POLYMER COMPOSITES

From Nano- to Macro-Scale

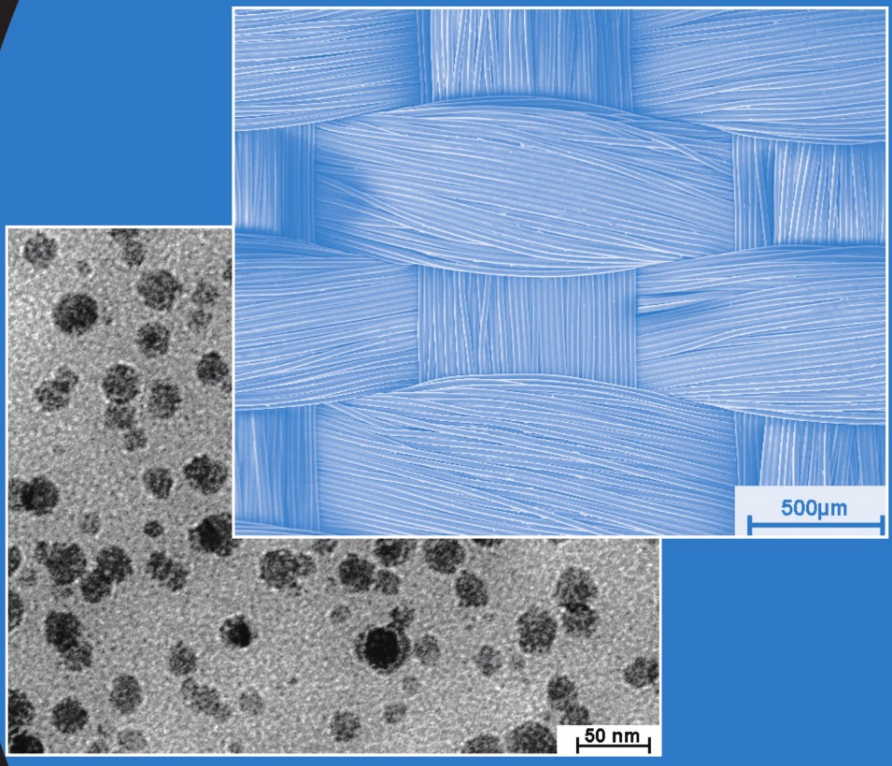

Klaus Friedrich, Stoyko Fakirov
and Zhong Zhang

Springer

POLYMER COMPOSITES
From Nano- to Macro-Scale

POLYMER COMPOSITES
From Nano- to Macro-Scale

Klaus Friedrich
Stoyko Fakirov
Zhong Zhang

Springer

Library of Congress Cataloging-in-Publication Data

Friedrich, Klaus, 1945-
Polymer composites: from nano-to-macro-scale/Klaus Friedrich, Stoyko Fakirov, Zhong Zhang.
p. cm.
Includes bibliographical references and index.
ISBN 10: 0-387-24176-0 ISBN 10: 0-387-26312-X (e-book)
ISBN 13: 9780387241760 ISBN 13: 9780387262130
1. Polymeric composites. I. Fakirov, Stoyko II. Zhang, Zhong, 1968- III. Title

TA418.9.C6F762005
620.1'92—dc22

2005050146

Printed on acid-free paper.

Printed in the United States of America.

9 8 7 6 5 4 3 2 1 SPIN 11053842

springeronline.com

Contents

Preface

The use of polymer composites in various engineering applications has become state of the art. This multi-author volume provides a useful summary of updated knowledge on polymer composites in general, practically integrating experimental studies, theoretical analyses and computational modeling at different scales, *i.e.*, from nano- to macroscale. Detailed consideration is given to four major areas: structure and properties of polymer nanocomposites, characterization and modeling, processing and application of macrocomposites, and mechanical performance of macrocomposites.

The idea to organize this volume arose from a very impressive workshop – The First International Workshop on Polymers and Composites at IVW Kaiserslautern: Invited Humboldt-Fellows and Distinguished Scientists, which was held on May 22-24, 2003 at the University of Kaiserslautern, Germany. The contributing authors were invited to incorporate updated knowledge and developments into their individual chapters within a year after the workshop, which finally led to these excellent contributions. The success of this workshop was mainly sponsored by the German Alexander von Humboldt Foundation through a Sofja Kovalevskaja Award Program, financed by the Federal Ministry for Education and Research within the "Investment in the Future Program" of the German Government. In 2001, the Humboldt Foundation launched this new award program in order to offer outstanding young researchers throughout the world an opportunity to establish their own work-groups and to develop innovative research concepts virtually in Germany. One of the editors, Z. Zhang, was among the 29 award winners in total, who was supported to establish an independent research team between 2001 and 2005 at the Institute for Composite Materials (IVW), University of Kaiserslautern, hosted by K. Friedrich.

The importance of promoting better knowledge in the field of polymer composites is demonstrated by the contents of this volume, which contains 18 independent chapters. The first part of this volume deals with the topic of structure and properties of polymer nanocomposites. In Chapter 1, Schulte *et al.* review the state of the art of carbon nanotube-reinforced polymers. The opportunity to apply carbon nanotubes as a filler for polymers and the improvement of the mechanical and functional properties are discussed. The application of non-layered nano-particles in polymer modification is described by M. Q. Zhang *et al.* in Chapter 2. A grafting polymerization technique is applied to inorganic nanoparticles, which helps to provide the composites with balanced performance. Chapter 3, authored

by Haupert and Wetzel, focuses on the reinforcement of thermosetting polymers by the incorporation of micro- and nanoparticles. Homogeneously distributed inorganic nanoparticles possess the potential to improve the mechanical performance of epoxy at very low filler contents. Privalko *et al.* present some interesting results concerning the synthesis and structure-property relationships of polyimide reinforced with a sol-gel derived organosilicon nanophase in Chapter 4, which suggest a good potential of low dielectric permittivity materials of this nanocomposite. Chapter 5 by Varghese and Karger-Kocsis focuses on the layered silicate/rubber nanocomposites *via* latex and solution intercalations. The structure-property relationships are discussed based on the dispersion state of the clay and the aspect ratio of the silicate layers. In Chapter 6, Sreekala and Eger report the property improvements of an epoxy resin by nano-silica particle reinforcement. The incorporation of SiO_2 nanoparticles into a reactive epoxy resin *via* a sol-gel process generated a new class of nanocomposites with perfect nanoparticle dispersion.

Part II focuses on some special characterization methods and modeling in the field of polymer composites. Chapter 7 by Goda *et al.* deals with micro-scratch testing and finite element contact and debonding analysis of polymer composites. A finite element macro/micro contact model has been introduced with the displacement coupling technique in order to study wear and failure mechanisms in real fiber-reinforced composites. Chapter 8, authored by Lauke *et al.*, concentrates mainly on the determination of the interface strength of polymer-polymer joints by a curved interface tensile test. A new experimental method for the determination of the adhesion strength between two different materials is proposed and the stress concentration at the interface as a function of applied load is derived by the finite element method. In Chapter 9, Evstatiev *et al.* present the manufacturing and characterization of microfibrillar reinforced composites from different thermoplastic polymer blends. Various examples of the manufacturing and processing of this new type of polymer-polymer composites are given and their structure-property relationships are investigated. Z. Zhang and Friedrich review the state of the art of the tribological properties of micro- and nanoparticle reinforced polymer composites in Chapter 10. Nanoparticles have a significant influence on the wear performance of polymers and composites.

"Macrocomposites: Processing and Application" is the topic of the third part of this volume. In Chapter 11, Nunes *et al.* consider the production of thermoplastic towpregs and towpreg-based composites. A purposely built powder-coating equipment was used to make thermoplastic matrix towpregs and pre-consolidated tapes (prepregs) from continuous fibers and a polymer powder. The mechanical properties of the composites were determined in order to assess the efficiency of this new process. Chapter 12 by Mitschang and Ogale deals with the manufacturing of tailored reinforcements for liquid composite molding (LCM) processes. Stitching and sewing processes exhibit high potential to generate various

advanced fiber-reinforced polymer composites based on LCM. Ye *et al.* describe the deconsolidation and reconsolidation of thermoplastic composites during processing in Chapter 13. A mechanistic model for void growth during thermal deconsolidation, and a transient heat analysis are introduced. An indicative void-closure model and a squeezed creep flow model are further discussed regarding to these important issues during thermoplastic composite processing. In Chapter 14, long fiber-reinforced thermoplastic composites and their automotive applications are discussed by Harmia *et al.* Advantages in processing and excellent performance suggest the use of these composites in the automobile industry.

In the last part of this volume, the mechanical performance of macro-composites is considered. Chapter 15 deals with deformation mechanisms of knitted fabric composites. Duhovic and Bhattacharyya provide a general understanding of the sheet forming behavior of knitted fabric thermoplastic composites gained from tensile, dome-forming, cup-drawing and V-bending experiments. Numerical simulations are carried out as well. Chapter 16, entitled "Impact Damage in Composite Laminates", is authored by Suemasu. A theoretical study, Rayleigh-Ritz approximation and finite element analysis are performed to obtain solutions on various levels of simplification for the damage problem and to clarify the mechanism of the initiation and growth of the low-velocity impact damage. Discontinuous basalt fiber-reinforced hybrid composites are discussed by Czigány in Chapter 17. Basalt fibers produced by melt blowing with proper surface treatments are recommended as a suitable reinforcement for both thermoplastic and thermoset polymers. An accelerated testing methodology for durability of polymer composites is the topic of Chapter 18, authored by Nakada *et al.* A prediction method of the fatigue strength of polymer composites and structures is introduced, which is applied to various fiber-reinforced plastics (FRP) and FRP/metal joints.

Various groups of readers may find particular interests in this volume: those who are active or intend to become active in the research on some aspects of polymer composites (material scientists, physical chemists, and mechanical engineers); those who have encountered practical problems in using polymer composites and wish to learn more updated approaches to their solution (designers, engineers and technologists in industries dealing with polymer composites' selection, processing and application); and teachers and students at universities.

Finally, the editors would like to thank all the contributing authors for their excellent chapters. Special gratitude is due to Dr. Greg Franklin, Springer, who contributed strongly to the publication of this volume. We would like also to thank the team in Sofia, Bulgaria, who helped the editorial work.

Klaus Friedrich
Stoyko Fakirov
Zhong Zhang

Editors Biographies

Klaus Friedrich – born in 1945, graduated in Fabrication Technology and in Mechanical Engineering before receiving his Dr.-Ing. (PhD) degree in Materials Science in 1978 from the Ruhr-University Bochum (RUB) in Germany. In addition to his industrial experience as a design engineer and his function as "Chief-Engineer" at the Institute for Materials, RUB, he was associated in 1980 as a Visiting Assistant Professor with the Center for Composite Materials, University of Delaware, USA. After that, he worked for eight years as a Professor of Polymers and Composites at the Technical University Hamburg-Harburg. Since August 1990, K. Friedrich became Research Director for Materials Science at the Institut für Verbundwerkstoffe GmbH (Institute for Composite Materials), University of Kaiserslautern. His major research interests include the fatigue and fracture properties as well as the friction and wear behavior of fiber-reinforced polymeric materials. Recent works are concentrating on fundamental aspects in the manufacturing of high performance composites with thermoplastic matrices. Prof. Friedrich was included in the Advisory Committees of many international conferences, and is a Scientific Board Member of various international journals in the fields of materials science, composites and tribology. In addition, he acted as consultant to various industrial companies within Europe and the USA. Together with his co-workers and students, he has published more than 600 papers in refereed journals and conference proceedings. Further, he is the Editor of three books on *Friction and Wear of Polymer Composites*, *Application of Fracture Mechanics to Composite Materials*, and *Advances in Composites Tribology*, respectively. In 1995, he was appointed as an Honorary Visiting Professor of the Zhongshan University, Guangzhou, China, for his achievements in the field of polymer tribology. At the end of 1996, his research group was awarded the innovation prize of the State of Rhineland-Palatine for applied research in the field of manufacturing of thermoplastic composite components. Besides, Prof. Friedrich has a long established track record in successful grant application from the German Science Foundation (DFG) and other research supporting establishments in Germany and Europe. In March 2001, he received an Honorary Dr. degree (Dr.h.c.) from the Budapest University of Technology and Economics, Hungary, and in June 2004, he was awarded the title of an Honorary Guest Professor of the University of Science and Technology of China, Hefei, which is among the best universities in China.

Stoyko Fakirov – got his MS degree in Chemistry from the Sofia University, Bulgaria, in 1959 and his PhD degree on Structure of Amorphous Polymers (1965) under the guidance of Prof. V. A. Kargin from the Lomonossov State University in Moscow. He received his DSc degree in 1982. In 1972, he became Associate Professor and in 1987, Full Professor of Polymer Chemistry. He is a co-organizer of the polymer education at the Sofia University (with obligatory courses on polymers for all chemistry students), as well as a founder and Head of the Laboratory on Structure and Properties of Polymers at the same university. He acted also as a Vice-Rector of this university for 3 years. Worth mentioning awards are Humboldt Fellow (1971, 88) and Humboldt Research Award Recipient (2000), Fellow of the Ministries of Education of Egypt, India, Spain, Turkey and Portugal, of the Japan Society for Promotion of Science, of the US Information Agency, of NATO-Spain, Member of the Advisory Board of the Institute for Polymer Research Dresden, Member of the Editorial Boards of three international journals on polymers. He has published about 300 papers in international polymer journals, has 11 US patents and contributed to about 150 international polymer meetings as well as delivered more than 100 invited seminar talks worldwide on his areas of interest: structure-properties relationships in polymers and composites, reactions in solid and molten condensation polymers, chemical healing, microfibrillar- and microplate-reinforced composites, microhardness of polymers, gelatin- and starch-based biomaterials. In addition, he acted as author, co-author, editor, co-editor and always as a contributor to 11 books on polymers, as for example, *Transreactions in Condensation Polymers* (1999), *Handbook of Thermoplastic Polyesters* (2002), *Handbook of Condensation Thermoplastic Elastomers* (2004) (all three of Wiley-VCH, Weinheim), *Microhardness of Polymers* (2000), Cambridge University Press, London, *Structure Development during Polymer Processing* (2000) Kluwer, Dordrecht. He was a Visiting Professor at the Universities of Mainz (Germany), Delaware, Newark (USA), Bosphorus, Istanbul (Turkey), Minho (Portugal), Kaiserslautern (Germany), CSIC, Madrid (Spain), NJIT, Newark, NJ (USA), and currently – Auckland (New Zealand). Here, he is focusing on new application opportunities of the concept of microfibrillar-reinforced composites (as developed in joint projects with the University of Delaware and the Institute for Composite Materials of the University of Kaiserslautern). These applications include commodity materials (with improved barrier properties), biomedical materials (scaffolds for tissue engineering and carriers for controlled drug delivery), materials for microelectronics (conductive elements), manufacturing of nanofibrillar reinforced composites, as well as the development of composites based on geopolymers.

Zhong Zhang – born in 1968, is a Guest Professor and a group leader at the Institute for Composite Materials (IVW) of the University of Kaiserslautern, Germany. He obtained his BS, MS, and PhD degrees from the University of Science of Technology of China, Hefei, China in 1990, 1996, and 1999, respectively. His

main research area involves the processing-structure-property relationships of polymers and composites. His research activities were mainly sponsored by the National Natural Science Foundation of China when he worked at the Cryogenic Laboratory (Beijing), Chinese Academy of Sciences between 1990 and 1996. In 1997 and 1998, he joined some world leading institutions, *e.g.*, Karlsruhe Research Centre, Germany, and Rutherford Appleton Laboratory, England, concentrating on low-temperature properties of polymers and composites. Parts of these results on failure processes in resins were of importance to support the design of large (11 m diameter) superconducting magnets for the Atlas experiment at CERN. He started to work at the IVW as an Alexander von Humboldt research fellow in September 2000. In 2001, he obtained a distinguished award from the same foundation, the Sofja Kovalevskaja Award financed by the Federal Ministry for Education and Research within its "Investment in the Future Program", and especially created for young and highly talented scientists. Zhong Zhang was selected in a worldwide competition as the only one from China, and one of only two in the field of Engineering Science, among 29 Sofja Kovalevskaja Award winners in total. The foundation has granted him one million Euros to establish an independent research team at the IVW from 2001 to 2005. The objective of his research is to investigate the long-term behavior (*e.g.*, tribological, creep and fatigue properties) of short fiber/nanoparticle-reinforced polymer composites, finally leading to an accelerative use of these materials in various industrial applications. Artificial neural networks are also used in his project to predict the performance of these materials as a function of their compositions and testing conditions. Dr. Zhang gave more than 20 invited lectures at world leading institutions, and some keynote and plenary lectures at international meetings. So far, he published more than 80 scientific papers in refereed journals and international conference proceedings.

Part I

Nanocomposites: Structure and Properties

Chapter 1

Carbon Nanotube-Reinforced Polymers: a State of the Art Review

Karl Schulte, Florian H. Gojny, Bodo Fiedler
Polymer Composites Section, Technical University Hamburg-Harburg, Hamburg, Germany

Jan K.W. Sandler
Department of Materials Science and Metallurgy, University of Cambridge, Cambridge, U.K.

Wolfgang Bauhofer
Materials in Electrical Engineering and Optics, Technical University Hamburg-Harburg, Hamburg, Germany

1 Introduction

The investigation of fullerenes and especially of carbon nanotubes (CNT) has opened a totally new window for the development of polymer matrix composites with novel properties and applications. CNT, which have a number of unexpected properties, both mechanical and electrical, seem to have huge potentials as a filler, *i.e.*, as a reinforcement in nanocomposites. With the addition of only 0.05 vol.% of CNT, the authors could achieve an electrical conductivity of less than 10^{-2} S/m in an epoxy matrix.[1,2] With the discovery of carbon nanotubes, the research efforts initially concentrated on the better understanding of their processing conditions, modification, and properties. Initially, the application of CNT as a filler material in matrix polymers in order to improve their properties has not been in the focus of research. However, the CNT potential of quite high mechanical properties gave rise to the assumption that the fracture mechanical properties and, especially, the fracture toughness of polymers can be improved. The extremely low diameter of CNT and their high aspect ratio make them an ideal material to improve the properties of the polymer matrix, compared to glass, carbon, or aramid fibers.

This should lead to a reduced sensitivity to delaminations, as the CNTs, having a diameter which is a couple of hundred times smaller than that of carbon fibers, can reinforce the tiny area in between the fibers of a laminated composite. They should also improve the elastic modulus of the matrix material itself. This last statement is mainly based on theoretical calculations and simulations, which predict a high fracture strength and elastic modulus for carbon nanotubes.[3-6]

In this chapter, we report technologies to produce CNT-nanocomposites, their resulting microstructures, and their mechanical properties. Tests were performed on various epoxy-based matrices, which were reinforced with catalytically and arc-grown multiple-wall carbon nanotubes (MWCNT). The arc-grown CNT were produced in a furnace, developed at the Technical University Hamburg-Harburg (TUHH), while the catalytically grown CNT were received from various sources. Carbon nonotubes were used as-received, but also after the application of chromatographic filter methods and oxidative chemical treatment. The latter enables a cleaning from the soot and can be used as a first step in the functionalization of the CNT surfaces. The oxidative treatment leads to the formation of carboxylic groups, which support *via* steric hindrance the dispersion of the tubes and stabilize them in solution or in the matrix material. This is an important step for the homogenous distribution of the CNT in polymers.

For the homogenous dispersion of the CNT in the matrix, a number of techniques were used. The quality of the nanotube distribution in the matrix was inspected by high resolution transmission electron microscopy (TEM).

2 General Problems in Nanocomposite Technology

The term *nanocomposites* means to distribute as much as possible amounts of nanoparticles in a polymer matrix. It has been shown that, when using fiber-reinforced polymers, the maximum amount of fibers in the matrix is about 70 vol.%. Actually, the fiber volume fraction in these materials varies between 20 and 60%. Figure 1 summarizes the values to be achieved for various fillers used in composites. In a volume element of 1 cm^3, it was assumed that we have continuous fibers with a diameter of 10 μm, particles (*e.g.,* talcum) with a diameter of 1 μm, and nanotubes with a diameter of 10 nm. The aspect ratios should be 20, 100, and 1000, respectively. If we further assume a volume content of 30% for both the fibers and the particles, and only 3% for the nanotubes, we already have quite interesting results:

The filler element numbers are ~10^6 fibers, ~10^{10} particles, and ~10^{15} nanotubes, respectively. The surface area amounts to ~0.1 m^2 for the fibers, ~1 m^2 for the particles, and ~100 m^2 for the nanotubes. There is another important aspect to be found, and that is the distance between the filler elements. For the fibers we calculated a distance of ~10 μm, for the particles ~1 μm, and for the nanotubes ~100 nm.

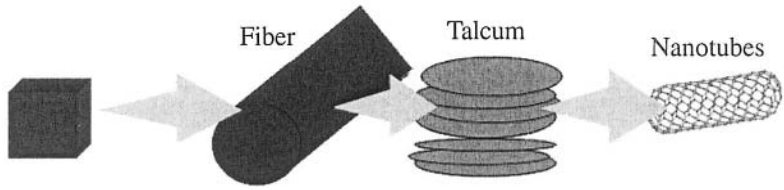

Particle size	10 μm	1 μm	10 nm
Volume content	30%	30%	3%
Number of particles	~ 10^6	~ 10^{10}	~ 10^{15}
Interface	~ 0.1 m^2	~ 1 m^2	~ 100 m^2
Aspect ratio	~ 20	~ 100	~ 1000

Figure 1. Influence of particles on the surface area.

These values already show the problems to overcome. *Nanotechnology* means that one has to deal with huge surface areas, a vast amount of nanofillers, and a small distance between them.

Figure 2 shows a calculation of the distance between nanotubes depending on their volume fraction. For this example, we assumed to have single-wall carbon nanotubes (SWCNT) with a diameter of *ca.* 1 nm. At a volume fraction of 3%, the distance between two tubes is just two times the diameter (*ca.* 3.2 nm). If we now assume to have isotactic polystyrene (iPS) as matrix polymer with a chain diameter

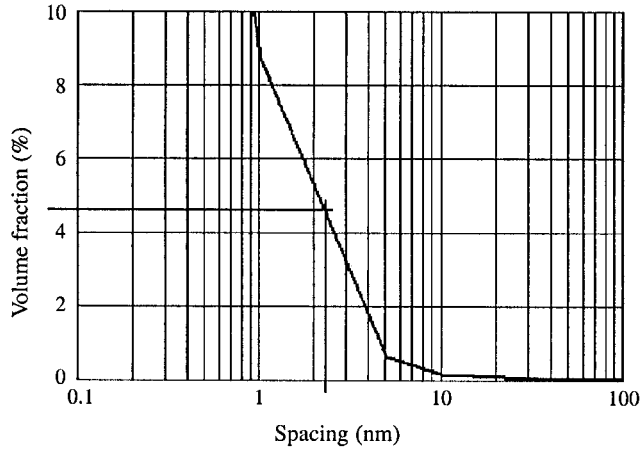

Figure 2. Correlation of the spacing between individual single-wall nanotubes (d = 1 μm) and their volume fraction.

of 0.8 nm, there is only a small gap for the polymer to penetrate between the tubes.

The main conclusion from this result is that it is extremely problematic to achieve high volume contents of nanotubes in a polymer matrix. All those who

report contents in the range of 10% or more might have agglomerates rather than a proper distribution.

3 Experimental

3.1 Manufacturing of Multiple-Wall Carbon Nanotubes

A number of methods have been developed to produce single- and multiple-wall carbon nanotubes. The most prominent are laser ablation, arc discharge, and catalytic growth (vapor deposition (CVD) and high pressure carbon monoxide (HipCO) process).

In the present chapter, the MWCNT were produced at the TUHH by the arc discharge method in a Krätschmer generator.[7] This method has previously been developed for the production of fullerenes, but today it is a common method to produce MWCNT without having a catalyst. It is based on the ignition of an electric arc between two graphite electrodes. A direct current of 20 to 30 V between the electrodes, in a helium atmosphere at a pressure of about 500 mbar, produces a plasma in which carbon is vaporized from the anode and reorganized at the cathode, forming a cylindrical deposit. During the process, the distance between the electrodes and the current density have to remain constant. Inside the deposit, which has a hard shell of turbostratic graphite, MWCNT are formed. Figure 3 is a scanning electron micrograph showing the nanotube-containing core of such a deposit, produced in a joint venture of TUHH and Trinity College, Dublin. In case that an

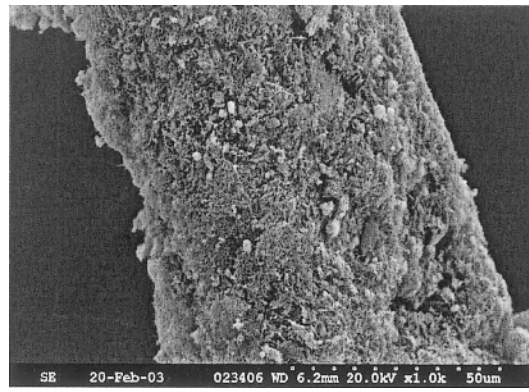

Figure 3. Scanning electron micrograph of the core of a deposit produced in a Krätschmer generator. The outer shell, consisting of tropostratic graphite, has been removed. The amorphous core material contains up to 50% multiple-wall CNT.

ultra-fine metal powder (Ni, Fe, Co, Cr) is added to the anode, single-wall carbon nanotubes can be found on the walls of the reactor.

The currently most successfully commercialized route is based on the CVD technique. Catalyst particles, such as Fe, Ni, or other metal catalysts, are introduced onto a substrate which is placed in a furnace. The growth of filaments (carbon nanotubes) is most sensitive to the reaction conditions, such as the pressure of the vaporized carbon source (benzene, toluene, *etc.*), the purity and flow rate of the carrier gas, the residence time for thermal decomposition, and the temperature of the furnace.[8]

In addition to the arc-grown CNT produced at the TUHH, catalytically grown CNT, received from various sources, were also used.

3.2 Treatment of Carbon Nanotubes

The dispersion of the nanotubes was performed either *via* direct stirring of the CNTs into the epoxy using an Ultraturrax T-25 disperser, or *via* a sonication method. The sonicator, a Bandelin Sonoplus HD2200, generates a pulsed ultrasound whereby the nanotubes were dispersed in the epoxy resin.[9]

A purification of the CNTs has been performed by oxidation using a mixture of sulfuric and nitric acid at 100 °C for 3 h. The separation of the oxidized nanotubes from the reaction solution was performed *via* centrifugation and membrane microfiltration.

The oxidized carbon nanotubes were then functionalized with different types of amines, such as triethylenetetramine, ethylenediamine and polyether-amines. The functionalization has been performed by refluxing a suspension of oxidized CNTs with the amine for 12 h to ensure a quantitative conversion. The separation of the nanotubes from the solution was again performed *via* centrifugation and membrane microfiltration.

3.3 Matrix Polymers

The epoxy resins Araldite LY556 with the hardener HY932 and Ruetapox LV 0164 with a polyetheramine hardener (Jeffamine® T-403) were used. The Jeffamine® T-403 can be used as hardener and/or as flexibilizer for epoxies and leads to thermosets with improved ductility.

3.4 Electron Microscopy

Transmission electron microscopy (TEM) was performed with an EM400 type microscope from Philips. Scanning electron microscopy (SEM) was performed with a Gemini GSMIC-848 apparatus.

3.5 Dynamic-Mechanical Thermal Analysis

The study of the thermo-mechanical behaviour was performed by dynamic-mechanical thermal analysis (DMTA), using a Gabo Eplexor 500 N equipment. Rectangular specimens, 50 mm long, 5 mm wide, and 2 mm thick, were prepared for the measurements. The tests were performed in tensile mode at a frequency of 10 Hz with a static strain of 0.6% and a dynamic strain of ±0.1%. The samples were measured between –120 °C and 150 °C at a heating rate of 3 °C/min.

4 Results

4.1 Comparison of the Multiple-Wall Carbon Nanotubes Studied

Arc-grown carbon CNT form relatively stiff rods consisting of concentric multiple-wall tubes (Figure 4). Due to this production process, graphitic nanoparticles can be observed next to the tubes. The amount of this so-called soot can exceed 30% of the total material. Therefore, a cleaning process is required before the use of CNT in the production of composites. The catalytically grown carbon nanotubes have not as much soot, but catalist particle remains are present as dark spots. Figure 5 is a transmission electron micrograph of catalytically grown CNT (produced at the University of Cambridge); CNT are extremely long, highly entangled, and with a cotton-like appearance. The tubes are highly crystalline, but compared to the arc-grown ones, they have a very high defect concentration, mainly within the outer

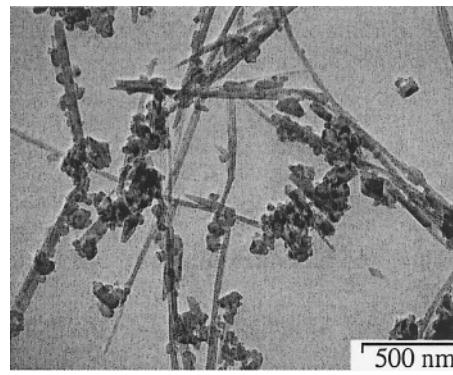

Figure 4. Transmission electron micrograph of arc-grown carbon nanotubes. A high amount of carbon nanotubes and the soot consisting of graphitic nanoparticles and carbon black are clearly seen.

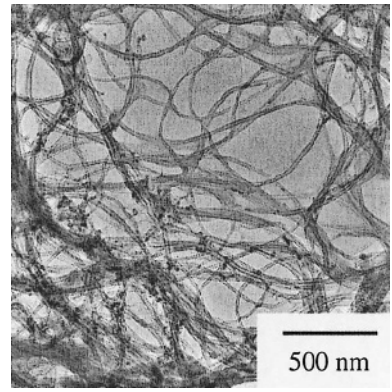

Figure 5. Transmission electron micrograph of catalytically grown multiple-wall carbon nanotubes with less impurities, but with a higher defect density and strongly entangled.

layers, which should affect the mechanical properties. Figure 6 is a scanning electron micrograph of CVD-grown MWCNT; they grow perpendicular to the catalyst but are extremely parallel and, in addition, pronounced entanglements forming the

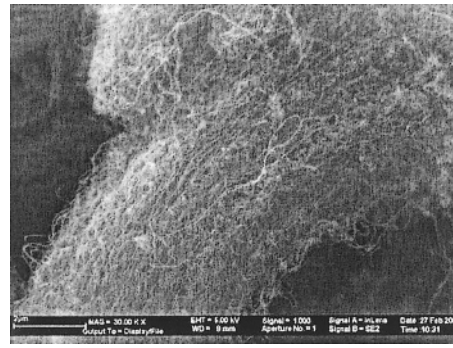

Figure 6. Scanning electron micrograph of catalytically grown multiple-wall carbon nanotubes. The cotton-like appearance is due to the manufacturing CVD process, where CNT grow onto a catalyst-covered substrate plate and, in addition to the strong entanglement, a generally parallel orientation of the tubes can be achieved.[18]

cotton-like structure are seen. Figure 7 is a transmission electron micrograph of CVD-grown MWCNT; the catalyst particles and the high defect density are clearly seen. These two findings suggest that arc-grown carbon nanotubes have a much lower defect density than the CVD tubes. As they are less entangled, they can be more easily dispersed than the catalytically grown tubes.

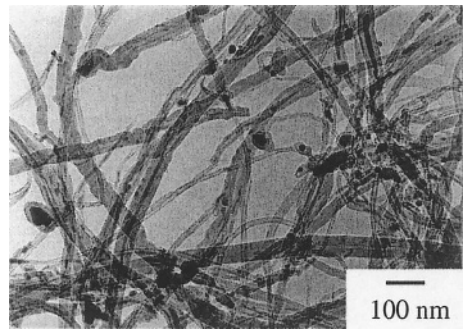

Figure 7. Transmission electron micrograph of catalytically grown multiple-wall carbon nanotubes with a high defect density. Catalyst particles are clearly seen.

4.2 Purification

As both the CVD- and arc-grown carbon nanotubes have impurities (amorphous carbon or catalyst residues), they should be cleaned. A number of purification methods have been described in the literature. In addition to chromatographic methods, the oxidative technique has been successfully used,[10-16] by taking into account the differences in the thermodynamic stability of carbon black, graphite, and the nanotubes. The wet chemical oxidation with a solution of sulfuric and nitric acids has been shown to be effective. In our studies, the nanotubes were refluxed in a solution of 3 parts of sulfuric and 1 part of nitric acid for 3 h at 130 °C. After centrifugation or membrane micro-filtration and washing with water, the nanotubes were refluxed for a couple of hours in a dilute sodium hydrogen carbonate solution to really eliminate the remaining acids. TEM clearly showed a reduction in impurities.

It could be also observed that, due to this purification process, the nanotubes start to be oxidized first at their caps and structural defects, and that functional groups (mainly carboxylic, which can be used for further modification) are formed on the surfaces (Figure 8). As this process injures the tubes, the caps of the

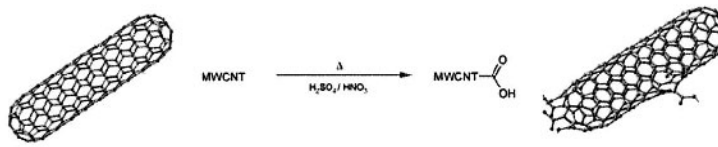

Figure 8. The oxidation process of the nanotubes leads to the formation of carboxylic and hydroxylic groups on the tube surfaces, preferentially on the caps or on structural defects. The cap opening cannot be avoided.

nanotubes can be opened or totally disappear (Figure 9), which is a disadvantage of the oxidative technique. The catalysts do not only help the formation and build up of CNT; in this special case, they also contribute to the degradation of nanotubes.

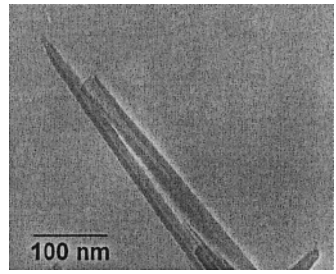

Figure 9. Transmission electron micrograph of oxidized carbon nanotubes. The opening of the caps due to the formation of functional groups is clearly seen.

4.3 CNT/Epoxy Composites: Dispersion, Matrix Bonding, and Functionalization

4.3.1 Dispersion

The use of nanoparticles as reinforcement elements in polymers is a common method to improve the mechanical and/or electrical properties of composites. The improvement of the fracture mechanics properties by the addition of particles can be achieved when a sufficiently good interaction between the nanoparticles and the matrix polymer takes place and when the particles are well dispersed within the matrix.

Our studies aimed at the improvement of the mechanical properties of epoxies by the addition of multiple-wall carbon nanotubes. The quality of the dispersion and the possible interaction between the CNT and the epoxy were investigated by light microscopy. For the homogeneous distribution of carbon black in an epoxy matrix, it was sufficient to use a high-speed disperser (Ultraturrax T-25), but for the dispersion of nanotubes this approach was not optimal (Figure 10a). The nanometer-scale size of the CNT and their aspect ratio make it necessary to develop new dispersion techniques in order to brake up the intermolecular bonds, leading to the formation of agglomerates.

In this respect, sonication has been found to be a promising alternative. A suspension of the CNT in an appropriate solvent (acetone) can be sonicated with a pulse ultrasound to break up the agglomerates. This suspension can later be mixed with the epoxy and the solvent is evaporated by simple heating. The nanotubes were sonicated for 20 min at a 30% amplitude, mixed with the epoxy resin and

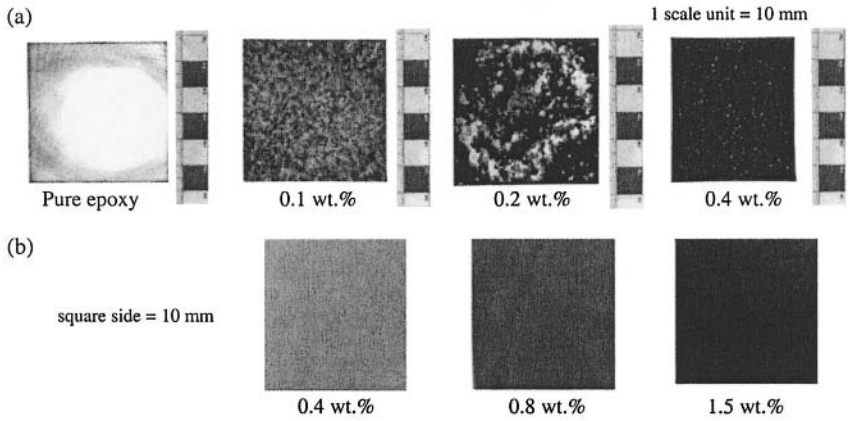

Figure 10: Light microscopy of a series of CNT/epoxy nanocomposites with different amounts of nanotubes: (a) CVD-grown CNT, 0, 0.1, 0.2, and 0.4 wt.%; (b) arc-grown carbon nanotubes, 0.4, 0.8, and 1.5 wt.%. The arc-grown carbon nanotubes tend to show less agglomerations than the CVD-grown CNT.

sonicated again for 10 min. During sonication, the samples have to be cooled to avoid curing of the composite. Finally, the composites were cured for 5 h at 80 °C and for 3 h at 130 °C in vacuum for the post curing. This approach allowed to substantially reduce the size of the agglomerates (Figure 10b).

A further reduction of the agglomerate size can be achieved by a combination of sonication and oxidative cleaning. The functional groups which develop on the surfaces on the CNT lead to steric hindrance and electrostatic interactions with the solvent, hence to a better distribution of the nanotubes in the epoxy matrix (Figure 11).

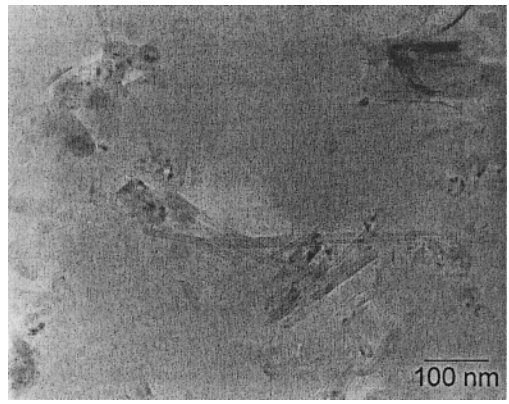

Figure 11. Transmission electron micrograph of a CNT/epoxy composite. Oxidation followed by sonication leads to an improved dispersion.[18]

4.3.2 Nanotube-Matrix Interaction

Another aim of this research was to achieve a good bonding between the nanotubes and the matrix. A load transfer between them can only be achieved with a sufficiently good bonding, which should result in an improvement of the fracture mechanical properties. TEM provides a possibility of obtaining useful qualitative information concerning the nanotube-epoxy matrix interaction.

Oxidized MWCNT were dispersed in an epoxy matrix by the above-mentioned techniques and visualized in Figure 12 as a series of TEM micrographs.[9] The TEM foil was loaded in the microscope by electron beam heating and it is seen that a nanotube embedded in the epoxy matrix bridges a void. Electron beam-induced void growth leads to an increasing load and to a rupture of the epoxy "bridge". Due to the low nanotube/matrix bonding no reinforcement of the bridging polymer occurs, but one can observe a pull-out of the nanotube from the matrix.

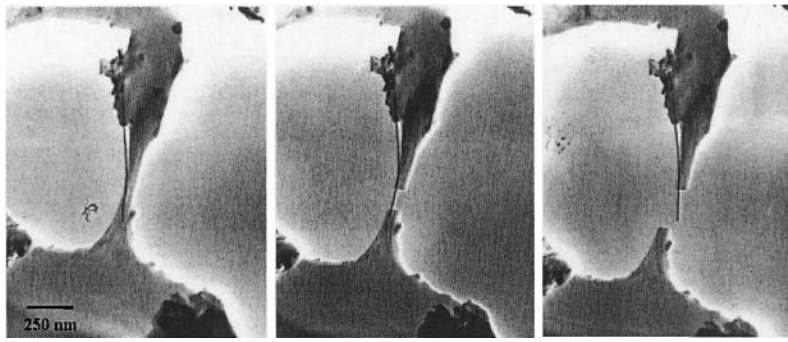

Figure 12. Transmission electron micrographs of oxidized CNT in an epoxy matrix. Void and crack growth results from thermal loading of the specimen with the electric beam. A tube bridging a crack is clearly seen; the weak nanotube-matrix bonding leads to pull-out.[9]

The conclusion can be drawn that the pull-out of oxidized CNT, regardless of the presence of carboxylic groups on their surfaces, points to an insufficient matrix bonding. Since the void formation and the loading of the test TEM foils took place by electron beam heating, only qualitative assessments can be made.

4.3.3 Functionalization

Only by a substantial improvement of the CNT-matrix bonding, an adequate reinforcement and, especially, an improvement of the composite fracture strength can be achieved. Therefore, the functionalization of the CNT surfaces is a key issue in order to realize a CNT reinforcement. The importance of functionalization

in the achievement of a strong CNT-matrix bonding was shown by Frankland *et al. via* a molecular simulation.[17] These authors have shown that an improvement in mechanical properties can already be achieved if less than 1% of the carbon atoms of the CNT form reactive bridges with the matrix.

A breakthrough in the development of CNT-reinforced epoxies could be made by chemical functionalization with multifunctional amines. In addition to the improvement of the bonding to the matrix, a better dispersion of the CNT could also be observed. A schematic representation of the functionalization process is shown in Figure 13.[9] After the oxidative treatment of the nanotubes, resulting in the development of carboxylic groups (Scheme (1)) they can react in a second

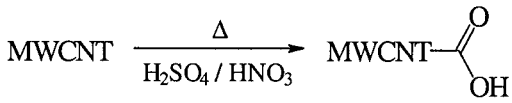

(1)

step with multifunctional amines and form ionic bonds (Scheme (2)).

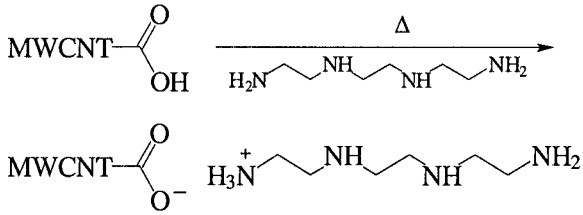

(2)

By the addition of the epoxy resin, the reactive free amino functions on the CNT surfaces form covalent bonds, improving the nanotube-matrix bonding (Scheme (3)).

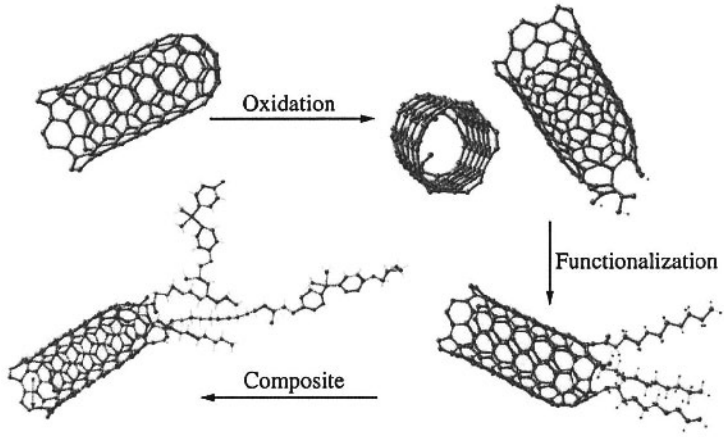

Figure 13. Schematic representation of the functionalization process, showing the entire cycle from the cleaning to the composite manufacturing.

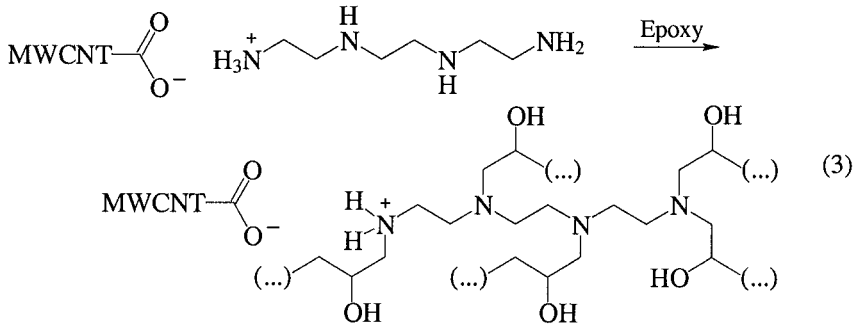

Amino functions were chosen because they are present in the hardener as well. The composites produced were observed in a TEM; for the first time matrix-rich areas could be seen alongside the surfaces of the nanotubes, together with crack bridging and telescopic pull-outs,[9] as described in detail in the next section.

4.4 Microscopy

4.4.1 Matrix Bonding to the Nanotubes

After the functionalization, CNT could be found which were entirely covered with the epoxy matrix, as shown in Figure 14a, where a nanotube sticks in the epoxy, a cone of the matrix is formed, and an epoxy layer spreads along the nanotube up to its tip, where the cap is also covered by epoxy. Due to the oxidation (leading to the formation of carboxylic groups) and the functionalization, the matrix can now directly react with the tube, forming covalent bonds.

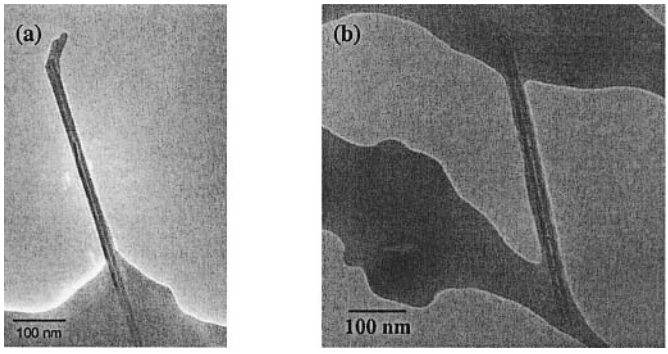

Figure 14. Transmission electron micrographs of functionalized carbon nanotubes in an epoxy matrix showing (a) the cone and the formation of a cap of matrix, and (b) the total coverage of the tube by the epoxy polymer.[9]

4.4.2 Crack Bridging and Telescopic Pull-Outs

A further indication of the improved CNT-epoxy bonding can be found in Figure 14b, where a nanotube bridges a pore. It is clearly seen that the tube is completely covered with matrix resin.[9] This result alone should suggest an improvement of the composite fracture toughness, because the nanotube is now able to bridge microcracks.

The improved bonding due to functionalization is visualized by the telescopic pull-out of nanotubes in Figure 15. Here again, a pore bridged by a matrix-covered nanotube and a multiple-wall carbon nanotube nicely bonded to the matrix are seen. Due to the void growth and the good CNT-matrix bonding, the outer layer of the tube remains bonded to the bridge, but the inner tubes are telescopically pulled out of the outer ones. This is possible because only weak van der Waals forces are present between the various concentric tubes and only the outer tube is covalently bonded to the matrix. In such a pull-out process, at least parts of the outer tube fail, indicating that a load transfer from the matrix to the outer tube occurs and that, due to the strong covalent bonding to the epoxy matrix, a consequent pull-out of the inner tubes takes place. This result can be further corroborated by the fact shown in Figure 16; a nanotube has been pulled out of the epoxy matrix. The outer shell of the tube remains in the epoxy matrix and continues into the void, whereas the inner tubes had been pulled out.

It can be assumed that for the adequate mechanical reinforcement of a matrix, MWCNT might not be the proper choice. The use of single- or double-wall carbon nanotubes might be more appropriate to achieve a good reinforcement.

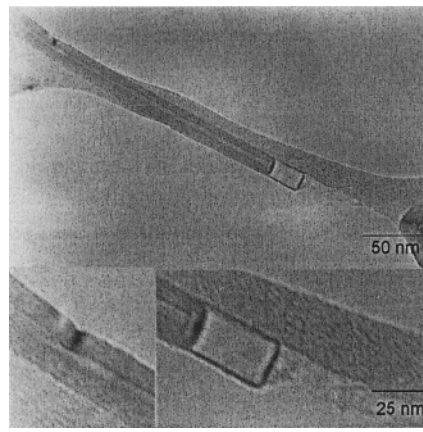

Figure 15. Transmission electron micrograph of functionalized carbon nanotubes. A nanotube bonded to a matrix crack bridge is pulled out of its outer shell (telescopic pull-out).[18]

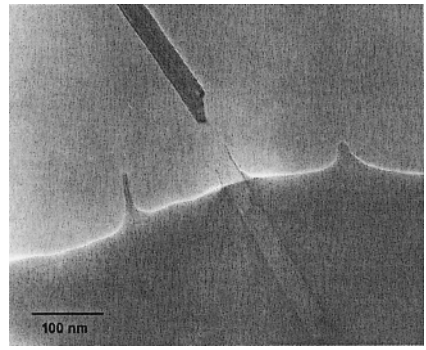

Figure 16. Transmission electron micrograph of a functionalized carbon nanotube in an epoxy matrix. The outer shell of this tube remains in the matrix and continues into the pore, while the inner tubes have been pulled out.[9]

4.5 Thermal and Mechanical Properties

Figure17a,b shows the results of the dynamic measurements of the complex modulus and the loss factor as a function of temperature. The thermo-mechanical properties were evaluated in order to verify the expected influence of the functionalization of CNT.[18] They did not show a general trend of the effect of the nanotubes on the complex modulus at temperatures below room temperature. This observation can be explained by the small amounts of nanotubes acting as a filler. Assuming a homogeneous dispersion, it can be expected that the nanotubes do not show an orientation and that only a small increase in the complex modulus should be observed.

A strong influence of the carbon nanotubes on the complex modulus of the composite is observed above room temperature. The increasing amounts of carbon nanotubes tend to result in a shift of the glass transition temperature towards higher values and an increase of the loss modulus E'' (Figure 18a,b).

This increase in thermal stability can be interpreted as a reduction of the mobility of the polymeric matrix through the nanotubes. This would explain the tendency in the shift of T_g. An even stronger effect was measured in composites containing functionalized nanotubes. Unlike the case of the composites containing non-functionalized CNT, these samples showed an almost linear dependence between the nanotube content and the shift of T_g (Figure 19). It can be assumed that covalent bonds between the amino-functions on the surface of the nanotubes and the epoxy matrix lead to an even stronger reduction of the matrix mobility, the latter expressing itself in a stronger shift of T_g. The different behavior of the two sample series is a further evidence of the influence of the chemical functionalization of the surface on the interfacial adhesion between the nanotubes and the epoxy resin. A detailed investigation should be carried out of the effect of

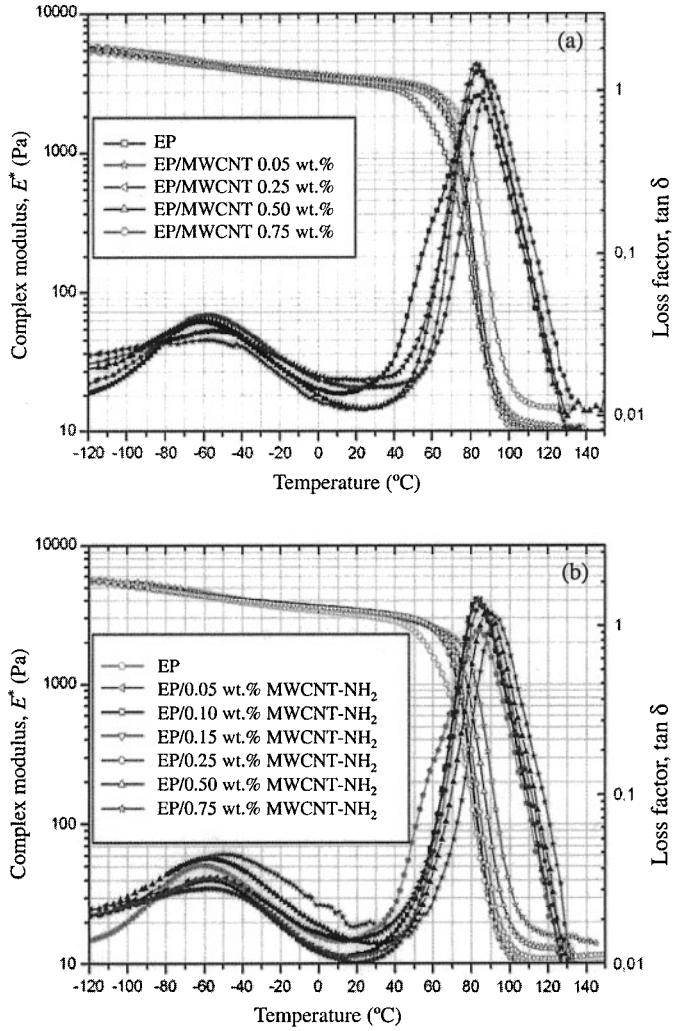

Figure 17. Complex modulus and loss factor of nanotube/epoxy nanocomposites with (a) non-functionalized nanotubes and (b) amino-functionalized nanotubes.[18]

the chemical functionalization of carbon nanotubes on the interfacial adhesion and the resulting mechanical reinforcement (Figure 20).

4.6 Electrical Properties

Carbon nanotubes dispersed as conductive fillers in an epoxy matrix result in electrical properties which can be compared to those obtained using an optimized

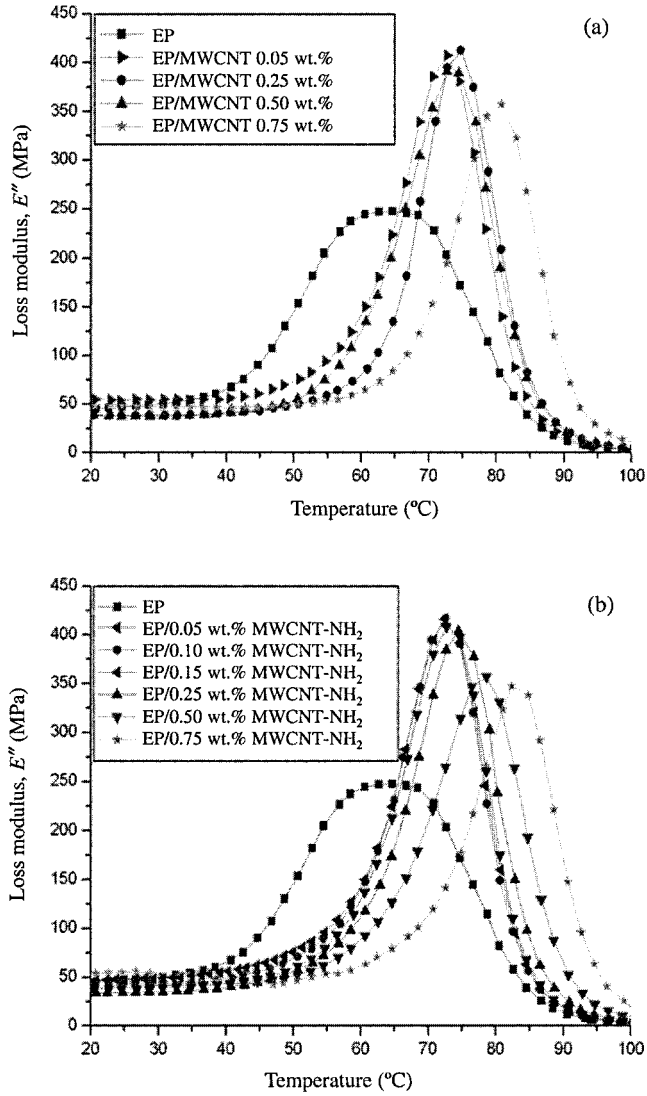

Figure 18. Loss modulus of nanotube/epoxy nanocomposites with (a) non-functionalized nanotubes and (b) amino-functionalized nanotubes.[18]

process with carbon black.[19] Sufficient matrix conductivity for anti-static applications can be achieved at lower filler concentrations using carbon nanotubes instead of carbon black. CNT reduce the percolation threshold to below 0.04 wt.% (Figure 21), and increase the overall conductivity achieved. At these low filler fractions, neither the processing behavior of the matrix nor the surface finish of

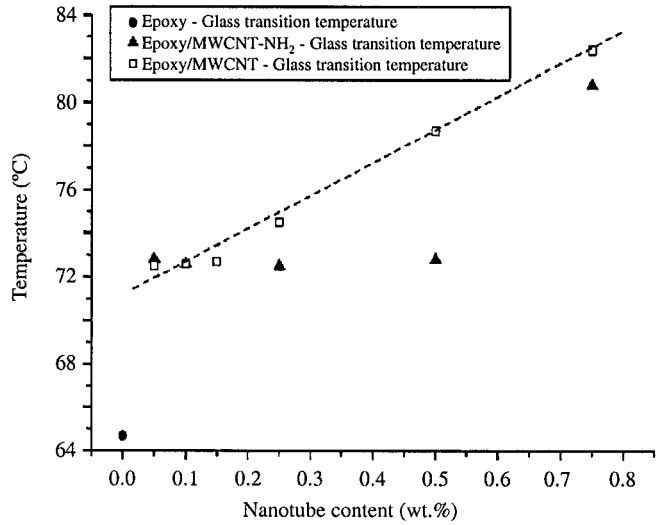

Figure 19. Glass transition temperature (from DMTA) as a function of nanotube content.[18]

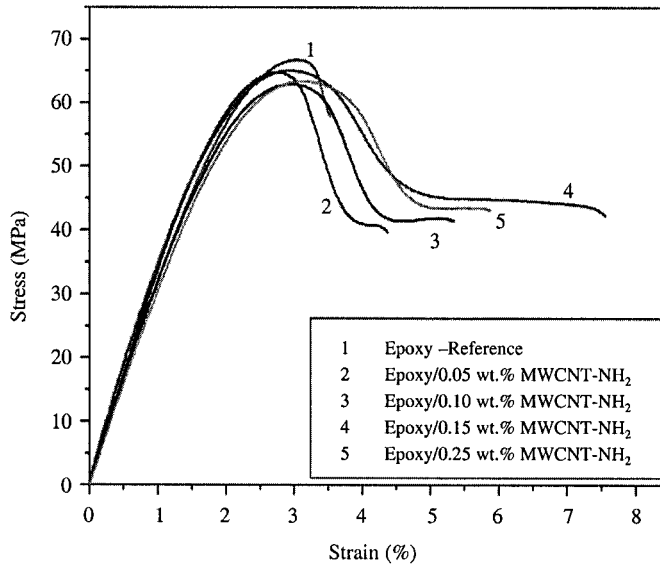

Figure 20. Stress-strain curves of functionalized carbon nanotubes in an epoxy matrix.

the samples are adversely affected.[1] Carbon nanotubes may offer new opportunities to modify both the electrical and the mechanical properties of an insulating matrix.

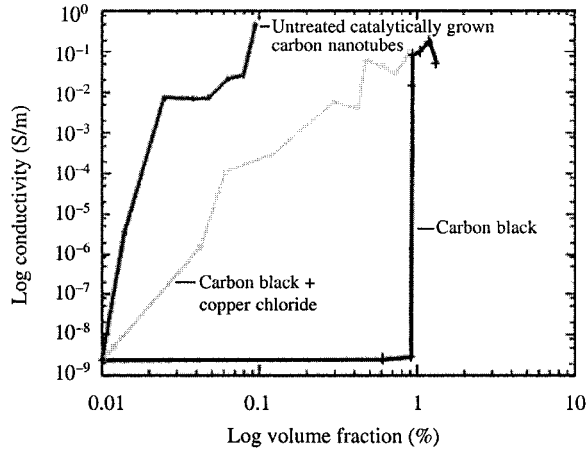

Figure 21. Comparative log-log plot of the conductivity of nanocomposites containing catalytically grown carbon nanotubes and carbon black as a function of the filler volume content.[1]

5 Conclusions

Compared to bulk materials, fiber-reinforced composites have already proven to exhibit superior properties in numerous applications. However, various desired combinations of properties, *e.g.*, strong reinforcing effects at high optical transparency combined with electrical conductivity or reinforced micro-injection molded parts, cannot be achieved by traditional composites. The further improvement of the fracture toughness of resin matrices is another important task. Nanocomposites possess the potential to fill this existing gap.

The excellent mechanical properties of carbon nanotubes and their high electrical and thermal conductivity make them ideal candidates for a wide range of applications where long carbon fiber-reinforced polymers cannot be employed. The present chapter shows the potential of the CNT as nanofillers in polymers, but also the need of further development for the achievement of optimal dispersion and orientation in order to attain the best possible properties.

CNT are capable of reinforcing polymers, making them electrically conductive and thermally more stable already at low volume fractions.

6 Acknowledgements

The support of the German Scientific Foundation (DFG) SFB 371-TP C9 and Schu 928/8 and of the European Commission (Scientific-Network "CNT-Net"; Contract N°: G5RT-CT-2001-050206) is gratefully acknowledged.

7 References

[1] J. Sandler, M. S. P. Shaffer, T. Prasse, W. Bauhofer, K. Schulte, A. H. Windle (1999) Development of a dispersion process for carbon nanotubes in an epoxy matrix and the resulting electrical properties, *Polymer* **40**, 5967.

[2] T. Prasse, A. Ivankov, J. Sandler, K. Schulte, W. Bauhofer (2001) Imaging of conductive filler networks in heterogeneous materials by scanning Kelvin microscopy, *J. Appl. Polym. Sci.* **82**, 3381.

[3] G. Overney, W. Zong, D. Tománek (1993) Structural rigidity and low frequency vibrational models of long carbon tubules, *Z. Physik D* **27**, 93.

[4] R. S. Ruoff, D. C. Lorents (1995) Mechanical and thermal properties of carbon nanotubes, *Carbon* **33**, 925.

[5] H. D. Wagner, O. Lourie (1998) Evaluation of Young's modulus of carbon nanotubes by micro-Raman spectroscopy, *J. Mater. Res.* **13**, 2418.

[6] H. D. Wagner, O. Lourie, Y. Feldmann, R.Tenne (1998) Stress-induced fragmentation of multiwall carbon nanotubes in a polymer matrix, *Appl. Phys. Lett.* **72**, 188.

[7] http://www.cnanotech.com/4-0_about.cfm

[8] http://www5.dsm.com.en_US/html/home/dsm_home.pl

[9] F. H. Gojny, J. Nastalczyk, K. Schulte, Z. Roslaniec (2003) Surface-modified nanotubes in CNT/epoxy-nanocomposites, *Chem. Phys. Lett.* **370**, 820.

[10] D. B. Mawhinney, V. Naumenko, A. Kuznetsova, J. T. Yates Jr. (2000) Infrared spectral evidence of the etching of carbon nanotubes: ozone oxidation at 298 K, *J. Am. Chem. Soc.* **122**, 2382.

[11] Y. Chen, R. C. Haddon, S. Fang, A. M. Rao, P. C. Eklund, W. H. Lee, E. C. Dickey, E. A. Grulke, J. C. Pendergrass, A. Chavan, B. E. Haley, R. S. Smalley (1998) Chemical attachment of organic functional groups to single walled carbon nanotube material, *J. Mater. Res.* **13**, 2423.

[12] J. L. Zimmerman, R. K. Bradley, C. B. Huffman, R. H. Hauge, J. L. Margrave (2000) Gas-phase purification of single-wall carbon nanotubes, *Chem. Mater.* **12**, 1361.

[13] K. Hernadi, A. Siska, L. Thiên-Nga, L. Forró, I. Kiricsi (2001) Reactivity of different kinds of carbon during oxidative purification of catalytically prepared carbon nanotubes, *Solid State Ionics* **141-142**, 203.

[14] I. W. Chiang, B. E. Brinson, R. E. Smalley, J. L. Margrave, R. H. Hauge (2001) Purification and characterization of single wall carbon nanotubes, *J. Phys. Chem. B* **105**, 1157.

[15] S. A. Curran, P. M. Ajayan, W. J. Blau, D. L. Carrol, J. N. Coleman, A. B. Dalton, A. P. Davey, A. Drury, B. McCarthy, S. Maier, A. Stevens (1998) Composite from poly(*m*-phenylenevinylene-co-2,5-dioctozy-*p*-phenylenevinylene) and carbon nanotubes: a novel material for molecular optoelectronics, *Adv. Mater.* **10**, 1091.

[16] B. McCarthy, J. N. Coleman, S. A. Curran, A. B. Dalton, A. P. Davey, Z. Konya, A. Fonseca, J. B. Nagy, W. J. Blau (2000) Observation of site selective binding in a polymer nanotube composite, *J. Mater. Sci. Lett.* **12**, 2239.

[17] S. J. V. Frankland, A. Calgar, D. V. Brenner, M. Griebel (2002) Molecular simulation of the influence of chemical cross-links on the shear-strength of carbon nanotube-polymer interfaces, *J. Phys. Chem. B* **106**, 3046.

[18] F. H. Gojny, K. Schulte (2004) Functionalisation effect on the thermo mechanical behaviour of multi-wall carbon nanotube/epoxy-composites, *Compos. Sci. Technol.*, in press.

[19] R. Schüler, J. Petermann, K. Schulte, H.-P. Wentzel (1997) Agglomeration and electrical percolation behaviour of carbon black dispersed in epoxy resin, *J. Appl. Polym. Sci.* **63**, 1741.

Chapter 2

Application of Non-Layered Nanoparticles in Polymer Modification

Ming Qiu Zhang, Min Zhi Rong
Key Laboratory for Polymeric Composite and Functional Materials of Ministry of Education, Zhongshan University, Guangzhou, P. R. China
Materials Science Institute, Zhongshan University, Guangzhou, P. R. China

Klaus Friedrich
Institut für Verbundwerkstoffe GmbH (Institute for Composite Materials), Kaiserslautern University of Technology, Kaiserslautern, Germany

1 Introduction

Polymeric nanocomposites can be considered as an important category of organic-inorganic hybrid materials, in which inorganic nanoscale building blocks (*e.g.*, nanoparticles, nanotubes, or nanometer-thick sheets) are dispersed in an organic polymer matrix.[1] They represent the current trend in developing novel nanostructured materials. When compared to conventional composites based on micrometer-sized fillers, the interface between the filler particles and the matrix in a polymer nanocomposite constitutes a much greater area within the bulk material, and hence influences the composite's properties to a much greater extent, even at a rather low filler loading.[2]

Currently, numerous procedures for the preparation of polymer nanocomposites have been proposed, using the following approaches: (i) direct incorporation of nanoscale building blocks into a polymer melt or solution,[3-6] (ii) *in situ* generation of nanoscale building blocks in a polymer matrix (*e.g.*, vacuum evaporation of metals, thermal decomposition of precursors, reduction of metal ions through an electrochemical procedure, *etc.*),[7-9] (iii) polymerization of monomers in the presence of nanoscale building blocks,[10,11] (iv) a combination of polymerization and formation of nanoscale building blocks (*e.g.*, sol-gel method, intercalation of

monomers into layered structures followed by polymerization, *etc.*).[12,13] The key issue of these techniques is that the geometry, spatial distribution, and volume content of the nano-fillers must be effectively controlled through adjusting the preparation conditions so as to ensure the structural requirements of nanocomposites stated above.

From the engineering point of view, large-scale and low-cost production routes, as well as a broad applicability of thermoplastic nanocomposites as structural materials should be considered. This can be achieved in the best way by the employment of commercially available, non-layered nanoparticles, and by the use of blending techniques already widely applied in the plastics industry. In fact, the authors have concentrated recently their major efforts on the latter approach.

It is noteworthy that the problem with dispersive mixing is that the nanoparticles commercially available usually exist in the form of agglomerates, which are difficult to disconnect by the limited shear force during mixing. This is true even when a coupling agent is used,[14] since it can only react with the nanoparticles on the surface of the agglomerates. The latter will maintain their friable structure in the composite and can hardly provide property improvements at all.

The positive effects of nanoparticles can be brought into play only if nanoparticle agglomerates themselves are reinforced prior to the compounding procedure, since a further promotion of the dispersion by existing methods might be too ideal to be realized. Nanoparticles can be pretreated by irradiation to introduce grafting polymers onto their surface not only outside but also inside the particle agglomerates. Owing to their low molecular weight, the monomers can penetrate into the agglomerated nanoparticles easily and react with the activated sites of the latters. The interstitial volume inside the nanoparticle agglomerates will be partly filled with grafting macromolecular chains, and the agglomerated nanoparticles will be separated further. In addition, the surface of the nanoparticles will also become "hydrocarbonated" due to an increased hydrophobicity resulting from the grafting polymer (Figure 1). This is beneficial for the filler/matrix miscibility and hence for the ultimate properties.[15] When the pre-grafted nanoparticles are mixed with the melt of a thermoplastic polymer, the filler/matrix interfacial adhesion can be improved by the grafting polymers chemically bonded onto the nanoparticles, in particular by creating entanglements with the matrix molecules.

In the case of a thermosetting matrix polymer, the grafted nanoparticles will keep their more stationary suspended state due to the interaction between the grafting polymer and the matrix. After curing such a mixture, the filler/matrix adhesion would also be substantially enhanced by chain entanglement and/or chemical bonding between the grafting polymer and the matrix material. In this context, the desired uniform dispersion of nanoparticles in the matrices on a nanometer level might no longer be critical.

The present chapter reviews our work dealing with the application of silica nanoparticles in the modification of polypropylene (PP) and epoxy resin according to the aforesaid concept. For the thermoplastic system, the improvement of the

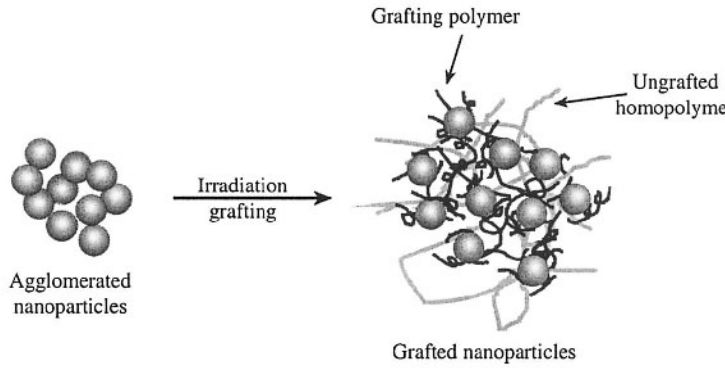

Figure 1. Schematic representation of the possible structures of nanoparticle agglomerates before and after grafting polymerization.

mechanical properties of the matrix is the main concern, while an increased tribological performance is desired for the thermosetting matrix composites.

2 Surface Treatment and Compounding

2.1 Raw Materials

General-purpose isotactic PP homopolymer (type F401, melting flow index (MI) = 8.5 g/10 min and 6.7 g/10 min, respectively) was provided by Guangzhou Petroleum Chemical Co., China. It should be noted that this is a rather brittle PP, compared to other PP types available on the world market. In addition, a bisphenol-A epoxy resin (type E-51) and 4,4′-diaminodiphenylsulfone (DDS) were provided by Guangzhou Dongfeng Chemical Co., China, as matrix materials.

The nanoparticles consist of pyrogenic colloidal SiO_2 (Aerosol 1380, Degussa Co., Germany) with an average particle size of 7 nm. Styrene, acrylamide, methyl methacrylate, butyl acrylate, ethyl acrylate, methyl acrylic acid, and vinyl acetate, were used as grafting monomers without further purification.

2.2 Pregrafting of the Nanoparticles by Irradiation

The typical pregrafting of SiO_2 proceeded as follows. Before being mixed with the monomers, the nanoparticles were preheated at 120 °C for 5 h in order to eliminate possible absorbed water on their surface. Then the mixture of monomer/particles and a certain amount of solvent (heptane or acetone, or ethanol, depending on the monomer/SiO_2 systems) was irradiated by ^{60}Co γ-rays under atmospheric

pressure at a dose rate of 1 Mrad/h at room temperature. After an exposure to a dose of 10 Mrad, the solvent was recovered and the dried residual powder could be compounded directly with the polymeric matrices chosen.

2.3 Characterization of the Irradiation Products

To differentiate between the amount of polymer grafted to the particles and the amount of material that was polymerized as a homopolymer during the irradiation process, certain parts of the irradiation products were extracted with solvents (benzene for polystyrene, acetone for poly(methyl methacrylate), poly(butyl acrylate), poly(ethyl acrylate) and poly(vinyl acetate), methanol for poly(methyl acrylate), and water for polyacrylamide, respectively). This procedure lasted over 37 h, using a Soxhlet's apparatus; the residual material was then dried under vacuum for 5 h at 80 °C. In this way, the homopolymer content was selectively separated from the irradiated powder. The weight increase in SiO_2 due to the presence of the non-extractable grafted material was then determined by thermogravimetric analysis (TGA, Shimadzu TA-50 thermogravimeter). In a second step, SiO_2 accompanied with the non-extractable grafting polymer was immersed in a 10-20% HF solution for 1-2 days to remove the SiO_2 particles, so that the grafting polymer could be recovered. A Nicolet 5DX Fourier transform infrared spectroscope (FTIR) was utilized to characterize changes in the particle surfaces and in the molecular structure of the grafted polymers.

2.4 Preparation of PP-Based Nanocomposites and Their Characterization

PP-based nanocomposites were prepared by tumble mixing the preweighed quantities of PP and the grafted fillers, followed by compounding this mixture on a lab-scale single-screw extruder. The manufacturing temperature was kept at 200 °C and the screw speed was 25 rpm. The specimens for mechanical tests were machined from compression molded plates ($65\times45\times3$ mm^3) of the extrudates. The filler volume fractions could be computed from the known weights of the polymer matrix, the fillers, and the polymer introduced by irradiation. The reinforcing efficiency of the nanoparticle agglomerates was assessed by measuring of the Young's modulus, tensile yield strength, and impact strength. Tensile tests were carried out on dumbbell shaped specimens by an LWK-5 universal testing machine at a crosshead speed of 10 mm/min. The fractured surfaces were observed by a HITACHI S-520 scanning electron microscope (SEM). An XJJ-5 tester was used for unnotched Charpy impact strength measurements.

2.5 Preparation of Epoxy-Based Nanocomposites and Their Characterization

Epoxy-based nanocomposites were prepared by mixing the preweighed quantities of epoxy and grafted fillers at 80 °C with stirring for 2 h and sonication for 1 h, respectively. Then the mixture was heated to 130 °C and the curing agent DDS was added under stirring for 10 min. For curing the composites, the following procedure was carried out step by step: 3 h at 100 °C, 2 h at 140 °C, 2 h at 180 °C, and 2 h at 200 °C.

The curing behavior of the epoxy and its composites was examined by differential scanning calorimetry (DSC, Perkin-Elmer DSC 7C) at a heating rate of 2 °C/min. Unlubricated sliding wear tests were carried out on a block-on-ring apparatus under a pressure of 3 MPa and a constant velocity of 0.4 m/s. The carbon steel ring (0.42-0.45 wt.% C, 0.17-0.37 wt.% Si, and 0.5-0.8 wt.% Mn; HRC 50) had a diameter of 40 mm and an initial surface roughness $R_a = 0.1$ μm. Prior to wear testing, all samples were pre-worn to an average surface condition, in order to reduce the running-in period. The actual steady-state test period was set to 3 h. The specific wear rates were calculated from weight measurements of the specimens before and after the actual steady-state test period. The morphologies of the worn surfaces were observed with a HITACHI S-520 SEM.

3 Thermoplastic Systems

3.1 Effect of Irradiation Grafting Polymerization on the Nanoparticles

In order to establish the effect of modified nano-silica on the mechanical behavior of PP composites, the variation in the chemical structure of the particles should be known at the very beginning of the discussion. FTIR spectra of untreated and treated nano-silica are shown in Figure 2. To eliminate the influence of homopolymers, both polystyrene-grafted nano-SiO_2 (SiO_2-g-PS) and poly(ethyl acrylate)-grafted nano-SiO_2 (SiO_2-g-PEA) used for the FTIR examinations were separated from the homopolymers in advance. Compared to the spectrum of SiO_2 as-received, the adsorptions at 690, 1460 and 2960 cm^{-1} appearing in the spectrum of SiO_2-g-PS represent the bending mode of C-H in benzene rings and the stretching modes of C-C and C-H, respectively. In addition, the band at 1725 cm^{-1} in the spectrum of SiO_2-g-PEA indicates the existence of carbonyl groups. These bands prove that PS and PEA have been chemically bonded to the nano-silica during the irradiation polymerization.

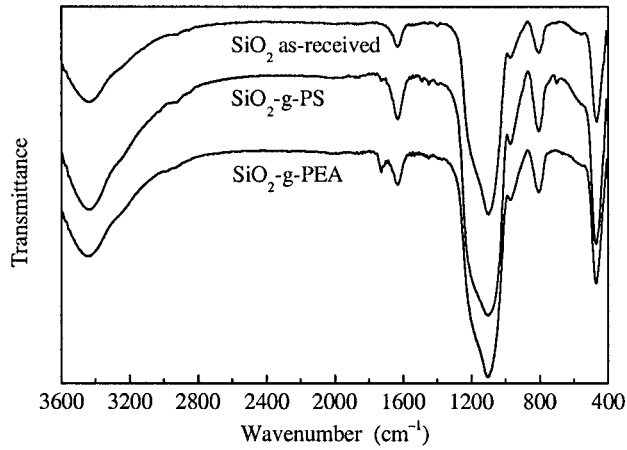

Figure 2. FTIR spectra of untreated and grafted SiO_2.

3.2 Tensile Properties

Typical tensile stress-strain curves of neat PP and its filled version are shown in Figure 3; as expected, both a reinforcing and a toughening effect of the nanoparticles on the polymeric matrix were fully brought into play. That is, a structural weakness, that would have been expected from the agglomerating behavior of the nanoparticles, could be fully eliminated by the grafting of macromolecular chains onto the individual particles.

By examining the composition-dependent tensile properties of the materials (Figure 4), it can be seen that the incorporation of untreated nano-SiO_2 decreases

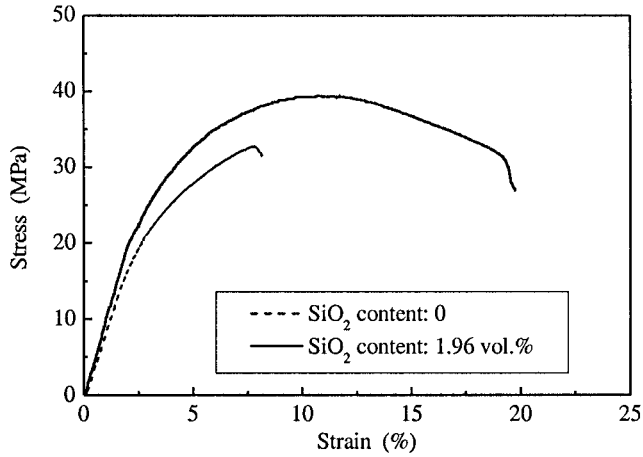

Figure 3. Typical tensile stress-strain curves of neat PP matrix (MI = 6.7 g/10 min) and the composites filled with SiO_2-g-PS.

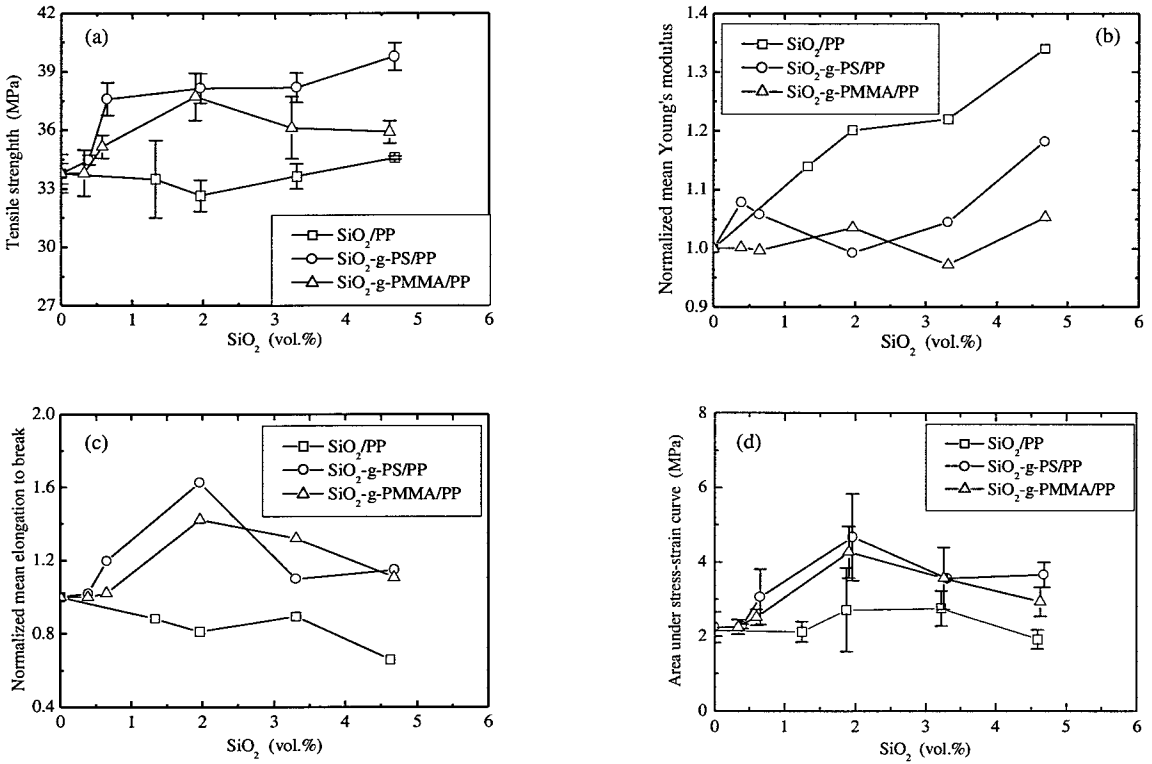

Figure 4. Tensile properties of PP (MI = 6.7 g/10 min) based nanocomposites *vs.* SiO_2 content: (a) tensile strength, (b) Young's modulus, (c) elongation to break, and (d) area under stress-strain curve.

the tensile strength of PP in the lower loading region, but then leads to a slight increase in strength when the particle fraction reaches 4.68 vol.% (Figure 4a). When the nanocomposites are filled with PS- or PMMA-grafted SiO_2, however, the situation is quite different. There is a considerable rise in the strength of SiO_2-g-PS/PP composites at a SiO_2 content as low as 0.65 vol.%, then the strength remains almost unchanged by a further addition of filler. A similar behavior can be observed in the case of SiO_2-g-PMMA/PP, except that a slight drop in strength occurs when the filler content exceeds 1.96 vol.%. Nevertheless, compared to the untreated case, it can be stated here that the mechanical loading seems to be more effectively transferred from the matrix to the filler particles owing to the interfacial bonding effect of the grafting polymers. This might result from interdiffusion and entanglement between the molecules of the grafting polymers and the matrix. The decrease in tensile strength of SiO_2-g-PMMA/PP above 1.96 vol.% can be interpreted by a change in the disperse state of the fillers. It is believed that a higher filler loading is detrimental to its uniform dispersion in the polymer matrix.

It is well known that the interface adhesion markedly influences the mechanical behavior of particulate filled polymer composites.[16-18] The present irradiation grafting pretreatment provides possibilities of interfacial design. As a result, the mechanical properties of the nanocomposites can be tailored accordingly. Table 1 lists the mechanical properties of nanocomposites filled with SiO_2 particles, grafted with various polymers, at a fixed SiO_2 fraction. Although the monomers of the grafting polymers should have different miscibilities with PP, all the grafting polymers except for PEA exhibit a positive effect on the tensile strength of the nanocomposites. These results contribute to the further understanding of the modified nanoparticles and their role in composites. That is, interdiffusion and entanglement of the grafting polymer segments with the polypropylene molecules (rather than a miscibility between the grafting polymer and the matrix) dominate the interfacial interaction in the nanocomposites. It can be concluded that a PP matrix with a higher molecular weight should entangle even more efficiently with the nanoparticles agglomerates, thus leading to a higher tensile strength increment (compare the results of Figure 3 with the data given in Table 1).

For the moment, it can be concluded that the reinforcing effect of nanoparticles on the polymeric matrices can be realized as long as the particles are grafted and a proper dispersion of the modified particles can be formed. In addition, the tensile properties of the nanocomposites can be purposely adjusted according to the interfacial viscoelastic properties provided by different grafting monomers.

As a parameter closely related to the static stress transfer at the interface, Young's modulus shows another aspect of the role played by the grafting polymers (Table 1). The increase in stiffness of the nanocomposites is obviously a result of the high modulus of the particulate fillers. However, taking into account that the tensile modulus was determined within a small strain range, the formation of a relatively compliant layer at the interface (*e.g.*, PBA, PVA, and PEA) tends to hinder the complete stress transfer under such a low stress level and thus masks

Table 1. Mechanical properties of PP (MI = 8.5 g/10 min) based nanocomposites[a] filled with polymer-grafted SiO_2[b].

	Nanocomposites						*Neat PP*
Grafting polymer	*PS*[c]	*PBA*[d]	*PVA*[e]	*PEA*[f]	*PMMA*[g]	*PMA*[h]	
Grafting[i] (%)	3.64	3.32	2.82	1.73	1.85	2.16	-
Homopolymer fraction[j] (%)	16.3	15.4	13.7	12.3	15.5	15.4	-
Tensile strength (MPa)	34.1	33.3	33.0	26. 8	35.2	33.9	32.0
Young's modulus (GPa)	0.92	0.86	0.81	0.88	0.89	0.85	0.75
Elongation to break (%)	9.3	12.6	10.0	4.6	12.0	11.9	11.7
Area under tensile stress-strain curve (MPa)	2.4	3.3	2.3	0.8	3.2	2.9	2.2
Unnotched Charpy impact strength (kJ/m^2)	19.8	19.4	22.9	14.6	20.5	4.7	8.0

[a]SiO_2 content 3.31 vol.%; [b]irradiation dose 10 Mrad in acetone solution, except for methyl acrylic acid/SiO_2 where the solvent was ethanol, monomer/SiO_2 = 2/10 (by wt.); [c]polystyrene; [d]poly(butyl acrylate); [e]poly(vinyl acetate); [f]poly(ethyl acrylate); [g]poly(methyl methacrylate); [h]poly(methyl acrylate); [i]grafting polymer/SiO_2 (by wt.); [j]homopolymer/SiO_2 (by wt.)

the stiffness of the filler particles. Figure 4b evidences this masking effect of the grafting polymers, showing that the modulus of the composites filled with untreated SiO_2 increases almost linearly with the addition of SiO_2, while PS- and PMMA-grafting greatly decrease the stiffening effect of SiO_2. Similar results were found in differently treated kaolin/high density polyethylene systems.[19]

The elongation to break of the nanocomposites exhibits a more complicated relation to the interfacial characteristics in the case of a lower molecular weight PP matrix (Table 1). Relative to the neat matrix, the values of the grafted SiO_2-nanocomposites remain on the same level, except for the PEA-treated system. For the matrix with the higher molecular weight (Figure 4c), however, the filler content dependence of the elongation to break seems to be clearly evident. The reduction in elongation to break of the composite by the addition of untreated SiO_2 implies that the fillers cause a reduction in matrix deformation due to an introduction of mechanical restraints. When the nanoparticles are grafted with PS and PMMA, on the other hand, an increase in elongation to break can be found because both interfacial viscoelastic deformation and matrix yielding can contribute to this value. The further tendency to a decrease in elongation to break above 1.96 vol.% suggests that matrix deformation is not only related to the interface features, but also to the disperse state of the fillers.

Compared with elongation to break, the area under the tensile stress-strain curve can characterize more reasonably the toughness potential under static tensile loading. In Table 1, it can be seen that the addition of modified nano-SiO_2 helps to improve the ductility of PP, except for the case of SiO_2-g-PEA. It is believed that

localized plastic deformation or drawing of the matrix polymer, being the main energy absorption process in particulate filled polymer systems, can be induced more efficiently by SiO_2-g-PS and SiO_2-g-PMMA than by untreated SiO_2 (Figure 4d).

The above discussion is focused mainly on the effects of modified SiO_2 due to the presence of grafting polymers. In fact, the internal structure of the grafted nanoparticles also plays an important role in determining the mechanical properties of nanocomposites. It can be assumed that the molecular weight, the branching degree and the content of both the grafting polymer and the homopolymer around the modified nanoparticles are closely related to the stress distribution of the dispersed phases. As shown in Table 2, both tensile strength and elongation to break of the nanocomposites decrease with a rise in irradiation dose from 2 to 20 Mrad, due to a possible crosslinked structure of PS as a result of over-irradiation. A uniform dispersion of the grafted nanoparticles in the polymer matrix would thus be obstructed during the compounding process. Table 3 demonstrates that the area under the tensile stress-strain curve of the nanocomposites decreases at higher styrene amounts; this is an indication of the importance of the arrangement of the SiO_2 particles inside the grafted agglomerates.

Table 2. Mechanical properties of PP (MI = 8.5 g/10 min) based nanocomposites[a] filled with SiO_2-g-PS[b] grafted at various irradiations.

Irradiation dose (Mrad)	*Tensile strength (MPa)*	*Young's modulus (GPa)*	*Elongation to break (%)*	*Area under tensile stress-strain curve (MPa)*	*Unnotched Charpy impact strength (kJ/m²)*
2	36.5	0.89	11.8	3.3	37.5
10	34.1	0.92	9.3	2.4	19.8
20	33.2	0.82	8.0	2.0	3.7
Neat PP	32.0	0.75	11.7	2.2	8.0

[a]SiO_2 content 3.31 vol.%; [b]styrene/SiO_2 = 2/10 (by wt.)

Table 3. Mechanical properties of PP (MI = 8.5 g/10 min) based nanocomposites[a] filled with SiO_2 grafted with various amounts of styrene[b].

Styrene/SiO_2 (by wt.)	*Tensile strength (MPa)*	*Young's modulus (GPa)*	*Elongation to break (%)*	*Area under tensile stress-strain curve (MPa)*	*Unnotched Charpy impact strength (kJ/m²)*
1/10	32.9	0.83	9.9	2.8	29.5
2/10	34.1	0.92	9.3	2.4	19.8
3/10	32.7	0.84	8.7	2.1	13.6
Neat PP	32.0	0.75	11.7	2.2	8.0

[a]SiO_2 content 3.31 vol.%; [b]irradiation dose 10 Mrad

3.3 Fractography

Neat PP has a relatively smooth surface and exhibits no signs of plastic deformation (Figure 5a). A coarser appearance can be found on the fracture surface of the composite containing untreated SiO_2, but it can still be characterized as semi-brittle, with only little plastic deformation of the matrix in some regions (Figure 5b). In contrast, the composites incorporating grafted SiO_2 particles show

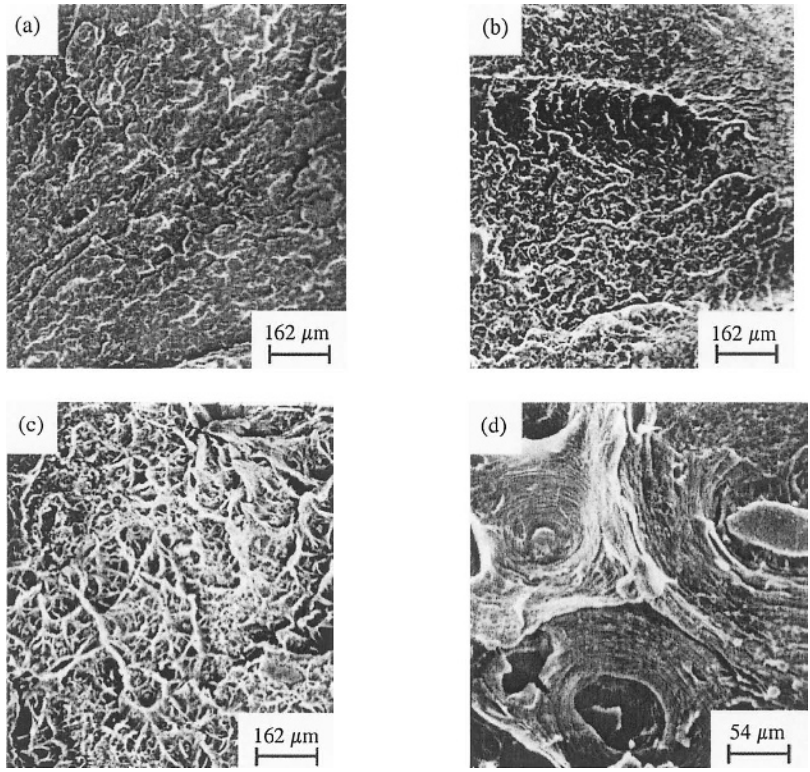

Figure 5. Scanning electron micrographs of the tensile fracture surface of: (a) neat PP (MI = 6.7 g/10 min), (b) as received SiO_2/PP (SiO_2 content 1.33 vol.%), (c) SiO_2-g-PBA/PP (SiO_2 content 3.31 vol.%), and (d) SiO_2-g-PS/PP (SiO_2 content 1.96 vol.%).

a clear evidence of plastic deformation (Figure 5c). The fracture surface is characterized by the formation of elongated matrix segments and extensive "cavitation" sites, as indicated by a number of concentric "matrix-fibrillated" circles around particle-like objects. A magnified micrograph (Figure 5d) indicates that the appearance of the fibrillated matrix circles is probably a result of a successive debonding of the modified nanoparticle agglomerates from the matrix due to the

interfacial stress concentrations. The debonding is accompanied by an unconstrained plastic stretching of the interparticle matrix ligaments. The voiding process can be described as follows. At the beginning of the deformation, the modified nanoparticle agglomerates act as stress concentrators, and the stress field is disturbed by the surrounding particle-clusters. Then shear yielding of the matrix occurs due to a maximum shear stress component at an angle of 45°.[20] Once debonding is initiated at both ends of the modified nanoparticle agglomerates (*i.e.*, at the poles), the shear stress is locally relieved and the deformation circles form due to a gradual contraction of the matrix. The concentric "fibrillar" circles around the nanoparticle agglomerations must have consumed a considerable amount of energy during the tensile procedure, which might account for the measured reinforcing and toughening effects.

4 Thermosetting Systems

4.1 Interfacial Interactions in the Composites

Polyacrylamide (PAAM) grafted SiO_2 (SiO_2-g-PAAM), with percent grafting and grafting efficiency of 10.3% and 53.7%, respectively, was prepared and incorporated into an epoxy matrix. PAAM was selected because the active hydrogen atoms of its amide groups might react with the epoxy groups and form three-dimensional networks throughout the composites, so that the nanoparticles can be connected covalently to the matrix.

As shown by the infrared spectrum of SiO_2-g-PAAM in Figure 6, the stretching modes of carbonyl and CN in amide groups appear at 1665 and 1454 cm^{-1}, respectively. The two peaks can also be observed in the spectra of homopolymerized PAAM and grafting PAAM, but the CN peak appears at a lower wavenumber of 1427 cm^{-1} in the spectra of grafting PAAM, suggesting that its chemical environment slightly differs from that of homopolymerized PAAM. For the grafting PAAM isolated from SiO_2-g-PAAM, the absorption due to intermolecular hydrogen bonds at 2900-3700 cm^{-1} is much broader than that of homopolymerized PAAM. In addition, there is a twin-peak at 3341 and 3413 cm^{-1} that is absent in the spectrum of PAAM homopolymer. This can be attributed to the hydroxyl groups on PAAM generated when silica in SiO_2-g-PAAM was removed by the HF solution. That is, during the grafting polymerization, PAAM had been covalently bonded to SiO_2.

To detect the possible reaction between PAAM and epoxy by infrared spectroscopy, a model system, consisting of PAAM homopolymer and epoxy (1/2 by wt.) with no other curing agents, was thermally treated following the same curing sequence as that applied for SiO_2-g-PAAM/epoxy composites. The visual inspection indicated that the blends of PAAM and epoxy became consolidated after curing. In addition, comparison of the infrared spectra of the materials can also yield interest-

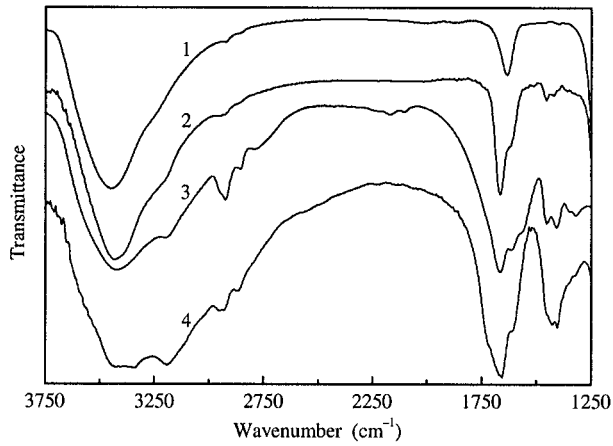

Figure 6. FTIR spectra of: (1) SiO_2, (2) SiO_2-g-PAAM, (3) homopolymerized PAAM, and (4) grafting PAAM.

ing information. As illustrated by the spectrum of PAAM in Figure 7, the C=O peak at 1665 cm^{-1}, the NH_2 peak at 1616 cm^{-1}, and the CN peak at 1454 cm^{-1} correspond to the primary amide. In the case of PAAM/epoxy blends, however, the spectrum profile has been changed as a result of a partial transformation of primary amide groups and band overlap due to the incorporation of epoxy. Since the CNH peak at 1530-1550 cm^{-1}, a characteristic peak of secondary amide, is not perceived, and the carbonyl peak appears at 1656 cm^{-1} instead, it can be assumed that this carbonyl peak in association with the low wavenumber shift (compared to the

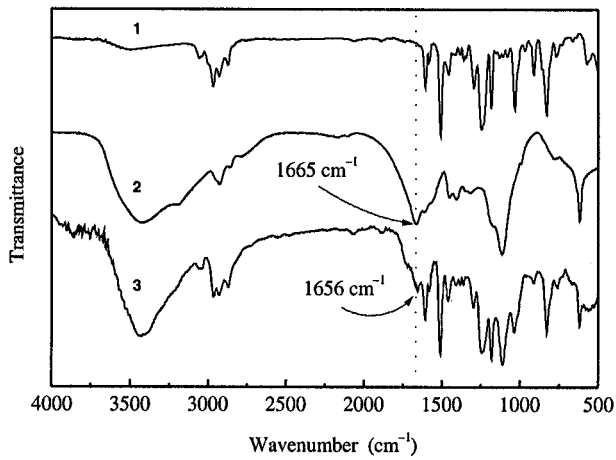

Figure 7. FTIR spectra of: (1) epoxy without any curing agent, (2) PAAM, and (3) cured blends of PAAM and epoxy (1/2 by wt.).

carbonyl peak position of primary amide) shows the existence of tertiary amide connected with a donor group. This evidences the reaction between PAAM and epoxy during curing. It can thus be concluded from the above visual observation and spectral analyses that PAAM can take part in the curing reaction of epoxy. Such a chemical bonding between the PAAM chains grafted onto SiO_2 nanoparticles and the surrounding epoxy networks would certainly enhance the filler/matrix adhesion in the composites.

4.2 Curing Behavior

To further understand the effect of the interaction between the nanoparticles and the epoxy resin, the curing reaction kinetics of the composites have been studied. Based on non-isothermal DSC measurements and the Kissinger equation,[21] the activation energy E, the pre-exponential factor A, and the reaction order n, of the curing kinetics are obtained (Table 4). Comparison of the kinetic data suggests that the presence of the nanoparticles in epoxy does not change the overall reaction

Table 4. Curing characteristics of the epoxy resin and its composites containing 2.17 vol.% nanosilica.

Parameter	*Epoxy*	*SiO_2/Epoxy*	*SiO_2-g-PAAM/Epoxy*
E^a (kJ/mol)	68.9	69.4	57.8
ln A^b	8.4	8.6	5.6
n^c	1.25	1.35	1.23

[a]Activation energy; [b]pre-exponential factor; [c]reaction order

mechanism. Compared to neat epoxy resin, the increase in the activation energy of the SiO_2/epoxy system suggests that the unmodified nanoparticles slightly decelerate the curing reaction. In contrast, the grafted nanoparticles tend to promote the curing of epoxy, as revealed by the decreased activation energy. The reduction in the pre-exponential factor of SiO_2-g-PAAM/epoxy composites is probably due to steric hindrance generated by the grafting polymers adhering to the nanoparticles.

4.3 Friction and Wear Performance

The sliding wear properties of the composites are plotted in Figures 8 and 9 as a function of the silica content. The frictional coefficient, μ, of the composites with unmodified silica nanoparticles remains almost the same as that of the neat matrix up to a filler fraction of about 4 vol.% (Figure 8). On the contrary, the grafted particles can obviously reduce the value of μ even at low filler loadings.

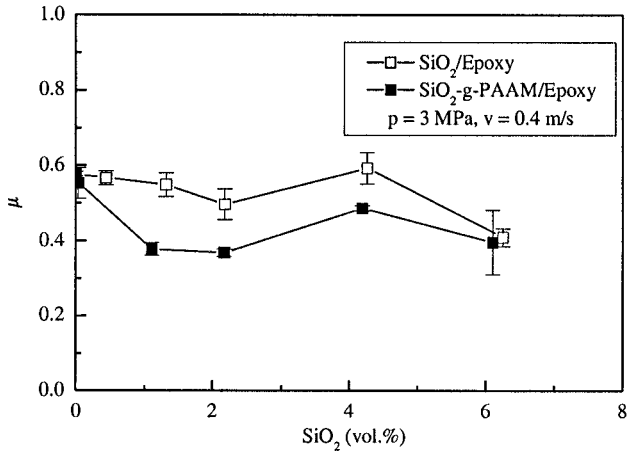

Figure 8. Dependence of the frictional coefficient, μ, of epoxy-based composites on the filler content.

Similarly, a substantial decrease in the specific wear rate, $\dot{w}_s$, can be observed in SiO_2-g-PAAM filled composites with the rise in filler content and all $\dot{w}_s$ values are lower than those of untreated nano-SiO_2-filled systems, although the untreated nanoparticles can also result in decreased $\dot{w}_s$ with respect to the unfilled epoxy. Within the filler content range from 2 to 6 vol.%, the wear resistance of epoxy is increased by a factor of about 20 by the addition of SiO_2-g-PAAM. Bearing in mind the fact that 40 wt.% micron-sized SiO_2 (180 μm) particles were needed to acquire a significant decrease in the wear rate of epoxy,[22] the present systems are clearly characterized by a broader applicability.

Nanoparticles can significantly reduce the wear rate of epoxy because the wear mechanism changes from severe abrasive to mild sliding wear.[23] A further improvement of the tribological performance of SiO_2-g-PAAM/epoxy composites may be caused by the excellent interfacial coupling between SiO_2 nanoparticles and epoxy resulting from reactions of the amide groups of grafted PAAM with the epoxy groups of the matrix. In addition, the remarkably reduced material removal due to wearing (Figure 9) and the lubricating effect provided by the nanoparticles tightly embedded in the matrix[24] should account for the low frictional coefficient characteristics of SiO_2-g-PAAM/epoxy composites over the filler content range studied (Figure 8). The lack of the above-mentioned interfacial chemical bonding between untreated SiO_2 nanoparticle agglomerates and the matrix resin results in higher wear rates and higher μ values of SiO_2/epoxy composites. The epoxy splinters (due to a severer material loss) entrapped at the interface between the steel counterpart and the composite pin might create a three-body abrasive wear situation, and thus counteract the lubricating effect of the nanoparticles, leading to μ values of SiO_2/epoxy composites similar to that of unfilled resin when the SiO_2 content is ≤ 4 vol.%.

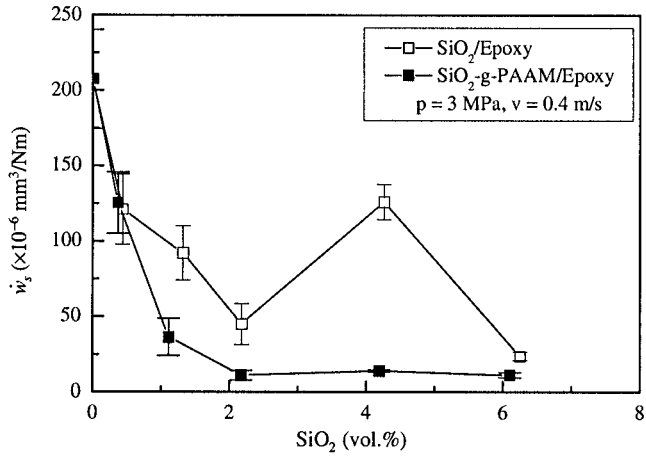

Figure 9. Filler content dependence of the specific wear rate, $\dot{w}_s$, of epoxy-based composites.

Figure 10 compares the coefficients of friction of epoxy and its composites determined at pressures of 3 and 5 MPa under a constant sliding velocity v = 0.4 m/s. It is seen that the frictional coefficient of epoxy keeps almost unchanged when the pressure increases from 3 to 5 MPa, which is in good agreement with other reports.[25] The frictional coefficients of nanosilica-filled composites are lower than that of unfilled epoxy and decrease with increasing pressure. The lowest value of μ is

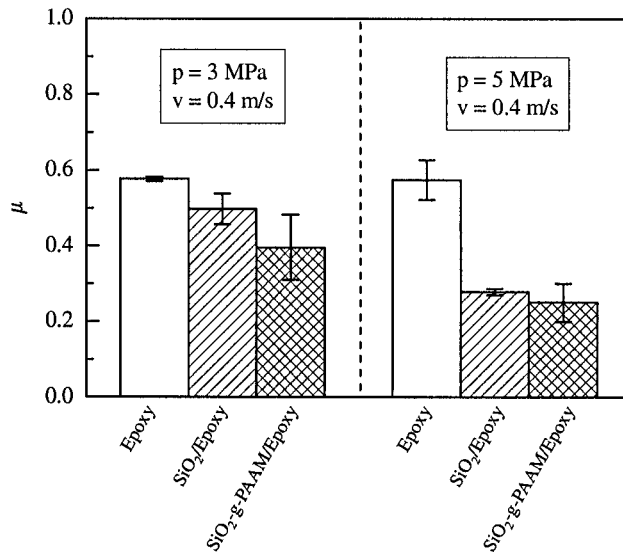

Figure 10. Frictional coefficients, μ, of epoxy and its composites at 2.17 vol.% SiO_2 content.

recorded at a load of 5 MPa for SiO_2-g-PAAM/epoxy composites. These observations imply that nanosilica can improve the friction-reducing ability of the composites, especially under higher loads.[26] The introduction of grafting PAAM further enhances the role of the particles. The effect of pressure on the specific wear rates of the materials is illustrated in Figure 11. Nanocomposites evidence a much higher wear resistance compared to the neat epoxy.

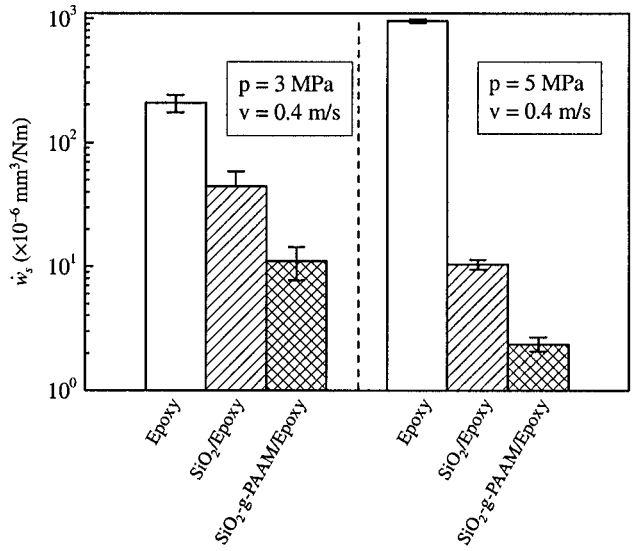

Figure 11. Specific wear rate, $\dot{w}_s$, of epoxy and its composites at 2.17 vol.% SiO_2 content.

Comparison of Figures 11 and 10 suggests that the decrement of the wear rate is greater than that of the frictional coefficient when the other conditions are the same. Silica nanoparticles seem to be more effective for improving the wear resistance of the composites. On the other hand, Figure 11 shows that the pressure dependences of the wear rate of unfilled epoxy differ from that of the frictional coefficient shown in Figure 10. With the rise in testing pressure, the wear loss of epoxy is increased, but that of the composites is decreased, suggesting that different wear mechanisms must be involved.

Fatigue wear has been regarded as the main mechanism responsible for the sliding of epoxy against a hard counterpart.[25,27] The model is based on the sub-surface crack nucleation and coalescence due to shear deformation of the softer surface induced by the traction of the harder asperities.[28] As shown in Figure 12a, scale-like removal of material has left traces on the worn surface of unfilled epoxy, clearly indicating fatigue-delamination generated under repeated loading during sliding. For SiO_2-reinforced composites, the basic wear patterns are characterized by a mild fatigue wear, resembling that of the matrix tested at 3 MPa (Figure 12a).

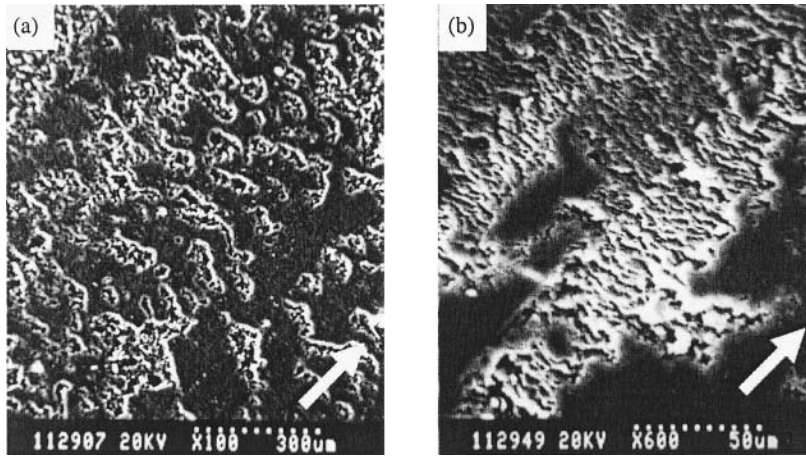

Figure 12. Scanning electron micrographs of the worn surface of (a) epoxy and (b) SiO_2-g-PAAM/epoxy composite. SiO_2 content 2.17 vol.%, sliding wear tests at p = 3 MPa, v = 0.4 m/s; the arrows indicate the sliding direction.

A careful examination of the wear grooves shows that the flaws' distribution produced on the worn surface change from a discontinuous mode (Figure 12a) to a continuous mode (Figure 12b). In particular, the uneven stress concentration built up inside the epoxy resin might have been homogenized to some extent in the composites due to the effect of the dispersion strengthening by the nanoparticles.[24] This is certainly beneficial for reducing the amount of material loss.

5 Conclusions

The modification of nanosilica by means of grafting polymerization helps to impart a balanced performance of the composites. In addition, different grafting monomers result in different interfacial interactions and different ultimate properties of the composites.

The addition of grafted silica nanoparticles into PP can bring in both reinforcing and toughening effects at rather low filler contents. Such a simultaneous improvement in modulus, strength, and elongation to break is hard to observe in conventional micron-sized particulate composites.

Grafting polymerization onto nanosilica can also increase the interfacial interaction between the particles and the epoxy matrix through chemical bonding. It proves to be an efficient way to further enhance the effect of the nanoparticles on the improvements of the tribological performance.

6 Acknowledgements

The authors gratefully acknowledge the support of the Volkswagen-Stiftung (No. I/76645) and thank the Deutsche Forschungsgemeinschaft (DFG FR675/40-4) for the cooperation between German and Chinese institutes on various topics of nanocomposites.

Further thanks are due to the National Natural Science Foundation of China (No. 50133020, 50273047) and the Team Project of the Natural Science Foundation of Guangdong, China (No. 20003038), especially for the support of young researchers working in the general field of nanoparticle treatment.

7 References

[1] R. Dagani (1992) Nanostructured materials promise to advance range of technologies, *C&EN* **70**, 18.

[2] M. Z. Rong, M. Q. Zhang, Y. X. Zheng, H. M. Zeng, K. Friedrich (2001) Improvement of tensile properties of nano-SiO_2/PP composites in relation to percolation mechanism, *Polymer* **42**, 3301.

[3] M. Yoshida, M. Lal, N. D. Kumar, P. N. Prasad (1997) TiO_2 nano-particle-dispersed polyimide composite optical waveguide materials through reverse micelles, *J. Mater. Sci.* **32**, 4047.

[4] M. Sumita, T. Okuma, K. Miyasaka, K. Ishikawa (1982) Effect of ultrafine particles on the elastic properties of oriented low-density polyethylene composites, *J. Appl. Polym. Sci.* **27**, 3059.

[5] S. W. Shang, J. W. Williams, K.-J. M. Soderholm (1992) Using the bond energy density to predict the reinforcing ability of a composite, *J. Mater. Sci.* **27**, 4949.

[6] M. Z. Rong, M. Q. Zhang, Y. X. Zheng, H. M. Zeng, R. Walter, K. Friedrich (2001) Structure-property relationships of irradiation grafted nano-inorganic particle filled polypropylene composites, *Polymer* **42**, 167.

[7] D. Y. Godovski (1995) Electron behavior and magnetic properties of polymer nanocomposites, *Adv. Polym. Sci.* **119**, 79.

[8] Y. Nakao (1995) Noble metal solid sols in poly(methyl methacrylate), *J. Colloid Interf. Sci.* **171**, 386.

[9] C. H. Griffiths, M. P. Ohoro, T. W. Smith (1979) The structure, magnetic characterization, and oxidation of colloidal iron dispersions, *J. Appl. Phys.* **50**, 7108.

[10] K. E. Gonsalves, G. Carlson, X. Chen, S. K. Gayen, R. Perez, M. Jose-Yacaman (1995) Surface functionalized nanostructured gold/polymer composites, *Polym. Mater. Sci. Eng.* **73**, 298.

[11] H. Liu (1997) Functional and structural investigation of nanometer particles/epoxy resin composites, MSc Thesis, Zhongshan University (in Chinese).

[12] E. P. Giannelis (1992) A new strategy for synthesizing polymer-ceramic nanocomposites, *JOM* **44**, 28.

[13] B. M. Novak (1993) Hybrid nanocomposite materials – between inorganic glasses and organic polymers, *Adv. Mater.* **5**, 422.

[14] W. Xu, R. Huang, B. Cai, W. Fan (1998) Nano-$CaCO_3$ filled HDPE composites, *Chin. Plast.* **12**, 30 (in Chinese).

[15] L. S. Schadler, K. O. Laul, R. W. Smith, E. Petrovicova (1997) Microstructure and mechanical properties of thermally sprayed silica/nylon nanocomposites, *J. Therm. Spray Technol.* **6**, 475.

[16] F. Sahnoune, J. M. Lopez-Cuesta, A. Crespy (1999) Effect of elastomer interfacial agents on tensile and impact properties of $CaCO_3$ filled HDPE, *J. Mater. Sci.* **34**, 535.

[17] Y. Long, R. A. Shanks (1996) PP-elastomer-filler hybrids. I. Processing, microstructure, and mechanical properties, *J. Appl. Polym. Sci.* **61**, 1877.

[18] B. Pukanszky (1990) Influence of interface interaction on the ultimate tensile properties of polymer composites, *Composites* **21**, 255.

[19] R. Walter, K. Friedrich, V. Privalko, A. Savadori (1997) On modulus and fracture toughness of rigid particulate filled high density polyethylene, *J. Adhesion* **64**, 87.

[20] G. M. Kim, G. H. Michler, M. F. Gahleitner (1996) Relationship between morphology and micromechanical toughening mechanisms in modified polypropylenes, *J. Appl. Polym. Sci.* **60**, 1391.

[21] H. E. Kissinger (1957) Reaction kinetics in differential thermal analysis, *Anal. Chem.* **29**, 1702.

[22] Y. Yamaguchi (1990) Improvement of lubricity, in *Tribology of Plastic Materials* (Ed. Y. Yamaguchi) Elsevier, Amsterdam, pp.143–202.

[23] L. S. Schadler, K. O. Laul, R. W. Smith, E. Petrovicova (1997) Microstructure and mechanical properties of thermally sprayed silica/nylon nanocomposites, *J. Therm. Spray Technol.* **6**, 475.

[24] M. Z. Rong, M. Q. Zhang, H. Liu, H. M. Zeng, B. Wetzel, K. Friedrich (2001) Microstructure and tribological behavior of polymeric nanocomposites, *Ind. Lubr. Tribology* **53**, 72.

[25] R. Bassani, G. Levita, M. Meozzi, G. Palla (2001) Friction and wear of epoxy resin on inox steel: remarks on the influence of velocity, load and induced thermal state, *Wear* **247**, 125.

[26] Q. Wang, J. Xu, W. Shen (1997) The friction and wear properties of nanometer SiO_2 filled polyetheretherketone, *Tribol. Int.* **30**, 193.

[27] W. Bonfield, B. C. Edwards, A. J. Markham, J. R. White (1976) Wear transfer films formed by carbon fibre reinforced epoxy resin sliding on stainless steel, *Wear* **37**, 113.

[28] N. P. Suh (1973) The delamination theory of wear, *Wear* **25**, 111.

Chapter 3

Reinforcement of Thermosetting Polymers by the Incorporation of Micro- and Nanoparticles

Frank Haupert, Bernd Wetzel
Institute for Composite Materials Ltd., Kaiserslautern University of Technology, Kaiserslautern, Germany

1 Introduction

A traditional way to improve the properties of polymeric materials, in order to make them more suitable for various loading conditions, is the incorporation of short fibers (*e.g.*, glass or carbon) or ceramic particles. The diameter of these reinforcements is usually in the range of several micrometers, and they provide an increase in thermal stability, stiffness and strength of the polymer matrix used. There are, however, some drawbacks by such fillers, as for example a reduction in strain to failure, impact strength and, sometimes also in fracture toughness.[1,2] To overcome this problem, an innovative approach takes advantage of particles with diameters in the range of several nanometers. This approach opens promising pathways to change fundamentally the characteristics of polymer matrices. The resulting nanocomposites may be characterized by a structure showing inhomogeneities in the size range between submicrons and nanometers.[3] According to Komarneni,[4] they include more than one solid phase, where at least one phase dimension is in the nanometer range (1 to 20 nm). Nanoparticle incorporation may lead to composite materials with superior properties than the neat matrix polymer,[5,6] even at particle sizes exceeding 20 nm and reaching into the submicron range. The degree of reinforcement depends on the material characteristics, such as the mechanical properties of matrix and fillers, but especially for this new class of materials the interface between matrix and fillers occurs to be most important.[7] If one considers that a large number of nanoparticles with a high specific surface

area are in contact with the surrounding polymer matrix, then the resulting composite behavior may be more and more interface-determined.

Figure 1 explains schematically why one must expect different, or even superior properties in the case of nanocomposites, when compared to traditional

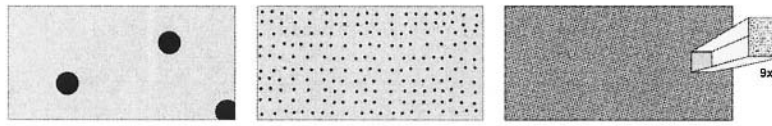

Figure 1. Correlation between the relative number n of particles and the particle size d at a constant filler content of 3 vol.% within a reference volume. Left: d = 10 μm, $n \sim 2.8$; center: d = 1 μm, n = 2860; right: d = 100 nm, n = 2 860 000 particles homogeneously distributed within a polymer.[8]

composites containing micro- or macroparticles. The correlation between the relative number of spherical particles, their size and specific surface area is demonstrated for a constant filler content of 3 vol.%. Within a reference volume of 50000 μm^3, one can detect only 3 particles when their diameter is 10 μm (Figure 1, left). However, the particle number increases enormously to more than 3 million, if nanoparticles of 100 nm diameter are used (Figure 1, right). Obviously, nanoparticles can provide a much higher interface area than the "large" particles. One can indeed speak of "interface-dominated" materials in this case, and it becomes clear that such increased interface area may widely determine the composite properties.

Considering, for instance, a small crack propagating through these different material structures, the crack will all the time interact with the particles in the case of the nanocomposite, whereas it may not "see" the particles at all when propagating in between the larger ones. The same conclusion can be drawn with regard to wear loadings, when considering a counterpart asperity scratching over the surface of such different material systems. In fact, it was verified by several researchers that inorganic nanoparticles possess the ability to reinforce effectively thermoplastic and also thermosetting polymer matrices.[8-17] A considerable improvement of the mechanical and tribological properties can already be achieved at very low filler volume contents, in the range of 1 to 5 vol.%. Specifically, such a reinforcement provides improvements of the elastic modulus, without losing strength, and at the same time, it can be accompanied by an enhancement in the material's fracture toughness[18] and impact energy.[19] Toughness improvement, however, depends strongly on the particle content[19,20] and, even more important, on the dispersion state of the fillers. Increasing the microstructural perfection of polymers by excluding flaws, inclusions or particle agglomerates, is always an option to improve toughness, and it is used as an important strategy for toughening.[21] Gaining a

homogeneous microstructure turned out to be of great importance also for the wear performance of epoxy nanocomposites filled with TiO_2 or Al_2O_3 particles.[22,23] The possible particle distribution depends on the particle type and size, the specific surface area, the volume content of particles, and the conditions during the mixing process. In order to find the optimum performance of nanocomposites, the best formulation must be established. This can be done by producing a series of nanocomposites with various nanoparticle contents, and by simultaneously evaluating the mechanical properties. Also, a combination of nanoparticles with conventional microparticles can be of great interest for many engineering applications, especially for cases when the friction and wear properties are quite important. Here, synergistic effects may be generated, which push the wear resistance of such composites to a much higher level.[8] Nanoparticles have also shown a capability to effectively improve the mechanical properties of filament wound carbon fiber-reinforced epoxy composites.[24] The expected excellent overall properties may then open the way towards new applications of high performance composites, leading to an innovative product development in industry.[25]

2 Manufacturing of Thermosetting Nanocomposites

The basic challenge in order to gain the desired nanocomposite properties is to disperse the nanoparticles as individual particles in the polymer matrix. So far, commercially available particle powders include agglomerates where the nanoparticles stick strongly together due to adhesive forces (Figure 2). Relative to particle mass forces, the adhesive forces increase with decreasing particle size. Furthermore, nanoparticles possess a very high specific surface area (Table 1).

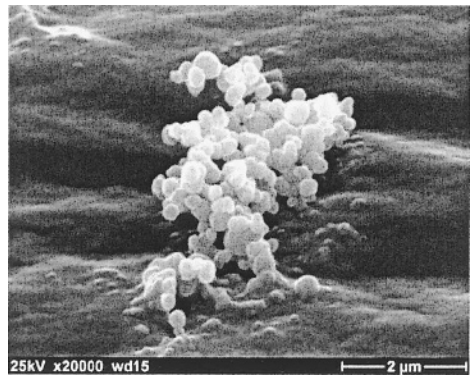

Figure 2. Titanium dioxide nanoparticle agglomerate.[8]

Table 1. Particle size and specific surface area of micro- and nanofillers.

Filler	*Particle size (nm)*	*Specific surface area (m^2/g)*
Al_2O_3	13	100
TiO_2	21	50
TiO_2	300	5
$CaSiO_3$	5000 - 10000	3.5

In order to obtain well dispersed nanocomposites with separated nanoparticles, the way of combining polymers and powders must be considered as the most important key to gain the desired material properties. Nanocomposite processing can be performed by different techniques, which are considered to be most important for the final nanocomposite properties.[26,27] Some methods aim at the incorporation of individual nanoparticles directly (*in situ*) into a polymer using chemical techniques.[28,29] For dispersing commercially available powders in liquids, mechanical methods have been established, which are often used in the lacquer and paint industries. These techniques apply high shear forces during a dispersion process in order to break up agglomerates and to distribute the individual fillers homogeneously in the polymer. A high local energy density can be realized by using different working principles, *e.g.*, rotating discs (Dissolver, Figure 3), rotor-stator-systems (Ultra-Turax), grinding effect of moving ceramic balls (Ball Mill),

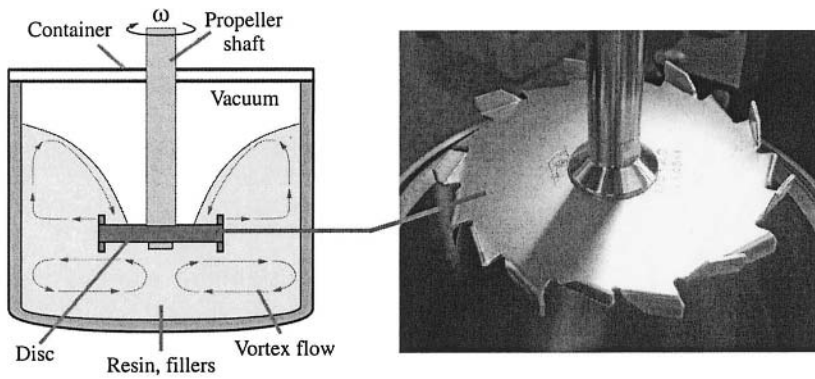

Figure 3. Dissolver technology (rotating disc) for the manufacturing of nanocomposites.

or combinations of these technologies (Torus Mill, Figure 4). The Dissolver technology applies high shear forces by the rotation of a metal disc in order to break up nanoparticle agglomerates, separate these particles and finally distribute them homogeneously within the matrix. The Torus Mill combines Dissolver and Ball Mill technology. Ceramic balls (*e.g.*, ZrO_2 of diameter 0.7-1.2 mm, Figure 4) introduce both a shear and a collision effect in order to achieve individual particles.

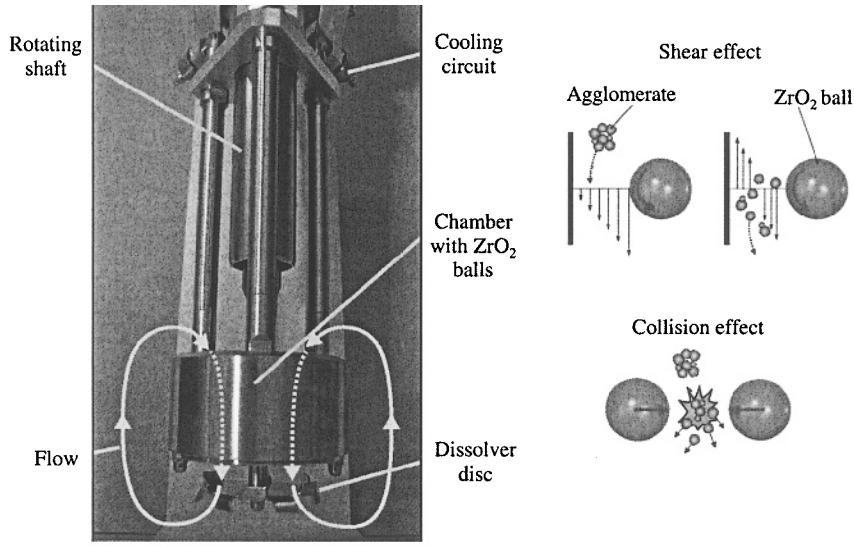

Figure 4. Torus Mill: combination of Dissolver and Ball Mill technology for the manufacturing of nanocomposites.

Figure 5 shows the influence of mixing processes on the state of dispersion in two nanocomposite materials. TiO_2 particles were mixed with insufficient quality

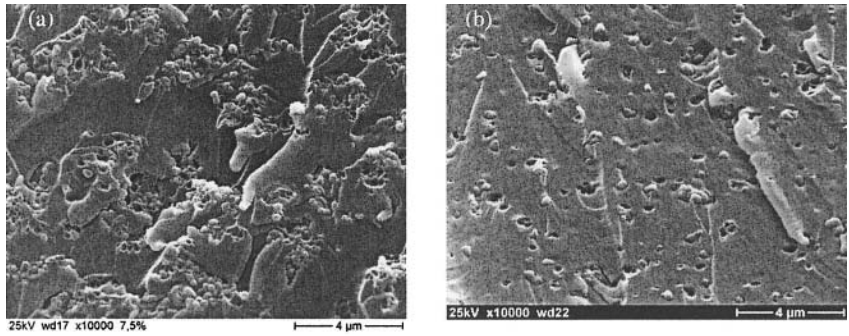

Figure 5. Fracture surface of epoxy resin containing (a) undispersed and (b) mechanically dispersed titanium dioxide nanoparticles (300 nm).

into epoxy resin by a laboratory propeller at low shear rates (Figure 5a). The agglomerates visible prove that such a device cannot fully disperse nanoparticles. On the contrary, the Dissolver technology is able to distribute the TiO_2 particles homogeneously in epoxy under high shear conditions (Figure 5b).

The efficiency of these methods may be further increased by the application of ultrasound.[30,31] Ultrasound techniques are able to combine the breakage of particle agglomerates with an effective mixing of the material components on a molecular level. In combination with mechanical stirring, ultrasound waves were able to successfully disperse carbon nanotubes in epoxy resin.[32]

Another approach to produce nanocomposites is to apply a special chemical pre-treatment of nanoparticles by grafting reaction before the mechanical dispersion process. A chemical treatment of the particle surface may enhance the composite's properties by improving the filler-matrix coupling quality.[33-35] Additionally, it can improve the dispersibility of the particles in the matrix. By this method, it is possible to enhance especially the wear properties of polymers.[36,37]

In the following sections, some work is presented in which the properties of nano- and microparticle filled composites were determined under variation of the filler contents. These materials were made on the basis of standard epoxy resins cured by amine hardeners. The nanofillers were aluminum oxide (Al_2O_3, 13 nm), titanium dioxide (TiO_2, 300 nm and 20 nm) and also calcium silicate ($CaSiO_3$, 5-10 μm) microparticles. All these fillers are commercially available as powders. The composites were prepared by mechanical mixing using a Dissolver mixing device, as shown in Figure 3.

3 Properties of Nanocomposites

3.1 Stress-Strain Behavior

The influence of particulate fillers on the stress-strain behavior of polymers is well known, at least for fillers in the size of micrometers and larger. Rigid microfillers commonly increase the stiffness on the one hand, but on the other hand, they may have a detrimental effect on the strain to break.[38] The flexural strength of microparticle-filled composites may also be reduced with rising filler content,[38,39] especially in the case when the load transfer between matrix and particles is insufficient and the interface is weak. This is true also for composites which contain particle agglomerates. Figure 6 depicts the flexural behavior of nanocomposites measured in three-point bending configuration at 2 mm/min under ambient conditions. Obviously, the nanocomposites offer a simultaneous increase of both flexural modulus and flexural strength with rising filler content.

Calcium silicate microparticles increase the modulus more efficiently than the nanoparticles. In this case, a silane-treatment of the $CaSiO_3$ surface ensures good filler-matrix bonding and favors stress transfer *via* the interface. The flexural strength decreases slightly, but remains above that of the neat matrix. The fracture surfaces of these composites (EP/Al_2O_3/$CaSiO_3$) occur extensively rugged and

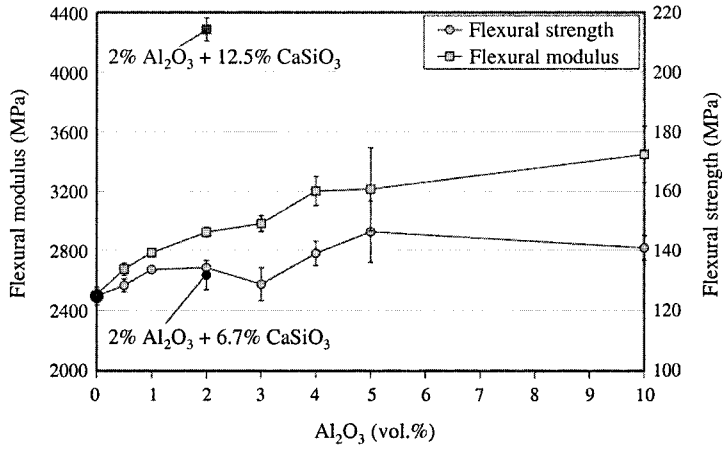

Figure 6. Bending properties of epoxy/Al_2O_3 (13 nm) nanocomposites *vs.* nanoparticle content.

brittle. The nanoparticle-modified matrix between the microparticles, however, shows a typical micro-rough structure, which indicates increased energy absorption.

Some important characteristics of composites have to be considered in order to explain the phenomena observed. The quality of the interface in composites, *i.e.*, the static adhesion strength, and the interfacial stiffness play usually a very important role in the materials' capability to transfer stresses and elastic deformation from the matrix to the fillers.[40] This is especially true for nanocomposites, because they impart a high portion of interface. If the filler-matrix interaction is poor, the particles are unable to carry any part of the external load. In this case, the strength of the composite cannot be higher than that of the neat polymer matrix. If the bonding between fillers and matrix is strong enough, the yield strength of a particulate composite can be higher than that of the matrix polymer.[41] A high interfacial stiffness corresponds in the same way to a high composite modulus. Hence, the gradual increase in stiffness and flexural strength, as observed for the nanocomposites, suggests that stresses are efficiently transferred *via* the interface.

As mentioned above, the strain at break usually tends to decline with rising rigid filler content. Depending on the fracture mechanisms involved and the adhesion quality between fillers and the matrix, a dramatic drop in the fracture strain may already be caused by low filler loadings. In the case of composites containing rigid fillers, most of the deformation comes from the polymer. The actual deformation of the polymer matrix is much larger than the measured deformation of the sample, with the result that the polymer reaches the failure strain limit at a lower total deformation. Thus, the total composite strain to break would generally decrease.

For nanocomposites it is surprisingly observed that the strain at maximum force and also the strain to break behave not exactly as it would be expected. They

stay on a nearly constant level at low particle contents up to 5 vol.%.[19] This suggests that the nanoparticles are able to introduce additional mechanisms of failure and energy consumption without heavily blocking the matrix deformation. However, at high filler contents the large number of filler particles may dominate and hinder the matrix deformation.

Another important aspect, which is more related to the dispersion state of the nanoparticles, may additionally play a significant role. In the case when relatively large agglomerates would remain in the matrix, a propagating crack could encounter a stress concentration locally and then easily induce the initiation of the final failure. Obviously, embrittlement effects occur at higher filler contents, where more agglomerates are likely to be found. The improved properties at low filler contents, on the other hand, testify lower stress concentrations and, therefore, the remaining nanoparticle clusters should be small. This shows again the importance to reach a homogeneous distribution of nanoparticles in the polymer.

Atomic force microscopy (AFM) on thin sections is a straightforward technique to depict individual particles and the dispersion quality within the matrix, as displayed in Figure 7. In this case, a relatively homogeneous particle distribution for the EP/Al_2O_3 nanocomposites at a low filler content was reached by using a Dissolver mixing device. Further methods to examine particle distributions would be transmission electron microscopy (TEM) and scanning electron microscopy (SEM).

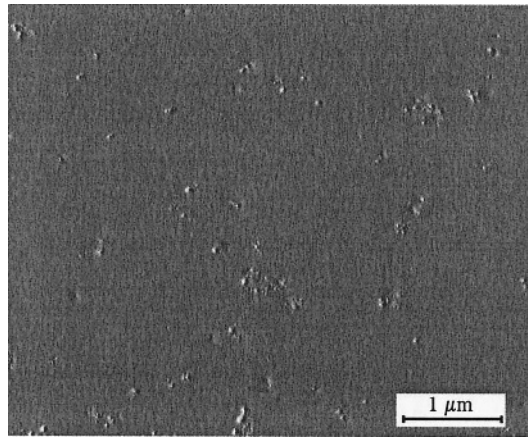

Figure 7. Atomic force microscopy image of a thin cut of epoxy/Al_2O_3 nanocomposite containing 1 vol.% filler. Homogeneous particle distribution.[19]

Visual examinations of the fracture surfaces (*e.g.*, from bending experiments) of neat epoxy resin (Figure 8) and particulate-filled epoxy resins (Figure 9), especially by SEM methods, can provide detailed information on the

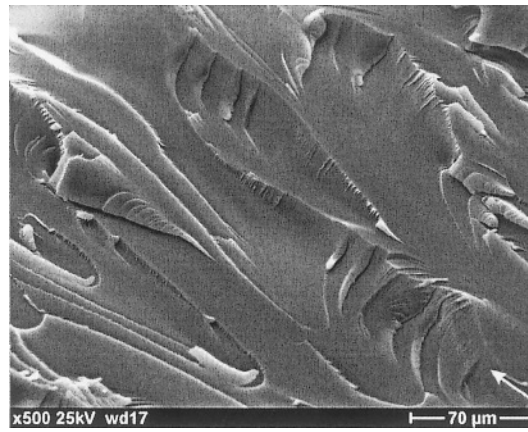

Figure 8. Fracture surface of neat epoxy resin from flexural testing. Brittle fracture with smooth areas.[19]

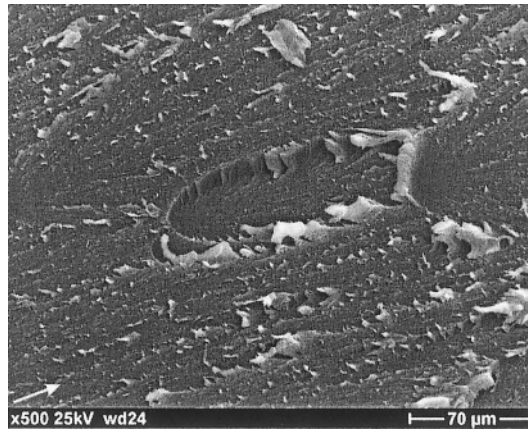

Figure 9. Epoxy/Al_2O_3 nanocomposite containing 1 vol.% filler. Micro-rough structure, hyperbolic markings indicate the formation of secondary cracks.[19]

cause and location of failure and, additionally, explain the reasons for the increase in energy absorption of nanocomposites. Several mechanisms of crack propagation and failure are commonly known to be applicable for filled epoxy resins, *e.g.*, filler/matrix debonding, shear yielding, banding, and step formation.[42-44] On the one hand, cracks may pass through the particles if the fillers are weak, or they may pass around if the particles are strong enough. On the other hand, failure may occur by interfacial debonding or by cohesive failure of the matrix. Some of these mechanisms were proved to act also for the micro- and nanocomposites.[19]

Figure 8 shows a fracture surface of the neat epoxy matrix, which reveals a brittle behavior characterized by large smooth areas. These are characteristic of Mode I loading and indicate a weak resistance to crack propagation. In contrast to the neat polymer, nanocomposite surfaces typically show a micro-rough structure characterized by flow patterns aligned in the direction of the main crack propagation, along with hackle-like features (Figure 9). Such matrix shear deformation (shear yielding) may occur by an energy-consuming mechanism in a particulate-filled epoxy resin, and the mechanism has been reported by several authors.[42-44] Other energy-consuming mechanisms are expected to be particle debonding, crack front pinning and the initiation of secondary cracks at local inhomogeneities indicated by hyperbolic markings.

3.2 Impact Behavior

Charpy impact tests are high speed fracture tests measuring the energy to break of a specimen under bending conditions. The specimens are deformed within a short time and therefore exposed to high strain rates. Since untoughened epoxy resin matrices can be classified as brittle materials, they are very sensitive to notches and local inhomogeneities, *e.g.*, particles, which may act as stress concentrators and reduce the absorbed impact energy of the composite when more particles are introduced. For instance, the impact energy of notched specimens is generally much lower than that of unnotched specimens. This is due to the fact that notches act as stress concentrators, and most of the deformation takes place in the neighborhood of the notch tip, where a higher apparent strain rate occurs than in similar unnotched specimens. One can assume that the same effect is observed in the case when the nanoparticles are not sufficiently dispersed in the polymer, and agglomerates remain as stress concentrators in the matrix. In general, it was found that the impact properties of polymers are more enhanced by small particles with low aspect ratio,[45] while large particles can act as flaws, and high aspect ratio particles are able to induce large stress concentrations near their edges.

In epoxy nanocomposites, the nanoparticles have a quite favorable effect on the impact behavior at low and also higher filler loadings (Figure 10). Strong reinforcement seems to be effective mainly at low filler contents. Especially for the small Al_2O_3 and TiO_2 particles, a maximum of impact energy is reached in the range of 1 to 2 vol.%. The nanocomposites containing the sub-micron TiO_2 (300 nm) exhibit a maximum of the impact energy at 4–5 vol.%. The impact energy decreases gradually at higher filler contents. Therefore, the smaller particles occur to be more effective. It is possible to interpret these results in terms of stress concentration effects around the inclusions. In the nanocomposites studied, the intensity of the stress concentration around particles is expected to be small, because the impact performance is not weakened by the nanoparticles. This means that the

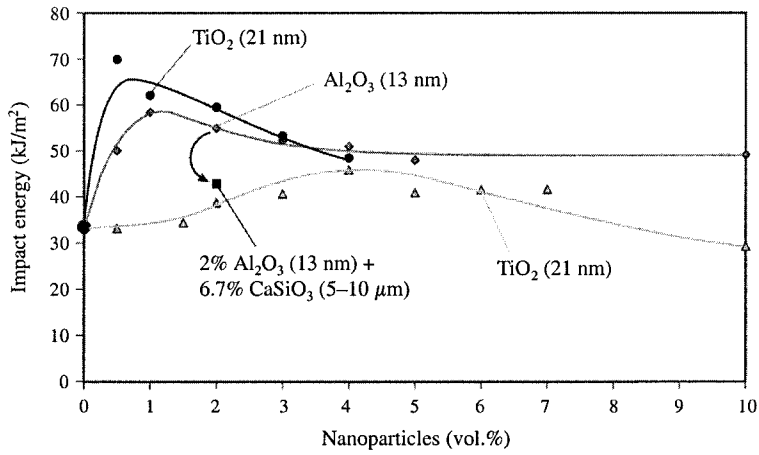

Figure 10. Improvement of the impact toughness of epoxy resin by nanoparticles.

nanocomposites do not become more brittle under high strain rate conditions and, therefore, the fillers may not act as failure sites.

The addition of $CaSiO_3$ microparticles into a nanocomposite reduces the absorbed impact energy (Figure 10). The increased brittleness may be caused by the inhomogeneous shape and size of the microparticles. Since some characteristic features of the $CaSiO_3$ particles are angularities and edges, they would facilitate failure under impact conditions due to localized stress concentrations.

3.3 Stiffness-Impact Energy Relationship

The special relationship between the flexural modulus and the impact energy can easily visualize the reinforcing effect of nanoparticles. The measured values for nanocomposites can be normalized by relating them to the values of the neat epoxy, yielding a normalized stiffness *vs.* normalized impact energy diagram (Figure 11), which summarizes the effect of nanoparticle reinforcement and the influence of the microparticles. Depending on the filler type, opposite effects can be observed.

On the one hand, it is possible to increase the toughness of polymers by incorporating rubber or polyurethane (HD-TPU) particles. Compliant particles, if well dispersed, may influence the deformation behavior towards a higher energy absorption by activating localized cavitational craze-like and shear yielding mechanisms. Their lower stiffness, however, has a disadvantageous effect on the composite's modulus.

If, on the other hand, stiff fillers are used instead, the modulus of the polymer can be enhanced, *e.g.*, by adding only silicon carbide or calcium silicate

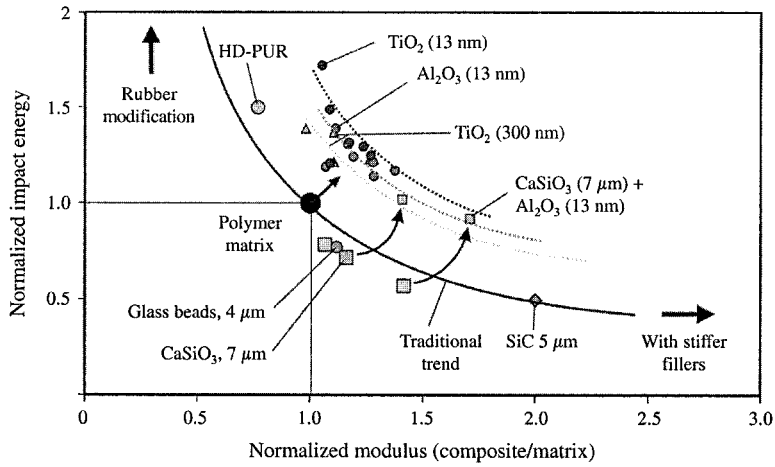

Figure 11. Relationship between stiffness and impact energy.

microparticles. Unfortunately, this turns out to be detrimental to the impact energy. The composite becomes more brittle and less tolerant to impact loads. The thick line in Figure 11 depicts the "traditional trend"; as both properties, modulus and impact energy, seemed impossible to be enhanced simultaneously so far, it turned out that nanoparticles are able to push these properties to a higher level, leading to the generation of polymer composites with superior mechanical properties. Microparticles ($CaSiO_3$) can improve the elastic modulus, however, at the expense of the impact energy. In the case when the introduction of microparticles is imperative, *e.g.*, in order to achieve an improved wear resistance of the polymer, it is very important to bear in mind that the nanoparticles obviously possess the ability to reduce the toughness loss induced by the microparticles.

3.4 Dynamic Mechanical Properties

The dynamic mechanical tests over a wide temperature range are very sensitive to the physical and chemical structure of polymers and composites. They allow the study of glass transitions or secondary transitions and yield information about the morphology of polymers. Experimental results of dynamic tensile tests (DMTA) conducted on nanocomposites are shown in Table 2 for selected temperatures (20 °C, 100 °C, 220 °C, and glass transition, T_g).

The rigid micro- and nanofillers push the complex modulus E^* of epoxy to a higher level. The modulus decreases with rising temperature. At elevated temperatures, in the rubbery plateau well above T_g, the nanocomposites retain higher modulus and damping than the neat epoxy, which probably indicates a higher network density. With rising filler content, the T_g of nanocomposites increases

Table 2. Dynamic mechanical properties at different temperatures and filler contents.

	Temperature								
	20 °C		*100 °C*		T_g			*220 °C*	
Filler content Al_2O_3 (vol.%)	*E* (MPa)*	*tan δ*	*E* (MPa)*	*tan δ*	*E* (MPa)*	*tan δ*	*T_g (°C)*	*E* (MPa)*	*tan δ*
0	2640	0.03	1880	0.026	109	0.854	171	32	0.02
2	2880	0.03	2090	0.025	130	0.79	175	41	0.029
5	3180	0.029	2280	0.027	167	0.734	177	53	0.033
10	3240	0.028	2360	0.025	212	0.666	181	66	0.026
2% Al_2O_3 + 12.6% $CaSiO_3$	4120	0.023	3040	0.02	212	0.75	174	71	0.026

slightly, while the damping peak decreases. These effects were also reported in the literature;[46,47] epoxy/alumina nanocomposites may show a behavior typical of antiplasticized systems, *e.g.*, increase in activation energy, temperature, and peak intensity for the β-relaxation. The nanoparticles can influence the composite's glass transition temperature stronger than the $CaSiO_3$ microparticles. The increase in T_g may be attributed to a loss in the flexibility of chain segments in the epoxy resin resulting from the nanoparticle/matrix interaction. Impeded chain flexibility is possible if the nanoparticles are well dispersed in the matrix. The particle surface-to-surface distances should then be relatively small, so that the chain segment movement may be restricted. Strong adhesion between nanoparticles and surrounding polymer matrix additionally enhances the dynamic modulus and T_g by reducing molecular flexibility to some extend. The hard particles incorporated into the polymer would act as additional virtual "network nodes".

3.5 Wear Performance

In general, the friction and wear properties depend on the whole tribological system rather than a material property alone. Such tribo-systems always consist of the following components: the sample material, a counterpart, a medium in between (*e.g.*, lubricant), the environment and also the stress conditions, such as pressure and sliding speed over a certain time period. The specimen needs to pass a running-in period, which may take some hours. Then, a steady state is reached and the frictional coefficient and the frictional force remain constant. An important question is, how the nano- and microparticles influence the wear properties of the epoxy resin under steady-state sliding conditions. Some aspects of the reinforcing role of ceramic micro-particles in the tribological behavior were already studied

by Durand,[48] who found that large particles (carbides) may protect the matrix better than small ones because they are able to shield the polymer from severe wear. Small particles, on the other hand, were removed out of the matrix and then involved in an abrading wear process. Hard and stiff microparticles (*e.g.*, SiC) are more beneficial to the composite's wear performance under abrasive conditions and high roughness of the counterpart. Under sliding conditions, it was found that nanoparticles change the wear mechanisms from abrasive wear to a mild fatigue wear when running against a steel counterpart.[49] The chemical treatment (*e.g.*, polyacrylamide (PAAM)-grafting) of nanoparticle agglomerates results in a further increase of the wear resistance of the nanocomposites.[49]

Figures 12 and 13 depict the wear performance of nanocomposites filled with Al_2O_3 (13 nm) and TiO_2 (300 nm), respectively. The nanoparticle content was varied between 0 and 10 vol.%. The results were obtained from unlubricated sliding wear experiments conducted on a block-on-ring apparatus. In this case, the specimens run against a carbon steel ring at constant pressure and rotating speed (*e.g.*, 1 MPa, 1 m/s). From the sample weight loss one can calculate the specific wear rate as follows

$$w_s = \frac{\Delta m}{\rho \cdot v \cdot t \cdot F_N} \left(\frac{\text{mm}^3}{\text{Nm}} \right)$$

where Δm is the worn specimen mass (g), ρ is the specific gravity of the specimen, v is the rotating speed of the counterpart, t is time and F_N is the normal force (N). Low wear rates indicate a high wear resistance of the material.

Nanocomposites containing TiO_2 or Al_2O_3 demonstrate an improved wear performance at low filler contents. However, the rise in filler loading to 10 vol.% obviously deteriorates the wear rate. Because of the large amount of hard ceramic particles in the polymer, a change in the wear mechanism is observed, causing higher abrasive wear. Alumina nanoparticles incorporated into a relatively wear resistant epoxy resin can improve the specific wear rate by about 30% at a filler content as low as 2 vol.%. For a less wear resistant epoxy system, the absolute gain occurs to be even higher at filler loadings lower than 1 vol.%.[48] Similarly, the 300 nm TiO_2 particles demonstrate their effectiveness in such epoxy systems. Here, the reduction of the specific wear rate is almost 300% (Figure 13). However, the filler content required to achieve this effect is considerably higher (4 to 5 vol.%).

Composites containing both nano- and microparticles possess an even higher wear performance for both types of epoxy matrices. To understand the beneficial effect of calcium silicate ($CaSiO_3$) and its role as internal lubricant, one has to consider the structure of the particles, characterized by silicate layers. Once in contact with the counterpart, the layers may detach and adhere on the metal surface and on the epoxy resin surface. Silicate layers provide protection and may prevent the polymer matrix from severe wear. The microparticles can also protrude out of the matrix and shield it. The steel ring then slides partially on the particle material that is harder than the matrix itself.

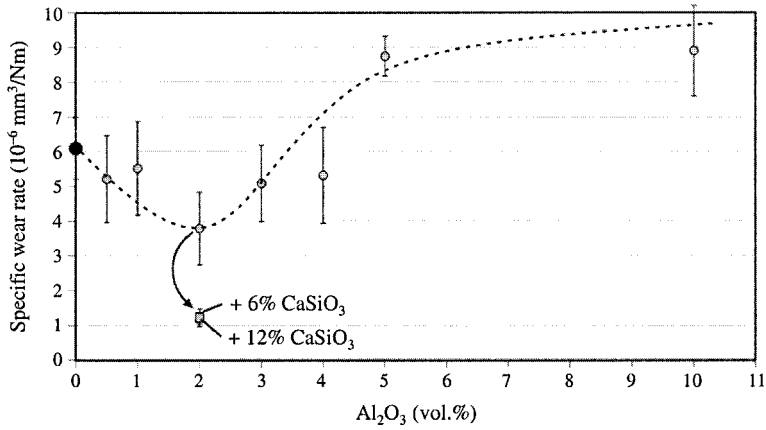

Figure 12. Specific wear rate for an epoxy system with relatively high wear resistance containing Al_2O_3 (13 nm) nanoparticles. Block-on-ring setup, speed 1m/s, pressure 1 MPa, time 20 h.

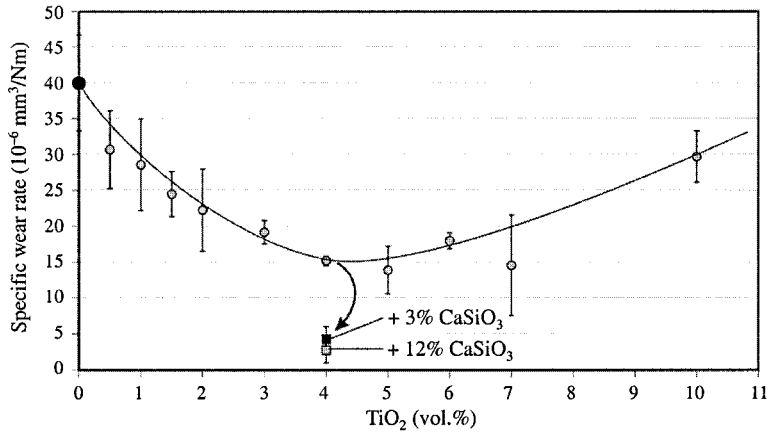

Figure 13. Specific wear rate for an epoxy system with relatively low wear resistance containing TiO_2 (300 nm) nanoparticles. Block-on-ring setup, speed 1m/s, pressure 1 MPa, time 20 h.

The nanoparticles incorporated into the polymer matrix generate remarkable improvements in material characteristics, like modulus, strength and toughness, and especially in wear resistance. The unique material property improvements observed for nanocomposites and presented in this chapter will offer new possibilities for innovative product development in the future.

4 Acknowledgements

Parts of this work, in the field of wear resistant thermosetting coatings development, were supported by the Volkswagen Stiftung, Federal Republic of Germany (Grant No. I/76645).

The development of a mixing technology for nanocomposites was supported by the BMBF (Grant No. 03N5044, Polymeric gradient materials).

5 References

[1] R. Walter, K. Friedrich, V. Privalko, A. Savadori (1997) On modulus and fracture toughness of rigid particulate filled high density polyethylene, *J. Adhesion* **64**, 87.

[2] B. Wetzel, F. Haupert, K. Friedrich, M. Q. Zhang, M. Z. Rong (2001) Mechanical and tribological properties of microparticulate and nanoparticulate reinforced polymer composites, *Proc. 13th ICCM*, Beijing, 1021.

[3] R. Roy (1986) Purposive design of nanocomposites: entire class of new materials, *Mat. Sci. Res.* **21**, 25.

[4] S. Komarneni (1992) Nanocomposites, *J. Mater. Chem.* **2**, 1219.

[5] B. J. Ash, D. F. Rogers, C. J. Wiegand, L. S. Schadler, R. W. Siegel, B. C. Benicewicz, T. Apple (2002) Mechanical properties of Al_2O_3/polymethylmethacrylate nanocomposites, *Polym. Compos.* **23**, 1014.

[6] Y. Ou, F. Yang, Z. Z. Yu (1998) A new concept on the toughness of nylon 6/silica nanocomposite prepared via in situ polymerization, *J. Polym. Sci. Part B: Polym. Phys.* **36**, 789.

[7] R. M. Laine (2001) Organic-inorganic nanocomposites with completely defined interfacial interactions, *Adv. Mater.* **13**, 800.

[8] B. Wetzel, F. Haupert, K. Friedrich, M. Q. Zhang, M. Z. Rong (2002) Impact and wear resistance of polymer nanocomposites at low filler content, *Polym. Eng. Sci.* **42**, 1919.

[9] B. Wetzel, F. Haupert, M. Z. Rong (2002) Nanoparticle-reinforced composites: preparation, structure, properties, *Proc. 8th Natl. Symp. SAMPE*, Deutschland e.V., Kaiserslautern (in German).

[10] M. Hussain, A. Nakahira, K. Niihara (1996) Fracture behavior and fracture toughness of particulate filled epoxy composites, *Mater. Lett.* **26**, 185.

[11] C. B. Ng, L. S. Schadler, R. W. Siegel (1999) Synthesis and mechanical properties of TiO_2-epoxy nanocomposites, *Nanostructured Mater.* **12**, 507.

[12] X. S. Xing, R. K. Y. Li (2004) Wear behavior of epoxy matrix composites filled with uniform sized sub-micron spherical silica particles, *Wear* **256,** 21.

[13] X. Shao, W. Liu, Q. Xue (2004) The tribological behavior in micrometer and nanometer TiO_2 particle-filled poly(phthalazine ether sulfone ketone) composites, *J. Appl. Polym. Sci.* **92**, 906.

[14] Q. Wang, W. Shen, Q. (1997) The friction and wear properties of nanometer SiO_2 filled polyetheretherketone, *Tribol. Int.* **30**, 193.

[15] Q. Wang, W. Shen, Q. Xue, J. Zhang (1998) The friction and wear properties of nanometer ZrO_2-filled poly-etheretherketone, *J. Appl. Polym. Sci.* **69,** 135.

[16] Q. Wang, J. Xu, W. Shen, Q. Xue (1997) The effet of nanometer SiC filler on the tribological behavior of PEEK, *Wear* **209**, 316.

[17] T. Naganuma, Y. Kagawa (2002) Effect of particle size on the optically transparent nanometer-order glass particle-dispersed epoxy matrix composites, *Compos. Sci. Technol.* **62**, 1187.

[18] M. Zhang, P. Singh (2004) Mechanical reinforcement of unsaturated polyester by Al_2O_3 nanoparticles. *Mater. Lett.* **58**, 408.

[19] B. Wetzel, F. Haupert, M. Q. Zhang (2003) Epoxy nanocomposites with high mechanical and tribological performance, *Compos. Sci. Technol.* **63**, 2055.

[20] R. P. Singh, M. Zhang, D. Chan (2002) Toughening of a brittle thermosetting polymer: Effects of reinforcement particle size and volume fraction, *J. Mater. Sci.* **37**, 781.

[21] A. S. Argon, R. E. Cohen (2003) Toughenability of polymers, *Polymer* **44**, 6013.

[22] M. Z. Rong, M. Q. Zhang, H. Liu, H. M. Zeng, B. Wetzel, K. Friedrich (2001) Microstructure and tribological behavior of polymeric nanocomposites, *Ind. Lubr. Tribol.* **53**, 72.

[23] M. Z. Rong, M. Q. Zhang, G. Shi, Q. L. Ji, B. Wetzel, K. Friedrich (2003) Graft polymerization onto inorganic nanoparticles and its effect on tribological performance improvement of polymer composites, *Tribol. Int.* **36**, 697.

[24] K. Niihara, K. Ishizaki, M. Isotani (1994) Effects of nano-sized filler dispersion on mechanical properties of carbon fiber reinforced epoxy composites, *Ceramic Transactions* **44**, 409.

[25] R. Mülhaupt, T. Engelhardt, N. Schall (2001) Nanocomposites – en route to application, *Plast. Eur.* **91**, 63.

[26] H. R. Dennis, D. L. Hunter, D. Chang, S. Kim, J. L. White, J. W. Cho, D. R. Paul (2001) Nanocomposites: the importance of processing, *Plastics Eng.* **1**, 56.

[27] J. W. Cho, D. R. Paul (2001) Nylon 6 nanocomposites by melt compounding, *Polymer* **42**, 1083.

[28] M. Avella, M. E. Errico, S. Martelli, E. Martuscelli (2001) Preparation methodologies of polymer matrix nanocomposites, *Appl. Organometal. Chem.* **15**, 434.

[29] T. Adebahr, C. Roscher, J. Adam (2001) Reinforcing nanoparticles in reactive resins, *Eur. Coatings J.* **4**, 144.

[30] Q. Wang, H. Xia, C. Zhang (2001) Preparation of polymer/inorganic nanoparticles composites through ultrasonic irradiation, *J. Appl. Polym. Sci.* **80**, 1478.

[31] S. S. Park, N. Bernet, S. De La Roche, H. T. Hahn (2003) Processing of iron oxide-epoxy vinyl ester nanocomposites, *J. Compos. Mater.* **37**, 465.

[32] J. Sandler, M. S. P. Shaffer, T. Prasse, W. Bauhofer, K. Schulte, A. H. Windle (1999) Development of a dispersion process for carbon nanotubes in an epoxy matrix and the resulting electrical properties, *Polymer* **40**, 5967.

[33] C. Becker, H. Krug, H. Schmidt (1996) Tailoring of thermomechanical properties of thermoplastic nanocomposites by surface modification of nanoscale silica particles, *Mat. Res. Soc. Symp. Proc.* **435**, 237.

[34] M. Z. Rong, M. Q. Zhang, Y. X. Zheng, H. M. Zeng, R. Walter, K. Friedrich (2000) Irradiation graft polymerization on nano-inorganic particles: an effective means to design polymer based nanocomposites, *J. Mater. Sci. Lett.* **19**, 1159.

[35] G. Carotenuto, L. Nicolais, X. Kuang, Z. Zhu (1995) A method for the preparation of PMMA-SiO2 nanocomposites with high homogeneity, *Appl. Comp. Mater.* **2**, 385.

[36] M. Q. Zhang, M. Z. Rong, S. L. Yu, B. Wetzel, K. Friedrich (2002) Improvement of the tribological performance of epoxy by the addition of irradiation grafted nano-inorganic particles, *Macromol. Mater. Eng.* **287**, 111.

[37] M. Q. Zhang, M. Z. Rong, S. L. Yu, B. Wetzel, K. Friedrich (2002) Effect of particle surface treatment on the tribological performance of epoxy based nanocomposites, *Wear* **253**, 1086.

[38] L. Nielsen, R. Landel (1994) *Mechanical Properties of Polymers and Composites*, Marcel Decker, New York.

[39] L. Nicolais, M. Narkis (1971) Stress-strain behaviour of styrene-acrylonitrile/glass bead composites in the glassy region, *Polym. Eng. Sci.* **11**, 194.

[40] M. Zhang, H. Zeng, L. Zhang, G. Lin, R. K. Y. Li (1993) Fracture characteristics of discontinuous carbon fibre-reinforced PPS and PES-C composites, *Polym. Polym. Compos.* **1**, 357.

[41] C. L. Wu, M. Q. Zhang, M. Z. Rong, K. Friedrich (2002) Tensile performance improvement of low nanoparticles filled polypropylene composites, *Compos. Sci. Technol.* **62**, 1327.

[42] A. C. Roulin-Moloney (1986) *Fractography and Failure Mechanisms of Polymers and Composites*, Elsevier Applied Science, London.

[43] F. Heutling, H. E. Franz, K. Friedrich (1998) Photomicrographic fracture analysis of the delamination propagation in cyclic loaded thermosetting carbon fiber-reinforced composites, *Materialwissenschaften und Werkstofftechnik* **29**, 239 (in German).

[44] J. Lee, A. F. Yee (2001) Inorganic particle toughening I: Micro-mechanical deformations in the fracture of glass bead filled epoxies, *Polymer* **42**, 577.

[45] A. M. Riley, C. D. Paynter, P. M. McGenity, J. M. Adams (1990) Factors affecting the impact properties of mineral filled polypropylene, *Plast. Rubber Proc. Appl.* **14**, 85.

[46] E. Vassileva, K. Friedrich (2003) Epoxy/alumina nanoparticle composites. I. Dynamic mechanical behavior, *J. Appl. Polym. Sci.* **89**, 3774.

[47] S. N. Goyanes, P. G. König, J. D. Marconi (2003) Dynamic mechanical analysis of particulate-filled epoxy resin, *J. Appl. Polym. Sci.* **88**, 883.

[48] J. M. Durand, M. Vardavoulias, M. Jeandin (1995) Role of reinforcing ceramic particles in the wear behaviour of polymer-based model composites, *Wear* **181-183**, 833.

[49] G. Shi, M. Q. Zhang, M. Z. Rong, B. Wetzel, K. Friedrich (2004) Sliding wear behavior of epoxy containing nano-Al_2O_3 particles with different pretreatments, *Wear* **256**, 1072.

Chapter 4

Polyimides Reinforced by a Sol-Gel Derived Organosilicon Nanophase: Synthesis and Structure-Property Relationships

Valery P. Privalko, Tatiana A. Shantalii, Eleonora G. Privalko
Institute of Macromolecular Chemistry, National Academy of Sciences of Ukraine, Kiev, Ukraine

1 Nanocomposites Based on Flexible-Chain Polymers

Polymer *nanocomposites* (PNC) reinforced by relatively small amounts of ultrafine, *nano*-particles (most often clay platelets) proved exceptionally promising engineering materials with unexpectedly high stiffness/toughness ratio, gas-barrier properties, flame retardance, *etc.*[1-3] In view of these outstanding properties, their further development and characterization are, on line with other areas of *nanotechnology*, among the major goals of the materials science in the oncoming millenium.

It is generally recognized[4,5] that a dramatic improvement of the performance of polymer/clay nanocomposites can be only achieved by the application of a special time/cost-consuming technology, ensuring the initial penetration (*intercalation*) of polymer molecules into the interlayer space (*galleries*) of clay tactoids and subsequent forcing these layers apart to the complete delamination (*exfoliation*) of clay nanolayers throughout a polymer matrix (Figure 1). Apparently, the major outcome of this technology is the achievement of a maximum possible area of polymer-filler interaction by elimination of the initial aggregated state of clay nanolayers. However, the structural implications of the observed extraordinary gain in the PNC mechanical properties are still poorly understood; in particular, the issue of the nanoparticle aspect ratio remains essentially unexplored.

The detailed viscoelastic studies of a series of commercial nanocomposites of polyamide 6 (PA6) prepared by melt compounding with organoclay hybrids (organically treated mica-like clay platelets with very high aspect ratio; specific

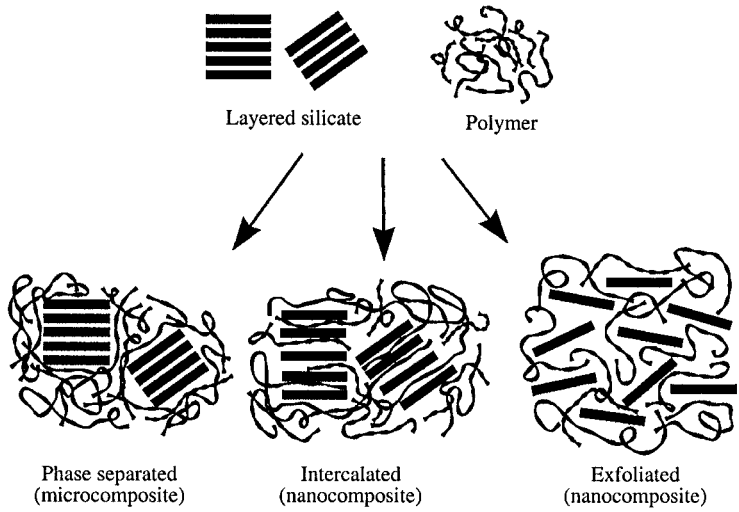

Figure 1. Schematic representation of the different composite types arising from the interaction of layered silicates and polymers.[5]

surface area of 700 m^2/g) have revealed[6,7] the formation of a fairly thick molten boundary interphase (BI) around the nanoparticles, resulting in the build-up of an "infinite cluster" of clay nanoparticles coated with BI at an unusually low clay loading (7.5 wt.%). The structural characterization of these PNC in the solid state by wide-angle X-ray scattering (WAXS) proved[8,9] that the organoclay nanoparticles induced the polymorphic $\alpha \rightarrow \gamma$ transition of PA6, while the matrix crystallinity in the PNC remained essentially unchanged (polymorphic transitions in polymers are discussed also in Chapter 5). Small-angle X-ray scattering (SAXS) experiments failed to detect the well resolved reflection close to $q \approx 0.62$ nm^{-1} (corresponding to the Bragg's periodicity $D \approx 10.1$ nm) of the neat PA6 due to the high intensity of the poly(ethylene naphthalate) (PEN) scattering in the same range. These results suggested a significant increase of structural heterogeneity of the PNC due to the appearance of new, strongly scattering entities (presumably, polymer nanoparticle interfaces and microvoids) with broad size distributions. The Young's moduli, E, and the linear thermal expansion coefficients, α_L, of the PNC derived from stretching calorimetry in the range of elastic (reversible) deformations proved to be several-fold higher and lower, respectively, than theoretically expected. These data were considered[8-10] as an evidence of the quite significant contribution of pre-stressed tie-chains in the interlamellar space of the PA6 matrix to the thermoelastic behavior of PNC in the solid state. Moreover, the substantial gain in the internal energy increments in the range of inelastic (irreversible) deformations for PNC compared to neat PA6 was an indication of fairly strong interactions at the polymer/organoclay interface, ruling out the possibility of eventual debonding effects.[8-10]

The assessment of the importance of the nanoparticle aspect ratio was among the main issues in subsequent studies of a PNC series prepared by melt compounding of isotactic polypropylene (PP) with essentially isometric (aspect ratio ≈ 1) nanoparticles of the standard pyrogenic silica (average particle size $<d> \approx 7$ nm), the surface of the latter being pregrafted by γ-irradiation with styrene to minimize the eventual agglomeration effects.[10-13] Viscoelastic studies of these PNC in the melt revealed surprising similarities with the salient rheological features of the PA6/organoclay hybrids (in particular, the formation of an "infinite cluster" of organosilica nanoparticles coated with BI at a filler volume content as low as 4.68%[10-12]). These data highlighted the structural significance of the ratio of the mean thickness of a polymer interlayer between neighboring nanoparticles, $<L>$, to the mean radius of gyration of a polymer coil, $<R_g>$. In the range of low filler loadings characterized by large scaled distances, $<L>/<R_g> \gg 1$, all PNC melts behaved as Newtonian liquids in which the self-diffusion of macromolecular coils was, however, slowed down. In this context, the eventual onset of plastic yield phenomena was regarded as an experimental evidence of the shear-resistant, infinite cluster of nanoparticles when the scaled distance approached the "critical" value, $<L>/<R_g> \leq 1$ (Figure 2a).[10-12] Within the frame of a standard definition,[14]

$$<L> \approx <d> [(\varphi_{max}/\varphi)^{1/3} - 1] \quad (1)$$

(where φ_{max} is the fraction with maximum packing), it is clear that the latter criterion of a structural *mesoscale*, $<L>/<R_g> \rightarrow 1$, can be met by three alternative approaches.

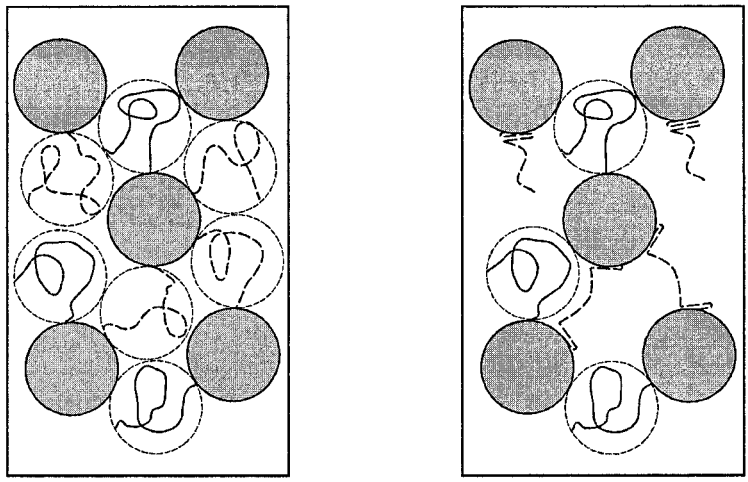

(a) (b)

Figure 2. Schematic representation of the inner structure of an infinite cluster in the melt (a) and in the solid state (b): nanoparticles (shaded circles); grafted PS chains (solid lines); PP chains (broken lines).[10]

The first (traditional) one relies on the continuous increase of the filler volume fraction φ (keeping both $<d>$ and $<R_g>$ constant), while the second and the third (largely neglected so far) approaches assume the continuous increase of the polymer molar mass (hence, $<R_g>$) and the decrease of the filler particle size, $<d>$. Since in Eq. (1), φ and $<d>$ are of the one-third and first power, respectively, it becomes obvious that the two latter approaches to the polymer structural mesoscale in a PNC should be much more effective (see Figure 1, Chapter 3).[13,15]

The structural features, as well as the thermoelastic behavior of PP/organosilica PNC in the solid state,[10,16] also turned out strikingly similar to those of the PNC of PA6/organoclay hybrids (*e.g.*, considerable increase in the Young's moduli together with small thermal expansivities, in the limiting strains for elastic behavior and in the strains at break, compared to reasonable theoretical predictions, absence of debonding at the polymer/organosilica interface, *etc.*). These results, combined with the X-ray diffraction data, were explained[10-13,16] by a model assuming that a non-negligible portion of polymer chains in the melt would be anchored by each end to the available adsorption-active sites of two different neighboring nanoparticles (Figure 2a). Presumably, during subsequent cooling a simultaneous lamellar growth at fixed positions of the same chains on adjacent nanoparticles would end up not only by a considerable extension of tie-chains, but also by a drop of the local packing density in the interlamellar space (Figure 2b).

2 Nanocomposites Based on Semi-Rigid Chain Polymers (Polyimides)

In the light of the above considerations, it seems reasonable to conclude that a significant improvement of, say, the mechanical performance of thermoplastic crystallizable polymers can be expected not only for the PNC containing well exfoliated organoclay platelets of very high aspect ratio, but also for the PNC filled with more common, isometric nanoparticles (by the condition of preliminary surface treatment of the latter with organic substances to avoid significant agglomeration effects). These arguments cannot be, however, readily extended to the case of semi-rigid non-crystallizable polymers, such as polyimides (PI). In fact, melt compounding with appropriately surface-treated nanoparticles can be definitely ruled out; the sol-gel technology ensuring the homogeneous, *in situ* generation of inorganic nanoparticles (most often silica and its derivatives) throughout a continuous polymer matrix is an attractive alternative route to the synthesis of PNC with improved performance.[17-19] Obviously, a further improvement of the mechanical properties was not the major concern in the preparation of PNC based on high-modulus, rigid-chain PI; however, these PNC containing the sol-gel derived

nanoparticles proved competitive to commercial PI packaging materials due to their better gas permeation, higher heat resistance, better flame retardance, *etc.*[20-24]

So far, the potential of PI-based PNC as low dielectric permittivity materials, another traditional field of PI application,[25,26] remained uncertain mainly due to the higher intrinsic dielectric permittivity of bulk silica ($\varepsilon' = 3.8\text{-}4.0$ at room temperature[27,28]) compared to that of neat PI ($\varepsilon' = 2.8\text{-}3.2$[25,26]). Somewhat unexpectedly, values of $\varepsilon' = 2.5\text{-}2.8$ were reported for several series of PI-based PNC at relatively high contents of sol-gel derived, silica-like nanoparticles.[29-31] These results, combined with the relevant morphological data, evidenced the striking difference between the inner structure of bulk silica and of the aggregates of sol-gel derived nanoparticles. Thus, it seemed interesting to gain a further insight into the structure-property relationships for such PNC in order to explore their potential as low dielectric permittivity materials.

2.1 *In Situ* Generation of an Organosilicon Nanophase

As described in detail elsewhere,[32,33] the preparation of PI-based PNC involved the following steps: (i) synthesis of a polyamic acid with ethoxysilane end-groups (PAAS), (ii) preparation of the nanocomposite precursors by the addition of the required amount of methyl triethoxysilane (MTS), (iii) MTS hydrolysis in the cast NCP films, and (iv) imidization of the PAAS to the corresponding polyimide by stepwise heating of the thin NCP films for 2 h at each of the following temperatures: 60, 100, 120, 150, 200, and 250 °C and by post-cure for 5 h at 300-315 °C.

The anticipated (ideal) structure of the final product can be represented schematically as follows:

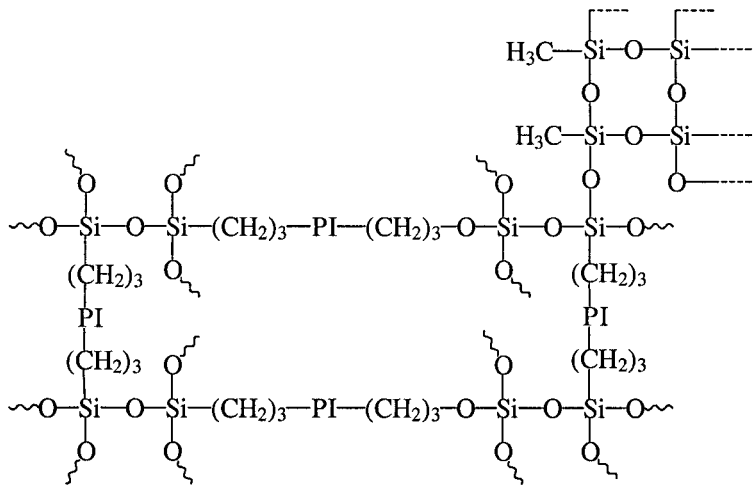

where

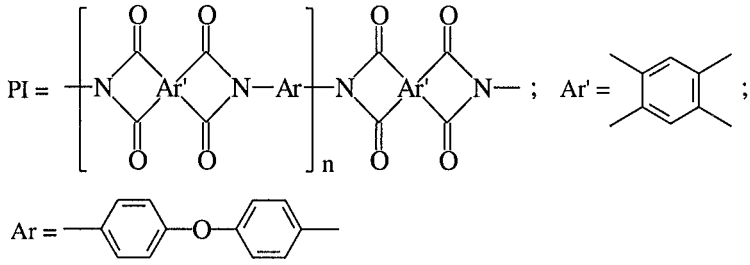

2.2 Structural Characterization

The diffuse maximum at $2\theta \approx 18.7°$ and the shoulder at $2\theta \approx 26.3°$ on the WAXS diagram for the pristine PI (Figure 3a) evidenced its non-crystalline (glassy) state with small-scale order parameters of 0.47 nm and 0.34 nm (presumably, characteristic interchain and intrachain spacings, respectively). The essentially similar WAXS patterns for the PNC imply little influence of the organosilicon nanophase on the small-scale structure of PI.

No evidence of a well developed long-range order could be detected from the SAXS curve of pristine PI, although a slight increase of the scattering intensity $I(q)$ at $2\theta < 1°$ (Figure 3b) suggested the existence of some structural heterogeneity. The SAXS patterns for the PNC were essentially similar; moreover, the SAXS invariants $Q = \int q^2 I(q)\,dq$ (calculated by integration in the interval $0 < q < 4$ nm^{-1}) also turned out almost composition-independent. Bearing in mind the physical significance of Q as a measure of the mean-square electron density fluctuations,

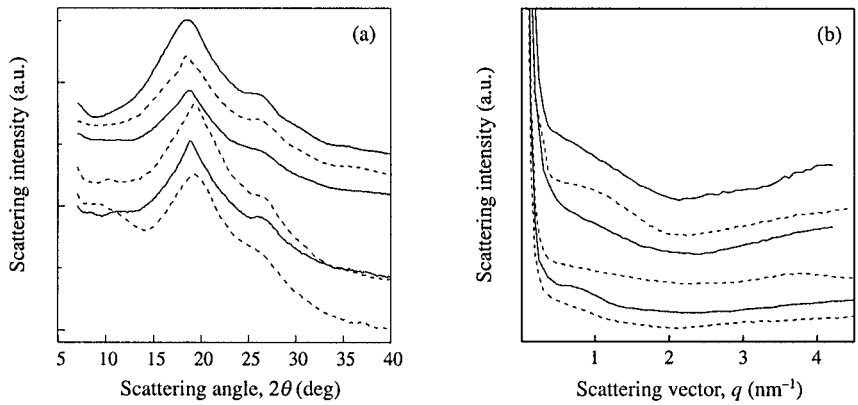

Figure 3. WAXS (a) and SAXS (b) patterns of samples S-0, S-8, S-16, S-20, S-40, and S-50 (from top to bottom). The curves are shifted vertically to avoid overlaps.[34]

$<\Delta\rho^2>$, these data implied little (if any) difference between $<\Delta\rho^2>$ of the pristine PI and of the PNC, respectively. These results evidence the loose internal structure of the organosilicon nanophase in the PI matrix.[34]

2.3 Water Uptake

As expected for diffusion-controlled processes, in all samples studied the initial water uptake, w, during the first 3 h increased linearly with $t^{1/2}$ up to a point with coordinates w^* and t^*, above which w continued to increase at a significantly lower, composition-independent rate to the final value, w_{inf} (corresponding to t_{inf} = 28 h). Formally, the apparent two-stage pattern of the w *vs.* $t^{1/2}$ plots is consistent with the dual-sorption model for glassy polymers, which assumes an initial fast filling by water molecules of the pre-existing microcavities (*i.e.*, loosely packed regions), and a subsequent slow water penetration into the defect-free (*i.e.*, densely packed) continuous matrix. The experimental data at $t < t^*$ were treated according to the standard relationship,

$$w/w_{inf} = 4(Dt/\pi d^2)^{1/2}, \quad (2)$$

to derive the apparent diffusion coefficients, D (here d is the film thickness). As can be seen in Table 1, the apparent water diffusivities D (estimated with a relative error of *ca.* 25%) were smaller by about an order of magnitude than those for the soft phase of segmented polyurethanes and tended to increase with the MTS content; the values of w_{inf} for the PNC were always higer than that for the pristine PI.

These results[32,33] support the above X-ray evidence of a rather loose inner structure of the organosilicon nanophase.

Table 1. Selected properties of nanocomposites.

*Sample**	ρ (g cm^{-3})	$10^{12}D$ (m^{2}s^{-1})	w_{inf} (%)	T_g (°C)	E (GPa)	σ_b (MPa)	ε_b (%)
S-0	1.3782	0.65	4.2	405	1.78	70.9	28.9
S-8	1.3771	1.6	5.8	420	2.07	73.6	14.0
S-16	1.3965	2.0	5.3	...	...	...	...
S-20	1.3899	...	...	395	2.04	75.5	18.1
S-40	1.3461	...	...	...	...	...	...
S-50	1.3614	2.2	4.7	400	1.75	61.0	12.6
S-60	1.3748	...	...	...	...	...	...
S-80	1.3823	2.5	4.8	400	1.82	62.5	13.0
S-100	1.3722	...	...	...	...	...	...
S-120	...	2.9	4.5	390	1.44	53.8	10.3

* S - MTS content

2.4 Thermomechanical Performance

The normalized thermogravimetric (TGA) traces for all samples exhibited the initial slight (a few percent) deflections at temperatures up to about 180 °C (presumably associated with evaporation of the traces of water and/or solvents) followed by plateaux extending over broad (*ca.* 300 °C) temperature ranges (Figure 4). The final accelerated weight losses set on at $T_{deg} \approx 580$ °C for the pristine PI and at $T_{deg} \approx 550$ °C for all PNC samples (except for S-8 and S-20, for which $T_{deg} \approx 520$ °C was observed); as expected, the char residues tended to increase with the MTS content. These data suggest that the thermal stability of the PNC remained almost the same as that of the pristine PI.

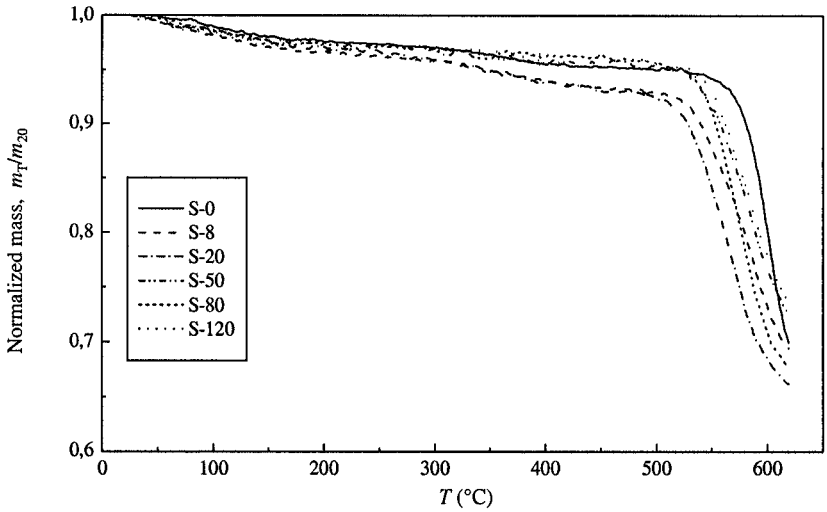

Figure 4. Normalized TGA traces for selected samples.[33]

The E^* *vs.* T plots in Figure 5a show that the complex moduli in the glassy state smoothly decreased from *ca.* 2.6 GPa at room temperature for all samples to *ca.* 1 GPa at about 300 °C. The almost composition-independent moduli in the glassy state imply similar values of E^* for both the pristine PI and the organosilicon nanophase. As usual, the onset of the main (α-) relaxation at T_g manifested itself as an abrupt decrease of E^*; however, the rubbery plateau moduli above T_g sharply increased with the MTS content. Taking into account the almost composition-independent moduli below T_g, the latter result suggested a significant reinforcement of the PI matrix in the rubbery state by the organosilicon nanophase. The tan δ *vs.* T plots (Figure 5b) exhibit weak relaxations in the glassy state at $T_g \approx 90$ °C and prominent main relaxation maxima at $T_g \approx 400$ °C for all samples except for S-8 ($T_g \approx 420$ °C, Table 1). As could be expected, the heights of the tan δ maxima at T_g decreased with the rise in the MTS content (S).

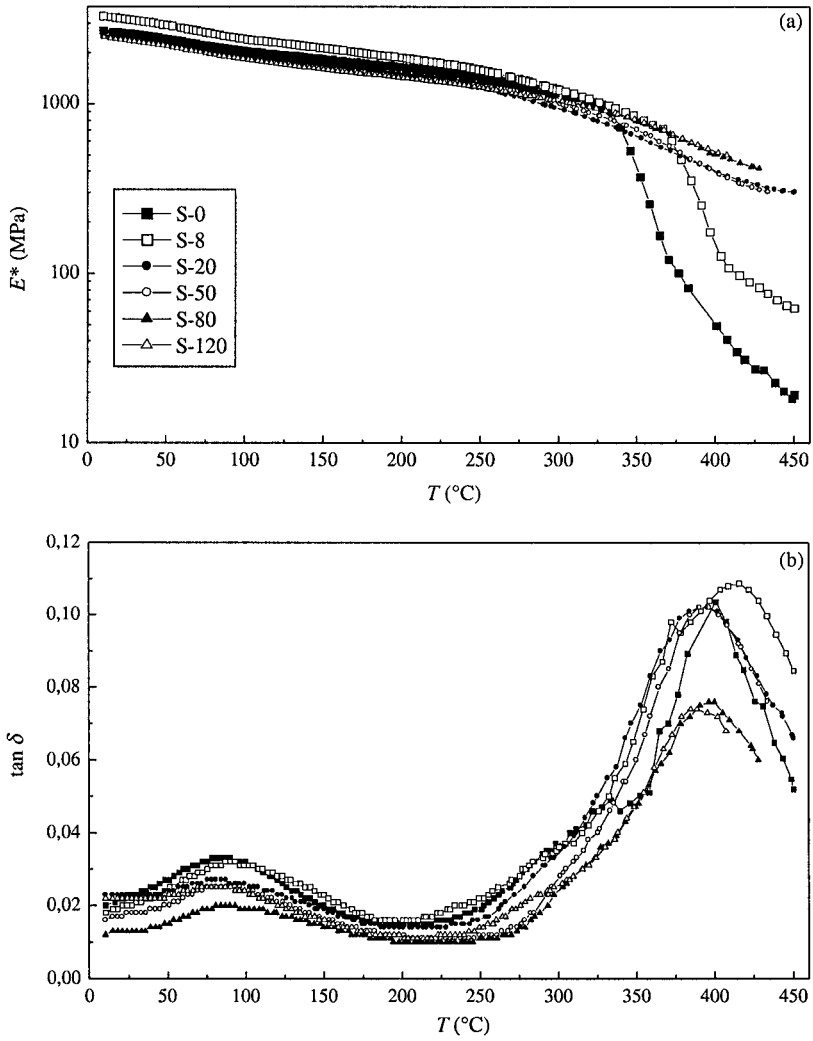

Figure 5. Complex Young's moduli (a) and mechanical loss tangents (b) for selected samples.[33,34]

The absence of yield-point maxima on stress-strain plots obtained at room temperature and the early mechanical failures observed with all samples studied were typical of the stretching of brittle glassy polymers far below their glass transition temperatures, T_g. As expected, the quasi-static Young's moduli E (Table 1) were always lower (by about 20-30%) than the dynamic moduli E^*; nevertheless, their composition dependence was essentially similar. The stresses, σ_b, and strains, ε_b, at break for the PNC (Table 1) also turned out comparable to (albeit slightly smaller than) those for the pristine PI.[33,34]

2.5 Dielectric Properties

A single maximum in the TSDC traces in the limited temperature range of our measurements for all samples studied presumably referred to the sub-glass (γ-) relaxation by the non-cooperative, localized motions of the imide cycle. The γ-peak temperatures, T_γ, in the PNC tended to decrease, while the relaxation strengths, $\Delta\varepsilon_\gamma$, increased with the MTS volume content, φ. Moreover, γ-relaxations could also be detected as maxima on the dielectric loss ε'' *vs.* temperature diagrams at different frequencies; the corresponding Arrhenius plots proved to be fairly linear. Table 2 shows that both the apparent activation energies for γ-relaxation, $\Delta E_\gamma/k$, and the pre-exponential factors, f_0, tended to decrease with the rise in the MTS content.[35]

Table 2. Parameters of the γ-relaxation.

PAAS/MTS mass ratio	T_γ(K)	$\Delta\varepsilon_\gamma$	$\Delta\varepsilon_{\gamma m} = \Delta\varepsilon_\gamma/(1-\varphi)$	$10^{-3}\,\Delta E_\gamma\ k^{-1}$ (K)	$\log f_0$ (Hz)
100/0	146	0.169	0.169	5.7	14.1
100/3	141	0.277	0.284	...	...
100/8	141	0.273	0.288	...	...
100/16	140	0.262	0.284	5.3	13.6
100/40	139	...	...	...	...
100/60	133	0.225	0.281	4.9	13.4
100/100	135	0.228	0.318	4.7	12.2
100/120	123	0.234	0.344	4.2	12.2

The above data are a clear evidence of the facilitated local mobility of the imide cycles in the PI matrix of PNC, which could be explained by a looser molecular packing of the PI chain fragments adjacent to the organosilicon nanophase. Obviously, this effect (*i.e.*, the apparent density decrease in the PI matrix) should become stronger at higher MTS contents; however, the reliable estimate of its magnitude remains the object of further studies.

As can be seen in Table 3, the values of ε'(at a fixed frequency f= 1 kHz) for the PNC decreased with the rise in the MTS content. This latter result was consistent with other relevant data[23-25] and was regarded as a further evidence of the invalidity of the reasonable expectation of an increase in dielectric permittivity from $\varepsilon' \approx 3.18$ for the precursor (PAAS) to $\varepsilon' = 3.8$-4.0 for the bulk silica.

A more quantitative assessment of the above data was attempted[35] within the frame of several theoretical treatments of dielectric permittivity-composition relationships in composite materials, by the implicit assumption that the dielectric permittivities of the matrix and of spherical inclusions (ε'_m and ε'_i, respectively)

Table 3. Experimental and calculated dielectric permittivities of nanocomposites.

PAAS/MTS mass ratio	ε'(at 1 kHz)	ε_i *derived by Eq.*			α
		(1)	(2)	(3)	
100/0	3.18	-	-	-	-
100/3	3.16	2.45	2.47	2.24	2.05
100/16	3.07	1.68	1.81	1.78	0.01
100/40	3.01	1.96	1.95	1.90	0.57
100/60	2.94	1.93	1.93	1.89	0.49
100/100	2.94	2.27	2.15	2.11	1.54
100/120	2.91	2.27	2.15	2.11	1.58

remain composition-independent, so that the volume fraction of inclusions, φ, and the fitting parameter, α, are the only factors responsible for the composition dependence of the dielectric permittivity of a composite, ε'. Therefore, although our data suggest that both a looser molecular packing of the PI chain fragments adjacent to the organosilicon nanophase (see the preceding section) and a loose inner structure of its spatial aggregates[33,34] might be responsible for a non-additive decrease of the experimental dielectric permittivity values for the PNC (Table 3); the values of ε' were treated by three different equations to derive the apparent values of ε'_i for the organosilicon nanophase (assuming ε'_m = const ≈ 3.18 for PI).

The apparent values of ε'_i estimated by different theoretical models (Table 3) exhibited a similar dependence on the PNC composition, remaining considerably lower than the dielectric permittivity of bulk silica. This result was explained[35] by the assumtion that the organosilicon nanophase is made up of nanoparticles of silica (ε'_m = 3.8-4.0) fused together into loose spatial aggregates with a considerable fraction, φ_e, of empty inner pockets ($\varepsilon'_i \approx 1$).

3 Conclusions

The crosslinked organosilicon nanophase formed by the sol-gel procedure possesses a rather loose inner structure, characterized by an enhanced water diffusivity and by mean-square electron density fluctuations and dynamic elasticity moduli comparable to those of the pristine, glassy PI.

The static mechanical and dynamic thermomechanical properties of the nanocomposites in the glassy state remain almost the same as those of the pristine PI, while a significant reinforcement effect is observed in the rubbery state above the main relaxation at T_g.

Both a looser molecular packing of the PI chain fragments adjacent to the organosilicon nanophase and a loose inner structure of its spatial aggregates are

believed to be responsible for the non-additive decrease of the experimental dielectric permittivity values for the PNC.

Organosilicon nanophase-reinforced polyimides may have a reasonably good potential as low dielectric permittivity materials.

4 Acknowledgements

Thanks are due to Drs. I. L. Karpova, V. Yu. Kramarenko, V. I. Shtompel, A. G. Charnetskaya, O. I. Gryshchuk, and to Ms. K. S. Dragan for their help in the experiments.

5 References

[1] Y. Fukushima, S. Inagaki (1987) Synthesis of an intercalated compound of montmorillonite and 6-polyamide, *J. Inclusion Phenom.* **5**, 473.

[2] P. C. LeBaron, Z. Wang, T. J. Pinnavaia (1999) Polymer-layered silicate nanocomposites: an overview, *Appl. Clay Sci.* **15**, 11.

[3] T. J. Pinnavaia, G. W. Beall (2001) *Polymer-Clay Nanocomposites*, John Wiley&Sons.

[4] E. P. Giannelis (1996) Polymer layered silicates nanocomposites, *Adv. Mater.* **8**, 29.

[5] M. Alexandre, Ph. Dubois (2000) Polymer-layered silicate nanocomposites: preparation, properties and uses of a new class of materials, *Mater. Sci. Eng.* **R28**, 1.

[6] V. M. Karaman, V. F. Shumsky, E. G. Privalko, V. P. Privalko, B. Lehmann, K. Friedrich (2003) Melt viscoelasticity of polyamide 6/organoclay nanocomposites, *Polym. Polym. Compos.* **11**, 663.

[7] V. M. Karaman, V. F. Shumsky, E. G. Privalko, V. P. Privalko, B. Lehmann, K Friedrich (2003) Viscoelastic behaviour of polyamide 6/organoclay nanocomposites in the melt state, *Phys. Condens. Polym. Syst.* (Rivne), in press.

[8] V. M. Karaman (2003) Structural and thermoelastic characterization of polyamide 6/organomineral nanocomposites, *5th Ukrainian Polym. Conf. Young Scientists*, Kiev, Abstract book, p. 48.

[9] V. P. Privalko, V. M. Karaman, E. G. Privalko, B Lehmann, K Friedrich (2003) Structure and thermoelasticity of polyamide 6/organoclay nanocomposites, *J. Macromol. Sci. Phys.* **B42**, 975.

[10] V. M. Karaman (2003) Thermo- and viscoelasticity of thermoplastic nanocomposites on the basis of polypropylene and polyamide 6, PhD Thesis, Institute of Macromolecular Chemistry, National Academy of Sciences of Ukraine, Kiev.

[11] V. F. Shumsky, Yu. S. Lipatov, E. G. Privalko, V. M. Karaman, V. P. Privalko, R. Walter, K. Friedrich, M. Z. Rong (2001) Rheological characterization of polypropylene-based nanocomposites in the melt state, *Proc. Natl. Acad. Sci. Ukraine*, No. 12, 130.

[12] V. F. Shumsky, E. G. Privalko, V. M. Karaman, V. P. Privalko, R. Walter, K. Friedrich, M. Q. Zhang, M. Z. Rong (2001) Viscoelastic behavior of polypropylene-based nanocomposites in the melt state, *Adv. Compos. Lett.* **10**, 191.

[13] V. P. Privalko, V. F. Shumsky, E. G. Privalko, V. M. Karaman, R Walter, K. Friedrich, M. Q. Zhang, M. Z. Rong (2002) Viscoelasticity and flow behavior of irradiation grafted nano-inorganic particle filled polypropylene composites in the melt state, *Sci. Technol. Adv. Mater.* **3**, 111.

[14] V. P. Privalko, V. V. Novikov (1995) *The Science of Heterogeneous Polymers*, John Wiley & Sons, Chichester.

[15] B. Wetzel, F. Haupert, K. Friedrich, M. Z. Rong (2003) Mechanical and tribological characterization of thermoplastic and thermosetting polymers reinforced with ceramic nanoparticles, *1st Int. Workshop Polym. & Compos.*, IVW, Kaiserslautern.

[16] V. P. Privalko, V. M. Karaman, E. G. Privalko, R. Walter, K. Friedrich, M. Q. Zhang, M. Z. Rong (2002) Structure and thermoelasticity of irradiation grafted nano-inorganic particle filled polypropylene composites in the solid state, *J. Macromol. Sci. Phys.* **41B**, 485.

[17] J. E. Mark, C. Y.-C. Lee, P. A. Bianconi (1995) *Hybrid Organic-Inorganic Composites,* American Chemical Society, Vol. 585.

[18] H. Schmidt (2000) Sol-gel derived nanoparticles as inorganic phases in polymer-type matrices, *Macromol. Symp.* **159**, 43.

[19] G. Kickelbick (2003) Concepts for the incorporation of inorganic building blocks into organic polymer on a nanoscale, *Progr. Polym. Sci.* **28**, 83.

[20]. C. Joly, S. Goizet, J. C. Schrotter, J. Sanchez, M. Escoubes (1997) Sol-gel polyimide-silica composite membrane: gas transport properties, *J. Membr. Sci.* **130**, 63.

[21] C. J. Cornelius, E. Marand (2002) Hybrid silica-polyimide composite membranes: gas transport properties, *J. Membr. Sci.* **202**, 97.

[22] Y. Chen, J. O. Iroh (1999) Synthesis and characterization of polyimide/silica hybrid composites, *Chem. Mater.* **11**, 1218.

[23] Z. Ahmad, J. E. Mark (2001) Polyimide-ceramic hybrid composites by the sol-gel route, *Chem. Mater.* **13**, 3320.

[24] J. Liu, Y. Gao, F Wang, M Wu (2000) Preparation and characterization of nonflammable polyimide materials, *J. Appl. Polym. Sci.* **75**, 384.

[25] M. I. Bessonov, M. M. Koton, V. V. Kudryavtsev, L. A. Laius (1987) *Polyimides – Thermally Stable Polymers,* Plenum Press, New York.

[26] D. Wilson, H. D. Stenzenberger, P. M. Hergenrother (1990) *Polyimides*, Blackie, Glasgow and London.

[27] J. J. Senkevich, S. B. Desu (1998) Poly(chloro-*p*-xylylene)/SiO_2 multilayer thin films deposited near-room temperature by thermal CVD, *Thin Solid Films* **322**, 148.

[28] M. G. Todd, F. G. Shi (2002) Validation of a novel dielectric constant simulation model and the determination of its physical parameters, *Microelectronics J.* **33**, 627.

[29] J. L. Hedrick, H.-J. Cha, R. D. Miller, D. Y. Yoon, H. R. Brown, S. Srinivasan, R. D. Pietro, R. F. Cook, J. P. Hummel, D. P. Klaus, E. G. Liniger, E. E. Simonyi (1997) Polymeric organic-inorganic hybrid nanocomposites: preparation of polyimide-modified poly(silsesqui-oxane) using functionalized poly(amic acid alkyl ester) precursor, *Macromolecules* **30**, 8512.

[30] M.-H. Tsai, W.-T. Whang (2001) Low dielectric polyimide/poly(silsesquioxane)-like nanocomposite material, *Polymer* **42**, 4197.

[31] W.-Ch. Liu et al. (2002) The structural transformation and properties of spin-on poly(silsesquioxane) films by thermal curing, *J. Non-Cryst. Solids* **311**, 233.

[32] T. A. Shantalii, I. L. Karpova, K. S. Dragan, E. G. Privalko, V. P. Privalko (2002) Synthesis and physical characterization of polyimides reinforced with the sol-gel

derived nanoparticles, *Int. Conf. "Polymerwerkstoffe'2002"*, Halle, Abstract book, pp. 171-172.

[33] T. A. Shantalii, I. L. Karpova, K. S. Dragan, E. G. Privalko, V. P. Privalko (2003) Synthesis and thermomechanical characterization of polyimides reinforced with the sol-gel derived nano-particles, *Sci. Technol. Adv. Mater.* **4**, 115.

[34] V. P. Privalko, T. A. Shantalii, I. L. Karpova, K. S. Dragan, E. G. Privalko (2003) Structure-property relationships for polyimides reinforced with the sol-gel derived organo-silicon nanoparticles, *Polym. Polym. Compos.* **11**, 213.

[35] V. Yu. Kramarenko, T. A. Shantalii, I. L. Karpova, K. S. Dragan, E. G. Privalko, V. P. Privalko, D. Fragiadakis, P. Pissis (2004) Polyimides reinforced with the sol-gel derived organo-silicon nanophase as low dielectric permittivity materials, *Polym. Adv. Technol.*, in press.

Chapter 5

Layered Silicate/Rubber Nanocomposites *via* Latex and Solution Intercalations

Siby Varghese
Rubber Research Institute of India, Kottayam, Kerala, India

József Karger-Kocsis
Institut für Verbundwerkstoffe GmbH (Institute for Composite Materials), Kaiserslautern University of Technology, Kaiserslautern, Germany

1 Concept of Nanoreinforcement

Nowadays, composite materials have replaced traditional ones in a variety of applications. Lightweight coupled with enhanced properties are the main reasons for their market acceptance and growth, and the optimization of their performance is a challenge worldwide. The high aspect ratio of the reinforcing particle and its adhesion to the matrix are of great importance, because they control the final properties of the composites. Polymer/clay nanocomposites meet these requirements due to the shape (platelet, disc) and nanometer-scale dispersion of the clay layers in the polymeric matrix. This type of composites has raised significant scientific interest due to the improved physical properties that can be achieved by adding a small fraction of clay (< 10 wt. %) into the polymer matrix.[1-5]

Best performance of the polymeric nanocomposites is achieved when the silicate layers are dispersed in the polymer matrix without agglomeration. An essential step in the preparation of a nanocomposite is the delamination of the layered silicates (LS), which is usually termed *exfoliation* in the literature. Both the layer thickness and the space (galleries) between the layers are of *ca.* 1 nm. The galleries are occupied by hydrated cations, which counterbalance the negative charge of the layers generated by the isomorphic substitution of some atoms in the silicate crystals.

The environment of the galleries is hydrophilic and thus inappropriate for the hydrophobic macromolecular chains to penetrate therein. The replacement of the inorganic cations by organic onium ions (surfactant, intercalant, tenside) overcomes this inconvenience. The cationic head of, *e.g.*, an alkylammonium compound is tethered to the layers *via* coulombic interactions, leaving the aliphatic tail to hover between the layers. The longer the surfactant chain length and the higher the charge density of the clay, the further apart the clay layers will be forced.[6] The presence of these aliphatic chains in the galleries renders organophilic the originally hydrophilic silicate. A value that characterizes each LS is the cation exchange capacity (CEC), expressed in meq/100 g, referring to the moderate negative charge of the clay layer surface. The effect of CEC has been checked for different types of clay.[7] It was claimed that a well exfoliated silicate structure can be obtained in polymers when layered silicates of optimum CEC (*ca.* 90 meq/100 g) are rendered organophilic.

Various models have been developed to trace the parameters forcing the macromolecular chain in the silicate layers and then causing their delamination.[8-11] The interplay of entropic and energetic factors determines the outcome of polymer intercalation/exfoliation. The entropy decrease due to confinement of the polymer molecules when entering between the galleries is overcompensated by the increase in the entropy of the tethered chains of the surfactant while the silicate layers are moving apart prior to their final separation. In addition, energetically favored interactions between the surfactant and polymer molecules may yield a negative mixing enthalpy. It should be noted that a molecular dispersion requires that the Gibbs' free energy of mixing become negative.

Vulcanized rubbers are usually reinforced by carbon black and inorganic fillers. Carbon blacks are excellent in reinforcement owing to the strong interaction with rubbers, but their presence often reduces the processability of rubber compounds, especially at high volume loadings. On the other hand, minerals of various shapes (*e.g.*, fibrous, platy) are suitable for rubber filling, but they have a poor interaction with rubbers ("inactive fillers"). Therefore, it is of paramount interest to disperse LS in rubber on a nanometer level. The required level of reinforcement in rubbers can be achieved at very low LS loadings, which offers easier processing without any property deterioration compared to traditional "active" fillers.

2 Production of Rubber/Clay Nanocomposites

Polymer/silicate nanocomposites are currently prepared in the following ways: (i) *in situ* polymerization, (ii) intercalation of the polymer from a solution (solution intercalation), (iii) direct intercalation of the molten polymer (melt intercalation), and (iv) sol-gel technology.

The preparation of rubber/clay nanocomposites slightly differs from the above scenario, since some methods are not applied (*in situ* polymerization, sol-

gel route) and rubbers are available in various forms (latex, solution, solid), which offer additional possibilities (*e.g.*, latex compounding). Figure 1 shows a scheme of the possible production routes of thermoset rubber/layered silicate nanocomposites (the methods indicated by dotted line are not yet practiced). The melt intercalation method which is strongly favored nowadays[12] is not discussed in this chapter.

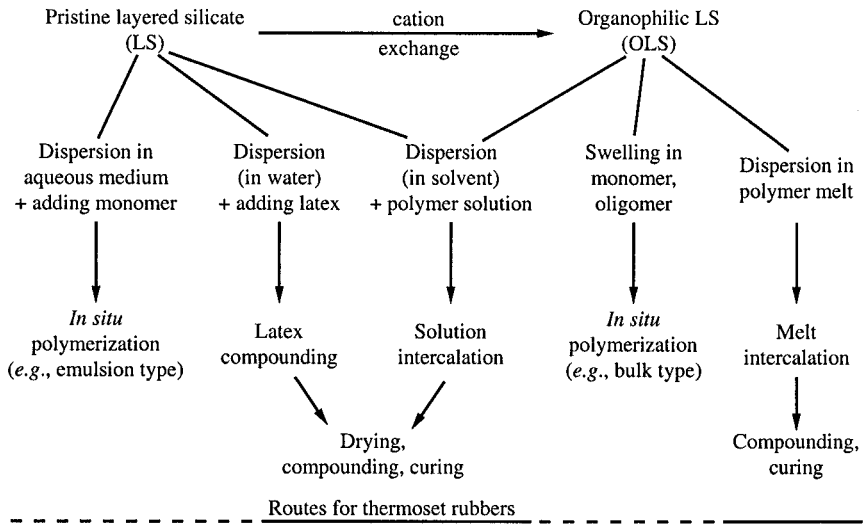

Figure 1. Scheme of the production routes to layered silicate/thermoset rubber compounds.

2.1 Latex Intercalation

The modification of the clay by organic molecules ("organophilization") is not always a necessary step in the production of polymer nanocomposites. In general, two types of organic/inorganic hybrids are distinguished: intercalated (polymer chains are diffused between the silicate layers preserving, however, some short-range order of the latter) and exfoliated (in which the silicate layers, *ca.* 1 nm thick, are fully delaminated and dispersed in the polymer matrix). Pristine layered silicates usually contain hydrated Na^+ or K^+ ions. In aqueous dispersions, the clay "swells" (*i.e.*, its layers are separated due to hydration of the interstitial cations), which facilitates the intercalation of the rubber molecules when the clay slurry is mixed with latex (Figure 1).

2.1.1 Nanocomposites from Rubber Latex

Since most of the rubbers exist in latex form and layered silicates can be easily dispersed in water, the production of nanocomposites from latices is rather

easy. Here the latex should be blended with the clay/water slurry without causing coagulation of the rubber. Wang and coworkers produced nanocomposites from styrene/butadiene rubber (SBR) and styrene/vinylpyridene latices by coagulating them afterwards.[13,14] Though they noticed some level of intercalation, the properties of the outcoming nanocomposites were not promising.

Varghese and Karger-Kocsis[15] tried the conventional latex compounding technique for producing nanocomposites from natural rubber (NR) latex. Two types of layered silicates were selected: sodium fluorohectorite (LS of synthetic origin showing an extremely high aspect ratio) and sodium bentonite (LS of natural origin). Dispersions of the layered silicates were prepared and compounded with NR latex along with dispersions of other latex chemicals for sulfuric vulcanization. A natural rubber composite loaded with an inert filler (non-layered clay) was used as reference material and the major properties of the vulcanized films were established. There was a slight increase in the moduli at various elongations for all composites except for the fluorohectorite-modified one (Figure 2a). On the

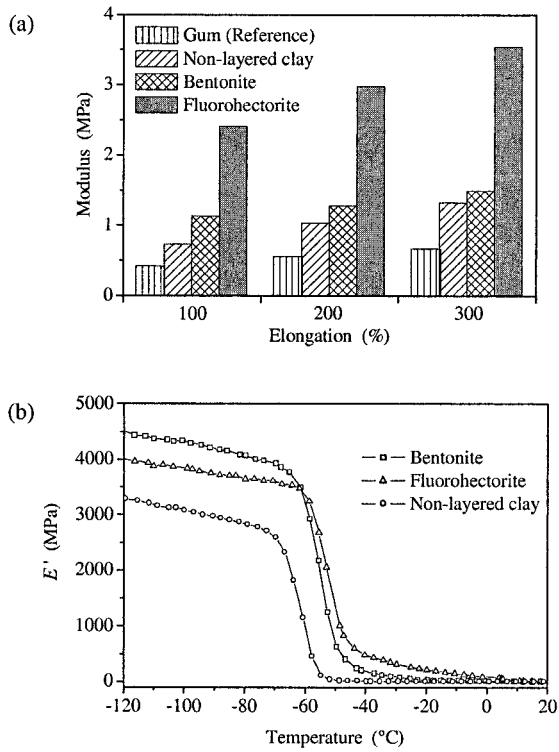

Figure 2. Moduli at various elongations (a) and complex storage moduli (b) *vs.* temperature for NR compounds with and without different reinforcements. Silicate content: 10 parts per hundred rubber (phr).

other hand, a remarkable increase in the storage modulus was noticed for both layered silicate-filled composites compared to the non-layered clay (Figure 2b). The increase in stiffness for LS-containing rubbers was accompanied with a shift in the glass transition temperature, T_g, toward higher values (Figure 2b).

The dispersion of layered silicate in the composites was observed by transmission electron microscopy (TEM) and is illustrated in Figure 3a,b. The TEM photographs represent the non-layered clay and Na^+-fluorohectorite-filled NR composites, respectively. In the non-layered silicate-filled composites, the filler is dispersed in very large particles (Figure 3a). The exfoliation and dispersion of fluorohectorite can be better understood from Figure 3b where clay layers are visible as regions of dark narrow bands within the polymer. The silicate layers produce a skeleton or "house-of-cards" structure. Even though the layers are "ceramic" in nature, because of their very large aspect ratio and nanometer thickness, they behave mechanically more like thin sheets rather than thick rigid plates. This flexibility (of elastic nature) of the silicate layers contributes to the elasticity of the rubber. It has been reported that intercalated and exfoliated clay layers orient in rubber along the strain direction during loading.[16,17]

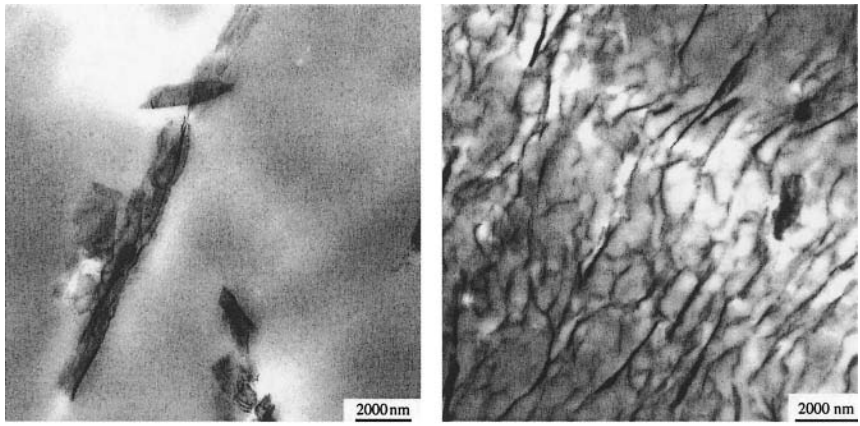

(a) (b)

Figure 3. TEM photographs of a non-layered clay (a) and sodium fluorohectorite-filled NR-based nanocomposite (b) produced by latex compounding. Silicate content of 10 phr.

2.1.2 Nanocomposites from Latex Blends

Polyurethane (PUR), being polar and having a lower molecular mass compared to natural rubber, was supposed to intercalate better with LS. Moreover, the addition of PUR latex to NR latex can make the former cheaper without affecting the mechanical properties. Latex blends with various PUR/NR ratios

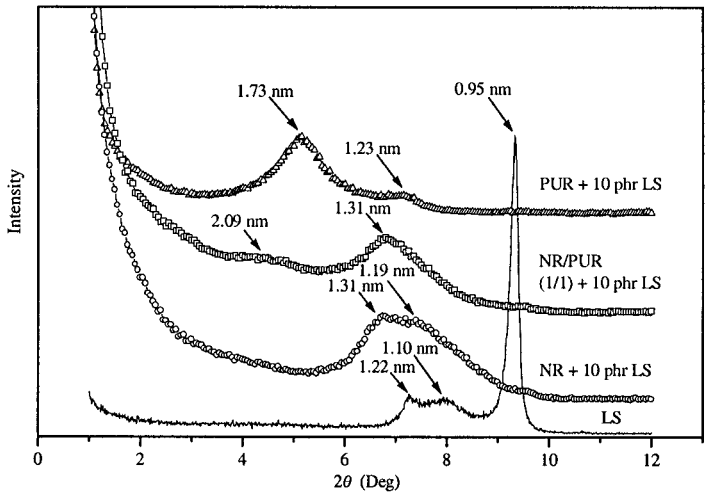

Figure 4. XRD spectra of layered silicate (sodium fluorohectorite) reinforced nanocomposites of various compositions.

(PUR/NR = 1/1 and 8/2), with and without LS, were produced by the film casting method.[18] Figure 4 shows the X-ray diffraction (XRD) spectra of the LS and the LS-containing films of various compositions. It should be noted that the LS (Na^+-fluorohectorite in this case) shows two smaller peaks at 1.22 and 1.10 nm, in addition to the major one at 0.95 nm, *i.e.*, the LS used contained some small fractions with greater intergallery distance than the bulk material. LS has been intercalated by NR in the related compound because the interlayer distance of the LS increased to 1.19-1.31 nm. The appearance of the related broad peak suggests that the degree of NR intercalation is different. A considerably better intercalation was noticed for the PUR latex where two peaks were also resolved. The major peak indicates that the interlayer distance of the LS widened to 1.73 nm from the initial 0.95 nm. This effect can be assigned to the higher polarity of PUR compared to NR which favors the compatibility with LS. Similar to PUR, the NR/PUR latex blend showed two XRD peaks. Albeit they appear at slightly greater interlayer distances than in PUR, these peaks are probably the same, but their intensity ratio is opposed to that of the pure PUR nanocomposite. Before discussing this aspect, attention should be paid to the results obtained by TEM studies.

The TEM images in Figure 5a,b evidence the good intercalation of LS by PUR. One may get the impression that a part of LS has been even exfoliated, and the high aspect ratio of the LS used (synthetic sodium fluorohectorite) is becoming obvious when the size of flat-on laying platelets (discs) is considered (Figure 5b).

The dispersion of LS in the PUR/NR (1/1) latex blend differs considerably from that of PUR. The TEM images in Figure 6 show that NR and PUR are incompatible. The particles of the sulfur-prevulcanized NR appear dark and layered silicate stacks can be located at the boundary of the PUR (light) and NR (dark)

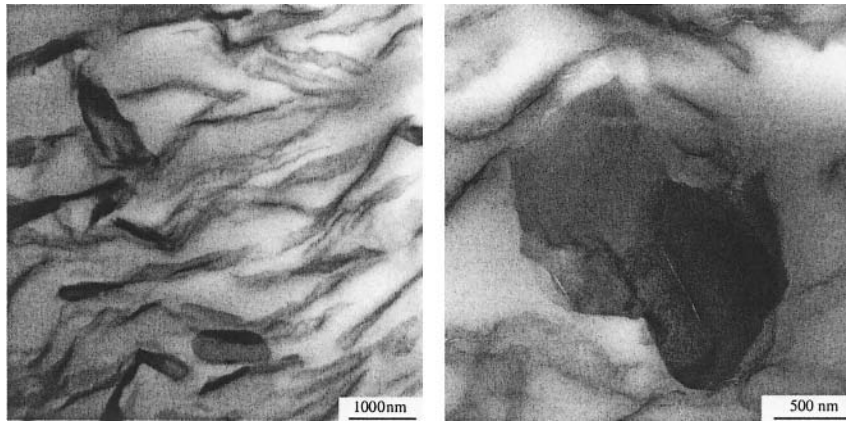

(a) (b)

Figure 5. TEM images taken at various magnifications from a film cast of PUR latex containing 10 phr LS (sodium fluorohectorite).

phases. A well pronounced intercalation and possible exfoliation took place only in the PUR phase (Figure 6b). The silicate layers and aggregates cover the NR particles, resulting in a skeleton ("house-of-cards") structure. This peculiar morphology is rather specific of NR nanocomposites produced by the latex route if the length of the LS is commensurable with the rubber particle size in the latex. Based on the TEM results, the difference in the XRD spectra of the PUR and PUR/NR latices (Figure 4) can be explained. Recall that LS is less intercalated by NR than by PUR and, in the case of the PUR/NR blend, PUR should intercalate

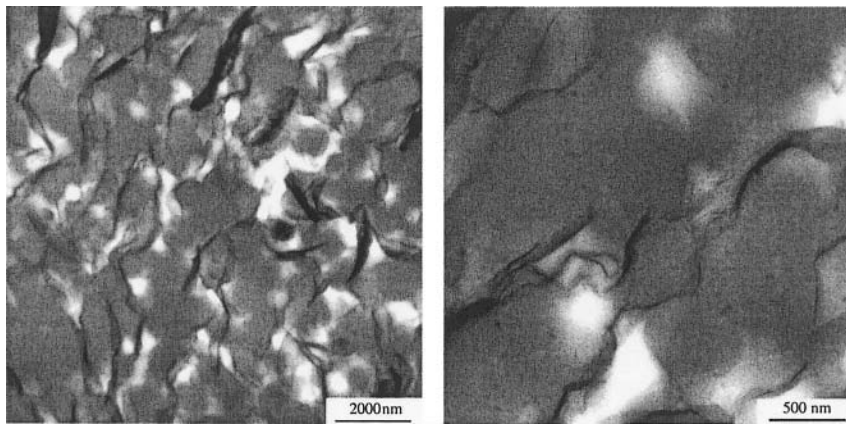

(a) (b)

Figure 6. TEM images taken at various magnifications from a film cast of PUR/NR (1/1) blend reinforced with 10 phr LS (sodium fluorohectorite).

the double amount of LS due to the volume excluded by NR. Bearing in mind that there is an optimum in the LS content with respect to intercalation/exfoliation phenomena, a substantial increase in the LS amount may cause its reaggregation (confinement). However, this does not lead necessarily to deterioration in the mechanical properties. Recall that the prevulcanized NR particles force the silicate aggregates in the neighboring PUR phase to cover their surface. This results in a skeleton morphology, since the length of the silicate layers is higher than the diameter of the particles (Figure 6). The formation of this skeleton structure results in improved mechanical properties, as listed in Table 1. The addition of LS resulted in a moderate increase in the tensile mechanical properties of NR, whereas in the cases of PUR and NR/PUR combinations, a remarkable improvement was found.

Table 1. Mechanical properties of the rubber nanocomposites before and after aging.[18] LS (sodium fluorohectorite) content: 10 parts per hundred rubber (phr) in all samples.

Before aging						
Property	*PUR*	*PUR+LS 10 phr*	*NR*	*NR+LS 10 phr*	*PUR/NR (1/1) + LS 10 phr*	*PUR/NR (8/2) + LS 10 phr*
Tensile strength (MPa)	4.0	15.9	19.6	23.5	12.4	11.4
Tensile modulus (MPa)						
100% Elong.	0.8	5.6	0.7	2.1	4.3	4.9
200% Elong.	0.9	7.8	0.9	3.1	5.9	6.7
300% Elong.	1.1	10.1	1.1	4.5	7.5	8.4
Elongation at break (%)	932	543	881	697	556	469
Tear strength (kN/m)	12.3	54.5	28.0	36.7	59.9	50.7
After aging in air at 70 °C for 7 days						
Tensile strength (MPa)	10.5	17.9	20.8	23.5	16.7	17.5
Tensile modulus (MPa)						
100% Elong.	1.1	7.6	0.7	2.7	6.7	7.4
200% Elong.	1.4	10.7	0.9	4.2	9.4	10.4
300% Elong.	1.8	13.5	1.1	6.0	11.6	13.0
Elongation at break (%)	772	444	768	620	484	447

2.1.3 Radiation-Vulcanized NR Latex

Radiation-vulcanized NR latex, where the hydrocarbon chains were linked directly by single bonds using γ-radiation, was mixed with layered silicates. The stress-strain curves of the composites containing different types of layered silicates are depicted in Figure 7. It can be seen that the gum compound (serving as reference)

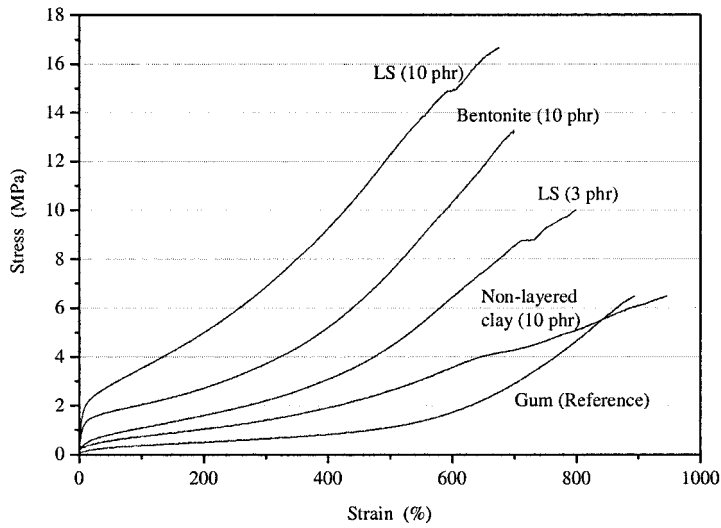

Figure 7. Stress-strain curves of radiation-vulcanized NR latex films as a function of their composition.

has the lowest stress at all strain levels except for the breaking point, where the strain-induced crystallization plays a major role. With the rise in the content of sodium fluorohectorite (LS), the stress-strain curves shift toward higher stress values. It is interesting to note that the effect of 10 phr (parts per hundred rubber) loaded non-layered commercial clay is still less than that of 3 phr sodium fluorohectorite. The large surface area achieved through exfoliation of this LS is the reason for this behavior. The stress values of the rubber nanocomposites at 10 phr bentonite are lower at the same strain values than those of the compound with 10 phr sodium fluorohectorite (Figure 7). The high reinforcing efficiency of sodium fluorohectorite is due to its high aspect ratio (more than twofold that of natural bentonite). The stress at lower elongations (which is a good measure of the reinforcement) is high for all LS-filled nanocomposites, and especially high for those with sodium fluorohectorite.

The TEM images of the NR nanocomposites loaded with bentonite (5 phr) at different magnifications are given in Figure 8a,b. It can be seen that the bentonite layers are exfoliated well in the latex. This is in agreement with the stress-strain behavior depicted in Figure 7. The network formation *via* the silicate layers is also obvious in Figure 8. It is interesting to note that the filler network is concentrated mainly on the boundaries of the rubber particles which fused together during vulcanization. Since a slurry with layered silicate was added to an already prevulcanized latex, the crosslinked rubber can hardly diffuse into the silicate gallery region. As a consequence, the silicate layers are mostly located in the boundary regions between the NR particles. Figure 9 represents a micrograph of

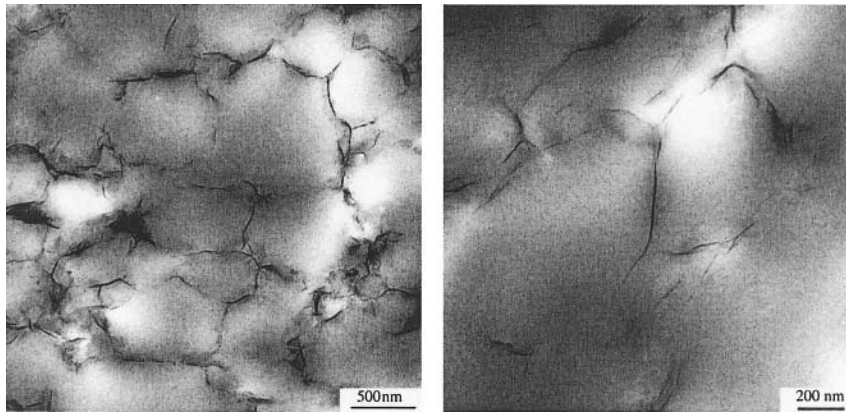

(a) (b)

Figure 8. TEM images taken at various magnifications from a film cast of radiation-vulcanized NR reinforced with 5 phr bentonite.

the fluorohectorite-containing (5 phr) NR nanocomposite, showing well exfoliated silicate layers. The network structure (skeleton or house-of-cards) of the silicate layers is also obvious. The skeleton structure with bentonite is needle-like (Figure 8), whereas that with fluorohectorite is ribbon-shaped (Figure 9). This ribbon shape indicates for a markedly higher aspect ratio of fluorohectorite (*i.e.*, larger lateral dimension) compared to bentonite, which, in fact, can be responsible for the outstanding mechanical properties of the related nanocomposites.

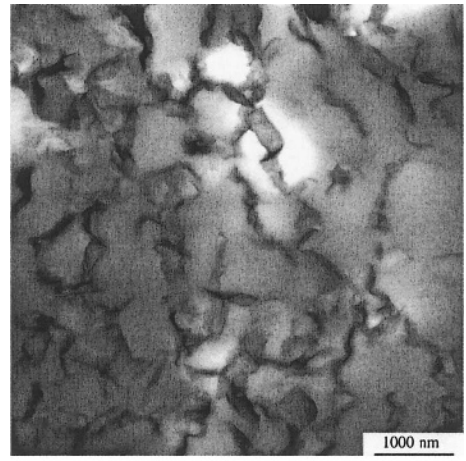

Figure 9. TEM image of a film cast of radiation-prevulcanized NR latex reinforced with 5 phr Na^+-fluorohectorite.

2.2 Solvent-Assisted Intercalation

Melt intercalation of high polymers is a powerful approach to produce polymers reinforced by organophilic layered silicates (OLS). It is quite general and broadly applicable to a range of commodity polymers.[12,19] This melt compounding method can be applied to dry forms of rubbers, as reviewed recently.[12] On the other hand, the dispersion of the silicate can be strongly improved by solvent-assisted techniques. In the latter case, the dry rubbers are dissolved in suitable solvents and an OLS is added. The latter swells more or less (depending on the organophilic intercalant used) in the solvent, as well. After removal of the solvent, the intercalated rubber is compounded with curatives by the traditional way and then vulcanized at a specific temperature (Figure 1). This method can thus be referred to as a solvent-assisted melt compounding one; the silicate dispersion is usually achieved in the solution step.

Ganter *et al.*[16,20] prepared rubber nanocomposites based on butadiene rubber (BR) and SBR containing OLS; the latter was swollen in rubber/toluene solution. The increase in interlayer distance of the silicates was monitored by wide-angle X-ray scattering (WAXS). The interlayer distance increased from the initial 1.26 nm (pristine montmorillonite) to 2.59 nm for the organoclay. The interlayer distance ranged from 3.59 nm to approximately 6 nm for the rubber-swollen organoclay. Fully vulcanized nanocomposites were prepared by compounding the rubber-swollen silicates with rubber chemicals in a three-roll mill followed by vulcanization at 165 °C for 35 min in a hot press under vacuum. The excellent dispersion of the organoclay (exhibiting intercalated and partially exfoliated layers) in rubber was demonstrated by TEM and atomic force microscopy (AFM).

The research group at Toyota Central Laboratories prepared an organophilic montmorillonite *via* cation exchange through amine-terminated liquid nitrile rubber (Hycar® ATBN). ATBN was also used for clay organophilization by the group of Mülhaupt.[20] The exchange reaction with ATBN occurred in a solvent mixture of N,N′-dimethylsulfoxide, ethanol, and water.[21] Then the organophilic montmorillonite was blended with acrylonitrile/butadiene rubber (NBR) by roll milling and the rubber was vulcanized with sulfur. According to TEM observations, the silicate layers were well dispersed in the rubber matrix. The tensile stress at 100% elongation of this organoclay/rubber nanocomposite at 10 phr organoclay content was equal to that of a rubber containing 40 phr of carbon black. In this rubber/clay nanocomposite, the hydrogen- and water-permeability decreased by 70% due to the incorporation of 3.9 vol.% organoclay.

Burnside and Giannelis discussed the nanostructure-property relationships in polydimethylsiloxane/LS nanocomposites.[22] The solvent uptake in this "nanostructured" silicon rubber was dramatically decreased when compared to conventional composites. Both swelling behavior and modulus were related to the excess amount of bonded rubber formed in the nanocomposites compared to conventional composites.

The conditions for dispersing clay nanolayers into both *cis*-1,4-polyisoprene (IR) and epoxidized natural rubber (ENR) have been reported.[23] The incorporation of the clays into these elastomers was achieved by mixing the components in a standard internal mixer/mixing mill (melt compounding) or by mixing their dispersions produced in toluene or methyl ethyl ketone solvents (solution intercalation). X-ray diffraction studies indicated the intercalation of IR and ENR into the silicate interlayers, followed by exfoliation (delamination) of the silicate layers. The reinforcing effect strongly depended on the extent of dispersion of the silicate layers.

Solvent-assisted techniques my be important also in the future. The reason behind this prediction is an interesting finding with melt compounded LS-reinforced, sulfur-cured rubbers. In such systems, considerable confinement (reaggregation) and even full deintercalation have been noticed.[24-26] This was believed to be the result of chemical reactions with the participation of the original surfactant of the OLS.[12,24-26] The solvent-assisted techniques offer some possibilities to circumvent the above problems observed in melt intercalation. The confinement and deintercalation of LS can probably be hampered due to the solvent molecules being also "intercalated".

3 Future Issues

The development of organoclay/rubber composites is still in its embryonic stage. The methods practiced so far are related to various solution (including the latex way) and melt intercalations. No direct (*in situ*) intercalation during rubber synthesis was reported in the open literature. Irrespective of the success with latex- and solution-assisted compounding, the R&D activities in the near future will likely focus on rubber melt intercalation techniques. Here the target issues are to clarify the role of polar rubbers as additives[26] and the effects of curing components,[26,27] to perform sulfurless vulcanization, to study the effects of processing oils, and to get experience with *in situ* melt intercalation (rendering the clay organophilic and achieving its intercalation/exfoliation during mixing/curing). Since the related research in the field of nanoreinforcement is far more advanced with thermoplastic resins than rubbers, attention should be paid to the related achievements (well reviewed in [19,28]), which may serve as guidance for the rubber-based nanocomposite development. Latex compounding will likely focus on rubber blends, whereas for solution intercalation, pristine layered silicates will be tried in the future.[29]

4 Acknowledgements

Dr. S. Varghese sincerely acknowledges the Alexander von Humboldt Foundation (AvH) for a post-doctoral fellowship. The authors are thanking

Mr. K. G. Gatos for his help in the artwork. J. Karger-Kocsis thanks the Fonds der Chemischen Industrie for the financial support.

5 References

[1] Y. Kojima, A. Usuki, Y. Kawasumi, A. Okada, T. Kurauchi, O. Kamigaito (1993) Synthesis of nylon 6-clay hybrid by montmorillonite intercalated with ε-caprolactam, *J. Polym. Sci. Part A: Polym. Chem.* **31**, 983.

[2] E. P. Giannelis (1996) Polymer layered silicate nanocomposites, *Adv. Mater.* **8**, 29.

[3] T. J. Pinnavaia, G. W. Beall, Eds. (2000), *Polymer-Clay Nanocomposites*, Wiley, New York.

[4] L. A. Utracki, M. R. Kamal, (2002) Clay-containing polymeric nanocomposites, *Arab. J. Sci. Eng.* **27**, 43.

[5] E. P. Giannelis, R. Krishnamoorti, E. Manias (1999) Polymer-silicate nanocomposites: model systems for confined polymers and polymer brushes, in *Advances in Polymer Science*, Vol. 138, Springer, Berlin, p. 107.

[6] P. C. LeBaron, Z. Wang, T. J. Pinnavaia (1999) Polymer-layered silicate nanocomposites: an overview, *Appl. Clay Sci.* **15**, 11.

[7] Lan, T., Kaviratna, P.D. and Pinnavaia, T.J. (1995) Mechanism of clay tactoid exfoliation in epoxy-clay nanocomposites, *Chem. Mater.* **7**, 2144.

[8] R. Krishnamoorti, R. A. Vaia, Eds. (2002) *Polymer Nanocomposites: Synthesis, Characterization, and Modeling*, ACS Symposium Series 804, ACS, Washington.

[9] R. A. Vaia, E. P. Giannelis (1997) Lattice model of polymer melt intercalation in organically-modified layered silicates, *Macromolecules* **30**, 7990.

[10] V. V. Ginzburg, C. Singh, A. C. Balazs (2000) Theoretical phase diagrams of polymer/clay composites: the role of grafted organic modifiers, *Macromolecules* **33**, 1089.

[11] R. A. Vaia, K. D. Jandt, E. J. Kramer, E. P. Giannelis (1995) Kinetics of polymer melt intercalation, *Macromolecules* **28**, 8080.

[12] J. Karger-Kocsis, C.-M. Wu (2004) Thermoset rubber/layered silicate nanocomposites. Status and future trends, *Polym. Eng. Sci.* **44**, 1083.

[13] L. Zhang, Y. Wang, Y. Sui, D. Yu (2000) Morphology and mechanical properties of clay/styrene-butadiene rubber nanocomposites, *J. Appl. Polym. Sci.* **78**, 1873.

[14] Y. Wang, L. Zhang, C. Tang, D. Yu (2000) Preparation and characterization of rubber-clay nanocomposites, *J. Appl. Polym. Sci.* **78**, 1879.

[15] S. Varghese, J. Karger-Kocsis (2003) Natural rubber-based nanocomposites by latex compounding with layered silicates, *Polymer* **44**, 4921.

[16] M. Ganter, W. Gronski, P. Reichert, R. Mülhaupt (2001) Rubber nanocomposites: morphology and mechanical properties of BR and SBR vulcanizates reinforced by organophilic layered silicates, *Rubber Chem. Technol.* **7**, 221.

[17] A. Mousa, J. Karger-Kocsis (2001) Rheological and thermodynamical behavior of styrene/butadiene rubber-organoclay nanocomposites, *Macromol. Mater. Eng.* **286**, 260.

[18] S. Varghese, K. G. Gatos, A. A. Apostolov J. Karger-Kocsis (2004) Morphology and mechanical properties of layered silicate reinforced natural and polyurethane rubber blends produced by latex compounding, *J Appl. Polym. Sci.* **92**, 543.

[19] J. Karger-Kocsis, Z. Zhang (2004) Structure-property relationships in nanoparticle/semicrystalline thermoplastic composites, in *Mechanical Properties of Polymers Based on Nanostructure and Morphology*, F. J. Baltá Calleja, G. H. Michler, Eds., Marcel Dekker, New York, in press.

[20] M. Ganter, W. Gronski, H. Semke, T. Zilg, C. Thomann, R. Mülhaupt (2001) Surface compatibilized layered silicates: a novel approach of nanofillers for rubbers with improved mechanical properties, *Kautschuk, Gummi, Kunststoffe* **54**, 166.

[21] Y. Kojima, K. Fukumori, A. Usuki, A. Okada, T. Kurauchi (1993) Gas permeabilities in rubber-clay hybrid, *J. Mater. Sci. Lett.* **12**, 889.

[22] S. D. Burnside, E. P. Giannelis (2000) Nanostructure and properties of polysiloxane-layered silicate nanocomposites, *J. Polym. Sci. Part B: Polym. Phys.* **38**, 1595.

[23] Y. T. Vu, J. E. Mark, L. H. Pham, M. Engelhardt (2001) Clay nanolayer reinforcement of *cis*-1,4-polyisoprene and epoxidized natural rubber, *J. Appl. Polym. Sci.* **82**, 1391.

[24] S. Varghese, J. Karger-Kocsis, K. G. Gatos (2003) Melt compounded epoxidized natural rubber/layered silicate nanocomposites: structure-properties relationships, *Polymer* **44**, 3977.

[25] S. Varghese, J. Karger-Kocsis (2004) Melt-compounded natural rubber nanocomposites with pristine and organophilic layered silicates of natural and synthetic origin, *J. Appl. Polym. Sci.* **91**, 813.

[26] K. G. Gatos, R. Thomann, J. Karger-Kocsis (2004) Characteristics of EPDM rubber/organoclay nanocomposites resulting from different processing conditions and formulations, *Polym. Int.* **53**, 1191.

[27] H. Usuki, A. Tukigase, M. Kato (2002) Preparation and properties of EPDM-clay hydrids, *Polymer* **43**, 2185.

[28] S. Sinha Ray, M. Okamoto M (2003) Polymer/layered silicate nanocomposites: a review from preparation to processing, *Progr. Polym. Sci.* **28**, 1539.

[29] H. S. Jeon, J. K. Rameshwaram, G. Kim, D. H. Weinkauf (2003) Characterization of polyisoprene-clay nanocomposites prepared by solution blending, *Polymer* **44**, 5749.

Chapter 6

Property Improvements of an Epoxy Resin by Nanosilica Particle Reinforcement

Meyyarappallil S. Sreekala
Institut für Verbundwerkstoffe GmbH (Institute for Composite Materials), Kaiserslautern University of Technology, Kaiserslautern, Germany

Christian Eger
Hanse Chemie AG, Geesthacht, Germany

1 Introduction and State of the Art

Polymer nanotechnology represents a new field in nanoscience. Recently, polymer nanocomposites attracted great attention especially because of their unexpected hybrid properties that are synergistically derived from the two components.[1-3] Due to the large boundary surface created by the nanofillers, polymer nanocomposites with new properties are possible. The advantages of nanoparticles include efficient reinforcement with minimal loss of ductility and impact strength, heat stability, flame retardance, improved abrasion resistance, better gas permeability, reduced shrinkage and residual stress, and altered electronic and optical properties. The decrease in size of the domains to less than 100 nm enables good optical transparency. The size of the particles is much smaller than the wavelength of visible light. This makes polymer nanocomposites a new perspective for optical materials. It has been reported that higher tensile properties and lower biodegradability were observed for aliphatic polyester/clay nanocomposites.[4] Thermal and mechanical property improvements in polypropylene/clay nanocomposites were achieved by Ma *et al.*[5] Various nanocomposites exhibit, therefore, exciting novel properties, which are very useful for automotive, aerospace, biomedical, and other engineering applications. They can be used successfully as gas and

solvent containers due to their excellent barrier properties. In addition, their good optical properties make them suitable for applications in the optoelectronic field.

Polymer/clay nanocomposites have lower water sensitivity, reduced permeability to gases, and a similar coefficient of thermal expansion. Further, it has been found that nanocomposites are flame retardant and UV resistant, which is not the case of neat polymers.[6] Most polymers exhibit these improvements in performance at relatively low clay loading (typically 2-10 wt.%). The incorporation of clay nanolayers increases the dimensional stability, thermal properties, and solvent resistance of the epoxy matrix.[7,8] It has also been found that the exfoliation of nanolayers in polymeric matrices results in higher dynamic modulus and higher decomposition temperature of the composite material.[9,10] In addition, exfoliated epoxy/clay nanocomposites have higher moduli than intercalated clay nanocomposites. Polymer/layered silicate nanocomposites also showed properties dramatically different from their conventional counterparts. They can attain a particular degree of stiffness, strength, and barrier properties with the added advantage of light weight.[11-13] Modified clays were found to be efficient in reinforcing rubber and latex matrices. Studies showed that exfoliation of the nanolayers occurs and the novel nanocomposites exhibit attractive advantages, such as improved optical and electrical properties, surface and interface modification, and good barrier properties; they are also flame retardant.[14,15]

Studies on the property improvements in polypropylene/silica nanocomposites were reported by Rong *et al.*[16] During the preparation of polymer nanocomposites by the conventional processing techniques, the main difficulty often encountered in achieving optimum properties is due to the strong tendency of nanoparticles to agglomerate. Radiation grafting of polystyrene onto the nanosilica particles and their incoroporation into the polypropylene matrix by conventional methods were tried.[16] It was found that polymer grafting onto the nanoparticles opens up the agglomerates and improves the dispersion of the particles in the matrix, thus resulting in a better performance of the nanocomposite. By proper modification of polypropylene, it is reported that an increase in the mechanical performance of PP/clay systems is possible.[17] Petrovicova *et al.*[18] observed higher scratch resistances in nylon/nanosilica composites due to the higher crystallinity. Studies on the nanosilica/PP system also revealed the role of the reinforcing nanosilica as nucleating agent during crystallization.[19]

Nanoparticle reinforcement in certain polymeric matrix materials can lead to significant property improvements, whereas in others they result only in marginal property improvements or in some cases even in a worsening of the properties.[20-22] This is because the strong tendency of nanoparticles to agglomerate in polymeric matrices can hardly be controlled by conventional processing techniques due to the limited shear force during the mixing procedure. Thus, it prevents a homogeneous dispersion in polymer melts, which are characterized by high viscosities. Consequently, clusters and aggregates of nanoparticles exhibit properties even worse than conventional particle/polymer systems. Therefore, a better break-down

of the nanoparticle agglomerates resulting in nanostructured composites, can be achieved by techniques, such as (i) *in situ* polymerization of metal alkoxides in organic matrices *via* a sol-gel approach, (ii) intercalation polymerization by inserting polymer chains into the sheets of smectite clay and other layered inorganic materials, (iii) addition of organically modified nanoparticles to a polymer solution, (iv) *in situ* polymerization of monomers in the presence of nanoparticles, *etc.* The property enhancement upon reinforcement of epoxies with silica-siloxane structures formed by *in situ* sol-gel process was investigated by Matejka *et al.*[23] They observed an increase in modulus of the system by two orders of magnitude. The molecular mixing of the reacting components in the sol-gel process results in fine dispersion of the inorganic phase in the organic matrix, which is difficult to achieve by mechanical mixing. The reaction conditions of the sol-gel process determine the fine structure and morphology of the system which contribute to the hybrid properties. Similar improvements were achieved by Hanse Chemie AG,[24] applying the sol-gel technique to silica-reinforced epoxy nanocomposites. The most inexpensive SiO_2 particle sources are sols prepared from aqueous sodium silicate using ion exchange techniques.[25] Sodium silicate solutions are commodities and the silica sols produced exhibit a narrow particle size distribution.

At present, the incorporation of the SiO_2 particles in a polymer matrix on a nanoscale level is a major challenge in this field. The formation of agglomerates which is observed in composites prepared by conventional techniques can deteriorate the final properties of the product. To overcome this problem, the sol-gel process for incorporating nanosilica particles into a reactive epoxy resin was tried in the works presented here. By this process, inorganic or inorganic-organic materials can be produced from liquid starting materials *via* a low temperature process. By employing chemical methods, nanoparticles can be produced elegantly and free of agglomerates. The major challenge is to transfer these nanosilica particles from the aqueous medium into the prepolymer of a reactive epoxy resin without affecting the particle distribution. In the liquid process, toxicological problems during handling of the pure nanoparticle substances do not exist or can be eliminated at the initial stage. The incorporation of nanosilica particles also aims at a low shrinkage upon curing because this improves the toughness and ductility of the cured products and also prevents debonding of the casting compound from the matrix. The special nano-scaled design of the particles is the key to a property enhancement. The silica phase consists of surface-modified, synthetic SiO_2 nanospheres with diameter of less than 50 nm and extremely narrow size distribution.

The most important benefits expected from the nanosilica reinforcement are the following: (i) lower viscosity of the resin formulation compared to common reinforcing fillers and a complete suppression of sedimentation, (ii) increased fracture toughness, impact strength, and modulus, (iii) improved scratch- and abrasion-resistance, (iv) reduced shrinkage upon curing and reduction of the coefficient of thermal expansion, (v) improved dielectric properties, (vi) improve-

ment of heat distortion, chemical resistance, glass transition temperature, durability and weathering stability, (vii) no adverse influence on the processing characteristics of the basic resin

The following section deals with the exact description of the preparation of nanosilica-reinforced epoxies by the sol-gel technique, and of the relation of their structure to various rheological, mechanical, and tribological properties.

2 Preparation and Characterization Techniques

2.1 Basic Material Components

Nanosilica-filled cycloaliphatic bisepoxide resin (3,4-epoxycyclohexylmethyl-3,4-epoxycyclohexane carboxylate), type ERL-4221, was produced by Hanse Chemie AG, Geesthacht, Germany. The nanosilica particles were incorporated into the epoxy resin *via* a sol-gel technique.[24] The neat resin is characterized by its low viscosity and low toughness. As a hardener for the curing reaction of the epoxy resin, 4-methylhexahydrophthalic anhydride (MHHPA) was used. Generally, a 1:1 stochiometric ratio of resin/hardener was recommended by Hanse Chemie. In addition, two different catalysts were used for accelerating the curing reaction and their properties were compared. The N,N-dimethylbenzylamine catalyst was also supplied by Hanse Chemie AG, whereas the cobalt(II) acetyl acetonate (CAA) catalyst was procured by Sachem Chemicals, The Netherlands.

2.2 Preparation of Nanosilica-Filled Epoxy Composites

The thermal curing of the epoxy resin was initiated by the addition of the anhydride hardner. The two catalysts, CAA (1.5 wt.% of the hardener amount) and N,N-dimethylbenzylamine (0.1 wt.% of the hardener amount), were used for accelerating the curing reaction. The thermal treatment comprised four different stages: (i) 90 min at 90 °C, (ii) 120 min at 120 °C, (iii) 120 min at 140 °C, and (iv) 60 min at 160 °C. DSC analysis of the cured samples showed, however, that the curing reaction was not completed under the above conditions. A peak was observed beyond T_g due to the incomplete reactions. The samples were additionally post-cured at 200 °C for about 2 h in order to complete crosslinking. This was again confirmed by DSC measurements. DMTA measurements showed the same results. Nanocomposites having various filler contents (0, 0.42, 0.92, 1.6, 2.97, 6.04, 10.35. and 13.64 vol.% of SiO_2) were prepared by mixing the master reinforced resin with neat ERL-4221 resin.

2.3 Structural and Mechanical Analysis

2.3.1 Microstructure

Transmission electron (TEM) and atomic force microscopy (AFM) have already been proved to be good characterizing tools for nanocomposites, especially in the study of the particle distribution. For TEM, ultra-thin sections of the nanocomposites were cut at room temperature using an ultramicrotome (LKB Ultrotome III) equipped with a diamond knife at a cutting speed of 20 mm/s, with a thermal feed of 50-60 nm. TEM images were taken on a Zeiss EM 10A transmission electron microscope, using an accelerating voltage of 80 kV. Atomic force microscopy studies of smooth fracture surfaces of the bulk materials were carried out by the use of a Nanoscope III from Digital Instruments. AFM images of the nanocomposite surfaces were taken in tapping mode. Forces acting on the tip due to the tip/sample interaction result in deflection or torsion of the cantilever, which are detected by a position-sensitive optical sensor. By detecting movements of the cantilever, the height differences of the surface can be resolved on an angstrom scale. A detailed description of the instrumentation and various modes of AFM imaging were reported earlier.[26]

2.3.2 Viscosity Studies of the Unfilled and Filled Resin

The change in the viscosity of the system upon nanosilica reinforcement was analyzed as a function of the filler content. The viscosity measurements were performed on a parallel plate viscometer from Couette-System/Mettler-Toledo GmbH. The viscosity change was monitored between room temperature and 100 °C.

2.3.3 Mechanical Properties

Three-point bending tests were carried out on a Zwick 1464 universal testing machine, in order to evaluate the bending strength and modulus of the composites as dependent on the SiO_2 nanoparticle content. An impact tester of Ceast Torino, Italy, was used to test the unnotched Charpy impact strength of the composites. The tests were carried out according to ASTM D 256. Dynamic microhardness studies of the nanocomposites were performed with a dynamic ultramicrohardness tester from DUH-202 Shimadzu Corporation, Japan. A load of 500 mN was used to make microindentations. Ten measurements were made on each sample, for which an average value was finally reported. For the fracture toughness measurements, compact tension (CT) specimens were cut and subjected to static tensile loading. The initial notch tip was prepared by a razor-blade indentation into the root of the saw cut. Loading was effected on a Zwick 1464 type universal tensile testing

machine at a crosshead speed of 0.5 mm/min. From the load-elongation (F-Δl) response of the CT specimens, the fracture toughness was determined as follows:

$$K_{IC} = \frac{F_{max}}{B \cdot W} \cdot a^{1/2} \cdot f(a/W) \quad (1)$$

where F_{max} is the maximum force in the F-Δl trace, B and W are the specimen thickness and width, respectively, a is the total notch length (produced by saw cut and razor blade indentation), and

$$f(a/W) = 1.99 - 0.41(a/W) + 18.7(a/W)^2 - 38.48(a/W)^3 + 53.85(a/W)^4 \quad (2)$$

is a geometry correction factor.

In order to calculate the K_{IC} value more accurately, the specimen parameters (a, W, and B) were measured on each individual specimen.

2.3.4 Tribological Properties

The friction coefficient and the specific wear rate of the nanocomposites were determined by sliding wear tests on a block-on-ring apparatus against a 100 Cr 6 (German standard) steel ring as the counterpart. A pressure of 1 MPa and a velocity of 1 m/s were used over a duration of 20 h for each sample. Additional wear tests of the composite systems were carried out under fretting test conditions against a ceramic ball as the counterpart.

2.3.5 Failure Analysis

Photographs of the fracture surfaces were taken on a JEOL JSM-5400 scanning electron microscope at an accelerating voltage of 20 kV. A sputtering device from Balzers (SCD 050) was used to make a conductive coating on the sample surface.

3 Microstructural and Rheological Details

3.1 Particle Distribution

Transmission electron micrographs of the representative samples were taken to study the distribution of the nanosilica particles in the composites prepared. A fine agglomerate-free and uniform dispersion of the nanoparticles became evident from the photographs at all filler loadings (Figures 1 and 2). Particle-particle contacts were not observed. The particle size was found to be in a narrow

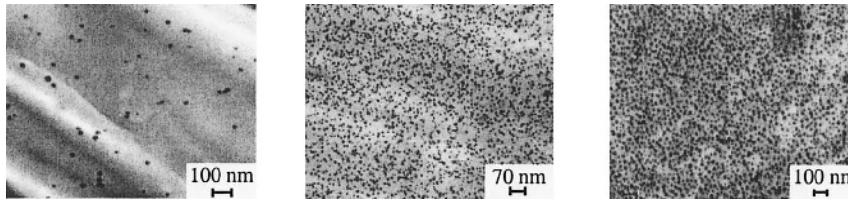

Figure 1. TEM images of the nano-SiO_2/epoxy composites: (a) SiO_2 0.42 vol.%, (b) SiO_2 2.97 vol.%, (c) SiO_2 13.64 vol.%.

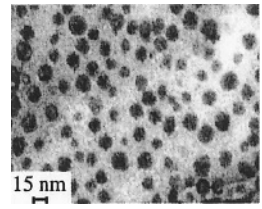

Figure 2. TEM image of the structure of the SiO_2 nanoparticles in epoxy matrix.

distribution range of 6 to 20 nm (Figure 3). In addition, the transparency of the resin was retained upon nanosilica reinforcement. This is due to the fact that light

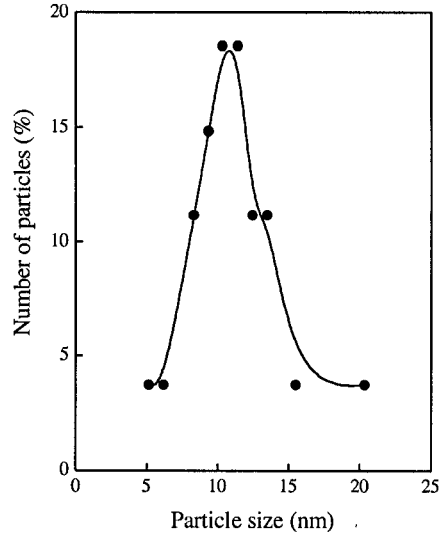

Figure 3. Size distribution of nano-SiO_2 particles in epoxy matrix.

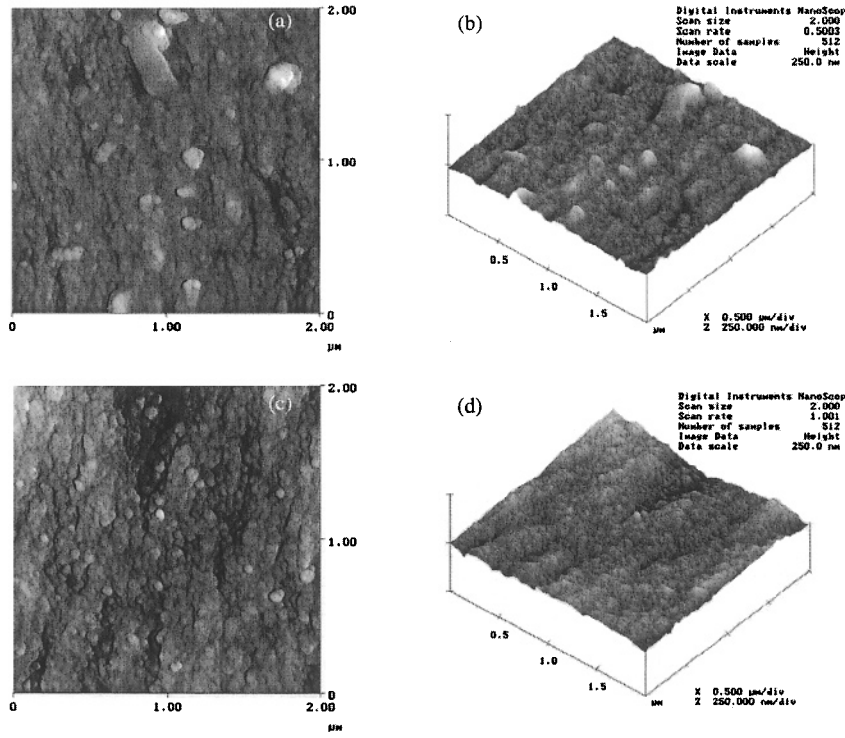

Figure 4. AFM images of the nano-SiO_2/epoxy composites: (a) SiO_2 0.42 vol.%, substracted hight-amplitude image, (b) SiO_2 0.42 vol.%, 3D image, (c) SiO_2 2.97vol.%, substracted hight-amplitude image, (d) SiO_2 2.97 vol.%, 3D image.

scattering is minimized owing to the good dispersion of the very small particles within the matrix. Atomic force micrographs, taken from the fractured surfaces of the nanocomposites, also revealed the distribution of the nanoparticles (Figure 4). In addition, a good coupling of the particles with the matrix is seen.

3.2 Viscosity

Figure 5 shows the temperature dependence of the viscosity of the epoxy matrix at various nanosilica contents. The viscosity of the resin remained unchanged at lower particle loadings. No considerable increase in the viscosity has been observed up to 3 vol.% loading of nanosilica particles. However, a gradual increase in viscosity was observed at higher filler contents. Compared to fumed silica-filled composites containing the same amounts of SiO_2, the rheological properties of the nanocomposites are drastically improved, thus allowing a better processabilty when such a nano-reinforced resin is used as matrix in fiber-reinforced composite systems.

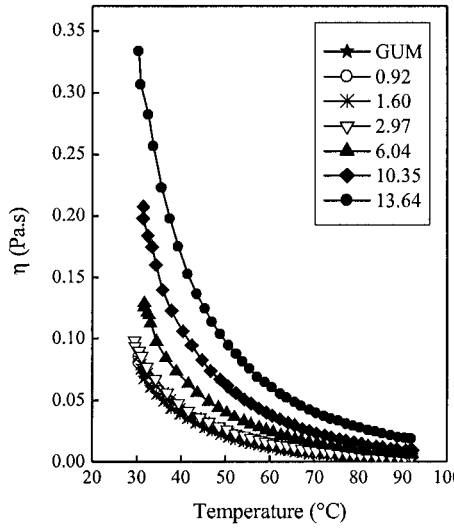

Figure 5. Temperature dependence of viscosity at various SiO_2 contents (vol.%).

4 Mechanical Properties

4.1 Three-Point Bending

The mechanical properties of the nanocomposites under consideration exhibited in almost all cases a more or less pronounced unexpected behavior in the lower filler content range. This was especially true for the bending modulus and strength which decreased within the range of 0 to 2 vol.% of SiO_2. Above this range, the values continuously increased, becoming higher by more than 40% at 14 vol.% SiO_2 filled epoxy, compared to that of the neat matrix (Figure 6). The unexpected behavior in the lower filler range was most probably due to a non-uniform distribution of the SiO_2 particles within the resin, thus leading to a variation in stress concentration sites within the composite specimens. When CAA was used as a catalyst during curing, the strength and modulus of the reinforced composite were enhanced by 5%. Similar results have been obtained by Petrovic *et al.*[27] with nanosilica-filled polyurethane composites.

4.2 Microhardness

Microhardness is a suitable test to detect the morphological and textural changes in polymers.[28] The microhardness values of the nanocomposites studied (amine-catalyzed during curing) showed a gradual increase with the filler content

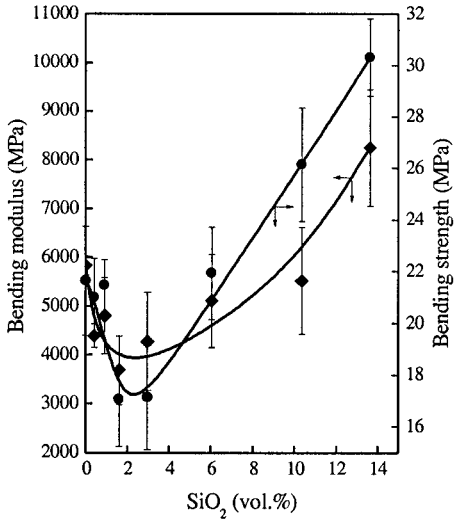

Figure 6. Strength and modulus of epoxy/SiO_2 nanocomposites *vs.* particle content under three-point bending (amine catalyst).

(Figure 7). It is supposed that this will also result in an improvement of the tribological properties of these materials (see Section 4.4), since during the application of an external frictional load, the presence of hard nanosilica particles imparts a higher load withstanding capability, thus preventing matrix deformation

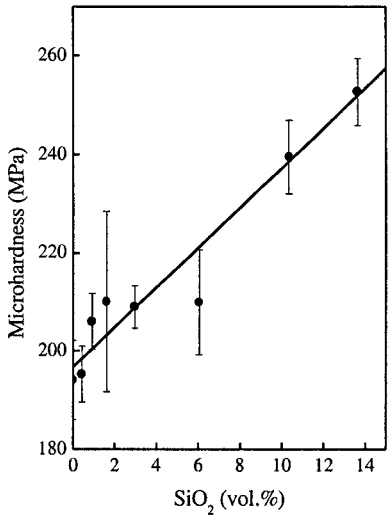

Figure 7. Microhardness of nanosilica-filled epoxy composites (amine catalyst).

and removal due to the sliding counterpart asperities. In the case of CAA-catalyzed nanocomposites, an additional 15% improvement in microhardness was observed. It is reported that in ERL-4221with anhydride system, the use of CAA as catalyst resulted in better adhesion between the silica particles and the epoxy matrix resin.[29]

4.3 Fracture Toughness

Upon nanosilica reinforcement, the fracture toughness of the amine-catalyzed epoxy matrix system was found to increase by 73% (Figure 8). Apart from some scatter in the lower volume fraction range, the values increased almost

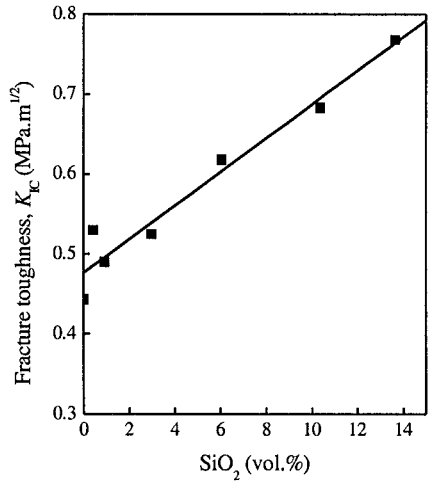

Figure 8. Fracture toughness of nanosilica-filled epoxy composites *vs.* filler content (amine catalyst).

linearly with the nanosilica content. Fracture toughness is a measure for the ability of a material to resist the growth of a pre-existing crack or flaw. It is assumed that the high stress concentration in front of the razor notch within the neat resin is changed into a more uniform stress distribution due to the fine distribution of the nanoparticles, thus enhancing the toughness of the system. Nevertheless, brittle crack growth has been observed in both the neat resin and the nanosilica-reinforced epoxy composites.

4.4 Tribological Properties

The variation in wear rate of epoxy/SiO_2 nanocomposites with particle content is shown in Figure 9a,b. As it was assumed from the microhardness results,

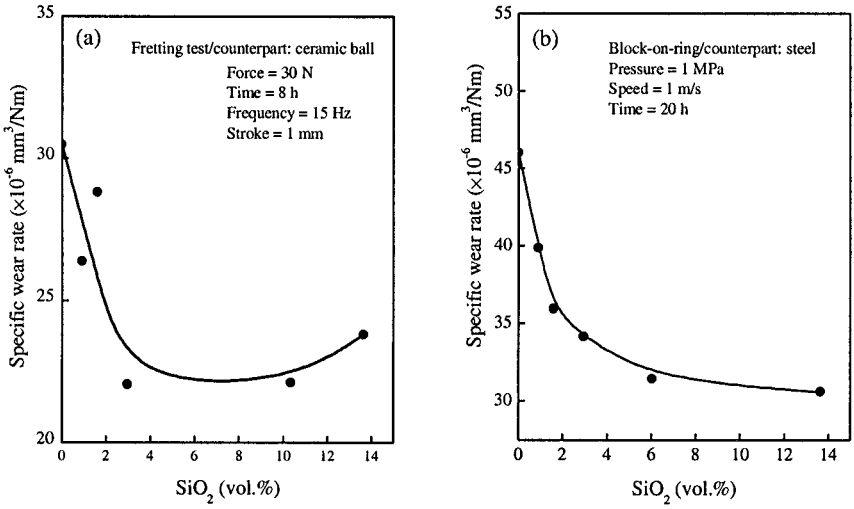

Figure 9. Wear rate of epoxy/SiO_2 nanocomposites *vs.* particle content (amine catalyst): (a) fretting test, (b) block-on-ring test.

the wear rate decreased considerably with the rise of the nanosilica volume fraction in both block-on-ring and fretting tests. Worn surfaces of the neat epoxy sample and the nanoparticle-reinforced composite after block-on-ring testing are given in Figure 10. It can be seen that the higher wear of the neat epoxy resulted in a rough

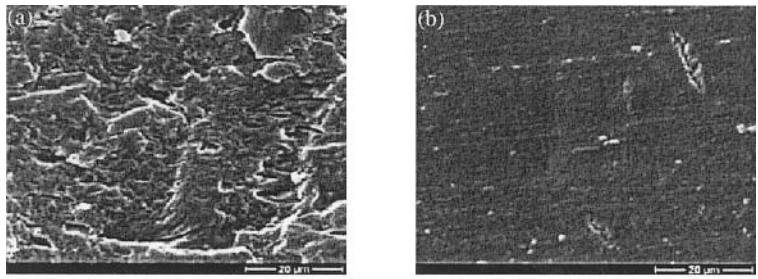

Figure 10. Scanning electron micrographs of the worn surface of epoxy/SiO_2 nanocomposite after block-on-ring test: (a) pure resin; (b) SiO_2 2.97 vol.%.

surface, whereas the nanoparticles impart some smoothening of the worn surface, associated with a lower amount of material removed.

On the other hand, it seems that upon nanosilica reinforcement, the friction coefficient slightly increases. The variation is irregular with the rise in nanosilica

content (Figure 11). This observation differs from the findings by other authors, who have shown a reduction in the friction coefficient by the mechanical incorporation of nanoparticles into various polymeric matrices.[30,31]

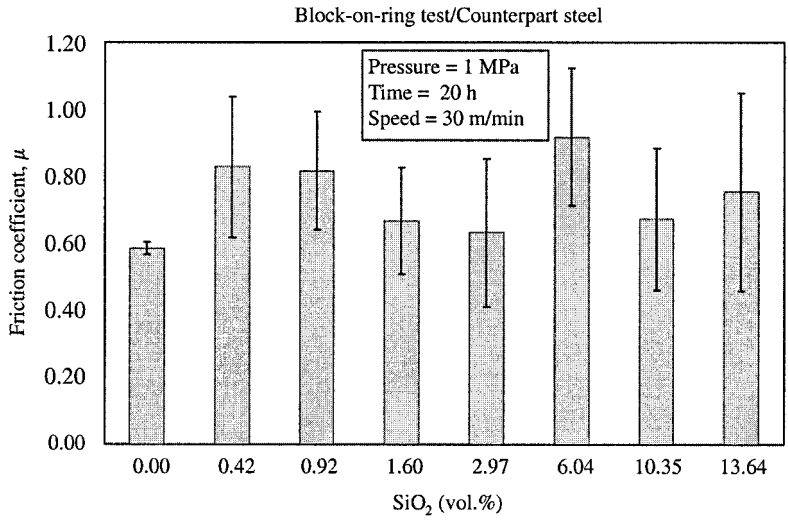

Figure 11. Friction coefficient of epoxy/SiO_2 nanocomposites *vs.* particle content (amine catalyst).

5 Conclusions

The incorporation of SiO_2 nanoparticles into a reactive epoxy resin *via* a sol-gel process generated a new class of nanocomposites, characterized by a monodisperse, non-agglomerated distribution of the spherical particles within a very narrow size range between 6 and 20 nm. The nanoparticles had no significant effect on the viscosity and the optical properties of the system. It was found that at a volume content of at least up to 14%, the particles cause an enhancement of various mechanical properties, including bending strength and modulus, microhardness, fracture toughness, and sliding wear resistance.

It is assumed that the use of such a nanocomposite as a matrix in continuous fiber-reinforced composites will definitely improve the matrix-related properties, such as interlaminar fracture toughness, transverse tensile strength and modulus, as well as interlaminar shear strength. The same should be true for polymer-based tribomaterials, in which such a nanoparticle-modified resin is used in combination with friction and wear improving fillers, such as short carbon fibers, PTFE particles, and graphite flakes.

6 Acknowledgements

M. S. Sreekala wishes to thank the Alexander von Humboldt Foundation for the post-doctoral research fellowship at the Institute for Composite Materials Ltd., University of Kaiserslautern, Germany. Further thanks are due to Prof. K. Friedrich for his valuable comments on the results of this work.

7 References

[1] N. Ogata, G. Jimmenez, H. Kawaki, T. Ogihara (1997) Structure and thermal/ mechanical properties of poly(l-lactide)-clay blend, *J. Polym. Sci. Part B Polym. Phys.* **35**, 389.

[2] Z. Wang, T. Lan, T. J. Pinnavaia (1996) Hybrid organic-inorganic nanocomposites formed from an epoxy polymer and a layered silicic acid, *Chem. Mater.* **8**, 2200.

[3] E. P. Giannelis, R. Krishnamoorthi, E. Manias (1998) Polymer-silicate nanocomposites: Model systems for confined polymers and polymers brushes, *Adv. Polym. Sci.* **138**, 107.

[4] S.-R. Lee, H.-M. Park, H. Lim, T. Kang, X. Li, W.-J. Cho, C.-S. Ha (2002) Microstructure, tensile properties, and biodegradability of aliphatic polyester/clay nanocomposites, *Polymer* **43**, 2495.

[5] J. Ma, Z. Qi, Y. Hu (2001) Synthesis and characterization of polypropylene/clay nanocomposites, *J. Appl. Polym. Sci.* **82**, 3611.

[6] J. W. Gilman, T. Kashiwagi, M. Nyden, J. E. T. Brown, C. L. Jackson, S. Lomakin, E. P. Giannelis, E. Manias (1999) Flammability studies of polymer layered silicate nanocomposites: polyolefin, epoxy, and vinyl ester resins, in *Chemistry and Technology of Polymer Additives* (Eds. S. Ak-Malaika, A. Golovoy, C. A. Wilkie) Blackwell Science Inc., Malden, MA, Ch. 14, p. 249.

[7] T. Lan, P. D. Kaviratna, T. J. Pinnavaia (1995) Mechanism of clay tactoid exfoliation in epoxy-clay nanocomposites, *Chem. Mater.* **7**, 2144.

[8] T. Lan, T. J. Pinnavaia (1994) Clay reinforced epoxy nanocomposites, *Chem. Mater.* **6**, 2216.

[9] X. Fu, S. Qutubuddin (2001) Polymer-clay nanocomposites: exfoliation of organophilic montmorillonite nanolayers in polystyrene, *Polymer* **42**, 807.

[10] Y. C. Ke, J. K. Lu, X. S. Yi, J. Zhao, Z. N. Qi (2000) The effects of promoter and curing process on exfoliation behavior of epoxy/clay nanocomposites, *J. Appl. Polym. Sci.* **78**, 808.

[11] R. Krishnamoorti, R. A. Vaia, E. P. Giannelis (1996) Structure and dynamics of polymer-layered silicate nanocomposites, *Chem. Mater.* **8**, 1728.

[12] E. P. Giannelis (1996) Polymer layered silicate nanocomposites, *Adv. Mater.* **8**, 29.

[13] E. P. Giannelis (1998) Polymer-layered silicate nanocomposites: synthesis, properties and applications, *Appl. Organometallic Chem.* **12**, 675.

[14] C. Zilg, P. Reichert, F. Dietsche, T. Engelhardt, R. Mulhaupt (1998) Polymer and rubber nanocomposites based upon layered silicates, *Kunststoffe - Plast. Europe* **88**, 1812.

[15] Y. Z. Wang, L. Q. Zhang, C. H. Tang, D. S. Yu (2000) Preparation and characterization of rubber-clay nanocomposites, *J. Appl. Polym. Sci.* **78**, 1879.

[16] M. Z. Rong, M. Q. Zhang, Y. X. Zheng, H. M. Zeng, R. Walter, K. Friedrich (2001) Structure-property relationships of irradiation grafted nano-inorganic particle filled polypropylene composites, *Polymer* **42**, 167.

[17] N. Hasegawa, H. Okamoto, M. Kato, A. Usuki (2000) Preparation and mechanical properties of polypropylene-clay hybrids based on modified polypropylene and organophilic clay, *J. Appl. Polym. Sci.* **78**, 1918.

[18] E. Petrovicova, R. Knight, L. S. Schadler, T. E. Twardowski (2000) Nylon 11/silica nanocomposite coatings applied by the HVOF process. II. Mechanical and barrier properties, *J. Appl. Polym. Sci.* **78**, 2272.

[19] M. S. Sreekala, B. Lehmann, M. Z. Rong, K. Friedrich, Nanosilica reinforced polypropylene composites: microstructural analysis and crystallisation behaviour, *Int. J. Polym. Mater.*, to be submitted.

[20] C. Zilg, R. Mulhaupt, J. Finter (1999) Morphology and toughness/stiffness balance of nanocomposites based upon anhydride-cured epoxy resins and layered silicates, *Macromol. Chem. Phys.* **200**, 661.

[21] C. Zilg, R. Thomann, J. Finter, R. Mulhaupt (2000) The influence of silicate modification and compatibilizers on mechanical properties and morphology of anhydride-cured epoxy nanocomposites, *Macromol. Mater. Eng.* **280**, 41.

[22] T. Lan, T. J. Pinnavaia (1994) Clay-reinforced epoxy nanocomposites, *Chem. Mater.* **6**, 2216.

[23] L. Matejka, O. Dukh, J. Kolarik (2000) Reinforcement of crosslinked rubbery epoxies by in-situ formed silica, *Polymer* **41**, 1449.

[24] www.hanse-chemie.com

[25] C. J. Brinker, G. W. Scherer (1990) *Sol-Gel Science*, Academic Press, Boston.

[26] Y. Han, S. Schmitt, K. Friedrich (1999) Nanoscale Indentation and scratch of short carbon fiber reinforced PEEK/PTFE composite blend by atomic force microscope lithography, *Appl. Compos. Mater.* **6**, 1.

[27] Z. S. Petrovic, I. Javni, A. Waddon, G. Banhegyi (2000) Structure and properties of polyurethane-silica nanocomposites, *J. Appl. Polym. Sci.* **76**, 133.

[28] F. J. Baltá Calleja, S. Fakirov, Eds. (2000) *Microhardness of Polymers*, Cambridge solid state science series, Cambridge University Press, Cambridge.

[29] S. Luo, T. Yamashita, C. P. Wong (2000) Study on the property of underfill based on epoxy cured with acid anhydride for flip chip application, *J. Electronics Manufacturing* **10**, 191.

[30] V. A. Bely, A. I. Sviridenok, M. I. Petrokovets, V. G. Savkin (1982) *Friction and Wear in Polymer-Based Materials*, Pergamon Press, Oxford.

[31] J. L. He, L. D. Wang, W. Z. Li, H. D. Li (1998) Experimental observations on the mechanical properties of nanoscale ceramic/teflon multilayers, *Mater. Chem. Phys.* **54**, 334.

Part II

Special Characterization Methods and Modeling

Chapter 7

Micro-Scratch Testing and Finite Element Simulation of Wear Mechanisms of Polymer Composites

Tibor Goda, Károly Váradi
Institute of Machine Design, Budapest University of Technology and Economics, Budapest, Hungary

Klaus Friedrich
Institut für Verbundwerkstoffe GmbH (Institute for Composite Materials), Kaiserslautern University of Technology, Kaiserslautern, Germany

1 Introduction

Reinforced polymers are widely used in different tribological applications, such as rollers, bearings, gears, *etc.* The design or selection of these structural elements is usually based on experiences gained by specific wear tests. A theoretical approach for the better understanding of the wear mechanisms is not so common, due to the complexity of the wear process, the specific material behavior of the polymers, and the inhomogeneity of the composite materials used.

The aim of the present chapter is to describe and to model the wear mechanisms of continuous fiber-reinforced polymer composites by using scratch tests, scanning electron microscopy, and finite element (FE) contact techniques applied to macro/micro-models, as well as a debonding algorithm developed.

The model material used is a unidirectional carbon fiber-reinforced, thermoplastic polyether-etherketone (PEEK) composite[1] with fiber diameter of $d = 8\ \mu m$. The fiber orientations studied are shown in Figure 1. The mechanical properties of this material are listed in Table 1. The first principal material direction, indicated by 1 in Table 1, is parallel to the fiber direction (Figure 1), the second and the third one are perpendicular to the fiber orientation. The anisotropic composite material properties were specified using the rule of mixture type equations.[2]

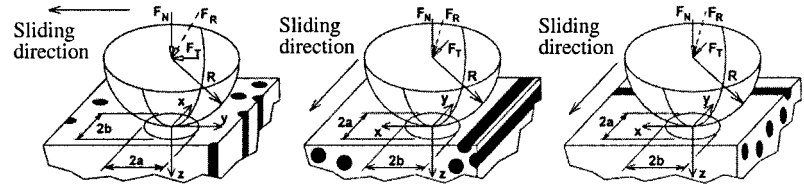

Figure 1. The studied fiber orientations with a hemispherical sliding asperity: (a) normal (N), (b) parallel (P), and (c) anti-parallel (AP).[2,3]

Table 1. Material mechanical properties (σ_Y - yield strength, E - elastic modulus, G - shear modulus, ν - Poisson's number).

$V_f = 0.61$*	*Steel*[4]	*Diamond*[5]	*CF*[6]	*PEEK*[7]	*Composite*
E_{11} (MPa)			235000		144921
E_{22} (MPa)	210000	850000	15000	4030	7276
E_{33} (MPa)			15000		7276
G_{12} (MPa)			6432		2734
G_{13} (MPa)	80769	354167	6432	1439	2734
G_{23} (MPa)			5357		2419
ν_{12}			0.166		0.257
ν_{13}	0.3	0.2	0.166	0.4	0.257
ν_{23}			0.4		0.504
σ_Y (MPa)		–	–	119	–

* Fiber volume fraction

2 Micro-Scratch Testing

To illustrate typical wear mechanisms caused by the sliding contact of an individual asperity with a polymer composite surface, a diamond indentor with a radius R = 100 μm can be compressed under a normal load F_N = 1 N onto a polished composite surface. Subsequently, the indentor is slowly moved, in order to create a scratch on the specimen surface. Scratch tests were carried out under normal (N), parallel (P), and anti-parallel (AP) fiber orientation. With repetition of the scratch tests on the same groove, the effects of cyclic loading can also be studied. However, in this case, it is very important to ensure the same contact path for the diamond indentor during the repetitions. The test apparatus used is described in Figure 2. In order to get an idea about the local failure events, the scratched surfaces of the composite specimens were examined by scanning electron microscopy. Typical SEM micrographs can be seen in Figures 3 to 7.

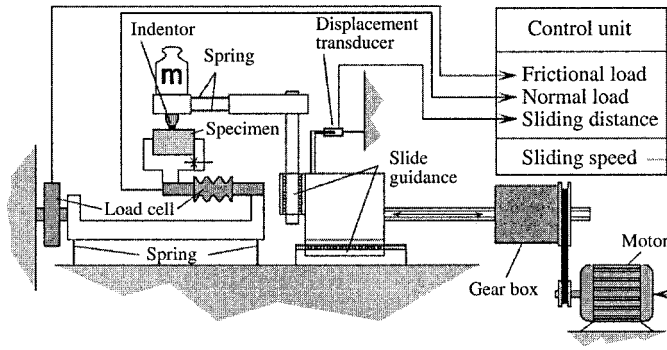

Figure 2. Scheme of the "Scratch-Tribometer".[2]

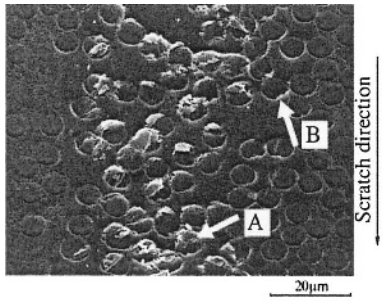

Figure 3. SEM micrograph of a normally oriented composite surface after five scratch repetitions.[8]

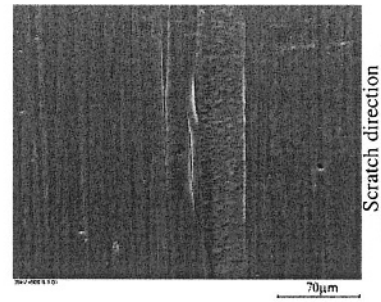

Figure 4. SEM micrograph of a composite surface in the case of P-fiber orientation.[9]

Figure 3 represents the conditions after five repetitions. The corresponding wear features are much more intensive than after one scratch. Most probably, already during the first scratch some sub-surface deformations have been induced (but were not yet visible), which allowed further damage mechanisms to occur during the subsequent scratches. "Pushed up" material is visible at the lateral fiber edges and at the front side of the fibers, including residual deformations and bent fibers after unloading. The difference in vertical direction is mainly between the fibers and matrix at the front side of the fibers. These phenomena end-up in characteristic mechanisms of wear debris formation, such as shearing and removal of small portions of the matrix material from the surface, and eventually their smearing-out by the formation of compacted wear debris layers.

Based on the micrograph in Figure 3, the following wear mechanisms can be listed: (i) small matrix shear lips or cracks, oriented transversely to the scratch direction, (ii) first indication of fiber edge cracking, which primarily occurred at

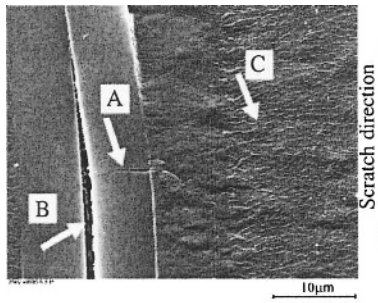

Figure 5. An enlarged segment of the contact area in the case of P-fiber orientation.

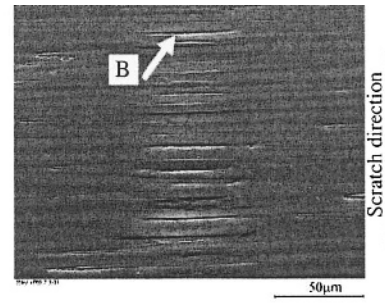

Figure 6. SEM micrograph of a composite surface in the case of AP-fiber orientation.[9]

the rear edge (compared to the sliding direction (A)) of the fibers, and (iii) the push-up of matrix material (B) at the lateral fiber edges (relative to the slightly lower level of the matrix, compared to the fiber ends on the polished and unscratched composite surface).

In the case of parallel fiber orientation, Figures 4 and 5 show other typical wear mechanisms: (i) fiber/matrix debonding, (ii) fiber bending, (iii) fiber cracking, and (iv) matrix shear. In Figure 4, right and left from the groove, the polished surface remained in its undamaged state. At a higher magnification of the scratched area (Figure 5), a fiber crack (A) and a fiber debonding (B) are noticeable. In addition, matrix shear (C) can also be detected.

Figures 6 and 7 show typical wear mechanisms in the case of AP-fiber orientation. Due to the compressive and frictional loads, the fibers bend in the depth and in the sliding direction, respectively. Both were associated with fiber fracture events in the center region of the contact area, as well as in the transition between the groove and the undamaged area. Some of the broken fiber segments were removed from the actual groove area, which can be a result of the additional

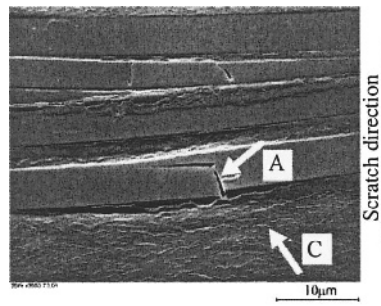

Figure 7. An enlarged segment of the contact area in the case of AP-fiber orientation.[9]

torsion acting in the scratched material surface. Repeated sliding of the counterpart may lead to cutting up of the fiber fragments at a later stage of the wear process.

Figure 7 shows an enlarged segment of the scratched area. Based on these observations, the following wear mechanisms can be noticed: (i) fiber cracking and removal from the fiber beds (A in Figure 7), (ii) fiber/matrix debonding (B in Figure 6), and (iii) shear of the matrix material between the broken fibers (C in Figure 7), as already described for the P-fiber orientation.

By replacing the diamond tip indentor with a small steel ball, the characteristic wear and failure events are very similar, although they do not appear so clearly.[2,3]

3 The Representative Wear Mechanisms

Figures 8 and 9 illustrate schematically the typical, experimentally observed wear mechanisms of the unidirectional fiber-reinforced polymer composites in the form of wear cycles based on different wear and scratch tests. Only the wear mechanisms of N- and P-fiber orientations are represented here because, in the case of AP-fiber orientation, they are similar to those observed for P-fiber orientation.

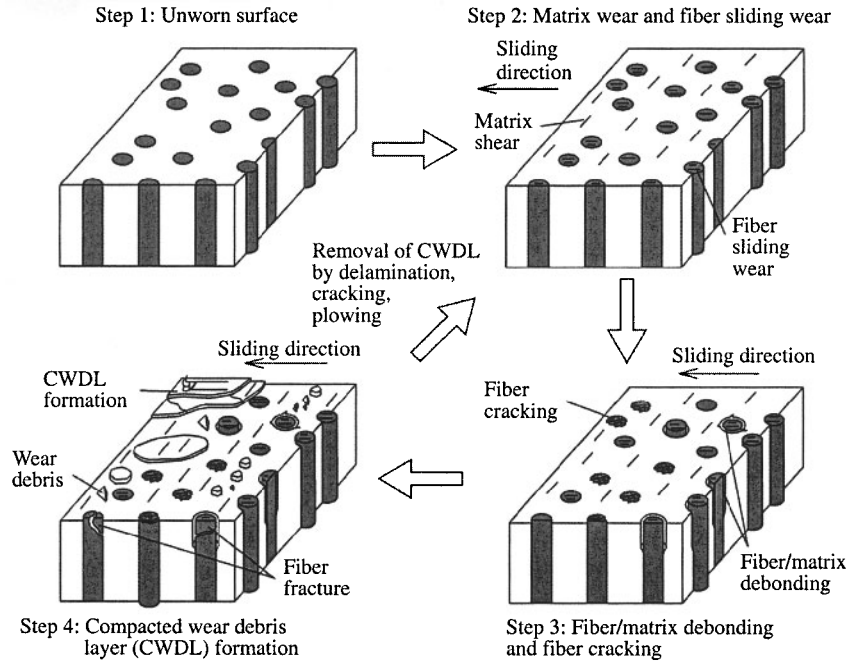

Figure 8. Typical wear mechanisms of a normally oriented unidirectional fiber-reinforced polymer composite.

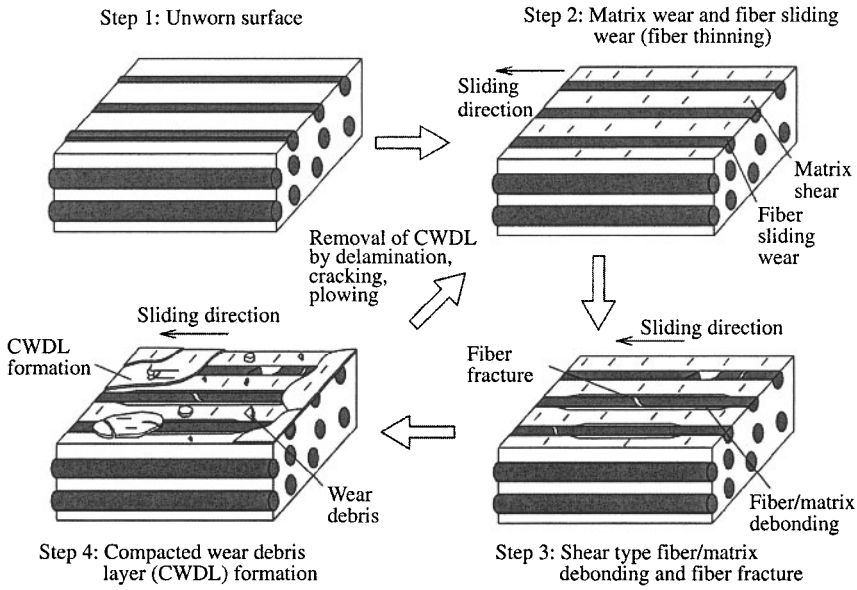

Figure 9. Typical wear mechanisms of a parallel oriented unidirectional fiber-reinforced polymer composite.

The wear sequence may occur as follows: matrix wear, fiber sliding wear, fiber cracking, wear by fiber/matrix debonding at the interface, and fiber edge cracking. As it is illustrated, at the initial stage of the wear process, matrix wear and fiber sliding wear occur. Then, fiber cracking appears due to the matrix removal and the asymmetric contact pressure distribution (see Section 4) produced by the sliding asperity.

In addition, as a typical failure mechanism, fiber/matrix debonding occurs due to the shear and tension type loading. If fiber/matrix debonding has taken place, the local separation initiates additional fiber cracking, wear debris formation, and a more intensive wear process. In the steady state wear process, a so-called compacted wear debris layer (CWDL) covers the surface; it is composed of pulverized wear debris and matrix material. During the wear process, this layer is continuously formed and removed by the surfaces sliding over each other.

4 Wear Considerations by Finite Element Contact Analysis

For the discussion of the wear mechanisms, it is worth to consider the contact and stress states developed between a counterpart asperity (*e.g.*, a diamond

tip or a small steel ball) and the fiber-reinforced polymer composite at different fiber orientations relative to the sliding direction. Since the numerical models and the detailed results can be found elsewhere,[2,3] only a brief review of the models is presented here. Due to the symmetry conditions, half models are used in the FE investigations. The results presented in this section are obtained with a hemispherical sliding steel asperity with a radius $R = 0.45$ mm and a normal load $F_N = 1$ N. The friction coefficients measured for N-, P- and AP-fiber orientation are as follows: $\mu_N = 0.45$, $\mu_P = 0.28$, and $\mu_{AP} = 0.3$.[10] The fiber volume fraction of the composite is $V_f = 0.61$.

4.1 Finite Element Macro/Micro-Contact Models

The sliding indentation problems for different fiber orientations were modeled, as shown in Figure 1. The normal and tangential forces, F_N and F_T, produce a frictional contact state, associated with stresses and strains. In order to obtain accurate contact results, a larger segment of the bodies should be involved in the model. At this level, a macroscopic approach, assuming anisotropic material properties (see last column in Table 1), is used. The micro-model can describe the fiber/matrix structure in a more realistic way, but it requires much more elements.

These two models are represented schematically in Figure 10. The micro-model can approximately represent the behavior of the larger macro-model if they are connected by the displacement coupling technique.[2] The contact results of the macro-model are not used in the further evaluations, and only the displacement results of the proper surfaces are transferred to the micro-model as boundary conditions. The contact problem is solved again in order to find the contact parameters (location of the contact area and the contact pressure distribution) for the micro-model. In order to solve the contact problem, contact elements were located between the contacting bodies. The contact solution follows a linear elastic material law for each component of the models.

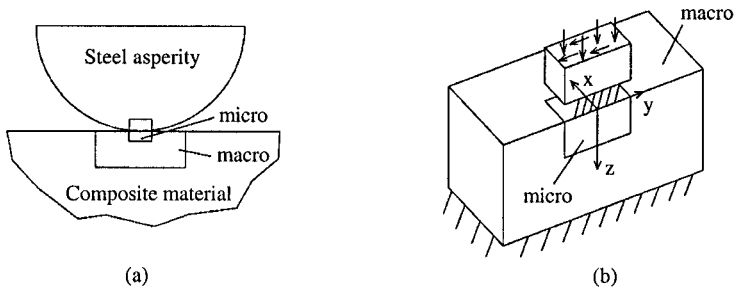

Figure 10. The global model (a) and the macro/micro-model with contact elements (b) (arrows describe the actual loading conditions of the steel asperity).[2]

4.2 Normal Fiber Orientation

Figure 11 shows the contact pressure distribution in the cases of normal fiber orientation. It can be seen that mostly fibers transfer the load. The frictional force induces an asymmetric contact pressure distribution on the top of the loaded fibers. The local pressure peaks appear at the rear edges of the loaded fibers located within the contact area.

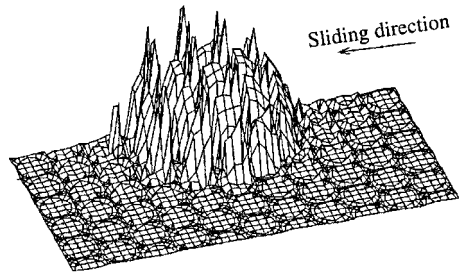

Figure 11. Contact pressure distribution in the case of N-fiber orientation.[2]

These results were obtained by FE macro/micro-models fitted by the displacement coupling technique.[2] In the case of N-fiber orientation, the deformed shape of the micro-model can be seen in Figure 12. Since in the present case (and in[2]), the radius of the steel ball differs from that of the diamond indentor, these results can, as a first approximation, only be regarded as illustrative of the wear processes.

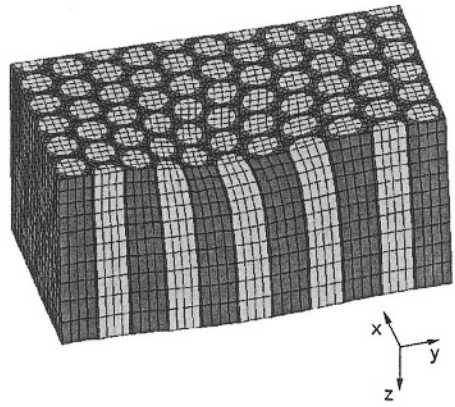

Figure 12. Deformed shape of the contact region in the case of N-fiber orientation (deformation scale 5:1).[2]

The vertical stress component, σ_z, that is the dominant component of the Von Mises equivalent stress (Figure 13), can cause failure at the rear edges on the top of the fibers. The compression limit strength of CF/PEEK composite is 1200 MPa.[11] As a rough assumption, the compression strength of a single carbon fiber is about 1900-2000 MPa, obtained by using a rule of mixture type relationship. This value and the maximum σ_z stress component at the rear edges of the mostly loaded fibers are almost in the same range, predicting fiber cracking in these local regions. This phenomenon can be explained by the asymmetric contact pressure distribution appearing on the top of the loaded fibers.

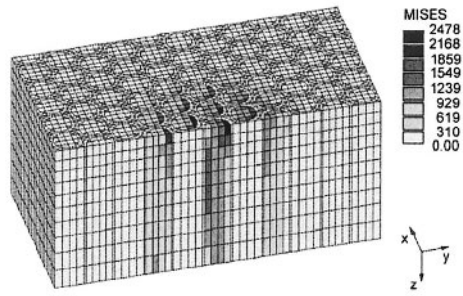

Figure 13. Von Mises equivalent stress in the composite for N-fiber orientation (MPa).[2]

Due to the high normal and shear stresses, equivalent stresses, exceeding the yield limit of the matrix material, are produced near the surface and along the fiber/matrix interfacial regions.[2] As a result, the matrix material becomes deformed and eventually can be sheared off in the form of thin wear debris layers.

The horizontal σ_y tensile stress component reaches its maximum at the rear edge of the contact area on the surface (Figure 14). During the sliding motion,

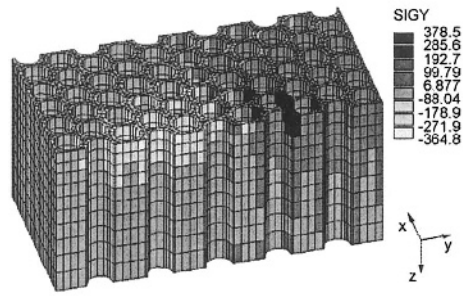

Figure 14. The σ_y (SIGY) stress component in the matrix for N-fiber orientation (MPa).[2]

these stresses are producing a repeated compression-tension loading along the fiber/matrix interfaces at the surface, resulting in fiber/matrix debonding events on both sides of these fibers (in the sliding direction). The tension type debonding appears on the surface of the composite material, from where it propagates in the depth. In addition, the normal loads induce high shear stresses along the fiber/matrix interface. Therefore, shear type debonding can also be initiated, propagating in the depth, similar to the tension one.

One can conclude that debonding seems to be one of the first phases of the wear process. If an asperity is sliding over the same region after debonding, the stresses produced (especially in the matrix) are substantially higher due to the separate deformation of the fiber and matrix components. At the same time, stronger bonding can reduce the debonding depth and, in this way, can increase the wear resistance of the composite material.

Comparing the failure mechanisms predicted, matrix shearing and fiber/matrix debonding seem to be the most dominant ones at the beginning of the wear process. They are followed by fiber cracking, as a further wear phenomenon, because the maximum compression stress at the top of the fibers is close to the compression strength limit.

4.3 Parallel Fiber Orientation

Figures 15 and 16 show the contact pressure distribution and the deformed shape of the micro-model, respectively. If no friction is considered, bending produces a symmetric stress distribution (without traction) relative to the x-z plane. An additional friction force, however, modifies the stress pattern (Figure 17). The combined loading of compression, traction, and bending can cause high σ_y stresses that may lead to fiber cracking, as it can be verified experimentally. Behind the contact area, tension appears in the mostly loaded fibers, and the magnitude of the maximum compression stress in the middle of the contact area is increased. The location of the maximum compression region is moved further to the sliding direction due to the effect of the friction force.

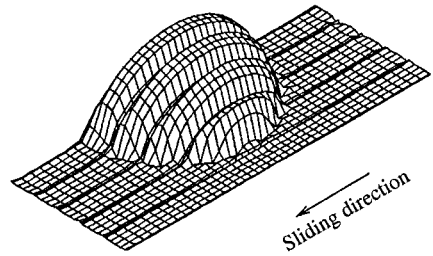

Figure 15. Contact pressure distribution in the case of P-fiber orientation.[3]

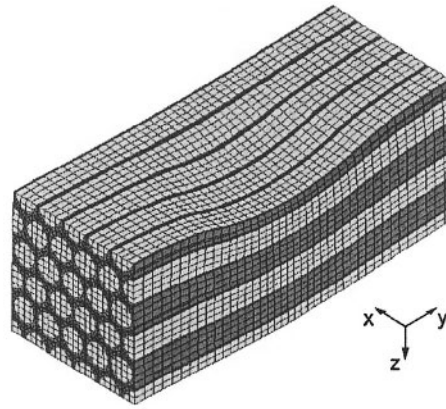

Figure 16. Deformed shape of the contact region in the case of P-fiber orientation (deformation scale 5:1).[3]

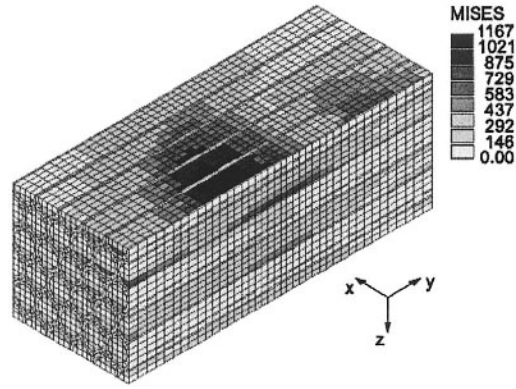

Figure 17. Von Mises equivalent stress in the composite for P-fiber orientation (MPa).[3]

With respect to the wear process, the most important wear mechanisms are fiber thinning, fiber/matrix debonding, fiber cracking, and shear events of the matrix material. Since the reinforcing fibers are oriented parallel to the contact plane, they are, first of all, subjected to bending.

The matrix material, in a small vicinity of the contact area and especially in the depth direction, is also subjected to high stresses. As a result, plastic deformation of the matrix under shear loading conditions should occur. The highest shear strain takes place around the mostly loaded surface fibers, at the front side of the contact area, and it is produced by the deformation due to normal and friction forces. According to these results, shear deformation and compression can finally yield a shear type failure of the matrix material. The high shear strains can also produce shear type fiber/matrix debonding. During the repeated sliding motion, it can propagate to the surface, producing a complete debonding of the

surface fibers. Therefore, it can be concluded that shear type debonding is a dominant failure mechanism in the case of P-fiber orientation. This debonding can produce a different, partly separated micro-structure that has less wear resistance than the original one, due to higher, more critical stresses.

4.4 Anti-Parallel Fiber Orientation

The deformed shape of the micro-environment can be seen in Figure 18. Considering the mostly loaded surface fibers, it can be concluded that the combined loading of compression/tension, bending, and torsion produces high fiber stresses (Figure 19). As a result, fiber cracking and fiber fragment removal can occur.

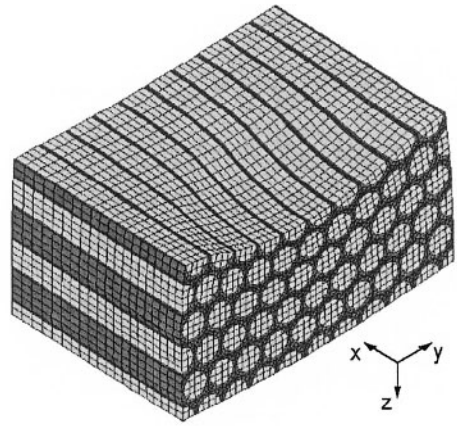

Figure 18. Deformed shape of the contact region in the case of AP-fiber orientation (deformation scale 5:1).[3]

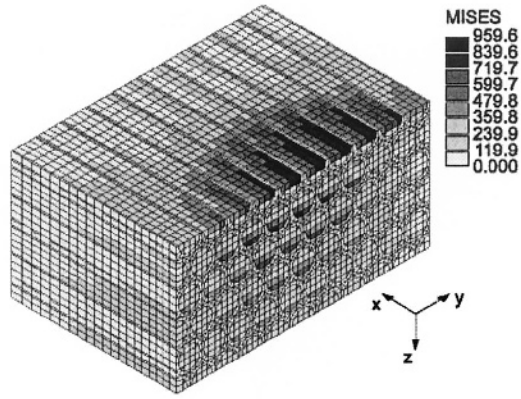

Figure 19. Von Mises equivalent stress in the composite for AP-fiber orientation (MPa).[3]

Similar to the P-fiber orientation, it can be concluded in this case also that in a small region of the contact area, especially in the depth direction, plastic deformation appears in the matrix material.

Based on the results,[3] the highest shear strains appear below the mostly loaded surface fibers, where they can produce shear type debonding. Furthermore the high horizontal σ_y stresses (Figure 20) can cause tension/compression type debonding. During the repeated sliding motion, the latter can propagate to the surface, producing complete debonding of the surface fibers.

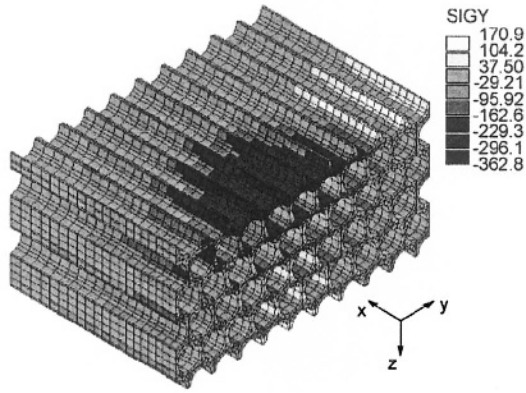

Figure 20. The σ_y (SIGY) stress component in the matrix for AP-fiber orientation (MPa).[3]

One can conclude that the shear and tension/compression type debonding is also one of the dominant failure mechanisms in the case of AP-fiber orientation. According to the results,[3] the AP-fiber orientation produces lower fiber and matrix stresses than the P-fiber orientation. This would imply a lower probability for wear failure under AP- compared to P-fiber orientation. This is, however, opposite to the impression one has from the scratch experiments, and also in contrast to previous sliding wear studies on this material.[12] Probably, in terms of the complete wear process and the complexity of wear mechanisms, the AP-fiber orientation is less advantageous, *i.e.*, the wear debris as a third abrasive have a more dominant effect on the wear process than in the case of P-fiber orientation.

5 Finite Element Simulation of the Fiber/Matrix Debonding

Due to the complexity of the problem, the frictional contact problem is first solved on two levels (by using larger macro- and smaller micro-models), followed by a non-linear debonding analysis.

The debonding models use a linear elastic-plastic material law for the matrix material that allows to study the plastic deformation in the matrix material. Due to this fact, the smaller diamond indentor ($R = 100\ \mu m$) with a normal load $F_N = 1$ N was used in the debonding simulation. The friction coefficient, obtained experimentally for N-fiber orientation, was $\mu_N = 0.1$. The results presented here are only for N-fiber orientation, although additional investigations were carried out also for P- and AP-fiber orientation.[9]

5.1 Debonding Model and Interface Elements

The debonding model obtains the boundary conditions over the sides of the model from the macro-contact model, and the contact pressure distribution is transferred from the micro-contact model. Additionally, it has an anisotropic "outer layer" of elements in order to apply the boundary conditions (obtained by the displacement coupling technique) in a "more uniform way", *i.e.*, by avoiding the direct loading of the softer matrix elements.

The model follows an incremental technique, *i.e.*, both the prescribed displacement and the load are incremented, and contains interface elements all the way around each fiber in order to model the debonding behavior (see Section 5.1.2).

For the material models, the following assumptions are made: (i) the fibers obey a linear elastic and anisotropic material law, (ii) the matrix follows an isotropic, linear elastic-plastic material law, (iii) the material behavior of the interface elements is described in Section 5.1.2, and (iv) the material model of the anisotropic "outer layer" is the same as that of the macro-contact model.

The micro-contact and the debonding model could be substituted by one model, but this task would require a huge computational effort, *i.e.*, to handle 750 contact elements, non-linear material behavior and a few hundred thousand degrees of freedom (DOF) in one model. For this reason, as an approximation, a linear elastic material law was assumed for the contact problems on both levels.

5.1.1 Interface Elements

Interface elements are located around each fiber, along its total length, as illustrated in Figure 21. The debonding analysis should detect the tension type (Mode-I) and the shear type (Mode-II) debonding, based on the tension and shear limit strain values, which characterize the initial and final phases of the debonding. In order to detect these types of debonding, local cylindrical coordinate systems are used to evaluate the representative stress and strain values. Figure 21 shows examples of tension and shear type debonding events. Tension type debonding can occur in the local radial direction (around the fiber), and shear type can take place in the local tangent plane (around the fiber) in any direction. In Figure 21, at

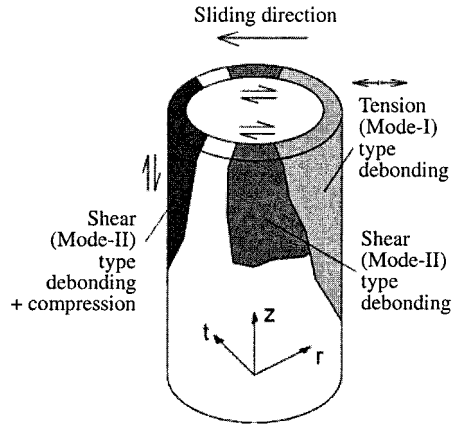

Figure 21. Schematic illustration of the locations where different types of debonding failure can occur.[8]

the upper left hand side of the model, shear is assumed in vertical direction, while compression is also present, modifying the debonding process.

The interface elements belong to the matrix material, therefore the material properties of the matrix and the interface are identical. Since the interface layer is modeled by eight-node solid elements, it has a finite thickness. In order to avoid degenerated element shapes, the thickness of the interface elements must be kept above a certain limit value, which is determined by the other two sizes of the eight-node interface elements. In the present study, the interface layer has a thickness of 0.5 μm.

5.1.2 Conditions of Debonding

Debonding is assumed to be the effect of an intensive plastic deformation, either a tensile, shear, or combined one. Figure 22 illustrates the different debonding criteria, assuming pure load cases.

The material behavior for debonding, based on the strain energy approach as an interface debonding criterion, is shown by the dotted line in Figure 22c,

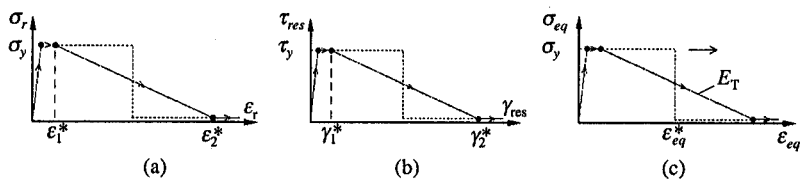

Figure 22. Debonding criteria (a) for pure tension, (b) for pure shear, and (c) a corresponding equivalent stress-strain curve.[8]

where ε_{eq}^* represents the equivalent debonding strain. Unfortunately, the non-linear FE technique available can only treat this behavior if a "light" degressive slope angle is used, assuming the same strain energy as for the case shown by the dotted line in Figure 22c. Therefore, the debonding model follows a linearly decreasing stress-strain curve specified by the tangent modulus E_T in Figure 22c.

In the case of combined stress and strain states, either the local radial strain ε_r or the local resultant shear strain γ_{res} controls the debonding process, depending on their magnitude. The debonding conditions are checked in the local cylindrical coordinate systems for ε_r (or later for γ_{res}), while the proper "segment" of the equivalent stress-strain curve controls the material behavior, *i.e.*, the proper (actual) material behavior is assigned to each interface element according to the equivalent stress-strain curve, as shown in Figure 22c. The material law applied is a Von Mises type elastic-plastic model.[13]

Tension type (Mode-I) debonding. Figure 22a illustrates the tension type debonding. If the interface element is subjected to tension in the radial direction, a linear elastic-perfectly plastic curve illustrates the first part of the material behavior. If the radial strain ε_r is greater than ε_1^*, local debonding starts showing a degressive stress-strain behavior. If the radial strain is as high as the limit strain ε_2^*, the debonding has ended, *i.e.*, the interface element cannot transfer load anymore.

Shear type (Mode-II) debonding under tension. In the local tangent plane (Figure 21), shear type debonding can occur in any direction. The resultant shear strain is

$$\gamma_{res} = \sqrt{\gamma_{rt}^2 + \gamma_{rz}^2}, \tag{1}$$

where γ_{rt} and γ_{rz} are the shear strain components in the local cylindrical coordinate system.

The shear type debonding process (Figure 22b) is similar to the tension type one. The strain values of γ_1^* and γ_2^* represent the initial and the final debonding in the case of pure shear. If the debonding has ended, the algorithm assigns practically zero material properties to the interface elements, according to Figure 22c.

Shear type (Mode-II) prevented and limited debonding under compression. The shear type debonding makes possible a "free sliding movement" between the debonding surfaces, if tension is present, *i.e.*, $\sigma_r > 0$. If, on the other hand, compression is active, this holds back the "free movement" after debonding has occurred. Two cases should be considered, based on the frictional behavior of the debonded surfaces.

If the compressive force, based on the radial stress σ_r and the coefficient of friction μ, produces a "potential" friction stress greater than the resultant shear stress τ_{res}, the "potential" friction force prevents the sliding motion of the debonded surfaces. The condition of prevented debonding is

$$\tau_{res} < \mu|\sigma_r|, \tag{2}$$

where

$$\tau_{res} = \sqrt{\tau_{rt}^2 + \tau_{rz}^2}\ , \tag{3}$$

and t_{rt} and t_{rz} are the shear stress components. If the friction force prevents the sliding motion of the debonded surfaces, it is assumed that the interface elements behave according to the original material law, shown by the dotted line in Figure 23.

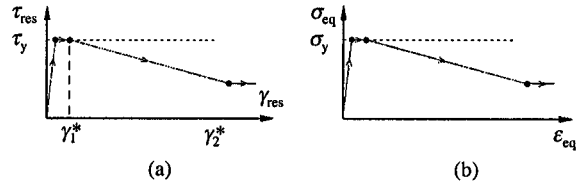

Figure 23. Debonding criteria (a) for pure shear under compression, (b) the corresponding equivalent stress-strain curve (dotted line shows the case of prevented debonding).[8]

The other case, *i.e.*, if

$$\tau_{res} \geq \mu|\sigma_r|, \tag{4}$$

allows a relative sliding, in which the friction force reduces the "free movement". This effect is roughly approximated by reducing the yield strength to half its original value, as illustrated in Figure 23b. This can be called "limited debonding".

5.1.3 Unloading Considerations

Finally, the total load is reduced to zero by a similar incremental technique. The unloading process follows the Von Mises type elastic-plastic model.[13] If the debonding has not ended yet, the unloading is controlled by the original modulus of elasticity. For the interface elements representing the final debonding, the unloading is executed according to a practically zero modulus of elasticity in order to avoid that stresses build up during unloading, *i.e.*, these elements cannot transfer loads anymore.

5.1.4 The Debonding Algorithm

The procedure developed is based on a non-linear FE analysis, using an incremental technique. At each load step, the algorithm selects the stress and strain results for each interface element, transforms them into the local cylindrical coordinate system, and checks if debonding has started or not. If debonding has started, the proper material properties are assigned to these elements, according to

the cases discussed in Figures 22 and 23; after this, the next load step is solved. These steps are repeated until the final load is reached.

5.2 Calculations for N-Oriented Carbon Fibers in a PEEK Matrix

To simulate debonding phenomena that can occur during the scratch test described in Section 2, at first contact calculation must be carried out. At a normal load $F_N = 1$ N, the measured coefficient of friction between the diamond indentor and the CF/PEEK specimen for N-fiber orientation was $\mu = 0.1$.

The debonding simulation is controlled by strain values representing the initial and the final debonding. For the PEEK material, the failure strain is in the range of 0.5-0.6.[1] In the case of a CF/PEEK structure, the failure of the interface layer seems to occur at a lower level, therefore, as a first approximation, a value of 0.35 was selected. It was considered as the equivalent debonding strain ε_{eq}^* (Figure 22c). In order to allow a numerical simulation, a limited slope angle has to be used for the debonding process. According to our test-calculations, the initial and final equivalent debonding strain values were taken as 0.05 and 0.65, respectively. The corresponding slope angle, *i.e.*, the representing tangent modulus was $E_T = -200$ MPa (Figure 22c). Considering the same equivalent strain conditions for the tension and the shear type debonding events, the following initial and final values were chosen:

$$\varepsilon_1^* = 0.056, \quad \varepsilon_2^* = 0.69 \tag{5}$$

$$\gamma_1^* = 0.09, \quad \gamma_2^* = 1.12. \tag{6}$$

Both ε_2^* and γ_2^* are higher than the real values, due to the limitation of the slope angle. The solutions for "more radical" degression of the stress-strain curves require further studies and probably a new solution technique.

Figure 24 shows the deformed shape of the contact area and its vicinity. The edge of the contact area can be identified by following the locations where debonding was more intensive. In particular, three fibers (next to "A" and "B" and the whole fiber between them) with prevailing deformation at their interface elements can be noticed. The difference in the vertical direction is mainly between the fibers and matrix at the front side of the contact area, similar to the push-up of matrix material in the real scratch test.

The debonding conditions in the problems studied were evaluated as in Section 5.1.2. At the maximum load, a total of 192 elements reached the final debonding state (*i.e.*, less than 0.7% of all interface elements). In the present case, final tension type debonding was not obtained. The reason for this is the rather low value of the coefficient of friction (as measured for the diamond indentor, *i.e.*, $\mu_{dia} = 0.1$). On the other hand, in previous wear studies with a steel disc and a normally oriented CF/PEEK material, the coefficient of friction was clearly higher ($\mu_{steel} = 0.45$).[10] In this case, debonding effects could probably occur much easier,

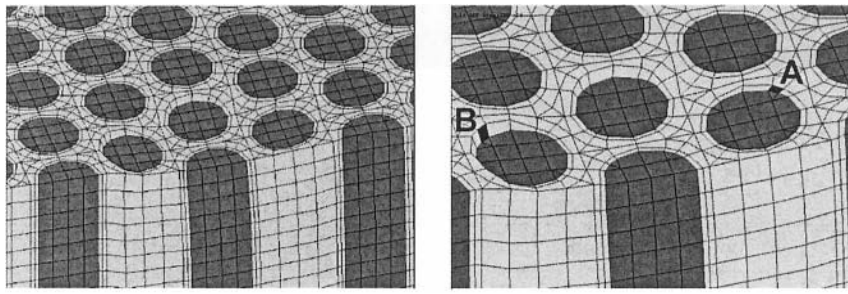

(a) (b)

Figure 24. Deformed shape of the contact area with debonding: (a) lower magnification, (b) higher magnification (shear type debonding under tension shown at *"A"*, limited shear type debonding under compression shown at *"B"*).[8] Sliding direction of the counterpart asperity from right to left.

and they were, in fact, also observed (Figure 25). This would be also in a better agreement with the results of Wu and Ovaert.[14]

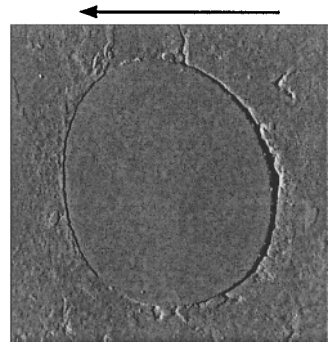

Figure 25. Tension type debonding of a normally oriented carbon fiber-reinforced epoxy composite, sliding against a steel counterpart, observed by AFM at the rear edge of a fiber.[15] The steel counterpart slides from right to left.

Shear type debonding, both under tension and compression, was analyzed here in detail within two vertical sections (Figure 26). Figure 27a,b illustrates the debonded interface elements in white and black. Shear type debonding under tension occurs on the side surfaces of the fibers relative to the sliding direction (see also Figure 21).

Shear type debonding under compression (Figure 27) is the most characteristic case (97% of the final debonding is of the shear type under compression), appearing mainly in front of the fibers, relative to the sliding direction. In the present case, prevented shear type debonding was not obtained.

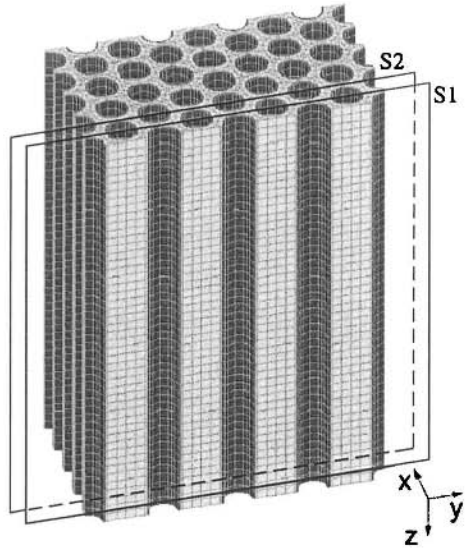

Figure 26. Schematic representation of the section planes: S1 located at $x = 5$ μm, S2 at $x = 10$ μm, respectively.[8]

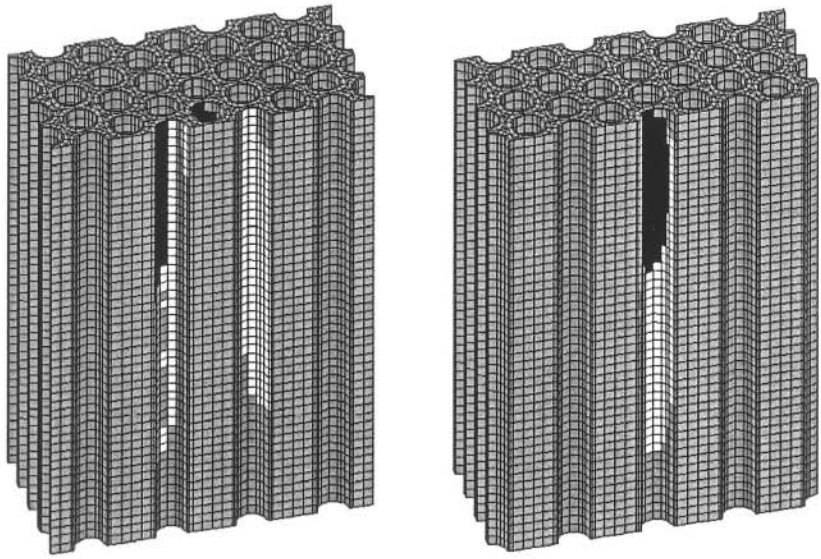

Figure 27. Limited shear type debonding under compression: (a) within S1 plane, (b) within S2 plane (initial debonding is shown in white, final debonding is shown in black).[8]

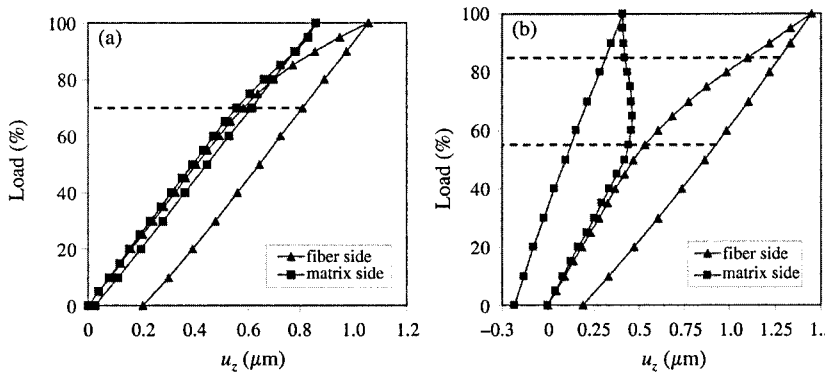

Figure 28. Vertical displacements, u_z, at the two sides of the selected interface elements in the vicinity of (a) *"A"* and (b) *"B"* in Figure 24 (dotted lines show the initial debonding, and at location *"B"* the final debonding as well).[8]

The debonding process is illustrated in Figure 28 at two locations. Figure 28a represents shear type debonding under tension (at the vicinity "A" in Figure 24), and Figure 28b shows an example for shear type debonding under compression (at the vicinity "B" in Figure 24). The vertical displacements of the two sides of the interface elements are plotted in terms of load (in percent of the maximum normal load of 1 N), showing the initial phase (at both locations) and the final phase (at the vicinity "B") of the debonding. Finally, the unloading process can also be followed.

6 Conclusions

When modeling the fiber/matrix micro-structure, in order to study wear and failure mechanisms in real fiber-reinforced composites, an FE macro/micro contact model (introducing the displacement coupling technique) is much more suitable than using an equivalent macro-model. As a result, the calculated contact, stress, and strain results are significantly closer to the real conditions.

Based on the FE micro-models, possible wear mechanisms of fiber-reinforced composites sliding in different directions against a counterpart asperity have been verified. For N-fiber orientation, surface failure of the matrix material is due to high shear stresses, producing thin layers of wear debris. The rear edges of the fibers located in the contact area can be cracked under high normal stresses. For P-fiber orientation, fiber/matrix debonding by shear type deformation and fiber sliding wear are the dominant failure mechanisms. If an AP-fiber orientation is considered, the shear and the tension/compression type debonding are the most dominant wear mechanisms.

Compared to the results of the experimental and the numerical investigations, typical failure mechanisms detected by FE models, such as matrix shear failure, fiber/matrix debonding, and fiber cracking were also observed on the scratched surfaces of such specimens.

An attempt was made to model the debonding process during sliding of a hard asperity on a fiber-reinforced polymer composite surface by introducing interface elements located around each fiber. The interface elements "can detect" the tension type and also the shear type debonding, the latter being under tension or compression. The complete solution consisted of the development of an anisotropic macro-contact model, a micro-contact model, and a debonding model. The first model provided the boundary conditions for the micro-models by a displacement coupling technique. The debonding model followed an incremental technique to study the process from the initial to the final debonding in terms of an increasing load.

In the case of a sliding diamond indentor, the smaller coefficient of friction produced prevailing shear type debonding mostly under compression. According to the results obtained, the high contact pressure maximum can produce fiber end breakage. For a polymer composite and steel sliding pair, the higher coefficient of friction could produce both tension and shear type debonding.

Regardless of the large number of elements in the micro-model (over 100 000), it is still too small when compared to the extent of the plastic deformation, therefore the present results can be regarded only as a first approximation of the real conditions.

7 Acknowledgements

The authors are grateful to the BMBF-TéT (UNG 020/99) and the Hungarian National Scientific Research Foundation (T 034746) for supporting the cooperation between the two institutions in the field of tribology of polymeric composites.

8 References

[1] ICI Thermoplastic Composites (1993) XC-2 wear resistant composites, Product Information.

[2] T. Goda, K. Váradi, K. Friedrich, H. Giertzsch (2002) Finite element analysis of a polymer composite subjected to a sliding steel asperity: Part I: Normal fibre orientation, *J. Mater. Sci.* **37**, 1575.

[3] K. Friedrich, K. Váradi, T. Goda, H. Giertzsch (2002) Finite element analysis of a polymer composite subjected to a sliding steel asperity: Part II: Parallel and anti-parallel fibre orientations, *J. Mater. Sci.* **37**, 3497.

[4] VDI Atlas of Heat (1997) (in German).

[5] M. Bauccio (1994) *ASM Engineered Materials Reference Book*, 2nd Edition, ASM International, Materials Park, OH.

[6] F. N. Cogswell (1992) *Thermoplastic Aromatic Polymer Composites*, Butterworth-Heinemann Ltd., Oxford.

[7] Victrex PEEK™, Material properties guide, http://www.victrex.com.

[8] K. Friedrich, T. Goda, K. Váradi, B. Wetzel (2004) Finite element simulation of the fiber/matrix debonding in polymer composites produced by a sliding indentor: Part 1 – Normally oriented fibers, *J. Compos. Mater.*, **38**, 1583.

[9] T. Goda, K. Váradi, B. Wetzel, K. Friedrich (2004) Finite element simulation of the fibre/matrix debonding in polymer composites produced by a sliding indentor: Part 2 – Parallel and anti-parallel fibre orientation, *J. Compos. Mater.*, **38**, 1607.

[10] J. Flöck, K. Friedrich (1998) Experimental investigations on the formation of a transfer film of carbon fiber-reinforced PEEK composites on a 100Cr6 steel ring, *Gft Tribologie-Fachtagung*, Göttingen, Vol. 1, p. 1 (in German).

[11] D. Hull (1990) *An Introduction to Composite Materials*, Cambridge University Press, Cambridge.

[12] J. Flöck (2001) Contribution to the experimental characterization and modeling of slidinig wear mechanisms of carbon fiber-reinforced PEEK composites, in *IVW Schriftenreihe* (Ed. M. Neitzel) Vol. 19, ISBN 3-934930-19-0, Kaiserslautern, Germany (in German).

[13] Structural Research and Analysis Corporation (2001) COSMOS/M User Guide V2.6.

[14] J. P. Wu, T. C. Ovaert (1994) Effect of asperity-scale tensile stresses on the wear behavior of normally oriented fiber-reinforced polymer composites, *Tribology Transactions* **37**, 23.

[15] Z. Zhang, C. Breidt, L. Chang, F. Haupert, K. Friedrich (2004) Enhancement of the wear resistance of epoxy: short carbon fibre, graphite, PTFE and nano-TiO_2, *Composites A* **35**, 1385.

Chapter 8

Determination of the Interface Strength of Polymer-Polymer Joints by a Curved Interface Tensile Test

Bernd Lauke, Konrad Schneider, Tobias Schüller
Institute for Polymer Research, Dresden, Germany

1 Introduction

The determination of the adhesion strength between two compact materials is still a problem under consideration. The main disadvantage of many tests is the creation of non-uniform, *i.e.*, singular stress states near the interface. Stress singularities cause initiation of debonding or material plasticization. In the first case, it is not clear how to determine a reasonable maximum stress (adhesion strength) with a finite value. It makes no sense to calculate an adhesion strength by dividing the maximum (critical) applied load by the loaded area. The occurrence of plastic deformations in a highly loaded region is not a general problem if it is considered by calculations. However, if there is no subsequent debonding, the experiment will be inappropriate for adhesion strength measurement. At least, it leads to the conclusion that the interface is stronger than the surrounding material.

There exist numerous tests to determine shear strength values, such as single- and double-shear lap tests, or tensile strength values, such as butt-like tensile tests.[1] However, the stress analysis of these testing arrangements reveals that the stress state is uniform only within the central regions of the samples, whereas it is singular at the edges.[2] The high local stress at the edges causes local failure of the interface or of one of the components. Kroupa *et al.*[3] and Pahr *et al.*[4] proposed the calculation of an average stress in the region near the sample edges according to the average stress criterion by Whitney and Nuismer.[5] However, this method introduces additionally the size of the region included into the averaging process, which is arbitrary. Haruna *et al.*[6] have applied the point stress criterion[5] to the butt test as a fracture criterion.

However, even this approach needs an additional characteristic length. Reddy and Guess[7] proposed the use of the critical intensity factors of the interface corner stress for the prediction of the interfacial quality. The so-called dominance zone of the stress intensity factor must be larger than the plastic zone in this case. This is a reasonable assumption only for certain materials, *e.g.*, ceramics and cleavage fracture of metals, but not for polymers.

In a recent publication, the authors proposed a new test set-up to measure the interfacial strength between polymer joints.[8] The joint is loaded parallel to the interface. Uniform stresses normal to the interface are caused indirectly by notches. There are no stress singularities in the whole sample and there are only normal interface stresses in the debonding region. Consequently, a simple strength criterion could be applied.

When a butt joint (flat interface) with elastic components is subjected to a remote uniaxial load, the stresses near the free edges are:[9]

$$\sigma_{ij}(r',\theta') = \frac{K}{(r'/a)^{\omega}} f_{ij}(\theta') + \sigma_{ij0}(\theta') \tag{1}$$

Here, r' and θ' are polar coordinates and a is a characteristic length, as given in Figure 1. The important exponent ω depends on the elastic constants of the two materials and on the angles θ_1 and θ_2 between the interface and the material boundaries. For positive values of ω, singular stresses are developed at the interface corners. For a flat joint, however, it was shown that there are cases when the

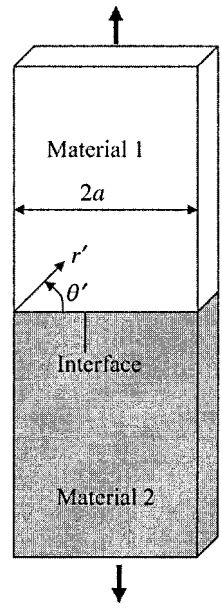

Figure 1. Geometry of a two-material joint with a flat interface.

exponent ω in Eq. (1) becomes negative, depending on the ratio between the elastic constants (Young's modulus and Poison's ratio) of the two materials.[9,10] This means that the stress field in the vicinity of the sample edge is not singular, which is a very important information concerning our aim of creating uniform stress states at the interface. It can be expected that also for other angles θ_1 and θ_2 there should be such a region of negative ω, depending on the ratio between the elastic constants of the two materials. This assumption for the zone near the edge ($r'/a \ll 1$) together with the knowledge that the stress field around an embedded particle has no singularities[11] and a maximum at the pole, *i.e.*, in the direction of the applied load, led us to the sample configuration shown in Figure 2. The use of such sample shapes has recently been described, but nothing has been reported about the failure initiation.[12]

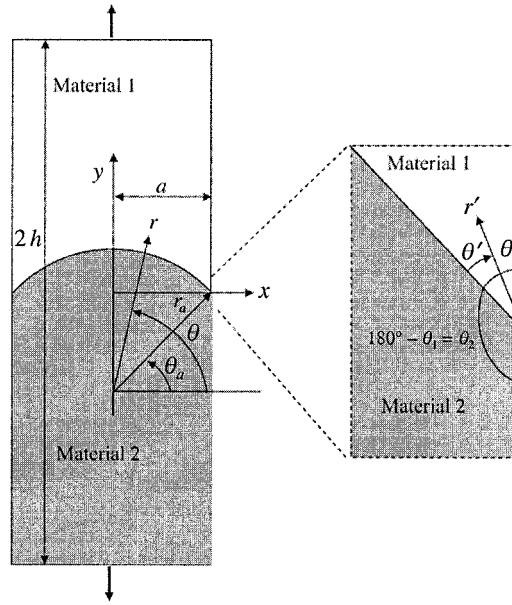

Figure 2. Geometry and coordinate system (x, y), respectively (r, θ), of a two-material joint with a curved interface. On the right hand side, the edge geometry and local coordinate system (r', θ') are shown.

This is not surprising because the material arrangement was chosen so that the common stress singularity (Eq. (1) with positive ω) develops at the edge of the sample. The maximum force has been divided by the sample cross section and these values have been used as the characteristic "composite strength". This method provides only a rough quantitative value to compare materials of the same geometry as in the experiment, but it does not provide a material parameter of the interface. It would be advantageous for the characterization of the adhesion between two

different materials to have an adhesion strength, which is independent of the sample geometry and dependent only on the interface quality.

In this chapter, a test method is proposed to determine the adhesion strength between two different polymers, where the interface fails under rather uniform stresses. The characterization of the adhesion quality by the strength at the interface makes only sense if a uniform stress state over a large enough interface region is created during application of the load. This is achieved by using samples with a curved interface between two different (or the same) glued or welded materials. A stress analysis provides the relation between the applied load and the created interfacial stress, as well as the optimum curvature of the interface for given material combinations.

2 Curved Interface Tensile Test

Figure 2 shows the general test set-up of the two-material sample under tensile load with the coordinate systems used for calculation of the stress distribution along the interface. Two polymer materials are bonded by a curved interface with the cylindrical coordinates $r = r_a$ and θ. Because of symmetry, only half of the sample needs to be considered, *i.e.*, $0 \leq x \leq a$ and $0 \leq \theta \leq 90°$. By choosing different radii r_a, different curvatures of the line and consequently different angles θ_1, respectively θ_2, can be realized at $x = a$. The geometrical situation near the point $x = a$ is shown at the right hand side of Figure 2. If the curvature of the interface in the very vicinity of that point is neglected, the typical open wedge problem[13] of two-material interfaces is faced.

During tensile loading of such samples, the interfacial failure would cause a drop in the load-displacement curve due to the change in the compliance. Also, the flanks of the failed joint separate. This separation will be visible if light transmission through the specimen is monitored. The adhesion strength results from the measured peak load of the force-displacement curve by means of a stress analysis. However, this method will be applicable only if there is no stress singularity at $x = a$ ($r = r_a$, $\theta = \theta_a$). One has to find the appropriate material arrangement and the appropriate curvature of the interface that ensure this assumption. There are at least two ways of doing this: analytically or numerically. The elastic solution of the two-material free edge problem by Williams[9] and other researchers gives Eq. (1), where the singularity parameter ω can be determined by a transcendental equation as a function of θ_1 and θ_2. Next, the stress intensities K and the angle functions f_{ij} have to be determined. The functions f_{ij} can be calculated analytically.[13] The stress intensity factor is usually defined in such a way that it is independent of the sample size, but depends on the applied load and a shape factor, as in the case of fracture mechanics (which represents the special case of $\theta_1 = \theta_2 = 180°$).

If no closed form analytical solution is available for the specific mechanical problem, a finite element analysis can be used for the determination of K, provided

that ω and f_{ij} are known. For a certain angle, usually along the interface ($\theta' = 0$), K can be determined by extrapolation of the stresses to $r' \rightarrow 0$:

$$\lim_{r' \to 0} \sigma_{ij} \times \left(\frac{r'}{a} \right)^{\omega} = K \tag{2}$$

This solution technique provides the stress distribution around a perfect interface between two materials. The term "perfect" means that normal stresses are continuous and there is no misfit in displacements. Our aim is now to find material combinations and interface geometry which do not cause stress singularities at the edge. For this reason, we follow here a more pragmatic way in using the finite-element modeling for the whole problem. With the knowledge of the form of the analytical solution available in the literature for the open wedge problem, the cases of importance for our aim were found by some trials. The geometry and material combinations that are inappropriate for measuring the adhesion strength provide the typical stress singularities and some results are shown only for the sake of comparison.

3 Stress Calculation by Finite-Element Analysis

The stress analysis provides the relation between the applied load and the created interfacial stresses, as well as the optimal curvature, respectively the radius r_a. The geometry shown in Figure 2 is modeled with a 2D (plane stress)-FE-analysis. Due to symmetry, only one half of the specimen is modeled. The following geometrical values have been used: $a = 5$ mm, $h = 30$ mm. The radius of the interface is given by: $r_a = f \times a$ with $f \geq 1$. The angles θ_1 and θ_2 depend on this value, and from the geometry it follows that $\theta_a = \arccos(a/r_a)$ and $\theta_1 = \theta_a$, $\theta_2 = 180° - \theta_a$.

The mesh is built using 8-node elements. A fine mesh is used at the edges of the interface between the two materials. The calculations are performed by using ANSYS 5.5® (PLANE82-elements). Since the implementation of ANSYS® is displacement-oriented, displacement-controlled boundary conditions are used. Symmetry implies that the nodes on the y-axis should be constrained, so that no displacement occurs in the x-direction.

The following elastic properties have been used for the stress analysis: Material 1, elastic modulus $E_1 = 0.33$ GPa, Poisson's ratio $\nu_1 = 0.49$; Material 2, $E_2 = 3$ GPa, $\nu_2 = 0.35$. The thermal residual stresses caused by the sample preparation are neglected.

For the composite shown in Figure 2 two different material combinations are considered for stress analysis: Case 1, Material 1 on the concave side of the interface and Case 2, Material 1 on the convex side of the interface.

3.1 Flat Interface

First, the problem of a flat interface between the two materials was considered. This should provide a typical stress distribution, as has already been calculated analytically, *e.g.*, by Williams,[9] and Munz and Yang.[10] Figure 3 shows the different interface stresses normalized by the applied load σ_y^0. The distribution of stress concentration of the normal tensile stress at the interface $\sigma_{yy}(y = 0)$ along the sample cross section shows that, within the middle part, it is slightly smaller than 1, but is counterbalanced at the edge by singular stresses. This behavior forbids the application of a strength criterion to evaluate the adhesion strength of the interface. Because of this non-uniform stress distribution, it makes no sense to normalize the critical applied load by the cross section A of the sample to obtain the debonding strength: $\sigma_{yy} = \sigma^0_{y,critical} = F^0_{y,critical}/A$. The shear stresses within the interface are almost zero in the middle of the sample and increase toward the edge. Because of the higher Poisson contraction of Material 1, it is under compression and Material 2 is under tension near the interface. Because the loading is symmetrical with respect to the interface, the stress concentration does not depend on the arrangement of the two materials.

3.2 Curved Interface

Case 1, low modulus Material 1 at the concave side. Let us consider the case when the stiffer of the two materials (Material 2) is placed at the convex side of the interface. When the radius $r_a = 2\times a$ is used, which implies a rather flat curvature of the interface, the stress distribution is similar to the case of a flat interface, as shown in Figure 3. This means that the stress exponent of Eq. (1) is positive for this material combination and geometry. Increasing the curvature, *i.e.*, decreasing the radius to $r_a = 1.1\times a$, provides the stress distribution shown in Figure 4.

The hoop stress in Material 2 now becomes rather high and tensile near the edge. The radial stress component slightly decreases near the edge but develops singularity at the edge. Consequently, the general situation does not change.

Case 2, low modulus Material 1 at the convex side. Several finite-element calculations for a radius $r_a \geq 2\times a$ led to the result that the radial tensile stress σ_{rr} at the interface shows the highest value at the edge of the two-material composite, rather than in the center. Decreasing the radius to $r_a = 1.5\times a$ ($\theta_1 = 48.2°$) suddenly changes the situation completely (Figure 5). The stress singularities disappear, so this is the material arrangement and geometry we are looking for. At the edges of the two-material composite, the stresses have finite values and, in the center part of the sample, the normal tensile stress, σ_{rr}, is rather uniform. Additionally, because of symmetry, the shear stresses at the center of the sample are zero. For this curvature, *i.e.*, for these angles $\theta_1 = 48.2°$ and $\theta_2 = 131.8°$ between the interface

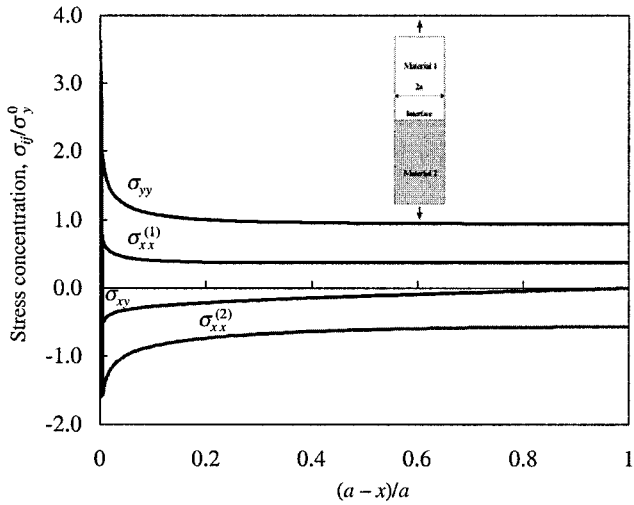

Figure 3. Stress concentration along the flat interface, in cartesian coordinates.

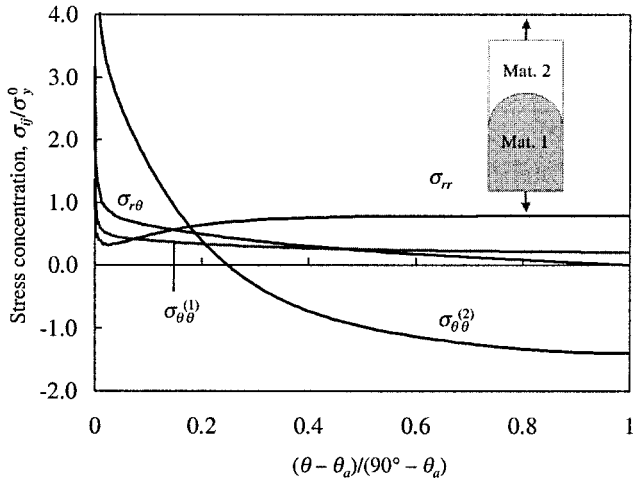

Figure 4. Stress concentration along the curved interface with $r_a = 1.1\times a$, Material 2 (stiff) on the convex side, in cylindrical coordinates.

and the sample boundary, the stress exponent ω of Eq. (1) becomes negative. Also for a radius $r_a = 1.01\times a$, which is nearly a semicircle geometry, the stresses remain finite. However, the hoop stresses near the pole in Material 1 increase to the order of the radial stresses at the interface. This may become critical for failure of Material 1 before debonding starts. Hence, whether this is critical or not must be established through experimental work.

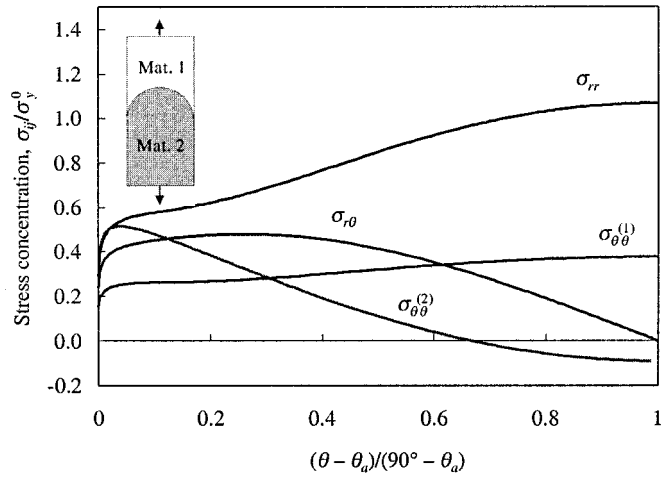

Figure 5. Stress concentration along the curved interface with $r_a = 1.5 \times a$, Material 1 (soft) on the convex side, in cylindrical coordinates.

This stress distribution is the basis for the determination of the adhesion strength at the interface. In such a case, the maximum stress criterion can be applied to determine the debonding strength:

$$\sigma_d = \frac{\sigma_{rr,\max}}{\sigma_y^0} \times \frac{F_{y,critical}^0}{A} = k_{rr}\, x\, \frac{F_{y,critical}^0}{A} \tag{3}$$

The maximum radial stress as a function of the mechanical properties of the components and the geometry are calculated by finite-element modeling. The critical load must be determined experimentally. It may be observed by a kink in the force-displacement curve, by direct optical observation, or by acoustic emission analysis. The calculated stress concentration factors for different curvatures of the interface are given in Table 1.

4 Experimental Observations

4.1 Materials and Specimen Preparation

Two different materials were chosen for the stiffer component (Material 2), polymethylmethacrylate (PMMA) and polycarbonate (PC). They were bonded to a much softer thermoplastic elastomer (TPE) (Material 1). The bulk mechanical

Table 1. Maximum stress concentration factor in the middle of the sample for different curvatures of the interface, Material 1 ($E_1 = 0.33$ GPa) on the convex side and Material 2 ($E_2 = 3$ GPa) on the concave side.

$F = r_a/a$	*Stress concentration factor,* $\sigma_{rr} = (\theta = 90°, r = r_a)/\sigma_y^0$
∞	0.944*
2	1.026*
1.5	1.058
1.1	1.109
1.01	1.128

* Stress singularities at the sample edges

Table 2. Mechanical properties of the components of the two-material samples.

Polymer	*Commercial grade*	*Tensile modulus (GPa)*	*Poisson's ratio*
PC	Lexan 121, GE Plastics	2.2	0.41
PMMA	Piacryl SG 90, Stickstoffwerk Piesteritz (comparable to Plexiglas 7N, Degussa)	3.1	0.37
TPE	Thermoplast TC 7 HAA (Styrene-block-copolymer/SEBS/70, Shore A), Fa. Krailburg	*ca.* 0.01	0.32

properties of the materials are summarized in Table 2. The two-material composite samples were produced by two-component injection-molding with a specially curved inlay into the mold.

As shown with the calculation of stress distribution, the semicircular sample geometry ($r_a/a \approx 1$) lacks singularities and has the advantage to avoid pre-cracks at the edges during the sample preparation. For this reason, we used the geometry shown in Figure 6 in our experiments.

Plates (80 mm×80 mm×2 mm) were produced by injection molding. From these plates, inlays for the injection molding tool were milled with different circular curvatures with radii $r_a = a = 0.5, 0.8, 1.0, 1.5, 2.0, 3.5, 5.0$ mm, and radii $r_a = 7.0$ and 10.0 mm with $a = 5$ mm ($r_a/a = 1.4$ and 2), as well as a flat interface with sharp edges at a width of 10 mm. The following geometrical parameters were used: h_p = 1-2 mm, $h_s \geq 10$ mm, $2b$ = 13.5-16.5 mm, specimen thickness $2t = 2$ mm. The testing speed was 5 mm/min.

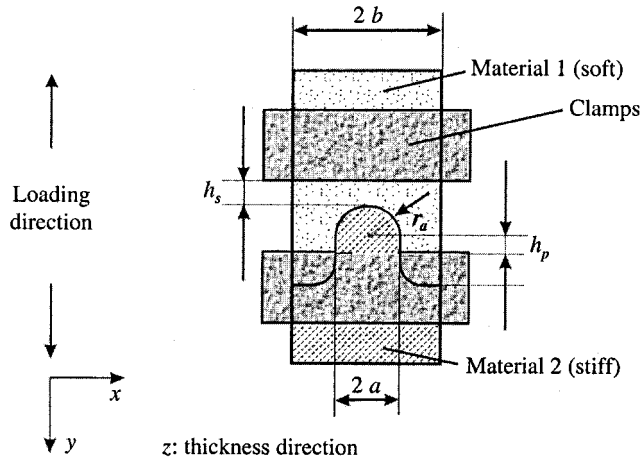

Figure 6. Specimen geometry for the curved interface tensile test; case of a circular interface ($r_a = a$) with supporting soft material at the edge.

4.2 Tensile Tests and Strain Estimation

The critical load for interface failure at the pole in the loading direction was determined experimentally by a kink in the force-displacement curve, as well as with direct optical observation. The drop in the load was nearly proportional to the ratio r_a/b. This is because a smaller radius r_a and a fixed width $2b$ would result in a smaller debonding area and therefore a lower compliance change during debonding. Typical stress-displacement curves of the PC-TPE-samples are shown in Figures 7 and 8 for the PC-TPE and PMMA-TPE samples, respectively. In most cases, instantaneous debonding took place along the whole interface.

To monitor the entire 2D-strain field at the samples surfaces, an optical grating method (ARAMIS, Fa. GOM Braunschweig, Germany) was used. It is based on a clearly visible random structure which is deforming along with the object. The deformation of this structure under different load conditions is recorded by a CCD camera and evaluated using digital image processing. The results obtained are the 2D-displacement and the strain field (lateral and transverse strain), based on a large number of data points. The high data point density and the graphical display of the results lead to a better understanding of the deformation behavior of the components.

Black paint spraying was applied to generate the optically active random structure. The CCD camera used had a resolution of 1280×1024 pixels. A grating was used with mesh width of normally 10×10 pixels, and each point was identified within a cell of 13×13 pixels.

In addition to the graphical display of 2D-displacements, also the displacement and tensile strain along the y-direction in the middle of the sample was investigated. This allows to trace the failure at the pole position of the interface.

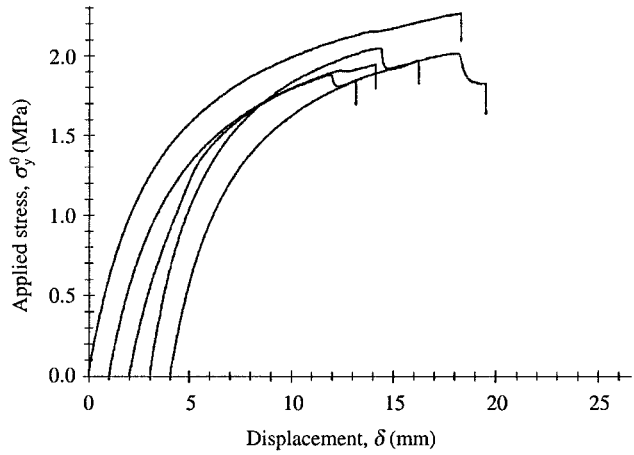

Figure 7. Typical stress-displacement curves of the PC-TPE samples (radii of curvature r_a = 0.5, 0.8, 1.0, 1.5, 2.0 mm, r_a/a = 1, curves shifted by 1 mm).

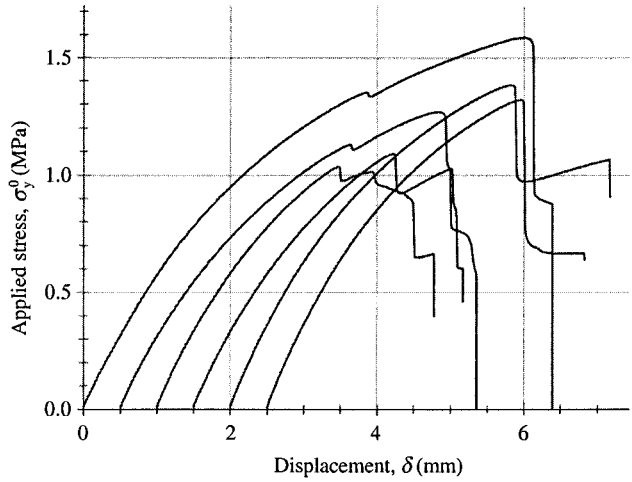

Figure 8. Typical stress-displacement curves of the PMMA-TPE samples (radii of curvature r_a = 0.5, 0.8, 1.0, 1.5, 2.0, 3.5 mm, r_a/a = 1, curves shifted by 1 mm).

The loading of a two-material composite perpendicular to the interface should show a clear step in the strain because of the different stiffness of the materials. A failed interface would exhibit a pole between the relatively moderate-strained components (*i.e.*, an offset of the borderlines of the two components). However, if a crack propagates from the surface of the specimen in the pole region into the specimen along the interface (through-thickness direction), one observes a large displacement of the cells close to the interface and a decreased strain

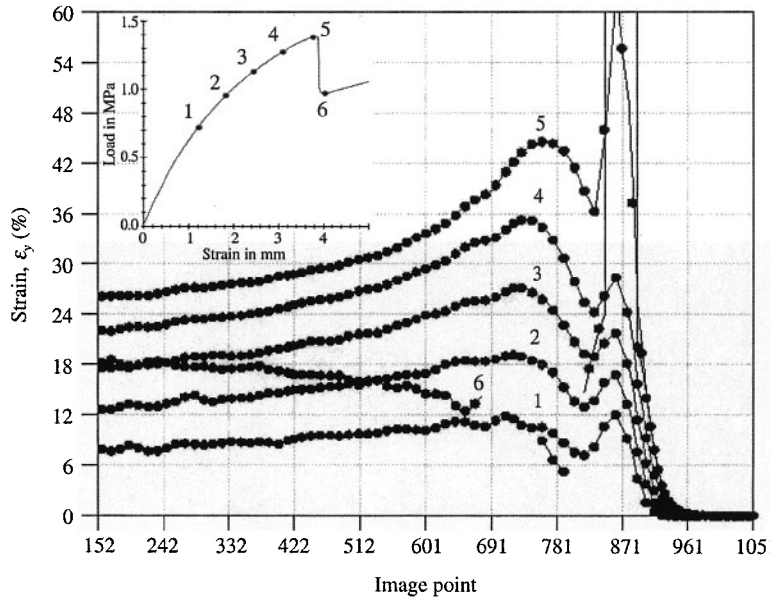

Figure 9. Longitudinal strain, ε_y, along the middle line ($x = 0$) of the sample surface at different strain states of a PMMA-TPE specimen with a radius of curvature r_a= 3.5 mm (r_a/a = 1). Abscissa: co-ordinate along the middle line of the sample (image points), the ordinate gives the strain in %. Numbers 1-6 refer to the load as indicated in the inset.

immediately behind it. Some typical strain curves of the PMMA-TPE specimen with a circular curvature (r_a = 3.5 mm) are shown in Figure 9.

With increasing load, the strain level grows steadily until failure. An additional strain tip establishes directly at the interface. It is relatively difficult to detect the exact moment of the crack initiation running from the surface to the specimen middle at the pole. After the interface failed, the total strain curve drops down.

The measurement allows us to draw the conclusion that failure starts at the surface in the pole region of the sample. This can be understood if the through-thickness (z-direction) geometry at the pole is considered. In this direction, Material 1 meets Material 2 under angles $\theta_1 = \theta_2 = 90°$. In such cases, a stress singularity ($\omega > 0$) develops. To avoid such high stresses at $z = \pm t$, $r = r_a$ double curved interfaces would be necessary.

4.3 Determination of the Adhesion Strength

The measurements of the load-displacement curves of the different samples, as shown in Figures 7 and 8, now provide the critical load to determine the debonding strength at the interface. The values of the debonding stress are collected

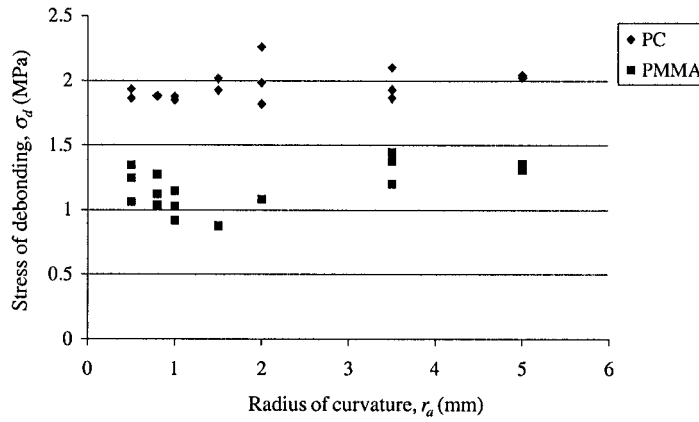

Figure 10. Critical applied stress of debonding at the pole position *vs.* radius of curvature r_a for $r_a/a = 1$.

in Figure 10 for different radii of curvature. As expected from the modeling, the stress concentration factor at the pole is mainly dependent on the ratio r_a/a. Samples with the same $r_a/a = 1$, but with different nose widths $2a$ should therefore provide the same debonding strength. The experiments show that the applied stress at failure is relatively independent of the nose width.

For the case of $r_a/a = 1.01$ (a circle-like shape of the interface), the finite-element calculations provide the stress concentration factors $k_{rr} = \sigma_{rr,max}/\sigma_y^0 = \sigma_{rr}(\theta = 90°, r = r_a)/\sigma_y^0$ for the two-material combinations, TPE-PMMA: $k_{rr} = 1.18$ and TPE-PC: $k_{rr} = 1.17$.

The diagram provides the mean critical applied stress for TPE-PMMA: $\sigma^0_{y,critical} = F^0_{y,critical}/A = 1.25$ MPa and for TPE-PC: $\sigma^0_{y,critical} = F^0_{y,critical}/A = 2.0$ MPa.

Together with the stress concentration factors, Eq. (3) provides the adhesion strength between PMMA and TPE to be $\sigma_d = 1.48$ MPa and between PC and TPE to be $\sigma_d = 2.34$ MPa.

5 Conclusions and Outlook

A new test method was proposed to determine the adhesion strength between materials of different elastic behavior. The stimulus came from the solution of two mechanical problems. First, in general, stress singularities are developed near the free edge of a bonded two-material composite. However, for special material combinations of flat interface geometry, this singularity disappears. Second, the radial stress at the surface of a hard sphere embedded within a softer matrix that is

under tensile load is maximum at the pole in the loading direction and decreases to the equator without any stress singularity. The answer to the following question led us to the new experimental set-up: Is there any geometry of an interface between two materials that does not cause stress singularities at the sample edges, but provides maximum normal stresses at the interface that change only smoothly? A curved interface with certain angles between the interface and the material boundaries and with the softer material on the convex side of the interface fulfils these requirements. For the two-material combinations considered here, Table 1 shows that for the ratio $f = r_a/a \leq 1.5$, no singularities appear at the edges. At the pole, the normal stresses are maximum and the shear stresses are zero. This allows the application of the simple uniaxial debonding criterion to determine the adhesion strength at the interface of a material joint.

However, samples are three-dimensional, so at the surface of the interface (in the thickness direction) stress singularities are again developed. To overcome this problem, the samples should have a double curvature. This requires a 3D-modeling for the calculation of the stress concentrations and respective experiments. For sample preparation, it is only necessary to modify the milling process of the polymer plates which are placed into the molding device, all other procedures being conventional.

6 References

[1] A. J. Kinloch (1994) *Adhesion and Adhesives*, Chapman & Hall, London, Glasgow, New York, Tokyo, Melbourne, Madras.

[2] K. Schneider, B. Lauke, W. Beckert (2001) Compression shear test (CST) – a convenient apparatus for the estimation of apparent shear strength of composite materials, *Appl. Compos. Mater.* **8**, 43.

[3] F. Kroupa, Z. Knesel, J. Zemankova (1992) Criteria for crack propagation at ceramic interfaces, *Proc. Int. Conf. Engineering Ceramics*, Smolnice Castle (Ed. M. Haviar) p. 102.

[4] D. H. Pahr, F. G. Rammerstorfer (2004) A fast multi-scale analysing tool for the investigation of perforated laminates, *Composites & Structures* **82**, 227.

[5] J. M. Whitney, R. J. Nuismer (1974) Stress fracture criteria for laminated composites containing stress concentrations, *Compos. Mater.* **8**, 253.

[6] K. Haruna, H. Hamada, Z.-I. Maekawa (1996) Strength prediction of adhasively bonded carbon/epoxy joints, *J. Adhesion Sci. Technol.* **10**, 1089.

[7] E. D. Reddy, Jr., T. R. J. Guess (1995) Butt joint tensile strength: interface corner stress intensity factor prediction, *Adhesion Sci. Technol.* **9**, 237.

[8] T. Schüller, B. Lauke (2002) Measuring the interfacial transverse strength: a novel test for evaluating polymer joints, *Int. J. Adhesion & Adhesives* **22**, 169.

[9] M. L. Williams (1952) Stress singularities resulting from various boundary conditions in angular corners of plates in extension, *J. Appl. Mech.* **19**, 526.

[10] D. Munz, Y. Y. Yang (1994) Stresses near the free edge of the interface in ceramic-to-metal joints, *J. Eur. Ceram. Soc.* **13**, 453.

[11] B. Lauke, T. Schuller, W. Beckert (2000) Calculation of adhesion strength at the interface of a coated particle embedded within matrix under multiaxial load, *Computational Mater. Sci.* **18**, 362.

[12] AIF-Research Report (2001) Interface reactive two component injection molding for hard-soft composites, AIF-Vorhaben-Nr. 12116B (in German).

[13] D. H. Chen (1994) General singular stress field in fracture mechanics, in *Computational and Experimental Fracture Mechanics* (Ed. H. Nisitani), Computational Mechanics Publications, Southhampton, UK, Boston, USA, p. 213.

Chapter 9

Manufacturing and Characterization of Microfibrillar Reinforced Composites from Polymer Blends

Michail Evstatiev, Stoyko Fakirov
University of Sofia, Laboratory on Polymers, Sofia, Bulgaria

Klaus Friedrich
Institut für Verbundwerkstoffe GmbH (Institute for Composite Materials), Kaiserslautern University of Technology, Kaiserslautern, Germany

1 Introduction

Blending polymers with other plastics, fibers, nano- or microparticles, and plates is a major route to improve the mechanical and barrier properties of polymeric materials. However, numerous polymer blend partners are thermodynamically immiscible and technologically incompatible. As a result, a great variety of morphologies of the dispersed phase can be formed *in situ* during processing, such as spheres or ellipsoids, co-continuous phases, ribbons or plates.[1-5] The shapes of the blend phases depend on the weight ratio, processing conditions, and chemical structure and properties of the components. It is well known that the physical properties of the matrix polymer, the shape and size of the dispersed phase, the nature of the interface, and the compatibility between the phases strongly affect the final properties[4-7].

The processing of an immiscible or incompatible polymer pair in which the dispersed phase forms *in situ* reinforcing fibrils can result in an appropriate morphology and improvement in the mechanical properties. This can be achieved by blending thermotropic liquid crystalline polymers (TLCP) with thermoplastics. These blends are often referred to as *in situ composites* because in the flow fields that occur during polymer processing operations, *e.g.*, in the advancing melt front

during injection molding, the TLCP phase can elongate into oriented fibrils that finally reinforce the thermoplastics matrix. TLCP are essentially rigid rod-like, long-chain molecules with some irregularity or flexibility incorporated into the polymer chain to lower the melting point below the decomposition temperature. The rigid-rod molecular structure allows these materials to exhibit molecular order in a liquid mesophase. The highly oriented nature of LCP produces highly anisotropic physical properties and makes thermotropic LCP quite attractive as a potential dispersed phase of the *in situ* reinforced materials. Blending LCP with conventional polymers has attracted much attention over the last decade.[8-18]

Recently, it was proved that the two-stage processing, which involves extrusion and injection molding of LCP blends at the matrix processing temperature, *i.e.*, below the melting temperature, T_m, of the LCP component in the blend, results in a much better product regarding its overall performance than the product obtained from single-stage direct injection molding. Two-stage processing minimizes the skin-core morphological difference and anisotropy, and leads also to a smoother surface of the polymer/polymer composite.[14-16] The extrusion and continuous drawing process in which *in situ* fibrillation occurs is very important for the obtaining of an optimal final product. The draw ratio (which in the present case is the ratio of the square of the die diameter to the square of the final extrudate diameter) is the factor, which finally determines the resulting properties. In general, LCP fibrillation and hence the mechanical performance of the resultant product become better at higher draw ratios.[14-18] Usually, the draw ratio depends on many factors, such as processing temperature, screw speed, die diameter, *L/D* ratio, and material feed rate.[15-18]

Unfortunately, the LCPs are often too expensive for general engineering applications. On the other hand, there are considerable supplies of engeneering plastics in the form of post-consumer scraps, which are a low cost source of raw materials for polymer blends. However, unlike LCPs, the molecules of common thermoplastics relax during melt processing; therefore a good molecular orientation is almost impossible.

A new type of polymer-polymer composites, the *microfibrillar reinforced composites* (MFC) from thermoplastic polymer blends, was created about ten years ago.[19-22] Unlike the classical macro-composites (*e.g.*, glass fiber-reinforced ones) and the *in situ* composites (TLCP rod-like macromolecules and mostly their aggregates as reinforcing elements), the MFC are reinforced by microfibrils of *flexible* chains. The microfibrils are created during the MFC manufacturing.

The preparation of MFC includes three basic steps: (i) melt blending with extrusion of the two immiscible polymers having different melting temperatures (*mixing step*), (ii) cold drawing of the extrudate with good orientation (*fibrillization step*), and (iii) thermal treatment at a temperature between the T_ms of the two blend partners (*isotropization step*). As a matter of fact, only after this last stage one deals with a reinforced composite material. The isotropization step can take place during the processing of the drawn blend *via* injection or compression molding.

The essential requirement is that the processing window is not too close to the T_m of the microfibrils, otherwise they will melt and take again a spherical shape.

The development of the described morphology during MFC manufacturing and processing was manifold proven by means of wide-angle X-ray scattering (WAXS),[5,6,19-29] light microscopy (LM),[21-23] scanning electron microscopy (SEM),[5,6,23-32] and transmission electron microscopy (TEM).[23,24,30]

It should be mentioned that a new approach to create *in situ* composites based on thermoplastic polymers (mainly poly(ethylene terephthalate) (PET) and polyolefins) was very recently proposed.[33-36] The preparation of these materials is quite similar to the MFC concept and could be generally described as follows: (i) in a first step, melt extrusion is followed by a high speed hot-stretching process at the T_m of the higher-melting component (*ca.* 270-280 °C), during which the fibrillar morphology of the higher-melting blend partner is created, and (ii) in a second step, the drawn blend is processed at a processing temperature of the lower-melting component (*ca.* 220 °C), in order to preserve the fibrilar structure of the higher-melting blend component.

The present chapter deals with investigations on MFC-structured blends of different thermoplastic polymers.[24,27,30-32] The main topics are concentrated on: (i) manufacturing of microfibrillar reinforced blends from recycled PET and polypropylene (PP), as well as from liquid crystalline polymers and poly(phenylene ether) (PPE) under industrially relevant conditions; (ii) processing of the drawn blends by injection and compression molding, and (iii) studies of the structure-property relationships of these MFCs after processing.

2 Materials, Processing, and Characterization Techniques

Recycled PET from beverage bottles (type FR 65, supplied by Rethmann Plano GmbH) (as reinforcing component) and commercial grade PP (type Novolen with MFI 5, provided by Basell) (as matrix), as well as a compatibilizer (C) (ethylene-glycidyl methacrylate (E-GMA), type Lotader AX 8840, commercial product of Atochem) were used.

From the dried components, various PET/PP/C blends (in wt. ratios 40/60/0; 40/59/1, 40/57/3, 40/54/6, and 40/51/9) were prepared and processed on a Brabender twin-screw extruder. The extrudate was cooled down to a temperature of 75-80 °C before it was continuously drawn to a draw ratio of about 10-12. Part of the drawn bristles (diameter of 0.6-0.7 mm) was pelletized for injection molding experiments.

All blends, as well as the neat PP, were processed by compression molding (CM) or by injection molding (IM). The IM was performed on a lab-scale Babyplast machine produced by Cronoplast S.L., Barcellona, at temperatures being either about 25-30 °C below T_m or above T_m of PET.

For the preparation of another set of MFC samples, amorphous PPE and four different kinds of thermotropic LCPs were used. Table 1 lists some of the

Table 1. Thermal (softening, T_s, glass transition, T_g, and melting temperature, T_m) and mechanical properties of the neat materials (no further specifications of their types were available).

Material	*T_s (°C)*	*T_m (°C)*	*Flexural modulus (GPa)*	*Flexural strength (MPa)*	*Flexural deflection (%)*	*Impact energy (kJ/m²)*
PPE	210 (T_g)	-	2.13	93.83	6.61	12
1-LCP	230	273	6.71	132.12	6.31	- *
2-LCP	250	316	6.54	125.55	3.77	58
3-LCP	260	324	6.09	125.17	3.94	25
4-LCP	290	316	8.56	133.39	3.33	34

* Did not brake

thermal and mechanical properties of the neat materials, and Table 2 shows the blend compositions. An additional set of the 4-LCP/PPE blends, containing different amounts of a compatibilizer (Table 3), was also prepared.

Table 2. LCP/PPE blend compositions.

Blend partners	Wt.%	Blend partners	Wt.%
1-LCP/PPE	5/95 10/90 20/80	3-LCP/PPE	5/95 10/90 20/80
2-LCP/PPE	5/95 10/90 20/80	4-LCP/PPE	5/95 10/90 20/80

The components were melt-blended using a Brabender twin-screw extruder with an *L/D* ratio of 22, at a screw rotation rate of 30-35 rpm. The temperature of the die was set between the softening temperature, T_s, and T_m of the respective LCP (Table 1). Immediately after leaving the die, the extrudate was continuously hot-stretched by a drawing device (draw ratio 6-11). By means of compression molding at 255 °C, *i.e.*, below T_m of LCP, plates with the dimensions 1.5×50×50 mm were prepared for mechanical testing. In addition, pellets of the materials were injection molded on the above mentioned lab-scale machine at temperatures below T_m of the LCPs (Tables 1 and 2), but in some cases also above or below T_s^{LCP} of the 4-LCP (Tables 2 and 3). The temperature profile, starting from the feeding zone, was 295, 300, 300 °C or 270, 275, 275 °C.

Table 3. Compositions of 4-LCP/PPE/C blends (wt.%, components blended together simultaneously)

Run	*4-LCP*	*PPE*	*Compatibilizer*
1	0	100	0
2	0	98.5	1.5
3	5	93.5	1.5
4	15	80.5	4.5
5	30	61	9
6	15	83.5	1.5
7	5	93.5	1.5

It should be pointed out here that the set temperatures were lower by about 30-40 °C than the T_m of the LCP types 2, 3, and 4, but by *ca.* 20 °C higher than the T_m of 1- LCP because of the relatively high processing temperature required for PPE (*ca.* 290-300 °C). *i.e.*, the blends containing 1-LCP were processed at a temperature higher than its T_m. Test samples with dimensions 4×10×80 mm were prepared from all drawn blends and neat polymers.

The morphological structure of the PET/PP and LCP/PPE blends at the various stages of MFC manufacturing and processing was investigated by means of SEM and WAXS. Mechanical tests (tensile and three-point bending (3PB) for the CM and IM samples) were performed at room temperature, using a Zwick 1464 testing machine.

3 Structure and Properties of MFCs

3.1 Structure and Properties of MFCs Based on PET/PP Blends

3.1.1 Morphology

Figure 1 shows SEM pictures of the cryofractured samples and WAXS patterns immediately after extrusion and also after drawing of the PET/PP blends without and with compatibilizer. The micrographs of the as-extruded samples show a rather homogeneous dispersion of PET in the PP matrix (Figure 1Aa,b). The spherical PET particles in the compatibilized blend are 3–4 times smaller (200 nm–1 μm, Figure 1Ab) than those in the blend without compatibilizer (1–3 μm, Figure 1Aa). The influence of the compatibilizer on the degree of dispersion becomes very obvious. After drawing, the blend components are transformed into a highly oriented state (Figure 1Ac,d). It should be mentioned here that the same morphology has been observed also for blends involving other polymers.[24-27,29-31]

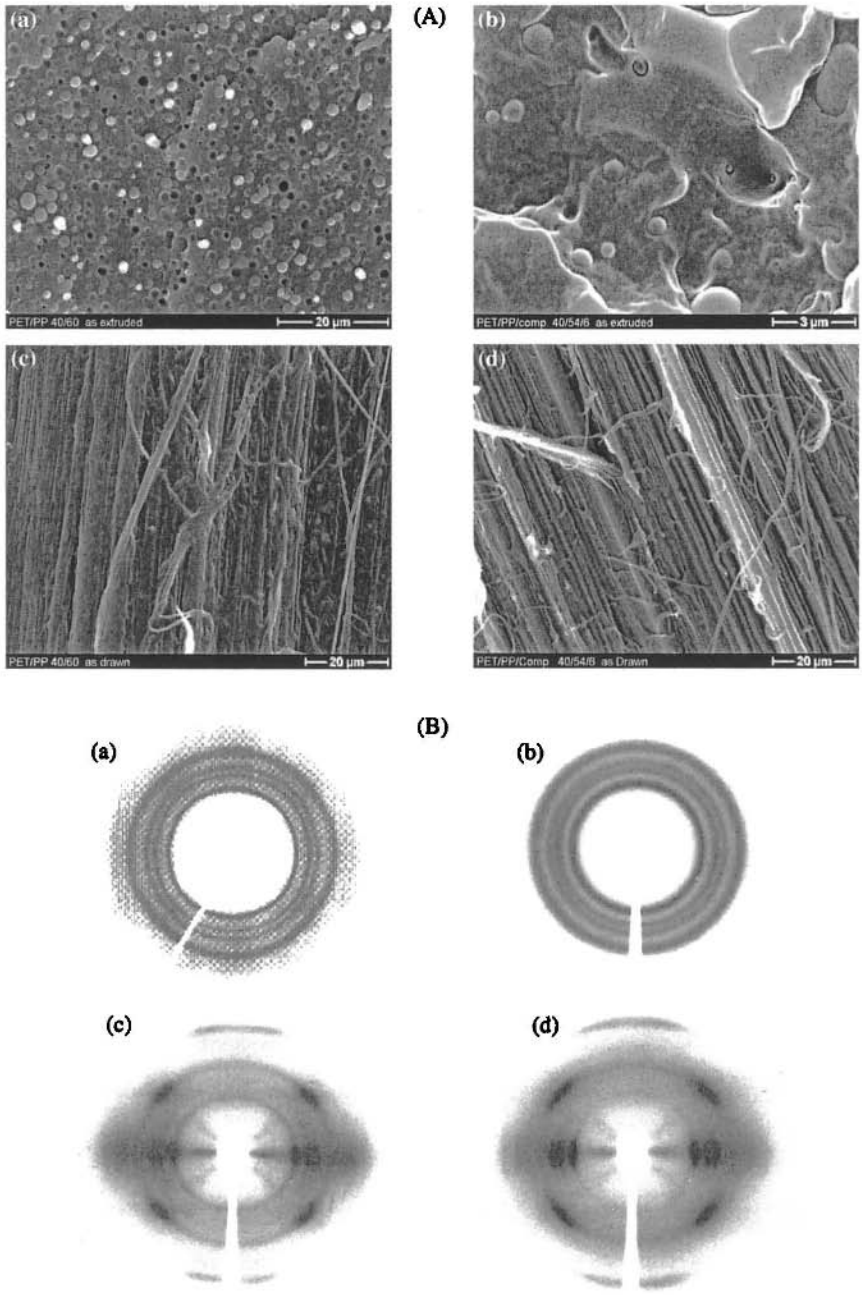

Figure 1. SEM micrographs of the cryogenic fracture surface (A) and WAXS patterns (B) of as-extruded PET/PP 40/60 blend (a) and PET/PP/C 40/54/6 blend (b), drawn PET/PP 40/60 blend (c) and PET/PP/C 40/54/6 blend (d). Here and further all compositions in wt.%.

The WAXS patterns show an isotropic chain distribution of the blend partners in the as-extruded bristles regardless of the presence or absence of compatibilizer (Figure 1Ba,b). This situation changes drastically after drawing, resulting in a very high degree of molecular orientation (Figure 1Bc,d).

The dramatic change in the orientation state, demonstrated by SEM and WAXS data, is also reflected in the mechanical properties of the blends. As can be seen in Figure 2, the tensile modulus of the drawn bristles is 2- to 4-fold higher than that after extrusion (Figure 2a). The same holds for the tensile strength. These values have shown a 5- to 7-fold increase after drawing (Figure 2b).

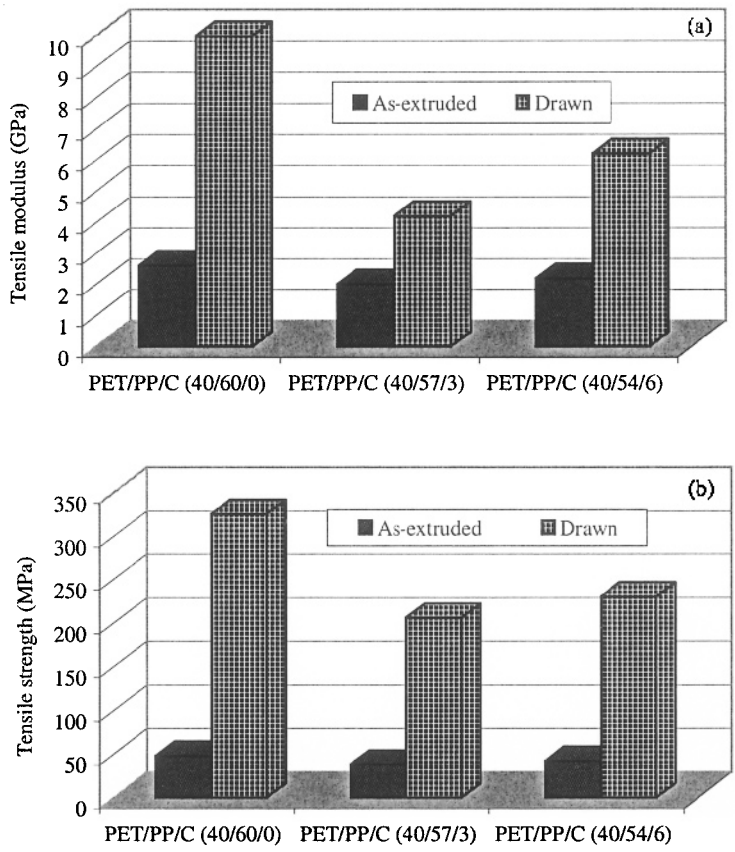

Figure 2. Tensile modulus (a) and tensile strength (b) of the as-extruded and drawn PET/PP bristles of different blend compositions.

Figure 3 shows microphotographs of the cryofracture surfaces of injection molded test samples processed above and below T_m^{PET}. As it was expected, proces-

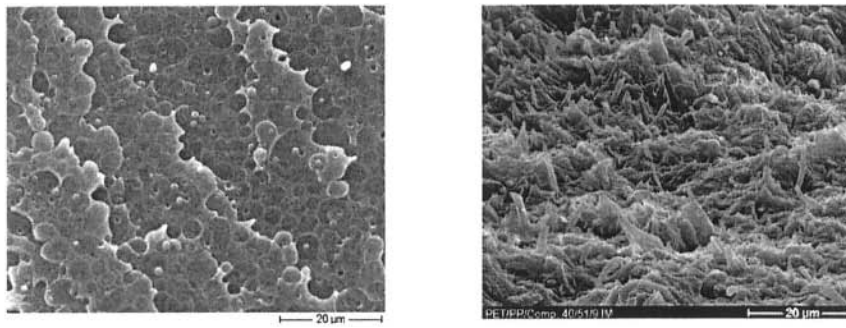

(a) (b)

Figure 3. SEM micrographs of the cryofracture surface of injection molded PET/PP blends above (a) and below T_m^{PET} (b).

sing above T_m^{PET} results in a conversion of the fibrils back into spherical particles (Figure 3a). When the processing temperature is below T_m^{PET}, the PP phase is transformed into an isotropic matrix, with a preservation of nearly randomly distributed PET fibrils as reinforcement (Figure 3b).

To get an idea about the length of the PET fibrils processed below T_m^{PET}, in some of the IM samples, the PP matrix was removed by means of a selective solvent. The SEM micrograph of the sample without compatibilizer shows fibrils with much higher aspect ratios and diameters between 300 nm and 1 µm (Figure 4a). In contrast to this observation, the blends with compatibilizer reveal significantly shorter fibrils (Figure 4b). This interesting fact could be explained by the formation mechanism of the fibrils. With the progress of the cold drawing, the spherical particles adopt an elliptic shape. Becoming thinner but longer, they start to contact each other and due to coalescence they build up uniform microfibrils comprising many starting

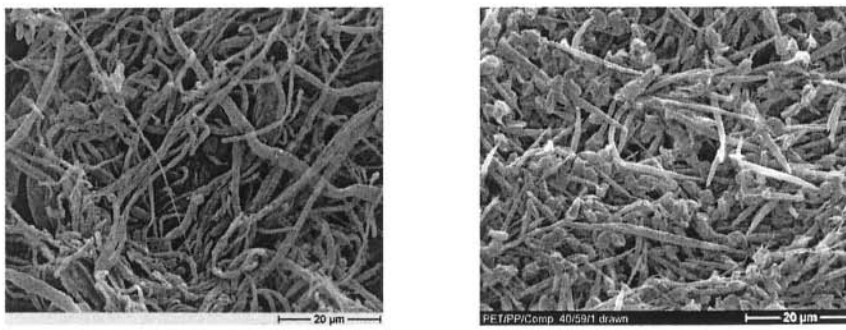

(a) (b)

Figure 4. SEM micrographs of the selectively dissolved matrix of PET/PP samples without (a) and with (b) compatibilizer (3 wt.%).

spheres. In the blends with compatibilizer, this process is hampered because the compatibilizer forms a thin shell around each PET sphere and does not allow their coalescence, which results in much shorter final microfibrils.

As can be seen in Figure 5, after compression molding of the drawn blend at a temperature between the melting temperatures of the two partners, the PP component undergoes also an isotropization, similar to the case of IM. At the same time, the PET fibrils preserve their uniaxial orientation and anisotropy, as well as their high aspect ratio, as can be concluded from Figure 5a, depicting a PET/PP blend without compatibilizer, after partial dissolution of PP at the surface. As expected (Figure 4), the fibrils in the blends with compatibilizer also kept their orientation, but they are much shorter than those without compatibilizer (Figure 5b).

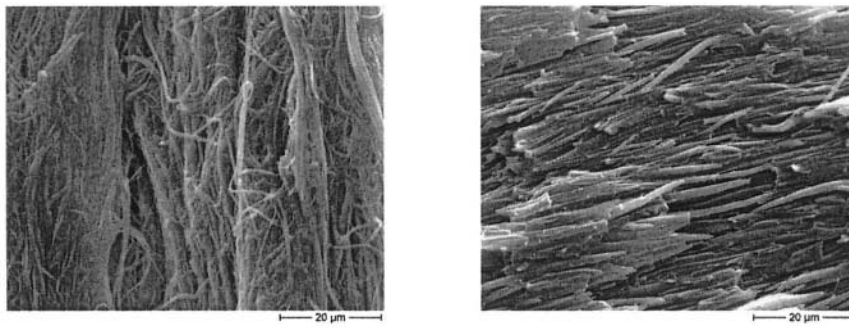

(a) (b)

Figure 5. Selectively dissolved PP on the surface of compression molded PET/PP/C blends with an MFC structure without (40/60/0) (a) and with compatibilizer (40/57/3 by wt.) (b).

Summarizing these morphological observations, it can be concluded that the type of processing (IM or CM) and the presence of a compatibilizer affect the morphology of the MFCs and therefore their properties, as it will be demonstrated in the next section.

3.1.2 Mechanical Properties of the Drawn Blends After Processing

In Figure 6, the flexural properties of IM PET/PP blends are presented. The flexural modulus of the samples with an MFC structure is almost two times higher than that of the samples without an MFC structure (the samples processed above T_m^{PET}). At the same time, it decreases with the rise in the compatibilizer amount (Figure 6a). On the contrary, the flexural strength of the blends with compatibilizer is higher than that of the samples without compatibilizer (Figure 6b). As expected, both parameters of the blends are by 60-70% higher than the values of the neat PP; this fact demonstrates the reinforcing effect of the PET fibrils.

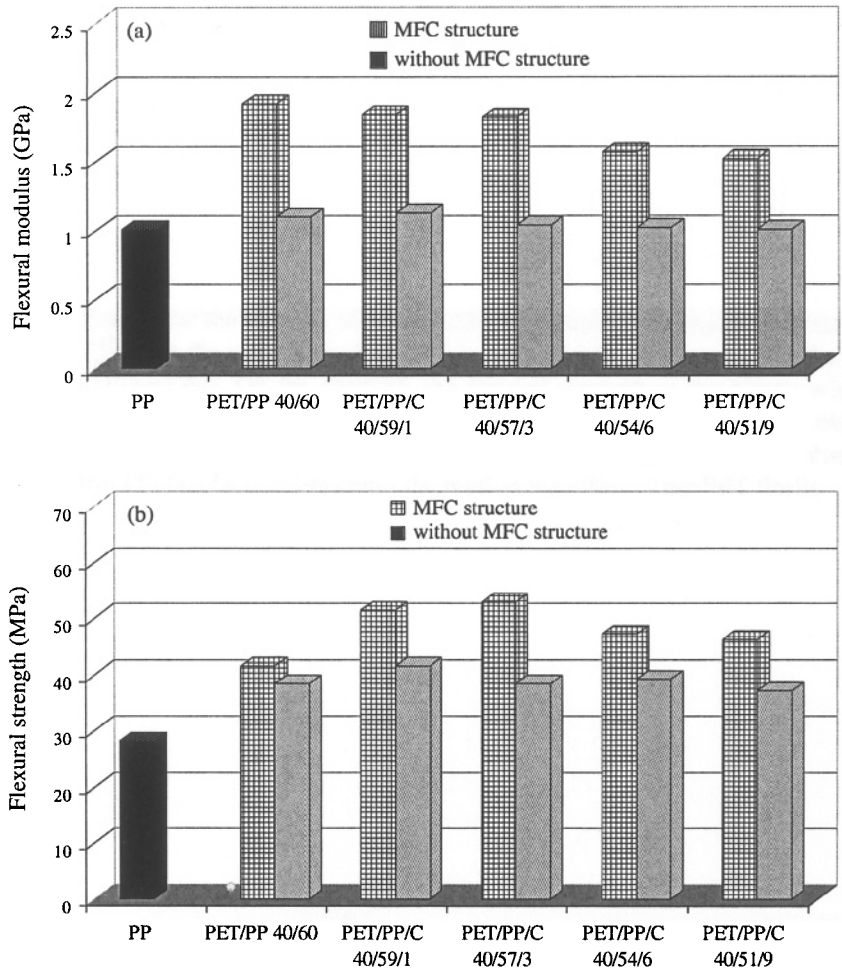

Figure 6. Flexural modulus (a) and flexural strength (b) of injection molded PET/PP/C blends of various compositions.

The flexural properties of CM samples (measured perpendicular and parallel to the PET fibril direction) are given in Figure 7. The flexural modulus increases with the rise in compatibilizer content, reaching values 3- to 4-fold higher then that of neat PP (Figure 7a). The same holds for the tensile strength (Figure 7b). The samples with more compatibilizer possess a 3-fold higher flexural strength than neat PP.

The values for CM samples, broken parallel to the fibril orientation direction, are somewhat different. The flexural modulus values (Figure 7a) are similar to those of the samples broken perpendicular to the orientation, but the flexural strength

(Figure 7b) is almost twice lower, because the reinforcing effect of the PET fibrils is strongly reduced in this case.

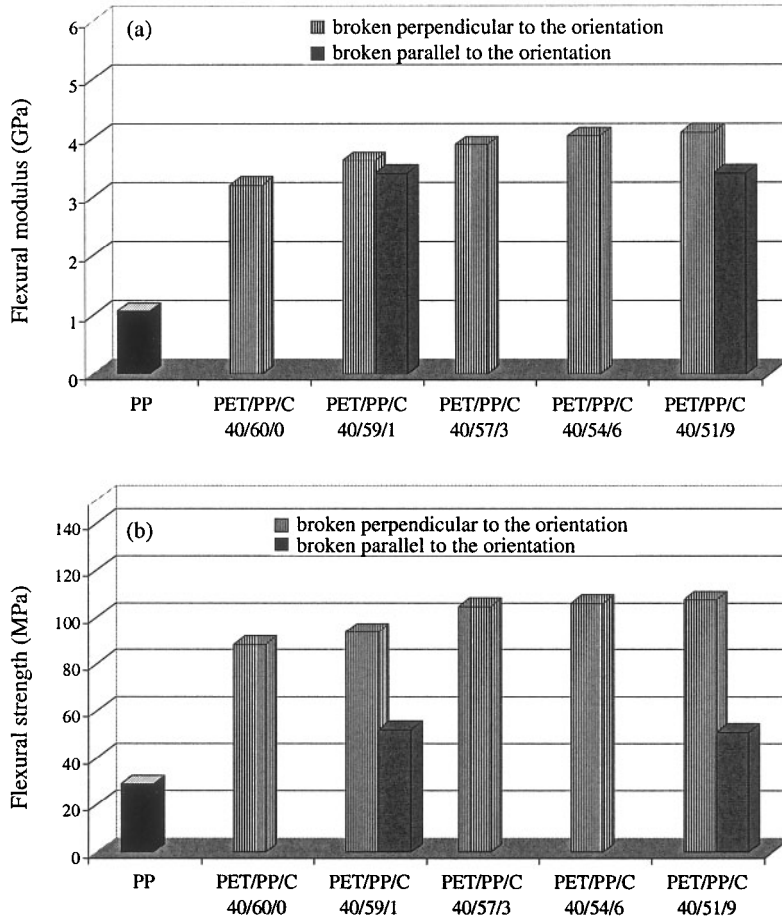

Figure 7. Flexural modulus (a) and flexural strength (b), measured across and parallel to the draw direction, of compression molded PET/PP/C blends of various compositions.

3.2 Structure and Properties of MFCs Based on LCP/PPE Blends

3.2.1 Morphology

SEM micrographs of the cryogenic fracture surface of the as-extruded blends are displayed in Figure 8. As in the previous cases (Figures 1a and 3a), a rather homogeneous distribution of spherical or elliptical LCP particles in the

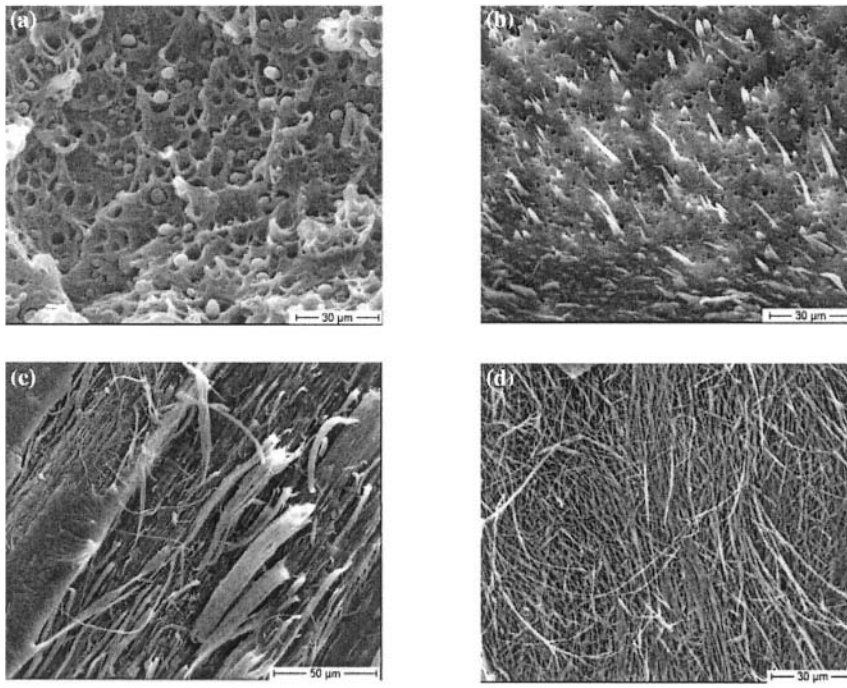

Figure 8. SEM observations of 1-LCP/PPE (10/90 by wt.) blend: cryofracture surface of the as-extruded sample (a), the same after hot drawing (b), peeled surface (c), and after selectively dissolved PPE matrix (d).

PPE matrix and holes with a diameter of 5-10 μm can be observed (Figure 8a). After drawing, the LCP spheres are transformed into fibrils oriented in the draw direction, with diameters between 1 and 3 μm (Figure 8b). The SEM observations of the peeled fracture surfaces show an excellent orientation of the fibrils in the draw direction (Figure 8c). In order to estimate the aspect ratio of the fibrils, some of the drawn bristles and compression molded films were treated with a selective solvent (toluene) for removing the PPE matrix. Since nearly no ends of the fibrils were observed (Figure 8d), it can be concluded that the aspect ratio of the fibrils is very high.

WAXS analysis provides further information concerning the structure of the neat polymers and their blends. The results are presented in Figure 9. As expected for the two homopolymers, PPE is completely amorphous and isotropic (Figure 9a), in contrast to the LCP, which is crystalline and relatively high-oriented (Figure 9b). Strikingly enough, drawing and compression molding do not affect the isotropic state of PPE, whereas the LCP improves its orientation after drawing (Figure 9c) and disorients slightly after compression molding (Figure 9d).

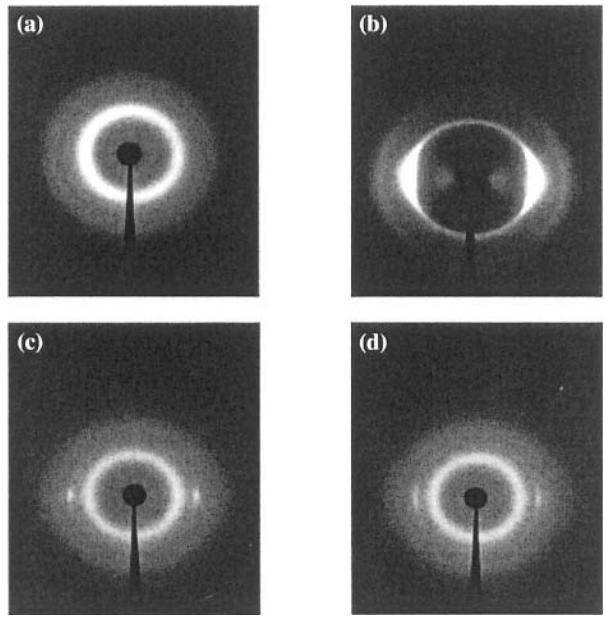

Figure 9. WAXS patterns of neat PPE (a) and neat 1-LCP (b), their hot drawn 1-LCP/PPE (10/90 by wt.) blend (c), and the compression molded drawn blend (d).

Further, the effect of the compatibilizer in the LCP/PPE blend on the morphology of LCP was studied. Micrographs of the cryogenic fracture surfaces of as-extruded and drawn bristles (4-LCP/PPE/C blend, 15/80.5/4.5 by wt.) are shown in Figure 10. It is seen that there is no difference in the structures of the blends with and without compatibilizer (compare Figure 8a,b and Figure 10a,b). It should be noted that the LCP fibrils are situated in holes in the matrix, with larger diameters than their own. This finding clearly evidences that the adhesion between the two components should be very poor, which is probably due to the difference in the thermal expansion coefficients ($\lambda = 60.10^{-6} K^{-1}$ and $\lambda = 0.25.10^{-6} K^{-1}$ for PPE and LCP, respectively).[7] This difference leads to different dimensional conditions of the LCP fibrils and the surrounding PPE matrix during cooling after processing, and during cryogenic fracturing and reheating to room temperature (for microscopic observation). Similar morphological peculiarities were observed for other drawn blends with different compositions (Table 2) and without compatibilizer.[32]

The SEM observations of the cryogenic fracture surfaces of the injection molded test samples from drawn 4-LCP/PEE/C blends (15/80.5/4.5 by wt.) are shown in Figure 11. IM processing was carried out below (275 °C) and at the T_s of the 4-LCP phase (300 °C, Table 1). As expected, during IM at T_s (Figure 11a), a large amount of the LCP fibrils in the drawn bristles (Figure 10 b), were transformed back into elliptical particles due to partial melting or relaxation of the 4-LCP in

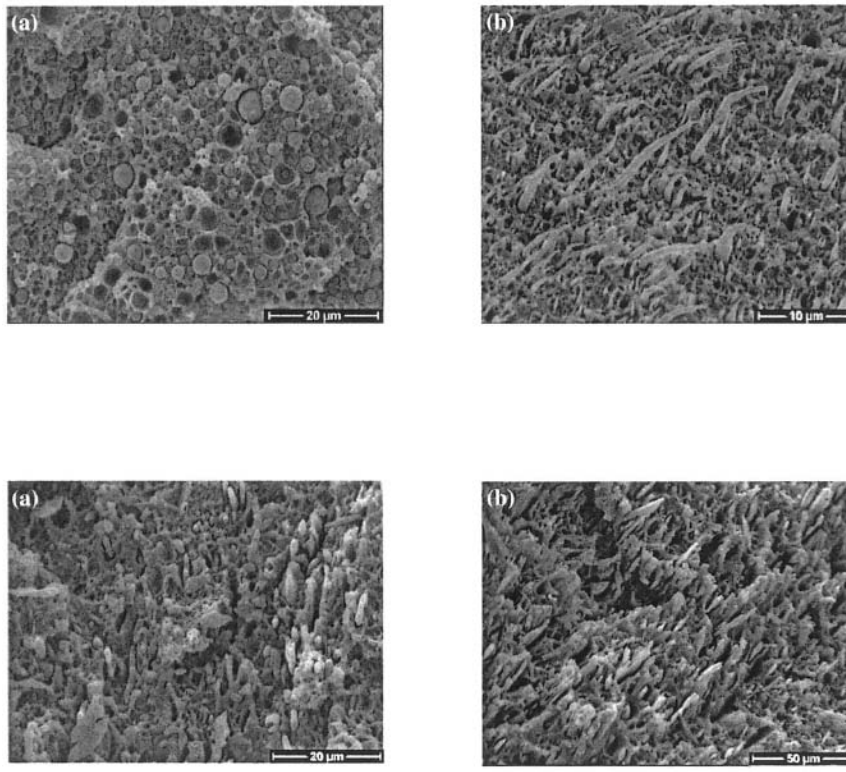

Figure 11. Cryofracture surfaces of injection molded samples of 4-LCP/PPE/C (15/80.5/4.5 by wt.) drawn blend processed at 300 °C (a) and 275 °C (b).

the surrounding PPE matrix. On the other hand, in the case of IM at 275 °C, a large amount of broken LCP fibrils, more or less oriented in the flow direction, can still be seen (Figure 11b).

It should be noted here that it was possible to process blends without compatibilizer below the T_s of the LCPs (types 1, 2 and 3) because their T_s values were relatively low (Table 1). After injection molding at 300 °C, the LCP fibrils took the shape of elliptical particles with a random distribution in the amorphous PPE matrix.[32]

3.2.2 Mechanical Properties of Injection Molded LCP/PPE Blends with MFC Structure

The flexural properties of the drawn and then injection molded (300 °C) LCP/PPE blends with different compositions are summarized in Figure 12. The flexural modulus of all blends increases with the rise of the LCP content in the

blends, reaching maximal values that are by about 50% higher than that of neat PPE (Figure 12a). At the same time, the highest values of the flexural strength were obtained for the LCP/PPE blends with the lowest (5 wt.%) LCP content. With the rise of the LCP fraction in the blends up to 20 wt.%, the strength decreases to the value of neat PPE (Figure 12b). In all these cases, the type of the LCP used (Table 1) was of less importance.

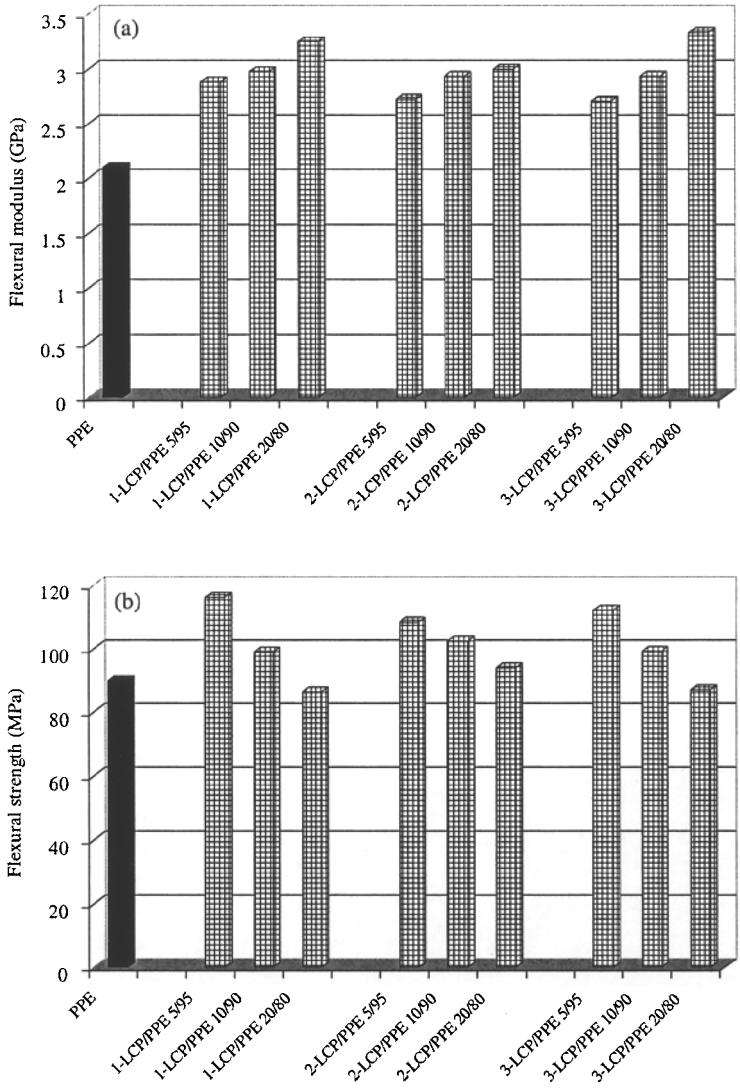

Figure 12. Flexural modulus (a) and flexural strength (b) of injection molded MFC based on LCP/PPE blends of different compositions.

The flexural modulus of the 4-LCP/PPE/C samples (injection molded at temperatures above $T_s^{4\text{-LCP}}$) increases slowly with the rise of the LCP amount, reaching values higher by about 40-70% than that of the neat PPE matrix. The flexural strengths of the blends and neat PPE (when processed at the same temperature) are almost on the same level.

On the other hand, a small increase (by about 15-20 MPa) of the flexural strength was observed for the samples processed at 275 °C (below $T_s^{4\text{-LCP}}$). This can be related to the morphological differences in the two sample types, as shown in Figure 11a,b.[32]

4 Conclusions

From the above results, it can be concluded that the MFC concept can be successfully applied to different polymer blends under industrially relevant production conditions. The drawn blends under investigation show a high level of orientation of the PET and LCP fibrils, as can be concluded from the WAXS analysis, and a relatively high aspect ratio demonstrated by the SEM observations.

The characteristic MFC structure in the PET/PP blends could be created after compression molding as well as after injection molding at temperatures below T_m of PET, although in the case of IM, the distribution of the PET fibrils in the PP matrix is almost random. The flexural strength and modulus of the IM blends with MFC structure are superior by 60-70% to those of the neat PP and blends without an MFC structure; this fact demonstrates the reinforcing effect of the PET fibrils. The compression molded PET/PP and LCP/PPE samples with an MFC structure possess much better mechanical properties in the draw direction than those of the IM specimens, because of the uniaxial orientation of the PET and LCP fibrils.

Processing by injection molding of the drawn LCP/PPE blends at temperatures below T_m^{LCP}, but above the softening temperature of the LCP, transforms the majority of the LCP fibrils into elliptical microparticles. This morphological restoration process affects negatively the mechanical properties of the blends. For the preservation of the LCP fibrils during processing, the injection molding should be performed slightly below T_m^{LCP}.

The addition of a compatibilizer to the LCP/PPE blend does not significantly improve the poor adhesion between the components and the mechanical properties. This is, at least partly, due to the great difference in the thermal expansion coefficients of the blend partners, which leads to different shrinkage conditions of the LCP fibrils and the PPE matrix, so that microholes appear and the compatibilizer cannot act at all.

5 Acknowledgements

The authors are grateful to the Deutsche Forschungsgemeinschaft for the support of the equipment for the production of the MFC (DFG FR 675/21-3). Further thanks are expressed to the German Ministry for Education and Research, which supported the German-Bulgarian cooperation on LCP/amorphous polymer blends (BMBF-WTZ Bulgaria). Thanks are also due to Mr. O. Evstatiev for his active participation in the performance of experiments. The SEM observations were made on the instrument donated by the Alexander von Humboldt Foundation to the Faculty of Chemistry at Sofia University, Sofia, Bulgaria.

6 References

[1] A. Leclair, B. D. Favis (1996) The role of interfacial contact in immiscible binary polymer blends and its influence on mechanical properties, *Polymer* **37**, 4723 .

[2] B. D. Favis (2000) Factors influencing the morphology of polymer blends in melt processing, in *Polymer Blends: Vol. 2, Formation* (Eds. D. R. Paul, C. B. Bucknall) John Wiley & Sons, New York, p. 501.

[3] J. Li, B. D. Favis (2001) Characterizing co-continuous high density polyethylene/ polystyrene blends, *Polymer* **42**, 5047.

[4] M. A. Huneault, Z. H. Shi, L. A. Utracki (1995) Development of polymer blends morphology during compounding in a twin-screw extruder, *Polym. Eng. Sci.* **35**, 115.

[5] S. Fakirov, M. Evstatiev, K. Friedrich (2002) Nanostructured polymer composites from polyetster blends: structure-property relationships, in *Handbook of Thermoplastic Polyesters* (Ed. S. Fakirov) Wiley-VCH, Weinheim, p. 1093.

[6] M. Evstatiev, S. Fakirov, K. Friedrich (2000) Structure-property relationships of injection- and compression-molded fibrillar reinforced PET/PA6 composite, *Adv. Polym. Technol.* **19**, 249.

[7] N. P. Cheremisinoff (1999) *Handbook of Engineering Polymeric Materials*, Marcel Dekker, New York, p. 44.

[8] D. G. Baird, M. A. Mcleod (2000) Liquid crystalline polymer blends, in *Polymer Blends: Vol. 2, Preparation* (Eds. D. R. Paul, C. B. Bucknall) J. Wiley & Sons, New York, p. 427.

[9] S. C. Tjong, S. L. Liu, R. K. Y. Li (1995) Structure and mechanical properties of the extruded blend of a liquid crystalline polymer with polypropylene, *J. Mater. Sci.* **31**, 479.

[10] H. Wang, G. Hinrichsen (1997) Influence of processing temperature on morphological and mechanical properties of a polycarbonate/thermotropic liquid crystalline polymer (PC/TLCP) blend, *Int. Polym. Proc.* **12**, 26.

[11] S. H. Kim, S. W. Park, E. S. Gil (1998) Crystallization kinetics of poly(ethylene terephthalate) with thermotropic liquid crystalline polymer blends, *J. Appl. Polym. Sci.* **67**, 1383.

[12] M. Kozlowski, F. P. La Mantia (1997) Study on compatibilization of polypropylene-liquid crystalline polymer blends, *J. Appl. Polym. Sci.* **66**, 969.

[13] A. G. C. Machils, J. V. Dam, A. P. D. Boer, B. Norder (1997) Stability of blends of thermotropic liquid crystalline polymers with thermoplastic polymers, *Polym. Eng. Sci.* **37**, 1512.

[14] A. Isayev (1993) Self-reinforced composite, US Patent 5,260,380.

[15] E. A. Sabol, A. A. Handlos, D. G. Baird (1995) Composites liquid on drawn strands of thermotropic liquid crystalline polymer reinforced polypropylene, *Polym. Compos.* **16**, 330.

[16] P. M. Thangamathesvaran, X. Hu, K. Chiu Tarn, C. Y. Yue (2001) In situ composites: effect of elongational flow velocity on thermotropic liquid crystalline co-polyester fibrillation in thermoplastic/TLCP systems, *Compos. Sci. Technol.* **61**, 941.

[17] H. Wang, K. W. Lee, T-S. Chung, M. Jaffe (2000) Rheology, morphology and properties of 2CP/Nylon 66 composite fibers, *Polym. Compos.* **21**, 114.

[18] A. A. Handlos, D. G. Baird (1996) Injection molding of microcomposites based on polypropylene and thermotropic liquid crystalline polymers, *Polym. Compos.* **11**, 82.

[19] M. Evstatiev, S. Fakirov (1992) Microfibrillar reinforcement of polymer blends, *Polymer* **33**, 877.

[20] S. Fakirov, M. Evstatiev, S. Petrovich (1993) Microfibrillar reinforced composites from binary and ternary blends of polyesters and nylon 6, *Macromolecules* **26**, 5219.

[21] S. Fakirov, M. Evstatiev (1994) Microfibrillar reinforced composites – new materials from polymer blends, *Adv. Mater.* **6**, 395.

[22] M. Evstatiev, N. Nicolov, S. Fakirov (1996) Morphology of microfibrillar reinforced composites from polymer blends, *Polymer* **37**, 4455.

[23] K. Friedrich, E. Ueda, M. Evstatiev, B. Krasteva, S. Fakirov (2002) Direct electron microscopic observation of transcrystalline layers in microfibrillar reinforced polymer-polymer composites, *J. Mater. Sci.* **37**, 4299.

[24] M. Evstatiev, S. Fakirov, B. Krasteva, K. Friedrich, J.A. Covas, A.M. Cunha (2002) Recycling of PET as polymer-polymer composites, *Polym. Eng. Sci.* **42**, 826.

[25] S. Fakirov, A. Apostolov, Z. Denchev, N. Stribeck, M. Evstatiev, K. Friedrich (2001) Crystallization in partly molten oriented blends of polycondensates as revealed byX-ray studies, *J. Macromol. Sci.-Phys.* **B40**, 935.

[26] M. Evstatiev, J. M. Schultz, G. Georgiev, S. Petrovich, S. Fakirov, K. Friedrich (1998) In situ polymer/polymer composites from poly(ethylene terephthalate), polyamide 6 and polyamide 66 blends, *J. Appl. Polym. Sci.* **67**, 723.

[27] M. Evstatiev, S. Fakirov, K. Friedrich (2000) Microfibrillar reinforced composites – another approach to polymer blends processing, in *Structure Development During Polymer Processing* (Eds. A. M. Cunha, S. Fakirov) Kluwer, Dordrecht, p. 311.

[28] D. Sapoundjieva. Z. Denchev, M. Evstatiev, S. Fakirov, N. Stribeck, M. Stamm (1999) Transcrystallization with reorientation in drawn PET/PA12 blend as revealed by WAXS from synchroton radiation, *J. Mater. Sci.* **34**, 3063.

[29] M. Evstatiev, S. Fakirov, J. Schultz, K. Friedrich (2001) In situ fibrillar reinforced PET/PA6/PA66 blend, *Polym. Eng. Sci.* **41**, 192.

[30] K. Friedrich, H. E. Kamo, M. Evstatiev, S. Fakirov (2004) Microfibrillar reinforced composites from PET/LDPE blend: morphology and mechanical properties, *J. Macromol. Sci.-Phys.* **B43**, 1.

[31] K. Friedrich, M. Evstatiev, S. Fakirov, O. Evstatiev, M. Ishii, M. Harrass (2005) Microfibrillar reinforced composites from PET/PP blends: processing, morphology and mechanical properties, *Comp. Sci. Technol.*, **65**, 106.

[32] O. Evstatiev, M. Evstatiev, S. Fakirov, K. Friedrich (2005) Manufacturing and characterization of MFC from liquid crystalline polymers and poly(phenylene ether) (LCP/PPE) blends, *Composites*, in press.

[33] X. D. Lin, W. L. Cheung (2003) Study of poly(ethylene terephthalate)/polypropylene microfibrillar composites. I. Morphological development in melt extrusion, *J. Appl. Polym. Sci.* **89**, 1743.

[34] Z. M. Li, M. B. Yang, B. H. Xie, J. M. Feng, R. Huang (2002) *In-situ* composite based on poly(ethylene terephthalate), polyamide and polyethylene with microfibres formed through extrusion and hot stretching, *J. Mater. Techol.* **18**, 419.

[35] Z. M. Li, M. B. Yang, J. M. Feng, W. Yang, R. Huang (2003) In-situ microfiber reinforced composite based on PET and PE via slit die extrusion and hot stretching: influences of hot stretching ratio on morphology and tensile properties at a fixed composition, *Polym. Eng. Sci.* **43**, 615.

[36] X. D. Lin, W. L. Cheung (2003) Study on PET/PP microfibrillar composites. I. Morphological development in melt extrusion, *J. Appl. Polym. Sci.* **88**, 3100.

Chapter 10

Tribological Characteristics of Micro- and Nanoparticle Filled Polymer Composites

Zhong Zhang, Klaus Friedrich
Institut für Verbundwerkstoffe GmbH (Institute for Composite Materials), Kaiserslautern University of Technology, Kaiserslautern, Germany

1 Introduction

The use of polymers in various tribological situations has become state of the art. This is a rapidly developing topic with the attractive advantages of self-lubrication and superior cleanliness. Furthermore, the inherent weakness of polymers could be improved successfully by using various special fillers; more and more polymer composites are now being used as sliding elements, which were formerly composed of metallic materials only. Nevertheless, new developments are still under way to explore other fields of application for these materials and to tailor their properties for more extreme loading and environmental temperature conditions.[1] An example for automotive applications is the new generation of control arm mountings or ball joints in the car chassis technology, in which higher loads and temperature are acting on a tribo-couple. In this case, polymer composites will be operated at relatively high environmental temperatures, *e.g.*, 120 °C, and the demand for high wear resistance becomes increasingly important. The understanding of these properties under severe operating conditions is directly related to the safety and service life of the technical components considered.

Inorganic particles are well known to enhance the mechanical and tribological properties of polymers, and this issue has been widely investigated in the past decades. It has been found that the particle size plays an important role in the improvement of the wear resistance. Reducing the particle size to a nano-scale level is assumed to improve significantly the composite efficiency; nanoparticle-filled polymers, the so-called *polymer nanocomposites*, are very promising

materials for various applications. They are expected to replace polymers, polymer blends, and their traditional composites in parts produced by melt processing techniques. This prediction is justified by the improvements in properties without sacrificing the melt rheological properties. Polymer nanocomposites are characterized by their huge interfacial surface area, which may result in a peculiar physical network structure of three-dimensional interphase.[2] Nano-fillers are expected to be able to strongly influence the wear performance of polymers and composites, which will be briefly reviewed in the present chapter. All cases discussed here are mainly related to sliding wear of polymer or composite specimens against polished metallic counterparts.

2 Influence of Particle Size: from Micro- to Nanometer

In order to enhance the modulus and hardness of polymers, micrometer size inorganic particles are frequently applied. However, a reduction in the material ductility may take place. Furthermore, either by diminishing the particle size or by enhancing the particle volume fraction, the strength can be improved, but in some cases the fracture toughness and modulus remain fairly independent of the particle size,[3] even when going down to the nanoscale.[4-6] The changes in other properties by the particle content and size depend on the type of loading applied. Of special concern here are the wear properties, which are rather complex, although they are to some degree correlated to the mechanical properties mentioned above.

In order to improve the wear resistance, various kinds of micrometer sized particles, *e.g.*, TiO_2, ZrO_2, SiC, and copper compounds (CuO, CuS, CuF_2), were incorporated into different polymer matrices, *e.g.*, polyetheretherketone (PEEK),[7] polyamide (PA),[8-11] polyphenylene sulfide (PPS),[12-15] polyoxymethylene (POM),[16] and polytetrafluoroethylene (PTFE).[17,18] The improvements of the wear resistance were due to either mechanical (the enhanced modulus and hardness) or chemical (the improved bonding between transfer films and metallic counterparts) reasons. PEEK, PPS, and PA are attractive semicrystalline thermoplastics for tribological applications due to their special features, *e.g.*, the high-temperature resistance of PEEK and PPS, and the good wear resistance of PA. The incorporation of micrometer scale inorganic particles led to two opposite trends in the wear resistance, as it was clearly demonstrated in studies of Bahadur and coworkers.[7-15] It was found that CuO and CuS are very effective in reducing the wear rate of PEEK[7] and PA11,[8-10] whereas ZnF_2, ZnS, and PbS increased the wear rate of PA11.[11] The wear resistance of PPS[12-15] could be improved by the addition of CuS, Ag_2S or NiS, but reduced by CaF_2, ZnF_2, SnS, PbSe or PbTe. It was concluded that a transfer film develops due to the adhesion and interlocking of the polymer fragments into metal asperities during sliding.[19] Some inorganic particles are of

help to enhance the bonding between the transfer film and the metallic counterpart, which leads to improved wear resistance. Others result in an adverse effect due to the generation of more discontinuities in the material.

In general, fine particles seem to contribute better to the property improvement under sliding wear conditions than larger particles. An example of this trend was detected in the case of glass particle-reinforced polymethylmethacrylate (PMMA) dental composites when tested against steel counterparts (superimposed by interfacial bond quality effects).[20] A similar trend was confirmed recently by Xing *et al.*[21] on the spherical silica particle-filled epoxy when the particle size varied from 120 to 510 nm. However, opposite size effects were found by Friedrich[22] in glass sphere-reinforced polyamides under abrasive wear conditions. Another example of the opposite size effects was reported by Durand *et al.*,[23] who conducted sliding wear tests using an epoxy matrix filled with various kinds of ceramic particles, *e.g.*, Al_2O_3, TiC, SiC, TiN, TiO_2, and ZrO_2; the particle sizes varied from 5 to 100 μm.

Once the particle sizes are diminished down to the nanoscale (< 100 nm), the wear performance of these nanocomposites differs significantly from that of micron particle-filled systems. Polymers filled with nanoparticles are recently under discussion because of some excellent properties they have shown under various testing conditions. Some results were achieved in various studies, suggesting that this method is also promising for new processing routes of wear resistant materials. For instance, Xue *et al.*[24] found that various kinds of SiC particles, *i.e.*, nano, micron and whisker, could reduce the friction and wear when incorporated into a PEEK matrix at a constant filler content, *e.g.*, 10 wt.% (≈ 4 vol.%). However, nanoparticles resulted in the most effective reduction. Nanoparticles were observed to be of help to the formation of a thin, uniform, and tenacious transfer film, which led to this improvement. The variation of ZrO_2 nanoparticles from 10 to 100 nm was conducted by Wang *et al.*[25] The results showed a similar trend as most of the micron particles, *i.e.*, the smaller the particles, the better was the wear resistance of the composites.

3 Influence of the Nanoparticle Volume Content

Agglomeration is considered as a general problem of polymer nanocomposites, especially for higher nano-filler contents. Figure 1 illustrates the correlation among particle diameter, distance, and volume content. Here, spherical particles were assumed in a cubic distribution with perfect dispersion in a polymer matrix. It should be noted that agglomerations may easily happen for smaller particles at higher filler contents due to the reduced interparticle distance.

So far, various inorganic nanoparticles, *e.g.*, Si_3N_4, SiO_2, SiC, ZrO_2, Al_2O_3, TiO_2, ZnO, CuO, $CaCO_3$, were incorporated into PEEK,[24-29] PPS,[30,31] PMMA,[32]

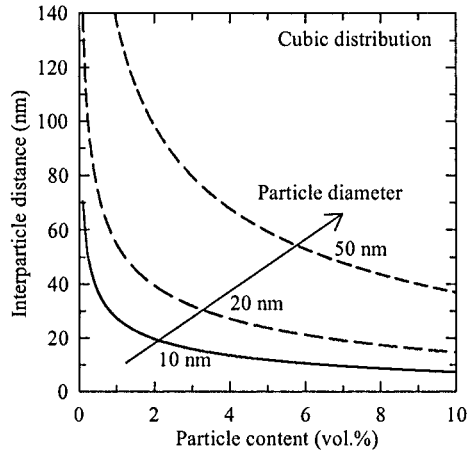

Figure 1. Correlation among nanoparticle diameter, interparticle distance, and volume content based on the assumptions of spherical particles, cubic distribution and ideal dispersion.

epoxy,[33-39] and PTFE[40,41] matrices, in order to improve their wear performance. In most of these cases, optimum nanoparticle filler contents could be acquired, at which the wear resistance of these polymers was the best. The results are summarized in Table 1. It can be seen that the optimum filler content of the small particles was always in the range between 1 and 4 vol.%, except for PTFE matrix composites (which will be discussed separately in the next section). Although in most of these works the morphologies of nanoparticle dispersions were not reported in detail, it should be clear that high filler contents lead to a deterioration of the wear properties, which may be due to a tendency of particle agglomeration. In general, it is of utmost importance that the nanoparticles are uniformly dispersed rather than being agglomerated in order to yield a good property profile.

For PEEK matrix nanocomposites,[24-29] a small amount of inorganic nanoparticles, such as Si_3N_4, SiO_2, SiC, and ZrO_2, contributed to a reduction in the frictional coefficient from about 0.4 for the neat matrix down to about 0.2 at high nano-filler contents. The dominant wear mechanisms were modified from adhesive and fatigue wear in the case of neat PEEK to a mild abrasive wear of the nanocomposites. However, with a further increase in nano-filler content, particle agglomeration occurred and resulted in a severe abrasive wear, as observed on the worn surfaces.[29]

A similar tendency was demonstrated by Bahadur *et al.*[30,31] for PPS filled with various kinds and amounts of nanoparticles. Al_2O_3 (2 vol.%) exhibited an optimum reduction in the wear rate of the composites at a surface roughness of the steel counterpart of 60 and 100 nm. However, with the roughness of 27 nm, which was smaller than the particle size (*ca.* 33 nm), any amount of nanoparticles

Table 1. Summary of wear resistant polymer nanocomposites.

Matrix/nano-particle	*Nanoparticle size*	*Lowest wear rate achieved (10^{-6} mm³/Nm)*	*Optimum particle content (vol.%)*	*Reference*
PEEK/Si_3N_4	<50 nm	1.3	2.8	Wang *et al.*[26]
PEEK/SiO_2	<100 nm	1.4	3.4	Wang *et al.*[27]
PEEK/SiC	80 nm	3.4	1~3	Wang *et al.*[28]
PEEK/ZrO_2	10 nm	3.9	1.5	Wang *et al.*[29]
PPS/Al_2O_3	33 nm	12	2	Schwartz *et al.*[30]
PPS/TiO_2	30-50 nm	8	2	Bahadur *et al.*[31]
PPS/CuO	30-50 nm	4.6	2	Bahadur *et al.*[31]
Epoxy/SiO_2	9 nm	45	2.2	Zhang *et al.*[34,35]
Epoxy/SiO_2-g-PAAM	9 nm	11	2.2	Zhang *et al.*[34,35]
Epoxy/Si_3N_4	<20 nm	2.0	0.8	Shi *et al.*[36]
Epoxy/TiO_2	300 nm	14	4	Wetzel *et al.*[37]
Epoxy/Al_2O_3	13 nm	3.9	2	Wetzel *et al.*[38]
Epoxy/SiO_2	13 nm	22	3	Sreekala *et al.*[39]
PTFE/ZnO	50 nm	13	15	Li *et al.*[40]
PTFE/Al_2O_3	40 nm	1.2	12	Sawyer *et al.*[41]

increased the wear rate. Normally, the surface roughness of the steel counterpart is directly correlated with the real average distance of two sliding surfaces,[42] which strongly affects the formation of a transfer film. Very recently, nano-size TiO_2 and CuO particles were found to be able to reduce wear in PPS matrix composites, whereas ZnO and SiC exhibited an opposite effect.[31] The optimum wear resistance was obtained with 2 vol.% of CuO or TiO_2. In an interesting experimental approach, which was used to observe the transfer film-counterpart bond strength by a peeling study, it was found that the bond strength strongly correlated to the wear resistance.

Recently, sliding wear studies using inorganic nanoparticle-filled epoxy were also carried out.[33-39] It was found that well dispersed nanoparticles could significantly improve both the mechanical and the tribological properties of the thermosetting matrix composites. The incorporation of SiO_2 nanoparticles (9 nm), grafted with another polymer (polyacrylamide (PAAM)) to enhance the adhesion of the particle agglomerates with the surrounding epoxy resin matrix, was conducted by Zhang *et al.*[34,35] The grafting polymerization technique increased the interfacial interaction between the nanoparticles and the matrix through chemical bonding, which in turn led to an improved tribological performance of these nanocomposites. Nano-Si_3N_4 particles (< 20 nm) seem to be very effective in reducing friction

and wear when incorporated into an epoxy matrix at a very low filler content (< 1 vol.%).[36] TiO_2 particles (300 nm) contributed to an improved wear resistance by changing from a severe abrasive wear of the neat epoxy to a mild abrasive wear caused by the formation of a compacted transfer film.[37]

4 Particle-Filled Polytetrafluoroethylene

PTFE is commonly used as a filler incorporated into most engineering polymers in order to improve their sliding properties. For special applications, where the unique properties of PTFE provide certain advantages, neat PTFE and PTFE-based composites are also approved. In general, PTFE and its composites are good candidates for applications in severe environments where no conventional lubrication is possible. PTFE possesses an extremely low frictional coefficient due to its peculiar molecular and morphological structure. PTFE itself has a relatively poor wear resistance due to its soft nature, which therefore needs to be improved by special fillers. Tanaka studied the sliding performance of TiO_2 and ZrO_2 particle-filled PTFE.[17] The TiO_2 was an agglomeration of fine particles of less than 300 nm in size, and the filler content was 20 wt.% (≈ 12 vol.%). The ZrO_2 particles applied ranged from several microns to about 50 μm and the filler content was 40 wt.% (≈20 vol.%). It was found that both particles could significantly improve the wear resistance of PTFE, although the frictional coefficient was increased. The bigger ZrO_2 particles preformed better with regard to a reduction in wear, but brought at the same time a higher frictional coefficient than the smaller TiO_2 particles. According to the observation of worn surfaces, ZrO_2 resulted in a greater abrasiveness against the steel counterpart than TiO_2, due to the bigger particle size and probably the greater hardness of ZrO_2. It seems, at least for a PTFE matrix, that diminishing the particle size does not always lead to an improved wear resistance. Bahadur *et al.*[18] presented another concept, assuming that the formation of a coherent transfer film of filled PTFE on the metallic counterpart contributed to the obviously enhanced wear resistance.

Inorganic nanoparticles, *i.e.*, ZnO and Al_2O_3, were recently incorporated into PTFE by Li *et al.*[40] and Sawyer *et al.*,[41] respectively. It was found that the optimum filler contents were relatively high, *i.e.*, more than 10 vol.%. Although the nanoparticles were agglomerated together, as shown in the case of nano-Al_2O_3,[41] wear was significantly reduced. From the reviewers' point of view, the reason may be the soft nature of the PTFE matrix. The improved mechanical properties, *e.g.*, stiffness and creep resistance, of PTFE by hard particles play a key role in such a reduction of wear. Agglomerated nanoparticles take over a similar function as the micron size particles.[17,18]

5 Integration of Inorganic Particles With Traditional Fillers

5.1 Inorganic Particles and Other Fillers

The integration of various functional fillers is a traditional route to achieve highly wear-resistant polymer composites.[1,43,44] In order to reduce the adhesion of polymers to metallic counterparts, internal lubricants, such as PTFE powders and graphite flakes, are frequently incorporated. Short aramid (AF), glass (GF) or carbon (CF) fibers are used to increase the creep resistance and the compressive strength of the polymer matrix. Not so many efforts have been undertaken so far in the development of such composites by integrating inorganic particles with conventional fillers.

PTFE powders were applied as an additional filler together with micron size CuS particles[45] or SiC nanoparticles,[46] respectively, in a PEEK matrix. Two opposite trends were observed. In the former case, the addition of PTFE contributed to a reduction of both the wear rate and the frictional coefficient. However, in the latter case, PTFE brought a negative effect to the tribological properties, which was believed by the authors to be due to a chemical reaction between the SiC nanoparticles and the PTFE.

Bahadur *et al.*[47,48] added micron size CuS or CuO particles together with PTFE powders into short carbon fiber- or glass fabric-reinforced PA. Neither CuS nor CuO alone contributed to the development of a good transfer film when added together with the fibers. However, the subsequent incorporation of PTFE was very efficient in the reduction of wear. An optimum wear resistant composition was found to be PA with 25 vol.% CuO, 11.3 vol.% glass fabric, and 10 vol.% PTFE. In this context, Palabiyik and Bahadur carried out also a study on composites consisting of PTFE, CuO particles, and short glass fibers in blends of PA and high-density polyethylene.[49] The effect of MoS_2 micron particles in PA was investigated recently by Wang *et al.*[50] Although MoS_2 particles alone did not result in a positive effect, their integration with short CF significantly improved the wear resistance of PA. It was believed that a synergism between carbon fibers and MoS_2 particles contributed to the formation of thin, uniform, and continuous transfer films, which were confirmed by scanning electron microscopic (SEM) observations of the worn surface.

5.2 Combinative Effect of Nanoparticles and Short Carbon Fibers

It is generally accepted that the overall behavior of multiphase materials can be considered as a function of the respective contribution of each phase, which is also true with regard to the wear properties. However, some special reactions were observed, which dominate the wear performance of polymer composites. In order to

fully promote the effect of nanoparticles, investigations were carried out recently by Zhang *et al.*[51,52] on a series of epoxy-based composites. The latter contained different amounts of PTFE powders and graphite flakes, additionally reinforced with various quantities of short carbon fibers (SCF) and nano-TiO_2 (300 nm). The best wear resistant composition was found to be a combination of nano-TiO_2 with conventional reinforcements. As an example, epoxy added with 15 vol.% graphite, 5 vol.% nano-TiO_2, and 15 vol.% SCF exhibited a specific wear rate of 3.2×10^{-7} mm^3/Nm at a pressure of 1 MPa and a sliding speed of 1 m/s, which is more than 100 times lower than that of neat epoxy.

Investigations have been carried out with a constant amount of graphite and SCF, but with a varying content of nano-TiO_2 particles. When either reducing the nanoparticle content to 2 vol.% or increasing it to 8 vol.%, the specific wear rates of the composites became higher. Figure 2 illustrates the dependence of the specific wear rate of epoxy-based composites with 5 and 15 vol.% of graphite and SCF on the nano-TiO_2 content. A comparison with the epoxy filled with various amounts of nanoparticles only[37] is also given. It is interesting to note that a content of 4-6 vol.% of nano-TiO_2 exhibited an optimum effect in all the three cases.

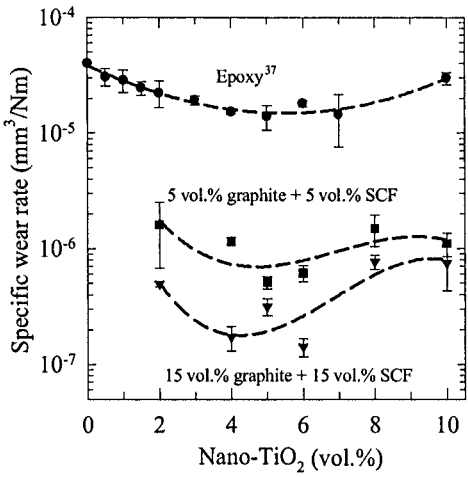

Figure 2. Dependence of the specific wear rate on the nano-TiO_2 content of epoxy nanocomposites. Wear conditions: normal pressure = 1 MPa, sliding velocity = 1 m/s, duration = 20 h, block-on-ring apparatus.

To evaluate the wear behavior of materials under different sliding conditions, *i.e.*, various contact pressures and sliding speeds, the time-related depth wear rate, W_t, was introduced

$$W_t = k * pv = \frac{\Delta h}{t} \tag{1}$$

where k^* is called wear factor (equivalent to the specific wear rate), p is the normal pressure, v is the sliding velocity, t is the test time, and Δh is the height loss of the specimen. In this equation, the wear factor, k^*, is supposed to be a material parameter, which also can be more or less dependent on the testing conditions, *e.g.*, p, v, and T (temperature). To reduce the basic wear factor, k^*, and to enhance the "limiting pv" value are the general targets of the design of wear resistant polymer composites.[22]

Figure 3 compares the time-related depth wear rate of filled epoxy composites, with and without nano-TiO_2, as a function of the pv factor.[53] W_t of the neat epoxy is already very high at a rather low pv value (1MPa•m/s) and cannot be drawn within this plot for higher pv values (*i.e.*, the material cannot be operated under these conditions). By incorporating traditional micron fillers, *i.e.*, 15 vol.% of SCF and 5 vol.% of each graphite and PTFE, the wear rate is significantly reduced. The depth wear rate generally increases with the increase in the pv factor. For the composite containing only these traditional micron fillers, the wear rate raises to a quite high value when the pv factor reaches 4 MPa•m/s. However, the depth wear rate of the composite with additional 5 vol.% of nanoparticles is much lower under this condition, and even at much higher pv factors, *e.g.*, 12 MPa and 1 m/s or 4 MPa and 3 m/s. Therefore, it is clear that the wear factor is reduced, and the "limiting pv" value is also enhanced by these nanoparticles.

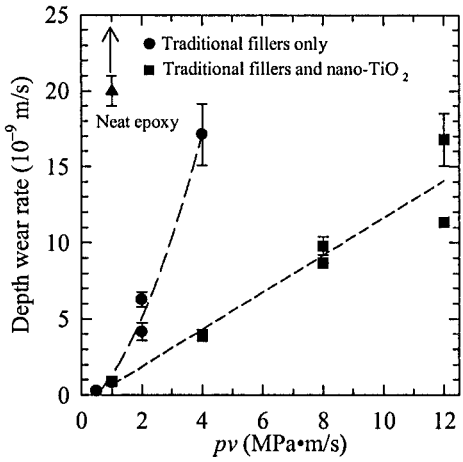

Figure 3. Comparison of the time-related depth wear rate of filled epoxy composites (5 vol.% graphite, 5 vol.% PTFE, 15 vol.% SCF) without and with 5 vol.% nano-TiO_2 as a function of the pv-factor. Wear conditions: pin-on-disk apparatus.

Investigations on the worn surfaces were performed using a scanning electron and an atomic force (AFM) microscope.[54,55] It is believed that SCF are

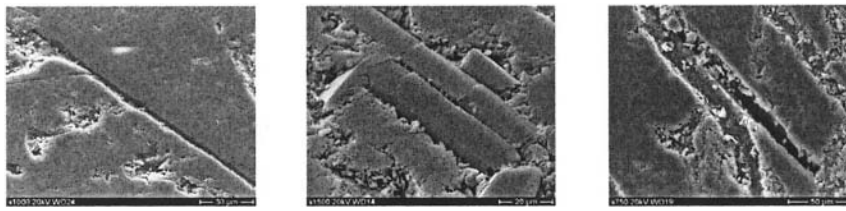

(a) (b) (c)

Figure 4. Wear process of short carbon fiber-reinforced epoxy composite (5 vol.% graphite, 5 vol.% PTFE, 15 vol.% SCF): (a) fiber thinning, (b) fiber breakage, and (c) fiber pulverization and interfacial removal. Wear conditions: normal pressure = 1 MPa, sliding velocity = 1 m/s, duration = 20 h, pin-on-disk apparatus.

the key filler to the improved wear resistance of polymers. Figure 4 shows the wear process of traditional SCF-reinforced composites without nanoparticles, in which fiber thinning, fiber breakage, and fiber pulverization and interfacial removal are the major mechanisms involved. Once nano-TiO_2 was incorporated, the worn surfaces seem to be much smoother (Figure 5a), even under severe wear conditions at 12 MPa and 1 m/s (Figure 5b) than in the case of Figure 4 (without nanoparticles).

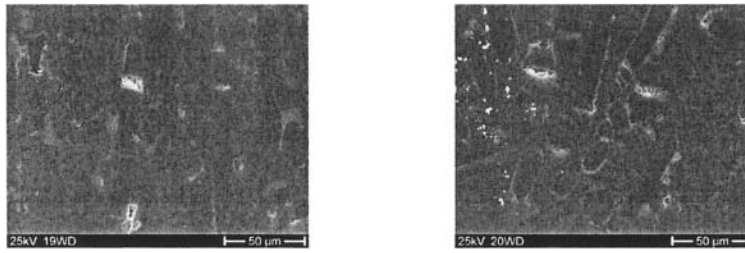

(a) (b)

Figure 5. SEM micrographs of the worn surfaces of a nanocomposite (epoxy, 5 vol.% graphite, 5 vol.% nano-TiO_2, 15 vol.% SCF) sliding at various contact pressures and constant velocity: (a) 1 MPa and (b) 12 MPa. Wear conditions: sliding velocity = 1 m/s, duration = 20 h, pin-on-disk apparatus.

AFM observations of the carbon fibers without nano-TiO_2 show that the fiber surface was quite smooth, but apparently tilted to the worn surface (Figure 6a,b). Interfacial damage between SCF and matrix occurred. However, the situation was different for the composition containing nanoparticles. In the latter case, the fiber surface was finely scratched by the tiny nanoparticles (Figure 6c,d, with scratches parallel to the sliding direction). Although the rear edges of the fibers (relative to

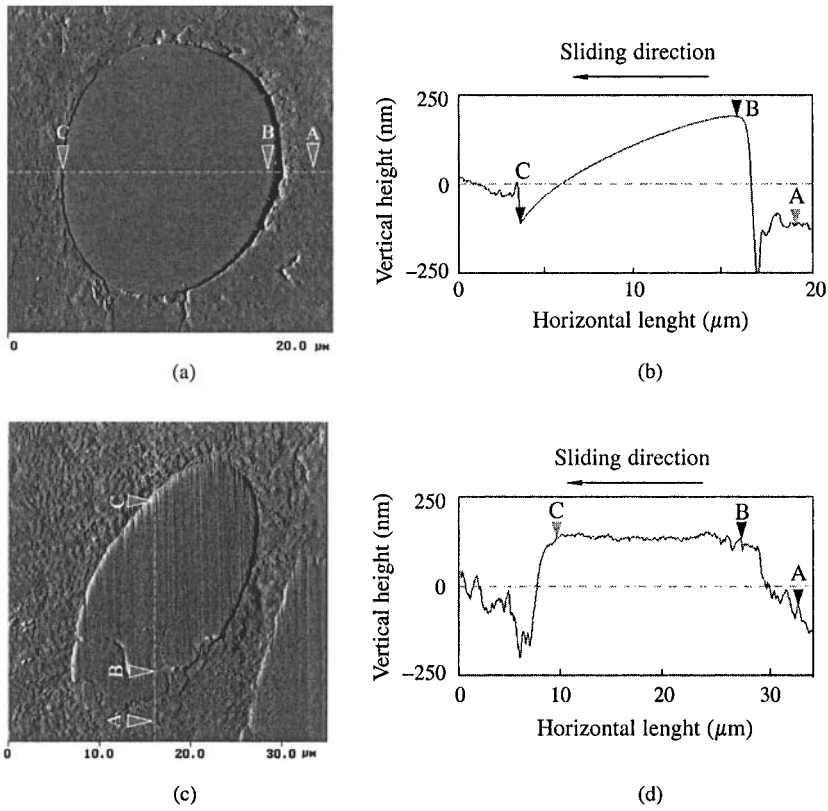

Figure 6. AFM images of carbon fibers on the worn surfaces of epoxy composites: (a,b) 15 vol.% graphite, 5 vol.% PTFE, 15 vol.% SCF and (c,d) 15 vol.% graphite, 5 vol.% nano-TiO_2, 15 vol.% SCF. The arrows indicate the sliding directions. Wear conditions: normal pressure = 1 MPa, sliding velocity = 1 m/s, duration = 20 h, pin-on-disk apparatus.

the sliding direction) were slightly damaged, the interface was maintained in good shape. From these observations, a positive rolling effect of the nanoparticles between the material pairs was proposed. This rolling effect helped to reduce the frictional coefficient during sliding and, accordingly, to reduce the shear stress and contact temperature. Also, this rolling effect protected the SCF from more severe wear mechanisms, especially at high sliding pressure and speed situations. Such a rolling effect was also reported for WS_2 nanoparticles as solid lubricants.[56,57]

This effect detected in epoxy composites was also found by preliminary investigations of thermoplastic composites, *i.e.*, PA66[58] and polyetherimide matrices.[59,60] Figure 7 shows typical trends of the frictional coefficient and contact temperature as functions of time for two PA66 composites, with and without nano-TiO_2. It is clear that at the beginning of the running-in stage, the sliding performance

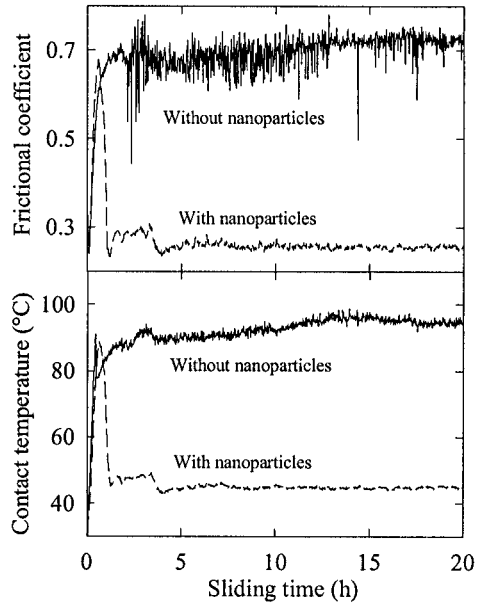

Figure 7. Frictional coefficient and contact temperature of PA66 composites (5 vol.% graphite, 15 vol.% SCF) without and with 5 vol.% nano-TiO_2. Wear conditions: normal pressure = 4 MPa, sliding velocity = 1 m/s, duration = 20 h, pin-on-disk apparatus.

is similar for the two compositions. However, the frictional coefficient and the contact temperature in the case of the nanocomposite were abruptly reduced after an initial stage of the contact period (about 1 h), *i.e.*, once the nanoparticles commenced to function. This is further supported by SEM observations of the worn surfaces. Figure 8a,c shows that the worn surfaces of the two compositions were not much different at a sliding duration of 30 min. However, after a sliding period of 2 h, the surface of the nano-TiO_2 filled composite looked much smoother (Figure 8d) than that without nanoparticles (Figure 8b). Lower magnification SEM photographs showing an overview of the worn surfaces, confirmed this impression (similar to Figures 4 and 5 for the epoxy matrix composites).

Figure 9 is a schematic representation of the effect of PTFE powders and TiO_2 nanoparticles on the changes in the frictional coefficient and contact temperature with time. PTFE is very helpful in keeping the frictional coefficient relatively low within the initiation or running-in period, whereas nano-TiO_2 becomes quite effective in the longer range. It is clear that a combination of SCF and solid lubricants (PTFE and graphite) together with TiO_2 nanoparticles can reach an optimum effect in both the running-in and the steady-state sliding stage.

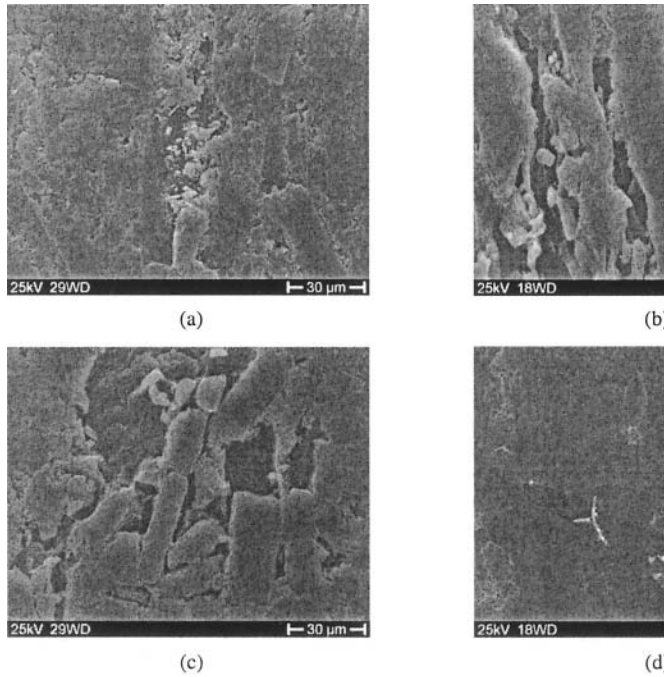

Figure 8. SEM micrographs of the worn surfaces of PA66 composites (5 vol.% graphite, 15 vol.% SCF): (a,b) without and (c,d) with 5 vol.% nano-TiO_2 after a sliding duration of (a,c) 30 min and (b,d) 2 h. Wear conditions: normal pressure = 2 MPa, sliding velocity = 3 m/s, pin-on-disk apparatus.

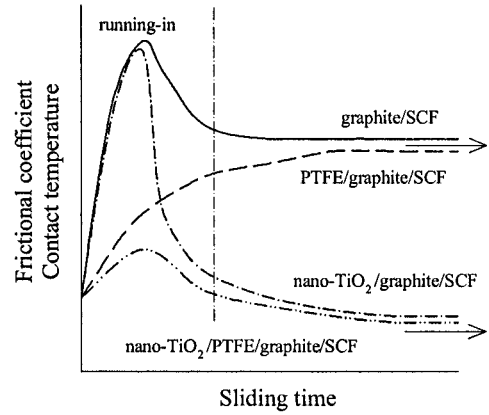

Figure 9. Schematic representation of the effects of PTFE powders and TiO_2-nanoparticles on the changes in the frictional coefficient and contact temperature of graphite and short carbon fiber-filled polymer composites.

6 Conclusion

In order to understand the mechanisms of the sliding wear of inorganic particle-filled polymers, two opposite aspects should be considered. On the one hand, hard particles improve the wear resistance of polymers, either by enhancing the mechanical properties (hardness and stiffness) or by improving the bonding between transfer films and metallic counterparts. On the other hand, abrasive wear may occur due to greater discontinuities in the material. Once the particle sizes are diminishing down to the nano-scale, significant improvements of the wear resistance of polymers were achieved at very low nano-filler contents (1-3 vol.%). It is still the subject of future studies to elucidate the reasons why the very reduced size of the fillers yields such a significant improvement in the wear properties.

The combination of nanoparticles and short carbon fibers exhibited a clear improvement in the wear resistance of both thermosetting and thermoplastic composites. In addition, this concept allowed the use of these materials under more severe wear conditions, such as higher normal pressures and sliding velocities. A topographic smoothening and a possible rolling effect due to the nanoparticles are supposed to be the reasons for this progress in the friction and wear performance.

7 Acknowledgement

Z. Zhang is grateful to the Alexander von Humboldt Foundation for his Sofja Kovalevskaja Award, financed by the German Federal Ministry of Education and Research (BMBF) within the German Government's "ZIP" program for investment in the future.

8 References

[1] K. Friedrich, Z. Zhang, P. Klein (2004) Wear of polymer composites, in *Wear - Materials, Mechanisms and Practice* (Ed. G. W. Stachowiak) The Institution of Mechanical Engineers, Professional Engineering Publishing Ltd., in press.

[2] J. Karger-Kocsis, Z. Zhang (2004) Structure-property relationships in nanoparticle/ semi-crystalline thermoplastic composites, in *Mechanical Properties of Polymers Based on Nanostructure and Morphology* (Eds. F. J. Baltá Calleja, G. Michler) Marcel Dekker Inc., New York, in press.

[3] A. C. Moloney, H. H. Kausch, T. Kaiser, H. R. Beer (1987) Parameters determining the strength and toughness of particulate filled epoxide resins, *J. Mater. Sci.* **22**, 381.

[4] C. B. Ng, L. S. Schadler, R. W. Siegel (1999) Synthesis and mechanical properties of TiO_2-epoxy nanocomposites, *Nanostructured Materials* **12**, 507.

[5] C. B. Ng, B. J. Ash, L. S. Schadler, R. W. Siegel (2001) A study of the mechanical and permeability properties of nano- and micron-TiO_2 filled epoxy composites, *Adv. Compos. Lett.* **10**, 101.

[6] Y. Ou, F. Yang, Z. Yu (1998) A new conception on the toughness of nylon 6/silica nanocomposite prepared *via in situ* polymerization, *J. Polym. Sci. B Polym. Phys.* **36**, 789.

[7] S. Bahadur, D. Gong (1992) The role of copper compounds as fillers in the transfer and wear behavior of polyetheretherketone, *Wear* **154**, 151.

[8] S. Bahadur, D. Gong, J. W. Anderegg (1992) The role of copper compounds as fillers in the transfer film formation and wear of nylon, *Wear* **154**, 207.

[9] S. Bahadur, D. Gong (1993) The transfer and wear of nylon and CuS-nylon composites: filler proportion and counterface characteristics, *Wear* **162-164**, 397.

[10] S. Bahadur, D. Gong, J. W. Anderegg (1993) Tribochemical studies by XPS analysis of transfer films of nylon 11 and its composites containing copper compounds, *Wear* **165**, 205.

[11] S. Bahadur, A. Kapoor (1992) The effect of ZnF_2, ZnS and PbS fillers on the tribological behavior of nylon 11, *Wear* **155**, 49.

[12] Q. Zhao, S. Bahadur (1999) The mechanism of filler action and the criterion of filler selection for reducing wear, *Wear* **225-229**, 660.

[13] Q. Zhao, S. Bahadur (1998) A study of the modification of the friction and wear behavior of polyphenylene sulfide by particulate Ag_2S and PbTe fillers, *Wear* **217**, 62.

[14] L. Yu, S. Bahadur (1998) An investigation of the transfer film characteristics and the tribological behaviors of polyphenylene sulfide composites in sliding against tool steel, *Wear* **214**, 245.

[15] C. J. Schwartz, S. Bahadur (2001) The role of filler deformability, filler-polymer bonding, and counterface material on the tribological behavior of polyphenylene sulfide (PPS), *Wear* **251**, 1532.

[16] L. Yu, S. Yang, H. Wang, Q. Xue (2000) An investigation of the friction and wear behaviors of micrometer copper particle-filled polyoxymethylene composites, *J. Appl. Polym. Sci.* **19**, 2404.

[17] K. Tanaka (1986) Effect of various fillers on the friction and wear of PTFE-based composites, in *Friction and Wear of Polymer Composites* (Ed. K. Friedrich) Elsevier, Amsterdam, p. 137.

[18] S. Bahadur, D. Tabor (1984) The wear of filled polytetrafluoroethylene, *Wear* **98**, 1.

[19] S. Bahadur (2000) The development of transfer layers and their role in polymer tribology, *Wear* **245**, 92.

[20] K. Friedrich (1993) Particulate dental composites under sliding wear conditions, *J. Mater. Sci.: Materials in Medicine* **4**, 266.

[21] X. S. Xing, R. K. Y. Li (2004) Wear behavior of epoxy matrix composites filled with uniform sized sub-micron spherical silica particles, *Wear* **256**, 21.

[22] K. Friedrich (1986) Wear of reinforced polymers by different abrasive counterparts, in *Friction and Wear of Polymer Composites* (Ed. K. Friedrich) Elsevier, Amsterdam, p. 233.

[23] J. M. Durand, M. Vardavoulias, M. Jeandin (1995) Role of reinforcing ceramic particles in the wear behaviour of polymer-based model composites, *Wear* **181-183**, 833.

[24] Q. Xue, Q. Wang (1997) Wear mechanisms of polyetheretherketone composites filled with various kinds of SiC, *Wear* **213**, 54.

[25] Q. Wang, Q. Xue, H. Liu, W. Shen, J. Xu (1996) The effect of of particle size of nanometer ZrO_2 on the tribological behavior of PEEK, *Wear* **198**, 216.

[26] Q. Wang, J. Xu, Q. Shen, W. Liu (1996) An investigation of the friction and wear properties of nanometer Si_3N_4 filled PEEK, *Wear* **196**, 82.

[27] Q. Wang, Q. Xue, W. Shen (1997) The friction and wear properties of nanometre SiO_2-filled polyetheretherketone, *Tribol. Int.* **30**, 193.

[28] Q. Wang, J. Xu, W. Shen, Q. Xue (1997) The effect of nanometer SiC filler on the tribological behavior of PEEK, *Wear* **209**, 316.

[29] Q. Wang, Q. Xue, W. Shen, J. Zhang (1998) The friction and wear properties of nanometer ZrO_2-filled polyetheretherketone, *J. Appl. Polym. Sci.* **69**, 135.

[30] C. J. Schwartz, S. Bahadur (2000) Studies on the tribological behavior and transfer film-counterface bond strength for polyphenylene sulfide filled with nanoscale alumina particles, *Wear* **237**, 261.

[31] S. Bahadur, C. Sunkara (2004) Effect of transfer film structure, composition and bonding on the tribological behaviour of polyphenylene sulfide filled with nano particles of TiO_2, ZnO, CuO and SiC, *Wear*, to be published.

[32] M. Avella, M. E. Errica, E. Martuscelli (2001) Novel PMMA/$CaCO_3$ nanocomposites abrasion resistant prepared by an *in situ* polymerization process, *Nano Lett.* **1**, 213.

[33] M. Rong, M. Zhang, H. Liu, H. Zeng, B. Wetzel, K. Friedrich (2001) Microstructure and tribological behavior of polymeric nanocomposites, *Industrial Lubrication & Tribology* **53**, 72.

[34] M. Q. Zhang, M. Z. Rong, S. L. Yu, B.Wetzel, K. Friedrich (2002) Improvement of tribological performance of epoxy by the addition of irradiation grafted nano-inorganic particles, *Macromol. Mater. Eng.* **287**, 111.

[35] M. Q. Zhang, M. Z. Rong, S. L. Yu, B. Wetzel, K. Friedrich (2002) Effect of particle surface treatment on the tribological performance of epoxy based nanocomposites, *Wear* **253**, 1088.

[36] G. Shi, M. Q. Zhang, M. Z. Rong, B. Wetzel, K. Friedrich (2003) Friction and wear of low nanometer Si_3N_4 filled epoxy composites, *Wear* **254**, 784.

[37] B. Wetzel, F. Haupert, K. Friedrich, M. Q. Zhang, M. Z. Rong (2002) Impact and wear resistance of polymer nanocomposites at low filler content, *Polym. Eng. Sci.* **42**, 1919.

[38] B.Wetzel, F. Haupert, M. Q. Zhang (2003) Epoxy nanocomposites with high mechanical and tribological performance, *Compos. Sci. Technol.* **63**, 2055.

[39] M. S. Sreekala, K. Friedrich, C. Eger (2004) Property improvements of an epoxy resin by nanosilica particle reinforcement, in *Polymer Composites - from Nano- to Macro-Scale* (Eds. K. Friedrich, S. Fakirov, Z. Zhang) Kluwer Academic Publishers.

[40] F. Li, K. Hu, J. Li, B. Zhao (2002) The friction and wear characteristics of nanometer ZnO filled polytetrafluoroethylene, *Wear* **249**, 877.

[41] W. G. Sawyer, K. D. Freudenberg, P. Bhimaraj, L. S. Schadler (2003) A study on the friction and wear behavior of PTFE filled with alumina nanoparticles, *Wear* **254**, 573.

[42] G. W. Stachowiak, A. W. Batchelor (2001) *Engineering Tribology*, 2nd Ed., Butterworth-Heinemann, Boston.

[43] K. Friedrich (Ed.) (1986) *Friction and Wear of Polymer Composites*, Composite Materials Series, Vol. 1, Series Editor: R. B. Pipes, Elsevier, Amsterdam.

[44] K. Friedrich (Ed.) (1993) *Advances in Composite Tribology*, Composite Materials Series, Vol. 8, Series Editor: R. B. Pipes, Elsevier, Amsterdam.

[45] J. Vande Voort, S. Bahadur (1995) The growth and bonding of transfer film and the role of CuS and PTFE in the tribological behavior of PEEK, *Wear* **181-183**, 212.

[46] Q. Wang, Q. Xue, W. Liu, J. Chen (2000) The friction and wear characteristics of nanometer SiC and polytetrafluoroethylene filled polyetheretherketone, *Wear* **243**, 140.

[47] S. Bahadur, D. Gong, J. W. Anderegg (1995) Studies of worn surfaces and the transfer film formed in sliding by CuS-filled and carbon fiber-reinforced nylon against a steel surface, *Wear* **181-183**, 227.

[48] S. Bahadur, V. K. Polineni (1996) Tribological studies of glass fabric-reinforced polyamide composites filled with CuO and PTFE, *Wear* **200**, 95.

[49] M. Palabiyik, S. Bahadur (2002) Tribological studies of polyamide 6 and high density polyethylene blends filled with PTFE and copper oxide and reinforced with short glass fibers, *Wear* **253**, 369.

[50] J. Wang, M. Gu, S. Bai, S. Ge (2003) Investigation of the influence of MoS_2 filler on the tribological properties of carbon fiber reinforced nylon 1010 composites, *Wear* **255**, 774.

[51] Z. Zhang, F. Haupert, K. Friedrich (2003) Enhancement of the wear resistance of polymer composites by nano-fillers, German Patent Application No.10329228.4.

[52] Z. Zhang, C. Breidt, L. Chang, F. Haupert, K. Friedrich (2004) Enhancement of the wear resistance of epoxy: short carbon fibre, graphite, PTFE and nano-TiO_2, *Composites A*, **35**, 385.

[53] L. Chang, Z. Zhang, C. Breidt, K. Friedrich (2004) Tribological properties of epoxy nanocomposites: I. Enhancement of the wear resistance by nano-TiO_2 particles, *Wear*, **258**, 141.

[54] L. Chang, Z. Zhang (2004) Tribological properties of epoxy nanocomposites: II. A combinative effect of short carbon fibre and nano-TiO_2, *Wear*, submitted.

[55] L. Chang, Z. Zhang (2004) Tribological properties of epoxy nanocomposites: III. Influence of solid lubricants - PTFE powders and graphite flakes, *Wear*, submitted.

[56] L. Rapoport, Yu Bilik, Y. Feldman, M. Homyonfer, S. R. Cohen, R. Tenne (1997) Hollow nanoparticles of WS_2 as potential solid-state lubricants, *Nature* **387**, 791.

[57] L. Rapoport, N. Fleischer, R. Tenne (2003) Fullerene-like WS_2 nanoparticles: superior lubricants for harsh conditions, *Adv. Mater.* **15**, 651.

[58] L. Chang, Z. Zhang, H. Zhang (2004) On the sliding wear of nanoparticles filled polyamide 6,6 composites, *Compos. Sci. Technol.*, submitted.

[59] G. L. Xian, Z. Zhang, K. Friedrich (2004) Tribological behaviour of micro- and nano-particles filled polyetherimide composites, *J. Appl. Polym. Sci.*, submitted.

[60] L. Chang, Z. Zhang, H. Zhang, K. Friedrich (2004) Effect of nanoparticles on the tribological behaviour of short carbon fibre reinforced polyetherimide composites, *Tribol. Int.*, submitted.

Part III

Macrocomposites: Processing and Application

Chapter 11

Production of Thermoplastic Towpregs and Towpreg-Based Composites

João P. Nunes, Ferrie W. J. van Hattum, Carlos A. Bernardo, António M. Brito, António S. Pouzada
Department of Polymer Engineering, Institute of Polymers and Composites, Minho University, Guimarães, Portugal

João F. Silva
Department of Mechanical Engineering, ISEP, Porto Polytechnic Institute, Porto, Portugal

António T. Marques
Department of Mechanical Engineering and Industrial Management, Porto University, Porto, Portugal

1 Introduction

During the last three decades, composites have replaced traditional materials in many engineering applications due to their excellent specific properties. Structural applications, requiring higher mechanical properties and, consequently, the use of long and continuous fibers, are still by far dominated by thermosetting matrix composites. However, continuous fiber thermoplastic composites are increasing their share of the composites' market. This is due to numerous advantages, *e.g.*, excellent toughness, durability and damping properties, possibilities of processing without chemical reactions, recycling, and reshaping.[1,2] However, the high viscosity of thermoplastic melts makes the impregnation of continuous fibers quite difficult, thus restricting the utilization of these materials in commercial applications. To overcome this problem is of great importance in the technology of continuous fiber thermoplastic matrix composites. The present chapter describes a research program envisaged with just this objective.

In this program, a powder-coating line was designed and used to make thermoplastic matrix towpregs and pre-consolidated tapes, *prepregs,* from continuous fibers and a polymer powder.[3-5] The operating conditions of the powder-coating equipment were optimized so that the system worked automatically, producing prepregs without significant impregnation difficulties. The prepregs were then processed by compression molding, pultrusion and filament winding, by adapting an equipment that is normally used to produce thermoset matrix composites.[6-13] At a later stage, long fiber-reinforced composites (LFTs) were also made from chopped towpregs. The mechanical properties of the composites were determined and used to assess the overall efficiency of the process. It was concluded that these properties are comparable to those of common engineering materials and quite appropriate for many structural applications.

2 Raw Materials

A polypropylene powder, Icorene 9184B P (supplied by ICO Polymers, France), and 2400 Tex 357D-AA glass fibers (supplied by Owens Corning, USA) were used in the production of the towpregs and pre-consolidated tapes. A polycarbonate powder, Makrolon 2458 (supplied by Bayer, Germany), and high strength Thornel T300/12/NT PAN carbon fibers (supplied by Amoco, USA) were also used in the consolidation model validations. Table 1 summarizes the properties of these materials.

Table 1. Properties of the raw materials (as determined experimentally[5]).

Property	*Unit*	*Glass fibers*	*Carbon fibers*	*Polypropylene*	*Polycarbonate*
Specific gravity	Mg/m^3	2.56	1.76	0.9	1.2
Tensile modulus	GPa	62.5	230	0.98	2.34
Poisson ratio	-	0.26	0.27	0.21	0.38
Tensile strength	MPa	1657	3500	19.0	63.2
Fiber diameter	μm	13.7	7.2	–	–

3 Production of Towpregs

3.1 Process and Equipment Description

The powder-coating equipment developed to produce the towpregs is composed of five modules (Figure 1): (i) fiber supplying system, (ii) pneumatic

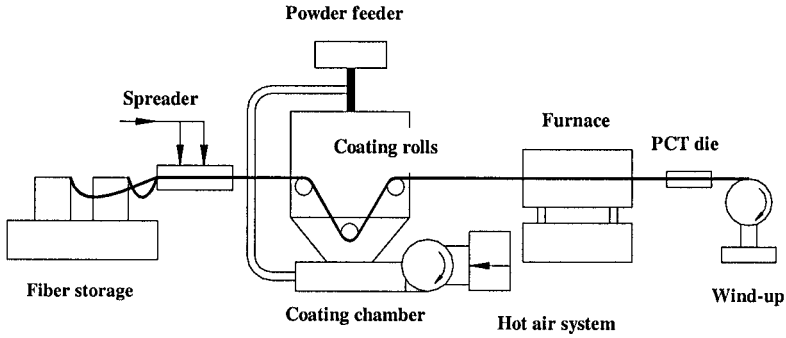

Figure 1. Schematic diagram of the powder coating line.

spreader, (iii) polymer powder feeder and coating chamber, (iv) furnace, and (v) terminal winding system.

The fibers are pulled from the roving and spread by a pneumatic device to facilitate polymer penetration. Then, in a deposition chamber, a thermoplastic powder is continuously supplied by a variable speed, double-screw miniextruder. By means of an air fan, the powder forms a cloud and adheres to the fibers. Three rolls conveniently placed inside the chamber increase the fibers' path and, consequently, the deposition time and amount of adhering thermoplastic powder. Next, the fibers pass through a furnace to soften the polymer particles and promote their adhesion to the surface. Finally, the towpregs are cooled down and wound-up on a spool with variable speed.

To increase the processability of the prepregs, the powder-coating line was modified to produce pre-consolidated tapes (PCTs).[8] By passing the towpregs through a heated die (Figure 2a) mounted immediately after the furnace, pressurization and consolidation of the towpreg at different temperatures is achieved before the final wind-up. Figure 2b depicts a PCT obtained from a glass fiber-polypropylene (GF/PP) towpreg. In this figure, and also in the SEM micrographs in Figure 3, it can be seen that a better impregnation is achieved in the case of the

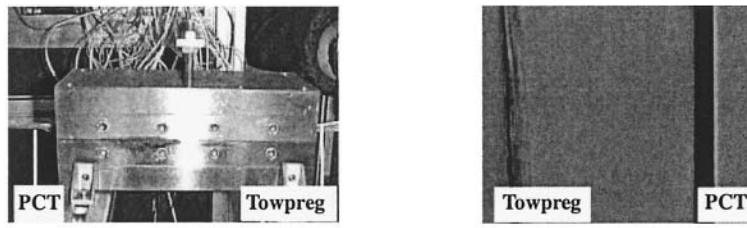

(a) (b)

Figure 2. Production of pre-consolidated tapes: (a) view of the die, (b) GF/PP towpreg and PCT samples.

PCT. This allows for a substantial saving of time in subsequent impregnation phases during processing.

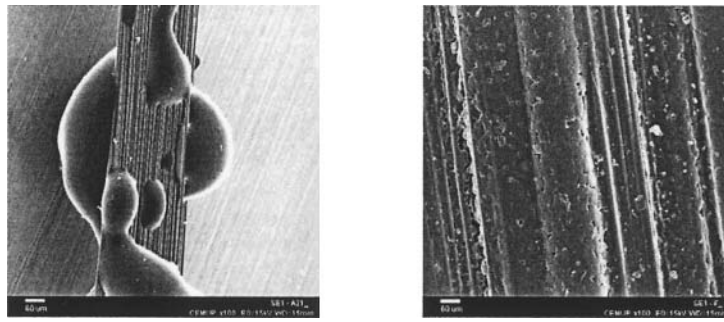

(a) (b)

Figure 3. SEM micrographs of the (a) towpreg and (b) PCT samples (magnification ×100).

The typical coating line operational conditions are summarized in Table 2.

Table 2. Typical coating line operational conditions.

Variable	*Unit*	*Value*
Linear fiber pull speed	m/min	0.7-1.2
PP powder feeder	g/min	11.8
Fan speed	rpm	825
PCT die temperature	°C	220
Furnace temperature	°C	240
Coating chamber temperature	°C	50
Spreader pressure	kPa	500

3.2 Relationships Between Final Properties and Processing Conditions

3.2.1 Parameters Affecting the Polymer Powder Deposition

The influence of the linear fiber pull speed, temperature and moisture content in the coating chamber, as well as the PP powder particle size on the amount of polymer deposited in the towpregs was established (Figure 4a-d). After setting each parameter, approximately 100 m of towpreg were produced, weighed, and the PP mass fraction was determined from the density of the components.

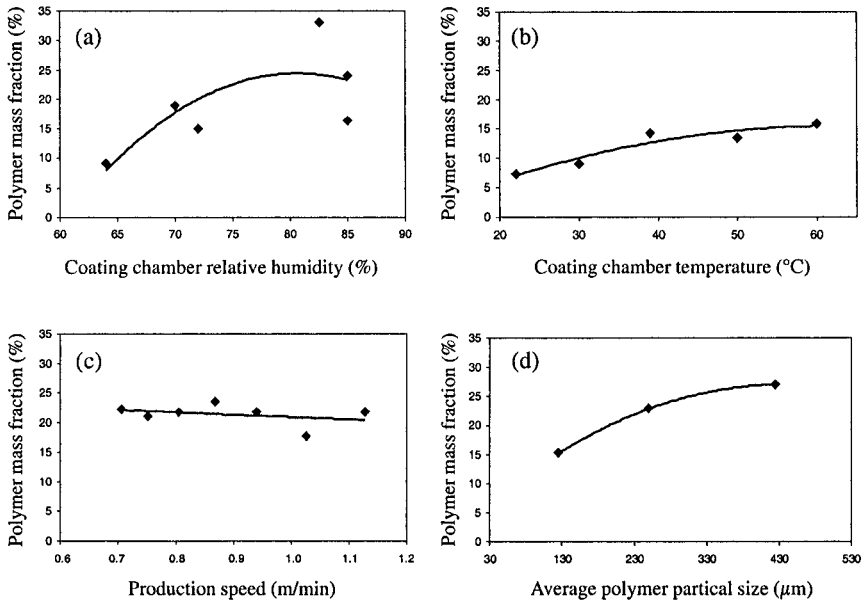

Figure 4. Influence of the processing conditions on the polymer mass fraction.

As can be seen in Figure 4, the PP mass fraction strongly depends on the powder particle size and on the moisture content in the coating chamber. On the other hand, it is almost insensitive to the linear pull speed. The amount of PP deposited on the fibers increases with the increment of moisture, temperature, and particle size until a maximum is reached for values around 80%, 50 °C, and 400 μm, respectively. These results lead to the conclusion that in order to optimize the coating process it is necessary to control the moisture content and temperature in the coating chamber. It is also highly desirable to control the particle size of the polymer.

3.2.2 Influence of the Processing Conditions on the Final Composite Properties

As a further step towards the optimization of the coating process, the influence of the operational variables on the final composite mechanical properties was studied. Four different parameters (polymer powder size, fiber pull speed, and furnace and PCT die temperatures) were independently varied. Then towpregs were produced under preset conditions, and composite plates were obtained by compression molding and subjected to mechanical testing (three-point bending and tensile tests). The overall results are summarized in Table 3.

Table 3. Coating line optimum processing conditions.

Variable	*Unit*	*Materials*			
		Pre-impregnated materials		*Composites made from:*	
		Towpregs	*PCTs*	*Towpregs*	*PCTs*
Polymer powder size	μm	400		280-320	
Linear fiber pull speed	m/min	0.6-1.2		1.1-1.2	≤ 0.88
PCT die temperature	°C	–	220-280	–	220-280
Furnace temperature	°C	280			
Coating chamber temperature	°C	55			
Coating chamber moisture	%	80			

It can be concluded that the polymer powder size is probably the most critical parameter for process optimization. In fact, the particle size found to be optimum to achieve high production rates (400 μm) should be reduced to 280-320 μm to guarantee adequate mechanical properties.

4 Production of Towpreg-Based Composites

Three high volume technologies were used to produce composite parts: compression molding, filament winding, and pultrusion. Furthermore, two compression molding techniques were used, one suitable for continuous fiber-reinforced and another for long chopped fiber-reinforced composites (LFTs).

4.1 Compression Molding

4.1.1 Process Description

The technique developed by Klett *et al.*[14] was followed: a wrapping wire mandrel was used to facilitate the towpreg lay-up and the coated tow is wrapped around an aluminum mandrel by rotating end-over-end. A limitation of this procedure is that the fibers in one layer are misaligned with respect to another layer.

4.1.2 Molding Conditions

Compression molding in an 800 kN SATIM press with two independently heated plates was started by heating the molding zone up to 230 °C and then

applying a pressure of 15 MPa. After 10 min, the mold was cooled down to room temperature and, finally, the laminate plate (*ca.* 2 mm thick) was removed.

4.2 Process Modeling

A theoretical model was developed to simulate the consolidation by compression molding, both in isothermal and non-isothermal conditions.[15,16] The model assumes a towpreg lamina as an array of fibers with attached particles (Figure 5a). The stacking of a number of these laminae together with different possible arrangements leads to a preform (Figure 5b).

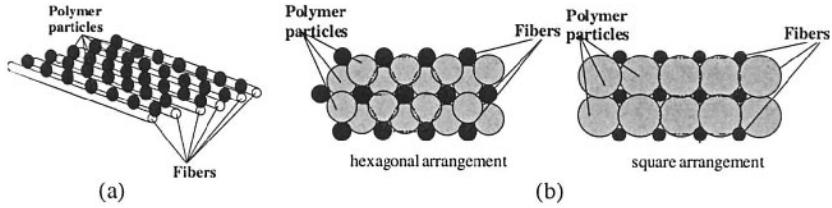

Figure 5. Geometry of a towpreg laminate: (a) towpreg lamina, (b) arrangements of laminae stacking.

The isothermal model was based on the following assumptions: (i) the fibers and polymer are at a constant temperature during the process, (ii) the fibers and polymer are incompressible, (iii) upon compression, the polymer bridges spread in the direction of the fibers and the pressure is considered constant through the thickness, (iv) the press closing speed is constant, (v) no voids are left after consolidation, and (vi) the polymer flow is laminar and steady, and inertial forces are negligible. It was also assumed that during consolidation each polymer particle is connected to the adjacent fibers (Figure 6). Hexagonal and square fiber/polymer arrangements were considered in the model derivation.

To model the consolidation stage, the final, L, and the momentary, $L(t)$, bridge lengths were related to the fiber volume fraction, v_f, the composite thickness,

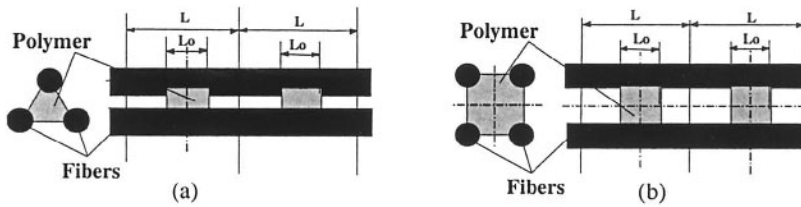

Figure 6. Schematic representation of a polymer bridge at the beginning of consolidation: (a) hexagonal and (b) square arrangement. L_0 and L are the initial and final bridge lengths.

$h(t)$, and the initial dimensions of the polymer particles. Then, the pressure gradient, dp/dx, required for the particle flow in the fiber direction was calculated as a function of the polymer properties for the hexagonal and square arrangements. In the case of isothermal consolidation and hexagonal arrangement, this can be done by applying the continuity, Darcy and Carman-Kozeny, equations to calculate the average polymer velocity.[15,17,18]

The derivation is formally the same for the hexagonal and square arrangements, only requiring the use of the correct expressions of v_f, L, and $L(t)$. The value of the viscous pressure thus obtained is:

$$p = -\frac{C}{\left[h(t) - h_{fi} v_{fi} \right]^6} \tag{1}$$

In this equation, C is a constant that depends on the towpreg properties, the press operation, and the fiber/polymer arrangement. The variables h_{fi} and v_{fi} are the final composite thickness and fiber volume fraction, respectively. For hexagonal and square packing, the values of C are, respectively:

$$C = \frac{64\eta\, s_p k_{xx} (h_{fi})^5 (v_{fi})^4 (1 - v_{fi}) (r_p)^6}{27\, (r_f)^6}; \qquad C = \frac{16\eta\, s_p k_{xx} (h_{fi})^5 (v_{fi})^4 (1 - v_{fi}) (r_p)^6}{9\, (r_f)^6} \tag{2}$$

where η is the polymer viscosity, r_f and r_p are the fiber and polymer particle radii, and k_{xx} is the Carman-Kozeny constant. According to Gutowski *et al.*,[18] this constant can be considered equal to 0.7.

For the utilization of the model, it is also necessary to consider the momentary shear rate, $\dot{\gamma}$, of the molten polymer through the fiber interstices. As can be seen from Eqs. (1) and (2), the pressure necessary to consolidate a towpreg with a hexagonal fiber/polymer arrangement is approximately 4/3 of that for a square arrangement. At this stage, using the viscosity, it is possible to express the temperature dependence of the pressure by Eq. (2) and to consider an isothermal and a non-isothermal approach.

4.2.1 Isothermal Consolidation

When the consolidation is isothermal, all composite layers are considered to be at the mold temperature. Then, using Eq. (1), the momentary pressure can be analytically determined if the fiber and polymer particle radii, the final molding thickness, and fiber volume fraction are known.

The polymer viscosity, η, at each mold temperature is derived by means of an Arrhenius power law. Finally, the expression modeling the evolution of the viscous pressure during isothermal consolidation can be obtained by introducing the value of η in Eq. (1).

4.2.2 Non-Isothermal Consolidation

Under non-isothermal conditions, the temperature varies through the thickness of the towpreg. As the polymer viscosity is temperature-dependent, the material layers deform at different rates. Thus, to calculate the momentary pressure, it is necessary to determine numerically the temperature gradient along the laminate z co-ordinate axis (Figure 7). Assuming the generation and transfer of heat by viscous dissipation and convection negligible, the momentary temperature at a point of z was calculated using finite differences by solving the following energy equation:

$$\frac{\partial T}{\partial t} = \alpha \frac{\partial^2 T}{\partial z^2} \tag{3}$$

where α is the thermal diffusivity ($\alpha = \dfrac{k}{\rho\, C_p}$, k is the thermal conductivity, C_p the specific heat, and ρ the density). The following boundary conditions were considered (see Figure 7):

$$T_{mold} = \text{constant; at } z = \pm\frac{h^{tot}}{2},\ T = T_{mold}$$

where h^{tot} is the total laminate thickness at any given moment.

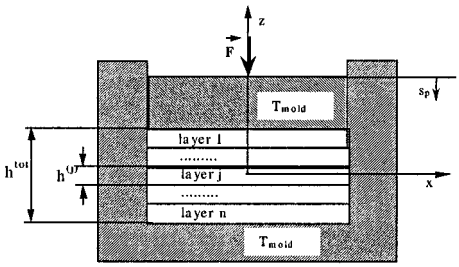

Figure 7. Scheme of the towpreg laminate used in the non-isothermal model.

Figure 8 shows the program flowchart used in the non-isothermal simulations. The determination of the temperature gradient is made in two steps

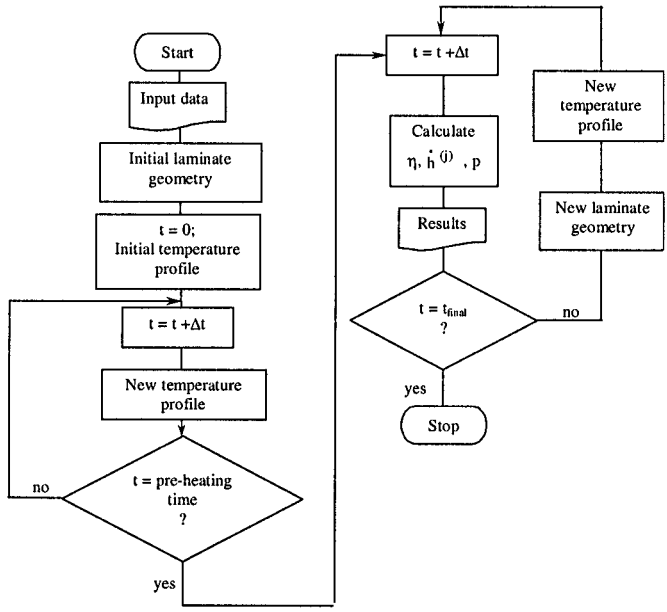

Figure 8. Non-isothermal simulation flowchart.

using small increments of time (Δt). In the first step, the composite, which consists of layers of equal thickness, is preheated without pressure, and the temperature field through the thickness is calculated. In the second step, the layers are considered to have different rheological and thermal properties, and to deform at different rates. At each moment during compression, t_i, the polymer viscosity is determined in every layer and the temperature calculated at its middle-plane.

Using Eqs. (1) and (2), the momentary deformation rate of each layer j, $\dot{h}^{(j)}$, can be calculated by solving the system of n equations:

$$\dot{h}^{(j)} = \frac{\eta^{(j+1)}\left[h^{(j)} - h_{fi}v_{fi}\right]^6}{\eta^{(j)}\left[h^{(j+1)} - h_{fi}v_{fi}\right]^6}\dot{h}^{(j+1)} \quad j = 1, \ldots, n-1 \quad \sum_{j=1}^{n}\dot{h}^{(j)} = s_p \qquad (4)$$

where the closing speed is considered to be equal to the sum of the deformation rates of all layers, and $\eta^{(j)}$ and $h^{(j)}$ are the momentary viscosity and thickness of the layer j, respectively.

4.2.3 Validation of the Consolidation Model

The SATIM press was used to produce laminates at four different temperatures. The pressure and platen displacement were continuously monitored

and recorded in a *x-t* recorder. Before consolidation, the laminate was preheated for 10 min.

The experimental values of the applied pressure, normalized with the closing speed and the viscosity of the material, are compared in Figure 9 with the simulation results, for both the hexagonal and the square fiber/polymer arrangements and quite good fits are observed. However, in the final stage of compression, the hexagonal model seems to fit better the experimental data. This may suggest that the hexagonal arrangement is closer to the actual packing assumed by the fibers during consolidation.

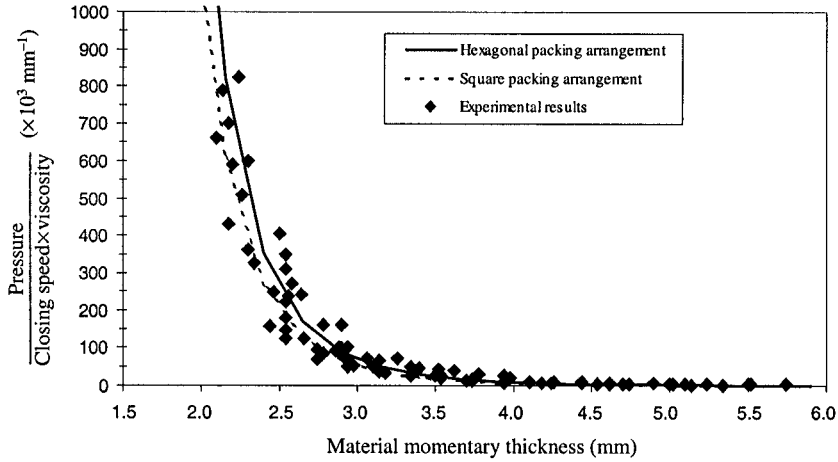

Figure 9. Comparison of experimental and theoretical consolidation pressure data.

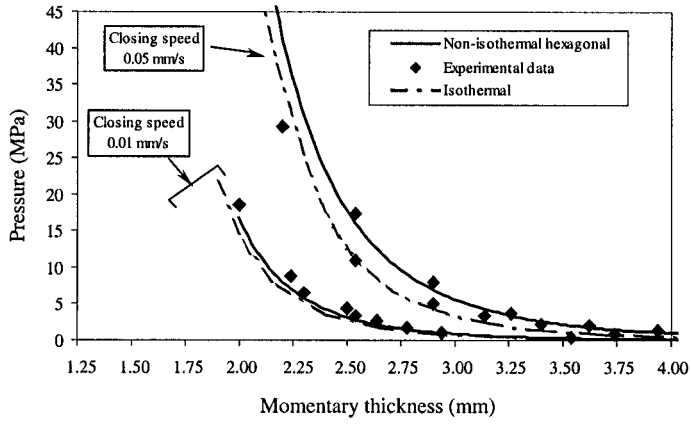

Figure 10. Experimental and theoretical consolidation pressure data at different closing speeds.

Despite the good fitting, the isothermal simulations provide little information about the influence of the preheating time and the closing speed on the pressure. For instance, with preheating times shorter than 10 min, experimental pressures greater than expected occurred at the beginning of compression. This results from the low temperature in the internal layers of the laminate and consequent viscosity increase. The same happened when the press closing speed increased. In this case, higher pressures are developed due to slow heat transfer that prevents the internal layers of reaching the set temperature.

In Figure 10, pressure data obtained from consolidation tests at 260 °C are compared with simulations for the isothermal and non-isothermal models using two different closing speeds. It is seen that the predictions of the non-isothermal model are closer to the experimental results, especially at the start of compression. The worst fit corresponds to the isothermal simulation at the higher closing speed.

4.3 Pultrusion

4.3.1 Process Description

A pultrusion head was designed, built, and mounted on a conventional 60 kN PULTREX pultrusion line (for thermoset matrix composites), thus adapting it to the production of continuous profiles made from thermoplastic matrix towpregs. The pultrusion head (Figure 11) includes three main parts: (i) preheating furnace, (ii) pressurization and consolidation die, and (iii) cooling die.

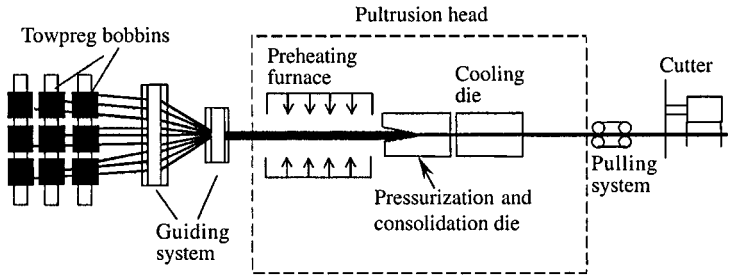

Figure 11. Schematic diagram of the pultrusion line.

The 4.8 kW preheating furnace allowed the processing of almost all fiber/thermoplastic-based towpregs. It has a 70×84 mm cross-section and a 625 mm long heating chamber that can be split opened to facilitate the passage of the towpregs at the start. Two type-K thermocouples and controllers enable the entry and the end zones of the chamber to be kept, when necessary, at different temperatures, leading to a progressive material heating. Two type-J thermocouples and controllers were also mounted in each of the two dies and the pressurization/consolidation

die was heated electrically. The temperature of the water that circulated inside the circular channels drilled in the cooling die was also controlled.

The process involves three phases. First, the towpregs are guided into the preheating furnace. Then, they pass through the first part of the pultrusion head, where the consolidation occurs. The consolidated material then enters the cooling die where it cools down to a required temperature. Finally, after leaving the pultrusion head, the profile is cut to specified lengths.

4.3.2 Processing Conditions

Table 4 lists the operating conditions typically used in preliminary tests on the pultrusion line. In these tests, well defined U-shaped profiles with smooth surfaces (cross-section 24×4 mm, 2 mm thick) were produced. The towpregs used in the process were made from the GF/PP system (Table 1).

Table 4. Typical pultrusion operating conditions.

Variable	*Unit*	*Value*
Pultrusion pull speed	m/min	0.5-0.8
Preheating furnace temperature	°C	200-250
Pressurization-consolidation die temperature	°C	300-320
Cooling die temperature	°C	60

4.3.3 Process Modeling

The model derived above to describe the consolidation of the towpregs was used in the design of the pultrusion-head dies, which are the critical elements in the profile consolidation and solidification. The recommendations by Astrom *et al.*[19-22] were taken into account in the design stage and the arrangement shown in Figure 12 was considered.

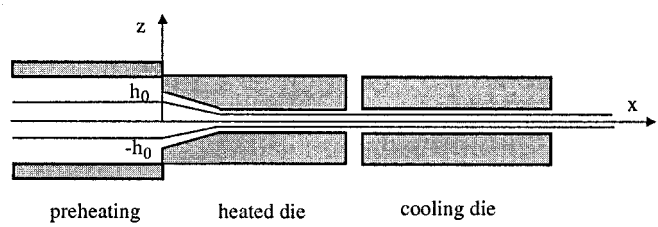

Figure 12. Pultrusion-head arrangement used (according to Astrom *et al.*[19-22]).

The length of the dies was determined taking into account that the temperature evolution in the towpregs during processing is given by the equation proposed by Astrom:

$$T(x,z) = T_{die} + \frac{2}{h_l}(T_0 - T_{die})\sum_{n=0}^{\infty}\left[\frac{(-1)^n}{\lambda_n}\exp\left(-\lambda_n^2\frac{\alpha_{tow}x}{U}\right)\cos(\lambda_n z)\right] \quad (5)$$

where

$$\lambda_n = \frac{(2n+1)\pi}{2h_l} \qquad n = 0, 1, 2, \ldots, n \quad (6)$$

and T is the temperature (°C), α_{tow} is the thermal diffusivity of the towpreg (m^2/s), T_0 – temperature of the towpreg at the die entrance (°C), T_{die} – die temperature (°C), and U – pulling speed (m/s).

The simulations indicated that a length of 200 mm was suitable for the steel heated and cooling dies, leading to an adequate consolidation and solidification of the GF/PP towpregs.

The pressurization and consolidation (heated) die was divided into three zones and designed to be opened horizontally. The first zone, about 40 mm long, has a large mouth to allow the easy entrance of the towpregs. The second zone is convergent and allows the pressure build-up for consolidating over a length of 115 mm. The prediction of the pressure field was made using an adaptation of the model derived for the consolidation by compression molding:

$$P_V = \frac{44.8\cdot\eta(\dot{\gamma},T)\cdot U\cdot\tan\theta\cdot(h_f)^5\cdot(V_f)^4\cdot(1-V_f)\cdot(r_P)^6}{27\cdot\left[r_f\cdot\left((h_0 - x\cdot\tan\theta) - h_f\cdot V_f\right)\right]^6} \quad (7)$$

where η is the polymer matrix viscosity, dependent on the temperature and shear rate (Pa.s), θ – angle of the convergent channel (°), h_f – final material thickness (m), V_f – final fiber volume fraction of the profile, h_0 – initial thickness of the towpreg at the entrance of the convergent channel (m), r_p – polymer particle radius (m), r_f – fiber radius (m), and x – distance to the convergent channel entrance (m).

Equation (7) shows that the pressure build-up in the convergent zone depends on the processing conditions (pulling speed), tool design (angle of the convergent channel, initial and final thickness), and towpreg characteristics (matrix viscosity, fiber volume fraction of the consolidated profile, polymer particle size and fiber radius).

Finally, a 45 mm long third zone allows the stabilization of the cross-section desired in the pultruded profile.

For heating the pressurization-consolidation die up to 300 °C within *ca.* 15 min, a power of 2 kW is required; ten 200 W heating cartridges were mounted in the die, five in each (upper and lower) side. The cooling die was designed at an overall length of 200 mm, with constant cross-section over its total length to

guarantee the maintenance of the final required dimensions of the pultruded profile during cooling. Cooling channels of 10 mm diameter were drilled in the die to allow uniform cooling, using water as the coolant fluid.

4.4 Filament Winding

4.4.1 Process Description

Figure 13 depicts schematically the filament winding system developed to produce GF/PP pipes and plates from towpregs and PCTs. This system was mounted on a laboratory CNC 6-axes conventional PULTREX filament winding machine. The equipment consists of a preheating furnace, a hot-air heater, and a pneumatically controlled consolidation roll.

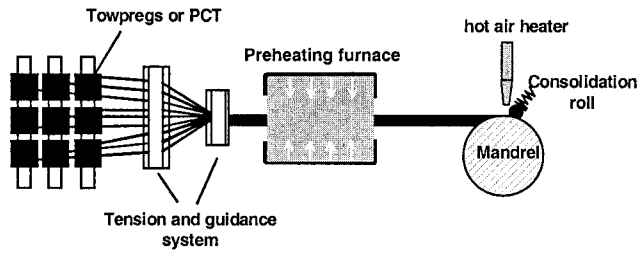

Figure 13. Schematic representation of the filament winding system.

Before being wound onto the mandrel, the towpregs or PCTs are guided, at a controlled and constant tension, through the preheating furnace at the desired temperature.[13] The final consolidation is achieved on the mandrel, at a required pressure, using a consolidation head consisting of a pneumatic force-controlled steel roll (diameter 30 mm), assisted by a hot-air heater. A type-J thermocouple allows the temperature to be adjusted during the consolidation. The machine program was specially designed to maintain the linear feeding speed constant and, therefore, to carry out the consolidation always under the same conditions.

4.4.2 Processing Conditions

GF/PP pipes with dimensions of $\varnothing 80 \times 2$ (mm) were produced from the two semi-products using the typical filament winding conditions shown in Table 5. The use of PCTs allows a 6-fold increase of the rotational speed, compared to that used in the production of towpregs (from 5 to 30 rpm), *i.e.*, much higher production rates are achieved. As stated before, this was the reason for the production of PCTs.

Table 5. Typical filament winding operating conditions.

Variable		*Unit*	*Value*
Mandrel rotational speed	Towpregs PCTs	rpm	5 30
Temperature	Preheating Air heater	°C	200–300–350
Consolidation force	–	N	80–100
Tow tension	–	N	10

The filament winding technology developed with thermoplastic towpregs and PCTs has already been transferred to a Portuguese composite manufacturer (Vidropol, SA). In this case, the system was adapted to a conventional 2-axes filament winding machine previously used to manufacture thermosetting composite pipes and vessels. With this system, encouraging preliminary results were obtained in the production of 100 mm diameter pipes from 15 tows, corresponding to a band width of 55 mm.

4.4.3 Relationships Between Final Properties and Processing Conditions

Different mandrel rotational speeds, consolidation pressures, and preheating and consolidation temperatures were used to manufacture pipes from towpregs and to verify the influence of these processing parameters on the mechanical properties. The circumferential tensile strength of the pipes was tested in an Instron 4505 machine using the split disk test method according to ASTM 2290 at a crosshead speed of 1 mm/min.

The circumferential tensile strength is strongly dependent on the fiber content. Therefore, to compare and normalize the results, the experimental data were divided by the average percentage of the specimen fiber mass fraction, determined from burn-off tests according to EN 60. These results are summarized in Figures 14 and 15 for pipes produced at a constant pulling tension of 10 N in each tow. The data in Figure 14 were obtained at constant consolidation temperature and pressure of 300 °C and 200 kPa, respectively. In Figure 15, these variables were increased to 360 °C and 500 kPa, respectively, to allow the use of lower preheating temperatures and to avoid polymer degradation.

The strength of the pipes preheated at 260 °C (Figure 14) is much lower because the consolidation is incomplete. For each preheating temperature, a processing window seems to exist in which maximum strength can be achieved. The strength decrease at lower rotational speeds is probably due to polymer degradation resulting from the longer stay in the preheating furnace. The lower

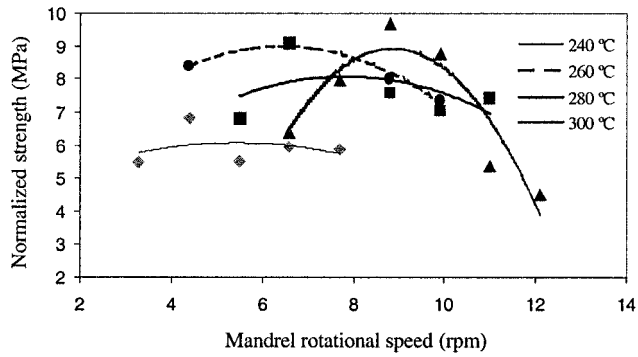

Figure 14. Influence of mandrel rotational speed on pipe strength for various preheating temperatures (tow tension = 10 N; consolidation temp. = 300 °C; consolidation pressure = 200 kPa).

strength values obtained at the higher rotational speeds are related to insufficient consolidation time. It may be concluded that the efficient preheating temperatures are in the range of 260–280 °C. Using such temperatures, the rotational speeds can be varied in a quite broad range, leading to fairly good mechanical properties. In fact, increasing the preheating temperature to 300 °C leads to a much narrower processing window.

Figure 15 shows that the rise in consolidation temperature and pressure allows a slight decrease of the preheating temperature, *i.e.*, the risk of polymer degradation also decreases. However, as the material stays very briefly under the consolidation roll, the consolidation temperature and pressure have much less influence on the pipe mechanical properties than the preheating temperature. It can be concluded that preheating temperatures in the range of 240–260 °C lead to the best combination of pipe strength and production rate.

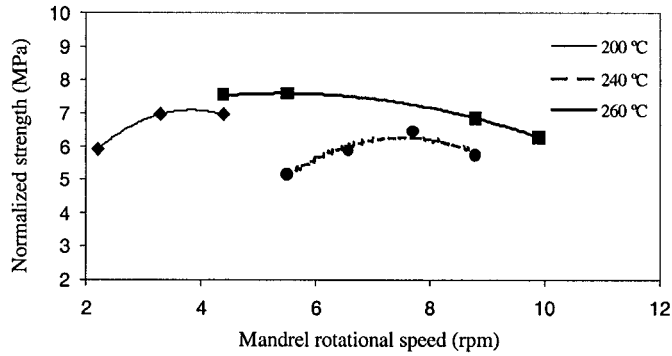

Figure 15. Influence of mandrel rotational speed on pipe strength for various preheating temperatures (tow tension = 10 N; consolidation temp. = 360 °C; consolidation pressure = 500 kPa).

4.5 Long Fiber-Reinforced Composite Stamping

4.5.1 Process Description

A novel, cost-efficient technology was developed to produce LFTs from towpregs in a patented piston-blender (specifically developed to promote melting while maintaining fiber length).[23,24] The towpregs are chopped to the desired length and mixed to the desired level with polymer material in the piston-blender. In this technology, the traditional concept of using an extrusion screw is replaced by a simple mechanism of rotating heated rods. The very low shear induced on the melt limits fiber breakage to a minimum. Due to its simple construction, the cost of the machine is much lower than those of other available LFT-extruders and offers the possibility of making LFTs with minor investments.

The LFTs and polymer powder are fed to the hopper and the heated rods then rotate to mix the material. At the same time, the cylinder wall (heated electrically from the outside) melts the material. Then a piston ejects the mixture that is cut by a cutting device and the material is ready for compression molding. By adding various amounts of virgin PP powder into the hopper, composites with varying fiber content can be obtained.

4.5.2 Processing Conditions

The GF/PP towpregs were melted in the piston-blender and compression molded to 300×300×4 mm plates under the processing conditions given in Table 6.

Table 6. LFTs compression molding processing conditions.

Variable	*Unit*	*Value*
Melt temperature	°C	220
Pressure	MPa	10
Compression time	s	30
Mold temperature	°C	85

5 Composite Properties

Due to their different nature and mechanical behavior, continuous and discontinuous fiber-reinforced composites are discussed separately in this section.

5.1 Mechanical Properties of Continuous Fiber-Reinforced Composites

The fiber mass fraction, and the flexural and tensile properties of the continuous fiber-reinforced composites produced by various techniques were determined according to ISO 1172, ISO 178, and EN 60, respectively. The split disk test method according to ASTM 2290 was employed to determine the circumferential strength and modulus of the pipes produced by filament winding.

The respective average values (AV) and their standard deviations (SD) are summarized in Table 7. The experimental results are also compared with those theoretically predicted in the composite fiber direction, using the rule of mixing (ROM), from the properties already determined for the fibers and the polymer.[5]

The composite theoretical strengths were determined by using the mean and the standard deviation values calculated for the fiber strength at the appropriate fiber length from the Weibull distribution.[5] The values of the fiber volume fraction were measured experimentally.

Comparison of the experimental and theoretical data in Table 7 suggests that the compression molded composites have the lowest mechanical properties; however, they are still appropriate for major commercial applications. As already mentioned, the lower strength seems to originate from the large fiber misalignment associated to this processing technique. Much better results were obtained for the composites produced by pultrusion and filament winding, the latter technique leading to the best mechanical properties.

A major improvement over the previous results was obtained with compression molded composites, by enhancing the fiber-matrix adhesion; small quantities of a carboxylic-acid-anhydride-modified polypropylene, Licomont AR 504 (supplied by Clariant, Portugal), were added in the coating chamber during the production of the towpregs.[25] The results are summarized in Table 8.

The Licomont/PP-containing composites (Table 8) reveal better tensile properties than those made without additive. Also, the flexural moduli and strengths are higher by a factor of 2.3 to 2.6 than those of composites with unmodified PP. In addition, the moduli are now in good agreement with the theoretically expected results. Furthermore, increases in the ease of processing as well as in fiber wettability and impregnation were observed.[25]

5.2 Mechanical Properties of Discontinuous Fiber-Reinforced Composites

Flexural test specimens (25 × 80 mm, 10 samples for each series) taken from the LFT-plates were tested according to ISO 178 at a crosshead speed of 2 mm/min. The fiber content was determined using density and matrix burn-off measurements.

Table 7. Mechanical properties determined for continuous fiber-reinforced composites.

Production technique	*Value*	*Properties*											
		Tensile strength (MPa)		*Tensile modulus (GPa)*		*Flexural strength (MPa)*		*Flexural modulus (GPa)*		*Fiber mass fraction (%)*		*Fiber volume fraction (%)*	
		AV	*SD*	*AV*	*SD*	*AV*	*SD*	*AV*	*SD*	*AV*	*SD*	*AV*	*SD*
Compression molding	Experimental	187.8	12.1	34.1	50.8	66.3	9.4	24.7	2.6	85.6	1.6	67.3	2.9
	Theoretical	789.1	260	42.4	8.8	789	260	42.4	8.8				
Pultrusion	Experimental	305	26	29.9	3.5	>117	4.3	22.5	0.3	78.4	1.4	56.2	2.8
	Theoretical	661.6	219	35.6	7.4	661.6	219	35.6	7.4				
Filament winding	Experimental	431.0	37.6	31.0	2.8	-	-	-	-	80.2	1.5	59.0	2.8
	Theoretical	693.7	229	37.3	7.7	-	-	-	-				

Table 8. Effect of the Licomont additive on the composite mechanical properties.

Property		*Unit*	*Determined values*							
			Pure PP		*Licomont/PP blends*					
					*0.5 phr**		*1.0 phr**		*2.5 phr**	
			AV	*SD*	*AV*	*SD*	*AV*	*SD*	*AV*	*SD*
Tensile strength	Exp.	MPa	187.8	12.1	–	–	–	–	–	–
	Theo.		789	80						
Tensile modulus	Exp.	GPa	34.1	5.8	35.9	8.3	45.6	4.6	38.1	5.7
	Theo.		42.1	8.8	38.6	9.5	42.2	8.8	41.3	8.6
Flexural strength	Exp.	MPa	66.3	9.4	164.1	17.8	155.6	26.0	156.1	30.1
Flexural modulus	Exp.	GPa	24.7	2.6	63.4	6.1	65.5	9.0	66.5	7.9
Fiber fraction	Mass	%	85.6	1.6	82.0	1.5	85.4	1.2	84.5	1.3
	Vol.	%	67.3	2.9	61.8	2.4	67.5	2.1	66.0	2.2

* Parts per hundred resin

Discontinuous fiber composites, like LFTs, have wide ranges of fiber lengths and broad fiber orientation distributions that significantly complicate the modeling of the properties. The purely analytical model proposed by Tandon and Weng[26] was used to obtain stiffness expressions from fiber and matrix data. Similar expressions, based on the well known Kelly-Tyson theory for the unidirectional strength of composites,[27] were derived to calculate the strength. The different fiber lengths were taken into account by simply substituting the average fiber lengths. From the several engineering constants thus obtained, the compliance and strength tensors were constructed and subsequently "orientation averaged" by the use of different fiber orientation tensors to account for orientation effects.[28,29]

Figure 16 shows experimental flexural data (modulus and strength *vs.* fiber volume fraction, at a constant fiber length of 25 mm), as well as theoretical results obtained as described above. For the sake of comparison, values obtained earlier with a different PP-based LFT material processed in the same way,[23] as well as data-sheet values of commercially available GMT (Azdel) and LFT (LNP-Verton), are also shown. The experimental values were obtained with the material properties presented in Table 1.

In Figure 16a, it is seen that the experimental modulus values are comparable to those obtained previously with the other LFTs[23] and to the data-sheet values of commercial GMT/LFTs. This indicates the feasibility of the present technology. The modulus values can be predicted quite well over the entire range of fiber volume fractions using the Tandon-Weng theory and assuming a random 2D fiber orientation distribution (solid line). It is interesting to note that the modified ROM, assuming random in-plane fiber orientation,[30] which is also plotted in the figure,

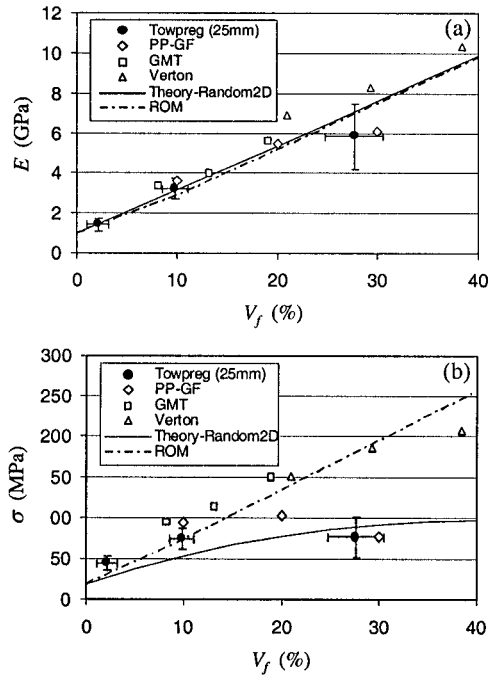

Figure 16. Theoretical and experimental dependences of the flexural properties on the fiber content: (a) modulus, (b) strength.

predicts modulus values close to all data. This shows that the modified ROM can be a useful tool to quickly predict, with a reasonable accuracy, the modulus of LFT composites.

Figure 16b shows that the experimental strength increases initially with fiber content until a limit is reached at higher fiber fractions, in agreement with previous results for the LFT material. However, the data are lower than those of commercially available GMT/LFTs at $V_f \geq 25\%$. An increase in mechanical properties, especially strength, is expected when a modified PP is used in the present LFTs in order to improve the fiber-matrix adhesion (as in the case of continuous fiber-reinforced composites). The strength model, assuming a random 2D fiber orientation distribution, leads to much lower values, although the non-linear dependence of the composite strength on the fiber fraction is predicted quite well. The ROM approach also gives inaccurate strength data predictions.

Finally, the results of the flexural tests as a function of the fiber length (at a constant fiber volume fraction) are given in Figure 17. It is seen that both modulus and strength decrease slightly when the length increases, but this effect is negligible, considering the reproducibility of the V_f data of the different samples.[31] These quasi-constant values can be explained by the fact that fiber lengths are above the critical value required for the obtaining of almost "continuous fiber" properties.[32]

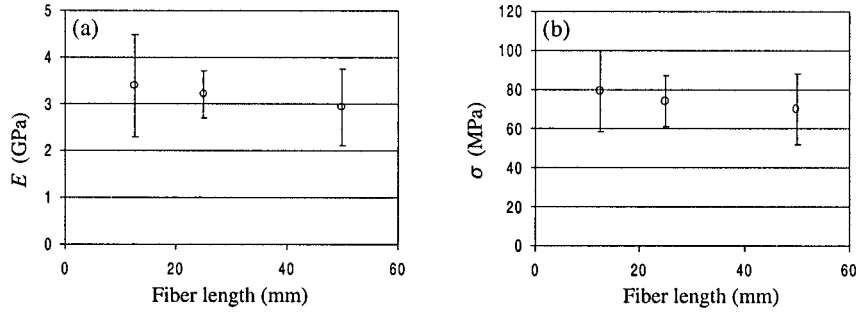

Figure 17. Dependence of the flexural properties on the fiber length: (a) modulus, (b) strength.

6 Conclusions

In the research program described here, new technological solutions, as well as the corresponding equipments, were developed to produce cost-effective long-fiber thermoplastic matrix semi-products and to process them into structural composites. It was possible to optimize the production conditions in order to achieve maximum mechanical properties of the composites. These properties are appropriate for structural applications and are superior to those of common engineering materials. On the basis of the results obtained, some of these technological solutions have already been implemented in an industrial environment. The program also demonstrated the large potential of the polymer powder deposition techniques to produce long-fiber thermoplastic matrix materials, especially towpregs, which can be easily processed into composites with adequate engineering properties.

7 Acknowledgements

The authors would like to thank the Centre of Lightweight Structures TUD-TNO, Delft, the Netherlands, for kindly allowing the use of their piston-blender and other equipment and the stay of one of them (FvH) on their site. The present project was carried out with partial funding of the Foundation for Science and Technology through the POCTI programme. The contribution of the Luso-American Foundation for Development to the mobility of the authors is also acknowledged. A research program like this one necessarily takes many years to accomplish and involves the collaboration of many people, post-graduation students, post-doctorates, and technicians, which is impractical to name personally. To these people, collectively, the authors wish to express their deep gratitude.

Gratitude is also due to Prof. Dan D. Edie, of Clemson University, SC, USA, who was the first to demonstrate to us the potential of the towpregs technology.

8 References

[1] J. Brandt, K. Drechsler, H. Richter (1993) The use of high-performance thermoplastic composites for structural aerospace applications, *Proc. 9th Int. Conf. Composite Materials – ICCM 9* (Ed. A. Miravete) Woodhead Publishing Ltd, Madrid, Vol. 6, p. 143.

[2] W. Malcolm, E. Todd (1993) Carbon fiber reinforced PPS thermoplastic materials implemented in cost sensitive commercial applications, *38th Int. SAMPE Symposium*, USA, p. 2055.

[3] J. P. Nunes, J. F. Silva, L. Silva, A. T. Marques, P. J. Novo (2000) The development of a dry coating process to produce glass reinforced thermoplastic matrix towpregs, *Proc. 9th European Conf. Composite Materials ECCM-9*, Brighton.

[4] J. P. Nunes, J. F. Silva, L. Silva, P. J. Novo, A. T. Marques (2002) Equipment to produce continuously powder coated thermoplastic matrix prepregs (towpregs), Int. Patent WO 02/06027, to University of Minho & National Institute of Engineering and Industrial Management.

[5] J. P. Nunes, J. F. Silva, A. T. Marques, N. Crainic, S. Cabral-Fonseca (2003) Production of powder coated towpregs and composites, *J. Thermopl. Compos. Mater.* **16**, 231.

[6] J. N. Mota, J. P. Nunes, A. S. Pouzada (2000) Production of profiles from thermoplastic matrix towpregs, *Proc. ANTEC'2000*, Orlando, USA.

[7] J. P. Nunes, J. F. Silva, P. J. Novo, A. T. Marques, A. S. Pouzada (2001) Production of structures from thermoplastic matrix towpregs, *Proc. ANTEC'2001*, Dallas, USA.

[8] J. P. Nunes, J. F. Silva, N. Crainic, A. T. Marques (2001) Technological developments to produce low-cost thermoplastic reinforced composites by filament winding, *Proc. 7th European Conf. Advanced Materials and Processes-EUROMAT'2001*, Rimini, Italy.

[9] J. P. Nunes, J. F. Silva, N. Crainic, P. Vieira, D. Rosin, A. T. Marques (2001) Filament wound pipes made with thermoplastic towpregs and coated tapes, *8th Int. Conf. Composites Engineering ICCE-8*, Tenerife, Spain.

[10] J. P. Nunes, J. F. Silva, P. Vieira, A. T. Marques (2002) Advances on filament winding technology to produce composites from thermoplastic towpregs and coated tapes, *Proc. ANTEC'2002*, San Francisco, USA.

[11] J. P. Nunes, J. F. Silva, M. J. Oliveira, A. T. Marques (2002) The influence of processing conditions in the production of glass reinforced thermoplastic matrix towpregs, *Proc. 10th European Conf. Composite Materials ECCM-10*, Belgium.

[12] J. P. Nunes, J. F. Silva, F. W. J. van Hattum, C. A. Bernardo (2002) Composite engineering structures from thermoplastic matrix towpregs, *Key-Note to the 18th World Conf. Polymer Processing Society – PPS 18*, Guimarães, Portugal.

[13] J. P. Nunes, J. F. Silva, P. Vieira, A. T. Marques (2002) Implementation of an industrial process to produce filament wound composites from thermoplastic towpregs and coated tapes, *Proc. 8th World Conf. Polymer Processing Society – PPS 18*, Guimarães, Portugal.

[14] J. W. Klett, J. Albiger, D. D. Edie, G. C. Lickfield (1992) Production and evaluation of a polyimide/carbon fiber powder-coated towpreg, *Proc. 7th Int. Conf. Carbon-Carbon'92*, Essen, Germany, p. 683.

[15] J. P. Nunes, C. A. Bernardo, A. S. Pouzada, D. D. Edie (1999) Modelling of the consolidation of polycarbonate/carbon fiber towpregs, *Polym. Compos.* **20**, 260.

[16] J. P. Nunes, A. M. Brito, A. S. Pouzada, C. A. Bernardo (2001) Non-isothermal consolidation of carbon fiber towpregs and composites, *Polym. Compos.* **22**, 71.

[17] J. P. Nunes (1998) A study of the processing and properties of sheet moulding compounds and unidirectional carbon fiber towpregs, PhD Thesis, University of Minho, Portugal.

[18] T. G. Gutowski, Z. Cai, S. Bauer, D. Boucher, J. Kingery, S. Wineman (1987) Consolidation experiments for laminate composites, *J. Compos. Mater.* **21**, 650.

[19] B. T. Astrom, P. H. Larsson, R. B. Pipes (1991) Development of a facility for pultrusion of thermoplastic-matrix composites, *Compos. Manuf.* **2**, 114.

[20] B. T. Astrom (1992) Development and application of a process model for thermoplastic pultrusion, *Compos. Manuf.* **3**, 189.

[21] B. T. Astrom, R. B. Pipes (1993) A modeling approach to thermoplastic pultrusion I: formulation of models, *Polym. Compos.* **14**, 173.

[22] B. T. Astrom, R. B. Pipes (1993) A modeling approach to thermoplastic pultrusion II: verification of models, *Polym. Compos.* **14**, 184.

[23] F. W. J. van Hattum, J. H. van Breugel (2001) Innovative processing and properties of long fiber reinforced thermoplastics. *Proc. 22nd SAMPE Europe Int. Conf.*, Paris, France, p. 207.

[24] A. Beukers, J. H. van Breugel, F. J. Wiltink (2000) Device and method for the preparation of a mixture comprising of fiber-reinforced thermoplastic pellets, Int. Patent WO 00/02718.

[25] J. P. Nunes, J. F. Silva, F. W. J. van Hattum, C. A. Bernardo, A. T. Marques (2003) Improving low-cost continuous fiber thermoplastic composites by tailoring fiber-matrix adhesion, *Proc. Int. Workshop on Thermoplastic Matrix Composites 2003*, Gallipoli, Italy, paper 26.

[26] G. P. Tandon, G. J. Weng (1984) The effect of aspect ratio of inclusions on the elastic properties of unidirectionally aligned composites, *Polym. Compos.* **5**, 327.

[27] A. Kelly, W. R. Tyson (1965) Tensile properties of fiber-reinforced metals: copper/tungsten and copper molybdenum, *J. Mech. Phys. Solids* **13**, 329.

[28] F. W. J. van Hattum, C. A. Bernardo (1999). A model to predict the strength of short fiber composites, *Polym. Compos.* **20**, 524.

[29] S. G. Advani, C. L. Tucker III (1987) The use of tensors to describe and predict fiber orientation in short fiber composites, *J. Rheology* **31**, 751.

[30] L. E. Nielsen (1974) *Mechanical Properties of Polymers and Composites*, Marcel Dekker, Vol. 2, p. 462.

[31] F. W. J. van Hattum, J. P. Nunes, C. A. Bernardo (2004) A theoretical and experimental study of the production of towpreg-based long fiber thermoplastic composites, *Composites Part A*, in press.

[32] W. Schijve (2002) Properties of long glass fiber polypropylene composites with varying length distributions, *Proc. 10th European Conf. Composite Materials – ECCM-10*, Brugge, Belgium.

Chapter 12

Manufacturing of Tailored Reinforcement for Liquid Composite Molding Processes

Peter Mitschang, Amol Ogale
Institute for Composite Materials Ltd., University of Kaiserslautern, Kaiserslautern, Germany

1 Introduction

The sewn textile preform technology is known to be a suitable engineering method to generate various fiber-reinforced polymer composites (FRPCs) based on liquid composite molding (LCM).[1] To manufacture a complex dry preform structure, there should be a specific preform process flow, which consists of several intermediate manufacturing steps. Thus, the stitching process used for preforming has a large potential for the automation and rapid processing.[2,3]

The adequate use of the available textile resources is one of the greatest advantages of preform manufacturing. Different textiles, *e.g.*, woven fabrics, knitted fabrics, non-crimp fabrics (NCFs), *etc.*, can be sewn into one preform assembly. Even the fabrics with tailored fiber placement (TFP)[4] are brought into the main structural assembly by means of the sewing technology. The process of bringing all the different textile material types into one structural assembly is called *multi-textile preforming*. This technology plays a vital role in introducing special materials at the exact load-carrying positions. For instance, a low cost FRPC product can be manufactured by using a glass fiber reinforcement, but at the quite critical zones, where the material performance needs to be very high, it is possible to use a small but adequate amount of carbon fibers by means of the stitching technology. Because of the debonding resistance capacity of sewn structures,[5] sewing processes are also used as a joining technology for load bearing metallic elements incorporated into the dry preform structure.

To innovate the applications of sewing, the stitching process itself and the seams or stitches have been classified. The definition of the various classes of seams focused on the demands imposed on the seams themselves (Figure 1).[6]

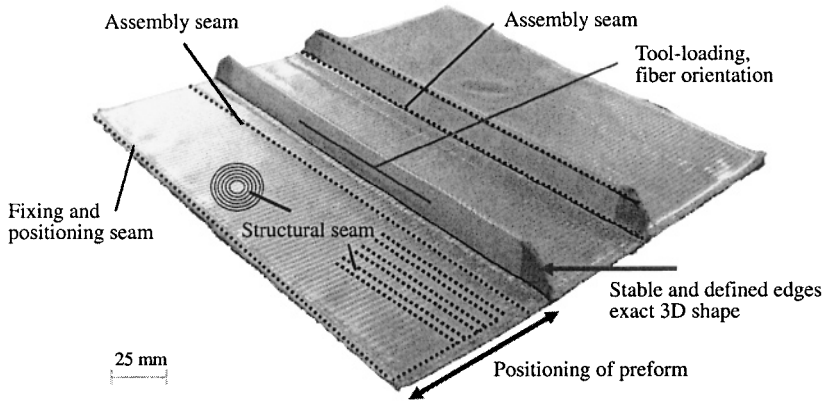

Figure 1. Seam types.[7]

Fixing and positioning seam. For manufacturing multi-textile sub-preforms, different layers of textile fabrics can be fixed and positioned according to the structural requirement of the composite component. Standard polyester threads with further epoxy-compatible treatment can be used for sewing purposes. Overlock seam and the sew-cut technology are used for making 2D sub-preforms.

Structural seams. The purpose of this seam type is to stitch the elements, which transmit the forces between various semi-finished goods or layers *via* tailored reinforcements (*e.g.*, ribs on support structures). These seams can also be used for positioning inserts or to enhance connections of inserts to the entire structure. Joining seams penetrate through the complete preform and are stitched by using threads made of carbon or glass fibers.

Assembly seam. Seams of this type are especially important for tool loading and the injection process. The sub-preforms can be assembled by using suitable types of threads,[7] which again assist the sewing operation. The preform assembly can either be two-dimensional or three-dimensional and the respective stitching parameters can be chosen to be different.

The requirements to the seams and preform structures define the usage of various stitch types. In general, chain stitches and lock stitches are well known in the garment as well as in the composite industry.[8,9,10] Also, one-sided stitches (OSS®),[11,12] blind stitches,[13] and tufting[14] can be helpful in 3D preform assembling. The modified lock stitch is advantageous in most of the stitching operations.

The differing functions of the seams require individually adaptable stitching parameters. Those are further differentiated into macro-stitching parameters, *e.g.*, stitch length, stitch density, *etc.*, and technology-driven stitching parameters, *e.g.*,

thread tension and pressure-foot height. Various stitching technologies offer different possibilities for the production of in-the-plain preparatory elements, as well as the 3D preform assembly.[15] In recent years, the LCM process and the use of process-compatible preforms are widely accepted in the composite industry. The strong interconnection between preforms and resin transfer molding brings the production of preforms to a top position. A new process chain of preform manufacturing, having FRPC as a final goal, is an introductory target. Figure 2 explains the process flow of the net-shape component manufacturing.

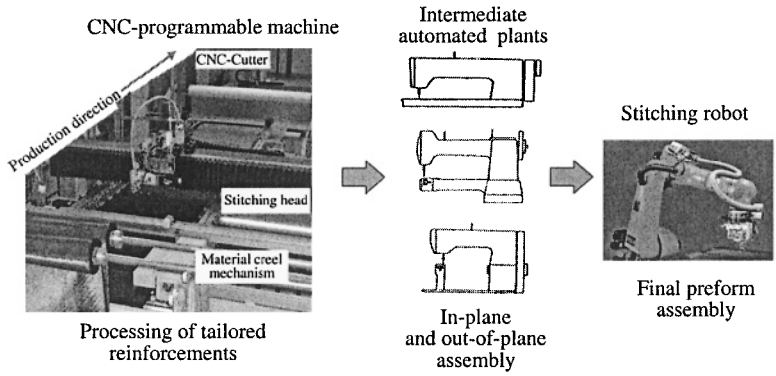

Figure 2. Steps in preform manufacturing.

2 Pre-selection of Sewing Thread

To specify the threads for FRPC manufacturing, it is obligatory to know the thread behavior throughout the process (from material lay-up to FRPC formation) and the impact of the selected thread on the quality of the finished product. Thus, the pre-selection of a thread for a specific sewing operation is a must.

For manufacturing a sewing thread, a continuous strand of textile fibers (yarn) is needed, which is then plied, twisted, and finished in subsequent processes according to the respective requirements. Sewing threads used in the life science or fashion are made of polymeric materials, such as polyester and polyamide, and the high performance threads are made of glass, carbon, or aramid fibers. Table 1 shows the classification of yarns for the manufacturing of sewing threads.

2.1 Selection Criteria

In the case of FRPCs, some requirements to a thread are: (i) compatibility with the resin system; effects on the thermal behavior of the resin in the components

Table 1. Yarn classification for sewing threads.

Yarn type	*Linear density (Tex)*	*Description*	*Mechanical properties*		*Suitable yarns for preform stitching*
			Strength (cN)	*Elongation (%)*	
Spun yarn	21-120	Made from short or long fibers with twist level around 400 turns/m	~750	18-25	As needle and bobbin thread
Twisted multi-filaments	16- 400	10-50 filaments, twisted ~150 turns/m (each filament 1-4 Tex), (filament diameter: PES - 13-30 μm, Nylon - 17-38 μm)	~ 1250	23-30	As needle and bobbin thread
Mono-filament	8-80	Single untwisted filament, thicker and stiffer than normal (100-500 μm in diameter)	~ 550	15-25	As bobbin thread
Textured yarn	8-105	Bulky, with inherent high elongation, tangled/looped filament orientation	~ 500	27-35	As needle and bobbin thread
Core spun yarn	18 - 135	Filament core, staple fiber sheath, high performance thread	~ 550	15-25	As needle and bobbin thread

are inadmissible, (ii) micro-impregnation should be possible; no voids inside the threads are allowed, (iii) flexibility or elongation should be high, resulting in little defects in the reinforcing structure, (iv) compatibility with the processing is required to prevent the release of gases from the thread into the FRPC, (v) in case of vacuum-assisted resin transfer molding (RTM) processes, the behavior of lubricated (finished) threads in vacuum has to be examined, (vi) automation of the sewing machines must be secured, and (vii) the thread diameter should be as low as possible.

Other various aspects of preform manufacturing should be considered for the achievement of excellent results. For instance, optically brightened threads are helpful where the seams are detected by using black light (on the automatic cutting machine). Table 2 lists the thread materials useable in the FRP preform manufacture; they are used to generate different seams, which again influence the preform in different ways. The selection must be done by considering the preforming purpose. For instance, for through-the-thickness reinforcement, it is necessary to apply load-carrying threads, such as glass- or carbon fiber-based sewing threads.

Table 2. Preform seam types and material options.

Seam type / *Material options*	*Fixing/positioning seam*	*Assembly seam*	*Structural seam (joining seam)*
Polyester	++	++	–
Glass fiber	+	+	+
Aramid	–	+	+
Carbon	–	–	+

Performance: ++ well suited; + suited; – not suited

2.2 Polyester Thread in Global Preform Sewing

During the selection of a textile yarn for manufacturing a sewing thread, all the existing and proposed properties of this yarn should be taken into consideration.[16] The thread parameters do not only influence the FRP properties; they also affect the productivity of the preforming process. In some cases, these controversial tendencies have to be balanced. Figure 3 describes the thread selection factors, such as possible machine speed limits for various threads, relative thread stiffness, and range of formed irregularities (ellipse-like, resin-rich regions) in the FRP.

In the overall preform manufacturing concept, the fixing and positioning seams, and the assembly seams have a tremendous contribution. The sewing operation should be performed at a very high speed with secured quality and at

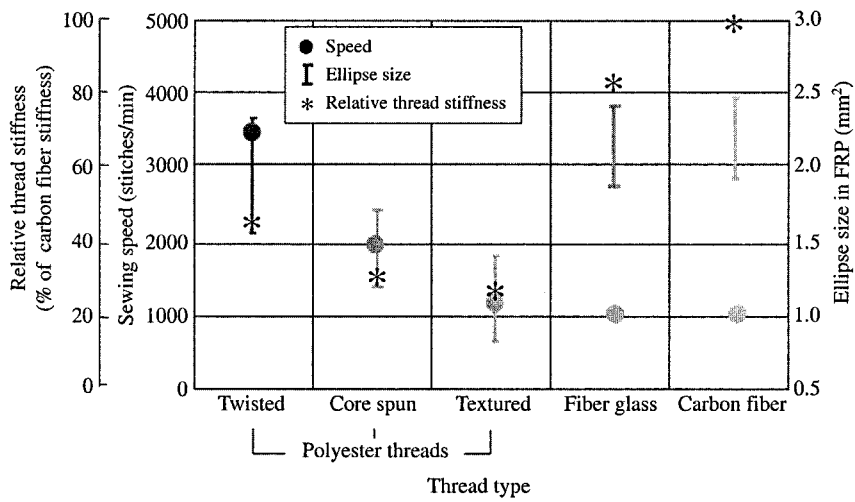

Figure 3. Thread selection factors: working speed, relative thread stiffness, and formed ellipse.

low process cost. Figure 3 shows the advantages of polyester threads over the glass and carbon threads. As far as polyester sewing threads are concerned, there are a variety of types available on the market, which are normally used in the garment industry. They are available in the range from highly extensible textured threads to rigid and thick plied threads and their usage depends on the specific preform manufacturing.

3 Tailored Reinforcements

The most important innovation is the introduction of a preparatory production step, called *tailored reinforcement* (TR). All of the required elements are integrated into the preform by means of a special stitching type, *e.g.*, structural 3D or TT (through the thickness) reinforcement, load-bearing elements, *etc.*[17]

The preparatory step deals with the standard textile, followed by the separation of the "tailored" intermediates or semi-finished products within the cutting process. This TR now assumes special characteristics that influence the subsequent process steps. Thus, each preform quality within the preform assembly steps should lead to different solutions. Therefore, the liquid composite molding quality depends on several preform parameters.

When the stitching process is introduced to produce "net-shape" preforms, their potential of automation should be considered. Typical problems of the sewing machine, such as first-stitch problems and missing stitches, should be solved. These problems are more or less the same for each single stitching type (double lock stitch, chain stitch, blind stitch, OSS®). Depending on the function of the seam, one missing stitch in the preform causes problems, such as edge-fraying, and thus difficulties in the tool loading.

Concerning the fibrous reinforcements for the FRPCs, the quality requirements are set to be high compared to the traditional sewing applications. Problems, such as thread rupture or varying thread tension, should be controlled over longer sewing distances. Although the stitching process is automated, problems can still occur because of static charge generation in the thread during stitching. The control over the stitching parameters, *e.g.*, the measurement of the thread tension, detects defective stitches. Some problems, *e.g.*, a thread is not being interlooped or a thread breaks, cause defective stitches. In addition to the technical possibilities of recognizing the thread breakage and re-positioning of the stitching head on the automatic CNC sewing machine, FRPC relevant consequences should also be considered. The re-start of stitching after a thread breakage has to be valued differently for FRPC applications. In this context, there is much more scope for automation of the sewing machine.

Because of the high fiber manufacturing costs, the consideration of fiber types, their interlaminates, and the consequences within the subsequent process

steps of preforming due to the stitching parameters, is an essential recourse to a quality management system. Based on the thread tension control and the compression brought into the structure *via* the presser-foot, which is attached to the special stitching paths, an on-line control can now be established.[18] The fixation of the acceptable machine tolerances can take place within the "preform engineering environment".

4 Stitching Parameters and Their Influence on the Fiber-Reinforced Polymer Composites

The significance of the stitching parameters to the preform quality becomes obvious when the following FRPC production process is discussed in parallel. Permeability, the most important parameter for the liquid infusion or injection is determined by the stitching parameters.[19] These parameters define the compression of the preform as well as the in-plane fiber displacement. For instance, the thread tension or presser-foot height are always selected by taking into account the thread construction and the lay-up of the structures to be sewn. In terms of preform quality, all these parameters need to be adjusted to the specifications of the preform given by the tool loading and injection process. As already mentioned, the lay-up of the textile with respect to the stitching direction also influences the entire process.

4.1 Machine Parameters

After considering the basic reinforcing material to be used and the thread material required for the preform stitching, the actual machine setting is a next step before starting the preform stitching. The sewing machine is a vital element which performs the preforming operations. The machine parameters are required to be set according to the type of preform application and the type of seam.[3] The basic machine parameters, such as applied thread tension, applied pre-compaction pressure on the lay-up, stitching pattern, program, and stitching velocity may influence the preforming operation. As far as the preform quality and the FRPC properties are concerned, the preform pre-compaction and the formation of a stable seam are essential. The sewing thread tension, the presser-foot pressure during the needle penetration, and the stitch pattern to be selected are of primary importance.

4.1.1 Thread Tension

The applied thread tension depends on the thread force being adjusted at the start of the stitching, so that knots are formed at the bottom of the laminate

(modified lock stitch, Figure 4). The thickness of the reinforcing fabric lay-up, sewing direction, and type of the material (woven, NCF, *etc.*) are the factors which govern the fluctuation of the thread tension. On-line thread tension monitoring

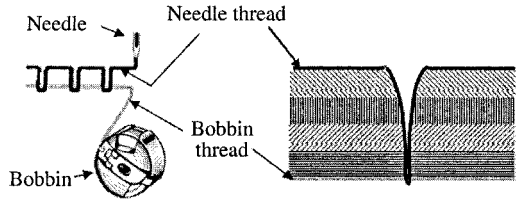

Figure 4. Modified lock stitch with upper and lower thread.[3]

and off-line tension measurement, before and after the preform stitching, improve the adjustment of the tension parameters. However, the final off-line preform quality must be checked after the data collection.

The thread tension set during the stitching assists to improve the compaction and fixation of the reinforcing fiber bundles. Figure 5 shows the compaction instrument which is developed at the Institute for Composite Materials Ltd., and

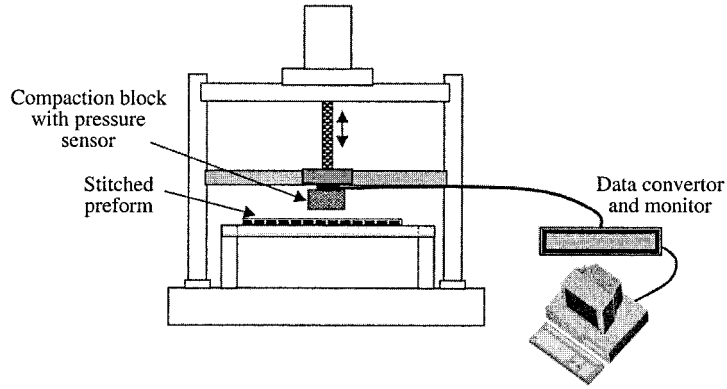

Figure 5. Compaction instrument.

used for off-line compaction measurement of the stitched preforms. Figure 6 shows the compression behavior of stitched and unstitched preforms and the corresponding maximum possible fiber volume fraction. Here, the influence of the thread tension on the preform compaction behavior is clearly visible. The stitched preforms are very well compacted. In this case, the porous compaction of the lay-up (pre-compaction due to presser-foot pressure and compaction due to thread tension) plays an important role.[20] After the initial application of the load, the sewn preforms

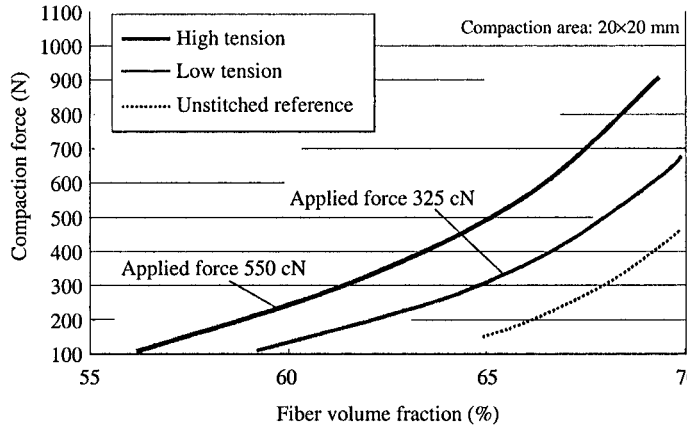

Figure 6. Influence of thread tension on the compaction behavior of a dry lay-up based on CF-woven 5H satin, $[0/90]_4$, polyester long fiber spun 73 tex, stitch length 2.5 mm, seam distance 40×40 mm, stitching direction ±45°, presser-foot height such that the foot rests on the dry lay-up.[18]

require lesser compaction force than the unstitched lay-up. With the progress of the compaction process, because of the presence of the seams, the localized displacement of the reinforcing fiber is obstructed and causes an increase in the compaction force. On the other hand, the unstitched lay-up is free to move and can result in a linear deformation of the reinforcing material.

4.1.2 Presser-Foot Pressure

During the stitching process, when the needle penetrates the fabric package and comes up, there is a slight vertical movement of the fabric package. To avoid this, the application of pressure at the needle penetration zone is a must. The presser-foot, a mechanical element, which itself has to be compatible with the FRPC process, is fixed at a certain height. This can be adjusted according to the fibrous material being used and the lay-up thickness. With the automated sewing units, this step can be done pneumatically. If the presser-foot is used as a measuring device, its on-line pressure can be analyzed. Consequently, deviations in the compression can be detected when the interlaminate characteristics change or when fiber packages are lacking within a fiber layer. If the variable thickness of the parts leads to stitching paths, the initial pressure has to be adjustable. The presser-foot pressure influences the pre-compaction and later the "bulk" material thickness. To obtain a high quality preform, the compression during the stitching process has to be interrelated with the parameters of the resin transfer molding process.

Figure 7 shows the compaction behavior of stitched and unstitched preforms, the corresponding maximum possible fiber volume fractions, and the

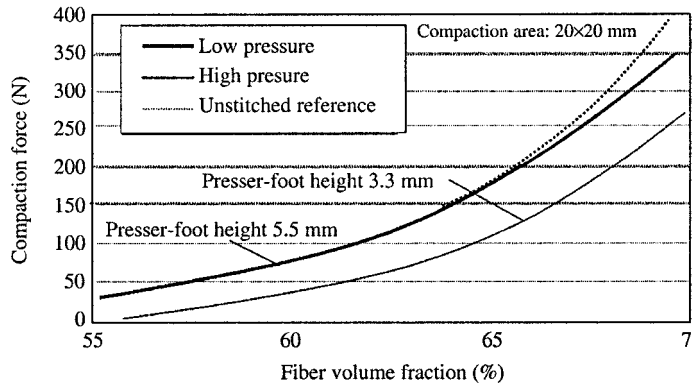

Figure 7. Influence of presser-foot height on the compaction behavior of a dry lay-up based on CF-woven 5H satin, $[0/90]_4$, polyester long fiber spun 73 tex, stitch length 2.5 mm, seam distance 40×40 mm, stitching direction ±45°, thread tension 400 cN.[18]

dependence of the compression upon the height of the presser-foot. The preform stitched at the high pressure (presser-foot height 3.3 mm) needs lower compaction force than that stitched at low pressure (presser-foot height 5.5 mm); in both tests, the thread tension was kept constant (400 cN). Due to the pre-compaction of the preform during stitching, the compaction force required at the initial stage is minimum in the case of stitched preforms and considerably higher in unstitched lay-ups.[18]

4.2 Stitching Pattern

The engineering aspects of the preform depend solely on the manufacturing techniques related to its ultimate use in the high performance FRPCs. The stitching pattern is one of the key points in the preform engineering. According to the requirements to the final product, preforms can be stitched in various patterns and geometries. The compaction of a preform, the fiber orientation factor, the preform permeability in the mold, the flexibility and drapability are factors influenced by the stitching pattern.

For different seam types, the stitch patterns should be different. The functionality of the seam can be organized by choosing a proper stitch pattern, *e.g.*, the fixing and positioning seam needs proper fixation of the lay-up with some compaction and locking of the reinforcing fibers. Thus, this type of seam has to be placed throughout the laminate surface with low stitch density. As far as a structural seam is concerned, the pattern should be generated with high stitch density. Thus, the stitches and the sewing thread itself can contribute to the mechanical properties of the laminate.

5 Quality Secured Preforming

The entire preform production technique and the finished ready-to-impregnate preform structure are not explored in detail. Thus, the concept of preform quality is at present in a developing stage. In general, a preform consists of a strand of arranged and locked fibers. This arrangement is then infused with the matrix (resin). The preparation of the preforms defines the usability of the package in the later manufacturing, *e.g.*, by the liquid molding process. Therefore, preform macro- and micro-characteristics have to be evaluated.

5.1 Macro-Preform Quality

The preform weight per unit area can be considered as one of the most important characteristic quality values. During the sewing process, a specific amount of threads is put into the fiber reinforcement. If it is not the purpose to increase the mechanical properties of the laminate in the thickness direction, the amount of fibers put into the arrangement is the dominating factor in terms of in-plane fiber movement. Thus, the thread has to be defined by taking into account these effects.

5.2 Micro-Preform Quality

The microscopic characteristics of the preform influence the quality of the part, as well as the production process. The parameters of the preforming process themselves (here, the stitching and the stitch formation) influence the permeability of the fibrous package and are, therefore, crucial in terms of the liquid infusion of the preform. The alternation of the thread tension within the stitching process can lead to a distraction of the fibers in the plain. The distraction causes gaps between the fiber packages and increases the preform permeability. These gaps, if not within the allowed and accepted tolerances, reduce the reproducibility of the LCM process and, consequently, lead to increased waste. Only matrix-compatible sizing of the sewing thread is allowed in order to reduce micro-defects in the product. Furthermore, it is mandatory not to lubricate the sewing machine (concept of oil-free machining).

During stitch formation, the needle interacts with the stitched substrates, the needle point penetrates the fibers, and meanwhile the needle shaft causes a "needle hole". The distraction of fiber packages is so far evaluated only in FRPC laminates (Figure 8). It is easy to evaluate either the dry preform surface or the FRPC laminate with respect to the stitched section.

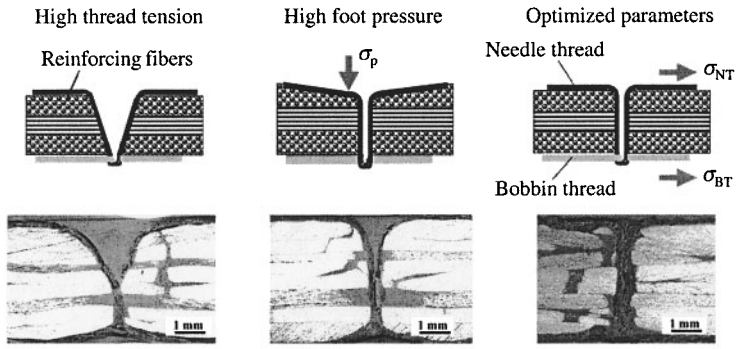

Figure 8. Influence of stitching parameters on the stitch geometry.[18]

5.3 Fiber Disturbance at Seams

The characterization of the fiber disturbance in the area of a needle hole can be performed based on the analysis of the various stitched preforms and FRPC laminates. To find out the critical elements in the stitching process (independent of seam, material layers, and the direction of stitch formation), the seam analysis is a must. The needle penetration causes the spreading of the fibrous package. This effect is dominated by the needle size. In the subsequent cycle of stitch formation, the penetrated needle comes out of the material and forms a stitch hole. Figure 9 describes the influence of a needle system on the intensity of formation of stitch holes at the dry preform stage. The interlacing is put on the upper side of

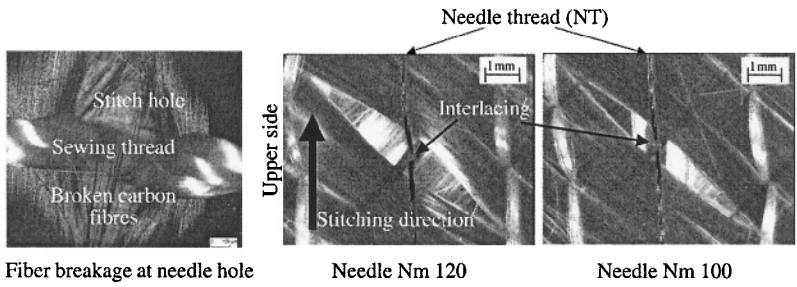

Figure 9. Fiber displacement around a lock stitch seam (left: fiber breakage at needle hole, right: influence of needle size on FRPC quality).[18]

the material to minimize the dynamic influence of the thread take-up and the acceleration spring, which helps to reduce the further widening of the stitch hole.

6 Liquid Composite Molding Process for Net-Shape Preforms

The net-shape preform manufacturing with a compact wall structure is an advantageous feature in terms of quick LCM processing. For closed-mold LCM, after placing the stitched 3D preforms inside the mold, the mold has to be closed without any further obstacles. The mold closure is very difficult if the preforms are of extra size. Net-shape preforms allow avoiding such inconvenience in the mold closing. The preform LCM process chain helps to correlate the preforming process with the LCM technique.

6.1 Preform LCM Process Chain

Quick placement of the preform into the mold, easy mounting, and fault-free single shot resin impregnation is an economical method of FRPC manufacturing. Preforms manufactured within the mold tolerances reduce the mold placement time and also avoid the possibility of resin channel formation. If the preform manufacturing is performed by keeping in mind the actual mold geometry and the tolerances, the next process tasks are easier and quicker than the conventional methods. Starting from the selection of textile material to the assembling of 2D preforms reduces the total molding time. As the preforms are cut to the exact shape, fiber trapping between the mold can be avoided, and there are limited difficulties in the mold closure.

Again, the inserts and other locally strengthening, toughening elements can be placed at the exact position and fixed by means of stitching. It takes less time to position these elements in the mold. Figure 10 shows the continuous chain

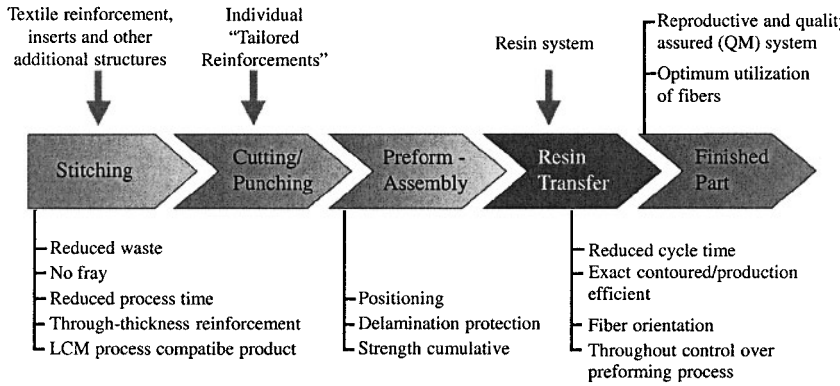

Figure 10. Preform liquid composite molding (LCM) process chain.[3]

from textile selection to the product manufacturing (3D preforms) with the required fiber orientation at different sections.

6.2 Thermal Behavior of Seam in FRPC

The FRP components may be subjected to considerably high temperatures, and it is essential to check the behavior of the threads at such temperatures, as well as in the resin. At the area of the stitch knot, a high amount of sewing thread is involved, so the thermal analysis of these small areas helps to check the actual thermal behavior of the thread inside the FRP laminate. Differential scanning calorimetry (DSC) tests of non-impregnated and impregnated threads in the FRP laminate reflect the heat sustention capacity of particular threads.

The polyester thread used for the tailored reinforcements should withstand the working temperature of the final product. Therefore, the micro-thermal behavior of a thread needs to be understood in detail. The glass transition temperature, T_g, of polyester threads is around 78 °C, which is much below the standard working temperature of most of the FRPC products. Fully impregnated threads do not show glass transition, *i.e.,* the occurrence of the next transition is at the crystallization temperature, T_c, which is again not visible in fully impregnated polyester threads. Thus, the sewn, completely matrix-bonded thread can withstand up to the melting temperature, T_m, of the polyester (260 °C).

7 Quality Management

The great variety of parameters and their dynamic changes during the stitching operation requires the introduction of an "on-line" quality management (QM)-tool. Following the TR-process, this QM-tool can be based on the "preform-engineering" environment (see below). Within this package, seam sections can be set with individual parameters that are then transferred into the preforming equipment. The integration of a thread tension controller offers the possibility of influencing the thread tensions *in situ*. For instance, when the software, which analyses the sensor signals during the stitching process, detects more than 10 stitches passing beyond the set range of the thread tension (Figure 11), the controller interface changes the thread tension. Tolerances for special stitching segments during the preforming operations are also defined during the preform-engineering. Figure 12 shows the usage of these tolerances within a later off-line control of the preform quality. However, an on-line regulation of the thread tension is also integrated. Thus, the waste rate of preforms is reduced. The documentation of the "actual state" compared to the "planned state" leads to a better knowledge of the

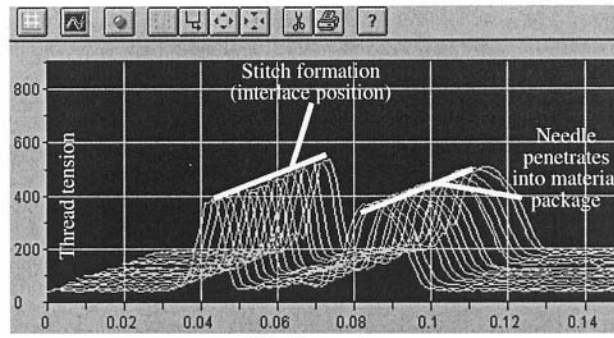

Figure 11. Thread tension: on-line data monitoring.

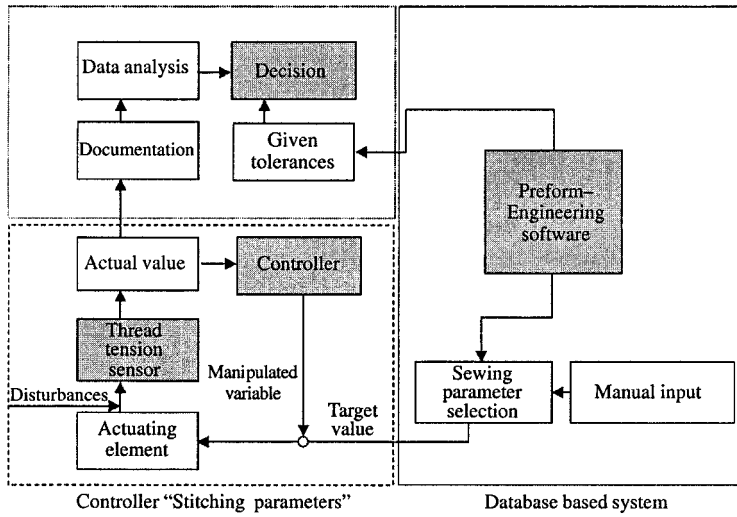

Figure 12. Thread tension control incorporated in a quality management (QM) tool for preform manufacturing.

preforming and LCM processes. The stitching parameters which are set for special stitching paths can be selected from a data bank system.

Addressing the reproducibility and quality of the stitched preforms, the complete process chain should be embedded in an engineering environment. This approach leads to a continuous transfer of data sets from the 3D design to the stitching data. Starting at the 3D model of a part, which must be designed according to the preforming manufacturing issues, 2D data sets need to be generated. Unwinding of 3D models is currently done using sheet-metal unwinding tools that are incorporated in commercial CAD software packages. These 2D data sets are then transferred to a new "preform engineering" software package *via* standardized interfaces. According to the newly developed "preform engineering" guidelines, the individual tailored reinforcements can be generated. During this step, the necessary seams are constructed in each reinforcement package. The attributes, *e.g.*, thread tension, of these seams are assigned.[6]

The different seam types require a machine specification that allows changes in the stitching parameters during the ongoing manufacturing process. Finally, the preform engineering allows the generation of the cutting path (including folding cuts) within the "tailored reinforcement". As shown in Figure 13, the stitched geometry, the cut preform, and the original shape of the needed part are different. The designed stitch path of a preform is then determined by the desired "shape" tolerance of the reinforcing member. These requirements lead to a certain stitching length, stitch density, *etc.* Assembly seams and structural seams have to be designed

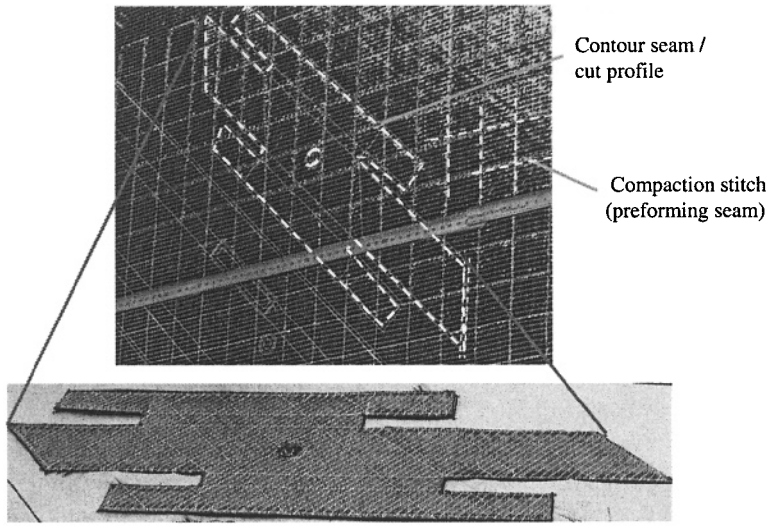

Figure 13: Example of tailored reinforcement (TR); sub-preform.

according to the guidelines set up by the processing requirements or mechanical properties.

8 Conclusions

By implementing tailored reinforcement processes, starting from dry fabric lay-up to the sew-cut-assembly, a ready to impregnate preform manufacturing can be targeted effectively. The concept of a continuous FRPC manufacturing process flow on the basis of "Engineered Tailored Reinforcements" has been developed. By keeping in mind that the proposed LCM forces act on the preform, "TRs" can be manufactured in a most advantageous way. The practice of preform manufacturing with optimization of the machine parameters is emerging successfully for producing quality FRPC products. In TR processing, complex, thick-walled, ready to impregnate preform manufacturing is an extremely critical, but achievable task. The "Preform-Engineering" environment was presented and based on the original data set; "Quality Management" can be introduced. Closed-loop control over the re-engineering of the preform and LCM process flow is possible by means of the selected data set. Hence, the product reproducibility can improve tremendously. The incorporation of the stitched preforms in the LCM process, which is in general a very flexible manufacturing process, is quite advantageous.

9 Acknowledgements

This research and development project is supported by the Federal Ministry for Education and Research (BMBF) within the project "Forschung für die Produktion von Morgen" (02PP2476) and attended by the Forschungszentrum Karlsruhe as the project executing organization of the BMBF for production and manufacturing technology.

10 References

[1] S. Hayse (2000) RTM as the low cost alternative, *Proc. 21st Int. SAMPE Europe Conf.*, Society for the Advancement of Material and Process Engineering (Ed. M. A. Earth) Paris, p. 35.

[2] K. Drechsler (2000) Advanced textile structural composites - needs and current developments, *Proc. 5th Int. Conf. Textile Composites*, Leuven, p. 418.

[3] P. Mitschang, A. Ogale, J. Schlimbach, F. Weyrauch, C. Weimer (2003) Preform technology: a necessary requirement for quality controlled LCM-processes, *Polym. Polym. Compos.* **11**, 605.

[4] D. Feltin (1999) New textile preform techniques for the manufacturing of cost-effective fiber-reinforced composite products, *Proc. 2nd Int. AVK-TV Conf. Reinforcing Composites and Molding Materials*, Baden-Baden, No. 10 (in German)

[5] L. A. Mignery, T. M. Tan, C. T. Sun (1985) *The Use of Stitching to Suppress Delamination in Laminated Composites. Delamination and Debonding*, ASTM STP 876 (Ed. W. S. Johnson) American Society of Testing and Materials, Philadelphia, PA, p. 371.

[6] C. Weimer, P. Mitschang (2002) Quality management during the manufacture of "Tailored Reinforcements" for LCM Processes, *Proc. ACUN-4 Composite Systems, Macrocomposites, Microcomposites, Nanocomposites*, University of New South Wales (Ed. S. Bandyopadhyay) ISBN 0 7334 1862 7, Sydney, Australia.

[7] A. Ogale, C. Weimer, P. Mitschang (2004) Seams and stitches used in preform manufacturing for fiber reinforced plastic composites, *Proc. Int. Conf. and Exhibition on Reinforced Plastics, ICERP 2004*, Chennai, India.

[8] A. P. Mouritz, L. K. Jain (1997) Interlaminar fracture properties of stitched fibreglass composites, *Proc. ICCM-11*, Gold Coast, Australia, pp. V116-127, 14-18.

[9] S. B. Shim, K. Ahn, J. C. Seferis, A. J. Berg, W. Hudson (1995) Cracks and micro-cracks in stitched structural composites manufactured with resin film infusion process, *J. Adv. Mater.* **7**, 48.

[10] K. U. Moll, B. Wulfhorst (1997) Quality assessment during stitching of reinforcing textiles for composites, *Proc. ICCM-11*, Gold Coast, Australia, p. 128.

[11] F. Rattay, Sewing machine, OS DE 197 51 011 A1, 18.11.1997 (in German).

[12] J. Wittig (2001) Robotic three-dimensional stitching technology, *Proc. Int. SAMPE Conf. "2001: A Material and Processes Odyssey"*, Long Beach, California.

[13] R. Keilmann, Blind stitch sewing apparatus, DE 01120143.1-2314 (in German).

[14] B. Räckers (2000) Textiles for advanced composites in commercial aircraft applications, *Proc. 1st Stade Composite Colloquium* (Ed. A. Stephan) Stade, Germany.

[15] C. Weimer, P. Mitschang (2001) Aspects of the stitch formation process on the quality of sewn multi-textile-preforms, *Composites Part A* **32**, 1477.

[16] J. O. Ukponmwan, A. Mukhopadhyay, K. N. Chatterjee (1998) Sewing threads, *Text. Prog.* **30**, 1.

[17] A. P. Mouritz, B. N. Cox (2000) A mechanistic approach to the properties of stitched laminates, *Composites A* **31**, 1.

[18] C. Weimer (2002) Sewing technology to assemble textile reinforcement for fiber-reinforced composites, PhD Thesis, University of Kaiserslautern, ISBN 3-934930-27-1, IVW Volume 31 (in German).

[19] T. Stöven, F. Weyrauch, P. Mitschang, M. Neitzel (2003) Continuous monitoring of three dimensional resin flow through a fibre prefrom, *Composites A* **34**, 475.

[20] B. Chen, T.-W. Chou (2000) Compaction of woven fabric preforms in liquid composite molding processs: nesting and multiplayer deformation, *Compos. Sci. Technol.* **60**, 2223.

Chapter 13

Deconsolidation and Reconsolidation of Thermoplastic Composites During Processing

Lin Ye, Meng Lu, Hong-Yuan Liu
Centre for Advanced Materials Technology, School of Aerospace, Mechanical and Mechatronic Engineering, The University of Sydney, Australia

1 Introduction

Over the past two decades, *thermoplastic matrix composites* have attracted considerable attention in engineering communities. With the development of manufacturing and processing technologies, the applications of thermoplastic composites have ranged from high-tech-only areas, such as the defence and aviation/aerospace industries, to more general purpose uses. For instance, thermoplastic composites have been widely used in the biomedical, automotive, marine and infrastructure industries. In comparison with thermosetting matrix composites, thermoplastic composites have some unparalleled advantages, such as fast mass production with a shorter manufacturing cycle time, better resistance to environmental hazards, and higher impact toughness. In particular, thermoplastic composites have the unique advantage of being reprocessable or recyclable through post-thermoforming and fusion bonding subject to a reheating/cooling cycle.[1-6] This advantage is appreciated by the relevant engineering communities, but some recent studies[7-11] report that it is not unconditionally available. Thermoplastic composites may suffer greatly from unexpected deterioration in performance during thermal processing. In fact, according to some experimental observations,[8,9] thermoplastic composites, even those that are initially well consolidated, may have a considerably negative change in their meso-structures as well as in their macro-performance when undergoing a reheating process. This change is referred to as thermal *deconsolidation.*

Microscopically, thermal deconsolidation is associated with an increase of the interior void content within the composite; its degree can be characterized by

the increment of void content. As observed,[8] the content of voids due to deconsolidation may exceed 10-20% of the entire volume of the composite. The deterioration of the mechanical properties of composites increases with the void content. For instance, for a glass fiber/polyamide 12 (GF/PA12) composite sheet,[8] if the void content increases from an initial 1% to 12%, the flexural strength decreases from 580 MPa to 360 MPa, or more than 20%. Meanwhile, Young's modulus decreases from 24 to 18.5 GPa, that is, by about 20% as well. Evidently, thermal deconsolidation may become a significantly critical event that greatly limits the reprocessability and on-line repairability of thermoplastic composites if void growth cannot be controlled. It is therefore imperative to suppress the occurrence of void growth and to develop relevant reconsolidation techniques in order to reduce its effect in practice.

In addition to void growth during thermal deconsolidation, it has been further observed[9] that some other relevant phenomena may appear in the reheating process. For instance, when a carbon fiber/polyetherimide (CF/PEI) thermoplastic composite laminate undergoes resistance-welding, in which only the lower surface of the laminate is heated, large-scale "movement" of voids can be observed, demonstrating that the voids "migrate" in the direction of the heat flux from a region where they were previously located to another region where voids were absent. This demonstrates that there is a propagating front behind which thermal deconsolidation takes place. Meanwhile, with the migration of voids, the voids in the deconsolidated region constantly disappear and "reconsolidation" resumes in the region, and then it appears that there is another propagating front behind which reconsolidation takes place. The migration of voids demonstrates the dynamic development of thermal deconsolidation in the composite, and its progress strongly depends on the thermal processing conditions. The in-depth understanding of the mechanisms involved is of practical significance in the thermoforming of thermoplastic composites, with questions of concern being, if thermal deconsolidation occurs, what amount of the composite would be influenced in a specific reheating operation, what duration of heating time is appropriate, and what thermal processing conditions are suitable to reduce the effect of deconsolidation. Unlike void growth in deconsolidation, reconsolidation following the migration of voids is apparently a positive event. Nevertheless, such reconsolidation may result in unexpected consequences. In fact, some side effects, such as squeezed creep flow of the matrix melt, can become a critical issue in certain instances. Therefore, it is also important to understand how reconsolidation resumes and what effect it may have on the composites.

This chapter summarizes some recent research advances in the understanding of deconsolidation and reconsolidation,[8-11] which include (i) a mechanistic model for void growth, in term of the degree to which thermal deconsolidation can be evaluated, (ii) an analysis based on transient heat transfer consideration for the so-called propagating fronts of both deconsolidation and reconsolidation, (iii) an indicative void-closure model relevant to reconsolidation, and (iv) a squeezed creep flow model.

2 Experimental Observations

An experiment for resistance welding of CF/PEI thermoplastic composites, shown in Figure 1, can be used to illustrate the events of void growth and migration of voids, as well as reconsolidation.[9] In this experiment, the CF/PEI laminates were consolidated from the woven fabric (plain weave) prepregs, and the initial void content of the laminates was less than 1% (with a consolidation pressure of 2MPa). The configuration and geometry of the specimen (only 1/8 of the whole

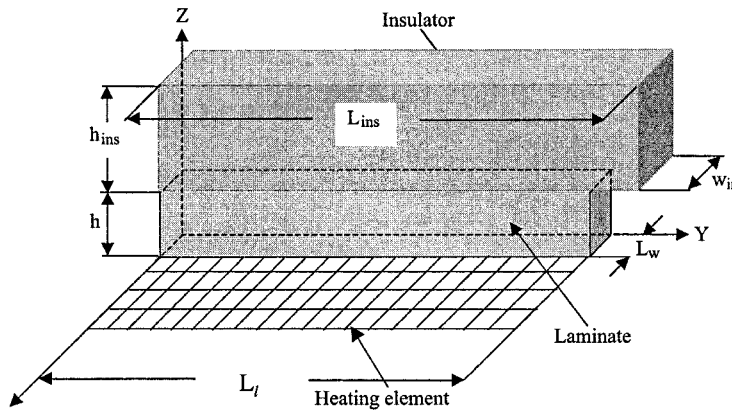

Figure 1. Schematic representation of resistance welding of a CF/PEI composite laminate.[9]

specimen in terms of its symmetry) are shown in Figure 1, where the width of the specimen, L_w, is 25 mm and the length, L_l, is 100 mm. The laminate of 10-layer of prepregs has a total thickness, h, of 2.032 mm, while the thickness of the insulator, h_{ins}, is 3 mm. The power level of the heating element was 46 kW/m^2. The laminate was subjected to an external pressure of 0.4 MPa during the thermal operation.

2.1 Void Growth

Void growth of deconsolidation can be readily observed in the reheating operation addressed above. Figure 2a,b shows the typical interior configurations of a CF/PEI composite laminate before and after deconsolidation,[9] respectively. Note that for the initially well consolidated laminate, the void content is only approximately 1% before deconsolidation (Figure 2a). In this case, the presence of voids can barely be seen by instant light microscopy. On the contrary, significantly large voids appear in the interior of the laminate after it has been reheated above the glass transition temperature, T_g, of the matrix (Figure 2b). The

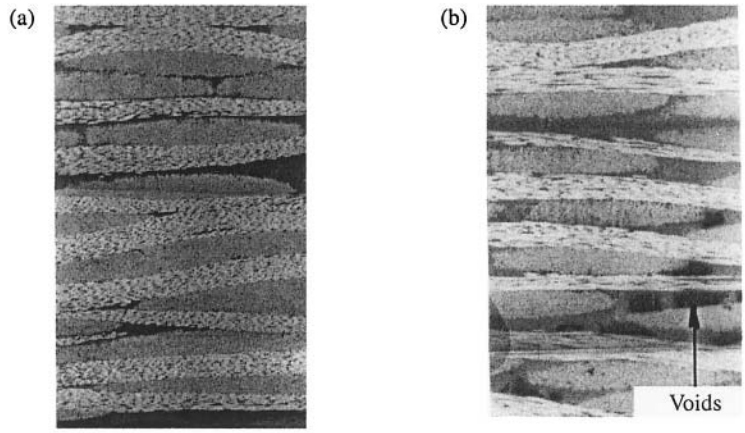

Figure 2. Interior configuration of a CF/PEI composite: (a) before thermal deconsolidation and (b) after thermal deconsolidation.

large voids predominantly occur in the matrix inside the fiber bundles or in the matrix-rich interlaminar regions. The voids are approximately elliptical in shape, randomly distributed and of different sizes. The characteristic dimension of some larger voids may be up to 200 μm.

According to the experimental observations,[8,9] the increase of void content is not sensitive to the maximum temperature when the specimen is reheated above T_g (for amorphous polymer matrices) or above the melting temperature, T_m (for semicrystallized polymer matrices). Also, it was found that the variation of void content is insensitive to the holding time in the reheating process, even when the processing period varied by several minutes. Yet the dependence of void content on the applied external pressure is quite clear. As shown for a GF/PA12 composite laminate,[8] the void content is about 10% at a pressure of 0.1 MPa, and then reduces to about 3% when the pressure increases to 0.5 MPa. No further variations of note are observed when the applied external pressure is over 1.0 MPa.

2.2 Migration of Voids

The phenomenon of migration of voids can be detected by observation of the internal profiles of the composite shown in Figure 2a,b at different heating times. In fact, when the laminate was heated for 1.5 min, large voids appeared in the composite near the heating element, as shown in Figure 3a, indicating that thermal deconsolidation had commenced in the composite. Let d denote the average distance of voids from the deconsolidation region to the heating element, then $d \approx 0.1h$ in this case. When the laminate was continuously heated for 3 min, more voids with increasing sizes could be found (Figure 3b). In particular, note that the

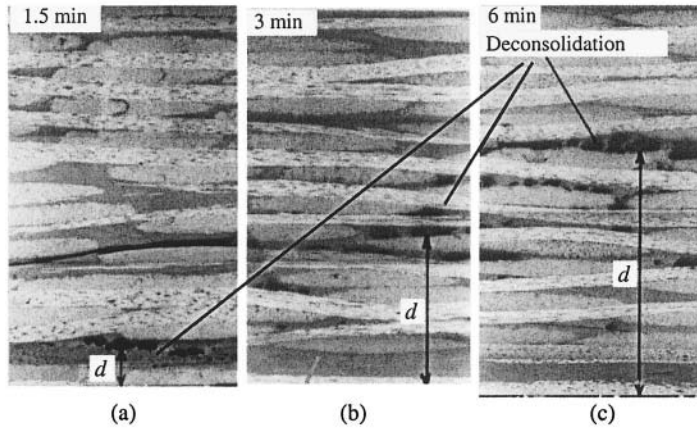

Figure 3. Void migration in a CF/PEI composite at various heating times.[4]

voids appearing in the region shown in Figure 3a have vanished and voids have occurred in a new region, demonstrating that voids migrate upwards along the direction of heat flux. Accordingly, the distance d increases to approximately $0.4h$ in comparison to the distance of $0.1h$ shown in Figure 3a. Reconsolidation occurs in this way, with the disappearance of voids in the previously deconsolidated region. After the laminate is heated for up to 5 min, the voids continue to migrate upwards along the direction of heat flux (Figure 3c). Furthermore, the regions where voids appeared in Figure 3a,b do not have visible voids any longer, with reconsolidation prevailing there, and d increases to approximately $0.65h$. Such a process can continue until all voids vanish in the composite laminate if there is a sufficient temperature rise throughout the composite thickness[9].

2.3 Squeezed Flow of Resin During Reconsolidation

Reconsolidation accompanying the migration of voids as shown in Figure 3a-c appears to be a positive event in terms of the structureproperty relationship of the composite material. It may be inferred from the results given in the last two sub-sections that reconsolidation can always resume when adequately high temperature (below the polymer thermal decomposition temperature) and external pressure are applied. However, experimental observations reveal that reconsolidation realized in this way may not be always without cost if the temperature and the external pressure in the reheating operations are too high.[9] Unnecessarily high temperature and external pressure may cause a considerable loss of matrix squeezing out from the free edges of the composite, particularly for specimens of small size.

An example of squeezed flow of resin is illustrated in Figure 4, where an aluminum/CF-PEI metal/composite joint was subjected to welding treatment.[9]

The heating power was 110 kW/m^2, while all other conditions and parameters were exactly the same as those shown in Figure 1. These photos show the profiles of deconsolidation and reconsolidation within the fusion bonding area in the composite laminate being heated for 4, 6, and 9 min, respectively. In particular, it should be noted that if the thickness of the laminate is taken as unit after being heated for 4 min, the thickness becomes $0.85h$ when it is heated for 6 min, and is further reduced to $0.67h$ when the heating time is 9 min.

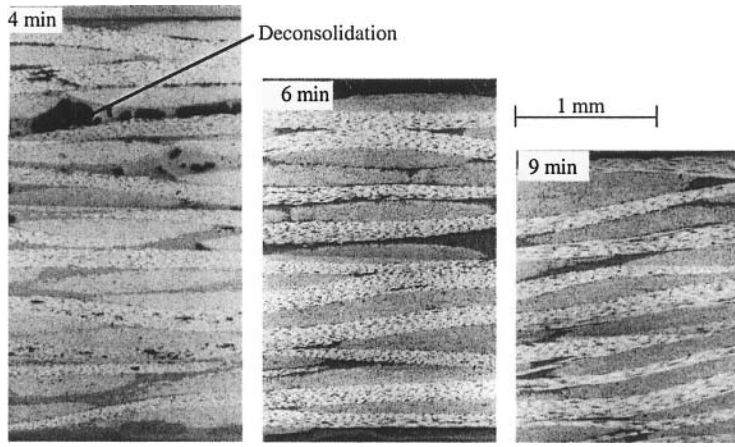

Figure 4. Reconsolidation in a CF/PEI composite at various heating times.[9]

Since the fibers and matrix are almost incompressible, the variation in the thickness of the composite laminate shown above can only originate from void growth or void closure, and from the loss of matrix melt (and fiber reinforcement towards nearby free edges in some extreme cases) because of the squeezed creep flow. Considering that the average contribution of voids to the volume of the composite was about 10% in the experiments,[8,9] the additional major change in thickness must be caused by the loss of matrix, the amount of which may be over 30% according to these experimental observations.

3 Mechanistic Model of the Void Growth

3.1 Discussion of the Mechanism

Thermal deconsolidation can be regarded in a certain sense as an inverse process of consolidation. To investigate the mechanisms of thermal deconsolida-

tion and to understand what forces cause the voids to grow, it is essential to examine the compressibility of the fiber reinforcement under consolidation.

Fiber reinforcements are compacted in a consolidation procedure in which external loads are applied to compress fibers, to squeeze air and resin out, to suppress voids, and to increase the fiber volume fraction. Before compaction, the fiber reinforcement networks are unable to carry traction stresses at/or below a certain initial critical fiber volume fraction, μ_{cf}^{0}. As the fiber volume fraction, μ_f, increases under compression, the network can carry a rapidly increasing load. Eventually, the fiber volume fraction of the network approaches a theoretical maximum based on the relevant close-packed geometry, and cannot increase without an enormous increase in load.[1] The compressibility of the fiber reinforcement network is dependent not only on the elastic properties of fibers, but also on the configuration of the fiber reinforcement network as well, that is

$$p|_{compaction} = \Gamma(\textit{fiber properties, configuration of fiber network, } \mu_f, \textit{ etc.}) \quad (1)$$

Here, $p|_{compaction}$ is the pressure required to compress the fiber reinforcement network to a specified μ_f.

After compaction of the fiber reinforcement network is completed and the matrix melt becomes a solid after cooling down (achieving consolidation), the elastic energy of the fiber reinforcement network is stored in the composite in the form of residual stresses. When the consolidated composite undergoes a reheating operation and its matrix commences to remelt, the elastic energy stored in the fiber reinforcement network tends to release, which is referred to as decompaction of fiber reinforcement. In this way, the decompaction of the fiber reinforcement network, denoted by $p|_{decompaction}$, should be proportional to $p|_{compaction}$, namely,

$$p|_{decompaction} \propto -p|_{compaction} \quad (2)$$

or

$$p|_{decompaction} = -k\Gamma. \quad (3)$$

Here, k is a factor relevant to the material and structural properties of the fiber reinforcement network, ranging from 0 to 1. The limiting case is that $k = 1$ for the compressibility of the fiber reinforcement network being fully "elastic" and $k = 0$ for it being fully "plastic". Since in most practical consolidation procedures the fiber reinforcement networks are not severely damaged, $k = 1$ can be taken as a reasonable first order approximation.

$p|_{decompaction}$ is clearly one source of "driving" forces for void growth and, as addressed later, it is actually the dominant source, while the other contributions, such as the thermal pressure inside a void, are usually not important.

It is believed that, in addition to the driving force acting on voids, void growth also depends strongly on the properties of the thermoplastic matrix. Hence, it is necessary to examine the properties of the polymer matrix in thermal deconsolidation. Amorphous thermoplastics become "brittle" below T_g, then

rubbery and flexible up to T_m of the crystalline phase. As the temperature rises above T_g, the viscosity usually diminishes rapidly; often the temperature T_g + 60~100 °C can be roughly taken as the onset of the truly liquid melt.[12,13] Therefore, when amorphous thermoplastic polymers are heated over T_g but below the temperature at which the polymer becomes truly liquid, the polymer melt still retains two basic properties, viscosity and elasticity. In particular, the latter property allows polymer melts to possess the characteristics of solids, enabling them to store elastic energy and to deform continuously under stress. When the stress is removed, the deformation may be recovered elastically. With such a rubber-like behavior, the driving force due to decompaction of fiber reinforcements will cause the microscopic voids that initially existed in the polymer matrix to grow under the traction, becoming larger voids. Such a driving force can also produce new voids through "cavitation" in the matrix.[14,15]

Thus, the void growth in thermal deconsolidation can be primarily attributed to three sources: (i) growth of microscopic voids under thermal pressure inside the voids due to an increase in temperature, namely, the thermal expansion of voids, (ii) coalescence of smaller voids into larger ones, and (iii) growth of microscopic voids under the traction of decompaction of fiber reinforcements, which includes the contribution of cavitation.

The thermal expansion effect can be estimated in a simplified way. Suppose that the initial average volume of voids in the composite is V_g^0, the temperature is T_0, and the corresponding pressure is p_g^0. Suppose that the air inside the void can be assumed as the ideal gas. During the reheating process, the temperature of the air increases from T_0 to T and correspondingly the voids expand from V_g^0 to V_g. Let the external pressure remain p_0 in the whole process. Then, ignoring the constraints of the elasticity of the polymer melt and surface tension, the equilibrium of the void expansion yields

$$V_g = \left(\frac{p_g^0}{p_0}\right)\left(\frac{T}{T_0}\right)V_g^0 . \tag{4}$$

Let T_0 = 293 K (20 °C), T = 500 K (227 °C), and $p_g^0 = p_0$ (=1 atmosphere pressure). Then Eq. (4) gives

$$V_g \approx 1.7\, V_g^0 . \tag{5}$$

Equation (5) shows that the volume of a void increases only around 0.7 times by thermal expansion. Therefore, its contribution is trivial compared to the increase of 10-20% in void content observed in thermal deconsolidation.[8] Moreover, the result shown in Eq. (5) is the upper limit of the estimation, as the effects of elasticity and surface tension were not taken into consideration, and these factors play a negative role in the thermal expansion of voids. It can thus be concluded that the thermal expansion of voids does not appear to be the primary source of growth of voids.

Regarding the coalescence of voids, it can be simply concluded that it is not the major source of the increase of void content either, as coalescence of voids itself does not add to the total void content in the material. In fact, while coalescence transforms smaller voids into larger ones, it correspondingly reduces the number of voids. As a result, the total void content is not considerably altered.

Thus, it appears that the traction induced by the decompaction of the fiber reinforcement network plays a major role in void growth at thermal deconsolidation, and a relevant model is discussed in the next section.

3.2 Void-Growth Model

In terms of the homogenization concept and within a first order approximation, an effective representative volume element is established.[10] As shown in Figure 5, the total initial volume of the representative element is supposed to be V_e^0. Inside the volume element, the volume of the effective void is V_g^0 at $t = 0$ and V_g at $t = t$. The volume equivalent radius of the void is $R_g^o = \sqrt[3]{V_g^0 \Big/ \left(\frac{4}{3}\pi\right)}$ and $R_g = \sqrt[3]{V_g \Big/ \left(\frac{4}{3}\pi\right)}$ at $t = 0$ and $t = t$, respectively. The void is surrounded by the matrix melt and further surrounded by the fiber network. The initial inner equivalent radius of the matrix is R_g^0 and the outer effective radius is R_M^0, which become R_g and R_M at time t, respectively.

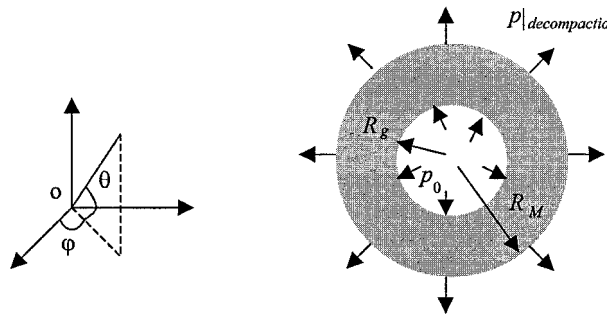

Figure 5. Schematic illustration of the representative volume element.

Let the initial void content of the representative volume element, α_e^0, equal the initial average void content of the composite, α^0. That is,

$$\alpha_e^0 \equiv V_g^0 / V_e^0 = \alpha^0. \tag{6}$$

Let the initial fiber volume fraction of the volume element, $\mu_{f_e}^0$, equal that of the composite μ_f^0,

$$\mu_{f_e}^0 \equiv (V_e^0 - V_M^0 - V_g^0)/V^0 = \mu_f^0. \tag{7}$$

After deconsolidation, we have

$$\alpha_e \equiv V_g/V = \alpha \tag{8}$$

and

$$\mu_{f_e} \equiv (V_e - V_M - V_g)/V = \mu_f. \tag{9}$$

Note that in comparison with the contribution of void growth to the composite, the volume variation of the melt and reinforcing fibers themselves can be ignored. That is, the melt and fibers can be regarded as incompressible. Thus, the equations of motion for the melt, in the spherical coordinates shown in Figure 2 and under the condition of sphere symmetry, give

$$\frac{1}{r}\frac{\partial}{\partial r}\left(r^2 v_r\right) = 0 \tag{10}$$

and

$$\rho_M\left(\frac{\partial v_r}{\partial t} + v_r\frac{\partial v_r}{\partial r}\right) = \frac{\partial \sigma_{rr}}{\partial r} + \frac{2\sigma_{rr} - \sigma_{\theta\theta} - \sigma_{\varphi\varphi}}{r} \tag{11}$$

where ρ_M is the density of the matrix, v_r is the radial velocity and σ_{ii} ($i = r$, θ, and φ) are stresses.

Since the matrix melt has both elastic and viscous properties, it can be described by a constitutive law of viscoelasticity. The non-linear Kelvin-Voigt equation is employed here

$$\sigma_{ij} = -p\delta_{ij} + (s_{ij})_{elastic} + (\tau_{ij})_{viscous}, \tag{12}$$

where p is the hydrostatic stress, $(s_{ij})_{elastic}$ is the elastic derivatoric stress which relates to the elastic shear deformation of the medium, and $(\tau_{ij})_{viscous}$ is the viscous stress.

Suppose that the elastic stress-strain relation of the matrix melt can be described by a linear function,

$$(s_{ij}) = \lambda(T)\varepsilon_{ij} \tag{13}$$

where $\lambda(T)$ is elastic modulus of shear, and ε_{ij} is strain. The shear moduli of thermoplastic melts are normally in the range of 1-1000 kN/m^2. For viscous properties the power-law is used, which gives

$$\tau_{ij} = \eta\dot{\gamma}_{ij} = \mathrm{C}\left|\dot{\gamma}_{ij}^{n-1}\right|\dot{\gamma}_{ij} \tag{14}$$

where $\dot{\gamma}_{ij}$ is the shear rate and C can be expressed by[12]

$$C(T)=\eta_0(T_g)\,e^{-\frac{C_1^0(T-T_g)}{C_2^0+(T-T_g)}} \tag{15}$$

in which T is temperature, while $\eta_0(T_g)$, C_1^0 and C_2^0 are material constants.

The void growth equation can be eventually derived as[10]

$$\ddot{R}_g=\Psi(\dot{R}_g,R_g,n,T), \tag{16}$$

where

$$\Psi=\kappa\left(p|_{r=R_M}-p|_{r=R_g}\right)+I_\varphi+E_\varphi+V_\varphi, \tag{17}$$

in which

$$I_\varphi=\omega\left\{-2\ln\frac{R_M}{R_g}+\frac{1}{2}\left[1-\left(\frac{R_g}{R_M}\right)^4\right]\right\}\dot{R}_g^2, \tag{18}$$

$$E_\varphi=-4\omega\lambda\left[\frac{1}{2}\left(\frac{R_g^0}{R_g}\right)^2-\frac{R_M^3-R_g^3+\left(R_g^0\right)^3}{2R_M^2}\right], \tag{19}$$

$$V_\varphi=-\frac{3\omega\left(\sqrt{6}\right)^{n-1}\eta_0(T)}{(3n+1)}\left[1-\left(\frac{R_g}{R_M}\right)^{3n-1}\right]\left(\frac{|\dot{R}_g|}{R_g}\right)^{n-1}\dot{R}_g, \tag{20}$$

$$p|_{r=R_g}=\left[\left(\frac{T}{T_0}\right)\left(\frac{R_g^0}{R_g}\right)^3 p_g^0-\frac{2\delta}{R_g}\right], \tag{21}$$

$$p|_{r=R_M}=p_0+\Delta p-p|_{de-compaction}, \tag{22}$$

$$\kappa=\frac{1}{\rho_M}\left[R_g\left(1-\frac{R_g}{R_M}\right)\right]^{-1}. \tag{23}$$

Here, T_0 is the initial temperature, p_g^0 is the initial pressure of the air inside the void, p_0 is the external pressure, which is normally 1 atm (1.03×10^5 MPa), Δp denotes the controllable external applied pressure in processing, δ is the surface tension coefficient, $\omega=\rho_M\,\kappa$, and

$$p|_{de-compaction}=\Gamma\equiv p_1\exp\left(\frac{\mu_f-\mu_{fc}^0}{C_r}\right) \tag{24}$$

where p_1 and C_r are material constants.

Note that in Eqs. (16)-(23) I_φ is related to the inertia effect of the void, E_φ to the elasticity of the matrix, and V_φ to the viscous effect of the matrix; $p|_{r=R_g}$ is the traction acting on the inner boundary of the void due to thermal expansion and surface tension; $p|_{r=R_M}$ is the traction action on the outer boundary of the void because of the decompaction of the fiber network against the applied pressure. It can be shown that $p|_{decompaction}$ is the major driving force for void growth.

3.3 Theoretical Predictions

A GF/PA12 thermoplastic composite is evaluated as an example.[10] The material properties used in the computation are $\lambda = 0.2\times10^5$ (N/m^2), $n = 0.4$,[12] $\eta_0(T_g) = 2\times10^5$ [Ns/m^2],[12] $T_g = 461$ (K), $C_r = 0.43$, $\rho_M = 1.04\times10^3$(kg/m^3), $\mu_{f_e}^0 = 46.5$ (%),[1] $\mu_f = 52$ (%), $T_0 = 288$ (K), $\alpha_0 = 1.0$ (%), $R_g^0 = 0.4\times10^{-4}$ (m), $p_0 = 1.03\times10^5$ (N/m^2), and $p_g^0 = 1.03\times10^5$ (N/m^2).

Figure 6a,b shows the void growth when $\Delta p = 0.1$ MPa and the temperature is 188 °C and 220 °C, respectively. It is seen that the dynamic behavior of the void is quite distinct and changes greatly at different temperatures. However, it will eventually approach the same steady state (Figure 7). This result is attributable to the fact that the melt viscosity influences the dynamic behavior of the void, but does not affect the final equilibrium state of the void. Note that in the present approach the effect of temperature on the melt elasticity is not taken into account. Also, it

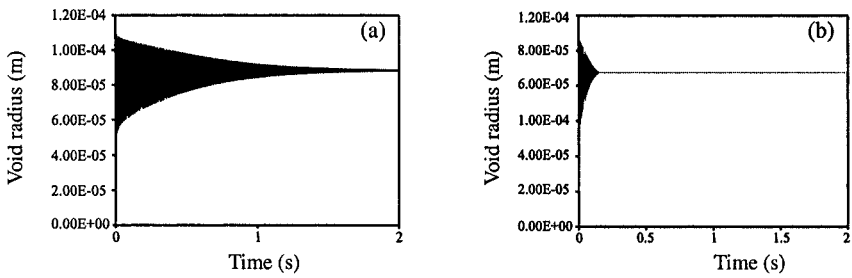

Figure 6. Void growth at different temperatures: (a) 188 °C and (b) 220 °C.

can be shown that the final state of the void appears to change very little when the elastic modulus of the melt is relatively small, *e.g.*, when λ is in the range 1-30 kN/m^2. When λ is higher, the elasticity of the matrix melt gradually becomes a significant factor, influencing the variation of void content. For instance, when $\lambda = 70$ kN/m^2 and the other conditions remain the same, as in Figure 3, the effective radius of the void R_g is 6.62×10^{-5} m, while R_g is approximately 9.67×10^{-5} m when $\lambda = 20$ KN/m^2. Correspondingly, the void content is 6.7% for $\lambda = 70$ kN/m^2, compared to 9.7 % for $\lambda = 20$ kN/m^2. This is an interesting result, indicating that for polymer melts with lower elasticity the variation of void content is insensitive

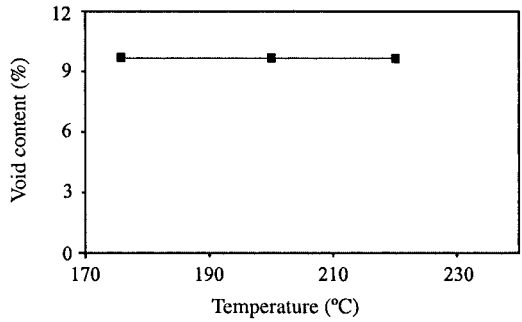

Figure 7. Void content at different temperatures (Δp = 0.1 MPa).

to λ, but for the melts with higher elasticity, λ may have a significant influence on void content.

It is also apparent in Figure 6 that the steady state of the void is reached within a few seconds. For instance, the expansion of voids takes only 0.2 s at 200 °C to reach a steady state, while it takes around 2.5 s to do so at 220 °C. This is in agreement with the experimental observation that the void content is insensitive to the holding time in a reheating process when the processing duration changes by several minutes.[9]

Figure 8 shows that the void content is rather sensitive to variations in the pressure Δp. When $\Delta p = 0.1$ MPa, the void content is 9.7 %, which is approximately 9 times the initial void content of 1%. With an increase of Δp, the void content decreases and approaches its initial value when $\Delta p = 1$ MPa. The experimental data[8] shown in Figure 8 agree well with the theoretical prediction.

The present analysis shows that the thermal deconsolidation of a thermoplastic matrix composite is primarily attributable to two essential factors: the

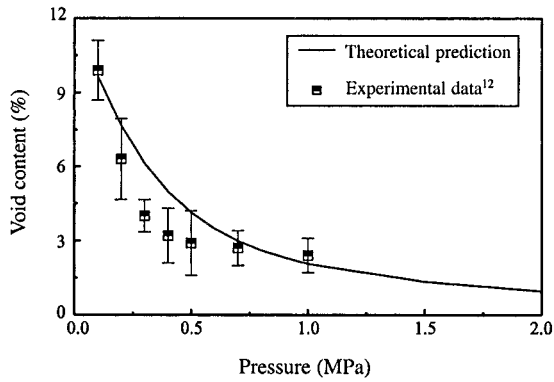

Figure 8. Void content at different applied external pressures.

decompaction behavior of the fiber network and the elasticity of the matrix melt. The former produces the driving force of void growth, while the latter enables the matrix melt to carry the traction.

4 Thermal/Mechanistic Models of Migration of Voids

4.1 Discussion of Mechanisms

It can be seen in Figure 3 that the heat flux is transferred from the heating element to the adjacent regions and, with the increase of heating time, the closer the region is to the heating element, the higher its temperature. According to the above analysis, when the temperature in a region exceeds T_g (or T_m, for crystallized or semicrystallized thermoplastics), the matrix there begins to melt and behaves in a rubber-like fashion. Hence, the residual stress in the region is released, and then voids are produced and grow under the traction of decompaction of the fiber reinforcement. Accordingly, thermal deconsolidation takes place. With heat fluxes further transferred from the deconsolidated region to adjacent regions, the temperature of these regions will also exceed T_g (or T_m), and new voids form, creating new deconsolidated regions. This process proceeds continuously from one region to another with the increase of heating time, and thus produces the propagating front of deconsolidation.

When the laminate is continuously heated, the deconsolidated region closer to the heating element experiences a constant rise of temperature; the matrix may eventually reach a fully liquid state with a very low viscosity, and the elasticity of the matrix melt vanishes. Note that the elasticity enables the matrix melt to carry the traction of decompaction of the fiber reinforcement, which is an essential factor for thermal deconsolidation. With its disappearance, the driving force of void growth due to the decompaction of fiber reinforcement also vanishes. Consequently, voids in the deconsolidated region would close under the applied pressure and the deconsolidation disappears, with reconsolidation resuming in the region. By a similar procedure as the propagation of the deconsolidation front just described, reconsolidation also proceeds continuously with time from one region to another in the direction of heat flux, creating a propagating front. Thus, it can be understood that the so-called migration of voids is not really due to any movement of voids. Rather, it is a process of void growth and closure.

4.2 Thermal Analysis

To simulate the propagation of the fronts of deconsolidation and reconsolidation associated with the welding test shown in Figure 1, transient heat

analysis is needed.[11] To this purpose the commercial FEM software, ABAQUS-58, is invoked here. Note that as a first order approximation, the thermal behavior in this analysis is decoupled from effects due to the presence of voids.

The initial and boundary conditions pertaining to the given problem are specified as follows. The initial temperature is T_0 (= 298.15 K) for the whole laminate, and the ambient temperature of the environment is also T_0. The boundary conditions are specified by free convection between the surfaces of the specimen and the surrounding media. In the present case, air is the medium to which heat transfers from the composite. The temperature-dependent expressions of the heat transfer coefficients of air[5,6] are directly invoked here.

In the analysis, the front of deconsolidation can be defined straightforwardly according to the T_g of the matrix, at which it begins to melt and behaves in a rubber-like fashion. However, the definition of the front of reconsolidation must be somewhat arbitrary, since there is usually no definite distinction to identify when the melting matrix becomes fully liquid. One way to define the fully liquid state of a melting polymer is based on its viscosity. For instance, when the viscosity of the melt is significantly less than that at the T_g, the melt is then considered to be in a fully liquid state. Here we consider that a matrix becomes fully liquid when the ratio stated above is less than 10^{-4} or 10^{-5}.

The temperature dependence of viscosity is reported in detail in many studies; here the form expressed by Eq. (15) is used and, again, for C_1^0 and C_2^0, their "universal values", $C_1^0 = 17.44$ and $C_2^0 = 51.6$, are employed.

Suppose that the temperature of reconsolidation is T_{melt} at which the viscosity of the thermoplastic melt is $\eta(T_{melt})$. Then, in light of Eq. (15) we have

$$T_{melt} = T_g + \gamma C_2^0/(C_1^0 - \gamma), \tag{25}$$

where

$$\gamma = -\ln\eta(T_{melt})/\eta(T_g), \tag{26}$$

is the logarithm ratio of T_{melt} against T_g. According to Eq. (26), when $\gamma = 10^{-4}$, $T_{melt} \approx T_g + 60$ K, and when $\gamma = 10^{-5}$, $T_{melt} \approx T_g + 100$ K.

For the CF-PEI laminate, the glass transition temperature of the matrix is $T_g = 492$ K and the melting temperature is then estimated as $T_{melt} = 552$ K. Other parameters and material constants used in computations[11] are: (for PEI) $\rho^{(m)} = 1270$ kg/m^3, $k^{(m)} = 0.22$ W/mK, $C^{(m)} = 1248$ J/kg K; (for carbon fiber) $\rho^{(f)} = 1790$ kg/m^3, $k_y^{(f)} = 9.1$ W/mK, $k_x^{(f)} = k_z^{(f)} = 0.43$ W/mK, $C^{(f)} = 1296$ J/kg K; (for wood) $\rho^{(w)} = 817$ kg/m^3, $k^{(w)} = 0.21$ W/mK. Here, $\rho^{(i)}$ is the density, $k^{(i)}$ the conductivity, and $C^{(i)}$ the specific heat ($i = m, f, w$), with m indicating the matrix, f the fiber, and w the wood.

Figure 9 illustrates the distribution of temperature in the z-direction at different times, while Figure 10 shows the variation of temperature of each layer with time. From these results, the propagation of deconsolidation and reconsolidation fronts can be obtained (Figure 11); note that the shaded region between the

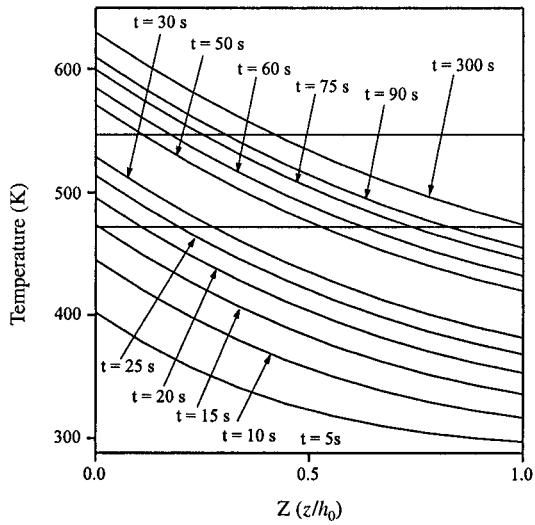

Figure 9. Temperature distributions at different times along the laminate thickness.

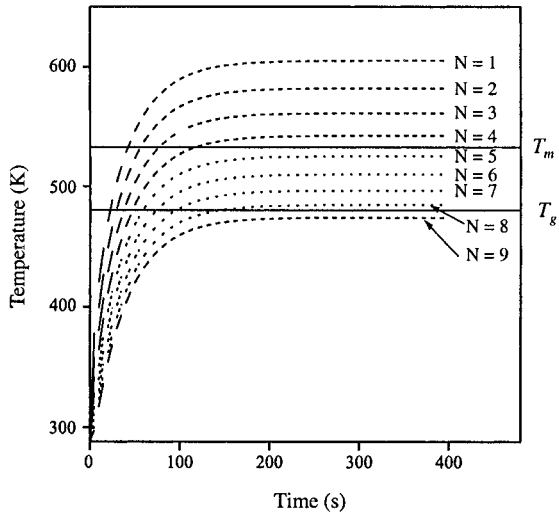

Figure 10. Time history of each layer of the composite.

two fronts denotes the zone where deconsolidation may occur. The corresponding experimental data[9] are also shown, and a satisfactory agreement between the theoretical prediction and the experimental results is achieved.

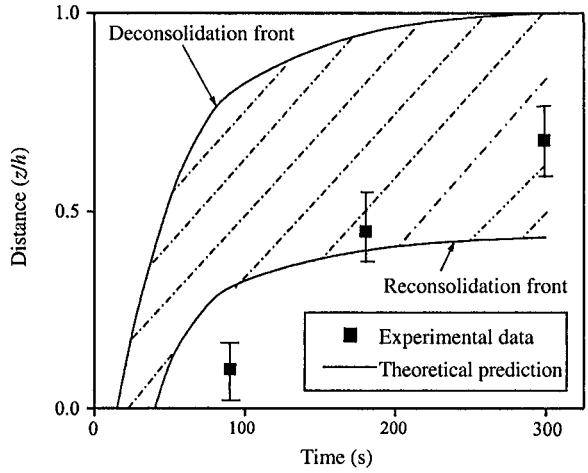

Figure 11. Propagation of fronts of deconsolidation and reconsolidation.

4.3 Void Closure

It should be pointed out that the fronts of deconsolidation and reconsolidation discussed above are based on the consideration of the matrix melting temperature only, and the properties of fiber reinforcement are not yet involved. However, when such a front of reconsolidation arrives at a region where deconsolidation has occurred previously, whether or not voids are really closed, another condition is necessary for reconsolidation to occur. This condition is that the compressibility of the fiber reinforcement, compared to the external load, must be negative, so that the matrix is subjected to recompression. This requirement implies that detachment between matrix melt and fiber reinforcement may occur if the external load is insufficient to suppress the decompaction of the fiber reinforcement, since the incompressible matrix melt cannot fully occupy the resulting "expanded space". In this case, reconsolidation does not take place. In contrast, when the external load is sufficient to suppress decompaction of the fiber reinforcement, reconsolidation will occur and deconsolidation may not happen at all. As shown in Figure 3a,c, both deconsolidation and reconsolidation, which require an opposite effect of the ratio of the compressibility of fiber reinforcement against the external load, take place under the same traction of the external load. According to the above discussion, it is plausible, therefore, to expect that the voids close behind the front of reconsolidation because the compressibility of the fiber reinforcement has deteriorated after deconsolidation, so that the matrix is under a recompression.

The results of the deterioration of the fiber reinforcement associated with repeated compaction are discussed elsewhere.[1] Void closure under such repeated compaction can be regarded to some degree as a process reverse to void growth.

The main distinction is that at reconsolidation the matrix becomes fully liquid and its elasticity vanishes. Thus, the equation for void closure can be given as follows:[11]

$$\ddot{R}_g = \Psi\left(\dot{R}_g, R_g, n, T, p|_{Reconsolidation}\right), \tag{27}$$

where

$$\Psi = \kappa\left(p|_{r=R_M} - p|_{r=R_g}\right) + I_\varphi + V_\varphi, \tag{28}$$

in which

$$I_\varphi = \alpha\left\{-2\ln R_M/R_g + \frac{1}{2}\left[1-\left(R_g/R_M\right)^4\right]\right\}\dot{R}_g^2, \tag{29}$$

$$V_\varphi = -3\alpha\left(\sqrt{6}\right)^{n-1}\eta_0(T)\Big/(3n+1)\left[1-\left(R_g/R_M\right)^{3n-1}\right]\left(|\dot{R}_g|/R_g\right)^{n-1}\dot{R}_g, \tag{30}$$

$$p|_{r=R_g} = \left[\left(p_g^0|_{Reconsolidation}/T_0|_{Reconsolidation}\right)\left(R_g^0|_{Reconsolidation}/R_g\right)^3 T - 2\delta/R_g\right], \tag{31}$$

$$p|_{r=R_M} = p_0 + \Delta p - p|_{Reconsolidation}, \tag{32}$$

$$\kappa = \rho_M^{-1}\left[R_g\left(1-R_g/R_M\right)\right]^{-1}, \tag{33}$$

$$R_M = \left[R_g^3 + \left(R_M^0|_{Reconsolidation}\right)^3 - \left(R_g^0|_{Reconsolidation}\right)^3\right]^{\frac{1}{3}}, \tag{34}$$

$$\alpha = \rho_M\kappa. \tag{35}$$

Here, R_g and R_M are the current effective volume-equivalent radii of void and matrix, respectively, while $R_g^0|_{Reconsolidation}$ and $R_M^0|_{Reconsolidation}$ are their initial counterparts in reconsolidation, which can be obtained in terms of the final values of R_g and R_M calculated for deconsolidation, T is the temperature and n is the viscous exponent of the matrix as defined in this study, δ denotes the surface tension coefficient, $T_0|_{Reconsolidation}$ and $p_g^0|_{Reconsolidation}$ are the initial temperature and pressure inside the void in reconsolidation, respectively, which, like $R_g^0|_{Reconsolidation}$ and $R_M^0|_{Reconsolidation}$, can be determined using the final values of T and p_g in deconsolidation, p_0 indicates the external pressure which is normally 1 atm (1.03×10^5 MPa), and Δp denotes the controllable external pressure during processing.

The initial conditions of Eq. (27) are

$$R_g|_{t=0} = R_g^0|_{Reconsolidation} \text{ and } \dot{R}_g|_{t=0} = 0 \tag{36}$$

Figure 12 shows the variation of void closure with time in reconsolidation, indicating that the normalized effective or volume-equivalent radius of void reduces to *ca.* half its initial value. Accordingly, the volume of the void is reduced to *ca.*

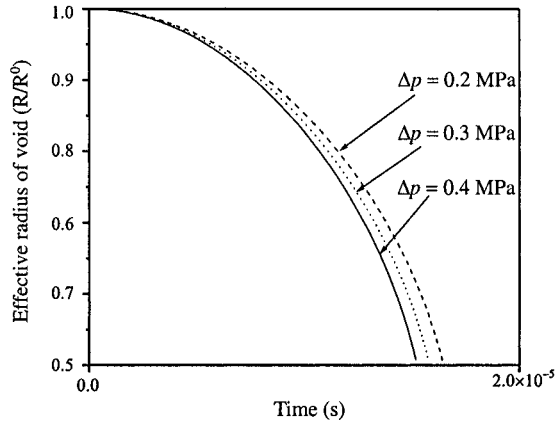

Figure 12. Time history of void closure.

one eighth of its initial counterpart. Figure 13 illustrates the corresponding variation of the fiber volume fraction, based upon a method described elsewhere;[3] it is seen that the fiber volume fraction increases to a final 0.52 from the initial 0.475.

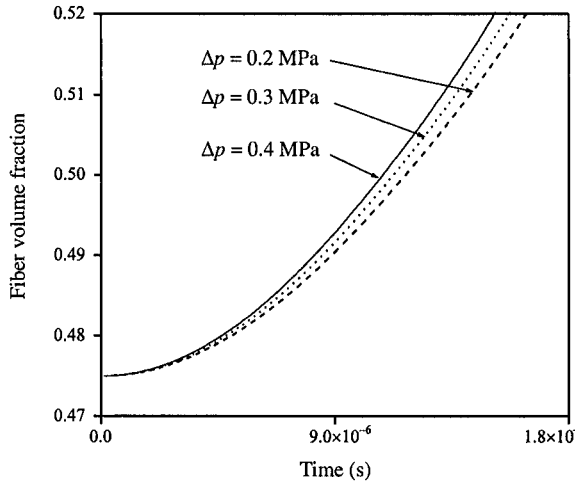

Figure 13. Variation of the fiber volume fraction with time due to closure of voids.

4.4 Squeezed Creep Flow of Resin

A simplified squeezed creep flow model is proposed here on the basis of the configuration shown in Figure 1. In this model, it is assumed that the effect of

fiber reinforcement can be ignored during the process of squeezed creep flow of the matrix melt. Considering the features of the strip specimens often used in experiments, namely, $L_l \gg L_w$, the squeezed flow in the y-direction can be ignored. Hence, the problem can be simplified to a 2D (in the x-z plane) case, as shown in Figure 14.

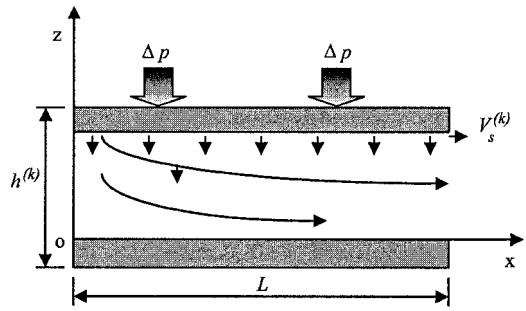

Figure 14. Schematic representation of the squeezed creep flow of the matrix melt.

For the composite laminate (Figure 1), $h_0^{(k)} = h_m$ = constant. Let $\xi = \rho L(h-h_0)/(\rho h_0 L) \equiv (h-h_0)/h_0$ be the relative loss of matrix volume due to squeezed creep flow, where $h_0 = \sum_k h_0^{(k)} = Nh_m$ is the initial total thickness of composite laminate. It is given[11] that

$$\xi = \frac{1}{N}\left\{\sum_{k=1}^{N}\left[1-\frac{L_w \Delta p}{4}\left(\frac{h_m}{L_l}\right)^2 \int_{t_k^0}^{t} \frac{1}{\eta^{(k)}} d\tau\right]^{-\frac{1}{2}}\right\}. \tag{37}$$

Since $(h_m/L_l) \ll 1$, expanding the right-hand side of Eq. (37) with respect to (h_m/L_l) and retaining the first order term give

$$\xi = \frac{L_w \Delta p}{8}\left(\frac{h_m}{L_l}\right)^2 \sum_{k=1}^{N} \int_{t_k^0}^{t} \frac{1}{\eta^{(k)}} d\tau + o\left[\left(\frac{h_m}{L_l}\right)^4\right] \approx \frac{1}{8}\left(\frac{F}{L_l}\right)\left(\frac{h_m}{L_l}\right)^2 \sum_{k=1}^{N} \int_{t_k^0}^{t} \frac{1}{\eta^{(k)}} d\tau \tag{38}$$

Since the viscosity coefficient $\eta^{(k)}$ depends on temperature *via* Eq. (15), the relationship between $\eta^{(k)}$ and time (t) can be obtained, provided that the temperature history in each layer, such as that shown in Figure 14, is known.

In Eq. (38), it can be readily seen that the loss of matrix is proportional to the external pressure Δp or the applied external force per unit length (F/L_l), and to the ratio of the matrix thickness in each layer against the length of the specimen, h_m/L_l. In practical reheating processes, relatively high external pressures, Δp, are often used to suppress the occurrence of thermal deconsolidation. In this case, small-sized specimens may suffer greatly from loss of matrix due to squeezed

flow of the melting matrix. Equation (38) also indicates that the loss of matrix is inversely proportional to the viscosity of the matrix melt, which depends strongly upon temperature. Since the matrix temperature depends on two factors, heating power and heating time, an appropriate balance should be established to reduce the loss of matrix material.

5 Conclusions

The present analysis shows that the thermal deconsolidation of thermoplastic matrix composites is primarily attributable to two essential factors. One is the decompaction behavior of the fiber network, and the other is the elasticity of the matrix melt. The decompaction of fiber network produces the driving force for void growth, and the elasticity of the matrix melt enables the matrix melt to carry the traction. Other phenomena, such as migration of voids and reconsolidation may also appear in a thermal deconsolidation process. These issues will be discussed in a future work.

It is shown in the present chapter that the apparent migration of voids during thermal deconsolidation is not really due to the movement of voids. Instead, it is actually a process of void formation and closure. Reconsolidation is another event associated with the migration of voids. In addition to the requirement that the temperature of the matrix must be sufficiently high so that the melt is in a fully liquid state, whether or not reconsolidation takes place also depends on the ratio of the external load to the compressibility of the fiber reinforcement in the second run of compression. An adequate external load is the sufficient condition for the suppression of deconsolidation and the realization of reconsolidation, but it may also result in a considerable squeezed flow of matrix,[9] which should be carefully considered to keep a balance between the two events.

6 Acknowledgement

This work was supported by the Australian Research Council, and the authors are grateful for this support.

7 References

[1] T. G. Gutowski, Ed. (1997) *Advanced Composites Manufacturing*, John Wiley & Sons, Inc., London, New York, Sydney, Toronto.

[2] D. M. Bigg, D. F. Hiscock, J. R. Preston, E. J. Bradbury (1988) High performance thermoplastic matrix composites, *J. Thermopl. Compos. Mater.* **1**, 146.

[3] F. N. Cogswell (1992) *Thermoplastic Aromatic Polymer Composites*, Butterworth-Heinemann Ltd, Oxford, London, Boston, Sydney, Tokyo, Toronto.

[4] I. W. Lee, G. S. Springer (1987) A model of the manufacturing process of thermoplastic matrix composites, *J. Compos. Mater.* **21**, 1017.

[5] I. Y. Chang, J. K. Lees (1988) Recent development in thermoplastic composites: a review of matrix systems and processing methods, *J. Thermopl. Compos. Mater.* **1**, 277.

[6] P. Davies, W. J. Cantwell, P. Y. Jar, P. E. Bourban, V. Zysman, H. H. Kaush (1991) Joining and repair of a carbon fibrereinforced thermoplastic, *Composites* **22**, 425.

[7] X. R. Xiao (1985) A model for the deconsolidation phenomenon in induction heating of thermoplastic resin composites, *Proc. 9th Int. Conf. Composite Materials (ICCM9)* (Ed. A. Miravete) Vol. II, p. 243.

[8] F. Henninger, L. Ye, K. Friedrich (1998) Deconsolidation behaviour of glass fibrepolyamide 12 composite sheet material during post-processing, *Plastics, Rubber and Composites and Applications* **27**, 287.

[9] C. Ageorges (2000) Resistance welding of thermoplastic matrix composite materials, PhD Thesis, University of Sydney.

[10] L. Ye, M. Lu, Y. W. Mai (2002) Thermal deconsolidation of thermoplastic matrix composites – I. Growth of voids, *Compos. Sci. Technol.* **62**, 2121.

[11] M. Lu, L. Ye, Y. W. Mai (2004) Thermal deconsolidation of thermoplastic matrix composites – II. "Migration" of voids and "reconsolidation", *Compos. Sci. Technol.* **64**, 191.

[12] R. I. Tanner (2000) *Engineering Rheology*, Oxford University Press, New York.

[13] R. M. Ogorkiewiz, Ed. (1974) *Thermoplastics – Properties and Design*, John Wiley & Sons, London, New York, Sydney, Toronto.

[14] C. O. Horgan, D. A. Polignone (1995) Cavitation of nonlinearly elastic solids: A review, *Appl. Mechanics Rev.* **48**, 471.

[15] A. N. Gent (1990) Cavitation in rubber: a cautionary tale, *Rubber Chem. Technol.* **63**, G49.

Chapter 14

Long Fiber-Reinforced Thermoplastic Composites in Automotive Applications

Tapio Harmia, Juha Hartikainen, Mathias Lindner
Future Advanced Composites and Technology Ltd., Kaiserslautern, Germany

1 Introduction

Long fiber-reinforced thermoplastics (LFT) are a relatively new class of fiber-reinforced materials in the field of composites. According to the fiber length, they take an intermediate position between injection molded short fiber-reinforced thermoplastics (SFT) and compression molded glass mat-reinforced thermoplastics (GMT).[1-9] However, LFT show better mechanical properties and even new property combinations compared to the corresponding SFT and GMT composites (Table 1).

Table 1. Typical mechanical properties of short- and long glass fiber-reinforced thermoplastics.

Material	*Tensile strength (MPa)*	*Tensile modulus (GPa)*	*Charpy impact at 23°C (kJ/m²)*
PP	30*	1.5	n.b.**
PP LGF 30	110	7.5	60
PP SGF 30	85	7	45
PA66	85*	3	n.b.
PA66 LGF 50	260	18	95
PA66 SGF 50	230	16	85
PA6	85*	3	n.b.
PA6 LGF 50	240	17	100
PA6 SGF 50	225	15	90

* Yield stress; ** Not breaking

LFT combine low production costs and high production rates of GMT with the superior properties, close to those of advanced continuous fiber-reinforced plastics (CFRP) and can be converted using compression, extrusion-blowing or injection molding equipment. To expand the range of these materials, more and more fiber-matrix combinations are constantly developed. So far, natural, glass, aramid, and carbon fibers are used in typical matrix polymers, such as polypropylene (PP) and various polyamides (PA). Other advantages of LFT composites over the competing SFT and GMT materials include: (i) no need for semi-finished pre-compounding (in-line extrusion, compression molding), less labor-intensive, great freedom in material modification, (ii) easy recycling, (iii) lower injection pressures during the injection molding, due to the better flow properties of long fiber materials, which reduces investment and production costs, (iv) very good surface quality of the produced parts, (v) shorter cycle times, and (vi) lower rejection rates.

The use of fiber-reinforced plastics and especially LFT composites in the automotive industry is steadily increasing, which is mainly a consequence of the low cost and good mechanical properties of the parts based on these materials. The increased safety in regard to high energy absorption offered by these materials and the design freedom enabled by thermoplastic parts and injection molding, cause an increasing demand of LFT materials. Applications in the automotive industry based on LFT materials range from interior instrumental panels, bottle holders, *etc.* (Figure 1), to parts "under the hood", such as components of the cooling system

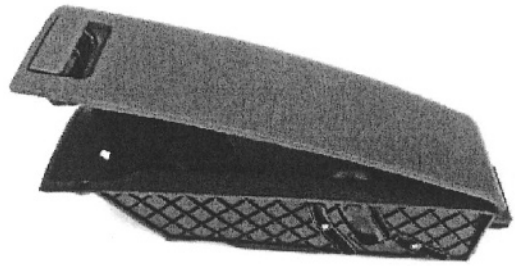

Figure 1. Bottle holder of VW T5 Multivan based on FACTOR polypropylene reinforced with 30 wt.% long glass fibers.

(Figure 2). The requirements to the parts in different applications define the level of, *e.g.*, material performance, surface quality and thermo-mechanical properties. In this chapter, the particularly interesting group of thermoplastic composite materials applied to different automotive applications is presented in a variety of cases. These cases show that the special needs of the automotive industry can be covered with the application of optimized LFT materials.

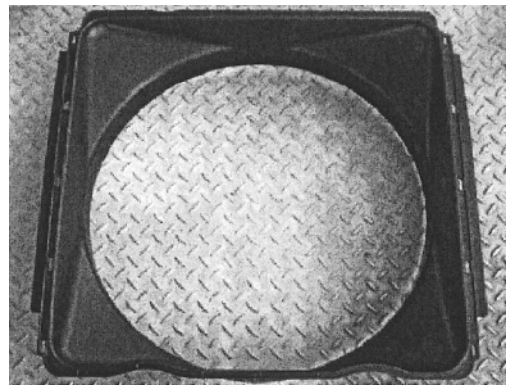

Figure 2. Housing of a cooling ventilator of a tractor (Fendt) based on FACTOR LGF-reinforced polypropylene.

2 Long Glass Fiber-Reinforced Polypropylene with Mineral Fillers

Part and material optimization is frequently related to the improvement of stiffness. In LFT materials, the stiffness is known to be higher compared to short fiber-reinforced composites, but even higher modulus than achieved by long fibres is required in some automotive parts. The diagram in Figure 3a shows that the stiffness of long glass fiber/polypropylene composites can be further improved by adding mineral fillers as a secondary "reinforcement", resulting in a multicomponent hybrid system. The advantages of the use of the secondary reinforcement are also shorter cooling time in the injection molding cycle due to the high thermal conductivity of the fillers and reduced warpage of the molded parts. As in the case of two-component systems comprising a thermoplastic matrix and mineral fillers,[10,11] the impact toughness and the tensile strength of LFT hybrid composites are usually slightly decreased compared to the corresponding materials without filler. However, property changes due to the filler addition are known to depend strongly on the fiber loading.[12] An LFT system with hybrid reinforcement is already used in automotive parts, such as the interior cover of a rear compartment (Figure 4).

The understanding of the effect of the fillers on the properties of LGF-reinforced polypropylene composites is a complex matter, since there is a considerable amount of different factors affecting the material behavior. In general, fiber loading improves the mechanical behavior of polypropylene, whereas the addition of fillers increases the modulus, but decreases the strength and toughness. However, at low fiber contents the decrease in strength and toughness is minor compared to the case of higher fiber concentration. This can be attributed to the fact that, in the

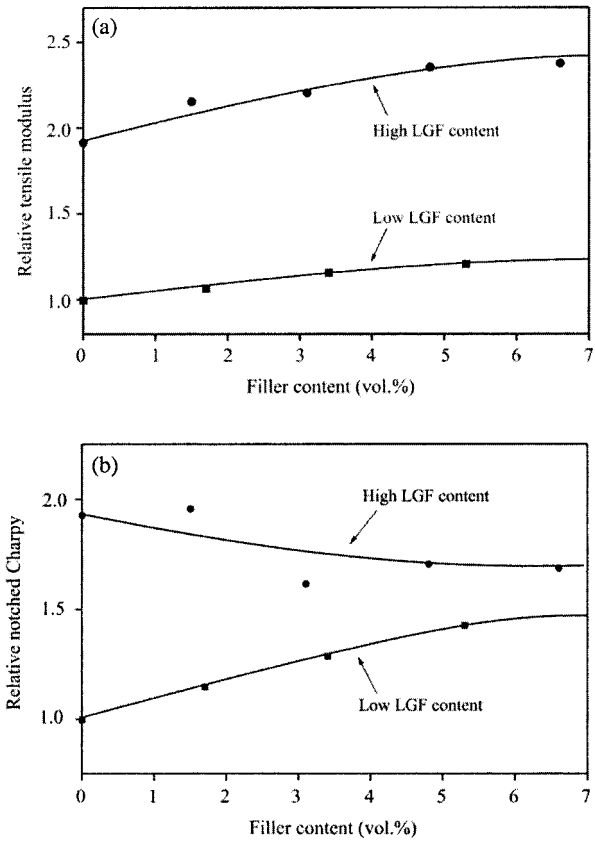

Figure 3. Normalized tensile modulus (a) and notched Charpy impact toughness (b) of PP reinforced with LGF and mineral filler at low and high fiber contents.

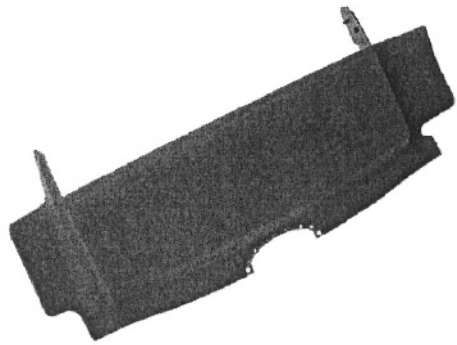

Figure 4. Interior cover of a trunk of Mercedes Benz SL. The material is based on FACTOR LGF-reinforced PP including a filler (molder: Intier Automotive).

former case, the matrix dominates the energy absorption mechanisms whereas the effect of fibers is predominant at higher fiber contents. Actually, even improved impact strength can be observed due to filler addition at low fiber content, which has been evidenced both by the pendulum and the falling weight impact toughness tests (Figure 3b).

3 Long Fiber-Reinforced Polyamide 66 with Minimized Water Absorption

Water absorption and stability of the materials based on hygroscopic polymers, such as polyamides, is an important matter in several automotive applications. For instance, the parts of the cooling system of a car are subjected to extreme conditions, *i.e.*, high temperature, high pressure, and chemicals for very long periods of time. In the case of LGF/polyamide composites, there are three main damages caused by water, chemicals, and heat: (i) plasticization of the polymer matrix by water, (ii) polymer chain degradation, and (iii) decrease of the interfacial properties between the glass fiber and polyamide. Plasticization is caused by the replacement of the interchain hydrogen bonds of polyamide by water molecules, resulting in improved toughness, but also in distinctly lower stiffness and strength. On the other hand, the two latter damages result in decreased long term mechanical properties. In order to minimize the reduction in mechanical properties as a function of time, expensive high temperature-resistant matrices, such as semiaromatic polyamides, are often needed. An alternative route to meet such requirements is to apply long glass fiber-reinforced polyamide 66 with a special stabilization of the matrix. In this case, the long fiber reinforcement provides high stiffness even at high temperatures and the special additives lead to decreased water uptake (Figure 5) and also good long term stability. These results suggest that more expensive high temperature polymers can be replaced by LGF/PA66, resulting in a good performance and economic benefits.

4 Long Fiber-Reinforced Thermoplastic Styrene Resins for Car Interior Applications

The main requirements to the interior parts of a car are attractive appearance combined with good mechanical properties and matching tight tolerances of the part after processing. Thermoplastic styrene-based polymers are often chosen due to the above mentioned aspects. In many cases, neat styrene-based thermoplastics need to be reinforced with glass fibres in order to fulfill these requirements. Depending

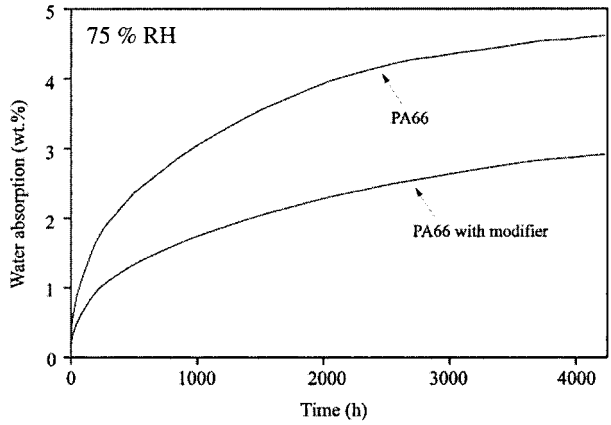

Figure 5. Water absorption of PA66 with and without a special modifier as a function of time at room temperature and at 75 % relative humidity.

on the actual application, different types of styrene thermoplastics are used, such as: polystyrene (PS), poly(styrene acrylonitrile) (SAN), acrylonitrile-butadiene-styrene (ABS), and also blends of polycarbonate (PC) and ABS (PC/ABS).

Figure 6 is a schematic representation of a novel concept in the manufacturing of automobile parts based on LGF-reinforced styrene-based thermoplastics.[13] One of the main benefits of this approach is high flexibility, allowing different adjustable levels of mechanical properties. Long glass fibers are provided as a LGF concentrate with 60 wt.% fiber content. The final fiber concentration in the parts is set during the processing by mixing with different neat "diluent" resins. Thus, the final properties, such as thermal behavior, stiffness or impact toughness, can be controlled during the part manufacture. Figure 7 shows DMTA curves for LGF-reinforced styrene composites based on this concept. It can be seen that the

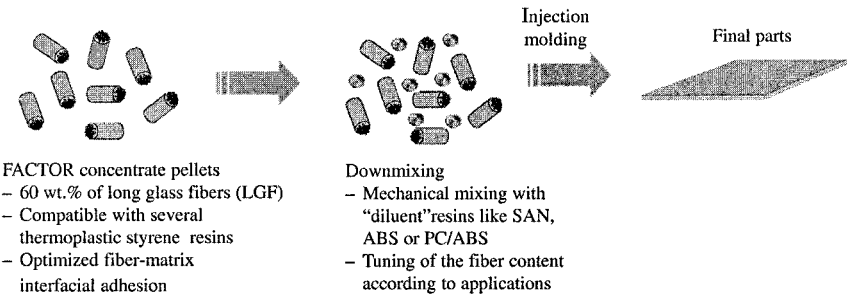

Figure 6. A novel concept in the manufacturing of long fiber-reinforced thermoplastic composites by using a base concentrate and different types of diluent polymers.

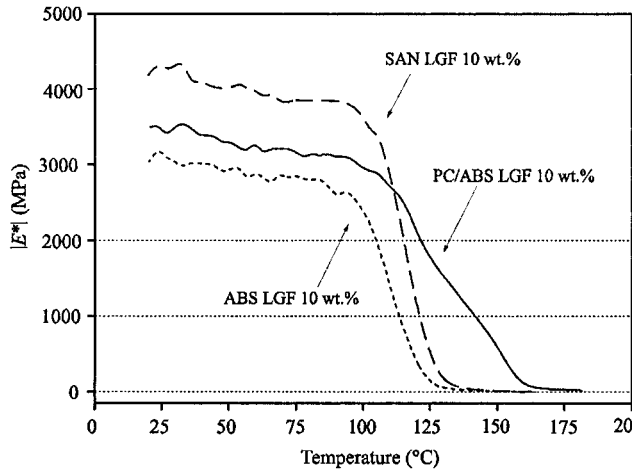

Figure 7. DMTA curves of styrene-based LGF composites with three different matrix systems: SAN, ABS, and a PC/ABS blend.

thermal properties, as well as the modulus at room temperature, can be modified just by using different diluent polymers.

5 Conclusions

The use of long glass fiber-reinforced thermoplastics in automotive applications was presented in three different cases, showing that the varying requirements can be met by choosing the right material system and tailoring the material properties. (i) The stiffness of LGF/PP can be improved and "fine-tuned" by using a hybrid reinforcement, such as mineral fillers. (ii) High temperature-resistant LGF/polyamide 66 composites are suitable materials for applications under the motor hood, such as parts of the cooling system. (iii) LGF-reinforced styrene-based thermoplastics are very interesting materials for car interior parts; the concentrate concept allows a very flexible adaptation of the material properties.

6 References

[1] F. van Hattum, S. van Breugel (2001) LFT: the future of reinforced thermoplastics?, *Reinforced Plastics* **45**, 42.

[2] D. E. Spahr, K. Friedrich, J. M. Schulz, R. S. Bailey (1990) Microstructure and fracture behaviour of short and long fibre-reinforced polypropylene composites, *J. Mater. Sci.* **25**, 4427.

[3] J. L. Thomason (2002) The influence of fibre length and concentration on the properties of glass fibre reinforced polypropylene: 5. Injection moulded long and short fibre PP, *Composites A* **33**, 1641.

[4] X. Zhou, Q. Lin, G. Dai (2002) Studies on mechanical properties of discontinuous glass fiber/continuous glass mat/polypropylene composite, *Polym. Polym. Compos.* **10**, 299.

[5] J. Karger-Kocsis, T. Harmia, T. Czigány (1995) Comparison of the fracture and failure behavior of polypropylene composites reinforced by long glass fibers and by glass mats, *Compos. Sci. Technol.* **54**, 287.

[6] L. W. Glenn, H. C. Kim, D. E. Miller, C. S. Ellis (1998) Toughness of long glass fiber reinforced thermoplastics, *J. Reinf. Plast. Compos.* **17**, 901.

[7] T. Harmia (1996) Fatigue behavior of neat and long glass fiber (LGF) reinforced blends of nylon 66 and isotactic PP, *Polym. Compos.* **17**, 926.

[8] J. Hollin, D. Miller, D. Vautour (1998) A comparison of transverse properties of 50% short and long glass fiber reinforced nylon 6/6 resin, *J. Reinf. Plast. Compos.* **17**, 1617.

[9] D. E. Mouzakis, T. Harmia, J. Karger-Kocsis (2000) Fracture behaviour of discontinuous long glass fibre reinforced injection moulded polypropylene, *Polym. Polym. Compos.* **8**, 167.

[10] J. Karger-Kocsis (1995) Microstructural aspects of fracture in polypropylene and in its filled, chopped fiber and fiber mat reinforced composites, in *Polypropylene: Structure, Blends and Composites* (Ed. J. Karger-Kocsis) Chapman & Hall, London, p. 142.

[11] B. Pukanszky B (1995) Particulate filled polypropylene: structure and properties, in *Polypropylene: Structure, Blends and Composites* (Ed. J. Karger-Kocsis) Chapman & Hall, London, p. 1.

[12] N. Hargarter, K. Friedrich, P. Catsman (1993) Mechanical properties of glass fiber/talc/polybutylene-terephthalate composites as processed by the radlite technique, *Compos. Sci. Technol.* **46**, 229.

[13] J. Hartikainen, M. Lindner, T. Harmia (2002) Long glass fibre reinforced styrene based polymers, in *Proc. 5th Int. AVK-TV Conf. Reinforced Plastics and Thermoset Moulding Compounds*, Baden-Baden, Germany, pp. A8.1–A8.6.

Part IV

Mechanical Performance of Macrocomposites

Chapter 15

Deformation Mechanisms in Knitted Fabric Composites

Miro Duhovic, Debes Bhattacharyya
Centre for Advanced Composite Materials, School of Engineering, University of Auckland, Auckland, New Zealand

1 Introduction

Over the past decade, there has been a significant amount of research interest in the field of thermoplastic composites, especially in the fabric-reinforced sheet materials. The understanding of the unique behavior of these sheet materials during forming and the practical viability of various forming processes is crucial in assessing their utilization and applicability. A relatively recent innovation in this field is the use of knitted textiles as the reinforcement. Knitted fabrics offer a number of potential advantages over straight-fiber fabrics: they can be stretched in both directions during forming, thus increasing the potential for forming complex and deeply curved components,[1-3] have excellent impact, fracture toughness and energy absorption properties,[4-6] and (in the case of 3D knits) exhibit improved out-of-plane mechanical properties.[2,7,8] Figure 1 compares knitted fabrics with some other existing reinforcement types.[9]

So far, the bulk of literature has concentrated on characterizing the mechanical properties of both thermosetting-[6,10,11] and thermoplastic-based[12,13] knitted composite materials. The modeling of the mechanical properties (mainly stiffness and tensile) has also been popular.[14-17] However, limited literature exists on the forming property characteristics of knitted fabric-reinforced thermoplastics[18,19] and their processing properties are still poorly understood. In fact, most of the literature on forming properties deals with unidirectional,[20,21] mostly woven[22-26] and, to a lesser extent, braided reinforcements,[27] rather than knitted reinforcements.

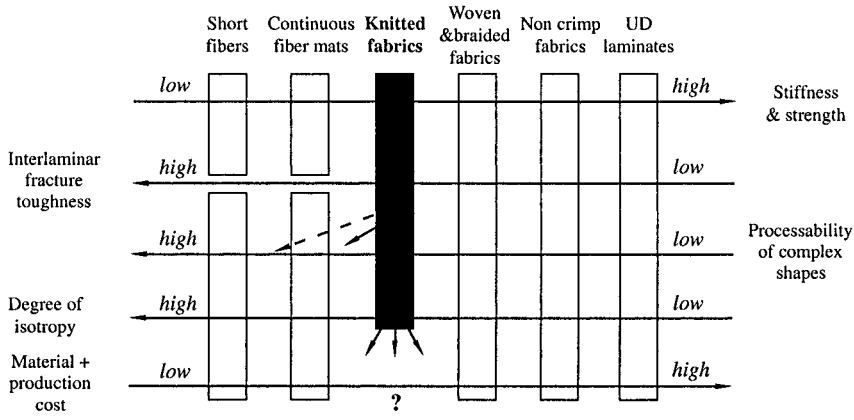

Figure 1. Overview and comparison of some composite properties of the existing reinforcements (modified from[9]).

Although the actual mechanism of sheet forming can be quite complex, a general understanding of the process and material characteristics can be gained through a series of simple experiments including hot-tension, dome-forming, cup-drawing, V-bending, and picture-frame experiments. They are designed to subject the material to selective modes of deformation allowing a more systematic approach to the analysis. One way of obtaining a physical measure of the forming behavior is to develop kinematic models based purely on geometrical changes. These changes can be measured using grid strain analysis (GSA) where grid points before and after the forming process are used to calculate forming strains. The experiments not only provide a general understanding, but also serve as a check for any predictive work.

When sufficient data regarding the material and other processing parameters are available, numerical simulations can provide time-saving predictions of the forming behavior. For materials with complex reinforcing structures, such as knitted fabrics, the material model must be able to accommodate the most important parameters, so that the material can be simulated accurately. Since the forming behavior of textile composites is governed by their reinforcing structures, the examination of the reinforcement can identify these important parameters. It has been shown that best results can be achieved using a low-viscosity matrix, *i.e.*, when the lubricating effects are significant. Therefore, the understanding of the deformation behavior of the reinforcing structure alone is of critical importance. To investigate these parameters physically would be very difficult, because of the scale and level of detail required; however, using advanced numerical simulations, a large quantity of information may be obtainable.

The overall approach to this study is based on experimental investigations and advanced micronumerical simulations forming the ground for the subsequent predictive macronumerical forming simulations.

2 Knitted Fabrics

Knitting is the process of manufacturing textile structures with a single yarn or a set of yarns moving in only one direction. Unlike weaving, where the yarns cross over one another, knitted fabrics are produced by looping the yarn through itself to make a chain of stitches which are then connected together (Figure 2). There are two knitted fabric types, those produced by weft knitting and those produced by warp knitting, where warp and weft refer to the knitting directions. In a weft knit, the fabric is essentially produced with one yarn, whereas in a warp knit the number of yarns used depends on the required fabric width. The knitting directions are also termed wale and course, as shown in Figure 2.

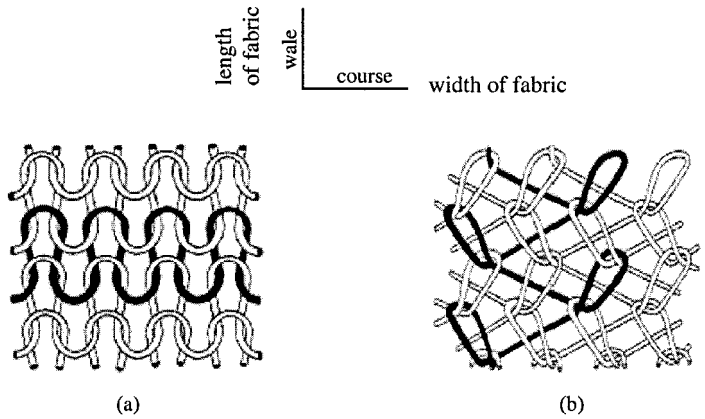

Figure 2. Schematic representation of knitted fabrics:[10] (a) weft knit, (b) warp knit.

In this study, two weft knitted structures, the "full milano" and "1×1 rib", are investigated. One reason for these structures to be chosen is that the rib structure generally possesses an unusually high degree of elasticity. As a result, yarns made form high performance fibers with very little inherent elasticity can produce a reinforcing fabric with significant stretchability. This is even more the case for the milano rib structure. These are also among the simplest weft knit configurations that generate a balanced fabric.

3 Material Characterization and Deformation Behavior

3.1 Raw Materials

Material characterization experiments were performed on E-glass fiber polypropylene specimens of standard or simple geometry with fiber volume content of 20%, under controlled experimental conditions, to yield data and qualitative results, which may be generally applied to a variety of situations.

3.2 Material Characterization

For the present research, a number of characterization and investigative tests were undertaken: (i) tensile testing, to study the in-plane elastic behavior of the material, (ii) V-bending, to investigate the forming of simple 2D components, (iii) dome forming, to assess the ability of the material to form 3D curved shells, and (iv) cup forming, to determine the drawing behavior of the material.

3.2.1 Tensile Testing

The main purpose of the tensile tests was to determine the stress-strain and modulus curves in the warp and weft directions for the material in its molten state, for later use in the construction of a numerical model in PAMFORM™. Experiments indicate that the elastic behavior of the dry fabric is very similar to that of the molten composite material at reasonably low forming rates (< 100 mm/min), which implies that viscous effects have a minimal impact on the stress-strain behavior of the molten composite under these conditions.

3.2.2 V-Bending

Previous research of the sheet forming of continuous fiber-reinforced plastic materials has included V-bending tests, which, due to the inextensibility of the continuous fibers, have focused on the viscous interply shear behavior of such materials during forming.[28] In the case of knitted fabric-reinforced thermoplastics, the extensibility of the fabric complicates the nature of the deformation mechanism, compared to straight or almost straight fibers and, in this context, V-bending tests offer a means of assessing the relative magnitude of the viscous shearing and fabric stretching mechanisms postulated to occur during 2D forming.

One of the goals of the matched die V-bending was to manipulate the tension in the material during forming, thereby dictating the degree to which the material stretched, with the aim of developing a correlation between the clamping force and the material strain. An evaluation of the spring-back/spring-forward

behavior was also of interest, as these phenomena are of critical importance for the part quality.

3.2.3 Dome Forming

The manufacture of hemispherical domes is well established, particularly in the field of composites, as a method of assessing the relative ability of the materials and processes to produce doubly curved shell components.[25] In the case of knitted fabric-reinforced thermoplastics, some of the key parameters relevant to product manufacture are: (i) material strain behavior (stretching *vs.* draw-in), (ii) surface finish, (iii) gross wrinkling and buckling of the sheet material, and (iv) interply shear in the laminate.

Dome forming experiments were undertaken to investigate these factors at a range of temperatures, with the aim of determining the optimum forming temperature (in terms of surface finish and absence of wrinkling) and assessing the overall feasibility of matched die forming resulting in doubly curved components from the weft knitted fabric-reinforced thermoplastics.

3.2.4 Cup Forming

Deep drawing experiments can be used to determine the practical forming limits of a material and to estimate the optimum forming parameters for a given drawing operation. Recent work in this area has focused on the relative amounts of stretching and drawing in cup forming operations with knitted material.[19] The aim of the cup-forming tests was to determine the stretch-forming limit of the material and to qualitatively examine the relationship between flange clamping and the onset of wrinkling.

4 Experimental Results and Grid Strain Analysis

4.1 Tensile Testing

The shapes of the stress-strain curves derived from the molten specimens exhibit similar characteristics of the fabric itself, with added lubricating and viscous effects due to the chemical sizing and the matrix. The general model is of loop stretching, becoming progressively more difficult with strain until the loops become fully extended and the fibers fail under direct tension, but more detailed micromechanical modes have been proposed[29,30] and are discussed in Section 5. The tensile modulus curves, which can be used for macronumerical simulation purposes, were derived by taking a moving average of five incremental stress-

strain gradients from the test results. Figure 3 shows the simplified modulus curves for the molten knitted composite material in the warp and weft directions.

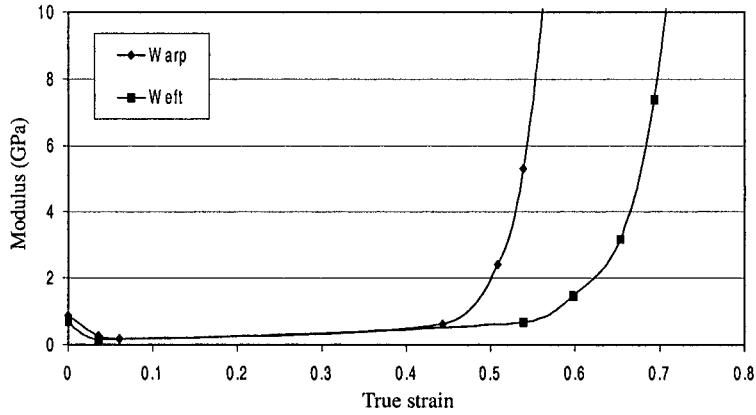

Figure 3. Modulus curves of warp and weft molten knitted fabric composites.

4.2 V-bending

To assess the strain and the interply shear in the material, a novel version of the GSA technique was adopted. Lines were marked on the upper and lower surfaces of the specimen at 10 mm intervals, so that the lines on both sides were exactly aligned prior to forming. After processing, the strain on each surface was assessed by measuring the grid intervals. The interply shear can be estimated from the misalignment of corresponding marks on the upper and lower surfaces. The lines remained coherent during forming and seemed to yield strains, which concurred with a visual assessment of strain from the changes in the fabric pattern. Four of the samples, two knitted and two woven specimens (for comparison), are shown in Figure 4. Inspection of the lines on the samples reveals that the knitted material deforms through pure bending (no interply shear) at 160 °C, with slight interply shear (*via* stretching of the individual layers) occurring at 170 °C. On the contrary, the biaxial material deforms purely through interply shear at all temperatures, with buckling observed at the inner nose radius of the 160 °C test specimen. Another interesting observation involves the variation in the spring-back/spring-forward behavior at the tested temperatures. In the softened state, the knitted material demonstrated spring-back, rather than the spring-forward observed in the molten samples. It appears that at the lower temperatures, the thermal effects are surpassed by the mechanical spring-back in the much stiffer material. Indeed, the thermal effects may be rendered less dramatic as there is no phase change in the matrix. Clearly, the spring-forward behavior of this material is a thermo-

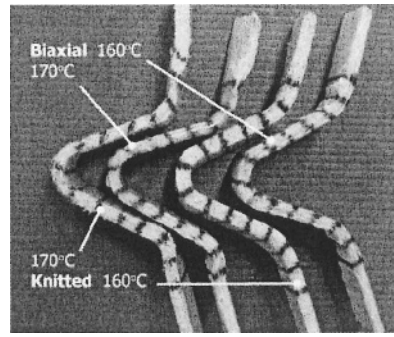

Figure 4. Knit and woven V-bend specimens.

mechanical phenomenon, which depends on the temperature (and hence the stiffness) of the matrix and on the effects of anisotropic thermal expansivity,[31] solidification, and changes in fiber distributions.

4.3 Dome Forming

Given the results of the V-bending experiments, which showed that the behavior of the molten knitted material varied little with temperature, multiply domes were formed from the softened material at 150-170 °C, as well as from molten sheets. A satisfactory surface finish proved difficult to achieve with the rigid aluminum male stamp, whereas a silicone rubber male stamp accommodated the thinning of the material during forming and allowed reconsolidation and superior finishing of the entire dome surface. The dome forming tests clearly demonstrated the extreme formability of the material; with no clamping of the blank whatsoever, the knitted fabric sheet readily formed hemispheres with no wrinkling or excessive draw-in over a range of forming temperatures.

The deformation mode of the knitted material varied with the blank temperature. Figure 5 shows a digitized representation of the grids on two of the 3-ply knitted fabric domes, along with a biaxial straight fiber-reinforced dome (for comparison). The orthogonal reference lines, showing the original grid axes, clearly indicate that when molten, the knitted fabric demonstrates larger amounts of draw-in (and correspondingly less stretching), as compared to the softened material. However, even when molten, the amount of draw-in does not reach the zero-strain extreme revealed by the biaxial material.

To further investigate the strain fields within the dome, the GSA software package was employed to calculate the principal strains in the material, shown as "arrow diagrams", as well as the changes in thickness due to stretching over the surface of the dome, shown using contour shading (Figure 6a-c). From these

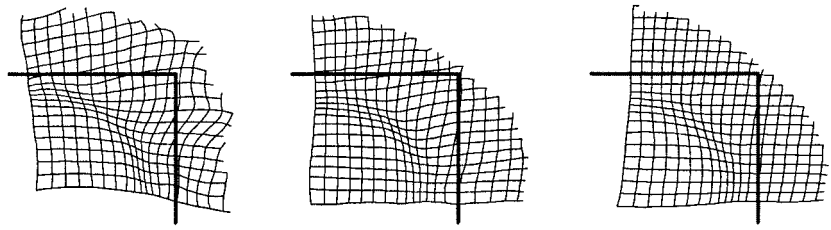

(a) Dome 1
Biaxial woven material
(180 °C)

(b) Dome 2
Molten knitted material
(180 °C)

(c) Dome 3
Softened knitted material
(150 °C)

Figure 5. Draw-in comparison of domes.

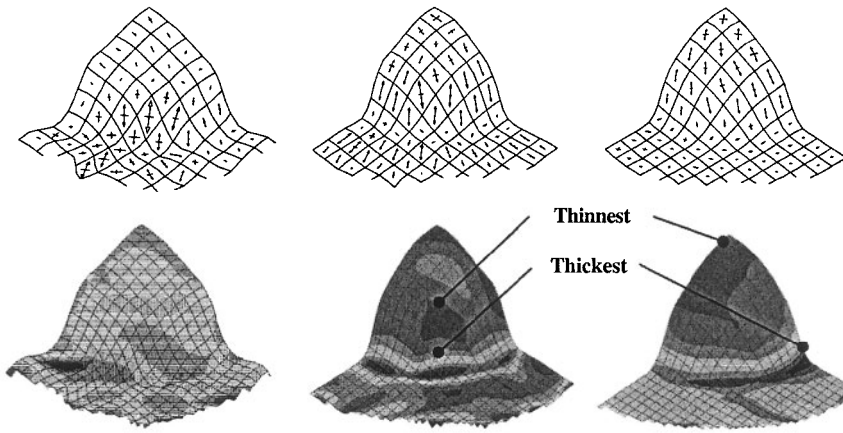

(a) Dome 1
Biaxial woven material
(180 °C)

(b) Dome 2
Molten knitted material
(180 °C)

(c) Dome 3
Softened knitted material
(150 °C)

Figure 6. GSA analysis of ∅100 mm domes.

diagrams, the different modes of deformation in the three domes may be clearly identified and the important observations are summarized in the following: (i) As expected, the biaxial dome shows no strain in the fiber directions, and deforms primarily through trellising (shear deformation) in the region at 45° to the fiber directions. It exhibits minimal variation in thickness, and there is no pattern evident in the thickness contours. This finding is in agreement with the results of earlier research.[14,25] (ii) The softened knitted dome forms almost exclusively by stretching, with fairly uniform strain around the middle of the dome and no significant strain in the flange whatsoever. There is a clear trend of decreasing thickness from the flange up to the top of the dome. (iii) The dome formed from molten knitted

material shows less stretching in the dome itself than for the softened specimen, with noticeable shear and linear strain in the flange. The stretching in the dome itself is less pronounced than in the softened specimen, and there is a definite region of thickening at the dome-flange transition due to draw-in. Interply shear of a similar magnitude to that observed in the V-bending tests has also been noted for this dome.

4.4 Cup Forming

In the cup forming experiments, maximum drawing depth without wrinkling was achieved with a fully clamped flange. Therefore, the test actually constituted stretch forming with no flange draw-in, resulting in tearing of the fabric, at which time the test was deemed to be complete. The final cup is shown in Figure 7, with the tear highlighted.

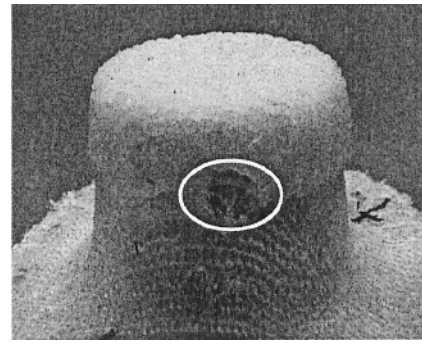

Figure 7. Final cup height with tear highlighted.

To draw a crude comparison with isotropic materials, such as sheet metals, this depth of cup constitutes an equivalent draw ratio (blank diameter/cup diameter) of approximately 2.9. Given that the theoretical maximum draw ratio for isotropic materials is about 2.7,[32] this result compares very favorably, although it must be stated that a superior ratio value does not necessarily indicate superior performance for sheet forming. Thinning and surface finish must also be taken into account, and it should be pointed out that in this case the surface finish is clearly very poor due to matrix migration. Another measure of relevance is the "areal draw ratio", the ratio of the final component area to the raw blank area. For woven fabrics, this has been found to be limited to 1.03,[28] although in this cup the ratio is 1.51, demonstrating far superior formability. The material's resilience to local failure was also tested. A sharp draw punch nose radius, which would be expected to cause failure with sheet steel at very small draw ratios, was not observed in the

knitted material due to the excellent strain transmission characteristics of the fabric.[33]

5 Textile Composite Deformation Mechanisms

When thermoforming parts from textile composite materials, it is useful to understand the deformation mechanisms, which take place inside them, so that the forming process can be optimized to produce parts of the best quality. The experimental observations and measurements considered in Section 4 are helpful for a general understanding, but do not provide enough detail to reveal the actual mechanisms. The following sections attempt to investigate these mechanisms in more detail.

The hierarchy of deformation modes for this family of composite materials can be divided into three categories: prepreg flow mechanisms, macro-level fabric deformation modes, and micro-level fabric deformation modes, each of which contains a number of different mechanisms.

5.1 Prepreg Flow Mechanisms

When the textile fabric reinforcement is combined with the matrix to form the composite prepregs, a set of deformation modes are introduced, which may be referred to as top-level deformation modes since they involve the movements of the reinforcement (macro- and micro-level fabric deformation mechanisms) and the matrix. They are in fact the conformation modes of the composite prepreg sheet or group of sheets, as is usually the case, during the forming process. The hierarchy of the top-level deformation modes consist of transverse flow, resin percolation, interply shear and intraply shear, as summarized by Cogswell[34] and revisited by Martin *et al.*[35,36]

5.2 Macro-Level Fabric Deformation Modes

The four types of macro-level fabric deformation modes, as shown in Figure 8, describe the deformations observed when looking at the fabric as a whole. However, the way in which each fabric complies to these modes is different and can be attributed to the deformations occurring within the textile structure itself. These sub-structure or micro-level deformation modes are the real mechanisms behind textile deformations and need to be identified in order to understand the material's behavior.

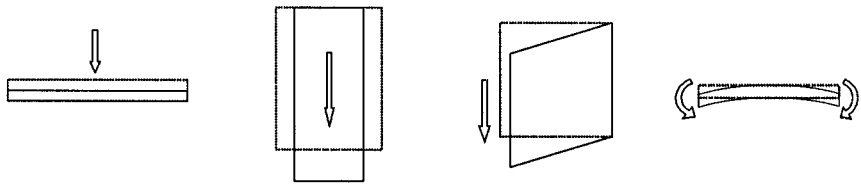

(a) Transverse compression (b) In-plane tension (c) In-plane shear (d) Out-of-plane bending

Figure 8. Macro-level fabric deformation modes.

5.3 Micro-Level Fabric Deformation Modes

Micro-level fabric deformation modes exist through the interaction of structured yarns within the fabric. Figure 9 shows what are generally believed to be the eight micro-level deformation modes for textile fabrics.

Inter-yarn slip, as shown in Figure 9a, occurs when the yarns that construct the fabric move over one another. It is one of the modes of deformation belonging almost exclusively to knitted fabrics. In this mode of deformation, the friction between the yarns becomes important since it determines where the onset of buckling will take place, as well as the magnitude of the forming forces required. Fortunately, the matrix and fiber chemical sizing (coatings) usually lubricate the yarn to help this mode of deformation.

Inter-yarn shear is a common mode of deformation in many woven fabrics. This is where the yarns rotate about their crossover points to accommodate the required deformation, Figure 9b. In fact, this type of mechanism has been reported

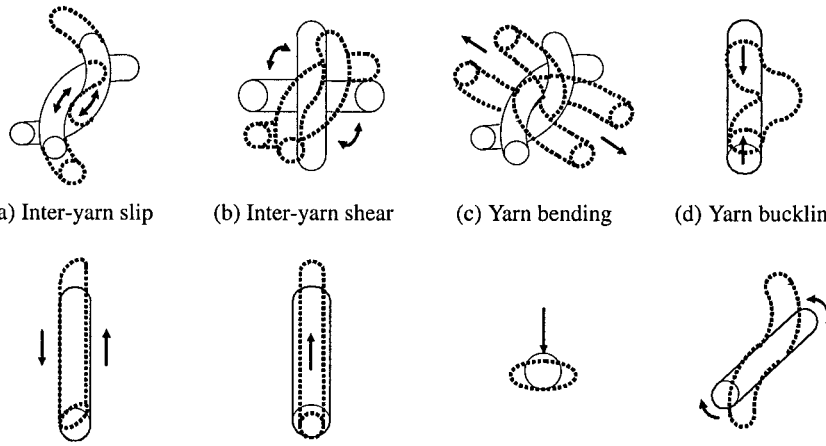

(a) Inter-yarn slip (b) Inter-yarn shear (c) Yarn bending (d) Yarn buckling

(e) Intra-yarn slip (Inter-fiber friction) (f) Yarn stretching (g) Yarn compression (h) Yarn twist

Figure 9. Micro-level fabric deformation modes.

to occur in multilayered continuous fiber-reinforced composites also, as outlined by Krebs *et al.*,[25] Martin *et al.*,[36] and Christie,[20] and is commonly referred to by many researchers as the "trellising effect". In knitted fabrics, depending on the orientation of the reinforcement, large in-plane tension and in-plane shear can be accommodated, but not in the same direction.

The yarn bending or "straightening" shown in Figure 9 is in many cases the most significant deformation mode in many textiles. It is the most influential mode in knitted fabrics because of the knit loop geometry. Straightening also occurs to a lesser extent in woven and braided fabrics depending on the amount of crimp or yarn undulation present in the fabric structure.

Out of all the different deformation modes, fiber buckling is the only unfavorable one since the material movement through this mode creates what is considered as defects, although it is quite difficult to observe with complex structures, such as knits and braids. Out-of-plane buckling usually occurs when the in-plane modes cannot accommodate the required deformation. In-plane buckling can also occur, but is less likely due to in-plane geometric constraints, Figure 9d.

The intra-yarn slip shown in Figure 9e coupled with yarn bending, Figure 9c, are the biggest contributors to a textile fabric force displacement curve. Intra-yarn slip is where the continuous fibers within the yarn slide past one another along the length of the fiber because of changes in fiber curvature during bending and unbending.

The yarn stretching, Figure 9f, while not so prominent at early stages of fabric deformation, is certainly present and contribute significantly to the deformation at larger strains. Although the reinforcing fibers used in composites are relatively brittle and exhibit very high stiffness moduli, strains of up to 5% can still occur through this mode.

Another fabric deformation mechanism to consider is yarn compression, Figure 9g, where forces at yarn crossover points compress the filaments in the yarn and cause them to flatten out and conform to the curvature of perpendicular yarns. Like fiber stretching, this can also be considered relatively insignificant and really starts to contribute to the load extension curve once the aforementioned mechanisms have been exhausted.

Finally, the yarn twist, Figure 9h, which has been observed in knitted fabrics and not so much in woven fabrics, imparts further resistance to the fabric deformation. This is where the yarn is subjected to one full turn during the manufacture of the fabric in order to create the looping structure of the knit. The twist creates a resistance to the increase in yarn curvature during fabric deformation.

5.4 Textile Fabric Force-Displacement Curve

The relative importance of each of these deformation mechanisms is fabric-specific and in some cases certain deformation modes may not be utilized at all.

During the deformation of a textile fabric, combinations of these mechanisms occur simultaneously and the influence of each mode changes continuously throughout the entire deformation. Figure 10 compares the force displacement curves for woven and knitted fabrics, with regions of the curves identified to show where certain deformation modes are thought to be of greatest influence.

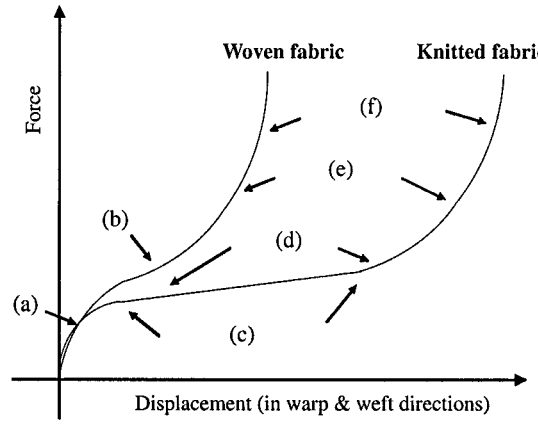

Figure 10. Textile fabric force displacement curves.

It can be seen that the curves for both the woven and knitted fabrics follow similar trends. Intra-yarn or inter-fiber friction (a) is most influential at the origins of both curves, starting out as the static friction that needs to be overcome to initiate the sliding of long fibers past one another.

For both fabrics, the next major regions (b) and (c) are caused by bending/unbending and resistance to twist. Friction is still present from here on, but is in the form of a lower dynamic friction force. Owing to its structure, a knitted fabric has more curved yarn to extend whereas a woven fabric, no matter what its degree of crimp, has far fewer. For knitted fabrics, inter-yarn slip (d) also contributes to the shape of the curve in this central region starting at around 10% extension and ending once the forces at the yarn crossover points become too large. Finally, yarn compression and extension (e) and (f), no doubt present throughout the entire extension, become most dominant at the final part of the curves and can contribute up to 5% of the total extension.

It is important to note that while the different regions of the force-displacement curves shown in Figure 10 have been drawn with similar orders of magnitude for explanation purposes, this is usually not the case in practice. For instance, actual force-displacement curves of woven fabric can look quite steep and linear, indicating that regions (e) and (f) are the most dominant. Furthermore, for most fabrics, region (a) will be significantly smaller than the rest of the curve.

5.5 Experimental Force-Displacement Curves

Experimental curves generated from warp direction tensile tests carried out on 1×1 rib fabric specimens produced from 68 tex E-glass fiber yarn are shown in Figure 11. The curves show that the initial inter-fiber friction, or region (a) in Figure 10, is a relatively small contributor to the fabric's total deformation energy. Other regions can be clearly identified and show similar characteristics to those described in Figure 10. Note that the specimens show a small mechanical property variation, as no two loops will have exactly the same geometry and may incur a varying degree of yarn damage during knitting. The tests provide an important part of the experimental verification for the numerical model discussed in Section 6.

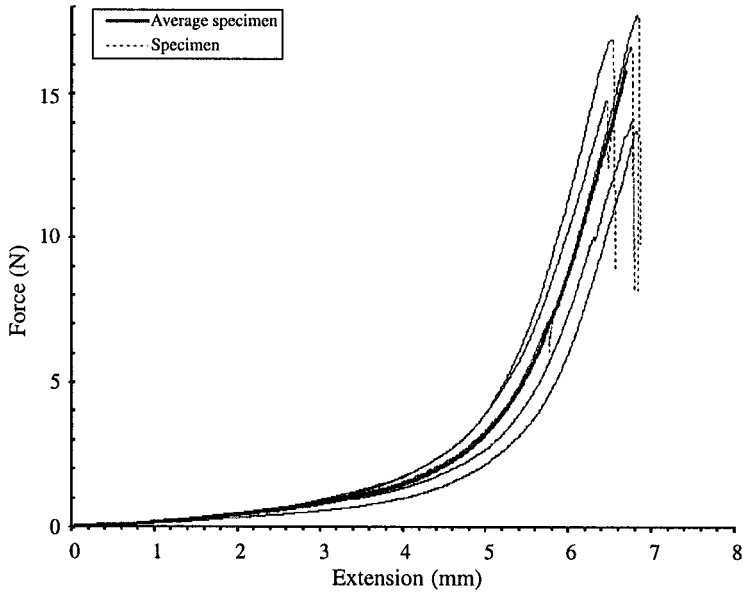

Figure 11. Average force-displacement curve for 1×1 rib specimen.

6 Modeling the Manufacture of the Reinforcement Architecture

In Section 4, it has been established that the most dominant factors influencing the sheet forming behavior of knitted fabric thermoplastics are associated with the micromechanics of their reinforcing structures. In this section, a model is developed to quantitatively analyze the contributions of the deformation

mechanisms described in Section 5. By setting up a model flexible enough to evaluate these mechanisms for some specific knit structures, more accurate simplified models can be developed for describing the forming behavior of textile composite materials in finite element software, such as PAMFORM™. Furthermore, the model could be developed to analyze the behavior of the knitted reinforcement in different forms of the matrix (*i.e.*, molten and solid), along with the failure modes, which could also be analyzed in detail. The knit manufacturing model is capable of producing models of many different weft-knit structures, their number being only limited by what can be produced on actual flatbed knitting machinery. In this study, the 1×1 rib structure has been chosen initially.

6.1 Model Set-Up

The manufacture of knitted fabrics is a high-speed dynamic contact problem, where knitting needles move back and forth at speeds of up to 1.5 m/s. This makes knit manufacture particularly suitable for modeling using the explicit dynamics code commonly utilized for crash and forming simulations. PAMCRASH™ has been used because of its extensive range of material models and contact algorithms most suited to the knitting process. Only a small quantity of the fabric is required for the analysis, therefore the number of needles used in the simulation has been limited to five. On real weft knitting machinery, there are hundreds of needles, their actual number depending on the desired fabric width and structure. For the 1×1 rib, it is possible to produce a coherent narrow strip of fabric that captures the repeating unit and can be used for experimental comparisons, as shown in Figure 12.

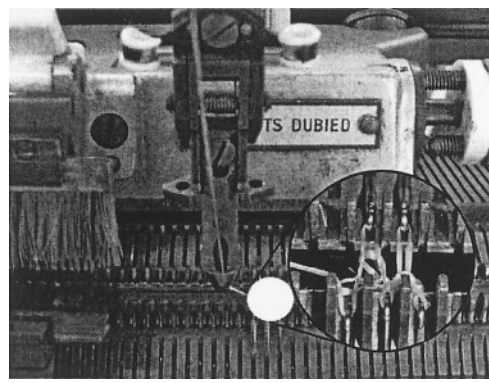

Figure 12. Real five needle knitting of 1×1 rib weft knitted fabric.

6.2 Model Input: Knitting Machine Parameters

Simulating the operation of a flatbed knitting machine requires the in-depth knowledge of all the physical parameters that make the machine work. Some of these important *knitting machine parameters* include: (i) the relationship between the knitting bed movement and displacement profiles of the front and back knitting needles or the cam profiles, (ii) the needle spacing or gauge, (iii) needle and bed geometries, (iv) yarn feed friction and take-up spring, (v) fabric take-up velocity and take-up spring, and (vi) knitting needle latch kinematics and friction, as summarized in Table 1.

While many of the knitting machine parameters can be modeled directly, the yarn feed mechanism including feed friction and the take-up spring is simulated using non-linear bar elements. Each filament in the yarn uses its own non-linear bar element describing the yarn feed properties; in this way, the definition is independent of the number of filaments and more or less filaments can be added depending on the computer resources available. Parameters, such as the fabric take-up velocity and the yarn feed friction, which are difficult to measure physically are estimated and adjusted according to the visual quality of the resulting knit, just as is done by technicians with real knitting machinery (*i.e.*, an insufficiently large numerical value for the yarn take-down velocity will cause poor loop formation, tangling, and needle jamming). The fabric take-up mechanism is simulated by moving springs attached to the take-up bar and applying an almost constant tension.

The needle latch friction moment is measured physically and then further reduced using needle-only simulations until a value, which sustains inertial effects of the needle movement, is obtained.

All the five knitting needles include kinematic pin joints that simulate the needle mechanism required to produce the fabric structure. The needle latches open and close according to the movements made by the needles and the contacts encountered by the needles against the yarn, and needle latches against the main body of the needle itself. A needle latch rotational friction resistance is also prescribed to restrict latch movement under its own inertial forces.

6.3 Model Input: Material Property Parameters

Material property parameters form another important part of the model. Fortunately, a continuous filament glass fiber yarn can be accurately represented as a purely linear elastic material. Each filament in the yarn is represented by a series of interconnected linear elastic circular beam elements, their bending, tension, and torsion forces being transmitted between one another. The element size, 0.2 mm, has been chosen carefully to allow an accurate representation of the fabric geometry, but also to keep the solving time reasonable. Other elements of the

Table 1. Summary of important knitting machine parameters.

Knitting machine parameters		*Description*
Geometrical	Cam dimensions (mm) (identical for both cams) A = 12.5 B = 72 C = 21.5	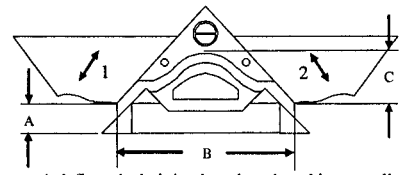 Parameter A defines the knitting loop length and is controlled via movable cams 1 and 2. Parameter B defines the needle cycle duration. Parameter C defines the needle stroke.
	Needle spacing, 10 gauge	Distance between adjacent knitting needles, 10 gauge equals a 2.54 mm spacing.
	Needle geometry, 5 needles	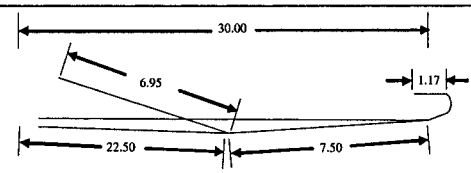 Needle head diameter = 0.5 mm
Mechanical	Yarn feed friction and feed take-up spring	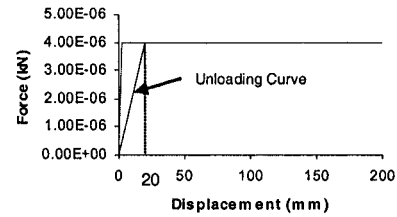
	Fabric take-up velocity	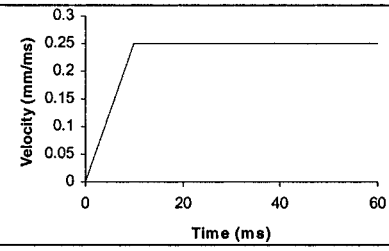
	Fabric take-up spring	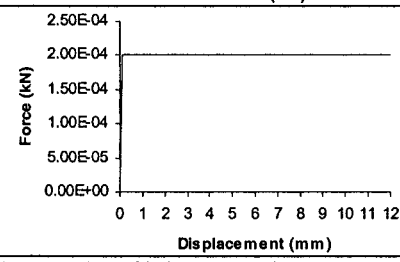
	Needle latch friction 5×10^{-07} N.m (kN.mm)	The needle latch friction moment is measured physically and then further reduced using needle only simulations until a value, which sustains inertial effects of the needle movement, is obtained.

machinery, such as knitting needles and the machine bed are treated as rigid bodies, since information on stresses and strains in these elements is not required. A summary of the yarn material properties is given in Table 2.

Table 2. Yarn material properties.

Material Property	*Value*
Filament diameter	17mm
Density, E-glass	2.54×10^{-06} kg/mm^3
Poisson's ratio, v	0.2
Tensile modulus, E	73 GPa
Second moment of area, Ix	4.1×10^{-09} mm^4
Second moment of area, Iy	4.1×10^{-09} mm^4
Polar second moment of area, J	8.2×10^{-09} mm^4

To simulate contact between the glass filaments and other elements of the knitting machinery, the code uses contact algorithms that check for penetrating nodes within a space around each element. In this simulation, the space is defined using the diameters of the filaments, 17 μm. Any penetration is then resisted by a contact stiffness (filament-filament, filament-needle compression stiffness in the presented case), calculated by averaging the tensile moduli of the two materials in contact.[37] For additional control, a scaling variable called the penalty scale factor is also introduced. Using the self-impacting contact type, contacts between individual filaments, filaments and the knitting machinery, as well as filaments contacting themselves can all be accounted for.

6.4 Model Input: Non-Physical Parameters

Apart from the physical parameters, many non-physical parameters, such as the time step scale factor (TSSF), contact search accelerator (CSA), penalty scale factor (PSF), and material damping factors play an important role in the simulation, ensuring solution stability and results within a sensible time frame. The most important non-physical parameters and their descriptions are presented in Table 3.

In explicit dynamic finite element procedures, the stable time step is calculated by using information about the element size, material density, and stiffness. To ensure the stability of the solution, this value is multiplied by the TSSF. For large strain simulations using shell elements, such as sheet metal forming, a suitable TSSF usually lies between 0.7 and 0.9. For crash simulations where elements undergo more radical movements during a single time step, the factor may need to be set as low as 0.3.[37] In the knitting simulation where only bar and

Table 3. Important non-physical parameters.

Non-physical parameter	*Abbreviation*	*Description*
Time step scale factor	TSSF	Time step control multiplier
Contact search accelerator	CSA	Controls search frequency per n cycles
Penalty scale factor	PSF	Contact stiffness multiplier based on E values
Material damping ratios	–	Control material oscillations

beam elements are used, the factor lies between 0.1 and 0.2. The reason for such a low value arises because of the ambiguity of one-dimensional element nodal rotations. For instance, if a beam element undergoes a rigid body rotation larger than a certain value during one time step, then it may be unclear which direction that element has rotated in order to get to that position. It is this shortcoming of the Lagrange (or even updated Lagrange) formulation when using bar or beam elements, which is the main factor influencing the solution stability in a knitting simulation.

With the large number of contacts involved, the contact search accelerator is another important non-physical parameter determining the frequency of the contact search per n time steps. To ensure that contacts are detected and maintained throughout the simulation, the search is performed at every time step.

6.5 Simulating the Mechanics of the Knitting Process

The duration of the model covers six full knitting cycles in total, producing enough fabric for the second stage of the simulation, where all the knitting machine elements will be removed and a numerical tensile test of the specimen will be performed. Given the linear density of the yarn, the density of E-glass, and filament diameter, the number of filaments in the real yarn can be calculated as approximately 120. While the present simulation uses only 20 filaments to help reduce solving time, a force-displacement curve of the resulting simulated fabric should exhibit a similar shape as that of the actual fabric (which contains 6 times the number of filaments), only lower in magnitude. The yarn itself is modeled as a hexagonal close packed arrangement of all the filaments, a simplification over real yarn, which is usually spun or air-textured to provide lateral cohesion and resistance to damage during knitting.[38] However, it is possible to simulate even these characteristics. Extra boundary conditions can be applied to the ends of the yarn, or the filaments can be assembled together with center distances smaller than their diameters, causing the filaments to fly apart initially, as if under the external force of an air jet.

The duration of the entire knitting simulation is 60 ms, somewhat faster, around 5 times, than practically achievable knitting speeds on conventional

machines due to the loss in yarn feed control and dangerously high needle bed movements. The six production stages of the simulation are shown in Figure 13. The simulation performs three full cycles, 6 passes, producing enough fabric for the second stage of the analysis.

7 Concluding Remarks

The most important validation of the model will be the comparison of the experimental and numerical force-displacement curves. If the numerical model is simulating the behavior of the knitted structure correctly, then the shapes of these curves should be very similar and the only difference should be the scale of force since the numerical simulation uses fewer filaments. Visual checks can also be used, *e.g.*, comparison of loop height and width or wale/course density given as number of vertical/horizontal columns/rows of loops per cm for both the experimental and numerical case.

In Section 5, eight micro-level fabric deformation mechanisms were identified and discussed in detail: inter-yarn slip, inter-yarn shear, intra-yarn slip, yarn bending, yarn twist, yarn stretching, yarn compression, and yarn buckling. These mechanisms can be separated into two further categories, those influenced by friction and those influenced by the material properties and geometry of the fibers. Inter-yarn slip, inter-yarn shear, and intra-yarn slip are all forms of inter-fiber friction, the difference being that inter-yarn slip and inter-yarn shear involve the relative translation or rotation of groups of fibers, whereas intra-yarn slip considers the axial sliding movements within these group reference frames. Even though friction is not activated in this simulation, in all three cases these movements can be measured. If friction was incorporated, then its influence could be closely analyzed, and the distribution of deformation energy could actually be quantified for the different values of the coefficient of friction. There is, however, the problem of element size which may induce an artificial form of friction, creating incorrect results or results corresponding to a particular unknown value of the coefficient of friction.

Yarn bending, compression, stretching, twist, and yarn buckling, which can be viewed as the reverse of yarn stretching or the result of axial compression upon a filament, belong to the second category. These mechanisms are directly related to the material properties and geometry of the fibers and can be compared using the simulation by plotting their energy contributions *vs.* wale direction strain.

This investigation has yielded a number of findings relating to the deformation behavior of knitted fabric-reinforced thermoplastic sheets, as well as conclusions regarding practical forming issues. It has also delved into the underlying mechanisms responsible for its unique behavior, both essential for the development and future use of these types of materials.

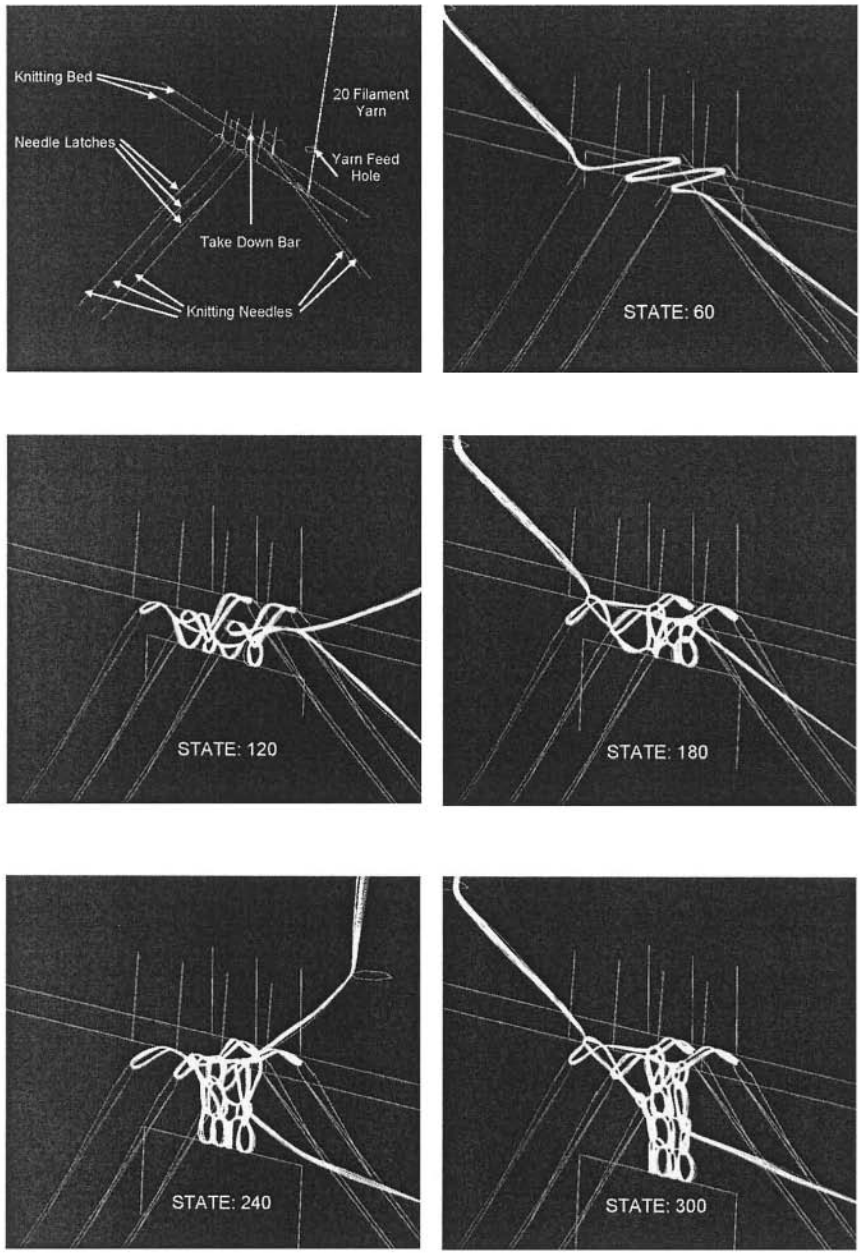

Figure 13. The six stages of the knitting simulation.

8 Acknowledgements

The authors would like to gratefully acknowledge the support of CRC-ACS Australia for arranging the use of material and software resources used in this project. The authors would also like to thank Allen Chhor and Damian McGuckin at Pacific ESI for their exceptional technical support of PAMCRASH™ and Fisher & Paykel for their financial assistance through the Maurice Paykel Scholarship.

9 References

[1] S. Savci, J. I. Curiskis, M. T. Pailthorpe (2000) A study of the deformation of weft-knit preforms for advanced composite structures Part 2: The resultant composite, *Compos. Sci. Technol.* **60,** 1943.

[2] A. P. Mouritz, M. K. Bannister, P. J. Falzon, K. H. Leong (1999) Review of applications for advanced three-dimensional fibre textile composites, *Composites A* **30**, 1445.

[3] J. Mayer, J. D. Haan, R. Reber, E Wintermantel (1998) Knitted carbon fibre reinforced thermoplastics: An overview, *First Asian-Australasian Conf. Composite Materials (ACCM-1)* Vol. 1, p. 401.

[4] S. D. Pandita, D. Falconet, I. Verpoest (2002) Impact properties of weft knitted fabric reinforced composites, *Compos. Sci. Technol.* **62**, 1113.

[5] R. Reber, J. D. Haan, M. Petitmermet, J. Mayer, E. Wintermantel (1998) Failure behaviour of weft-knitted carbon fibre reinforced PEEK, *First Asian-Australasian Conf. Composite Materials (ACCM-1)* Vol. 1, p. 407.

[6] M. K. Bannister, O. A. Khonder, K. H. Leong, I. Herszberg (1998) The effect of architecture on the impact properties of knitted fabrics, *First Asian-Australasian Conf. Composite Materials (ACCM-1)* Vol. 1, p. 402.

[7] A. Miravete, Ed. (1999) *3-D Textile Reinforcements in Composite Materials*, Woodhead Publishing Limited, Cambridge.

[8] L. Tong, A. P. Mouritz, M. K. Bannister (2002) *3D Fibre Reinforced Polymer Composites*, Elsevier, Boston.

[9] P. V. Houtte, I. Verpoest, B. Gommers (1998) Analysis of knitted fabric reinforced composites: part I. Fibre orientation distribution, *Composites A* **29**, 1579.

[10] S. Ramakrishna (1997) Characterisation and modelling of the tensile properties of plain weft-knit fabric-reinforced composites, *Compos. Sci. Technol.* **57**, 1.

[11] P. V. Houtte, I. Verpoest, B. Gommers (1998) Analysis of knitted fabric reinforced composites: part II. stiffness and strength, *Composites A* **29**,1589.

[12] J. D. Haan, R. Reber, J. Mayer, E. Wintermantel (1998) Tensile properties of plain weft knitted carbon fibre reinforced polyamide 12 composites, *First Asian-Australasian Conf. Composite Materials (ACCM-1)* Vol. 1, p. 403.

[13] I. Putnoki, E. Moos, J. Karger-Kocsis (1999) Mechanical performance of stretched knitted glass fibre reinforced poly(ethylene terephthalate) composites produced from commingled yarn, *Plastics, Rubber and Composites* **28**, 40.

[14] P. Tan, L. Tong, G. P. Steven (1997) Modelling for predicting the mechanical properties of textile composites – a review, *Composites A* **28**, 903.

[15] S. Ramakrishna, H. Hamada, K. B. Cheng (1997) Analytical procedure for the prediction of elastic properties of plain knitted fabric-reinforced composites, *Composites A* **28**, 25.

[16] Z. M. Huang, S. Ramakrishna (2000) Micromechanical modelling approaches for the stiffness and strength of knitted fabric composites: A review and comparative study, *Composites A* **31**, 479.

[17] P. V. Houtte, B. Grommers, I. Verpost (1996) Modelling the elastic properties of knitted-fabric-reinforced composites, *Compos. Sci. Technol.* **56**, 685.

[18] N. Takano, Y. Ohnishi, M. Zako, K. Nishiyabu (2001) Microstructure-based deep-drawing simulation of knitted fabric reinforced thermoplastics by homogenization theory, *Int. J. Solids Structures* **38**, 6333.

[19] T. C. Lim, S. Ramakrishna, H. M. Shang (1998) Improvement of knitted fabric composite sheet formability by simultaneous deep drawing and stretch forming, *First Asian-Australasian Conf. Composite Materials (ACCM-1)*Vol. 1, p. 409.

[20] G. R. Christie (1997) Numerical modelling of fibre-reinforced thermoplastic sheet forming, PhD Thesis, Department of Mechanical Engineering, University of Auckland.

[21] A. K. Pickett, J. E. Cunningham (1996) Numerical techniques for the pre-heating and forming simulation of continuous fibre reinforced thermoplastics, *SAMPE European Conf. and Exhibition.*

[22] M. J. Clifford, A. C. Long, P. Luca (2001) Forming of engineered prepregs and reinforced thermoplastics, *The Minerals, Metals & Materials Society (TMS) Annual Meeting.*

[23] P. Boisse, A. Gasser, G. Hivet (2001) Analyses of fabric tensile behaviour: determination of the biaxial tension-strain surfaces and their use in forming simulations, *Composites A* **32**, 1395.

[24] L. Ye, H. R. Daghyani (1997) Characteristics of woven fibre fabric reinforced composites in forming process, *Composites A* **28**, 869.

[25] J. F. Krebs, D. Bhattacharyya (1998) A direct comparison of matched-die versus diaphragm forming, *Composites A* **29**, 183.

[26] A. Cherouat, J. L. Billoet (2001) Mechanical and numerical modelling of composite manufacturing processes deep-drawing and laying-up of thin pre-impregnated woven fabrics, *J. Mater. Proc. Technol.* **118**, 460.

[27] W.-S. Kuo, J. Fang (2000) Processing and characterization of 3D woven and braided thermoplastic composites, *Compos. Sci. Technol.* **60**, 643.

[28] R. J. Dykes, T. A. Martin, D. Bhattacharyya (1998) Determination of longitudinal and transverse shear behaviour of continuous fibre-reinforced composites from vee-bending, *Composites A* **29**, 39.

[29] M. Duhovic, D. Bhattacharyya, L. R. Baxter, A. R. M. Douglas (2002) Kinematic and numerical analyses of knitted fabric composites forming. *3rd Asian-Australasian Conf. Composite Materials (ACCM-3)* p. 737.

[30] O. Rozant, P.-E. Bourban, J.-A. E. Mason (2000) Drapability of dry textile fabrics for stampable thermoplastic preforms, *Composites A* **31**, 1167.

[31] K. Friedrich, M. Hou, J. Krebs (1997) Thermoforming of continuous fibre/thermoplastic composite sheets, in *Composite Materials Series* (Ed. D. Bhattacharyya) Elsevier Science, Amsterdam, p. 119.

[32] W. H. Hosford, R. M. Caddell (1983) *Metal Forming Mechanics and Metallurgy*, Prentice-Hall, New Jersey, p. 279.

[33] T. C. Lim (2000) *Sheet Forming of Knitted Fabric Composites*, Department of Mechanical Engineering, The National University of Singapore, Singapore, p. 171.

[34] F. N. Cogswell (1992) *Thermoplastic Aromatic Polymer Composites*, Butterworth-Heinemann, Oxford (England), Boston.

[35] D. Bhattacharyya (1997) Composite sheet forming, in *Composite Materials* (Ed. R. B. Pipes) Elsevier, Amsterdam, New York, Vol. 11.

[36] T. A. Martin, G. R. Christie, D. Bhattacharyya (1997) Grid strain analysis and its application in composite sheet forming, in *Composite Sheet Forming* (Ed. D. Bhattacharyya) Elsevier, New York, p. 217.

[37] Pam-System-International PAM-CRASH™ version 2000 level 18 Notes Manual. 2000.

[38] J. W. S. Hearle (11969) *Structural Mechanics of Fibers, Yarns and Fabrics*, John Wiley and Sons, New York, Vol. 1.

Chapter 16

Impact Damage in Composite Laminates

Hiroshi Suemasu
Department of Mechanical Engineering, Sophia University, Tokyo, Japan

1 Introduction

Composite laminates find numerous applications, especially for aerospace structures, due to their high specific strength and stiffness. However, structures made of composite laminates, *e.g.*, carbon fiber-reinforced plastics (CFRP), are susceptible to impact damage, such as transverse cracking, delamination, *etc.* The impact damage, being difficult to detect, may cause a serious reduction of the structural performance, *e.g.*, the compressive strength (compression after impact).[1-3] Design loads of the airplane structures are often limited by this reduced compressive performance. The mechanism of damage accumulation due to impact should be well understood in order to take full advantage of the use of composite laminated structures and many experimental and numerical studies treat the impact damage problem.[1-6] The low velocity impact response is already reported to be similar to the deformation due to a static concentrated load and, *vice versa*, the low velocity impact may be defined as an impact event where the dynamic effect is relatively small. The study of the damage accumulation process under a quasi-static transverse concentrated load helps the better understanding of the low velocity impact behaviors. There are few works focusing on the multiple delaminations developing at the impact point from the fracture mechanical point of view.

In the present chapter, an analytical research on the damage in composite laminates due to a concentrated transverse load is reported. Special emphasis is placed on the interlaminar delaminations below the loading point, which usually occur in the form of multiple delaminations. Figure 1 shows an ultrasonic image of a damage in a quasi-isotropic CFRP laminate created by transverse indentation. Delaminations tended to propagate radially at all interfaces, with accompanying

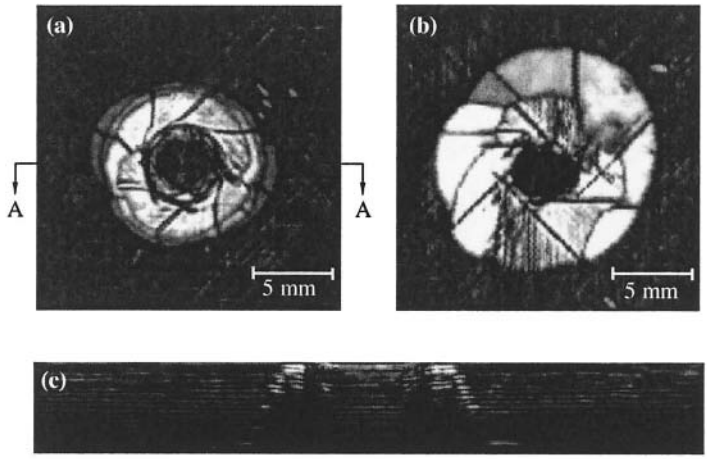

Figure 1. Ultrasonic images of a damage due to a transversely applied concentrated load in a quasi-isotropic CFRP laminate: (a) view from the loaded surface, (b) view from the back surface, (c) cross-section along A-A.

transverse cracks. There are clear straight lines of transverse cracks at the delamination edges. The damage size increases with the depth from the loaded surface to the back surface. Figure 2 is a micrograph of a cross-section of the damaged CFRP laminate. Transverse cracks making 45° angles with the horizontal surface were continuously extended to delaminations. Transverse cracks at 90° to the plate surface are observed in the bottom layer, and are caused by the strong tensile normal stress due to bending.

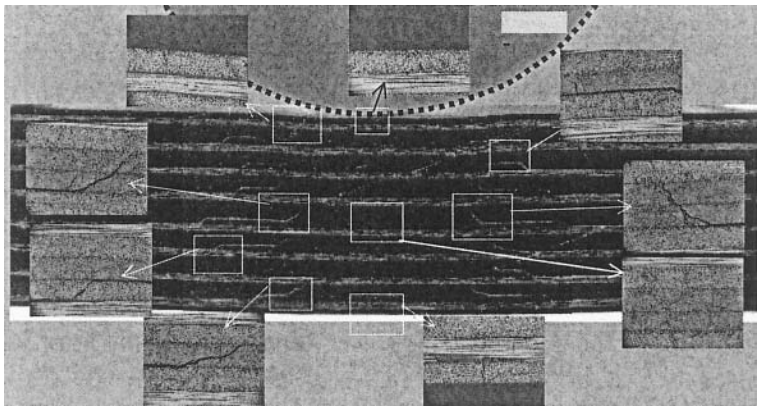

Figure 2. A micrograph of the cross-section of a damaged CFRP quasi-isotropic laminate.

2 Deformation and Energy Release Rate of Axisymmetric Plates with Multiple Delaminations

2.1 Axisymmetric Plate with Multiple Delaminations of the Same Size[8]

A transverse concentrated load, P, is applied at the center of a clamped circular plate of radius R and thickness h with multiple circular delaminations, as shown in Figure 3. The damaged portion is divided into N pieces of the same thickness by N-1 equal in size delaminations of radius a. The values relating to the intact and delaminated portions are indicated by subscripts 0 and d, respectively.

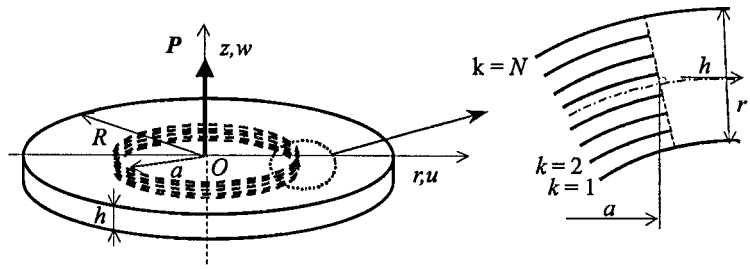

Figure 3. Axisymmetric plate with multiple delaminations.

The following assumptions are made in order to simplify the problem. Displacements are small and a linear analysis is valid. The plate is isotropic and the material is uniform. No delamination opens and the frictional force is neglected. Kirchhoff's hypothesis is valid even in the neighborhoods of the delamination edges. The boundary conditions at $r = R$ are

$$w_0 = w_0' = 0 \tag{1}$$

where w is a transverse displacement. The prime sign means differentiation with respect to r. Owing to Kirchhoff's hypothesis, the continuity conditions of displacements and forces at the delamination edge ($r = a$) are simply written as

$$w_0 = w_d,\ w_0' = w_d',\ u_k = u_0 - z_k w_0'(a) \tag{2}$$

$$Q_0 = \sum_{k=1}^{N} Q_{dk},\quad M_0 = \sum_{k=1}^{N} \left(M_{dk} + z_k T_{rk}\right) \tag{3}$$

where u, Q, T, and M denote the radial displacement of the mid-plane, the transverse shear forces, the in-plane resultant force and the bending moments, respectively. The subscript k means k-th delaminated portions and z_k is the distance from the

mid-plane of the plate to the middle surface of k-th delaminated portion. The transverse displacements of delaminated portions are equal, by the assumption of no delamination opening. Under the condition of small displacement, u_0 can be assumed to be zero, while u_k cannot be set zero because the slope of the mid-plane at the delamination front causes radial displacements. The in-plane resultant stresses, T_{rk},contribute to the moment. As no friction is assumed on the delaminated surface, the in-plane stresses become uniform in each delaminated portion. Then,

$$T_{rk} = T_{\theta k} = \frac{Eh}{1-\nu}\frac{z_k}{a} w_0'(a) \tag{4}$$

where E and ν are Young's modulus and Poisson ratio, respectively.

When only a concentrated force is applied at the center of the plate, the governing equation with respect to the deflection w is written as

$$D\left(\frac{d^2}{dr^2}+\frac{1}{r}\frac{d}{dr}\right)\left(\frac{d^2}{dr^2}+\frac{1}{r}\frac{d}{dr}\right)w=0 \tag{5}$$

where D is the bending rigidity. The exact solution is given as

$$w(\rho) = W_0[\phi(\rho)+(N^2-1)\alpha^2\phi(\rho/\alpha)], \tag{6}$$

where $\rho = r/R$, $\alpha = \alpha/R$, $W_0 = PR^2/(16\pi D)$ and

$$\phi(\xi) = \begin{cases} 1-\xi^2+2\xi^2\log\xi & \xi \le 1 \\ 0 & \xi > 1 \end{cases}.$$

The stored energy V is

$$V(\alpha) = \frac{1}{2}Pw_d(0|P,\alpha) = \frac{P^2R^2}{32\pi D}\left\{1+(N^2-1)\alpha^2\right\} \tag{7}$$

where $w_d(0|P,\alpha)$ means the center displacement when the load and the delamination radius are P and α, respectively. When all the delaminations propagate by a same amount $\delta\alpha$ under a constant load, the energy release rate G can be given by the following equation

$$G = \lim_{\delta\alpha\to 0}\frac{V(\alpha+\delta\alpha)-V(\alpha)}{2\pi(N-1)R^2\alpha\delta\alpha} = G_0(N+1) \tag{8}$$

where $G_0 = P^2/(32\pi^2 D)$. G is independent of R and a and proportional to the number N+1 and D^{-1}. The critical load P_{cr} at which the delaminations become unstable is given by the condition $G = G_{cr}$.

$$P_{\mathrm{cr}} = \pi\sqrt{\frac{32DG_{\mathrm{cr}}}{N+1}}. \tag{9}$$

The stored energy at $P = P_{cr}$ is

$$V_{cr} = \frac{\pi R^2 G_{cr}}{N+1}. \tag{10}$$

The impact energy V_{imp}, being equal to the area below the load-displacement curve, can be given as

$$V_{imp} = P_{cr} w_d\left(0 \mid P_{cr}, \alpha\right) - \frac{1}{2} P_{cr} w_d\left(0 \mid P_{cr}, 0\right).$$

Since the energy to cause the damage is $V_{imp} - V_{cr}$, the total area of multiple delaminations $(N-1)\pi a^2$ is

$$(N-1)\pi a^2 = \frac{V_{imp} - V_{cr}}{2G_{cr}}. \tag{11}$$

The total delamination area increases linearly with the impact energy after the impact energy exceeds V_{cr}.

2.2 A Delamination is Larger or Smaller than the Rest[8]

Let us consider the cases when the M-th delamination is larger or smaller than the rest, as shown in Figure 4. The values relating to the three portions are indicated by subscripts 0, s and d, respectively. The boundary conditions and assumptions are the same as in the previous section. When a delamination is larger or smaller than the rest, the continuity conditions about displacements and forces at $r = b$ and a are, respectively,

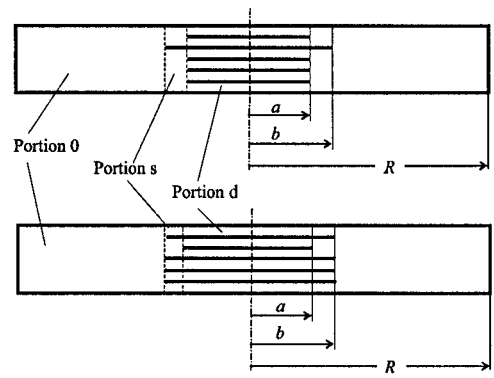

Figure 4. One of the multiple delaminations is larger or smaller than the rest.

$$w_0 = w_s,\ w_0' = w_s',\ u_0 - z_{sj}w_0' = u_{sj}$$

$$Q_0 = \sum_{j=1}^{N_s} Q_{sj},\quad M_0 = \sum_{j=1}^{N_s}\left(M_{sj} + z_{sj}T_{rsj}\right) \text{ at } r = b \tag{12}$$

$$w_s = w_d,\ w_s' = w_d',\ u_{sk} = u_{dk} - (z_{dk} - z_{sj})w_s'$$

$$\sum_{j=1}^{N_s} Q_{sj} = \sum_{k=1}^{N} Q_{dk},\quad \sum_{j=1}^{N_s}\left(M_{sj} + z_{sj}T_{rsj}\right) = \sum_{k=1}^{N}\left(M_{dk} + z_{dk}T_{rdk}\right) \text{ at } r = a$$

where N_s is the number of delaminated ligaments in the portion s, that is, $N_s = 2$ when one ligament is larger, and $N_s = N - 1$, when the ligament is smaller than the rest. The general solutions of w_0, w_s and w_d are obtained as

$$w(\rho) = W_0[\phi(\rho) + S_s\beta^2\phi(\rho/\beta) + S_d\alpha^2\phi(\rho/\alpha)] \tag{13}$$

where $\beta = b/R$ and

$$S_s = \begin{cases} \dfrac{N^3}{M^3 + (N-M)^3} - 1 & \text{(a delamination is larger)} \\ \dfrac{N^3}{N+6} - 1 & \text{(a delamination is smaller)} \end{cases}$$

$$S_d = N^2 - S_s - 1$$

The stored energy V is

$$V = \frac{1}{2}Pw_d(0) = \frac{P^2}{32\pi D}\left[1 + S_s\beta^2 + S_d\alpha^2\right] \tag{14}$$

When the load is constant, the energy release rate of the M-th delamination and the average energy release rate of the other $N-2$ delaminations of the same radius can be given as follows

$$G_b = -\lim_{\Delta\beta\to 0}\frac{V(\alpha,\beta+\Delta\beta) - V(\alpha,\beta+\Delta\beta)}{2\pi R^2\beta\Delta\beta\times(N_s - 1)} = G_0\frac{S_s}{N_s - 1}$$

$$G_a = -\lim_{\Delta\beta\to 0}\frac{V(\alpha+\Delta\alpha,\beta) - V(\alpha,\beta)}{2\pi R^2\alpha\Delta\alpha\times(N - N_s)} = G_0\frac{S_d}{N - N_s} \tag{15}$$

The energy release rate at the smaller delamination edge or edges is always higher than those of larger delaminations. The shorter delamination(s) tend to propagate to reach the longer delaminations, *i.e.*, once multiple delaminations are created, all of them tend to propagate simultaneously.

2.3 Effect of Geometrical Nonlinearity[9]

Geometrical nonlinearity due to in-plane stress should be considered when the deflection of the plate reaches the order of the plate thickness or that of the delaminated portions. This order of the deflection is often realized in composite materials when the propagation of multiple delaminations takes place. The clamped circular plate with multiple penny-shape delaminations of the same radius a is considered again. The boundary and the continuity conditions are the same as those in Section 2.1. Since no exact solution is available, the Rayleigh-Ritz approximation method is adopted. The total potential energy $\Pi = U - V$ is written as the sum of the total strain energy

$$U = \pi D\int_a^R \left(\kappa_r^2 + 2\nu\kappa_r\kappa_\theta + \kappa_\theta^2\right)rdr + \frac{\pi h}{E}\int_0^R \left\{\left(\frac{\chi'}{r}\right)^2 - 2\nu\frac{\chi'\chi''}{r} + (\chi'')^2\right\}rdr$$
$$+ \sum_{i=1}^{N}\left[\pi D_i\int_0^a \left(\kappa_r^2 + 2\nu\kappa_r\kappa_\theta + \kappa_\theta^2\right)rdr + \frac{\pi Eh}{N(1-\nu^2)}\int_0^a \left(\varepsilon_{ri}^2 + 2\nu\varepsilon_{ri}\varepsilon_{\theta i} + \varepsilon_{\theta i}^2\right)rdr\right] \tag{16}$$

and the work done by the external force $V = Pw_d(0)$, where $k_r\,(= -w'')$, $k_q\,(= -r^{-1}w')$ and $\varepsilon_{ri} = \varepsilon_{\theta i}\,(= -(z_i/a)w_0(a))$ are the curvatures of the plate and in-plane strains of the i-th delaminated portion. χ is Airy's stress function ($\sigma_r = \chi'/r$, $\sigma_\theta = \chi''$). The first derivative, χ',can be written as a function of the normalized deflection $W = w/h$ as

$$\chi' = -\frac{Eh^2}{4R}\left[\int_0^\rho \left(\frac{\rho}{\xi} - \frac{\xi}{\rho}\right)(W')^2 d\xi + c_0\rho + c_1\rho^{-1}\right] \tag{18}$$

Considering the exact solution (Eq. (6)) of the linear case, the displacement field is assumed as

$$W = q_0\phi(\rho) + q_1\alpha^2\phi(\rho/\alpha) \tag{19}$$

Substituting Eq. (19) into Eq. (18) and considering the in-plane boundary conditions at $r = 0$ and 1, we have the following expression of χ' as a function of the generalized coordinates q_0 and q_1.

$$\chi' = -\frac{Eh^2}{8R}\left(q_0^2 A_{00}(\rho) + 2q_0q_1A_{01}(\rho) + q_1^2A_{11}(\rho)\right) \tag{20}$$

$$A_{00} = \rho^3\left\{7 - 12\log\rho + 8(\log\rho)^2\right\} - (8+\kappa)$$

$$A_{01} = \begin{cases} \rho^3\left\{7 - 12\log\rho + 8(\log\rho)^2 + (6 - 8\log\rho)\log\alpha\right\} & \rho \le \alpha \\ -\rho\left\{8\alpha^2(1-\log\alpha) + \kappa\alpha^4(1-2\log\alpha)\right\} - \alpha^4(1-2\log\alpha)\left(\rho^{-1} + \kappa\rho\right) & \alpha < \rho \le 1 \end{cases}$$

$$A_{11}=\begin{cases}\rho^3\left\{7-12(\log\rho-\log\alpha)+8(\log\rho-\log\alpha)^2\right\}-\rho\left\{8\alpha^2+\kappa\alpha^4\right\} & \rho\le\alpha\\ -\alpha^4\left(\rho^{-1}+\kappa\rho\right) & \alpha<\rho\le 1\end{cases}$$

where $k=(1+\nu)/(1-\nu)$. By substituting the equations for W and χ' into Eq. (16), we have a potential energy function Π of a forth-order polynomial of q_0 and q_1.

$$\Pi=\frac{8\pi Dh^2}{R^2}\Big[q_0^2\left\{1-\alpha^2\left(1-N^{-2}\right)\right\}+2q_0q_1\alpha^2N^{-2}+q_1^2\alpha^2N^{-2}$$
$$+\frac{3}{128}(1-\nu^2)\left(B_0q_0^4+B_1q_0^3q_1+B_2q_0^2q_1^2+B_3q_0q_1^3+B_4q_1^4\right)-2p\left(q_0+\alpha^2q_1\right)\Big] \quad (21)$$

The coefficients B_i (i = 0,1,···,4) are obtained by numerical integration. The equations derived by differentiating Π by q_0 and q_1 are numerically solved. The energy release rate is numerically obtained as

$$G\left(a+\frac{\Delta a}{2}\,|\,p\right)=\frac{\Pi(a+\Delta a\,|\,p)-\Pi(a\,|\,p)}{2\pi a\Delta a} \quad (22)$$

2.4 Finite Element Analysis[8,9]

A finite element analysis (FEM, NISA II) is conducted to prove the validity of the present theoretical results. An eight-node isoparametric axisymmetric element is used to divide a circular isotropic plate (R = 50 mm, h = 2 mm, a = 10 mm) with multiple delaminations, as shown in Figure 5. Young's modulus, E, and Poisson ratio, ν, are 71.5 GPa and 0.345, respectively. The finite element mesh is refined at the neighborhood of the delamination edges. The energy release rate is obtained through the virtual crack closure technique.[10] Double nodes, where the relative displacement in the thickness direction is constrained, are used to prevent the delaminated portions from overlapping. The nodal forces at the crack fronts are obtained by using very short stiff bar elements connecting the relating nodes for the numerical convenience. The effect of the bar elements on the response of the plate and the related energy release rate are negligible.

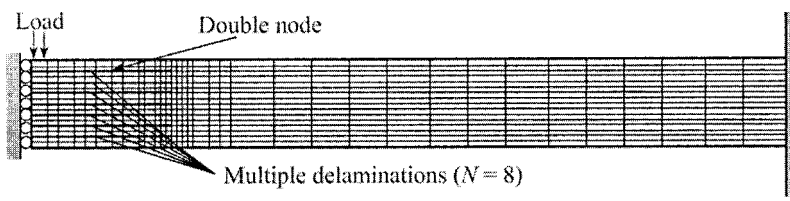

Figure 5. A finite element mesh of a delaminated circular plate.

2.5 Some Derived Relationships

The normalized energy release rates are listed in Tables 1 and 2. The theoretical results which are averages of the energy release rates of all the delaminations agree well with the numerical ones. Some important features of damage growth during the impact can be explained on the basis of the present explicit forms of the linear solution. A body of multiple delaminations tends to grow when delamination cites are created in the laminate. The load is constant during delamination growth. The damage size may be estimated as a function of the impact energy and material properties when the number of the delaminations is prescribed.

Figure 6 shows the relationships between the normalized center deflections w/h and the nondimensional load $p = P/(16\pi Dh/R^2)$ for $N = 4$. The analytical results coincide with the finite element ones when the deflection is small, because the assumed deflection includes the exact solution of the linear problem. The nonlinear effect is eminent when $W > 0.5$ for the intact plate and $W > 0.2$ for the delaminated plate of $\alpha = 0.4$. As expected, the discrepancy between the theoretical results and the finite element analysis increases with the load and/or the size of delaminations. This is because the nonlinearity increases with the load and delamination radius, and the deformed shape of the plate differs considerably from that of the linear solution. The square root of the nondimensional energy release rate $G^{1/2}$ is plotted against p for $N = 4$ in Figure 7. The results for $\alpha = 0$ should be assumed as a limiting case $\alpha \to 0$. The analytical relation between the energy release rate and

Table 1. Normalized energy release rate, G/G_0, for delaminations of the same size.[8]

N		*FEM*			*Theory*
		$a/R = 0.1$	$a/R = 0.2$	$a/R = 0.4$	
2	1	2.979	3.022	3.019	3
4	1	4.522	4.636	4.658	-
	2	5.550	5.673	5.692	-
	3	4.522	4.636	4.658	-
	Average	4.866	4.981	5.003	5
8	1	6.759	6.988	7.051	-
	2	8.890	9.158	9.221	-
	3	9.702	9.976	10.036	-
	4	9.931	10.210	10.264	-
	5	9.702	9.976	10.036	-
	6	8.890	9.158	9.221	-
	7	6.759	6.988	7.051	-
	Average	8.661	8.921	8.983	9

Table 2. Normalized energy release rates, G/G_0, when a delamination is larger or smaller than the rest ($N = 8$, $a = 10$ mm, $b = 12$ mm, $a = 8$ mm, $b = 10$ mm).[8]

	a/R or b/R	*FEM*	*Theory*		*a/R or b/R*	*FEM*	*Theory*
1	0.2	9.18	-	1	0.2	3.14	-
2	0.2	11.38	-	2	0.2	4.79	-
3	0.2	9.18	-	3	0.2	9.76	-
4	**0.24**	**3.02**	**3**	**4**	**0.16**	**27.27**	**27.43**
5	0.2	9.18	-	5	0.2	9.76	-
6	0.2	11.38	-	6	0.2	4.79	-
7	0.2	9.18	-	7	0.2	3.14	-
Average	0.2	9.91	10	Average	0.2	5.90	5.929
1	0.2	5.88	-	1	0.2	7.32	-
2	**0.24**	**1.30**	**1.286**	**2**	**0.16**	**27.28**	**27.43**
3	0.2	9.13	-	3	0.2	10.02	-
4	0.2	12.24	-	4	0.2	5.70	-
5	0.2	12.95	-	5	0.2	4.96	-
6	0.2	12.41	-	6	0.2	4.29	-
7	0.2	9.24	-	7	0.2	3.11	-
Average	0.2	10.31	10.286	Average	0.2	5.90	5.929

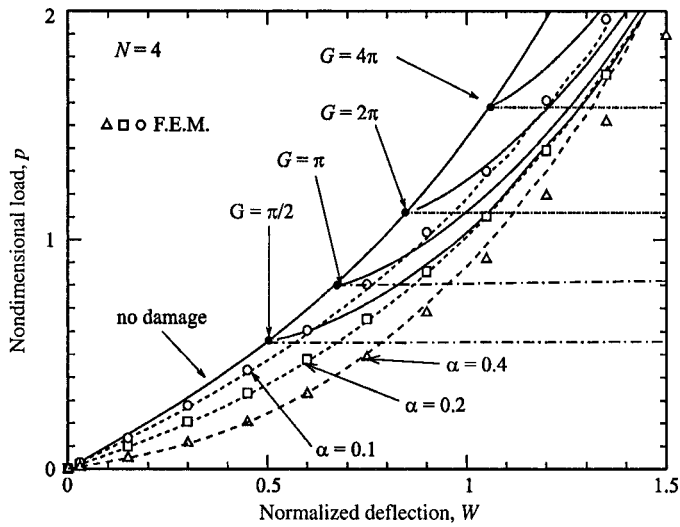

Figure 6. Applied nondimensional load *vs.* normalized deflection for the plate with three delaminations ($N = 4$). The thinner solid curves starting from the black points are the expected equilibrium relations of applied load and deflection when the delamination is assumed to propagate at a constant energy release rate.[9]

the load is sufficiently accurate. As expected from the linear solution at low load levels, $G^{1/2}$ increases linearly with the same slope in all cases. The slopes of the curves reduce at higher loads and the reduction rate is higher when the size of the delaminations is larger. The expected load-deflection paths are drawn in Figure 7, when the delaminations are assumed to propagate under a constant energy release rate. In contrast to the linear case, the load must be increased so as to keep the delaminations to propagate.

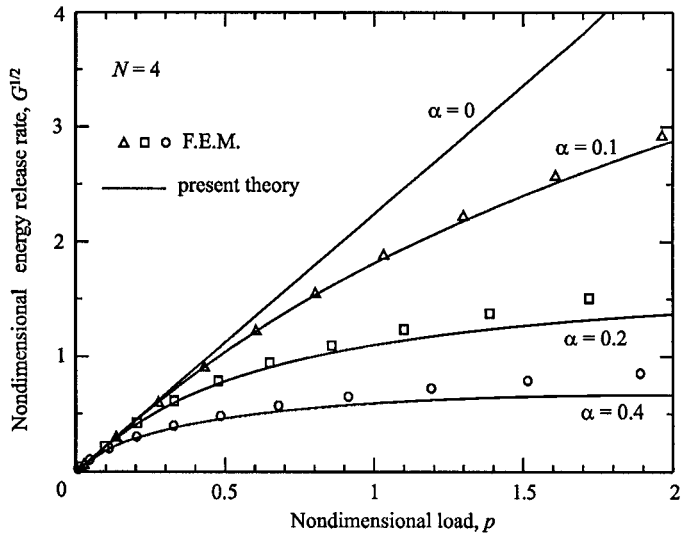

Figure 7. Nondimensional energy release rate *vs.* nondimensional load for the plate of $N = 4$.[9]

The relations between p and α are plotted in Figure 8. The solid lines show the results in the case of $N = 4$ and the broken lines those in the case of $N = 8$. When more delaminations exist, they start to propagate at a lower load but tend to stop at the smaller size. The point where the curve bends upward can be derived from the linear solution. The nonlinear effect of the delaminated plate becomes appreciable when the local deflection, the second term of Eq. (6), exceeds the order of the thickness of the delaminated layers. The load p_{nl} at which w_d reaches $\beta h/N$ can be given as

$$P_{nl}\alpha^2(N^2 - 1) = \beta/N \tag{23}$$

where the coefficient β is a constant of the order of 1. At this point, $G \approx p_{nl}^2(N+1)$. The normalized delamination radius α_{nl} at which the load must be appreciably increased to keep the delaminations to propagate farther is given approximately as

$$\alpha_{nl}^2 \approx \frac{\beta/N}{p_{nl}\left(N^2-1\right)} = \sqrt{\frac{N+1}{G_{cr}}}\,\frac{\beta}{N\left(N^2-1\right)} = \frac{\beta}{\sqrt{G_{cr}}}\,\frac{1}{N\left(N-1\right)\sqrt{N+1}} \tag{24}$$

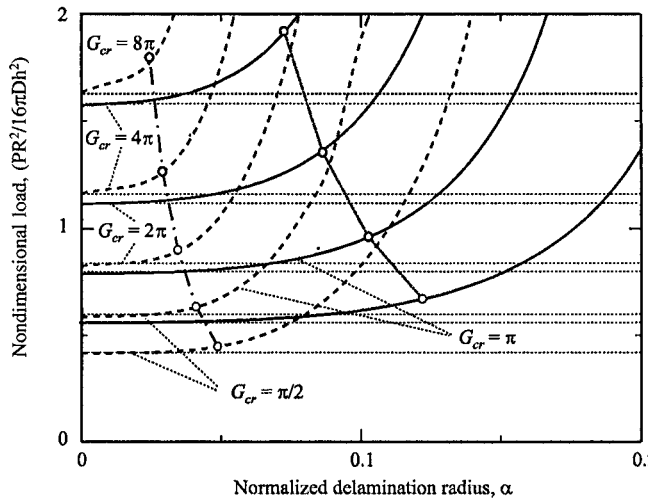

Figure 8. Nondimensional load *vs.* the size of multiple delaminations.[9]

From the present results for the load deflection curves, the value of 0.5 is appropriate for β. The condition of Eq. (24) is plotted in Figure 8 with dotted lines for $N = 4$ and 8. The plots are found to give a rough estimate of the delamination radius over which delaminations become difficult to grow farther.

3 Effect of the Stacking Sequence[11,12]

A square quasi-isotropic composite laminate (150 mm×150 mm×4 mm) and the stacking sequence $[-45°/90°/45°/0°]_4$ were numerically studied. The elastic properties of each ply are $E_L = 142$ GPa, $E_T = 10.8$ GPa, $G_{LT} = 5.49$ GPa, $G_{TT} = 4.15$ GPa, and $\nu_{LT} = 0.3$. Circular delaminations are present at each interlaminar plane, as shown in Figure 9a. Model A (discussed below) has just delaminations and model B has both delaminations and transverse cracks. We used a finite element code[14] (ABAQUS 5.8). Three-dimensional 20-node isoparametric brick elements and 15-node wedge elements (only at the center of the delaminated area) were used to divide the square laminates with circular damage, as shown in Figure 9b. The geometrical nonlinearity was considered. The contact problem at the delaminated surfaces was almost overcome by using a nonlinear spring element which had high stiffness in the compressive direction and no resistance in the tensile direction. The energy release rates were calculated using the virtual crack closure technique. The relations between the center displacements and the applied load are similar to those of the circular plate (Figure 6). The stiffness of the plate of the large delamination (not shown owing to space limitations) was very small at the low load level,

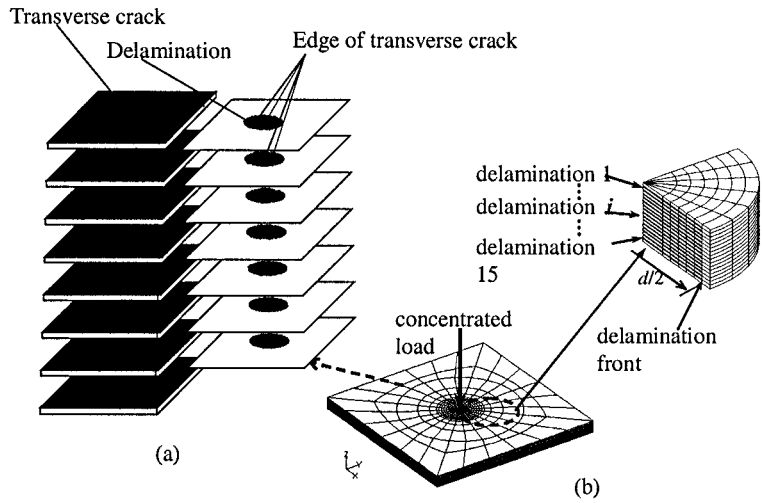

Figure 9. An analytical model of a damaged quasi-isotropic laminate and finite element discretization.

because the local bending stiffness of the delaminated portion was roughly $1/16^2$ (the laminate was divided into 16 layers by 15 delaminations). The damaged plates showed a significant geometrical nonlinearity when the displacement exceeded the thickness of the delaminated portions, which is 1/16 of the total laminate thickness. Since this displacement is quite small, the geometrical nonlinearity should be considered in the damage accumulation problem of the composite laminate.

The energy release rate distributions along the delamination edges were computed. Despite that the division of the model may not be sufficiently small to obtain an accurate energy release rate because of the computer capacity, this accuracy, however, is thought to be sufficient to assess qualitatively the delamination propagation process. Figure 10 shows the distributions of the total energy release rates along the delaminations for model A when $d = 20$ mm and $P = 300$ N, which are plotted in the radial direction. The center displacement was about 0.4 mm in this case, and the nonlinearity was small at this displacement level. The energy release rate tends to be large near the mid-surface, where the transverse shear stress, τ_{xz} and τ_{yz}, is usually large. The energy release rate component, G_{II}, was also dominant for the quasi-isotropic laminate, as in the case of homogeneous plate. The energy release rates at the delaminations near the front and back surfaces (1, 2, 3, 13, 14, 15) had preferred directions, which coincided with the stiffer principal material directions of the delaminated portion outside the corresponding delamination. At the delaminations 4-12, the distributions are almost uniform and the graphs are circular, because the orthotropy of the delaminated portions is weak and, what is more, the delaminated portions separated by the delaminations 4, 8 and 12 are quasi-isotropic. The energy release rate for model B (not shown owing to space

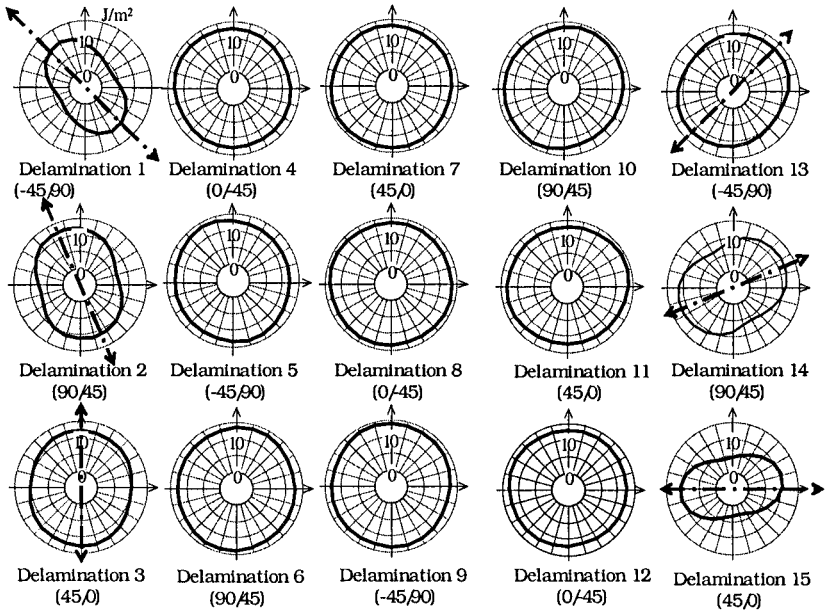

Figure 10. Energy release rate distributions along the delamination edges for model A ($d = 20$ mm, $P = 300$ N). The thin arrows indicate the principal material direction of the layers outside the delamination.[12]

limitation) was slightly higher than for model A and the distribution shapes were similar to those of model A except that they were slightly elongated in the direction of the transverse cracks.

Figure 11 shows the distributions of the total energy release rates along the delaminations for model A ($d = 20$ mm, $P = 2280$ N). The center displacement is about 1.5 mm, which is 6-fold larger than the delaminated layers. The fiber directions of the layers just above and below each delamination are indicated by the shorter and longer arrows in each figure. At this load level, the direction of the maximum energy release rate changes from the material principal direction of the upper layers in the linear case to the fiber direction of the layer just below. The energy release rate of the delamination in the tensile side tends to be large. The difference of the moduli in the radial directions of the layers above and below the delamination is plotted in Figure 12. The shape of this distribution is quite similar to the energy release rate distribution. The latter is dominated by the stiffness difference of the laminates below and above the delamination and is shown for model B ($d = 20$ mm, $P = 2560$ N) in Figure 13. The distribution shape is basically similar to that of model A, but a little more deformed in the transverse crack directions. Maximum energy release rate is attained in the fiber direction of layer 16 at delamination 15. This is an interesting result that could explain the large

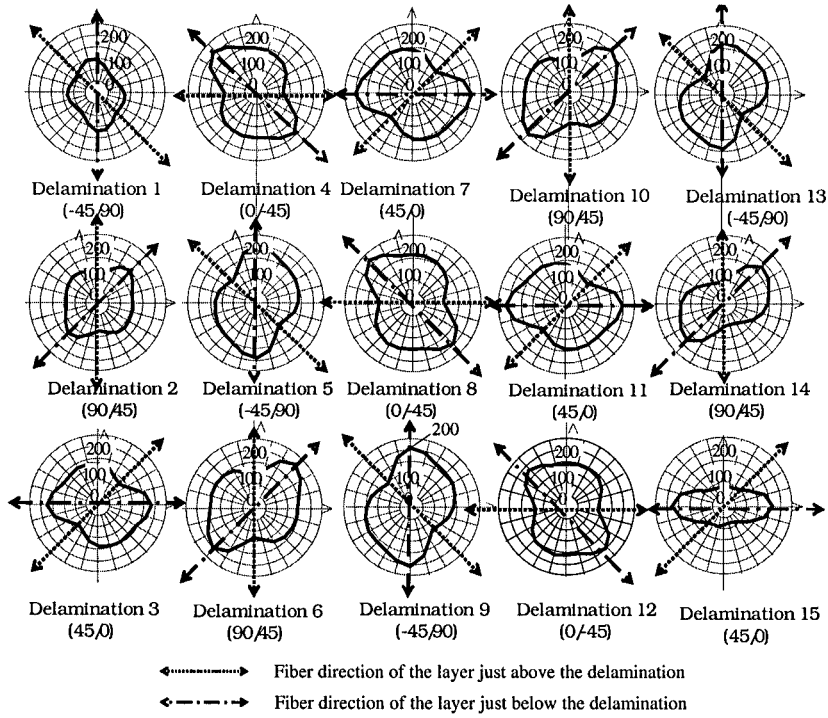

Figure 11. Energy release rate distributions along the delamination edges for model A (P = 2280 N, d = 20 mm).[12]

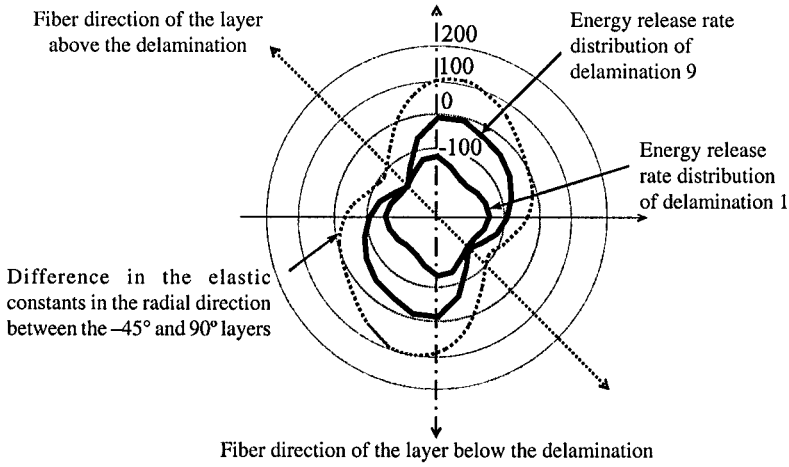

Figure 12. The stiffness difference between the layers differing in fiber orientation by $45°\{E_{90}(\theta)\text{-}E_{-45}(\theta)\}$.[12]

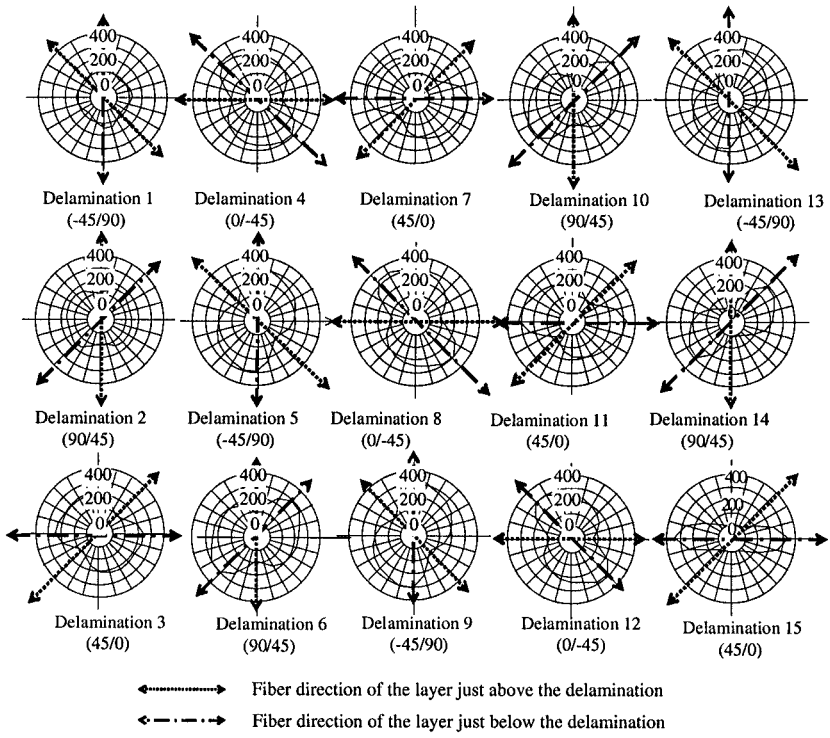

Figure 13. Energy release rate distributions along the delamination edges for model B (P = 2560 N, d = 20 mm).[12]

delamination at the interface near the back surface of the impact damaged specimens.

4 Simulation of Delamination Growth in Composite Laminates[13]

The two-dimensional propagation of delaminations in isotropic plates and cross-ply laminates $(0°/90°)_{2S}$ was analyzed by using an interface element. The dimensions of the laminates and the material properties of each layer are the same as in the models of the previous section. Owing to the symmetry, a quarter of the plate was analyzed. Circular initial delaminations of radius 2.5 mm were situated at its center. Figure 14 shows the relationships between the applied load and the center deflection where a finite element mesh is shown. The propagation of delaminations occurred first at the center interlaminar plane where the energy

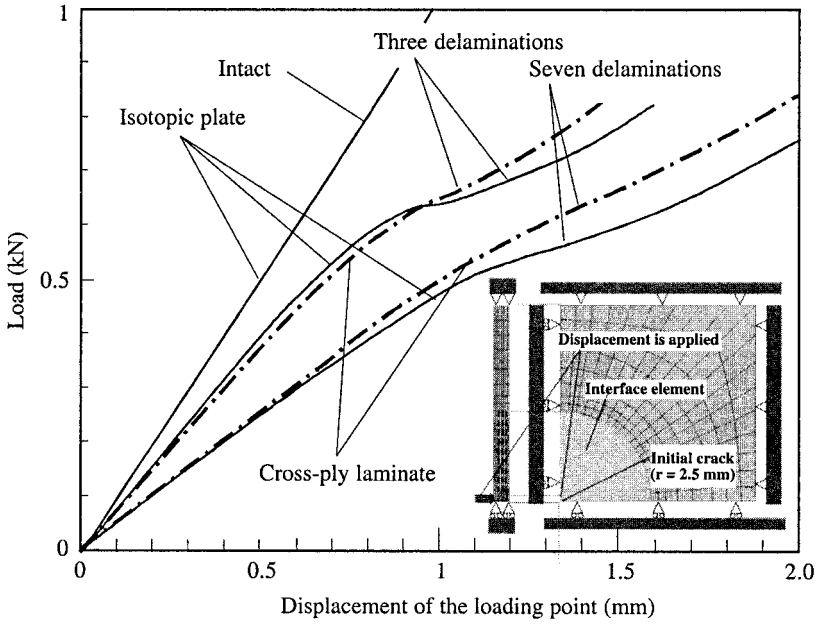

Figure 14. Relationships between the center deflection and the applied load. A finite element discretization is also shown.[13]

release rate was the highest, when it was accompanied by some stiffness reduction. However, the latter was not eminent until all the delaminations started to propagate. The delaminations propagated in a circular pattern for the isotropic plate and in the fiber directions of the layers just below them for the cross-ply laminates, as expected from the results of the previous section. The delamination near the loaded surface was obviously small compared to the rest. The delamination patterns are compared with the distributions of the energy release rate in Figure 15. The delaminations tended to propagate only in the direction of maximum energy release rate. The overlapping of the delaminations in 0° and 90° layers was small, indicating that the energy release rate distributions must change with the delaminations' growth. The growth history of the damage is quite important and must be considered to assess the impact damage in laminates.

5 Conclusion

A theoretical study, Rayleigh-Ritz approximation and finite element analysis were performed to obtain solutions at various levels of simplification for the damage problem in composite plates and to clarify the mechanism of the initiation and

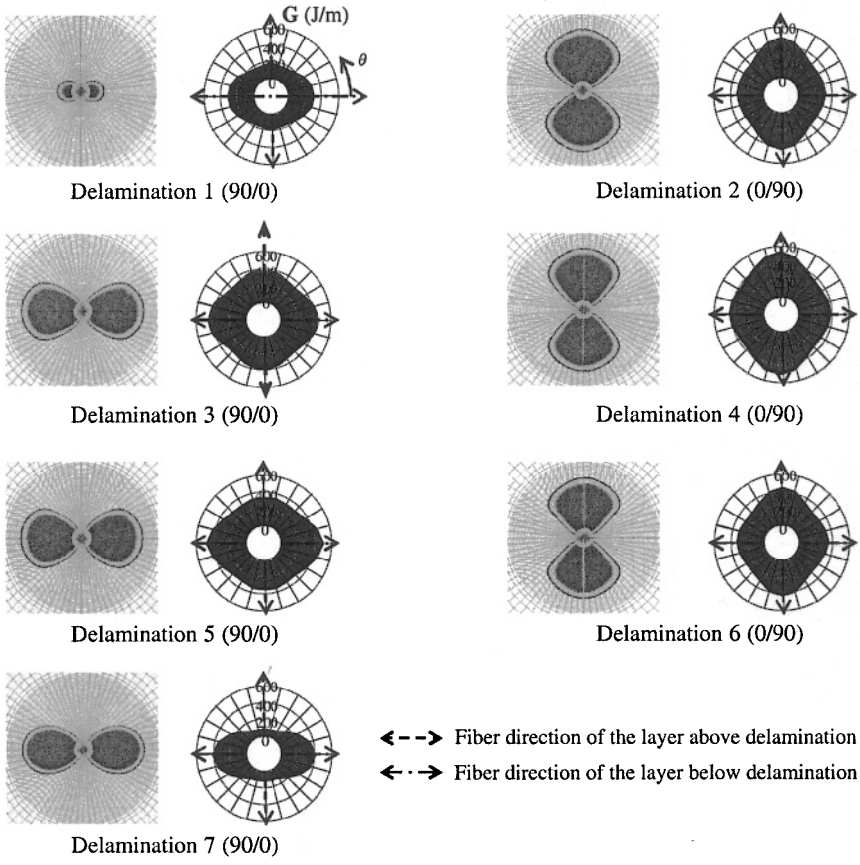

Figure 15. Damage patterns obtained and energy release rate distributions (P = 1.04 kN, d = 20 mm).[13]

growth of the low velocity impact damage. The mechanism of the damage growth is clearly explained by the reasons of the nucleation of multiple delaminations and the effects of the geometrical nonlinearity, the stacking sequence, the damage growth history, the transverse cracks, *etc.*

6 References

[1] T. Ishikawa, S. Sugimoto, M. Matsushima, Y. Hayashi (1995) Some experimental findings in CAI tests of CF/PEEK and conventional CF/Epoxy flat plates, *Compos. Sci. Technol.* **55**, 349.

[2] S. M. Lee (1986) Compression-after-impact of composite with toughened matrices, *SAMPE Journal*, 64.

[3] E. F. Dost, L. B. Ilcevicz, W. B. Avery, B. R. Coxon (1991) The effects of stacking sequence on impact damage resistance and residual strength for quasi-isotropic laminates, ASTM STP 1110:476.

[4] J. D. Whitcomb, K. N. Shivakumar (1989) Strain energy release rate analysis of plates with postbuckled delamination, *J. Compos. Mater.* **23**, 714.

[5] P. O. Sjobolm, J. T. Hartness, T. M. Cordell (1988) On low velocity impact testing of composite materials, *J. Compos. Mater.* **22**, 30.

[6] S. Liu, F. K. Chang (1994) Matrix cracking effect on delamination growth in composite laminates induced by a spherical indenter, *J. Compos. Mater.* **28**, 940.

[7] H. Suemasu, M. Maier (1994) An analytical study on impact behavior of axisymmetric composite plates, *Adv. Compos. Mater.* **5**, 17.

[8] Suemasu H and Majima O (1996) Multiple delaminations and their severity in circular axisymmetric plates subjected to transverse loading, *J. Compos. Mater.* **30**, 441.

[9] H. Suemasu, O. Majima (1998) Multiple delaminations and their severity in non-linear circular plates subjected to transverse loadings, *J. Compos. Mater.* **32**, 123.

[10] K. N. Shivakumar, P. W. Tan, J. C. Newman (1988) A virtual crack-closure technique for calculating stress intensity factors for cracked three dimensional bodies, *Int. J. Fracture* **36**, R43.

[11] Y. Aoki, H. Suemasu, O. Majima (2001) Damage accumulation in composite laminates during quasi-static transverse loading, *Adv. Compos. Mater.* **10**, 219.

[12] Y. Aoki, H. Suemasu (2001) Fracture mechanical study on mechanism of damage accumulation in composite laminates, *Tran. JSME (A)* **67**, 1563 (in Japanese).

[13] Y. Aoki, H. Suemasu, O. Majima (2003) Damage analysis in composite laminates by using an interface element, *Adv. Compos. Mater.* **12**, 1.

[14] ABAQUS/Standard User's Manual Vol. I-III.

[15] Y. Aoki (2003) A study on impact damage problem of fiber reinforced composite laminate, DSc Thesis, Sophia University, Tokyo.

Chapter 17

Discontinuous Basalt Fiber-Reinforced Hybrid Composites

Tibor Czigány
Department of Polymer Engineering, Budapest University of Technology and Economics, Budapest, Hungary

1 Introduction

Structural materials are usually classified into three groups: polymers, metals, and ceramics. Their combinations are composites, which show unique properties. If the matrix has a multiphase structure or the reinforcement consists of more than one material, the resulting composite is called *hybrid composite*. Hybrid composites are at the peak of the pyramid in the hierarchy of structural materials due to their special properties.

The large-scale and fast growing applications of polymer composites in all industrial fields are characteristic of the modern market-oriented technology and economy. The reason for this development is primarily the favorable price/weight ratio of composites. The most rapidly developing branch is the automotive industry where traditional metals are continually being replaced by corrosion-resistant polymer composites. This yields a significant reduction in the weight of the automotive parts. Hence, fuel is saved and the impact on environment is reduced. Nowadays, the reinforcing material in polymer composites is usually glass fiber (GF, volume fraction of *ca.* 85%), which has good strength, ensures a relatively good adhesion to the polymer matrix, and has a low price. Carbon fiber (CF) is used in more demanding applications with special requirements (*e.g.*, aerospace technology, aircraft industry, military applications, sports and leisure). The production expenses of CF are much higher than those of GF and the sufficient adhesion between matrix and CF is also more difficult to obtain. Recently, natural fibers are spreading: flax and

hemp are preferentially produced and used in Europe, while sisal is preferred in countries of warmer climate. Note that these fibers are cheap and possess acceptable strength properties in addition to biological degradability. However, their properties cannot be guaranteed (they depend on the duration of sunshine, the amount of precipitation, the quality of the soil, *etc.*) and a good adhesion to the polymer matrix is difficult to achieve.

In addition to the above-mentioned fibers, several other reinforcements are used, such as aramid (AF), ceramic (CeF), bast wood, ramie, *etc.* fibers, but their application is not yet significant. Considering the competition in the market and the ever-increasing economic and environmental requirements for reinforcements in polymer composites, the reinforcement potential of newer and newer fibers is investigated in the leading research institutes of the world. During the last decade, the possible applications of basalt fiber as a reinforcing material for polymers are the object of intensive research. Basalt is a mineral of volcanic origin. The fiber made of basalt rock is really cheap and has several excellent properties (good mechanical strength, excellent sound and thermal insulator, non-flammable, biologically stable, *etc.*). The disadvantages of basalt fibers (BF) are related to their stiff and brittle nature, hence their processing and application require special caution. BFs are available in both discontinuous and continuous forms. The aim of this chapter is to summarize the hybrid polymer composites containing discontinuous BF produced by a melt-blown technology. As already mentioned, the hybridization concept holds for both polymer matrix and reinforcement. As polymer matrices, both thermoplastic and thermosetting resins will be considered.

2 Basalt Fibers

2.1 Characteristics, Applications

Rock wool fibers can be characterized by their acidity modulus, M_s, which describes the ratio of acidic to basic oxides. If $M_s < 1.2$, the fiber is called slag wool, the base material of which is cinder. Nowadays, such low quality fibers are not produced any more because they are very brittle and show a poor chemical resistance. If $M_s = 1.2–1.5$, the fiber is considered to be a mineral wool, the base materials of which are basic volcanic rock and cinder. These fibers are brittle, but have acceptable insulation properties, hence their significance in the construction industry is high. If $M_s > 1.5$, the fiber is called rock wool, and if its base material is basalt then it is named basalt wool (basalt fiber, BF). The base of basalt fiber is basalt, which is a volcanic, over-ground, effusive rock saturated with 45-52 wt.% SiO_2. Due to the circumstances of its formation, basalt has several excellent properties. In addition to its high elasticity modulus and excellent heat resistance,

its fibers have a significant capability of heat and acoustic damping and are outstanding vibration isolators.

BF has been a well known insulating material for almost 50 years, but the reports in the literature are far less abundant than those on GF and CF; exhaustive reports on GF and CF covered their production, properties, and applications. On the other hand, only few papers dealt with BF and even much less is known about their incorporation into polymer matrices. The first papers were published by researchers of the former Soviet Union in the late 1970s and early 1980s. The authors studied BFs as insulating materials and as raw materials for the textile industry.[1,2] It is interesting to note that at that time basalt fibers were used in the insulation layer of the astronauts' spacesuits in the Soviet Union.

Before reviewing the state of the art with BF and BF applications in composites, it should be noted that all reports used high quality continuous BFs or their chopped versions. BF as a possible polymer reinforcing material was mentioned for the first time by Subramanian and Austin,[3] who reported that BF can be applied in polymer matrix composites instead of GF. The authors recognized the importance of the BF-to-matrix adhesion and studied it in single BF-reinforced thermosetting polyester matrix composites. It was established that the surface treatment of BF with silanes improved the adhesion to the matrix, reflected also in the bending strength of the composites. Park and Subramanian embedded single BF treated by different types of silanes in an epoxy resin and concluded that 3-aminopropyl-triethoxy-silane and dimethoxysilane increased the interfacial shear strength.[4,5]

As BFs were tried as reinforcing materials in the 1990s, the following questions arose more and more frequently: what are the useful properties and the drawbacks of BFs, what the application fields are, and what are their advantages over other fibers? Wojnárovits compared the corrosion resistance of BF and GF, as the stability against air pollution, water, and high temperature is crucial in terms of the service life of thermal insulations.[6] It was found that if the design is not adequate, corrosion damages both BF and GF to such a great extent that the insulating material fails. It was also observed that the chemical resistance of the fibers does not correlate with their mechanical properties. This work covered different silicate fibers (basalt, kaolin, glass, and ceramic) and the factors influencing the mechanical properties were clarified. The fibers containing the smallest pore volume, and especially the smallest ratio of large mesopores (*ca.* 0.03-0.15 μm) showed the best mechanical performance. On the other hand, no direct relationship could be deduced between the chemical compositions of the fibers and their mechanical properties. Jung and Subramanian investigated the tensile strength of BF and concluded that if alumina (2 wt.%) is added to the basalt, the fiber strength can be improved by *ca.* 15%.[7]

The increasing application of basalt (primarily as an insulating material in the construction and automotive industry) raised the question whether BF is harmful to the health. Kogan and Nikitina carried out a comparative analysis on asbestos and basalt fibers.[8] They forced rats to inhale air containing asbestos and basalt fibers

for six months. In the case of asbestos fibers at a dose of 1.7 g/kg (referred to the body weight of the rat), one third of the animals died, while a dose of 2.7 g/kg killed all the rats. In the case of BF, the animals survived even when the dose reached 10 g/kg. Similar investigations were conducted by McConnell *et al.*[9] and also by Adamis *et al.*[10] These authors also concluded that BFs pose no risk to humans, hence asbestos fibers can be replaced by BFs.

In the second half of the 1990s, mainly Park *et al.* from Korea published several papers on BF-reinforced composites. They tested polycarbonate (PC)[11,12] and epoxy resin (EP)[13,14] based polymer composites with the methods of single fiber fragmentation and acoustic emission. It was found that in the case of PC matrix composite (when aminosilane was used as a treating agent), the number of acoustic events correlated well with the value of the interfacial shear strength determined from the fragmentation tests.

Bashtannik *et al.*[15] produced polypropylene (PP) matrix/short BF composites with an extrusion technology. The same authors also concluded that BF-reinforced polymer composites have excellent wear properties.[16] Botev *et al.*[17] also examined PP matrix/short BF composites and reported that their mechanical properties were very poor when no coupling agent was used.

A further impetus to develop BF-reinforced composites was given by Goldsworthy's leading article in the journal of Composites Technology issued in August, 2000.[18] This work devoted to the past, present, and future of polymer composites was entitled "New Basalt Fiber Increases Composite Potential". The author emphasized the potential of BF as a new reinforcing material of natural origin and predicted its large-scale utilization.

Gurev *et al.*,[19] as well as Morozov *et al.*[20] examined the production of continuous BF as a function of the chemical composition of Russian basalt. The reason behind was that the technological parameters had a decisive effect on the mechanical properties of BF. It was concluded that the most suitable basalt rock for continuous BF production was the one with high SiO_2 and Al_2O_3, and low CaO and MgO content.

Zihlif and Ragosta[21] produced short (1-3 mm) BF-reinforced polystyrene (PS) composite plates and found that the strength of the composite went through a maximum whereas both Young's modulus and the impact resistance increased monotonically with increasing BF content. Bashtannik *et al.*[22] investigated the fiber-matrix interfacial adhesion in BF composites with high density polyethylene (HDPE) matrix. It was found that the properties of BF-reinforced polymer composites were much more sensitive to the BF surface treatment than traditional fiber-reinforced systems.

On the basis of the above literature survey, it can be concluded that BF may become an alternative to GF and a suitable replacement of the already banned asbestos fibers if good adhesion to the polymer matrix can be provided in addition to adequate fiber quality and low price.

2.2 Production and Properties of Melt-Blown Basalt Fibers

The BF used in the thermoplastic and thermoset composites reported here was produced by the so-called Junkers technology (Toplan Ltd., Tapolca, Hungary). The essence of this method is that the basalt melt coming from the 1580 °C furnace is fed to a horizontal shaft fiber spinning machine. This has three centrifugal heads and consists of one accelerating and two fibrillizing cylinders. The fibers formed as a result of the centrifugal force are blown off with high-pressure air as depicted in Figure 1.

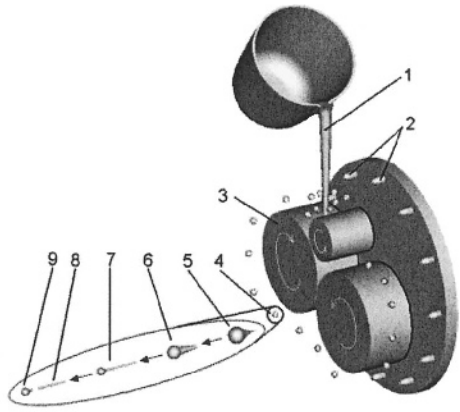

Figure 1. Scheme of the Junkers type BF production by melt blowing: 1 – molten basalt rock, 2 – blowing valves, 3 – fibrillizing cylinder, 4 – droplets, 5-7 fiber formation, 8 – fiber, 9 – fiber head.

This fiber spinning technology is very efficient and cheap. However, it has the disadvantage that the fibers cool down gradually and hence smaller or larger "heads" remain at their ends depending on the fiber length and affect adversely the strength and toughness. Scanning electron microscopic (SEM) images taken from the fracture surface of a BF-reinforced PP composite show the effect of the BF head (Figure 2). To avoid the negative effects caused by broken heads, the latter were removed by settling in water. This was a necessary step, especially when the performance of the hybrid reinforcement was investigated.

The tensile strength and Young's modulus of BF (Toplan Ltd., Tapolca, Hungary) were determined according to the JIS R 7601 standard using single fibers. The properties of the melt-blown discontinuous BF are listed in Table 1 together with the related data for a GF, a CF, and a CeF. For the sake of better comparison, not only the clamping length of the fibers was kept constant (20 mm), but their initial surface finish was also removed (by burning in a furnace at 400 °C for 4 h).

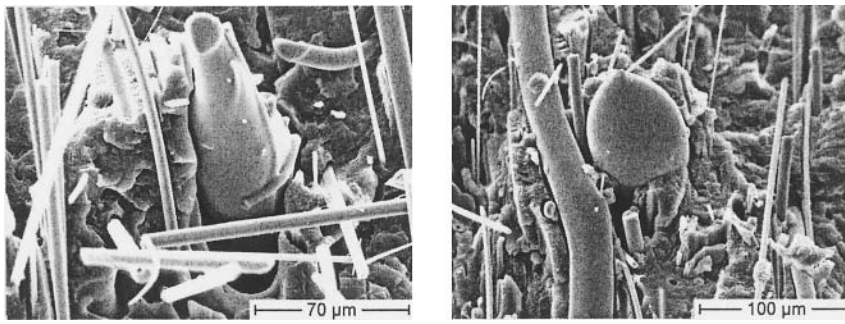

(a) (b)

Figure 2. SEM images taken from the fracture surface: (a) broken BF head and (b) headed BF in PP/BF composites.

Table 1. Properties of the reinforcing fibers used (ρ – density, d_{av} – average diameter, σ_t – tensile strength, ε_t – elongation, E_t – Young's modulus).

Fiber and manufacturer	ρ *(g/cm³)*	d_{av} *(μm)*	σ_t *(MPa)*	ε_t *(%)*	E_t *(GPa)*
Basalt (BF, Toplan Ltd.,Hungary)	2.70	9.0±2.7	586±267	1.12±0.45	60.4±18.9
Glass (GF, Sokoplast, Slovakia)	2.54	12.2±1.4	1540±556	3.10±1.18	52.2±18.2
Carbon (CF, Zoltek Co., Hungary)	1.76	7.9±0.9	2372±977	0.02±0.01	157.9±58.6
Ceramic (CeF, Carborundum Ltd., France)	2.55	5.9±1.1	828±306	1.50±0.62	59.9±13.0

3 Hybrid Composites

3.1 Concept and Realization

The word "hybrid" is of Greek-Latin origin and can be found in numerous scientific fields. However, this term is most commonly used in biology for the cross-breeding of different animal and plant species. Analogously, the engineering science uses this word in various cases, but the common principle is that this term means a "mixture" of different materials. In the case of polymer composites, *hybrid composites* are these systems in which one kind of reinforcing material is incorporated in a mixture of different matrices (blends),[23] or two or more reinforcing and filling materials are present in a single matrix,[24,25] or both approaches are combined.

Researchers have long been interested in the use of different reinforcing fibers in composites, in order to tailor their mechanical properties. Note that the hybrid concept may have a positive or negative effect on the properties of the resulting composites. Until the mid-1990s, the works focused on fiber (reinforcement) hybridization combining GF, CF, and AF. Bunsell and Harris,[26] as well as Summerscales and Short[27] revealed in their early papers that the hybrid effect is strongest in composites containing both GF and CF. It was concluded that if GF is added to CF-reinforced composites, the price can be reduced dramatically while the impact resistance increases. On the other hand, if CF is added to GF-containing composites, the flexural modulus increases to a great extent. Marom *et al.*[28,29] improved the impact resistance and flexural strength by adding AF to CF-reinforced epoxy matrix (EP) composites. Chaudhuri and Garala[30] found that the compressive strength of CF/EP composites could be optimized just by adding 15 wt.% GF. This finding was supported by the work of Fu *et al.*[31] on PP matrix-based hybrid fiber composites. They examined the Charpy impact energy of 25 wt.% short fiber-reinforced injection-molded specimens as a function of the GF/CF ratio. It was found that the mean fiber length depends on the GF/CF ratio in the hybrid composites. If the relative GF content was higher, the fibers were longer, while higher relative CF contents led to a decrease in the fiber length due to melt processing (extrusion, injection molding). Note that during processing the brittle fibers break owing to fiber/fiber and fiber/machine part (screw, barrel) interactions. In the case of Charpy tests, a small increase in the impact energy was noticed when the GF content increased.

The beneficial effect of CF on the flexural strength of polyphenylene sulfide (PPS)/GF composites was shown by Jang and Lee.[32] They examined the changes in the flexural strength and modulus as a function of the GF/CF ratio in isotropic specimens. It was found that the CF content was directly proportional to both flexural strength and modulus.

Failure modes were examined by Sohn and Hu[33] in the case of continuous CF/EP composites. The delamination strength increased by more than 100% when AF (15 wt.%) was added, but the compressive strength decreased.

Hybrid fiber composites do not only have favorable effects when considering mechanical properties. Friedrich and Jacobs[34] examined the friction properties of GF-, CF-, and AF-reinforced EP, polyetheretherketone (PEEK), and polyamide (PA) matrix composites toward steel. The AF/CF hybrid composites showed the best wear resistance.

Only in the second half of the 1990s, reports appeared in the literature describing hybrid composites containing other reinforcements than the traditional fibers (GF, CF, AF). The reason behind this fact was that natural fibers gained attention due to environmental concerns. Kalaprasad *et al.*[35,36] examined sisal/GF hybrid fiber/LDPE matrix composites at various fiber orientations. Benevolenski *et al.*[37] investigated the impact properties of flax/glass/PP matrix hybrid composites produced by hot compression molding technique from a needle-felted preform.

This felt contained all components of the composite (*i.e.*, matrix and reinforcement) in short fiber form. It was found that even a relatively small amount of GF (45 wt.% flax, 5 wt.% glass) resulted in a significant improvement in the dynamic impact properties. If the GF content was 20 wt.% and flax 30 wt.%, a twofold increase in the impact resistance was observed.

Several more recent papers deal with natural fibers of tropical origin and glass fiber-reinforced hybrid composites, mainly based on the work of Asian researchers. Rozman *et al.*[38] examined PP composites reinforced with the fruit bast of oil palm and GF. It was reported that PP has to be maleated and the natural fibers have to be surface treated (with trimethoxysilyl-propylmethacrylate) in order to improve the mechanical properties of the hybrid composites. Rout *et al.*[39] investigated coir/GF/thermosetting polyester (13/7/80 wt.%, respectively) hybrid composites. If coir was alkaline-treated, a significant increase could be achieved in the tensile strength of the hybrid composites and the moisture uptake decreased abruptly. Thwe and Liao,[40] as well as Mishra *et al.*[41] observed the same behavior (decrease in moisture uptake and slight improvement in mechanical properties) in the cases of bamboo fiber/GF/PP and pineapple/sisal/GF/polyester hybrid composites.

3.2 Property Prediction

The early theoretical considerations of the hybrid effect showed that the calculations based on the simple rule of mixtures contradicted the experimental results, suggesting the complexity of the "hybridization". Thus, the rule of hybrid mixtures (RHM, Eq. (1)) was introduced to characterize the mechanical properties of hybrid composites:

$$P_H = P_I \cdot V_I + P_{II} \cdot V_{II} \tag{1}$$

where P_H is any mechanical property of the hybrid composite $P_{I,II}$ are the properties of the simple composites *I* and *II*, respectively, $V_{I,II}$ are the volume fractions of the reinforcing fibers *I* and *II* ($V_I + V_{II} = 1$). In the case of hybrid composites, the simple rule of mixtures cannot be applied in the calculations of the components because it does not involve the strength of the fiber-matrix interfacial adhesion and the interaction of the fibers that build up the hybrid composite, hence experimental results should be considered.

Most studies carried out in this field examine the appearance of the so-called hybrid effect and characterize the synergistic effect of the reinforcing materials. According to Marom *et al.*,[42] a positive hybrid effect occurs when the properties of the composite are better than the values calculated from the RHM, while a negative hybrid effect appears when the calculation with the rule of mixtures results in a higher value than the real one. Positive and negative effects in hybrid composites with different reinforcing and matrix materials were measured by many researchers, but the most significant results can be credited to Fu *et al.*[43]

Hayashi[44] drew attention to the inaccuracy of the rule of mixtures. Based on own measurements, he argued that the RHM cannot be applied when there is a huge difference in the elongation at break of the reinforcing materials.

3.3 Applications

The application of hybrid composites is widespread owing to their favorable properties and the abundant related literature. Zhu *et al.*[45] used GF/CF-reinforced epoxy matrix hybrid composites instead of steel for pipes and tanks. These composite parts had an excellent resistance to creep, besides being corrosion resistant and having sufficient strength. Chiu *et al.*[46] recommended the usage of braided AF/CF-reinforced epoxy matrix hybrid composite tubes and profiles in the automotive industry due to their excellent energy absorbing capability. Shan and Liao[47] recommended the use of GF/CF/epoxy hybrid composites in marine applications since their investigations showed that the fatigue strength of these materials in water is higher than that of the composite containing only GF. Hybrid composites have opened a new chapter in the history of sporting plane construction when the gliding plane family of the LAK type was developed in 2000. The weight of this plane assembled from GF/CF/AF-reinforced panels is only 200 kg and it can reach the maximum speed of 270 km/h. The newest application of hybrid composites is wheel blades of wind turbine power stations.[48] In 2003, a 9 m-long GF/CF-reinforced hybrid composite wind blade was developed in the USA. It is expected that hybrid composites will be produced in large scale, especially as parts of large dimension.

4 Thermoplastic Hybrid Composites

4.1 Polypropylene with Hybrid Reinforcement Containing Basalt Fibers

PP composites containing various short (nominal initial length of 20 mm) fibers were produced by melt compounding in a Brabender internal mixer. Recall that the fibers used along with their characteristics are given in Table 1. The compositions prepared are summarized in Table 2.

To avoid severe fiber breakage, the fibers were added to the PP melt (T = 190 °C, kneader revolution 50 rpm, mixing time = 3 min) and homogenized for additional 5 min. Composite test sheets were produced from the compounds by compression molding. Specimens cut of the sheets were subjected to static (subscript "s") and dynamic (subscript "d") flexural tests using the 3-point bending configuration. Static tests were carried out at a deformation rate of 1 mm/min,

Table 2. Reinforcement content and composition of the hybrid composites studied (wt.%).

Fiber	*Batch*										
	1	*2*	*3*	*4*	*5*	*6*	*7*	*8*	*9*	*10*	*11*
PP	100	70	70	70	70	70	70	70	70	70	70
BF	–	30	–	–	–	20	20	20	10	10	10
GF	–	–	30	–	–	10	–	–	20	–	–
CF	–	–	–	30	–	–	10	–	–	20	–
CeF	–	–	–	–	30	–	–	10	–	–	20

whereas dynamic ones at 3.6 m/s, both at room temperature. In addition, the static and dynamic fracture toughness (K_s and K_d, respectively) values were determined by the concept of linear elastic fracture mechanics, and notched specimens with varying notch length were used. The flexural strength, σ, modulus, E, and K data are summarized in Table 3.

Table 3. Mechanical properties of the hybrid fiber-reinforced composites: σ_s – static flexural strength, σ_d – dynamic flexural strength, E_s – static flexural Young's modulus, E_d – dynamic flexural Young's modulus, K_s – static fracture toughness, K_d – dynamics fracture toughness. For batch numbering, see Table 2.

Batch	σ_s *(MPa)*	σ_d *(MPa)*	E_s *(GPa)*	E_d *(GPa)*	K_s *(MPam$^{1/2}$)*	K_d *(MPam$^{1/2}$)*
1	36.6±1.4	26.6±2.3	1.1±0.0	0.9±0.1	2.2±0.3	4.6±1.0
2	26.2±0.5	23.0±0.8	2.4±0.1	1.0±0.1	1.1±0.1	4.0±0.6
3	40.4±3.5	38.1±6.5	2.6±0.2	1.2±0.1	1.9±0.3	6.0±0.6
4	58.3±4.5	51.3±7.4	4.1±0.4	1.9±0.1	2.3±0.1	7.3±0.8
5	43.6±2.2	31.0±1.5	2.5±0.2	1.1±0.1	2.0±0.1	4.3±0.6
6	31.9±3.5	25.1±3.4	2.3±0.2	1.3±0.2	1.6±0.1	3.1±0.5
7	32.2±3.3	31.7±2.1	2.7±0.1	1.5±0.1	1.7±0.1	4.9±0.4
8	31.0±2.0	22.1±0.7	2.7±0.0	0.9±0.0	1.3±0.1	3.2±0.8
9	31.7±4.2	29.6±3.2	2.5±0.4	1.3±0.2	1.5±0.2	3.8±0.4
10	43.3±5.6	40.8±2.5	4.0±0.1	1.8±0.2	2.2±0.2	6.6±0.7
11	26.7±1.7	24.9±2.0	2.4±0.1	0.8±0.1	1.3±0.2	2.4±0.3

As expected, the CF-reinforced PP composites showed the best properties, since the modulus and strength of CF are the highest among all examined fibers (Table 1). However, if the production costs are also considered, attention should be focused on the fact that these properties are coupled with high expenses since

the price of CF is by 1.5 orders of magnitude higher than that of BF. The good properties of the composite containing 20 wt.% CF and 10 wt.% BF prove that BF can successfully be applied in hybrid composites and the material costs can be reduced significantly. This statement is based on the RHM, showing that a positive hybrid effect was achieved only in the composite containing 20 wt.% CF and 10 wt.% BF. Surprisingly, the properties of the CeF-reinforced and CeF-containing composites were the poorest. This is likely an effect of severe CeF breakage during compounding. Note that the price of CeF is almost the same as that of CF. Results also revealed that the stiffness increased for all composites and the BF/CF-reinforced hybrid composites possessed improved strength, too.

SEM micrographs taken from the fracture surfaces evidence that the dominating failure mode of short fiber hybrid composites is fiber pull-out. Recall that fiber pull-out strongly depends on the quality of the interfacial adhesion. The remaining voids after the fibers were pulled out indicate for poor interfacial adhesion; the maximum pull-out length of the fibers was *ca.* 100 μm.

At the beginning of this chapter, it was stated that the cheap BF can be used as an alternative of GF (the price of BF is *ca.* one third that of GF), since they have almost the same strength properties and density. However, BF is a less efficient reinforcement than GF if it is not treated (finishing, surface coating, *etc.*) accordingly. On the other hand, attention should be paid to the fact that the melt-blown BF used belongs to the low quality BF versions.

4.2 Basalt Fiber-Reinforced Polymer Blends

Our study was extended to BF-reinforced blends containing non-polar PP/polar PA12 polymers. The strategy with this polymer pair was to coat and encapsulate the BF *in situ* by the polar PA12 and disperse it in the PP matrix.[49] This *in situ* formed coating was expected to rise the resistance of BF against fracture during compounding. As PA12 and PP are incompatible, a compatibilizer, maleated PP (PP-g-MAH), was added. The PA12 content of the blends was varied between 0 and 50 wt.% in 10 wt.% steps, whereas the amount of PP-g-MAH was kept constant (5 phr; parts per hundred resin). The BF content was also varied between 0 and 20 wt.% in 10 wt.% steps (Table 4).

Hybrid composites were produced by extrusion melt compounding and dumbbell specimens were injection-molded for testing. Specimens were subjected to static and dynamic flexural tests using the 3-point bending configuration. Static tests were carried out at a deformation rate of 2 mm/min, whereas dynamic ones at 2.9 m/s, both at room temperature. In addition, the K_s and K_d values were determined. The σ, E, and K data are summarized in Table 5.

The results show that for the plain PP matrix the strength decreases with increasing BF content. This leads to a conclusion that during processing BFs break into pieces shorter than the critical length, hence they are present as fillers in the

Table 4. PA12/PP and BF content of the hybrid composites studied (wt.%).

Component	*Batch*																	
	1	*2*	*3*	*4*	*5*	*6*	*7*	*8*	*9*	*10*	*11*	*12*	*13*	*14*	*15*	*16*	*17*	*18*
Polypropylene (PP)	100	90	80	70	60	50	90	81	72	63	54	45	80	72	64	56	48	40
Polyamide (PA)	–	10	20	30	40	50	10	9	18	27	36	45	0	8	16	24	32	40
Basalt fiber (BF)	–	–	–	–	–	–	10	10	10	10	10	10	20	20	20	20	20	20

Table 5. Mechanical properties of BF-reinforced hybrid matrix composites: σ_t – tensile strength, σ_f – flexural strength, E_t – tensile Young's modulus, E_f – flexural Young's modulus, K_s – static fracture toughness, K_d – dynamics fracture toughness. For batch numbering, see Table 4.

Batch	σ_t *(MPa)*	σ_f *(MPa)*	E_t *(GPa)*	E_f *(GPa)*	K_s *(MPam$^{1/2}$)*	K_d *(MPam$^{1/2}$)*
1	26.5±0.5	48.7±0.2	1.3±0.1	1.7±0.1	2.4±0.1	2.6±0.2
2	28.9±0.4	53.5±0.2	1.4±0.1	1.9±0.1	1.5±0.1	3.2±0.1
3	29.7±0.6	61.1±0.6	1.5±0.1	2.1±0.1	1.5±0.1	3.8±0.1
4	27.4±0.1	51.8±1.1	1.2±0.1	1.6±0.1	1.7±0.1	3.6±0.2
5	26.6±0.1	47.8±1.3	1.1±0.1	1.6±0.1	1.7±0.2	3.0±0.5
6	26.4±0.3	46.2±1.2	1.0±0.1	1.6±0.1	1.8±0.1	2.9±0.2
7	25.1±0.1	51.9±0.5	1.8±0.1	2.5±0.1	2.4±0.1	3.5±0.2
8	29.8±0.3	63.1±0.4	1.9±0.1	2.5±0.1	2.5±0.2	3.7±0.1
9	30.0±0.7	62.8±1.5	1.9±0.1	2.7±0.1	2.7±0.2	3.9±0.3
10	28.7±0.6	57.1±1.4	1.7±0.1	2.5±0.1	2.5±0.1	3.9±0.4
11	28.2±0.4	53.7±0.6	1.6±0.1	2.2±0.1	2.5±0.2	3.7±0.1
12	26.5±0.1	50.6±0.3	1.3±0.1	2.0±0.1	2.4±0.1	3.7±0.2
13	24.9±0.1	53.3±0.4	2.2±0.3	2.9±0.1	2.2±0.1	4.2±0.2
14	30.7±0.2	64.3±0.5	2.6±0.1	3.2±0.1	2.7±0.2	4.3±0.3
15	30.4±0.4	64.7±0.1	2.5±0.1	3.2±0.1	2.8±0.5	4.5±0.2
16	28.7±0.2	59.9±0.4	2.0±0.2	2.8±0.1	2.5±0.2	4.4±0.1
17	28.2±0.1	57.0±0.5	1.9±0.1	2.5±0.1	2.3±0.1	3.8±0.4
18	26.7±0.1	54.3±0.4	1.9±0.1	2.5±0.1	2.2±0.2	3.7±0.2

composite. On the contrary, when PA12 was added to the PP matrix, the strength of the composite increased significantly.

SEM inspection allowed us to shed light on the effect of PA12. When the PA12 content of the blend was low, it was coarsely dispersed in the PP matrix. Figure 3a shows that the PA12 domains did not coat preferentially the basalt fibers. With increasing PA12 content, however, the polar PA12 wets and coats the BFs (Figure 3b). In this way, the critical fiber length is changing and, consequently, the fiber pull-out length alters, as well.

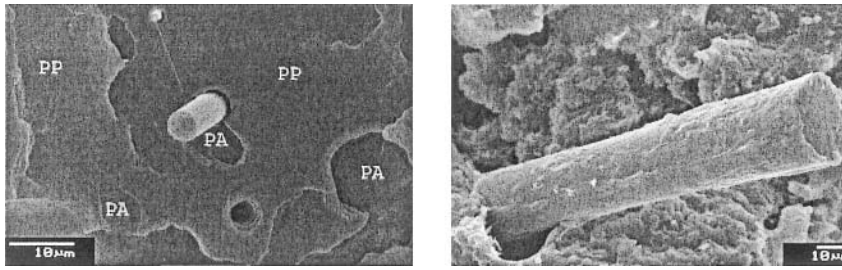

(a) (b)

Figure 3. SEM images taken from the fracture surface composed of (a) 81/9/10 wt.% PP/PA/BF and (b) 48/32/20 wt.% PP/PA/BF single edge notched specimens.

5 Thermoset Hybrid Composites

Due to its inherent brittleness, BF is probably more suitable for thermoset reinforcement than for thermoplastics. Note that the mechanical loading of the reinforcement during resin infiltration is markedly lower than in melt compounding procedures. To check this concept, basalt fiber mat-reinforced thermoset composites were produced by resin transfer molding (RTM). Note that the reinforcing mat was always a felt consisting of short fibers, the handling of which was ensured by needling.

5.1 Basalt Fiber Mat-Reinforced Hybrid Thermosets

Hybrid thermosets of interpenetrating network (IPN) structure were developed recently.[50,51] Albeit the major target was to improve the toughness by IPN formation, the related resins were of great importance for composite applications. Combining vinylester (VE) with amine-crosslinkable EP resins is beneficial for composites due to the low viscosity, fast curing and IPN structure of the outcoming thermosets. Note that low viscosity owing to the presence of styrene (crosslinking agent for VE) is helpful for wetting out the reinforcement. The fast curing of VE compared to EP alone allows to reduce the production cycle time. However, the

most interesting aspect is given by the IPN structuring. As the average width of the IPN constituting bands is of *ca.* 100 nm, an intermittent bonding of the reinforcing fiber can be achieved *via* the matrix structure. Intermittent means that good-poor-good-... bonding may occur on the nano-scale, if the fiber surface is appropriately "finished" for one (*i.e.*, VE or EP) of the resin components. In order to check this concept, BF mat-reinforced composite sheets were produced by RTM. The VE/EP hybrid resin and the parameters of the RTM processing are described in previous works of ours.[52,53] The surface chemistry of the BF mat containing discontinuous fibers (length ≤50 mm) was varied. To vary the sizing (finish) of the BF, the original sizing was removed by burning (500 °C, 3 h).The organosilane sizings of the BF were performed in aqueous solutions containing silanes of epoxy (ES) or vinyl (VS) functialities.[54] From the composite sheets containing *ca.* 30 wt.% BF mat of various surface treatments, rectangular specimens were cut and subjected to standardized tension and flexural loading. The related results are summarized in Table 6.

The data in Table 6 clearly show the reinforcing effect of the BF mat as a function of sizing. The tensile and flexural mechanical values of the composites are comparable for mats containing as-received and burned BF. Sizing of BF by VS and ES strongly improved both strength and stiffness. Note that sizing has a strong effect on the strength properties. On the other hand, stiffness should be insensitive to BF sizing as it depends on the reinforcement amount, which is not the present case. This can be explained by the fact that due to the ES and VS sizing the initial IPN structure has been changed at least close to the fiber surfaces. So, BF is likely encapsulated by an EP- or VE-rich layer depending on whether ES or VS sizing was applied. This might have changed the stiffness and strength characteristics of the matrix *via* differences in the crosslinking reactions (*i.e.*, VE crosslinking with styrene through free radical mechanism and polyaddition between the epoxy groups

Table 6. Mechanical properties of BF mat-reinforced VE/EP resins of IPN structure as a function of the BF surface treatment: T – tensile, F – flexural.

	Loading	σ *(MPa)*	*E (GPa)*	ε *(%)*
VE/EP matrix	T	40.8±1.7	2.4±0.1	4.5±0.8
	F	75.9±1.5	2.2±0.1	5.2±0.2
With as-received BF mat	T	47.5±3.8	4.8±0.6	2.1±0.4
	F	100.3±3.1	6.2±0.2	2.1±0.1
With burned BF mat	T	44.3±0.9	4.3±1.0	0.9±0.2
	F	77.2±9.1	5.8±0.9	3.0±0.7
With ES-treated BF mat	T	58.8±0.7	6.0±0.5	1.6±0.5
	F	115.4±0.1	9.0±0.3	1.4±0.1
With VS-treated BF mat	T	58.0±1.1	6.5±0.1	1.5±0.2
	F	109.5±6.4	9.5±0.5	1.3±0.1

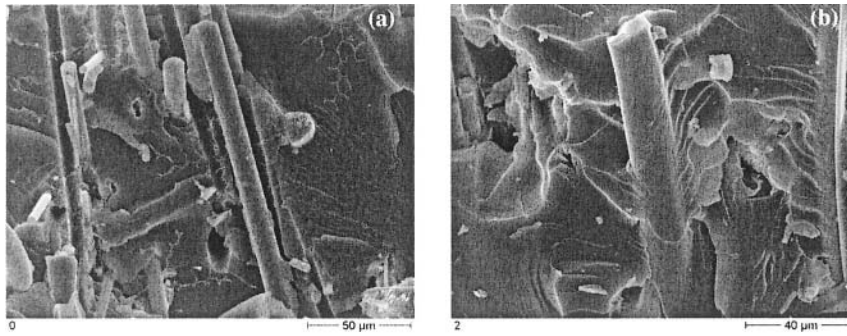

Figure 4. SEM pictures taken from the fracture surfaces of BF mat-reinforced VE/EP matrix composites with: (a) burned BF and (b) vinylsilane-treated BF.

of EP and amine groups of the hardener). Changes in the interface/interphase characteristics should be observable on the fracture surface of the composites by fractography. Figure 4 displays the difference between burned and VS-treated BF mat reinforcements.

If the above scenario is correct, preferrential wetting by one of the resins (encapsulation) takes place instead of intermittent bonding. At present, this issue is under investigation.

5.2 Hybrid Fiber Mat-Reinforced Hybrid Thermosets

The composite materials reported here were produced under the conditions described in Section 5.1. Even the sizing of the fibers was changed as described

Table 7. Tensile and flexural mechanical properties of hybrid fiber mat-reinforced (CeF/GF) hybrid composites as a function of the fiber surface treatment: T – tensile, F – flexural.

	Loading	*σ (MPa)*	*E (GPa)*	*ε (%)*
VE/EP matrix	T	40.8±1.7	2.4±0.1	4.5±0.8
	F	75.9±1.5	2.2±0.1	5.2±0.2
With as-reeceived CeF/GF mat	T	56.8±1.6	2.7±0.1	4.5±0.3
	F	99.3±0.1	2.6±0.1	4.9±0.1
With burned CeF/GF mat	T	58.4±1.6	4.8±0.1	2.5±0.2
	F	119.4±0.1	4.8±0.1	2.9±0.6
With ES-treated CeF/GF mat	T	86.1±0.2	6.6±0.1	3.4±0.5
	F	145.3±4.1	6.4±0.1	2.5±0.1
With VS-treated CeF/GF mat	T	96.6±0.3	7.6±0.5	3.8±0.2
	F	133.1±2.5	6.5±0.1	4.3±0.2

above. The only difference was that the reinforcing mat, present here also in 30 wt.%, consisted of 70 wt.% CeF (10–50 mm long, diameter 9±1 μm) and 30 wt.% GF (10–50 mm long, diameter 11±2 μm). The difference in the mechanical characteristics between GF and CeF is not substantial. Thus, the effect of surface treatment may override the fiber hybridization effect. The data in Table 7 show that probably this was the case, since the effect of the fiber surface treatment was very strong. As expected, again the VS and ES treatments of the fibers proved to be most suitable for the VE/EP hybrid resin-based mat-reinforced composites.

6 Conclusions and Outlook

Due to their favorable price/weight characteristics, good mechanical properties, and corrosion resistance, fiber-reinforced polymer composites are indispensable nowadays in many applications. The results described in this chapter demonstrate that discontinuous BF produced by melt blowing is a suitable reinforcement for polymers of both thermoplastic and thermoset nature. However, due to the brittleness of BF, "gentle" technologies have to be selected during preforming (*e.g.*, to produce mats by carding instead of needling) and processing. For melt processing, some adjustments in the machinery could be necessary (*e.g.*, screw configuration) and proper processing conditions should be selected. Thermoset processing methods, such as resin transfer molding, production of sheet molding compounds, and reinforced reactive injection molding with polyurethanes may be very interesting for BF applications. Fiber hybridization with BF is a straightforward method to reduce the materials cost without sacrificing the mechanical property profile of the composites. In some cases, even a positive hybrid effect can be achieved.

Matrix hybridization seems to be a useful tool for both thermoplastics and thermosets. The encapsulation of BF by one of the polymers may have various beneficial effects, such as resistance against breakage and tailoring of the interphase properties.

It was established that the surface treatment of BF is crucial in order to reach useful composite properties. This issue should be considered, however, still in the BF production stage.

It is worth noting that high quality continuous and discontinuous BF, produced by traditional melt spinning technologies, will be marketed in the near future. This may give a new impetus to BF applications in polymer composites.

Future research on BF/polymer composites will focus on the use of the exceptional properties of BF, namely fire and corrosion resistance. Concerning the matrix development, the use of recyclable polymers can be predicted.

7 Acknowledgement

This work was supported by the Hungarian Ministry of Education (Széchenyi-plan NKFP 3/001/2001) and the Hungarian-German Intergovernmental Science and Technology Project (TéT D-16/02 and HUN 02/024, respectively).

8 References

[1] D. D. Dzhigiris, R. P. Polevoi, P. P. Polevoi (1976) Life of refractories of tank furnace for production of superfine basalt fiber, *Glass Ceram.* **33**, 223.

[2] D. D. Dzhigiris, M. F. Makhova, V. D. Gorobinskaya, V. D. Bombyrlin (1983) Continuous basalt fiber, *Glass Ceram.* **40**, 467.

[3] R. V. Subramanian, H. F. Austin (1980) Silane coupling agents in basalt-reinforced polyester composites, *Int. J. Adhes. Adhes.* **1**, 50.

[4] J. M. Park, R. V. Subramanian (1991) Interfacial shear strength and durability improvement by monomeric and polymeric silanes in basalt fiber epoxy single-filament composite specimens, *J. Adhes. Sci. Technol.* **5**, 459.

[5] J. M. Park, R. V. Subramanian, A. E. Bayoumi (1994) Interfacial shear strength and durability improvement by silanes in single-filament composite specimens of basalt fiber in brittle phenolic and isocyanate resins, *J. Adhes. Sci. Technol.* **8**, 133.

[6] I. Wojnárovits (1995) Factors influencing the mechanical properties of silicate fibers, *Glass Sci. Technol.* **68**, 360.

[7] T. Jung, R. V. Subramanian (1993) Strengthening of basalt fiber by alumina addition, *Scripta Mater.* **28**, 527.

[8] F. M. Kogan, O. V. Nikitina (1994) Solubility of chrysotile asbestos and basalt fibers in relation to their fibrogenic and carcinogenic action, *Environ. Health Persp.* **102**, 205.

[9] E. E. McConnell, O. Kamstrup, R. Musselman, T. W. Hesterberg, J. Chewalier, W. C. Miller, P. Thevenaz (1994) Chronic inhalation study of size-separated rock and slag wool insulation fibers in Fischer 344/N rats, *Inhal. Toxicol.* **6**, 571.

[10] Z. Adamis, T. Kerényi, K. Honma, M. Jackel, E. Tátrai, G. Ungváry (2001) Study of inflammatory responses to crocidolite and basalt wool in the rat lung, *J. Toxicol. Env. Health* **62**, 409.

[11] J. M. Park, E. M. Chong, W. G. Shin, S. I. Lee, D. J. Yoon, J. H. Lee (1996) Interfacial properties and micro-failure mechanisms of SiC fiber reinforced high temperature thermoplastic composites using fragmentation technique and acoustic emission, *Polym.-Korea* **20**, 753.

[12] J. M. Park, E. M. Chong, D. J. Yoon, J. H. Lee (1998) Interfacial properties of two SiC fiber-reinforced polycarbonate composites using the fragmentation test and acoustic emission, *Polym. Compos.* **19**, 747.

[13] J. M. Park, W. G. Shin (1997) Interfacial aspects of dual basalt and SiC fibers reinforced epoxy composites using fragmentation technique and acoustic emission, *Korea Polym. J.* **5**, 114.

[14] J. M. Park, W. G. Shin, D. J. Yoon (1999) A study of interfacial aspects of epoxy-based composites reinforced with dual basalt and SiC fibres by means of the fragmentation and acoustic emission techniques, *Compos. Sci. Technol.* **59**, 355.

[15] P. I. Bashtannik, V. G. Ovcharenko, Y. A. Boot (1997) Effect of combined extrusion parameters on mechanical properties of basalt fiber-reinforced plastics based on polypropylene, *Mech. Compos. Mater.* **33**, 600.

[16] P. I. Bashtannik, V. G. Ovcharenko (1997) Antifriction basalt-plastics based on polypropylene, *Mech. Compos. Mater.* **33**, 299.

[17] M. Botev, H. Betchev, D. Bikiaris, C. Panayiotou (1999) Mechanical properties and viscoelastic behavior of basalt fiber-reinforced polypropylene, *J. Appl. Polym. Sci.* **74**, 523.

[18] W. B. Goldsworthy (2000) New basalt fiber increases composite potential, *Compos. Technol.* **8**, 15.

[19] V. V. Gurev, E. I. Neproshin, G. E. Mostovoi (2001) The effect of basalt fiber production technology on mechanical properties of fiber, *Glass Ceram.* **58**, 62.

[20] N. N. Morozov, V. S. Bakunov, E. N. Morozov, L. G. Aslanova, P. A. Granovskii, V. V. Prokshin, A. A. Zemlyanitsyn (2001) Materials based on basalts from the European North of Russia, *Glass Ceram.* **58**, 100.

[21] A. M. Zihlif, G. Ragosta (2003) A study on physical properties of rock wool fiber-polystyrene composite, *J. Thermoplast. Compos.* **16**, 273.

[22] P. I. Bashtannik, A. I. Kabak, Y. Y. Yakovchuk (2003) The effect of adhesion interaction on the mechanical properties of thermoplastic basalt plastics, *Mech. Compos. Mater.* **39**, 85.

[23] J. Karger-Kocsis (2000) Reinforced polymer blends, in *Polymer Blends* (Eds. D. R. Paul, C. B. Bucknall) John Wiley & Sons, New York. Vol. 2, p. 395.

[24] S. Y. Fu, G. Xu, Y. W. Mai (2002) On the elastic modulus of hybrid particle/short-fiber/polymer composites, *Composites Part A* **33**, 291.

[25] B. Pukánszky (1995) Particulate filled polypropylene: structure and properties, in *Polypropylene. Structure, Blends and Composites* (Ed. J. Karger-Kocsis) Chapman & Hall, London. Vol. 3, p. 1.

[26] A. R. Bunsell, B. Harris (1974) Hybrid carbon and glass fiber composites, *Composites* **4**, 157.

[27] J. Summerscales, D. Short (1978) Carbon fibre and glass fibre hybrid reinforced plastics, *Composites* **9**, 157.

[28] G. Marom, E. Drukker, A. Weinberg, J. Banbaji (1986) Impact behaviour of carbon/Kevlar hybrid composites, *Composites* **17**, 150.

[29] G. Marom, H. Harel, S. Neumann, K. Friedrich, K. Schulte, H. D. Wagner (1989) Fatigue behaviour and rate-dependent properties of aramid fibre/carbon fibre hybrid composites, *Composites* **20**, 537.

[30] R. A. Chaudhuri, H. J. Garala (1995) Analytical experimental evaluation of hybrid commingled carbon glass epoxy thick-section composites under compression, *J. Compos. Mater.* **29**, 1695.

[31] S. Y. Fu, B. Lauke, E. Mäder, X. Hu, C. Y. Yue (1999) Fracture resistance of short glass-fiber-reinforced and short-carbon-fiber-reinforced polypropylene under Charpy impact load and its dependence on processing, *J. Mater. Process. Tech.* **89-90**, 501.

[32] J. Jang, C. Lee (1998) Performance improvement of GF/CF functionally gradient hybrid composite, *Polym. Test.* **17**, 383.

[33] M. Sohn, X. Hu (1998) Processing of carbon-fibre epoxy composites with cost-effective interlaminar reinforcement, *Compos. Sci. Technol.* **58**, 211.

[34] K. Friedrich, O. Jacobs (1992) On wear synergism in hybrid composites, *Compos. Sci. Technol.* **43**, 71.

[35] G. Kalaprasad, S. Thomas, C. Pavithran, N. R. Neelakantan, S. Balakrishnan (1996) Hybrid effect in the mechanical properties of short sisal/glass hybrid fiber reinforced low density polyethylene composites, *J. Reinf. Plast. Comp.* **15**, 48.

[36] G. Kalaprasad, K. Joseph, S. Thomas (1997) Influence of short glass fiber addition on the mechanical properties of sisal reinforced low density polyethylene composites, *J. Compos. Mater.* **31**, 509.

[37] O. I. Benevolenski, J. Karger-Kocsis, K. P. Mieck, T. Reussmann (2000) Instrumented perforation impact response of polypropylene composites with hybrid reinforcement flax/glass and flax/cellulose fibers, *J. Thermoplast. Compos. Mater.* **13**, 481.

[38] H. D. Rozman, G. S. Tay, R. N. Kumar, A. Abusamah, H. Ismail, Z. A. Mohd Ishak (2001) Polypropylene-oil palm empty fruit bunch-glass fibre hybrid composites: a preliminary study on the flexural and tensile properties, *Eur. Polym. J.* **37**, 1283.

[39] J. Rout, M. Misra, S. S. Tripathy, S. K. Nayak, A. K. Mohanty (2001) The influence of fibre treatment on the performance of coir-polyester composites, *Compos. Sci. Technol.* **61**, 1303.

[40] M. M. Thwe, K. Liao (2002) Effects of environmental aging on the mechanical properties of bamboo-glass fiber reinforced polymer matrix hybrid composites, *Composites A* **33**, 43.

[41] S. Mishra, A. K. Mohanty, L. T. Drzal, M. Misra, S. Parija, S. K. Nayak, S. S. Tripathy (2003) Studies on mechanical performance of biofibre/glass reinforced polyester hybrid composites, *Compos. Sci. Technol.* **63**, 1377.

[42] G. Marom, S. Fisher, F. R. Tuler, H. D. Wagner (1978) Hybrid effects in composites: conditions for positive or negative effects *versus* rule of mixture behaviour, *J. Mater. Sci.* **13**, 1419.

[43] S. Fu, Y. Mai, B. Lauke, C. Yue (2002) Synergistic effect on the fracture toughness of hybrid short glass fiber and short carbon fiber reinforced polypropylene composites, *Mat. Sci. Eng.* **323**, 326.

[44] T. Hayashi (1972) Development of new material properties by hybrid composition, *Compos. Mater.* **1**, 18.

[45] X. Zhu, Z. Li, Y. Jin (1994) Creep behaviour of a hybrid fibre (glass/carbon)-reinforced composite and its application, *Compos. Sci. Technol.* **50**, 431.

[46] C. H. Chiu, K. H. Tsai, W. J. Huang (1999) Crush-failure modes of 2D triaxially braided hybrid composite tube, *Compos. Sci. Technol.* **59**, 1713.

[47] Y. Shan, K. Liao (2001) Environmental fatigue of unidirectional glass-carbon fiber reinforced hybrid composite, *Composites B* **32**, 355.

[48] J. R. Hazen (2003) Carbon/fiberglass wind blades planned, *High-Performance Compos.* **11**, 13.

[49] D. Yu, J. Wu, L. Zhou, D. Xie, S. Wu (2000) The dielectric and mechanical properties of a potassium-titanate-whisker reinforced PP/PA blend, *Compos. Sci. Technol.* **60**, 499.

[50] J. Karger-Kocsis, O. Gryshchuk, N. Jost (2003) Toughness response of vinylester/epoxy-based themosets of interpenetrating network structure as a function of the epoxy resin formulation: Effects of the cyclohexylene linkage, *J. Appl. Polym. Sci.* **88**, 2124.

[51] J. Karger-Kocsis, O. Gryshchuk, S. Schmitt (2003) Vinylester/epoxy-based thermosets of interpenetrating network structure: An atomic force microscopic study, *J. Mater. Sci.* **38**, 413.

[52] J. S. Szabó, G. Romhány, T. Czigány, J. Karger-Kocsis (2003) Interpenetrating vinylester/epoxy resins reinforced by flax fibre mat, *Adv. Compos. Lett.* **12**, 115.

[53] J. S. Szabó, J. Karger-Kocsis, O. Gryshchuk, T. Czigány (2004) Effect of fibre surface treatment on the mechanical response of ceramic fibre mat-reinforced interpenetrating vinylester/epoxy resins, *Compos. Sci. Technol.* **64**, 1717.

[54] D. M. Laura, H. Keskkula, J. W. Barlow, D. R. Paul (2002) Effect of glass fiber surface chemistry on the mechanical properties of glass fiber reinforced, rubber-toughened nylon 6, *Polymer* **43**, 4673.

Chapter 18

Accelerated Testing Methodology for Polymer Composite Durability

Masayuki Nakada, Yasushi Miyano
Materials System Research Laboratory, Kanazawa Institute of Technology, Yatsukaho, Matto, Ishikawa, Japan

Rokuro Muki
Civil & Environmental Engineering Department, University of California at Los Angeles, Los Angeles, CA, USA

1 Introduction

The mechanical behavior of polymer resins exhibits time and temperature dependences, called *viscoelastic* behavior, not only above, but also below the glass-transition temperature, T_g. Thus, it can be presumed that the mechanical behavior of polymer composites also depends on time and temperature even below T_g, which is within the normal operating-temperature range. Examples in this respect are given by Aboudi *et al.*,[1] Sullivan,[2] Gates,[3] and Miyano *et al.*[4-6]

The time-temperature dependence of the flexural constant strain-rate (CSR), creep, and fatigue strengths of various carbon fiber-reinforced plastics (CFRP) has been studied by McMurray *et al.*[7] and Miyano *et al.*[5] It was observed by Enyama *et al.*[8] that the fracture modes are almost identical for the above three types of loading over wide ranges of time and temperature. Similar results were also reported by Karayaka *et al.*[9] at room temperature. The literature survey indicates the validity of the two hypotheses for CFRP: the same failure process and the same time-temperature superposition principle for CSR, creep, and fatigue failure.

In our previous publication,[10] we proposed a prediction method for fatigue strength of fiber-reinforced plastics (FRP) under arbitrary frequency, stress ratio, and temperature based on the above two hypotheses and two additional ones: the

linear cumulative damage law for monotonic non-decreasing loading and the linear dependence of the fatigue strength on the stress ratio. Further, we applied the method to our experimental data for various FRP and FRP/metal joints from tensile and three-point bending tests[10-18] and discussed the cause of limitation when the method fails.[14,15] In this chapter, we summarize the validity and limitations of the fatigue-prediction method for typical FRP and FRP/metal joints.

2 Prediction Procedure of Fatigue Strength

The prediction method[10] rests on the four hypotheses: (A) same failure process under CSR, creep, and fatigue loadings, (B) same time-temperature superposition principle for all failure strengths, (C) linear cumulative damage law for monotonic non-decreasing loading, and (D) linear dependence of fatigue strength on stress ratio.

When these hypotheses are valid, the fatigue strength under an arbitrary combination of frequency, stress ratio, and temperature can be determined based on the following test results: (i) master curve of CSR strength and (ii) master curve of fatigue strength for zero stress ratio. The master curve of CSR strength is constructed from the test results at various constant strain-rates and temperatures. On the other hand, the master curve of fatigue strength at zero stress ratio can be constructed from the test results at a single frequency for various temperatures based on hypothesis (B).

The outline of this method is shown schematically in Figure 1 together with definitions of some notations. The detail of the method will be presented with experimental data.

3 Some Experimental Details and Relationships Obtained

3.1 Experimental Procedure

The satin-woven CFRP laminates were made from carbon fiber Torayca T400 (Toray) and a matrix resin #3601 with a high glass transition temperature of 236 °C.[10] The volume fraction of the fibers in the CFRP was approximately 65.5%.

The three-point bending tests for CSR, creep, and fatigue loadings were conducted at various temperatures. The span, width and thickness for these tests were $L = 50$ mm, $b = 15$ mm, and $h = 2.7$ mm, respectively.

The CSR tests were conducted using an Instron type testing machine with a constant temperature chamber. The tests were conducted at three loading rates $V = 0.02$, 2, and 200 mm/min at ten constant temperatures from $T = 50$ °C to 250 °C.

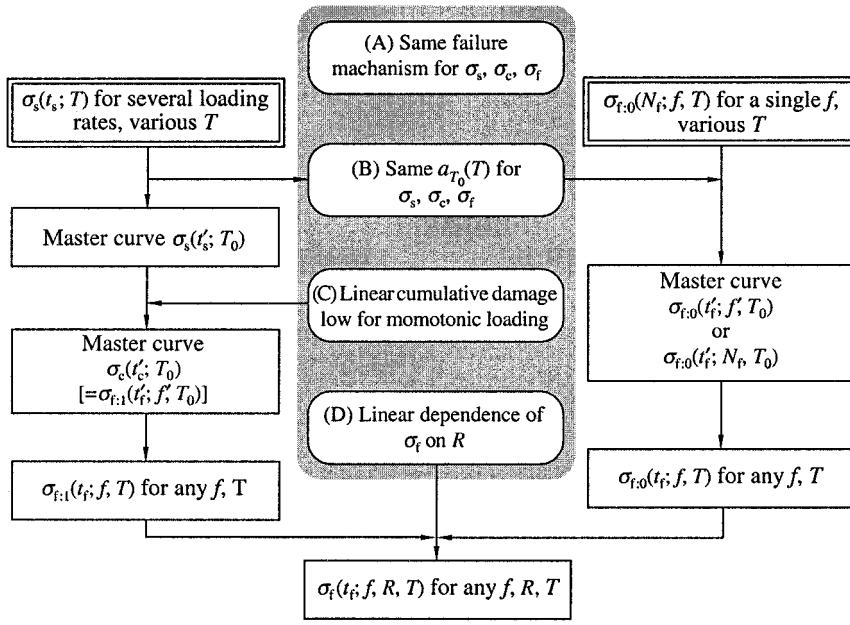

Figure 1. Prediction procedure of fatigue strength. T, T_0: temperature, reference temperature; f, f': frequency, reduced frequency; t_s, t_c, t_f: time to failure under CSR, creep, and fatigue loadings; t'_s, t'_c, t'_f: reduced times to failure; a_{T_0}: time-temperature shift factor ($a_{T_0} = t_s/t'_s = t_c/t'_c = t_f/t'_f = f'/f$); R: stress ratio ($R = \sigma_{min}/\sigma_{max}$); N_f: number of cycles to failure ($N_f = f \cdot t_f$); σ_s, σ_c, σ_f: CSR, creep, and fatigue strengths; $\sigma_{f:0}$, $\sigma_{f:1}$: σ_f for $R = 0$ and $R = 1$.

The creep tests were conducted at three constant temperatures using a creep testing machine with a constant temperature chamber. The fatigue tests were conducted using an electro-hydraulic servo testing machine with a constant temperature chamber at five constant temperatures and two loading frequencies ($f = 2$ and 0.02 Hz) and a stress ratio (minimum stress/maximum stress), $R = 0.05$. Additionally, the fatigue tests were also conducted at $R = 0.5$ and three different temperatures.

3.2 Failure Mechanism

We summarize here the failure mechanism under CSR, creep, and fatigue loading for satin-woven CFRP laminates tested by three-point bending. Figure 2 shows the side view of flexural failure of T400/3601 under CSR, creep, and fatigue loadings at various temperatures. In the CSR test for the temperature of 200 °C or below, faint sounds were heard without any visible sign of failure preceding the

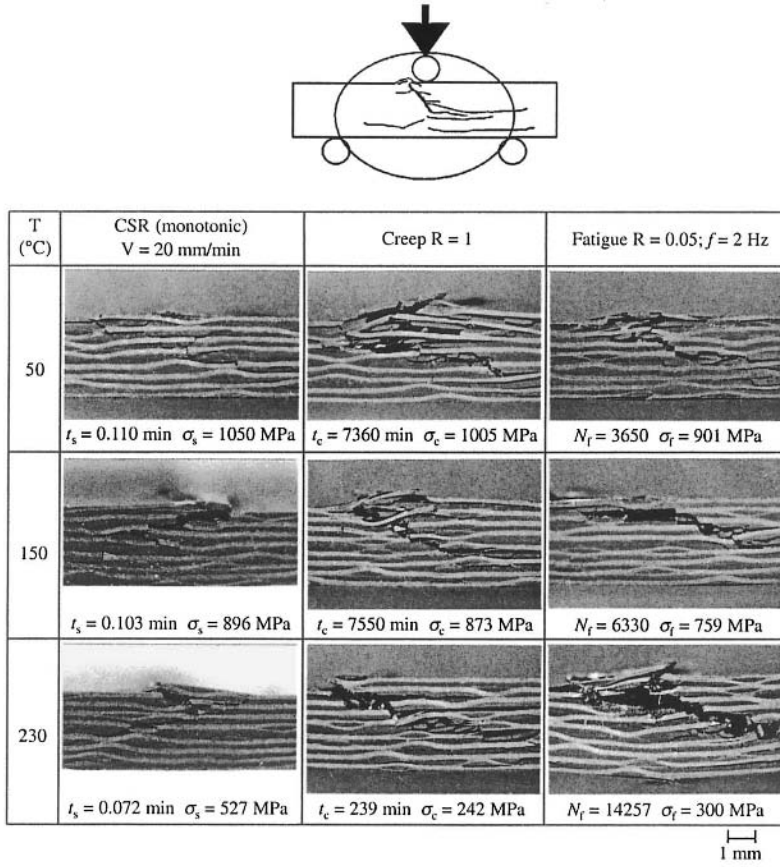

Figure 2. Side view of the flexural failure of T400/3601 under CSR, creep, and fatigue loadings at various temperatures.

warp fiber buckling on the compressive side of the specimen near the loading point. Then, a crack initiated in the matrix at the site of the warp fiber buckling propagated into the thickness of the specimen at some angles up to a plane slightly in the tensile side. Finally, delamination took place leading to the failure of the specimen, accompanied by a loud sound. The entire failure process took a very short period of time for the temperatures below 200 °C. On the contrary, for the test temperature above 200 °C, no sounds were heard during the failure process and the crack propagated more slowly, though the same fracture process as for the test temperatures below 200 °C was observed. Therefore, we assume that the specimens fail in a similar manner with different time scales depending on the temperature regardless of the loading pattern.

3.3 Master Curve for the CSR Strength

The left hand side of Figure 3 shows the CSR strength, σ_s, *vs.* time to failure, t_s, at ten temperatures, T, where t_s is the time period from the initial to the maximum loading. The master curve was constructed by shifting σ_s at constant temperatures other than the reference temperature, T_0, along the log scale of t_s, so that they overlap on σ_s at the reference temperature or on each other to form a single smooth curve, as shown in the right hand side of Figure 3. Since σ_s at various temperatures can be superimposed smoothly, the time-temperature superposition principle is applicable to σ_s.

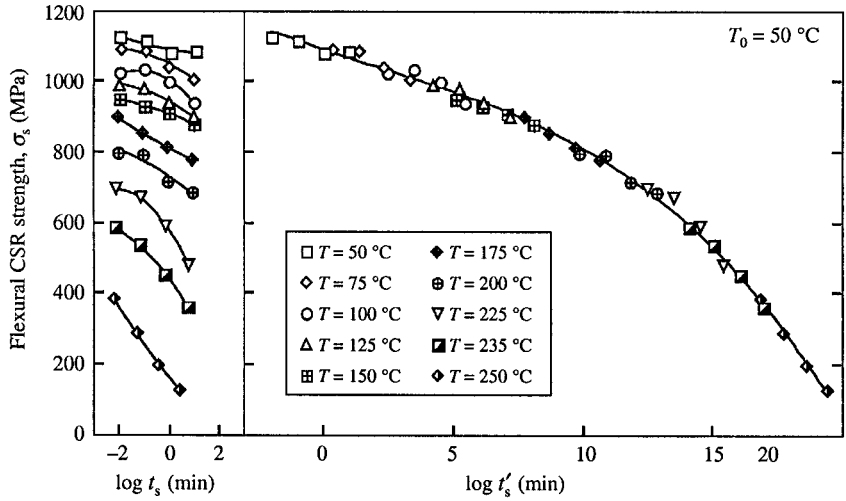

Figure 3. Master curve of CSR strength.

The time-temperature shift factor $a_{T_0}(T)$ is defined by

$$a_{T_0}(T) = \frac{t_s}{t'_s} \tag{1}$$

where t'_s is the corresponding time at the reference temperature T_0, called the reduced time to failure. The shift factors for the CSR strength of T400/3601 obtained experimentally in Figure 3 are plotted in open circles in Figure 4; the solid circles in Figure 4 are the shift factors for the storage modulus of matrix resin. They agree well with each other, indicating that the time and temperature dependence of the CSR strength is controlled by the viscoelastic behavior of the matrix resin.

All of these shift factors are quantitatively in good agreement with two Arrhenius' equations with different activation energies ΔH:

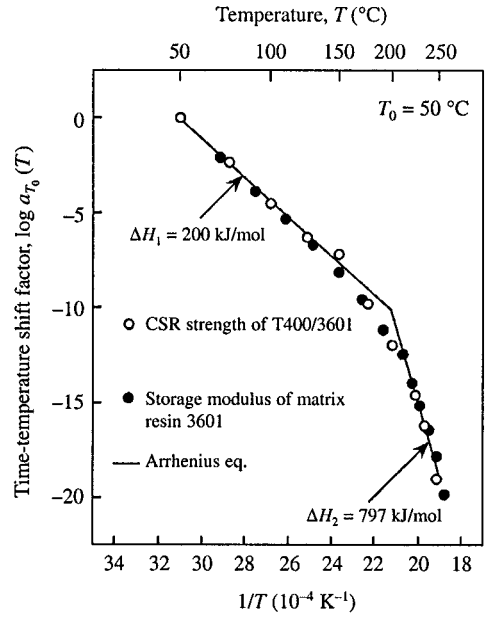

Figure 4. Time-temperature shift factors for CSR strength.

$$\log a_{T_0}(T) = \frac{\Delta H}{2.303G}\left(\frac{1}{T} - \frac{1}{T_0}\right) \tag{2}$$

where G is the gas constant, 8.314×10^{-3} [kJ/(K.mol)].

3.4 Master Curve for Creep Strength

A prediction method for the creep strength, σ_c, from the master curve of the CSR strength using the linear cumulative damage law was presented in our previous publication.[10] Let $t_s(\sigma)$ and $t_c(\sigma)$ be the CSR and creep failure time, respectively, for the stress σ. Suppose that the material experiences a non-decreasing stress history $\sigma(t)$ for $0 < t < t^*$ where t^* is the failure time under this stress history. The linear cumulative damage law states

$$\int_0^{t^*} \frac{dt}{t_c[\sigma(t)]} = 1 \tag{3}$$

When $\sigma(t)$ is a constant stress σ_0, the above formula yields $t^* = t_c(\sigma_0)$.

The left hand side of Figure 5 shows the creep strength σ_c at three temperatures which are shifted using the shift factor for the CSR strength to the data at $T_0 = 50$ °C on the right hand side. There, the dashed curve represents the master

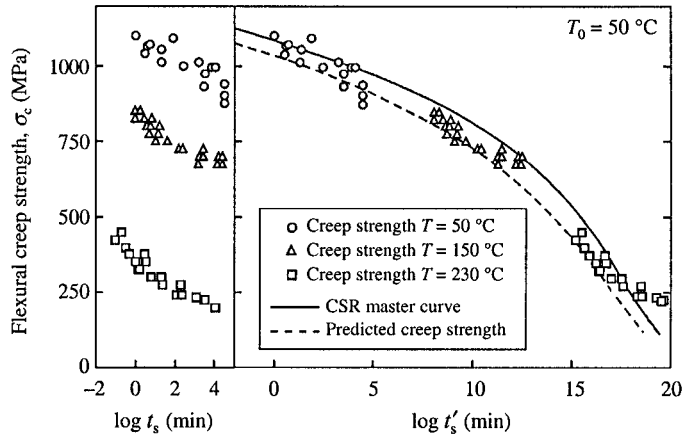

Figure 5. Prediction of creep strength.

curve of the creep strength calculated on the basis of Eq. (3) using the master curve of CSR strength (solid line). The agreement between the predicted curve and the creep test data is satisfactory; this indicates the validity of the linear cumulative damage law and a common shift factor.

3.5 Master Curve for the Fatigue Strength at Zero Stress Ratio

We regard the fatigue strength, σ_f, either as a function of the number of cycles to failure, N_f, or of the time to failure $t_f = N_f/f$ for a combination of frequency f, stress ratio R, and temperature T, and denote it either $\sigma_f(N_f; f, R, T)$ or $\sigma_f(t_f; f, R, T)$. Further, we consider the CSR strength $\sigma_s(t_f; T)$ the fatigue strength at $N_f = 1/2$, $R = 0$, and $t_f = 1/(2f)$; this is motivated by the closeness of the line connecting the origin and $(\pi, 1)$ and the curve $[1 + \sin(t - \pi/2)]/2$ for $0 < t < \pi$. At this point, we introduce special symbols for fatigue strength at zero and unit stress ratios, $\sigma_{f:0}$ and $\sigma_{f:1}$, where the latter corresponds to creep strength.

To describe the master curve for $\sigma_{f:0}$, we need the reduced frequency f' in addition to the reduced time t'_f, each defined by

$$f' = f \cdot a_{T_0}(T), \; t'_f = \frac{t_f}{a_{T_0}(T)} = \frac{N_f}{f'} \tag{4}$$

We introduce two alternative expressions for the master curve for zero stress ratio: $\sigma_{f:0}(t'_f; f', T_0)$ and $\sigma_{f:0}(t'_f; N_f, T_0)$. In the latter expression, the explicit reference to frequency is suppressed in favor of N_f. Equation (4) enables one to construct the master curve from the tests at a single frequency and various temperatures.

Curves of the flexural fatigue strength, $\sigma_{f:0}$, *vs.* the number of cycles to failure N_f, $\sigma_{f:0}$-N_f curves, are shown in Figure 6 where $\sigma_{f:0}$ at $N_f = ½$ is represented by σ_s at $t_s = (2f)^{-1}$. The upper graph is for $f = 2$ Hz, while the lower is for $f = 0.02$ Hz

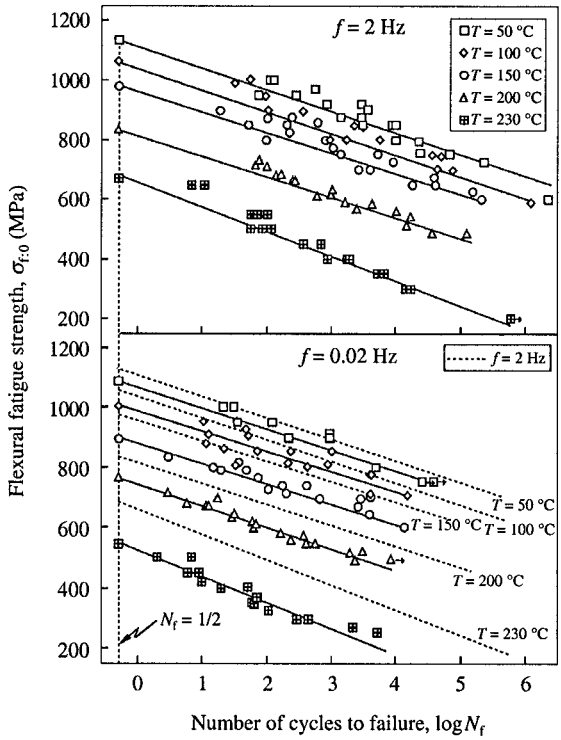

Figure 6. σ-N curves for $f = 2$ and 0.02 Hz, $R = 0.05$.

where the curves for $f = 2$ Hz are also included (dotted lines). The $\sigma_{f:0}$-N_f curves are found to be linear with a same slope for all frequencies and temperatures tested over the six decades of N_f. Furthermore, hypothesis (B) is valid for the fatigue strength since the frequency-temperature dependence of the $\sigma_{f:0}$-N_f curves is controlled by σ_f at $N_f = ½$, which is equal to $\sigma_s\{(2f)^{-1}; T\}$, obeying hypothesis (B). We thus confirmed that tests at a single frequency are sufficient to construct the master curve of $\sigma_{f:0}$.

The fatigue strength $\sigma_{f:0}$ *vs.* the reduced time to failure t_f' dependences for ten reduced frequencies f' are depicted by dotted lines in Figure 7; they are evaluated from Figure 6 using Eq. (4). The master curves of $\sigma_{f:0}$-t_f' for fixed N_f are constructed by connecting the points of the same N_f on the curves for a fixed reduced frequency, as shown by the solid curves in Figure 7.

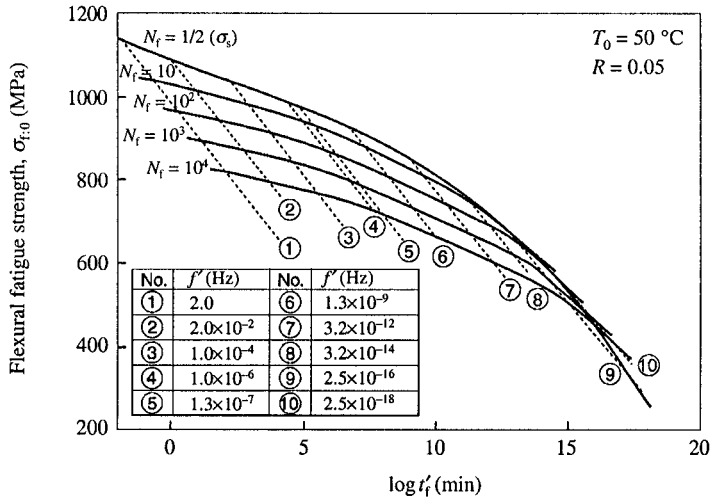

Figure 7. Master curves of fatigue strength for $R = 0.05$.

3.6 Prediction of Fatigue Strength for Arbitrary Stress Ratios

The creep strength at any temperature T can be taken from the master curve for creep strength $\sigma_c(t_f'; T_0)$. The creep strength, in turn, may be regarded as the fatigue strength $\sigma_{f:1}(t_f; f, T)$ at unit stress ratio $R = 1$ and arbitrary frequency f with $t_c = t_f$. Further, the master curves for the fatigue strength $\sigma_{f:0}(t_f', f', T_0)$ can be obtained, in principle, from tests with a single frequency and various temperatures, as evident from Eq. (4); the master curves in Figure 7 were constructed based on the two frequencies, 0.02 and 2 Hz. The fatigue strength $\sigma_{f:0}(t_f; f, T)$ at zero stress ratio for any combination of t_f, f, T can be read off from Figure 7 after evaluating the corresponding reduced time t_f' and frequency f' by using Eq. (4).

Implementing hypothesis (D), we propose a formula to estimate the fatigue strength $\sigma_f(t_f; f, R, T)$ at an arbitrary combination of f, R, T by

$$\sigma_f(t_f; f, R, T) = \sigma_{f:1}(t_f; f, T)R + \sigma_{f:0}(t_f; f, T)(1-R) \tag{5}$$

Figure 8 shows experimental data for σ_f-t_f for $f = 2$ Hz, $R = 0.05$, 0.5, 0.8, 1.0, and $T = 50$, 150, 230 °C. The solid lines represent the least-square fits for $R = 0.05$ which we assume as the curves for $R = 0$, while the dashed lines are the creep strengths obtained from the master curve of the CSR strength using the linear cumulative damage law. The dash-dotted and dash-double-dotted lines are calculated from Eq. (5) on the basis of the curves for $R = 0$ and $R = 1$, respectively. As can be seen, the predictions agree well with the experimental data for all temperatures tested. Therefore, the validity of hypothesis (D) for the fatigue strength is confirmed.

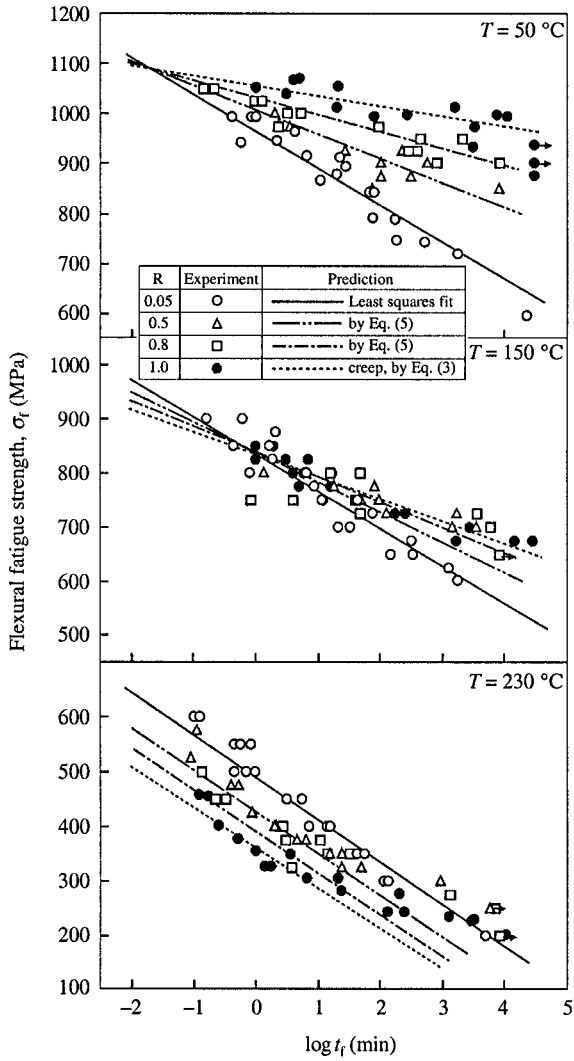

Figure 8. Prediction of fatigue strength for various stress ratios.

4 Applicability of the Prediction Method

We applied the prediction method to the fatigue strengths of various FRP and FRP/metal joints; typical results are shown in Table 1, where the symbols ○, △, and × denote complete agreement, partial agreement, and disagreement with the hypotheses, respectively.

Table 1. Applicability of the prediction method.

Carbon fiber	Matrix	Type	Fiber/Matrix	Loading direction	Hypothesis (A)	(B)	(C)	(D)
PAN	Epoxy	UD	T400/828	LT	○	○	○	○
			T300/2500	LB	○	○	○	○
				TB	○	○	○	○
		SW	T400/3601	LB	○	○	○	○
	PEEK	UD	T300/PEEK	LB	○	×	×	△
				TB	△	×	×	×
Pitch	Epoxy	UD	XN40/25C	LB	○	△	×	○

GFRP/Metal Joint System		Hypothesis (A)	(B)	(C)	(D)
Conical shaped joint		○	○	○	○
Adhesive joint	Brittle epoxy	○	○	○	○
	Ductile PMMA	○	○	○	○
Bolted joint		○	○	○	○

UD: Unidirectorial; SW: Stain woven; LT: Longitudinal tension; LB: Longitudinal bending; TB: Transverse bending

The tensile fatigue strength in the longitudinal direction, the flexural fatigue strengths in the longitudinal and transverse directions of unidirectional PAN-based carbon fiber/epoxy resin, and the flexural fatigue strength of satin-woven PAN-based carbon fiber/epoxy resin can be predicted using this method, because the hypotheses (A)-(D) are valid.[10,13,15,16] In these cases, the time-temperature superposition principle for the CSR strength also holds for creep and fatigue strengths. The flexural fatigue strengths of PAN-based carbon fiber/PEEK resin and pitch-based carbon fiber/epoxy resin cannot be predicted, because the time-temperature superposition principle for the CSR strength does not hold for the creep strength, which is caused by the crystallization of the PEEK resin and the time-dependent behavior of the pitch-based carbon fiber.[14,15] The tensile fatigue strengths of the GFRP/metal tapered joint[11], adhesive joint,[12,17] and bolted joint[18] can be predicted using this method.

5 Conclusion

This chapter describes a prediction method of the fatigue life of polymer composites and structures which we proposed in 1997[10] and applied to various FRP and FRP/metal joints. We summarize here the results of our previous experiments and show the validity and limitations of the fatigue-prediction method for various FRP and FRP/metal joints under several loading conditions.

Our proposed approach leads to a simpler estimate of the life of polymer composites than the traditional σ-N approach and may be extended to life-prediction of polymer-composite structures having combined loading and temperature histories.

6 References

[1] J. Aboudi, G. Cederbaum (1989) Analysis of viscoelastic laminated composite plates, *Compos. Struct.* **12**, 243.

[2] J. Sullivan (1990) Creep and physical aging of composites, *Compos. Sci. Technol.* **39**, 207.

[3] T. Gates (1992) Experimental characterization of nonlinear, rate dependent behavior in advanced polymer matrix composites, *Experimental Mechanics* **32**, 68.

[4] Y. Miyano, M. Kanemitsu, T. Kunio, H. Kuhn (1986) Role of matrix resin on fracture strength of unidirectional CFRP, *J. Compos. Mater.* **20**, 520.

[5] Y. Miyano, M. K. McMurray, J. Enyama, M. J. Nakada (1994) Loading rate and temperature dependence on flexural fatigue behavior of a satin woven CFRP laminate, *Compos. Mater.* **28**, 1250.

[6] Y. Miyano, M. K. McMurray, N. Kitade, M. Nakada, M. Mohri (1994) Role of matrix resin on the flexural static behavior of unidirectional pitch-based carbon fiber laminates, *Adv. Compos. Mater.* **4**, 87.

[7] M. K. McMurray, J. Enyama, M. Nakada, Y. Miyano (1993) Loading rate and temperature dependence on flexural fatigue behavior of a satin woven CFRP laminate, *Proc. 38th SAMPE* (Society for the Advancement of Material and Process Engineering) *Symp.* No. 2, p. 1944.

[8] J. Enyama, M. K. McMurray, M. Nakada, Y. Miyano (1993) Effects on stress ration on flexural fatigue behavior of a satin woven CFRP laminate, *Proc. 3rd Japan SAMPE* (Society for the Advancement of Material and Process Engineering) *Symp.* Vol. 2, p. 2418.

[9] M. Karayaka, P. Kurath (1994) Deformation and fatigue behavior of woven composite laminates, *J. Eng. Mater. Technol.* **116**, 222.

[10] Y. Miyano, M. Nakada, M. K. McMurray, R. Muki (1997) Prediction of flexural fatigue strength of CFRP composites under arbitrary frequency, stress ratio and temperature, *J. Compos. Mater.* **31**, 619.

[11] Y. Miyano, M. Nakada, R. Muki (1997) Prediction of fatigue life of a conical shaped joint system for fiber reinforced plastics under arbitrary frequency, load ratio and temperature, *Mechanics of Time-Dependent Mater.* **1**, 143.

[12] Y. Miyano, S. W. Tsai, M. Nakada, S. Sihn, T. Imai (1997) Prediction of tensile fatigue life for GFRP adhesive joint, *Proc. 11th Int. Conf. Composite Mater.*, Gold Coast, Australia, p. 26.

[13] Y. Miyano, M. Nakada, H Kudo, R. Muki (1999) Prediction of tensile fatigue life under temperature environment for unidirectional CFRP, *Adv. Compos. Mater.* **8**, 235.

[14] Y. Miyano, M. Nakada, R. Muki (1999) Appicability of fatigue life prediction method to polymer composites, *Mechanics of Time-Dependent Mater.* **3**, 141.

[15] M. Nakada, M. Maeda, T. Hirohata, M. Morita, Y. Miyano (1996) Time and temperature dependences on the flexural fatigue strength in transverse direcion of unidirectional CFRP, *Proc. Int. Conf. Experimental Mechanics*, Singapore, p. 492.

[16] M. Nakada, T. Ishiguro, Y. Miyano (1997) Prediction of flexural fatigue life for unidirectional CFRP laminates, *Proc. 11th Int. Conf. Composite Mater.*, Gold Coast, Australia, p. 167.

[17] M. Nakada, S. Sihn, T. Imai, Y. Miyano, S. W. Tsai (1998) Prediction of tensile fatigue life for GFRP/metal adhesive joints, *Proc. 2nd Joint Canada-Japan Workshop Composites*, Montreal, Canada, p. 67.

[18] T. Yonemori, M. Nakada, Y. Miyano, S. W. Tsai (1999) Time and temperature dependence on failure load of GFRP/metal bolted joints, *Proc. 6th Japan Int. SAMPE* (Society for the Advancement of Material and Process Engineering) *Symp.*, Tokyo, Japan, Vol. 2, p. 1201.

Contributing Authors

Wolfgang Bauhofer – born in 1947 in Linz, Austria. He grew up in Austria and continues to hold Austrian citizenship. From 1965 to 1974, he studied physics at various German universities in Kiel, Freiburg and Stuttgart, and received his PhD in 1974 with a thesis in solid state physics. After a year in industry at the BAYER AG in Leverkusen, he joined the Max-Planck-Institut für Festkörperforschung in Stuttgart where he was involved in fundamental research. During this time, he spent several months at the Academia Sinica Semiconductor Institute in Beijing and at the IBM Research Center in Yorktown Heights, NY, USA. He is Full Professor of Microelectronic Materials in the School of Electrical Engineering, Technical University Hamburg-Harburg (TUHH) since 1990. His research focuses on the development and characterization of new materials for applications in electrical engineering. In recent years, he has been actively involved in the establishment of international Master's Programs at the TUHH.

Carlos António Alves Bernardo – born in 1946, graduated in Chemical Engineering at the Instituto Superior Técnico in 1971. In 1975 he was granted the Diploma of Imperial College (London, UK) and in 1978 the PhD degree of the University of London. In 1986, he obtained the degree of "Agregado" at the University of Minho, where he is now Full Professor at the Polymer Engineering Department. He is a member of the Society of Plastics Engineers (USA), the Portuguese Society of Engineers and the Sigma Xi Society (USA). He was a Member of the Management Committees of the European Commission VALUE II and INNOVATION programs (1992-1997) and also acted as an expert for the Council of Europe (1999-2001). Carlos Bernardo co-directed six NATO Advanced Study Institutes. His present research interests are the processing and characterization of composites with polymeric matrices and glass and carbon fibers and the recycling of thermoplastics. He has authored more than 100 publications, including 55 articles in international refereed journals, co-edited 4 books and oriented successfully 7 PhD dissertations.

Debes Bhattacharyya – holds a Personal Chair in Mechanical Engineering at the University of Auckland, New Zealand where he is currently the Head of Department and the Director of the Centre for Advanced Composite Materials. His research interests involve primarily the mechanics of manufacturing composite products that include both synthetic and natural materials. He has travelled widely and has held visiting professorships/fellowships at various places, such as McMaster

University (Canada), the Center for Composite Materials (University of Delaware, USA), the Institute for Composite Materials (IVW, University of Kaiserslautern, Germany) and the University of Queensland (Australia). He was awarded the prestigious German Science Foundation Fellowship in 1996 and had a Du Pont Fellowship in 1991. He has given plenary, keynote and invited lectures in many different countries and has more than 200 scientific/technical publications including a volume on *Composite Sheet Forming* (published by Elsevier), three monographs and several book chapters. He has successfully implemented and commercialized several international patents in the composites area and has done extensive consulting in many countries. He is on the Editorial Boards and Technical Panels of several journals and scientific/technical organizations. He is a Fellow of the Royal Society of New Zealand and the Institution of Professional Engineers New Zealand. He is currently the President of the Asian-Australasian Association of Composite Materials.

António M. Brito – born in 1956 in Braga, Portugal, he received his Mechanical Engineering degree from the University of Coimbra in 1980 and the PhD in Polymer Engineering from the University of Minho, Portugal in 1996. Since then, he has been Assistant Professor at the Polymer Engineering Department and researcher at the Institute for Polymers and Composites of the same university. His main research interests are in the area of the injection mold design and computer simulation. A. M. Brito is an affiliate member of the Society of Polymer Engineering. He is a co-author of 1 book chapter, 6 papers published in international refereed journals, and 27 papers published in proceedings of international conferences, 12 national book chapters and 19 papers published in national journals and conference proceedings.

Tibor Czigány – Head of the Department of Polymer Engineering, Budapest University of Technology and Economics (BUTE). He received his Mechanical Engineering degree from the Technical University of Budapest in 1988 and started his scientific carrier in the same university at the Institute of Machine Design. He worked two years as Guest Researcher in the University of Kaiserslautern, Institute for Composite Materials. T. Czigány received his PhD and Dr.-habil. degrees in Mechanical Engineering in 1997 and 2002, respectively. His main research areas are development of new composite materials and technologies; examination of glass, carbon, ceramic, flax and basalt fiber-reinforced plastics; theoretical and practical investigation of crack initiation and propagation; fracture mechanics of composites; acoustic emission examination of composites and exploration of different failure modes; determination of the size of damage zones; welding and weldability of polymers; quality control. Due to his outstanding scientific results, he was awarded the Bolyai Scholarship from the Hungarian Academy of Sciences and the Széchenyi Professor Scholarship from the Hungarian Ministry of Education.

Dr. Czigány is a member of the Hungarian Academy of Sciences Committee of Materials Science and Technology. Since 2001, he is the Head of the Department of Polymer Engineering, which is a leading department in the Mechanical Engineering Faculty of BUTE.

Miro Duhovic – Mr. Duhovic received his BE in Mechanical Engineering with first class honors from the University of Auckland, New Zealand in 1999. In the final year of his BE, he developed a strong interest in composite materials and was involved in a project entailing the design and manufacture of complex thermoplastic composite components for racing wheelchairs. Currently, while working on the completion of his PhD thesis at the Centre for Advanced Composite Materials, he is holding a full time position as a member of the academic staff in the Department of Mechanical Engineering at the University of Auckland. His principal research area is in the forming properties of knitted fabric composites although he has a keen interest in the areas of design, production and manufacturing technology, where he does most of his teaching. His particular interest in CAD/CAM and FEA manufacturing simulation has involved him in many projects, resulting in several publications in this field.

Christian Eger – Business Unit Manager at Hanse Chemie AG, Geesthacht, Germany. Dr. Eger received his PhD degree from Hamburg University in 1999, where he was involved in macromolecular and technical chemistry. The topic of his PhD thesis was pyrolysis of polymethylmethacrylate. He joined Hanse Chemie AG in 1998, where he is working in the field of silicone-modified resins and nanoparticles. Since 2002 he is in charge of the Performance Materials group.

Michail Evstatiev – Professor in the Faculty of Chemistry, Sofia University, Bulgaria. He received his PhD in 1987 and his DSc degree (Chem. Eng.) in 2001. He is author or co-author of about 100 scientific contributions and has more than 300 hits according to the Science Citations Index. His research interest areas are materials science, design with composites and blends, solid state reactions in condensation polymers (basics and commercial application), physical and chemical modification of polymers, polymer laminates, processing and recycling of polymers, polymer composites and blends, microfibrillar- and nano-composites. He has been many time visiting Professor and Scholar at the Institute of Composite Materials, University of Kaiserslautern, Germany; at the University of Delaware, Department of Chemical Engineering and CCM; at the University of Minho, Department of Polumer Engineering, Portugal. At present, he is the Director of the Laboratory on Structure and Properties of Polymers, Sofia University, Bulgaria.

Bodo Fiedler – works as a senior scientist in the Polymer Composites Section, Technical University Hamburg-Harburg. He studied Material Science, within the

Mechanical Engineering program, at the Technical University Hamburg-Harburg. His Diploma thesis was performed in the Advanced Ceramic Group and dealt with the crack propagation in metal reinforced ceramic composites. For his PhD, he moved in 1993 to the Polymer Composites Group. His research areas focused on the investigation of fiber failure in fiber-reinforced polymer composites and modeling of the failure process. In 1998, after receiving his PhD degree, he moved to Kyoto University, Japan, in the position of an Invited Lecturer for Advanced Research at the Mesoscopic Materials Research Center of Prof. S. Ochiai. His research concentrated on failure criteria for the matrix rupture in CFRP and modeling of failure by consideration of thermal residual stresses in composite materials. He further worked on crack initiation and propagation in CFRP and the failure process of superconducting composites. Since 2004, Dr. Fiedler is Head of the research group at the Technology Centre Hamburg Finkenwerder consisting of 4 full time scientists and two technicians, which is a group with great experience in the characterization, testing and modeling of polymer composites.

Tibor J. Goda – Docent, Bánki Donát Faculty of Mechanical Engineering, Technical College of Budapest. Dr. Goda received his Mechanical Engineering degree from the Budapest University of Technology and Economics (BUTE) in 1999, where he was involved in research on the tribological behavior of polymer composites. From 1999 to 2002, he spent several months at the Institute for Composite Materials (IVW GmbH) as Guest Scientist. After one and a half years as a Research Scientist at the Chair of Particle Technology of the University of Kaiserslautern, he joined the Technical College of Budapest, where he is presently a Docent at the Faculty of Mechanical Engineering. Dr. Goda received his PhD in Mechanical Engineering from the BUTE in 2003. His research areas include finite element analysis of contact problems and modeling of the mechanical behavior of granular materials by discrete element methods.

Florian H. Gojny – studied chemistry at the University of Hamburg, focusing on Technical and Macromolecular Chemistry. In 2001, he obtained his Diploma in Chemistry. His Diploma thesis dealt with the "Synthesis and photophysical characterization of 1,4-disubstituted 2,5-phenylene-vinylene oligomers". In 2001, he moved to the Technical University Hamburg-Harburg, Polymer Composites Group and has since then successfully worked on his PhD thesis: "Evaluation of the potential of carbon nanotubes for a mechanical reinforcement of epoxy matrices". He presented the results of his research at numerous international conferences and already published several papers in the field of nanotube research.

Tapio Harmia – Managing Director, FACT GmbH, Germany. He received his Doctoral degree in the area of long fiber-reinforced thermoplastics from the Kaiserslautern University of Technology, Institute for Composite Materials Ltd.

(IVW), Germany, in 1996. Dr. Harmia has over 30 publications and several patents in the field of composite materials. He has been involved in the development of new methods in the manufacturing of long fiber-reinforced thermoplastics. His current research interests are in the area of mechanical properties and tailoring of properties of composite materials. Dr. Harmia is the founder of FACT GmbH and has successfully managed the company since 1998.

Juha Hartikainen – Project Manager of FACT GmbH, Germany. Mr. Hartikainen got his degree in Material Technology from the Helsinki University of Technology, Finland, in 1999. He worked as a researcher in the field of electrically conducting polymers in Finland for one and a half years. Mr. Hartikainen carried out his doctoral studies in Kaiserslautern University of Technology from 2001 to 2004. His studies were in the field of long fiber-reinforced thermoplastics.

Ferrie W. J. van Hattum – born in 1971 in Amersfoort, The Netherlands, holds a MSc in Mechanical Engineering (Design with Plastics), from the University of Twente, The Netherlands and a PhD in Polymer Engineering (Carbon Nanofiber Composites) from the University of Minho, Portugal (UM). He is a member of the European Society of Composite Materials. He worked at the Centre of Lightweight Structures TNO-TUD, Delft, The Netherlands, performing contracted research on composite applications, and was a lecturer at the Department of Polymer Engineering, UM. Dr. van Hattum is currently full-time Researcher at the Institute for Polymers and Composites, UM, where his main research is in the field of polymer composites. He is a co-author of 2 book chapters, 6 invited lectures, 12 papers published in international refereed journals, and 21 papers published in proceedings of international conferences.

Frank Haupert - Research Scientist and Group Leader, Technical University of Kaiserslautern, Institut für Verbundwerkstoffe GmbH. Dr. Haupert studied Mechanical Engineering and received his PhD in materials science from the Technical University of Kaiserslautern in 1997. The main topic of his research was the influence of processing parameters on the material structures and characteristics during thermoplastic filament winding. Since 1997, he has the position of a group leader in the materials science division at the Institute for Composite Materials in Kaiserslautern. Here, one research topic are nanoparticle-reinforced polymers and composites, strongly focused on the structure-property relationships. Another important field of his activity is the tribology of polymeric materials. In this field, material compositions were developed for very special applications, such as *e.g.*, journal bearings for automotive applications, pump bearings for seawater or calendar covers for the paper-making industry.

József Karger-Kocsis – born in 1950, worked first in the Research Institute for the Plastics Industry in Budapest, Hungary. He received his PhD (Chemical

Engineering) at the Lomonossov Moscow Institute of Fine Chemicals Technology in 1983. Later he was employed by the Taurus Hungarian Rubber Works as chief engineer in a factory in Budapest. After a two-years research stay as Alexander von Humboldt (AvH) fellow and an additional two-years period as scientific co-worker in the Composites Group of the Technical University Hamburg-Harburg, he has joined the Institute for Composite Materials (Institut für Verbundwerkstoffe GmbH, IVW) at the University of Kaiserslautern as group leader of the Materials Science Division in 1990. He got his DSc degree (Chemical Engineering) from the Hungarian Academy of Sciences in 1991. He was invited as a Professor at the Department of Plastics and Rubber at the Technical University of Budapest in 1992, but did not follow this call. In 1994, he received a fellowship of the Japan Society for Promotion of Science (JSPS). His DSc degree was accepted by the University Kaiserslautern in 1995. Dr. Karger-Kocsis was awarded the Honorary Doctorate (Dr.h.c.) of the Budapest University of Technology and Economics in 2004. He is (co)author of about 400 scientific contributions and patents.

Bernd Lauke – Institute of Polymer Research Dresden. Dr. Lauke studied physics at the Technical University Dresden. He joined the Institut für Technologie der Polymere in 1975 and got his PhD in 1979 in the field of deformation behavior of composite shells. He investigated the fracture behavior of short fiber-reinforced polymers and got the habilitation in 1989. The year 1991 he spent as a Visiting Scientist at the Institute of Composite Materials, University of Kaiserslautern in the group of Prof. Klaus Friedrich, working on thermoplastic filament winding. Then he created a group of researchers within the Institute of Polymer Research dealing mainly with the deformation and fracture of composites and fracture mechanics of interface cracks. During that time he has supervised the preparation of six PhD and two master works. He has been the leader of numerous projects supported by the EU, DFG and the Saxony Ministry. He is currently active in research on stress and failure analysis (analytical and finite element modeling) of particle-reinforced polymers and bi-material composites as well as in teaching of fracture mechanics.

Mathias Lindner – Head of R&D, FACT GmbH, Germany. Mr. Lindner got his degree in Mechanical Engineering in 1997. He has been active in several research subjects in the field of long fiber-reinforced thermoplastics. His interests are especially in the field of mechanical properties of composite materials, as well as in the manufacturing methods of long fiber-reinforced thermoplastics. He holds several patents in the field of composite materials.

Hong-Yuan Liu – Research Fellow at the Centre for Advanced Materials Technology of the University of Sydney. Her research projects include interface mechanics of fiber composites, bridging mechanism of through-thickness

reinforcement, dynamic fracture of a fiber/z-pin bridged crack, fracture monitoring and control in active fiber composites.

Meng Lu – Senior Research Scientist at the Commonwealth Scientific and Industrial Research Organization (CSIRO). He has extensive working experience in three universities (Beijing University of Aeronautics and Astronautics, Korean Advanced Institute of Science and Technology, and the University of Sydney) either as an academic or a research staff. His research interests include the behaviors of materials/structures, such as damage, fracture, constitutive relations, and permeability/diffusion in porous media, as well as various mechanics issues during material processing.

António Torres Marques – born in 1950 in Porto, Portugal, received his Mechanical Engineering degree from the Faculty of Engineering of Porto University in 1972 and the MSc (Option polymers) and PhD (Creep behavior of glass fiber-reinforced polyester laminates in air and liquid environment) degrees from the Cranfield Institute of Technology, UK, in 1977 and 1981, respectively. He is Full Professor at the Faculty of Engineering, University of Porto, since December 2002, with research interests focussed on the design, manufacturing and testing of composite systems (experimental work and numerical modeling), product development, and biomechanics. He has been supervisor or co-supervisor of 28 MSc theses and 15 PhD theses and has participated or coordinated several R&D national and international projects. He authored, with other researchers, a Portuguese patent, published 32 papers in international scientific journals and 12 in national journals, and presented 130 communications at international conferences and 65 at national conferences. He published various book chapters and co-edited two publications. He has also published 40 didactical texts for undergraduate courses, and international and national short courses. He is an Honorary Member of the Senate of the Polytechnic University of Bucharest, Romania.

Peter Mitschang – born in 1960 in Ramstein, Germany, Prof. Dr.-Ing. Mitschang is the Research Director for Manufacturing Science since 1999 at the Institut für Verbundwerkstoffe GmbH, Kaiserslautern. He completed his academic training at the University of Kaiserslautern. His field of specialization was Mechanical Engineering and he received his diploma in 1987. In 1990, he got his Doctor's degree in Mechanical Engineering, University of Kaiserslautern. From 1987 to 1996, he gathered experience at G. M. Pfaff AG Kaiserslautern and was employed there at the Research and Development Center. His last position at the Pfaff AG was Head of the Department "Analysis and Technology-Development". In 1996, he moved to the Institut für Verbundwerkstoffe GmbH; in 1999, he was appointed Research Director Manufacturing Science and in 2003 was promoted to Professor. He is lecturing on manufacturing of polymer composites and joining of fiber-reinforced plastics since 2000.

Yasushi Miyano – received his BS (1964), MS (1966) and PhD (1969) degrees from Keio University in Japan. After graduation, he was employed at Hitachi Research Laboratory, Hitachi Ltd., until 1977. He is a Professor in Kanazawa Institute of Technology since 1977, and also the Director of the Materials System Research Laboratory at this school. He is investigating the durability of advanced fiber-reinforced plastics, focusing on the residual stress analysis in polymers and the experimental viscoelastic analysis.

Rokuro Muki – received his BS (1951) and PhD (1956) degrees from Keio University in Japan. After graduation, he was an Associate Professor at Keio University and a Visiting Associate Professor at California Institute of Technology. He moved to the University of California Los Angeles as a Professor at the School of Engineering and Applied Science in 1969. Dr. Muki retired from the School's Department of Civil and Environment Engineering in 1993. He was investigating the field of elasticity and is best known for his seminal work on elasticity, entitled *Asymmetric Problem of the Theory of Elasticity for a Semi-infinite Solid and a Thick Plate*. He passed away on February 10, 2004.

Masayuki Nakada – received his PhD in Mechanical Engineering from the Kanazawa Institute of Technology, Japan, in 1991. In 1990 and 1991, he was awarded a fellowship from the Japan Society for Promotion of Science (JSPS). After receiving his PhD, he worked in the University of Tokyo as a researcher of JSPS. He is employed at the Kanazawa Institute of Technology since 1992. He was promoted to an Associate Professor in 1998. He stayed at the Institute for Composite Materials (IVW), University of Kaiserslautern as a Guest Professor funded by the Deutsche Forschungsgemeinschaft (DFG) from September 2001 to August 2002. His major interests are focused on the experimental and theoretical research related to the durability of polymer composite materials.

João Pedro Nunes – born in 1958 in Coimbra, Portugal, received his Mechanical Engineering degree from the Faculty of Engineering of Porto University in 1981 and the MSc (SMC Rheology) and PhD (Development of New Thermoplastic Matrix Composites) in Polymer Science and Engineering from the University of Minho in 1992 and 1998, respectively. He began working in composite design and technology in 1982 as technical manager of a Portuguese manufacturer, Vidropol. After six years of industrial experience, he became junior lecturer at the University of Minho, where he is now Assistant Professor at the Polymer Engineering Department. He co-authored two Portuguese and two international patents and authored or co-authored 2 book chapters and more than 50 papers in international refereed journals and international or national conferences. Since 2000, Dr. Nunes is also Director of Engineering at Vidropol and started a career as private consultant to the composite industry. J. P. Nunes is a Member of the Portuguese Standardization Committee for Plastic Reinforced Products and

nominated Portuguese Delegate to the European Technical Standardization Committees 155 and 210. He is a Member of the Portuguese Society of Engineers, the Society of Polymer Engineers and the European Society of Composite Materials.

Amol Ogale – Research scientist, Institut für Verbundwerkstoffe GmbH, Kaiserslautern, Germany. Mr. Ogale received his MS degree in Textile Engineering from the Indian Institute of Technology, New Delhi, India, in 2000. During the Master's program, he was working on the fire retardant fibers and textiles manufactured from them. He worked in the field of research and development of textile machinery at the Indian Institute of Technology, Bombay, India for one year. Since 2001, he is involved in the research group of preform manufacturing, especially the sewn preforms, and resin transfer molding at the Institut für Verbundwerkstoffe GmbH.

António Sérgio Pouzada – a Mechanical Engineer, MS in Applied Polymer Engineering, PhD, and Doctor of Science (Minho, 1997). He is a Chartered Engineer of the Portuguese Society of Engineers, Fellow of the Institute of Materials (UK) and Senior Member of the Society of Plastics Engineers (USA). His academic career started in 1972 at the Department of Mechanical Engineering of the University of Luanda (Angola) and continued at the Department of Polymer Engineering of the University of Minho where he is a Full Professor in Design with Polymers. Since 2001, he is the Dean of the School of Engineering at the University of Minho. His research interests include flow studies in molds for thermoplastics and composite materials, prediction of mechanical properties of molded polymeric plates, design of plastics' products and injection molds, and design and manufacturing of testing and processing equipments. He authored over 150 publications and has been granted 2 patents.

Eleonora G. Privalko – Senior researcher, Department of Polymer Thermophysics (DePTh), Institute of Macromolecular Chemistry, National Academy of Sciences of Ukraine. She graduated in Polymer Chemistry from the Shevchenko State University (Kyiv) and got her PhD (Polymer Chemistry) in the Institute of Macromolecular Chemistry, National Academy of Sciences of Ukraine (1989). Areas of research: thermodynamic properties and mechanical performance of heterogeneous polymer materials (filled polymers, polymer blends, interpenetrating polymer networks, polymer nanocomposites). Visiting positions: NATO Research Fellow, National Technical University of Athens, Greece. Publications: over 50 papers in refereed journals.

Valery P. Privalko – Head, Department of Polymer Thermophysics (DePTh), Institute of Macromolecular Chemistry, National Academy of Sciences of Ukraine. He graduated in Chemical Engineering from the Kyiv State Polytechnic University

and held different research positions at the Institute of Macromolecular Chemistry, National Academy of Sciences of Ukraine, since 1966. He got his PhD (Physical Chemistry) in 1970, DSc (Polymer Science) in 1976, and became a Full Professor (Physics and Mechanics of Polymers) in 1986. Area of research: materials science of polymers, with special emphasis on the molecular structure-physical property relationships, and the interfacial interactions in heterogeneous polymer materials (filled polymers and nanocomposites, polymer blends, block copolymers, interpenetrating polymer networks). Honors and awards: Research Professorship, Institute of the Structure of Matter, Supreme Council of Scientific Studies, Madrid, Spain; Lady Davis Professorships, Technion – Israel Institute of Technology, Haifa, Israel; Leo Pissarzhevsky prize in physical chemistry, National Academy of Sciences of Ukraine; Marquis *Who's Who in Science and Engineering*. Publications: over 350 papers in the refereed international journals and 5 books. Member of the Editorial Advisory Boards of 5 international journals.

Min Zhi Rong – Mr. Rong obtained his PhD degree in Polymer Chemistry and Physics in 1994, in Zhongshan University, China. He is now a Professor in the Materials Science Institute, Zhongshan University, China, and serves as the Secretary-General of the Guangdong Society for Composites. He has gained over twenty-year systematical experience in polymeric materials, with particular interests in thermosetting/thermoplastic blends, polymeric functional materials, structure of polymer networks, polymer nanocomposites, natural fiber composites, and dynamic mechanical properties of polymers and polymer composites. He has published more than 100 papers in refereed scientific journals and books as well as over 40 conference papers on the general topics of polymers and polymer composites.

Meyyarappallil Sadasivan Sreekala – received her Master of Philosophy in Chemistry in 1995 and PhD degree in Chemistry in 2001 from Mahatma Gandhi University, Kottayam, Kerala, India. She has been awarded a junior research fellowship from Mahatma Gandhi University and senior research fellowships from the Council of Scientific and Industrial Research (CSIR), New Delhi, India during her research work at Mahatma Gandhi University. Her major area of research is polymer science and technology. Specifically, she is interested in the research in the field of polymer nanocomposites, development of fully biodegradable macro-, micro- and nano-"green" composites and natural and synthetic fiber-reinforced polymer composites. She bagged the Best Paper Award in a technical symposium, "Elastofest'99" held at Chennai, India in 1999. Also she has been awarded a major scientific project for young scientists in the field of polymer composites from the Department of Science and Technology, New Delhi, India for the year 2000-2001. In 2001, she has been awarded the prestigious Alexander von Humboldt (AvH) post-doctoral research fellowship from the Alexander von Humboldt Foundation,

Germany. She has been selected for the ICS-UNIDO fellowship on environmentally degradable plastics in Trieste, Italy, in 2002. Dr. Sreekala has made contributions to books, many research papers to international journals and contributions to international conferences. She has been awarded the prestigious JSPS post-doctoral research fellowship from the Japan Society for Promotion of Science, Tokyo, Japan in 2003 and is currently undertaking the same at Yamaguchi University, Ube, Yamaguchi, Japan.

Jan K.W. Sandler – studied Mechanical Engineering at the Technical University Hamburg-Harburg and obtained his Master degree in 1999. Following a brief stay at the Materials Science Centre in Manchester, UK, he began his PhD course at the Department of Materials Science and Metallurgy at the University of Cambridge, UK, in October 2000. Since January 2004, he is at the University of Bayreuth, Germany, as the Chief Engineer of the Polymer Engineering group of Prof. Dr.-Ing. Volker Altstädt. Jan Sandler has been active in the field of polymer nanocomposites for the last 5 years. His focus has been the evaluation of carbon nanotubes and nanofibers, both with regard to their intrinsic mechanical and physical properties as well as their potential as reinforcements for polymeric matrices. His publications cover the structure-property relationships of a wide variety of nanocomposites, with additional emphasis on the exploitation of such carbon-based fillers in polymer foams and in electrically conductive composite materials.

Konrad Schneider – Institute of Polymer Research Dresden. Dr. Schneider studied Physics and Polymer Physics at the Institute of Technology Leuna-Merseburg and got there his PhD in 1984 in the field of glass transition of amorphous polymers. Since 1984, he works in the Institut für Technologie der Polymere and later the Institute of Polymer Research Dresden in various experimental fields, mainly the field of mechanical characterization of polymers and composites on different levels. He is the Head of the Department Mechanics and Fibre Formation.

Tobias Schüller – Institute of Polymer Research Dresden. Dr. Schüller received his Master degree in Physics from the TU Dresden in 1997. He went to the IPF in 1998 to work in the fields of micromechanics, fracture mechanics, interface cracks in heterogeneous materials and of finite element simulation. He received his PhD in Engineering Science from the University of Kaiserslautern in 2004. He is currently senior developer of Micro-Optronic Messtechnik GmbH.

Karl Schulte – Head of the Polymer Composites Section of the Technical University Hamburg-Harburg. A research staff of 12 full-time scientists plus three technicians form a group which has great experience in the area of characterization, testing and modeling of polymer composites and the generation and characterization

of carbon nanotube (CNT)/carbon nanofiber (CNF) based polymer composites. He has a more than 20 years experience in polymer matrix composites research and published more than 200 papers in this field. He is at present the European Editor of Composite Science and Technology. Prof. Schulte is the co-ordinator of the scientific network "Carbon Nanotubes for Future Industrial Composites" CNT-Net (http://www.cnt-net.com) with 18 European members from both industry and academia.

Tatiana A. Shantalii – Senior researcher, Department of Polymer Thermophysics (DePTh), Institute of Macromolecular Chemistry, National Academy of Sciences of Ukraine. She graduated in Organic Chemistry from the Kuban State University (Krasnodar) and got her PhD (Polymer Chemistry) in the Institute of Macromolecular Chemistry, National Academy of Sciences of Ukraine (1994). Area of research: synthesis and structure-property relationships for semi-rigid chain polymers reinforced with the sol-gel derived inorganic nanophase. Publications: over 30 papers in refereed journals.

João Francisco Gomes da Silva – born in 1968 in Porto, Portugal. He holds an MS in Mechanical Engineering (Mechanical Design) from the Faculty of Engineering of Porto University, Portugal, and is now Assistant Professor at the Mechanical Engineering Department of Porto Polytechnic. Since 1992, he is a researcher at INEGI – Institute of Mechanical Engineering and Industrial Management, presently finishing a PhD thesis on the *Production and Processing of Continuous Fiber-Reinforced Thermoplastic Composites*. He is a co-author of 1 book, 1 international patent, 2 invited lectures, 6 papers published in international refereed journals and 30 papers published in the proceedings of international conferences.

Hiroshi Suemasu – born in 1952, he received a Doctor of Engineering degree from the Department of Aeronautics at the University of Tokyo in 1980. He worked first in the Aerospace Laboratory at the University of Tokyo as a Research Associate from 1980 to 1986. During this period, he worked as a Visiting Research Assistant Professor in the University of Illinois from 1983 to 1985. He was employed by Sophia University as an Associate Professor at the Department of Mechanical Engineering in 1986. He was a Visiting Researcher at the National Aerospace Laboratory, Japan, from 1988 to 1991 and a Visiting Associate Professor at the Institute of Space and Astronautical Science of Japan from 1989 to 1991. He stayed as an Alexander von Humboldt (AvH) fellow in the Institute for Composite Materials (IVW), University of Kaiserslautern, from 1992 to 1993. He was promoted to Professor in 1994 in Sophia University. He was awarded twice in 1987 and 2001 by the Japan Society for Composite Materials.

Károly Váradi – Professor at the Institute of Machine Design, Budapest University of Technology and Economics (BUTE). He received a Mechanical Engineer degree in 1972, specialized in applied mechanics, and a PhD degree for his thesis entitled *Increasing the Lifetime of Ball Bearings by Contact, Friction, and Stress State Analysis* in 1983. He received the Dr. habil. title in 1997. Since 1980, Dr Váradi has been employed at BUTE, first as a Research Fellow, Associate Professor, and, since 1998, as a Professor, teaching the subjects of Machine Elements, Structural Analysis; Structure Optimization; Product Modeling and Simulation; Finite Element Analysis of Mechanical Structures and Numerical Methods in Machine Design. He spent the academic year 1989-90 as Exchange Professor in the United States. He has acted as Deputy Dean for Science at the Faculty of Mechanical Engineering of BUTE for the period 1997-2001. In 2001-2002, he stayed at the Institute of Composite Materials, Kaiserslautern University, as a DAAD Guest-Professor, teaching FEM in Engineering Design I and II. Several prize winner studies for the Scientific Student Circle, degree projects, and three doctoral theses have been completed under his professional supervision. Since 1980, he has been involved in finite element systems development. Software systems for elastic-plastic and transient heat transfer problems as well as for pipes and fiber-reinforced hoses have been developed in cooperation with his colleagues. In the course of the past few years, the main field of his research has been the analysis of contact, stress and thermal states of rough (measured) metal-metal and composite-metal surfaces in sliding contact. This approach included macro/micro models jointed with the displacement coupling technique, debonding simulation as well as modeling the transfer film formation. He has more than 200 publications, mainly in cooperation with co-authors, in journals including *Tribology International*, *Tribotest*, *Wear*, *Tribologia*, *Composites Science and Technology*, *Journal of Materials Science*, *Advanced Composite Letters*, *Int. J. of Machine Tools and Manufacture*, *Mechanics of Composite Materials and Structures*, and *Tribology Transactions*.

Siby Varghese – a scientist at the Rubber Research Institute of India, who received his Doctorate in 1992. He did his post-doctoral research (1996 to 1998) under the JSPS (Japan Society for Promotion of Science) post-doctoral program at the University of Tokyo, Japan in the area of radiation processing of polymers. For his scientific contributions he has received the Indian Young Scientist Award in 1996. His responsibilities include designing and leading of polymer projects of popular interest, trouble shooting of factory processes, conducting training programs for polymer students and entrepreneurs, supervision of PhD students, *etc.* In 2002, he has been selected for the prestigious AvH (Alexander von Humboldt) post-doctoral fellowship at the Institute for Composite Materials (IVW), University of Kaiserslautern, Germany. He has 70 international publications and several presentations on international level, and has been granted 6 patents. His

specific area of research interest includes polymer composites, blends, rubber nanocomposites, latex allergy, recycling, *etc.*

Bernd Wetzel – Research Associate at the Institut für Verbundwerkstoffe GmbH, University of Kaiserslautern. Mr. Wetzel received his Mechanical Engineering degree at the Universität Karlsruhe (TH), Germany. During his studies, he specialized on materials science as well as conventional and regenerative energy systems. He was first introduced to composite materials while working on a research thesis collecting design principles from nature, in order to set up bionic design catalogues. The compressed information in such catalogues serves as a useful tool for engineers to develop innovative products on the basis of solutions from nature. To further satisfy his curiosity about composite materials, he went to the Graduate Aeronautical Laboratories, California Institute of Technology (Caltech), Pasadena, to accomplish his studies by working on his Master thesis dealing with the creep behavior of rocket propellant mock composites. Now he is working on his PhD thesis and has chosen much smaller dimensions of fillers: the nanoscale. In the year 2000, he joined the Institut für Verbundwerkstoffe GmbH (IVW), University of Kaiserslautern, Germany where he develops thermosetting polymer nanocomposites for industrial applications. His research aims to reinforce polymers with ceramic micro- and nanoparticles, in order to improve their mechanical and tribological performance and furthermore to find reinforcing mechanisms and also structure-property relationships.

Lin Ye – Full Professor at the School of Aerospace, Mechanical & Mechatronic Engineering of the University of Sydney. His major research interests are in the general areas of composites science and technology, smart materials and structures, nano-materials and nano-composites, structural integrity and durability. He received one of approximately 10 Friedrich Wilhelm Bessel Research Awards in 2004 from the Alexander von Humboldt Foundation for young, top-flight scientists and scholars already recognized as outstanding researchers in their fields.

Ming Qiu Zhang – Professor of Materials Science, Director of the Key Laboratory for Polymeric Composite and Functional Materials of the Ministry of Education of China, and the Materials Science Institute of Zhongshan University, China, Deputy Dean of the School of Chemistry and Chemical Engineering of Zhongshan University, China. He is also a Member of the Standing Councils of the Chinese Society for Composites and the Chinese Materials Research Society, and the President of Guangdong Society for Composites. He is on the Editorial Boards for 5 scientific journals. His research interests include structure-property-processing relationships, characterization techniques and applications of polymers and polymer composites. He has been granted 7 patents and published over 200 papers in refereed journals and books.

List of Acknowledgements

The authors gratefully acknowledge permissions to reproduce copyrighted materials from a number of sources. Every effort has been made to trace copyright ownership and to give accurate and complete credit to copyright owners, but if, inadvertently, any mistake or omission has occurred, full apologies are herewith tendered.

Chapter 1 Carbon Nanotube-Reinforced Polymers: a State of the Art Review

1. Figures 6, 11, 15, and 17-19 reprinted from *Compos. Sci. Technol.*, in press, 2004, Authors: F. H. Gojny, K. Schulte, Title: Functionalisation effect on the thermomechanical behaviour of multi-wall carbon nanotube/epoxy-composites, Copyright (2004), with permission from Elsevier Science.

2. Figures 12, 14, and 16 reprinted from *Chem. Phys. Lett.*, Vol. 370, 2003, Authors: F. H. Gojny, J. Nastalczyk, K. Schulte, Z. Roslaniec, Title: Surface-modified nanotubes in CNT/epoxy-nanocomposites, p. 820, Copyright (2004), with permission from Elsevier Science.

3. Figure 21 reprinted from *Polymer*, Vol. 40, 1999, Authors: J. Sandler, M. S. P. Shaffer, T. Prasse, W. Bauhofer, K. Schulte, A. H. Windle, Title: Development of a dispersion process for carbon nanotubes in an epoxy matrix and the resulting electrical properties, p. 5967, Copyright (2004), with permission from Elsevier Science.

Chapter 2 Application of Non-Layered Nanoparticles in Polymer Modification

1. Figure 2 reprinted from *Compos. Sci. Technol.*, Vol. 62, 2002, Authors: C. L. Wu, M. Q. Zhang, M. Z. Rong, K. Friedrich, Title: Tensile performance improvement of low nanoparticle-filled polypropylene composites, p. 1327, Copyright (2004), with permission from Elsevier Science.

2. Figures 3, 4, 5, and Tables 1, 2, and 3 reprinted from *Polymer*, Vol. 42, 2001, Authors: M. Z. Rong, M.Q. Zhang, Y. X. Zheng, H. M. Zeng, R. Walter,

K. Friedrich, Title: Structure-property relationships of irradiation grafted nano-inorganic particle filled polypropylene composites, p. 167, Copyright (2004), with permission from Elsevier Science.

3. Figures 6, 7, 10, 11, 12, and Table 4 reprinted from *Wear*, Vol. 253, 2002, Authors: M. Q. Zhang, M. Z. Rong, S. L. Yu, B. Wetzel, K. Friedrich, Title: Effect of particle surface treatment on the tribological performance of epoxy based nanocomposites, p. 1086, Copyright (2004), with permission from Elsevier Science.

4. Figures 8 and 9 reprinted from *Macromol. Mater. Eng.*, Vol. 287, 2002, Authors: M. Q. Zhang, M. Z. Rong, S. L. Yu, B. Wetzel, K. Friedrich, Title: Improvement of tribological performance of epoxy by the addition of irradiation grafted nano-inorganic particles, p. 111, Copyright (2004), with permission from Wiley-VCH.

Chapter 3 Reinforcement of Thermosetting Polymers by the Incorporation of Micro- and Nanoparticles

1. Figures 1 and 2 reprinted from *Polym. Eng. Sci.*, Vol. 42, 2002, Authors: B. Wetzel, F. Haupert, K. Friedrich, M. Q. Zhang, M. Z. Rong, Title: Impact and wear resistance of polymer nanocomposites at low filler content, p. 1919, Copyright (2002), with permission from the Society of Plastics Engineers, Inc.

2. Figures 7-9 reprinted from *Compos. Sci. Technol.*, Vol. 63, 2003, Authors: B. Wetzel, F. Haupert, M. Q. Zhang, Title: Epoxy nanocomposites with high mechanical and tribological performance, p. 2055, Copyright (2003), with permission from Elsevier Science.

Chapter 7 Micro-Scratch Testing and Finite Element Simulation of Wear Mechanisms of Polymer Composites

1. Figures 1a, 2, 10, 11, 12, 13, and 14 reprinted from *J. Mater. Sci.*, Vol. 37, 2002, Authors: T. Goda, K. Váradi, K. Friedrich, H. Giertzsch, Title: Finite element analysis of a polymer composite subjected to a sliding steel asperity: Part I: Normal fibre orientation, p. 1575, Copyright (2002), with permission from Kluwer Academic Publishers.

2. Figures 1b, 1c, 15, 16, 17, 18, 19, and 20 reprinted from *J. Mater. Sci.*, Vol. 37, 2002, Authors: K. Friedrich, K. Váradi, T. Goda, H. Giertzsch, Title: Finite element analysis of a polymer composite subjected to a sliding steel asperity:

Part II: Parallel and anti-parallel fibre orientation, p. 3497, Copyright (2002), with permission from Kluwer Academic Publishers.

3. Figures. 3, 21, 22, 23, 24, 26, 27, and 28 reprinted from *J. Compos. Mater.*, Vol. 38, 2004, Authors: K. Friedrich, T. Goda, K. Váradi, B. Wetzel, Title: Finite element simulation of the fiber-matrix debonding in polymer composites produced by a sliding indentor: Part I – Normally oriented fibers, p. 1583, Copyright (2004), with permission from SAGE Publications.

4. Figures 4, 6, and 7 reprinted from *J. Compos. Mater.,* Vol. 38, 2004, Authors: T. Goda, K. Váradi, B. Wetzel, K. Fiedrich, Title: Finite element simulation of the fiber-matrix debonding in polymer composites produced by a sliding indentor: Part II – Parallel and anti-paraller fiber orientation, p. 1607, Copyright (2004), with permission from SAGE Publications.

Chapter 8 Determination of the Interface Strength of Polymer-Polymer Joints by a Curved Interface Tensile Test

1. Figures 1, 2, 3, 4, and 5 reprinted from *Compos. Interfaces,* Vol. 10, 2003, Authors: B. Lauke, K. Schneider, T. Schüller, Title: Determination of interface strength of polymer-polymer joints by a curved interface tensile test, p. 1, Copyright (2004), with permission from VSP, International Science Publishers.

2. Figures 6, 7, 8, 9, and 10 reprinted from *Compos. Interfaces*, Vol. 10, 2003, Authors: K. Schneider, B. Lauke, T. Schüller, Title: Determination of interface strength of polymer-polymer joints by a curved interface tensile test: Preliminary experimental results, p. 581, Copyright (2004), with permission from VSP, International Science Publishers.

Chapter 10 Tribological Characteristics of Micro- and Nanoparticle Filled Polymer Composites

Figures 2 and 6 reprinted from *Composites A*, Vol. 35, 2004, Authors: Z. Zhang, C. Breidt, L. Chang, F. Haupert, K. Friedrich, Title: Enhancement of the wear resistance of epoxy: short carbon fibre, graphite, PTFE and nano-TiO_2, p. 385, Copyright (2004), with permission from Elsevier Science.

Chapter 12 Manufacturing of Tailored Reinforcement for Liquid Composite Molding Processes

1. Figure 1 reprinted from *Proceedings of the International Conference and Exhibition on Reinforced Plastics, ICERP 2004*, Authors: A. Ogale, C. Weimer, P. Mitschang, Title: Seams and stitches used in preform manufacturing for fiber reinforced plastic composites, Copyright (2004), with permission from Y. J. Jayakumar, Executive Secretary, FRP Institute, Chennai 600 097, India.

2. Figures 4 and 10 reprinted from *Polym. Polym. Compos.*, Vol. 11, 2003, Authors: P. Mitschang, A. Ogale, J. Schlimbach, F. Weyrauch, C. Weimer, Title: Preform technology: a necessary requirement for quality controlled LCM-processes, p. 605, Copyright (2004), with permission from Kate Evans, Rapra Technology Ltd., Shawbury, Shrewsbury, Shropshire, SY 4 4NR, UK.

Chapter 14 Long Fiber-Reinforced Thermoplastic Composites in Automotive Applications

1. Figures 1, 2, and 4 reprinted from *JEC Composite Magazine,* Vol. 1, 2003, Authors: J. Hartikainen, M. Lindner, T. Harmia.

Chapter 18 Accelerated Testing Methodology for Polymer Composite Durability

1. Figures 1-8 reprinted from *J. Compos. Mater.*, Vol. 31, 1997, Authors: Y. Miyano, M. Nakada, M. K. McMurray, R. Muki, Title: Prediction of flexural fatigue strength of CFPP composites under arbitrary frequency, stress ratio and temperature, p. 619, with permission from Sage Publications Ltd.

Author Index

Subject Index

D

E

F

G

H

I

K

L

M

N

O

P

R

S